The University Of Sheffield.

Zeolite Catalysts for Water Treatment: Catalytic Wet Peroxide Oxidation (CWPO) of Phenol

A thesis submitted to The University of Sheffield for the degree of Doctor of Philosophy in the Faculty of Science

Changyan Zhou

The University of Sheffield

Department of Chemistry

8/12/2021

Declaration

I, the author, confirm that the Thesis is my own work. I am aware of the University's Guidance on the Use of Unfair Means (www.sheffield.ac.uk/ssid/unfair-means). This work has not been previously been presented for an award at this, or any other, university.

Acknowledgement

First of all, I would like to thank my supervisor, Dr. Marco Conte, sincerely for his selfless help, guidance, and kindly encouragement throughout this project. His insight and knowledge into this research area helped me complete this project successfully. He was always enthusiastic to help and support in any way he could during the research process and I can not imagine a better supervisor than him. Besides, I would also like to thank my second supervisor, Dr. Kirill Horoshenkov and my independent advisor, Dr. Anthony Haynes for their help and advice.

Next, I would like to thank the members of our research group, Prea, Dedi, James, Baozhai, Rebecca, Mengyuan, Mohamed, Ghadeer and Bahhaj. It is so lucky to meet you in this foreign country, my friends, I enjoyed all the time I have spent in the UK with your accompany.

I would also like to thank all the staff who worked for the chemistry department, especially Rob Hanson, Dan Jackson, Neil Bramall, Heather Grievson, Craig Robertson, and Garry Turner, who provided direct help and assistance to complete this project. Special thanks also go to Dr. Robert Dawson from our department for the BET tests, Dr. David Morgan from the UK catalysis Hub, Harwell, UK for the XPS analysis and Prof. Xi Liu from Shanghai Jiaotong University for the TEM tests.

I would also like thank the Grantham Centre for Sustainable Futures for their financial support to allow us to complete this research project.

Last but not least, I would like to thank my father, mother, and sister for their warm care and support. They encouraged me a lot and always stood by me when I was upset and frustrated during hard times which gave me the courage to move on.

Abstract

The discharge of wastewater into the environment without adequate treatment aggravates water shortage worldwide, which prompts the development of efficient wastewater treatment technology as an active area of research in recent years. The catalytic wet peroxide oxidation (CWPO) based on Fenton and Fenton-like reactions, as one of the most promising techniques, is applied in the decomposition of the aromatic pollutants in water by using phenol as representative compound in this research.

Although some catalysts with high phenol removal efficiency in the CWPO process have been reported in the literature, most of them emphasized the high activity, in the sense of phenol consumption but without considering the actual degradation products (that is in some cases can be as dangerous as phenol). Furthermore, most of the current literature is also lacking of appropriate knowledge of the deactivation mechanism of catalysts and accordingly, the design and development of a stable catalyst in the CWPO process. For these reasons, the screening of active catalysts, the assessment of catalytic activity and more importantly, the design of highly stable catalysts in the CWPO of phenol were investigated in detail in this PhD project.

The assessment of the water purification efficiency based on the identification and determination of phenol and the intermediate products (both aromatics and acids) formed during the reaction process is the groundwork of this project. Fe- and Cu- supported ZSM-5 catalysts showed high activity in the CWPO of phenol, especially the Cu/ZSM-5 with high phenol conversion (100%), complete removal of aromatic intermediates, high H_2O_2 consumption (>90%) and high CO_2 formation (around 90%) under the reaction conditions (initial phenol concentration 1 $g \cdot L^{-1}$, phenol: H_2O_2 ratio 1: 14, M: S ratio 1: 30, temperature 80 ^oC, endogenous pressure, time 4 h). However, all the metal-supported Cu/ZSM-5 catalysts tested in this project suffered from low stability in the form of high metal leaching (> 50%), which is due to their low resistance of the supported metal oxides to the acid intermediates

(especially oxalic acid) that were formed during the reaction process.

The metal incorporated zeolite (or silica) catalyst is one of the promising solutions to the leaching issue. In this project, the catalysts, such as Fe-ZSM-5-HTS, Cu-ZSM5/SiC, and Cu-MCM-48, with metal incorporated into the zeolite (or silica) matrix were synthesized by hydrothermal synthesis and were tested in the CWPO of phenol reaction with the Fe-ZSM-5-HTS catalyst as a benchmark. The synthesized materials were characterized by an array of analytical techniques including XRD, N_2 adsorption-desorption, ATR-FTIR, TEM and ICP-OES. The catalytic results showed that the Fe-ZSM-5-HTS(80) had high activity (100% phenol conversion, 100% H_2O_2 consumption, 60% CO_2 formation) and high stability (< 0.4 $mg \cdot L^{-1}$ Fe leaching) in successive 8 runs of reaction without loss of activity, indicating the potential of the metal incorporated zeolite catalysts in the CWPO of phenol. Besides, the Cu-containing MCM-48 catalysts were also synthesized and the synthesis parameters were optimized to improve the metal incorporation ratio. The Cu-MCM-48 with highly ordered structure, uniform mesopore size, and heteroatom metal loading of 0.2% (total Cu loading of 1.2%) was obtained, which showed steady phenol conversion (> 70%), H_2O_2 consumption (> 40%) and CO_2 formation (> 30%) throughout 5 runs of reaction and more importantly, it could be easily regenerated by calcination at 550 ^oC in air.

Thesis content

Abbreviations

(Alphabetically)

13X: zeolite 13X

a_0: unit cell parameter

AC: activated carbon

AOPs: advanced oxidation processes

ATR-FTIR: Attenuated Total Reflectance Fourier Transform Infra-Red

BE: binding energy

BEA: zeolite Beta

BET: Brunauer-Emmett-Teller

BJH: Barrett-Joyner-Halenda

C18: chain length (octadecyl) of alkyl bonded phase

CAT: catechol

CHA: Chabazite

CMB: carbon mass balance

CNT: carbon nanotube

COD: chemical oxygen demand

CTAB: Cetyltrimethylammonium bromide

CWPO: catalytic wet peroxide oxidation

DHS: direct hydrothermal synthesis

DIPE: diisopropyl ether

DMSO: dimethyl sulfoxide

DP: deposition-precipitation

D_p: pore diameter

EC50: median effect concentration

EDX: Energy Dispersive X-Ray

EPA: Environmental Protection Agency

EtOH: ethanol

FAU: Faujasite

FWHM: full width at half maximum

GC: gas chromatography

HPLC: high-performance liquid chromatography

HQ: hydroquinone

HTS: hydrothermal synthesis

HY: zeolite Y hydrogen

HZSM-5: Zeolite Socony Mobil-5, Hydrogen form

IC: ion chromatography

ICP-OES: inductively coupled plasma - optical emission spectroscopy

IE: ion exchange

IRE: internal reflection element

IUPAC: international union of pure and applied chemistry

IZA: international zeolite association

k: rate constant

LC50: median lethal concentration

LOD: limit of detection

LTA: Linde Type A

M: S: metal to substrate ratio

MCM-41: Mobil Composition of Matter No. 41

MCM-48: Mobil Composition of Matter No. 48

MCM-50: Mobil Composition of Matter No. 50

MFI: Mordenite Framework Inverted (zeolites)

MIBK: methyl isobutyl ketone

MOF: metal-organic framework

MOR: Mordenite

NDIR: non-dispersive infrared

NH_4ZSM-5: Zeolite Socony Mobil-5, ammonia form

NIST: national institute of standards and technology

nm: nanometer (10^{-9} m)

NMR: nuclear magnetic resonance

NPRI: National Pollutant Release Inventory

OBQ: *o*-benzoquinone

OPOD: N-octanoylpyrrolidine

PBQ: *p*-benzoquinone

pKa: $-\log_{10}$ of acid dissociation constant

ppb: parts per billion

PPI: pores per inch

ppm: parts per million

PSSF: paper-like sintered stainless fibre

R: correlation coefficient

RC: relative crystallinity

RES: resorcinol

RF: radiofrequency

ROS: reactive oxygen species

rpm: revolutions per minute

R_s: resolution

SBA-15: Santa Barbara Amorphous No.15

S_{BET}: BET surface area

SEM: scanning electron microscopy

SiC: Silicon Carbide

TBP: tributyl OF phosphate

TC: total carbon

TEM: transmission electron microscopy

TEOS: tetraethyl orthosilicate

TIC: total inorganic carbon

TOC: total organic carbon

TPAOH: Tetrapropylammonium hydroxide

TPD: temperature-programmed desorption

TPO: temperature programmed oxidation

t_R: retention time

UV: ultraviolet

UV-vis: ultraviolet-visible spectroscopy

V_p: pore volume of zeolite

VSB-5: zeolite VSB-5

WHO: World Health Organization

WI: wet impregnation

W_t: wall thickness

XPS: X-ray photoelectron spectroscopy

XRD: X-ray diffraction

Y: zeolite Y

ZSM-5: Zeolite Socony Mobil-5

Chapter 1. Introduction

1.1 Overview

Water covers 70% of the Earth's surface and is critical to life and human activities. If there was no water there would be no life on the earth as all plants and animals must have water to survive. However, the amount and quality of freshwater available in the world continues to decrease due to growing water demands which combined with climate change, are threatening the survival of millions of lives. The WHO reported that, in 2019, 1 in 3 people globally, approximately 2.2 billion, did not have access to safe drinking water service [1], while by 2025, half of the world's population will be living in water-deprived areas. This situation is being worsened by global challenges such as COVID-19 [2]. On the other hand, the generation of a large amount of wastewater from domestic use and industrial production worldwide is another significant factor that is contributing to water shortage [3]. An estimated 2,212 km^3 of water in the world (corresponding to the volume of 44 Garda lakes) is released into the environment per year as wastewater from urban and industrial effluents as well as agricultural drainage water, which accounts for 56% of the annual consumption of the global freshwater [4]. More importantly, it is estimated that more than 80% of the wastewater in the world doesn't undergo adequate treatment before discharge, which further aggravates the water shortage, as reported by the United Nations World Water Development Report 2021 [2]. Therefore, the reuse of wastewater to recover water is an important strategy to relieve the stress of water shortage. Against this background, developing novel technologies to clean up and decontaminate wastewater is crucial to guarantee water recycle and thus improve the accessibility of more people worldwide to clean water. In this context, the aim of this project is to develop a novel and high-efficient method for wastewater purification, especially targeted to aromatic compounds.

1.2 General aspects of organic contaminants in water

Public's awareness of the nature of water as a finite resource and the importance of water purification is progressively growing, as a consequence of increasing concern on

environmental protection in the last decades. Meanwhile, stricter wastewater discharge standards and environmental regulations are introduced in efforts to reduce the environmental impacts of industrial processes.

In general terms, pollutants in water from rivers, lakes or reservoirs include: suspended solids and sediments, pathogens, nutrients and agriculture runoff, as well as organic pollutants, inorganic pollutants (salts and metals) from industrial and domestic processes, and radioactive pollutants. In some cases, even effluents from chemical plants at a higher temperature than water reservoirs can also contribute to pollution, known as thermal pollution, as it can lead to an uncontrolled proliferation of algae, with a detrimental effect on aquatic life. Among these harmful pollutants and contaminants, organic pollutants have been a hot area of research for years, owing to the serious impacts on human health and the ecological environment originating from their high toxicity, strong corrosivity, unpleasant odour, slow biodegradability and so on. Among these, the organic pollutant, phenol, has received increasing attention as one of the priority toxic pollutants listed by US EPA since 1977 [5], and members of pollutant substances recorded in Canada NPRI Substance List since 1995 [6]. Phenol is widely studied not only due to its toxicity and prevalence in industrial processes but also because phenol is an intermediate or a by-product obtained during the oxidation of higher molecular weight aromatic compounds. It has been estimated, for instance, that more than 10 million tons of phenols are yearly discharged to the environment [7]. In view of these factors, phenol is often selected as a model contaminant in the field of organic wastewater abatement. For these reasons, together with its chemical nature, aromatic compounds are known to be difficult to be removed, converted and disposed, phenol will also be at the centre of this thesis work.

1.3 Sources and hazards of phenol in water

Phenolic compounds are a class of organic compounds containing a hydroxyl group(s) directly bonded to one or more aromatic rings. The first member of chemicals belonging to

this category of organic compounds is called phenol (also known as benzenol, carbolic acid, phenylic acid, phenic acid, hydroxybenzene [8,9]), while other members are derivatives of phenol. Phenol is a colourless crystalline solid with a sickeningly sweet and acrid odour and is volatile. The structure and the physical and chemical properties of phenol are shown in figure 1.1 and table 1.1, respectively. Phenol is one of the most widely used organic compounds in existence and is a basic structural unit for a variety of synthetic organic compounds including agricultural chemicals and pesticides [10], for example, the use of phenols for the synthesis of carbamate (one of the main components of pesticides) was reported [11]. The water solubility of phenol reaches over 90 $g \cdot L^{-1}$ at room temperature (in table 1.1 [12]), indicating the potential threats of the organic compounds to water safety.

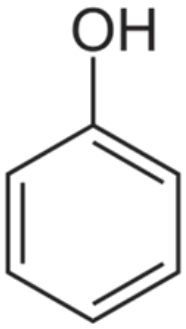

Figure 1.1. Chemical structure of phenol

Table 1.1. Physical and chemical properties of phenol [12]

Molecular formula	C_6H_5OH
Molecular weight	93 $g \cdot mol^{-1}$
Melting point	40.9 °C
Boiling point	181.75 °C
Solubility in water (at room temperature)	93 $g \cdot L^{-1}$
pK_a	9.89
Flammability limits in air	1.7 vol%
Flash point	79 °C
Autoignition temperature	715 °C

1.3.1 Sources of phenol

Phenol is widely used in different branches of industry and is commonly found in aquatic environments. The presence of phenol in water originates from both natural and anthropogenic activities.

1.3.1.1 Anthropogenic sources

The most important phenol emission results from industrial production as phenol is a significant precursor in the production of many materials, especially the manufacture of phenolic resins [13]. For example, phenol is widely used in the manufacture of household chemicals (such as plastics, drugs, sockets, textiles) or involved in the fuel/energy sector (like oil, petroleum, coal processing and metallurgy, manufacture of dyes). On the other hand, some industrial activities involving combustion processes (including wood) also produce phenol and phenolic compounds. Besides, the use of pesticides, insecticides and herbicides, in the form of agricultural sources, also contribute to water pollution with phenolic compounds. In addition, household chemicals such as disinfectants, antiseptics, soaps, body lotions, ointments, mouthwashes, oral sprays, paints and perfumes contain small amounts phenol, for which however the cumulative effect on disposal can be large. Furthermore, effluents and influents emanating from municipal waste treatment plants, and leachates from municipal solid waste landfill sites, are another sources of phenolic compounds into water bodies. Industrial processes release high concentrations (10 $g \cdot L^{-1}$ was reported in [14]) and considerable amounts of phenol, with consequences to both atmosphere and water resources.

1.3.1.2 Natural sources

The common natural sources of phenol in water include the degradation of organics, such as plants and animals, synthesis by microorganisms or plants [13]. For example, the waste generated by agro-based industries, such as empty fruit bunches, seed, fibre, shell, wood and bagasse, is found to be rich in phenolic derivatives [15]. Besides, benzene, which widely

exists in organic wastes, may produce phenol via metabolic degradation, as reported by Rothman [16]. The bio-synthesis process of some plants, conversion of amino acids contained in plants' hemicelluloses under UV irradiation or sunlight [17], and tyrosine transformation in mammalian (including human) digestive tract [18] are all possible natural sources of phenol. Furthermore, phenol is also formed as a result of chemical reactions in condensed water vapour that forms clouds, in natural fires as well as in lignin degradation. Direct decomposition of these organics in water and/or indirect introduction from runoffs and rainfall result in the contamination of water with phenol [13]. The effects of the phenol produced naturally on environments are smaller than those produced in human activity due to the much lower production.

1.3.2 Toxicology of phenol

When discussing the toxic effects of some substances, their dosages or concentrations are priorities to be considered. The toxicity of phenol in water is closely associated with its concentration. For example, international regulatory bodies set strict discharge limits for phenols for a sustainable environment while the EPA set a water purity standard of lower than 0.5 ppb (also written as $\mu g \cdot L^{-1}$) in potable and mineral waters, 0.5 ppm (also written as $mg \cdot L^{-1}$) in wastewater discharge to surface waters and 1 ppm for the sewerage system [19]. The hazards of phenol in water to both aquatic life and human health are serious or even fatal when phenol concentration exceeds the threshold value strictly limited by regulations. Generally, the concentrations of phenol in natural water, i.e. non-contaminated sources of water like lakes or rivers, as a consequence of metabolic processes, are in the range of 0.01-2.0 $\mu g \cdot L^{-1}$ [14,20], which are harmless to the environment. In comparison, the phenol concentrations in industrial wastewater sometimes reach as high as 10 $g \cdot L^{-1}$ [14,20], i.e. more than 100 million times higher than that in natural water thus the toxicity is considerable.

Phenol is readily soluble in water, thus its toxicology researches were mainly focused on its effects on aquatic life and human health. Phenolic compounds reveal unpleasant odour to

water bodies, cause damaging effects on aquatic organisms, including algae and aquatic life and even affect the survival and reproduction of fish. In toxicological studies, LC50 and EC50 are usually used to characterize the toxicity of a chemical to a living organism. There are a number of reviews and papers on the toxicology of phenol and its derivatives to aquatic life [20-23], however, the LC50 and EC50 values of phenol basically varied from 0.26 to 2200 $mg \cdot L^{-1}$ due to the different test objects and test conditions. As reported, carp (*Cirrhinus mrigala*) was the most sensitive freshwater organism with a 96 h-LC50 of 1.56 $mg \cdot L^{-1}$ for phenol while opossum shrimp (*Archaeomysis kokuboi*) was the most susceptible marine organisms to phenol with a 96 h-LC50 of 0.26 $mg \cdot L^{-1}$ [20]. Phenol also affected the growth of marine microalgae with the 96 h EC50 values of *Dunaliella salina*, *Platymonas subcordiformis*, *Phaeodactylum tricornutum Bohlin*, and *Skeletonema costatum* to phenol solutions of 72, 93, 27, and 27 $mg \cdot L^{-1}$, respectively [24]. Furthermore, phenol was also harmful to waterborne bacteria. For example, the 14-day EC50 value of *S. horneri* on the basis of the specific growth rate was 58 $mg \cdot L^{-1}$ phenol [25]. Worst of all, the organic toxins accumulating in these organisms may affect the related food webs and indeed the entire aquatic ecosystems [20].

With the increase of phenol concentration in water, human health is also affected. This imparts medicinal taste and objectionable odour to drinking water even at a much lower concentration of 2 $\mu g \cdot L^{-1}$. In an incident of contamination of groundwater caused by spillage of phenol in Wisconsin (US) in 1974, many villagers who consumed the contaminated water were diagnosed as subacute poisoning [26,27]. The maximum concentration of phenol in the contaminated water actually ingested by the victims is uncertain, while Baker et al. [27] estimated the exposures of 10 to 240 mg/person/day. Moreover, it is reported in some literature that the toxicity levels are in the range of 1024 $mg \cdot L^{-1}$ for humans [28] (this is the reason why the initial concentration of phenol is 1 $g \cdot L^{-1}$ in this project). If exceeding the range, exposure to phenol will cause various health problems. Acute effects of phenol exposure include anorexia; eyes, nose, and throat irritation, while chronic effects include weight loss, lassitude (weakness, exhaustion), muscle ache, and pain. Moreover, it may trigger dark urine,

cyanosis, skin burns, dermatitis, tremor, convulsions, and twitching. In the long term, some human organs include skin, eye, respiratory tract, liver, and kidney may get damaged if exposed to phenol for long time. Phenolic compounds are also fatal for human by inhalation, ingestion, skin or eye absorption, as it quickly penetrates the skin and may cause severe irritation to the eyes, the mucous membranes, and the respiratory tract. Oral exposure to phenol may cause severe damage to the liver and kidney and ingestion of 1 g of phenol is reported to be lethal to an adult man [29,30], though individual tolerance for this compound is different.

1.4 Phenol treatment and abatement methods

The increasing environmental pollution leads to progressive deterioration in our quality of life and prompts us to develop effective technology with the aim of human health and nature preservation. Some techniques, either aim to separate or destroy phenol from water, are emerging in recent years and have been applied in different processes. When screening the most appropriate technology from these methods, the concentration and nature of the pollutants, the actual volume of wastewater, as well as economic factors need to be carefully considered. The application of the appropriate method for the removal of phenol from water not only eliminates possible harms associated with the pollutant but allows the attainment of value-added phenolic compounds as by-products.

1.4.1 Separation of phenol from wastewater

Separation-based methods, compared to other technologies, are usually non-destructive and purify phenol-containing water by moving phenol from the water phase to another phase, thus phenol can even be recycled as high-value chemicals after treatment. In addition, separation methods are superior to other treatments in terms of low cost, large capacity, easy operation, and flexible design. The frequently used separation methods include adsorption [31,32], solvent extraction [33,34], steam distillation [35,36], membrane pervaporation [37,38], reverse osmosis [39,40], nanofiltration [41,42]. Among them, adsorption and extraction are

most commonly applied at industrial level, as they are cheap, however they also have a few drawbacks as briefly described in the next sections.

1.4.1.1 Adsorption

Among the separation-based techniques, adsorption is the most popular method and aims to isolate certain compounds from water by preferentially accumulating pollutants from solution onto the surface of adsorbents (usually solid materials). It is usually used to purify wastewater with a wide range of phenol concentrations.

The typical adsorption mechanism of the adsorbate molecules from the bulk liquid phase into the solid (adsorbent) phase includes four steps [43]: 1) the mass transfer of the adsorbate molecules across the external boundary layer toward the solid particle, 2) adsorbate molecules are transported from the particle surface into the active sites by diffusion within the pore-filled liquid and migrate along the solid surface of the pore, 3) solute molecule adsorption on the active sites on the interior surfaces of the pores and 4) the molecule gets approached inside the pores of the adsorbent. The efficiency of the adsorption process depends on a number of factors such as: the physical properties of adsorbent (e.g. functional group composition, pore structure like pore size and its distribution, surface area, ash content), the conditions of solution (e.g. pH, temperature, degree of polarity, ionic strength, the concentration of the adsorbate) and the nature of the adsorbate (e.g. solubility, polarity, size, molecular weight) [12]. Many porous materials, e.g. bentonite [31,44], clay [45,46], resin [47,48], carbon nanotube [49,50] and zeolite [51,52], are applied in the adsorption of phenol in water whereas the most commonly used adsorbent is activated carbon due to the high adsorption capacity, well-developed porous structure, special surface characteristics [53]. In addition to the commercial activated carbon, other potential alternative adsorbents derived from other carbonaceous material, especially materials with high carbon content and low inorganic components, are used as a precursor to produce activated carbon to further decrease the cost of the adsorption process (table 1.2).

However, two significant drawbacks make adsorption unfavourable as a stand-alone process. On the one hand, the adsorption suffers easy blockage of adsorbent and incomplete elimination of pollutants (in table 1.2). As reported by Mukherjee and his co-workers [54] the adsorption efficiency of phenol with three carbonaceous materials (activated carbon, bagasse ash and wood charcoal) at 24 ± 1 ^{o}C for 1 h (initial phenol concentrations of 30 and 50 mg·L^{-1}, adsorbent of 50 g·L^{-1}, pH 6.8) were 98%, 90% and 90%, respectively. In fact, further destructive post-treatment of the wastewater after the adsorption process is needed to reach a high purification level. Besides, the adsorption process per se is a concentration process of the contaminants from water onto adsorbent, thus the further treatment of the concentrated contaminants brings another problem, regeneration of adsorbents (or desorption of contaminants). The conventional regeneration of adsorbent is thermal technique [55], in which the loaded adsorbent is heated for desorption and recovery of the pollutant. However, heating and cooling in each of the adsorption-desorption cycles exert thermal stress on the adsorbent which causes loss of activity [56]. Moreover, the desorbed adsorbates require secondary treatment otherwise it would re-renter the cycle.

Table 1.2. Various adsorbents reported in the literature for phenol removal

Adsorbent	Experimental condition	Adsorption capacity	Ref
coconut shell-based activated carbon	100-500 mg·L^{-1} phenol, 30 ± 1 °C	205.8 mg·g^{-1}	[57]
hydroxyapatite nano-powders	400 mg·L^{-1} phenol, 60 °C, pH 6.4	10.33 mg·g^{-1}	[58]
beet pulp carbon	25-500 mg·L^{-1} phenol, 60 °C, pH 6.0	89.5 mg·g^{-1}	[32]
rice husk-based mesoporous carbon	3.187 mmol·L^{-1} phenol, 20 °C, pH 2.7	0.235 mmol·g^{-1}	[59]
chitin	300 mg·L^{-1} phenol, 40 °C, pH 1.0	21.5 mg·g^{-1}	[60]
polymeric resins	100 mg·L^{-1} phenol	81.68 mg·g^{-1} (Amberlite XAD1), 96.13 mg·g^{-1} (Duolite S861)	[61]
basic anion exchange resin	100 mg·L^{-1} phenol, pH 11.2	92.9 mg·g^{-1}	[47]
polyethyleneimine/SiO_2	200 mg·L^{-1} phenol, 20 °C, pH 7	160 mg·g^{-1}	[62]
activated carbons from wood chips	25 °C, pH 7	667.9 mg·g^{-1} (ZnCW-1.5), 256.5 mg·g^{-1} (FeZnCW-1.0)	[63]
Seaweed-based activated carbon	150 mg·L^{-1} phenol, 50 °C, pH 3.0	98.31% removal	[64]
corn grain-based activated carbon	100 mg·L^{-1} phenol, 293.15 K	232 mg·g^{-1} (R-1/2), 185 mg·g^{-1} (R-1/3), 176 mg·g^{-1} (R-1/4)	[65]
aluminium impregnated fly ash	200 mg·L^{-1} phenol, 34.44 °C, pH 5.65	12.67 mg·g^{-1} (86.4% removal)	[66]
dye-affinity hollow fibres	20 °C, pH 6.0	145.9 μmol·g^{-1}	[67]
granular activated carbon	200 mg·L^{-1} phenol, 30 °C, pH 8	79.9% removal	[68]
HZSM-5 (SiO_2/Al_2O_3 of 80)	100 mg·L^{-1} phenol, 30 °C, 30 min	50.5% removal	[69]
Cu/coconut-shell based activated carbon	300 mg·L^{-1} phenol, 30 °C, pH 8	71.43% removal	[70]

1.4.1.2 Liquid-liquid extraction

The liquid-liquid extraction, also known as solvent extraction, is also attractive in industry not only because it is applicable for a wide range of phenol concentrations (50-2200 $mg \cdot L^{-1}$ [28]) but also due to the characteristics of large production capacity, high selectivity and ease of automation. In principle, the target compound can be transferred from one liquid phase to another and then gets separated from the aqueous phase by this technique, based on its different solubility or distributions in two immiscible liquids (usually water and an organic solvent). The compound can be even completely moved into the organic phase when the solubility of phenol in some selected extractants is much higher than that in water, although more than one extraction operation is sometimes necessary.

Many factors such as extractant, the distribution ratio of phenol in water and extractant, process conditions, affect the extraction performance, while the selection of extractant is the key part as it defines the separation efficiency and selectivity [71]. Various solvents have been used for the extraction of phenol from water, such as tributyl phosphate (TBP) [72], N-octanoylpyrrolidine (OPOD) [73], methyl isobutyl ketone (MIBK) and diisopropyl ether (DIPE) [74], in which the solubility of phenol is much higher than that in water. For instance, Xu et al. [75] investigated the extraction of phenol in wastewater with QH-1 extractant (the amine mixture) and annular centrifugal contactors, it is observed that the extraction rate and the stripping efficiency of the three-stage cascade reached more than 99%. However, some shortcomings such as: difficult or impossible regeneration of the extraction media, large use of samples and organic extraction agent, make solvent extraction expensive, time-consuming and environmentally unfriendly [76]. The severe drawbacks make this method a short term solution for the removal of contaminants and not a long term since the extracting phase is contaminated afterwards and this will also be need to be disposed.

1.4.2 Destruction of phenol from wastewater

In comparison with separation methods, the destruction-based techniques are usually able to effectively destroy the pollutants in an environmentally benign and cost-effective way, namely, high conversion of pollutants to inorganic mineral constituents or harmless intermediates, leading to a higher degree of purification. The representative methods include microbial degradation [14,77], enzymatic treatment [78,79], advanced oxidation process [80,81], supercritical water gasification [82,83]. Among these methods, microbial degradation and advanced oxidation process are the most mentioned techniques due to high removal efficiency, low cost and sustainable routes.

1.4.2.1 Microbial degradation

Biological treatment as one of the most promising and economical approaches for the control of many organic water contaminants such as phenol, has been greatly developed in recent years. However, conventional microbial degradation is inapplicable in highly concentrated phenol purification processes because microorganisms generally cannot survive in the conditions of a high concentration of phenol (> 1000 $mg \cdot L^{-1}$) and salt (5%) [33]. Therefore the biological method that involves microorganisms is usually feasible for water containing a medium/low concentration of phenol (5-500 $mg \cdot L^{-1}$ [84]) only.

One of the widely applied biological methods is microbial treatment, which utilizing phenol as the sole carbon and energy source in the degradation process. Both aerobic and anaerobic microorganisms were reported to be capable of degrading phenol, while conventional aerobic processes are preferred because aerobic microorganisms grow faster, thus they are more efficient for phenol degradation. A typical pathway for metabolizing phenol is to hydroxylate the ring, by the enzyme phenol hydroxylase, form catechol, and then open the ring through ortho- or meta- oxidation [29]. The hydroxylation reaction in phenol metabolism was the key determinant of biodegradation velocity. Other factors such as temperature, pH, oxygen content, substrate (phenol) concentration, microbial completion and microbial adaptation can

also affect the degradation ability or metabolism of microorganisms by either preventing or stimulating the growth of the organisms. The substrate concentration is particularly important because the growth of microbial cells is inhibited by phenol itself, especially at higher concentrations. Many microbial strains capable of degrading phenol have been studied such as *Pseudomonas putida*, *Pseudomonas fluoroescens, Acinetobacter*, *Trichosporon cutaneum* and *Candida tropicalis* in free and immobilized forms, using different types of bioreactors (table 1.3). Among them, *Pseudomonas putida* is a rod-shaped, Gram-negative bacterium that has been known for its ability to degrade organic solvents, especially its high removal efficiency of phenol [85]. For example, Gonzalez and co-workers [86] introduced the study of the biodegradation of phenolic industrial wastewaters by a pure culture of immobilized cells of *Pseudomonas putida* ATCC 17484, and the bioreactor showed phenol degradation efficiency higher than 90% after 25 h of degradation at 30 ^{o}C, even for a phenol loading rate of 0.5 g phenol$\cdot L^{-1}\cdot day^{-1}$. In addition to bacteria and fungi, the capabilities of some algae for phenol biodegradation were also confirmed. The biodegradation of phenol by microalgae occurs only under aerobic conditions. For instance, Tepe and Dursun [87] tested the capabilities of calcium-alginate immobilized *Ralstonia eutropha* for phenol degradation in a batch stirred reactor and phenol removal of 68% was obtained after degradation time of 24 h at 30 ^{o}C and pH 7 with 100 mg$\cdot L^{-1}$ initial phenol concentration.

Table 1.3. Various microorganisms capable of degrading phenol reported in the literature.

organism	Specific name	Experimental condition	Degradation time	Removal efficiency	Ref.
bacteria	*Pseudomonas putida*	1000 mg·L^{-1} phenol, 29.9 ± 0.3 °C, pH 7.1	162 h	100%	[88]
	Pseudomonas putida	500 mg·L^{-1} phenol, 30 °C, pH 6.6	25 h	>90%	[86]
	Acinetobacter sp. stain	500 m·L^{-1} phenol, 30 °C	9 h	99.6%	[89]
	Alcaligenes faecalis	1600 mg·L^{-1} phenol	76 h	100%	[90]
	Pseudomonas putida	1-2 mg·L^{-1} phenol	28 h	99%	[91]
	Acinetobacter sp.	800 mg·L^{-1} phenol	30 h	96%	[92]
	Acinetobacter sp. B9	47 mg·L^{-1} phenol, 30 °C	96 h	100%	[93]
	Brevibacillus sp.	200 mg·L^{-1} phenol, 30 °C	93.1 h	100%	[94]
	Acinetobacter sp. XA05 and Sphingomonas sp. FG03	800 mg·L^{-1} phenol, 30 °C, pH 7.2	35 h	> 95%	[95]
	Acinetobacter sp. BS8Y	600 mg·L^{-1} phenol, pH 7.2	24 h	99.2%	[92]
fungi	*Graphium sp.stain*	10 mM phenol, 30 °C	168 h	75%	[96]
	Phanerochaete chrysosporium	500 mg·L^{-1} phenol, 30 °C	30 h	100%	[97]
algae	*nkistrodesmus braunii, Scenedesmus quadricauda*	400 mg·L^{-1} phenol, 30 °C	5 days	70%	[98]
	Ralstonia eutropha	100 mg·L^{-1} phenol, 30 °C, pH 7	24 h	68%	[87]

1.4.2.2 Advanced oxidation processes

Chemical destruction and biological degradation, as destructive techniques, both destroy phenol completely to harmless products, however, chemical methods are usually more efficient as they degrade phenol in hours while biological methods need days (as shown in table 1.3). In addition, chemical destruction is usually able to oxidize non-biodegradable, recalcitrant and toxic organic pollutants. Moreover, chemical methods are proper to high organic loading and can partially cover the application range of biological methods, as it could, as reported, be used in water purification with phenol concentration up to 15 $g \cdot L^{-1}$ [99]. Thus it can be used in almost all the phenol-containing wastewater without pre-dilution as the phenol concentration in industrial wastewater are usually lower than 10 $g \cdot L^{-1}$.

Classical chemical methods for phenol decomposition from water known as advanced oxidation processes (AOPs), are a group of techniques with a common chemical feature: generate and use reactive oxygen species (ROS) as strong oxidant to destroy organic compounds efficiently. Different oxidants used in the AOPs to generate highly reactive species (including but not limited to hydroxyl free radicals (HO·)) and their oxidation potentials (indicates the availability of the free electrons and the oxidizing tendency) are summarized in table 1.4. As shown, hydroxyl radical (HO·, $E_0 = 2.80$ V) is an effective strong oxidant with the oxidation potential second only to fluorine (F_2, $E_0 = 3.06$ V). Besides, the hydroxyl radical is non-selective for most of the organic contaminants and the reaction rate between HO· and organic molecules usually reaches 10^6-10^9 $mol^{-1} \cdot s^{-1}$, which is 10^6–10^{12} times faster than ozone [100]. This high reactivity for the hydroxyl radical is a consequence of its high instability (the half-life period is less than 1 μs [101]), thus it is usually obtained indirectly from other sources in wastewater treatment applications.

Table 1.4. Standard redox potential of various oxidants among them, the hydroxyl radical (HO·) with high oxidation potential is a good choice. [102]

Oxidant	Oxidation potential (V)
fluorine	3.06
hydroxyl radical	**2.80**
atomic oxygen	2.42
ozone	2.08
persulfate	2.01
perbromate	1.85
hydrogen peroxide	1.78
perhydroxyl radical	1.70
hypochlorite	1.49
bromate	1.48
chlorine	1.36
dichromate	1.33
chlorine oxide	1.27
permanganate	1.24
oxygen (molecular)	1.23
perchlorate	1.20
bromine	1.09
iodine	0.54

Given that the hydroxyl radical is such an unstable and reactive species, it must be generated continuously 'in situ' through chemical reactions. Known methods form literature for the production of ·OH include: Fenton-based reaction [103,104], ozonation [105,106], photocatalysis [107,108], electrochemical oxidation [109,110], plasma [111,112] and so on. Compared with other AOPs, Fenton oxidation process with Fe^{2+} as the catalyst and H_2O_2 as the oxidant, is still a core theme of research and the most popular technique because of the

following advantages [113]: 1) ·OH radicals are usually generated at mild temperature (T , 100 °C) and ambient pressure, which avoids the requirement of complicated reactor facilities or large energy consumption, 2) the simple and flexible nature of the technique as it can be used alone or combined with other water treatment methods such as biological degradation, 3) the activation of H_2O_2 and the production of hydroxyl radicals are fastest among all other AOPs due to the rapid Fenton reaction (Fe^{2+} and H_2O_2), 4) the use of the high-abundant, high-reactive and low-toxic catalyst iron catalyst as well as efficient and the environmentally friendly oxidant (H_2O_2, decompose to H_2O and O_2), makes the Fenton process cost-effective and practically viable, and 5) the high efficiency of mineralization enables the transformation of organic pollutants into non-toxic CO_2 (though needs further treatments such as carbon capture to avoid the greenhouse gas effect, it is harmless in comparison with toxic organic contaminants).

Among various factors that influence the effectiveness of the degradation process in the Fenton oxidation system, the operating pH (3-5), initial concentrations of the substrate and dose of catalyst (or in other words, a molar metal to substrate, M:S, ratio), concentration of H_2O_2 are the most significant [114], because these parameters determine the efficiency of hydroxyl radical generation as well as overall reaction efficiency. For example, Inchaurrondo [115] investigated the effects of temperature, catalyst load and hydrogen peroxide concentration on phenol mineralization and hydrogen peroxide consumption efficiencies. The results revealed a complete phenol removal together with final total organic carbon (TOC, defined as the amount of carbon found in an organic compound and is often used as one of the indicators of water quality) conversion close to 94% at optimal conditions (343 K, 25 $g \cdot L^{-1}$ of catalyst, hydrogen peroxide 3.9 times the stoichiometric ratio), indicating the high efficiency of the Fenton oxidation method.

Overall, to choose the most appropriate technology multiple aspects, such as the applicability (concentration of the pollutants), purification efficiency, technical cost and secondary

contamination, must be comprehensively considered. From the above point of view, the chemical AOPs method, especially the Fenton process, is the most appropriate option in this research for phenol degradation if considering the criteria listed above.

1.5 Fenton and Fenton-like processes

The majority of studies for catalytic wet peroxide oxidation (CWPO) mainly focus on the removal of reactant and TOC conversion, however, sufficient knowledge for reaction mechanisms and pathways as well as reaction kinetics is essential as well to optimize the reaction conditions and to develop the effective catalysts required for industrial applications.

1.5.1 Reaction mechanism of Fenton reaction

Though formally defined in 1987 by Glaze et al. [116], AOPs can be traced back to the 1890s when Henry John Horstman Fenton published a detailed research concerning a pioneering work on the use of a mixture of H_2O_2 and Fe^{2+} (called Fenton's reagent later) for the oxidation of tartaric acid [117]. However, the definite mechanism of the Fenton process for pollutant decomposition has not been fully established over the last decades thus the actual elementary steps of the Fenton systems are still subject of study.

The traditionally proposed Fenton process includes more than 20 chemical reactions [118-120], and its generally accepted core reaction is the “Fenton reaction” (Eq. 1.1). The system containing hydrogen peroxide and Fe(II) salts is known as Fenton reagent, the system involves the oxidation of ferrous to ferric ions, to decompose H_2O_2 into hydroxyl radicals as follows [114,119,120]:

$$H_2O_2 + Fe^{2+} \rightarrow Fe^{3+} + HO^- + HO\cdot \qquad \text{(Eq. 1.1)}$$

The reaction is very fast (k = 63-76 $M^{-1}s^{-1}$ at 25 ^oC [113]), and induces a series of chain reactions due to the combination of ferrous iron and hydrogen peroxide and the generation of hydroxyl radicals initiated by the conversion of hydrogen peroxide.

The ferric ions produced in the above reaction are reduced by Eq. (1.2) [114,118-120], called Fenton-like reaction, with excess hydrogen peroxide to form ferrous ions, allowing Fe^{2+} regeneration in an effective cyclic mechanism.

$$Fe^{3+} + H_2O_2 \rightarrow Fe^{2+} + HOO\cdot + H^+ \quad \text{(Eq. 1.2)}$$

Eq. 1.2 is associated with a two-step transformation in which the adduct $[FeOOH]^{2+}$ formed in the equilibrium reaction (Eq. 1.3) is subsequently converted into Fe^{2+} and hydroperoxyl radical ($HOO\cdot$) following the Eq. 1.4 [120,121]:

$$Fe^{3+} + H_2O_2 \leftrightarrow [FeOOH]^{2+} + H^+ \quad \text{(Eq. 1.3)}$$

$$[FeOOH]^{2+} \rightarrow HOO\cdot + Fe^{2+} \quad \text{(Eq. 1.4)}$$

The net result of the first two equations (Eq. 1.1 and Eq. 1.2) is the formation of large amounts of reactive radicals such as $HO\cdot$ and $HOO\cdot$, which can attack and degrade organic contaminants to oxygenated, and often smaller compounds or even CO_2 and H_2O, as shown in figure 1.2. It is noted that the Fenton-like reaction (Eq. 1.2, k = 0.001-0.01 $M^{-1}s^{-1}$ at 25 °C [113,119] is usually slower than Fenton reaction (Eq. 1.1, k = 63-76 $M^{-1}s^{-1}$ [113,119]) and the hydroperoxyl radicals ($E^0(HOO\cdot/ H_2O_2)$ = 1.50 V) are less sensitive than hydroxyl radicals (($E^0(HO\cdot/H_2O)$ = 2.73 V)) [119,121].

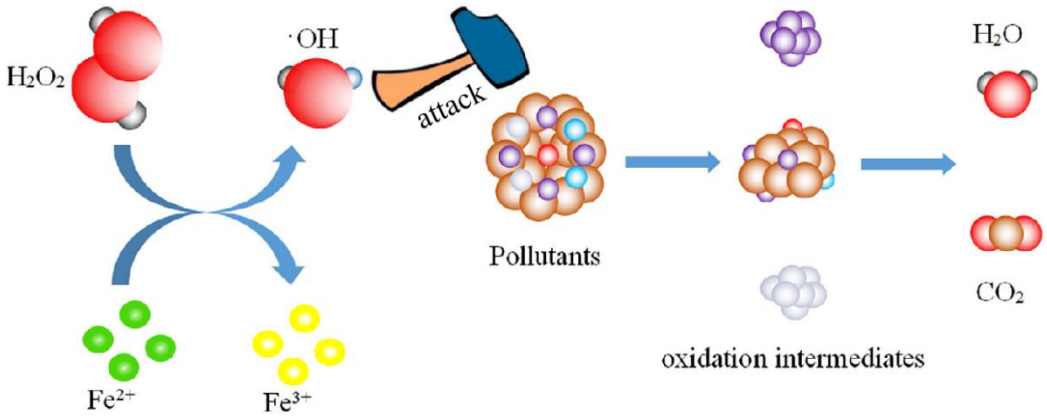

Figure 1.2. Mechanism of Fenton process for organic pollutant decomposition. Phenol decomposed to intermediates under the attack of hydroxyl radicals rather than the direct effects of the catalyst (Fe^{3+}) or the oxidant (H_2O_2). Figure reproduced from [114] with permission.

The generation of the radicals involves a complex reaction sequence in an aqueous solution [114]:

$$Fe^{2+} + HO\cdot \rightarrow Fe^{3+} + HO^{-} \quad \text{(Eq. 1.5)}$$

$$Fe^{2+} + HOO\cdot \rightarrow Fe^{3+} + HOO^{-} \quad \text{(Eq. 1.6)}$$

$$Fe^{3+} + HOO\cdot \rightarrow Fe^{2+} + H^{+} + O_2 \quad \text{(Eq. 1.7)}$$

For example, when reacting with ferrous ion (Eq. 1.5 and Eq. 1.6), the free radicals formed in Eq. 1.1 and Eq. 1.2 are scavenged and thus lead to negative effects on organic compounds degradation. When reacting with ferric ions (Eq. 1.7), the free radicals can also reduce Fe^{3+} back to Fe^{2+}.

In addition, they also react with free radicals (radical–radical reactions) and hydrogen peroxide (hydrogen peroxide–radical reaction), as shown in Eq. 1.8-1.13 [119,120].

$$HO\cdot + HO\cdot \rightarrow H_2O_2 \quad \text{(Eq. 1.8)}$$

$$2HO\cdot + 2HO\cdot \rightarrow O_2 + 2H_2O \quad \text{(Eq. 1.9)}$$

$$HO\cdot + H_2O_2 \rightarrow HOO\cdot + H_2O \quad \text{(Eq. 1.10)}$$

$$HOO\cdot + HOO\cdot \rightarrow H_2O_2 + O_2 \quad \text{(Eq. 1.11)}$$

$$HOO\cdot + H_2O_2 \rightarrow HO\cdot + H_2O + O_2 \quad \text{(Eq. 1.12)}$$

$$HO\cdot + HOO\cdot \rightarrow H_2O + O_2 \quad \text{(Eq. 1.13)}$$

Likewise, the radicals generated from the Fenton and Fenton-like reaction react with each other or with the excess H_2O_2 in an aqueous solution, which also leads to the scavenging of the free radicals. The overall reaction is the decomposition of hydrogen peroxide to molecular oxygen and water, as presented follows:

$$2\ H_2O_2 \rightarrow 2\ H_2O + O_2 \quad \text{(Eq. 1.14)}$$

It also suggests that part of H_2O_2 would be consumed regardless of the absence or presence of organic molecule to be oxidized, resulting in waste of oxidant H_2O_2 and thus leading to an unnecessary increase of cost.

While in the presence of the organic substrate (here denoted R−H), the generated hydroxyl radical degrades organic pollutant by abstracting a hydrogen atom from R−H and generates an organic radical (R·) [113,119].

$$RH + HO\cdot \rightarrow R\cdot + H_2O \quad \text{(Eq. 1.15)}$$

Like the hydroxyl radical, organic radical also experiences a series of chemical transformation to form various oxidation products, as displayed in Eq 1.16 - 1.20 [119]:

$$R\cdot + H_2O_2 \rightarrow ROH + HO\cdot \quad \text{(Eq. 1.16)}$$

$$R\cdot + O_2 \rightarrow ROO\cdot \quad \text{(Eq. 1.17)}$$

$$R\cdot + R\cdot \rightarrow RR \quad \text{(Eq. 1.18)}$$

$$R\cdot + Fe^{2+} \rightarrow R^- + Fe^{3+} \quad \text{(Eq. 1.19)}$$

$$R\cdot + Fe^{3+} \rightarrow R^+ + Fe^{2+} \quad \text{(Eq. 1.20)}$$

The above equations (Eqs. 1.1-1.18) demonstrate the complex mechanism of the Fenton process. During the whole process, the formation of the hydroxyl radical is the most important part. Hydroxyl free radicals, as the most active species for pollutants degradation in the Fenton reaction, are generated mainly from Eq. 1.1, which is the chain initiation step. The efficiency of the Fenton system in generating the active HO· radical oxidant largely depends on the catalytic cycling of iron between the Fe^{3+} and Fe^{2+} states. Then the reaction system involves the chain propagation step (Eq. 1.15): the reaction of highly reactive species with organic compounds to generate alkyl radicals (R·) and their further transformations. During the reaction process, reactive species can be scavenged by ferrous ions (Eq. 1.15), hydrogen peroxide (Eq. 1.10), hydroperoxyl radicals (Eq. 1.13), and/or even maybe auto scavenged (Eq. 1.8 and Eq. 1.9), which leads to the chain termination. Meanwhile, the foregoing analysis indicates that hydrogen peroxide acts both as a radical generator (Eq. 1.1) and as a scavenger (Eq. 1.10) [120].

In the past decades, new practically acceptable and economically viable Fenton-like processes (Fe^{3+}/H_2O_2 or M^{n+}/H_2O_2 system) were also developed to generate HO· from H_2O_2. For example, cupric ions show strikingly similar redox properties to ferric ions in terms of their reactivity towards H_2O_2. Both the cuprous (Cu^+) and cupric (Cu^{2+}) oxidation states react easily with H_2O_2 (Eq. 1.21) and 1.22), analogous to the Fe^{2+}/H_2O_2 and Fe^{3+}/H_2O_2 reaction systems, as shown in the following reactions (Eq. 1.21 and Eq. 1.22) [113]:

$$H_2O_2 + Cu^+ \rightarrow Cu^{2+} + HO^- + HO\cdot \qquad \text{(Eq. 1.21)}$$

$$Cu^{2+} + H_2O_2 \rightarrow Cu^+ + \cdot OOH + H^+ \qquad \text{(Eq. 1.22)}$$

Similarly, the reaction rate of Eq. 1.21 with a rate constant of 1.0×10^4 $M^{-1}s^{-1}$ (at 25 °C) [122] is much faster than that of Eq. 1.22 with a rate constant of 1.15×10^{-6} $M^{-1}s^{-1}$ (at 25 °C) [122]. The HO· radicals formed from the above two equations attack organic compounds effectively and thus the Cu^+/H_2O_2 system is one of the alternatives of traditional Fenton reagent. Other metal ions such as Ce^{4+}/Ce^{3+} [113,123], Mn^{3+}/Mn^{2+} [113,123] are also active in the decomposition of H_2O_2 to generate hydroxyl radicals.

1.5.2 Reaction pathways of phenol

Although the capability of ·OH radicals for decomposition of phenol has been well accepted over the past decades, the actual details of the oxidation pathway is still an open question as phenol is usually not directly oxidized to CO_2 and water but via some organic intermediates, such as aromatic compounds (e.g. hydroquinone) and short-chain acids (e.g. acetic acid). Moreover, it is reported in the literature that the reaction pathway of phenol decomposition to some extent depends on catalysts (e.g. active species) and reaction conditions (e.g. pH), making the actual reaction pathways of phenol decomposition highly complex.

Various phenol oxidation routes involving different intermediates have been proposed so far [124-127]. The reasons for different reaction pathways in the literature include the use of different active species (Cu [124], Fe [128]), oxidants (H_2O_2 [124], O_2 [129]) as well as

reaction parameters (acidic medium [124], basic medium [125]), which all have influences on the mechanism and the intermediates formed in the oxidation process. In the three representative oxidation pathways shown in figures 1.3, 1.4 and 1.5, the involved intermediates, as well as the precursor and product of specific compounds (e.g. maleic acid and oxalic acid), are different. For instance, one of the phenol oxidation routes using the classical Fenton reagent (Fe^{2+} salt) as catalyst is shown in figure 1.3, which indicating that over 10 intermediates would be produced during the process of phenol decomposition to CO_2 and H_2O. As shown, phenol decomposition by Fenton reagent proceeds initially through hydroxylation of the aromatic ring to yield dihydroxybenzenes, mainly catechol and hydroquinone, which are in redox equilibrium with benzoquinones. Then ring-opening of the aromatic intermediates results in the formation of muconic acid and maleic acid. All of the intermediates are finally oxidized to acetic acid, formic acid and oxalic acid, thus, a pH decrease takes place. Among these acids, formic acid can be oxidized to CO_2 and H_2O, whereas oxalic acid shows quite refractory behaviour and remains in solution. The final products based on this oxidation route are acetic acid and CO_2.

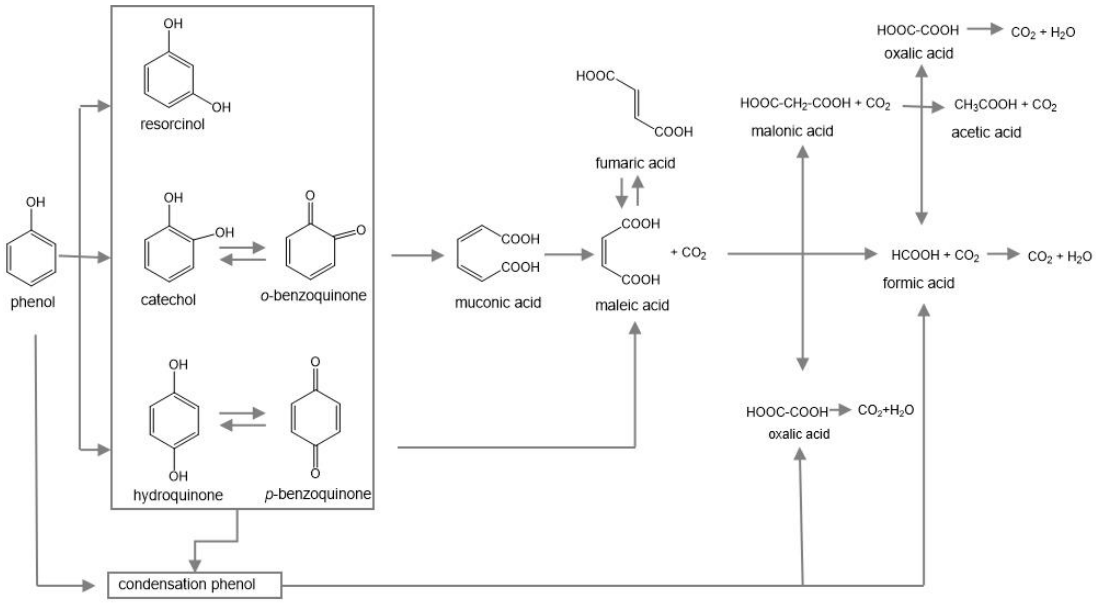

Figure 1.3. Accepted pathway of phenol decomposition in water with homogeneous Fe^{2+} catalyst and H_2O_2 oxidant [128]

The oxidation route proposed based on Cu supported catalyst is exhibited in figure 1.4, where phenol is decomposed to catechol and hydroquinone and the two intermediates develop two separate pathways respectively. The formation of catechol leads to a polymerization product and then to oxalic acid. Oxalic acid formed in the oxidation reaction is oxidized to CO_2 or complexes with Cu catalyst to form Cu oxalate, which is also one of the reasons for metal leaching in an aqueous phase reaction [130,131]. The other direct intermediate, quinones, contribute to the formation of various acids including maleic, fumaric, acetic, formic, malonic and oxalic acid. Besides, it is reported that the phenol oxidation pathway at acidic [124] and basic conditions [125] are completely different when using a commercial copper catalyst under the same reaction conditions (except pH).

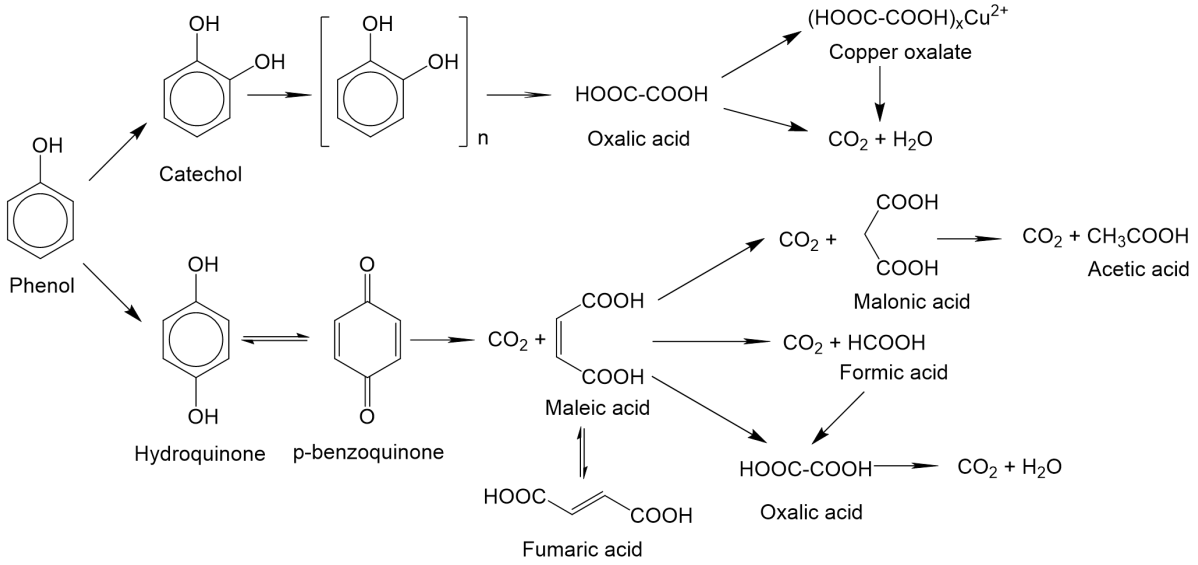

Figure 1.4. Accepted pathway of phenol decomposition in water with Cu supported catalyst [124]

Another possible oxidation pathway over noble metal catalysts like Ru, Pt and Rh is displayed in figure 1.5. It is stated the formation of maleic acid is crucial and it acts as the bridge between the decomposition of C6 compounds and the formation of smaller organic acids (C1, C2 and C3). Unlike the other two samples presented in figure 1.3 and figure 1.4, the oxidation route suggests that all intermediates can be further oxidized and CO_2 is the final product when ideal reaction conditions such as efficient catalyst are provided. .

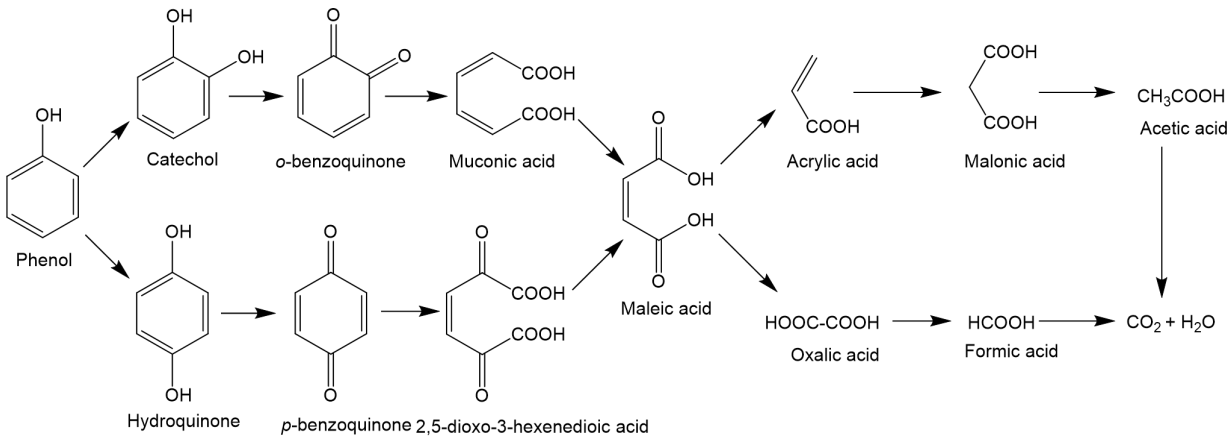

Figure 1.5. Accepted pathway of phenol decomposition in water with noble metal catalyst [126]

However, as it can be seen, regardless of their differences, all the reaction pathways suggested so far, consider the hydroxylation of phenol to hydroquinone and catechol as the first step in two parallel reactions, followed by oxidation of the dihydroxyl benzenes to benzoquinones, while the quinone intermediates would be further decomposed to short-chain acids such as acetic acid and formic acid, and then to CO_2 and water. Within the oxidation pathway, the details from the ring-opening of quinone intermediates to the formation of specific acid are strongly dependent on actual reaction conditions. Furthermore, it is widely accepted that the final products of phenol oxidation were some acids that are resistant to further oxidation like acetic acid, formic acid and CO_2. Overall, the deep understanding of the phenol oxidation route and in particular, the identification of intermediates, are of great importance to increase the selectivity of harmless products such as CO_2 and acids, as well as to decrease the toxic level of the reaction mixture, since some of the intermediates (like hydroquinone and *p*-benzoquinone) are even more toxic than the initial reactant [132,133].

1.5 3 Homogeneous and heterogeneous Fenton reaction

Though the traditional Fenton process has been developed over the past decades, there are still drawbacks that need to be tackled: 1) narrow range of pH [123,134]. The optimal pH for the Fenton reaction was found to be around 3, regardless of the target substrate [118,134]. In fact, at a pH below 2.5, the decomposition efficiency of phenol decreases due to: a) the

formation of $[Fe(H_2O)_6]^{2+}$ which reacts slowly with H_2O_2, giving rise to a less amount of ·OH radicals; b) the significant increase of the scavenging effect of ·OH by hydrogen protons; c) the inhibition of the reaction between Fe^{3+} and H_2O_2; and d) the formation of stable $[H_3O_2]^+$ in the presence of high concentrations of H^+ which make H_2O_2 more stable, thereby reducing its reactivity with Fe^{2+}. In contrast, at pH above 4, the formation and precipitation of ferric oxyhydroxides inhibit both the production of ·OH radicals and the regeneration of Fe^{2+} [113]. Besides, the oxidation potential of ·OH decreases as the pH increases and, finally, the decomposition of H_2O_2 into O_2 and H_2O is accelerated at high pH values [121,134]. 2) Formation of ion sludge in the form of oxyhydroxide [114,135]. The efficiency of hydroxyl radicals generation decreases with the precipitates of Fe^{3+} at pH above 4, leading to the loss of activity. 3) Difficult recovery of catalyst. In the conventional Fenton system, the catalyst, Fe^{2+}, added as a soluble salt, cannot be recovered after reaction and cause secondary contamination, thus an additional separation step is required to remove or recover the metal ions from the treated effluent, and accordingly increases operational costs and limits the application. In this context, the use of heterogeneous catalysts offers a practical and promising alternative to the conventional homogeneous routes, and it is precisely at the centre of this project.

Table 1.5. Comparison of homogeneous and heterogeneous catalyst [136]

	Homogeneous	**Heterogeneous**
Activity		
Active centres	All metal atoms	Only surface atoms
Concentration of substrate	Low	High
Selectivity	High	Lower
Diffusion	Practically absent	Present (mass-transfer controlled reaction)
Reaction conditions	Mild	Severe
Applicability	Limited	Wide
Activity loss	Irreversible reaction with products (cluster formation); poisoning	Sintering of metal crystallites; poison; metal leaching
Catalyst properties		
Structure/stoichiometry	Defined	Undefined
Modification possibilities	High	Low
Thermal stability	Low	High
Catalyst separation	Sometimes laborious (chemical decomposition, distillation, extraction)	Fixed-bed: unnecessary Batch: filtration
Catalyst recycling	Possible	Unnecessary or easy
Cost of catalyst losses	High	Low

The main drawbacks of homogeneous Fenton reaction can be overcome by immobilizing the active metal on a solid phase thus giving rise to heterogeneous Fenton reaction, a particular and the most representative case of the so-called CWPO. In comparison with the homogeneous process, using a heterogeneous catalyst in the Fenton reaction has many advantages (table 1.5), for instance, heterogeneous inorganic catalysts are often quite thermally robust, which makes them especially useful for chemical reactions that operate

under hostile conditions. Owing to those merits, heterogeneous catalyst has become basic to more than 80% of current bulk chemical processes used in the chemical and petrochemical industries [137], especially in the Fenton process, not only can the treatment tolerate more severe conditions (wider pH range, higher temperature), but, in principle, the catalyst can also be easily recovered, regenerated, and reused.

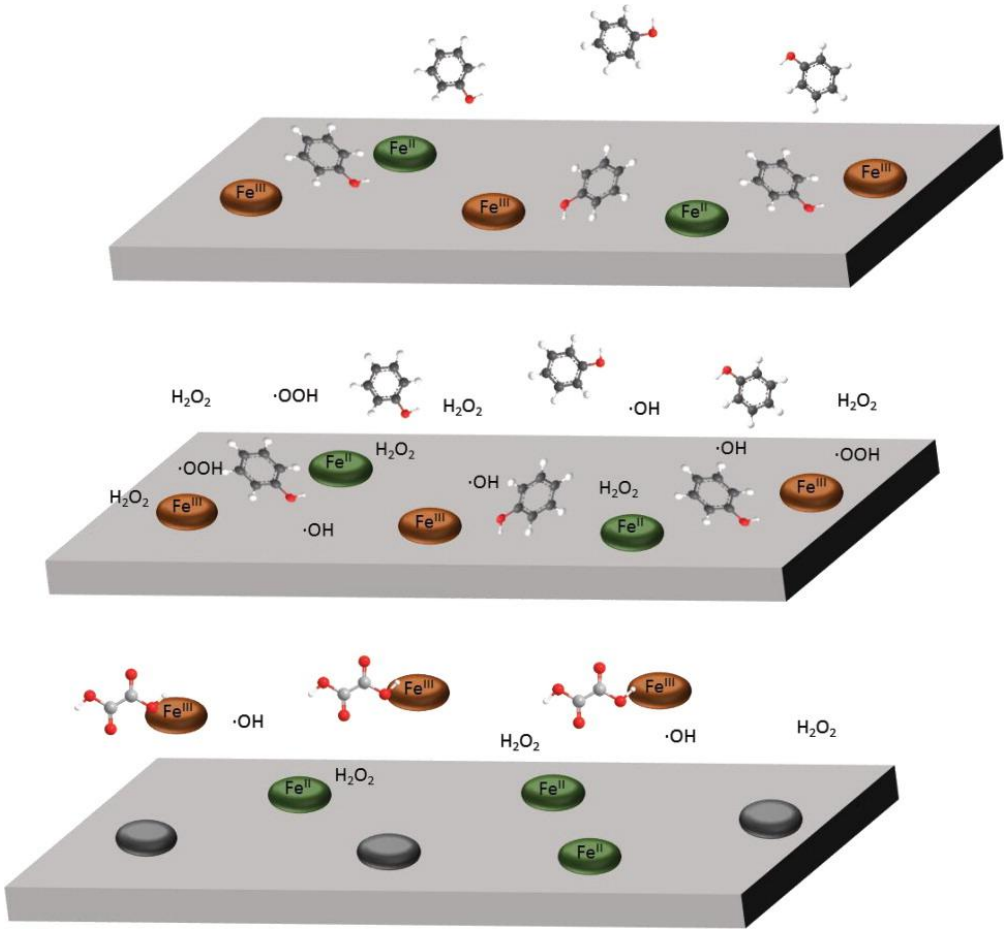

Figure 1.6. General reaction scheme of phenol degradation over Fe supported catalyst, where oxalic acid, one of the intermediates formed during phenol oxidation causes Fe leaching from the catalyst surface into the reaction mixture. Figure reproduced from [121] with permission.

It is noteworthy that the Fenton system can be translated into a heterogeneous phase. Similar to the classic Fenton, the CWPO process is a reaction between H_2O_2 and Fe in a solid matrix, such as Fe oxide and Fe supported porous materials, to produce highly oxidizing species (e.g. ·OH and ·OOH), as shown in Figure 1.6. The basic difference between the

homogeneous and heterogeneous Fenton-like processes involves the different phases where the catalytic reactions occur. In the homogeneous system, by definition the catalysis process occurs in the whole liquid phase, while in the heterogeneous system the catalysis process always occurs on the surface of the catalyst. Hence, the reaction mechanism begins with the diffusion of organic pollutant in the reaction media and the adsorption of the organic pollutant into the surface, which is further degraded by the radicals formed. Moreover, in the CWPO process with phenol as substrate, short-chain organic acids are common reaction intermediates and they can sometimes leach metal ions by forming metal complexes, contributing to deactivation of heterogeneous catalyst (this will be discussed in section 4.4.2 in chapter 4), and if the leached species is also active this can contribute itself to homogeneous catalysis.

It also follows that a heterogeneous catalyst should not be prone to metal leaching to avoid the homogeneous reaction and catalyst deactivation. Thus it is well accepted that the most important issue in the CWPO process is the development of a heterogeneous catalyst capable of combining activity and long-term stability at a reasonable cost.

1.6 Catalytic wet peroxide oxidation

In comparison with homogeneous catalysts, most heterogeneous catalysts show either low catalytic activity or unsatisfactory product selectivity or even low stability, and some of them require complex or lengthy synthesis processes. To solve these problems, the design of low-cost, highly active, highly selective and stable catalysts still remains the main focus of this process. In this section, the main content is the research and development of active heterogeneous catalysts in the CWPO process, including the constitution of a heterogeneous catalyst, potential catalytic materials for phenol decomposition, traditional catalysts and novel catalysts with resistance to leaching as well as catalyst preparation methods.

1.6.1 Heterogeneous catalyst

As mentioned in section 1.5.3 homogeneous catalysts operate in the same phase as the reactants, while heterogeneous catalysts are present in a phase different from that of the reactants. Typically though, the reactants are in the gas or liquid phase, whereas the catalyst is a solid material. A typical supported metal heterogeneous catalyst comprises three components: metal active species, support (catalyst carrier) and in some cases a promoter. Active species are typically metal clusters or active centres dispersed on the surface and/or in the pores of supports in the form of nanoparticles (1-50 nm in diameter). Catalyst supports are porous, usually, high-surface-area materials, having significant pore volume and capacity for preparing and preserving stable, well-dispersed catalytic species during reactions. Promoters are usually added in relatively small quantities (i.e., 1-5% [136]) to enhance the texture or catalytic surface and to increase the catalytic activity and/or stability. For example, Pd/C catalyst with the introduction of Fe_2P promoter was reported as an efficient way of improving its catalytic activity in formic acid electro-oxidation in fuel cells reactions [138]. In this project, the research was mainly focused on the active species comprising Cu and Fe metals and supports using an array of zeolites. We also explored the possibility to prepare thin films of zeolites over an inert material like SiC, as well as the incorporation of Fe or Cu centre within the framework of the zeolite rather than nanoparticles.

1.6.1.1 Metal active species

The nature of the active species, or metal active centre, is always the most important factor in the design of a heterogeneous catalyst, whereas in the CWPO process, it is essential that the metal used for catalyst development exists in multiple oxidation states so that it able to transform H_2O_2 to hydroxyl radicals. Basically, Fe (one of the key components in the Fenton reagent) that has the capability of activating H_2O_2 (as shown in Eq. 1.1) is the ideal metal employed in the CWPO of phenol as the formation of the hydroxyl radicals controls the pollutant degradation efficiency. Besides, other metal species (called Fenton-like reagents in the presence of H_2O_2 in aqueous solution) are also potential active species in the CWPO

process since they are able to decompose H_2O_2 to generate free radicals as well in Fenton-like reactions, as illustrated in figure 1.7.

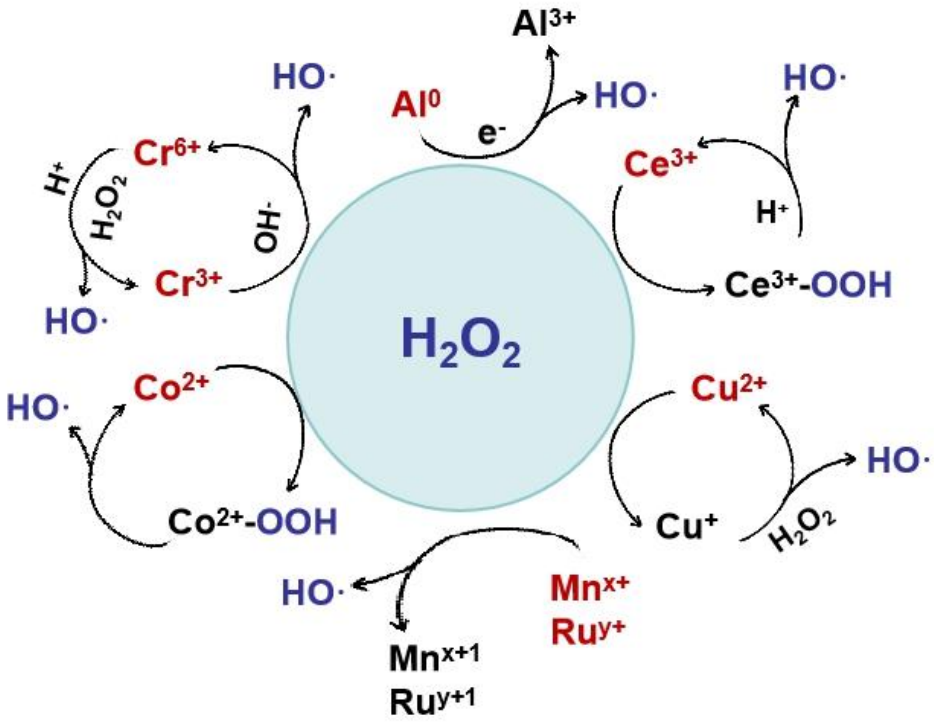

Figure 1.7. Schematic illustration of H_2O_2 activation mechanisms using different nonferrous Fenton-like catalysts, figure reproduced from [119] with permission.

Common active species including Ag [139], Au [140], Ru [141], Pt [142], Ce [143], Cr [144], Mn [145], Cu [146], are all capable of decomposing H_2O_2 to radicals, both in single or combined forms [142,147] were reported. However, catalysts with precious metals (e.g. Ag, Au, Pt) as active species show a certain tendency to deactivation by poisoning during the oxidation [148], which together with the relatively high cost limit their application. As a consequence, recent research in this field focused on the use of earth-abundant transition metals and their oxides owing to their high activity and stability, low cost, and resistance of deactivation. It is well established in the literature that many non-precious metal catalysts including Cu, Fe, Mn, Co, and Ni catalysts are active for the complete removal of phenol from water (as summarized in Table 1.6) in terms of phenol conversion and total organic

conversion (TOC) conversion. All these reported catalysts displayed high activity in phenol oxidation, and among them, those based on copper and iron, are more active and frequently used in the classical Fenton oxidation process due to their higher capability of generating ·OH radicals (as discussed in 1.5.1). Especially Cu, which is even superior over Fe, it presents higher catalytic activity in the CWPO of phenol since it has a higher rate constant (as shown in Eq.1.1 and Eq.1.21) in the decomposition of H_2O_2 to hydroxyl radicals. On the other hand, it can be used in a broader reaction condition, for example, $Cu(OH)_2$ precipitates at around pH 6 [149], which would offer a few more advantages compared to iron (which precipitates at around 4 [113]) in an aqueous reaction, as water at pH 4 does need pre-treatment before reaction but water at pH 6 can be used directly. As such these metal oxides are also investigated in this project either to further improve their activity and stability or as benchmarks.

Table 1.6. Summary of transition metal oxides supported catalysts for the CWPO of phenol reported in the literature.

Active species	Support	Reaction condition	Catalytic activity	Ref.
Fe	pillared clay	70 ºC	X_{Ph}=100%, X_{TOC}= 80%	[150]
	pillared clay	70 °C	X_{Ph}=100%, X_{TOC}= 80%	[151]
	activated carbon	50 °C	X_{Ph}=100%, X_{TOC}= 85%	[152]
	SBA-15	80 °C	X_{Ph}=100%, X_{TOC}= 66%	[153]
	ZSM-5	80 °C	X_{Ph}=99%, X_{TOC}= 78%	[154]
	MCM-41	80 °C	X_{Ph}=98%, X_{TOC}= 75%	[155]
	VSB-5	70 °C	X_{Ph}=100%	[156]
Cu	13X zeolite	60-80 °C	X_{Ph}=100%, X_{TOC}= 50%	[157]
	ZSM-5/PSSF	80 °C	X_{Ph}=100%, X_{TOC}= 85%	[158]
	γ-Al_2O_3	70 °C	X_{Ph}=100%, X_{TOC}= 80%	[159]
	MOF	70 °C	X_{Ph}=99%, X_{COD}= 93%	[160]
	MFI	20 °C	X_{Ph}=78%, X_{TOC}= 61%	[161]
	Activated carbon	80 °C	X_{Ph}=100%, X_{COD}= 90%	[162]
	HY-5	80 °C	X_{Ph}=100%	[163]
	Silicalite-1	70 °C	X_{Ph}=95%	[164]
	polymer	30 °C	X_{Ph}=93%	[165]
Au	Activated carbon	80 °C	X_{Ph}=100%	[166]
Ag	CeO_2	70 °C	X_{Ph}=30%	[139]
Fe/Mn	diatomite	90 °C	X_{Ph}=100%	[167]
Fe/Cr	pillared bentonite	45 °C	X_{Ph}=100%	[168]
Ce/Zr	pillared clay	25 °C	X_{Ph}=100%	[169]
Co-Ni	--	--	X_{Ph}=94%	[170]

Where X_{Ph} was denoted as phenol conversion, X_{TOC} and X_{COD} meant total organic carbon (TOC) conversion and chemical oxygen demand (COD), respectively. The higher activity of catalysts is presented in terms of both the higher phenol conversion and/or the higher TOC conversion.

1.6.1.2 Support

Supports in heterogeneous catalysis are fundamental, otherwise the supported metal species would have the tendency to sinter or aggregate to a bulk form, with detrimentally low dispersion and loss of catalytic activity, as shown in figure 1.8. Whereas using a support to disperse the chosen metal will help to increase the surface area and extend the catalysts' lifetime. Besides, it can also enhance metal-support interactions, which ultimately influence catalyst performance [48]. Hence, the selection of good or appropriate support is also an important step for catalyst development.

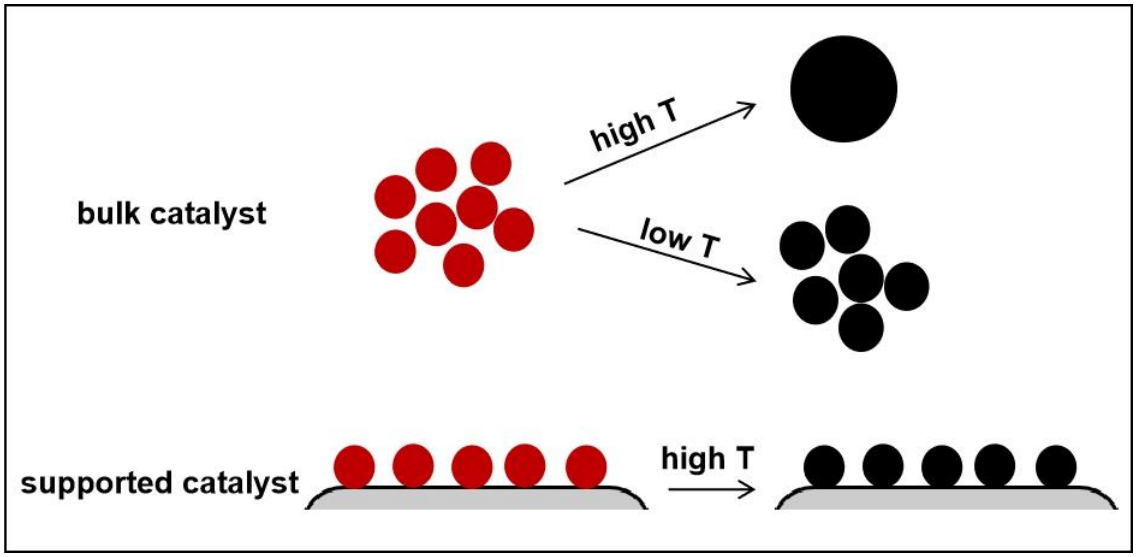

Figure 1.8. Schematic representation of the effect of temperature on catalyst particle size where red points and black points are metal ions and metal oxides, the growth of the size suggests the agglomeration of metal oxides. Figure reproduced from [171] with permission.

In addition, good catalyst supports must fulfill several criteria [172]. They need to have physical and mechanical resistance to stand the temperature, pressure, and stresses encountered in a reactor for a long period of time. It should interact enough with the catalytically active species to provide good physical dispersion and mechanical support, but should not react to the extent of degrading performance of the catalyst itself. The support should not itself catalyse some other, undesired reaction, although it is beneficial when a

support can further promote the reaction of interest, either by intruding geometrical constraints, like in the case of zeolites, or providing acids or basic centres, or by stabilizing one oxidation state of supported metal with respect to another. The support should have an adequate surface area and porosity to provide a facile reaction with little or no diffusion resistance in the pores. Ideally, the support should also be relatively inexpensive. In practical terms, although tens of support can be found in literature, only a few are actually capable to satisfy all of these criteria at the same time. Among the most relevant are: alumina [173,174], silica [175,176], titania [177,178] pillared clays [151,179], activated carbon [162,180], zeolite [157,181] and diatomite [182,183], which are frequently used in phenol oxidation reactions (in table 1.6).

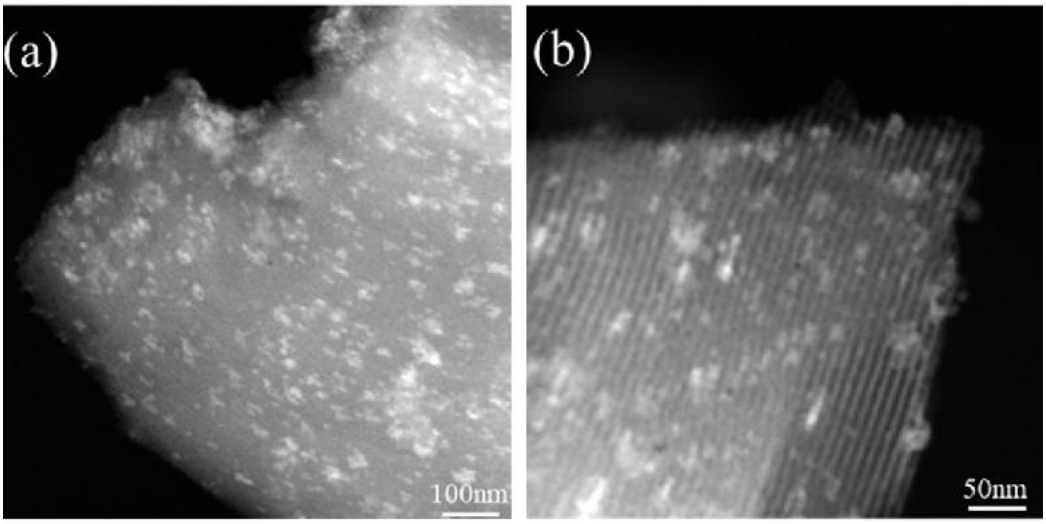

Figure 1.9. TEM images of Fe_2O_3/SBA-15 prepared by the incipient wetness method, where the white particles on the surface of SBA-15 are supported metal oxide particles. Figure reproduced from [142] with permission.

Among those reported materials, zeolites are one of the most widely employed supports for phenol oxidation due to their unique properties such as: uniform and reproducible pore size (0.3 - 2 nm range [184,185]), large specific surface area (> 200 $m^2 \cdot g^{-1}$), adjustable acidity, and the possibility to incorporate transition metal ions into their framework. For example, a larger pore size than the substrate molecular allows reaction occurs in the pore/channel of

zeolites; the high surface area improves metal dispersion; the acid sites originated from Al incorporation increase the activity of phenol decomposition whereas the metal species that replacing Al sites in the framework may contribute to the better catalytic performance of catalysts. Iron oxides, as shown in the image of metal-supported zeolite catalyst in figure 1.9, were uniformly dispersed on the surface of the zeolite support in the form of the small white particles (< 20 nm) owing to the large surface area, which evidencing the positive effects of the catalyst support. Thus, zeolites are also the main supports used in our project.

1.6.2 Zeolite catalysts in the CWPO process

The name ‘zeolite’, first recognized in 1756, was termed by the Swedish mineralogist Axel Fredrik Cronstedt to describe stilbite, the first classified zeolite mineral. ‘Zeolite’ is a combination of the two Greek words ‘zeo’, meaning ‘to boil’, and ‘lithos’, meaning ‘a stone’ [186]. This describes the ability of zeolites to reversibly release and take up water depending on the temperature and moisture level of the external environment.

Zeolites are hydrated crystalline aluminosilicates of natural or synthetic origin with highly ordered structures [136]. They consist of SiO_4 and AlO_4 tetrahedra (written as TO_4 (T = Si, Al)), which are interlinked through oxygen atoms to give rise to building blocks that are octagonal, hexagonal, cubic, polyhedral (pentasil for ZSM-5 zeolite), as shown in figure 1.10. The negative charges of aluminum-oxygen tetrahedron are compensated with cations.

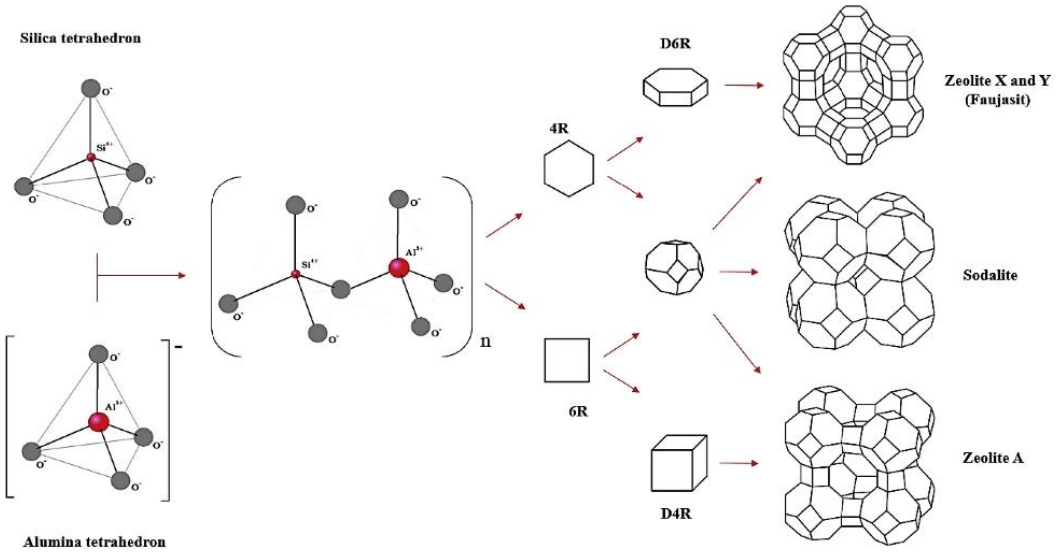

Figure 1.10. The framework structures of zeolites with AlO_4 and SiO_4 as basic unit (O atoms - dark grey balls, Si atoms - small red balls, Al atoms - big red balls). Figure reproduced from [187] with permission.

The chemical composition of a zeolite can hence be represented by a formula as follows [188]: $M^{n+}_{x/n}[(AlO_2^-)_x(SiO_2)_y]\cdot wH_2O$, where M represents the exchangeable cation and is generally a Group I or II ion (e.g. Na^+, K^+, Ca^{2+}, H^+), although other metal, non-metal and organic cations may also balance the negative charge created by the presence of Al in the structure [189], (n) is the valence of the cation, (w) is the number of water molecules per unit cell, (x+y) is the number of tetrahedra per crystallographic unit cell and x/y is the so-called framework silicon/aluminium ratio, n_{Si}/n_{Al} (or simply Si/Al). Typically, the formula of ZSM-5 zeolite is $Na_nAl_nSi_{96-n}O_{192}\cdot 16H_2O$.

Zeolites are also called molecular sieves. Some of them occur naturally as minerals (and identified by using a framework code to distinguish them, e.g. CHA, FAU, MOR), while most of them are prepared synthetically (which most common frameworks identifiers are known as MFI, BEA, LTA). At present, there are more than 200 unique zeolite frameworks identified, and over 40 naturally occurring zeolite species are known, as recorded by International Zeolite Association (IZA).

1.6.2.1 Zeolite catalysts with different structural properties

Zeolites are crystalline solids with very regular porous structures which have a very significant bearing on their applications, such as catalysis and adsorption [190]. A particular pore system exerts a steric influence on the reaction, controls the access of reactants and products, by shape-selectivity. Apart from the geometrical aspects related to the pore structure, zeolites can be fine-tuned by changing the composition both of the structure itself (changing the Si/Al ratio) and of the cations that serve as counter-ions to the structure itself (namely by ion-exchange of these cations). The specific characteristics of zeolites are, to some extent, responsible for their ability to catalyse chemical reactions while changing structure and composition allows us to have zeolites with different properties. Among the various zeolites, both natural and synthetic, have been discussed in the CWPO of phenol so far.

For example, the effects of framework and pore size of different supports on the activity of phenol degradation were investigated. Zeolites, in terms of pore size, are classified as microporous (pore size less than 2 nm) and mesoporous (pore size of 2-50 nm) zeolites, examples are ZSM-5 (pore size of 5.4−5.6 Å, namely, 0.54−0.56 nm) zeolites, and SBA-15 (pore diameter of 5-15 nm) silica respectively. The pore size and distribution of catalyst or support sometimes play important role in chemical reactions. On the one hand, the existence of the pores provides more surface area to disperse the active sites more uniformly, while the metal dispersion is to some extent related to the reaction rate. On the other hand, the distribution of pore sizes also affects the selectivity of a reaction. A microporous catalyst might be advantageous if it is desired to react selectively to the small molecules in a complex mixture since large molecules would have difficulty penetrating the micro-pores. Inversely, a macro-porous catalyst might be preferred if the reactant is a large molecule. For example, Calleja [191] studied the activity of iron supported catalysts with different structure such as Fe-SBA-15, amorphous SiO_2-Fe_2O_3 mixed oxide and Fe-Silicalite-1 in the CWPO of phenol under the same reaction conditions. Among them, the Fe_2O_3 supported mesostructured

SBA-15 material showed the best performance, reaching a 100% removal of aromatic compounds with TOC reductions up to ca. 70% in only 10 min. The possible reason for this trend is that the organic matter is more accessible to the active iron sites owing to the larger pore size. Similarly, Vakaj [192] investigated the catalytic activity and stability of Cu/Y5 and Cu/ZSM-5 zeolites in phenol oxidation with hydrogen peroxide as oxidant. It was found that the activity of Cu/Y5 catalyst (phenol conversion of 99% at 60 ^{o}C) was generally higher than that of Cu/ZSM-5 (phenol conversion of 66% at 60 ^{o}C) as it catalysed phenol oxidation more efficiently, which is due to the lower diffusion resistance of molecules in the pore of the Cu/Y5 catalyst.

In addition, zeolite catalysts with different Si/Al ratios (either expressed as SiO_2:Al_2O_3 or Si:Al) were also frequently investigated. In general, silicon is the main component responsible to maintain the framework structure of molecular sieves as it is present in much larger amount, while alumina provides acid sites, so adjusting the Si: Al ratio often leads to different results. Acidity is one of the most important characteristics of zeolites which makes them very useful in catalysis. Zeolites with various Si: Al ratios have been widely investigated, even pure silica zeolite since it always shows higher thermal stability. For instance, Chen [193] tested the three catalysts, Fe/ZSM-5-1 (Si: Al of 181), Fe/ZSM-5-2 (Si: Al of 37), Fe/ZSM-5-3 (Si: Al of 21,) prepared by incipient-wetness impregnation method in the CWPO reaction of cresol at 30 ^{o}C. Among these three catalysts, the catalytic activities of all the Fe/zeolites followed the sequence: Fe/ZSM-5-3 > Fe/ZSM-5-2 > Fe/ZSM-5-1, indicating that the Si: Al ratio is an important parameter influencing the catalytic degradation of cresols. The authors explained the difference by the higher ability of the zeolite with lower Si: Al ratio to accelerate HO· generation. Moreover, Cihanoğlu [194] investigated the acetic acid degradation over catalysts in the presence of H_2O_2 at 60 ^{o}C. In his study, a series of Fe/ZSM-5 zeolite catalysts with different Si/Al ratio (12.4-42.0) were prepared by ion-exchange method. The iron content, Brønsted acidity and catalytic activity of the catalysts were all affected by the Si/Al ratio of the zeolites. In addition to cresol and acetic acid, the influence of Si/Al ratio of zeolite on the

decomposition of formic acid was also proved. As reported by Taran [195], Cu-ZSM-5 zeolites (atomic Si: Al ratio of 17, 30 and 45) prepared by ion exchange showed apparently different efficiency in formic acid removal. The highest catalytic activity is observed over catalysts based on zeolite with Si: Al ratio of 30, the lowest with the zeolite with Si: Al of 17.

1.6.2.2 Zeolite catalysts with different metal-support interactions

A heterogeneous catalyst is a material, characterised by the relative amounts of different components (active species, physical and/or chemical promoters, and supports), size, pore volume and distribution, surface area and so on. The optimal catalyst is the one that provides the necessary combination of properties (activity, selectivity, lifetime, ease of regeneration and toxicity) at an acceptable cost. Thus, except for the structural properties of zeolite, other aspects such as the metal-support interactions, are also important to determine the final activity of these materials, this important aspect of a catalyst structure is briefly described here.

Different metal-in-zeolite structures are defined according to the location of the nanoparticles and their interactions with the zeolite support, as shown in figure 1.11. As it can be seen, the metal species exist in the form of: (1) isolated clusters, (2) covalent metal centres and (3) heteroatoms incorporated into the framework. Besides, the three categories of catalysts with different metal-support configurations can be usually classified as metal-supported zeolite catalyst (sample i and sample ii in figure 1.11) and metal-substituted zeolite catalyst ((sample iii in figure 1.11) according to the location of the metal species.

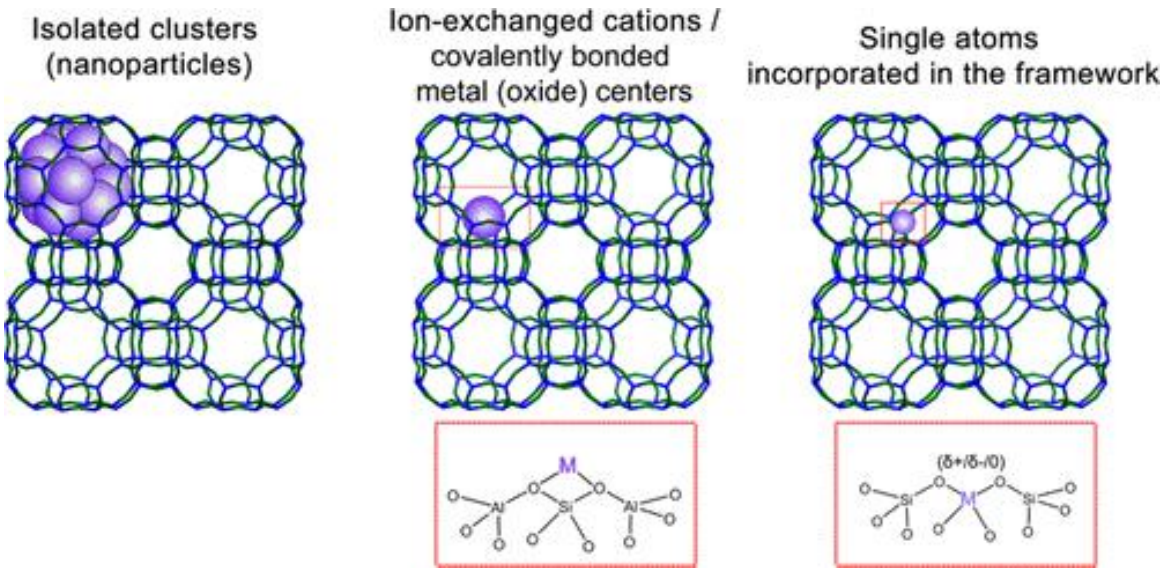

Figure 1.11. Possible zeolite–metal composite configurations: (i) isolated clusters/nanoparticles on the surface (left), (ii) covalently bonded metal oxides on the surface (middle), (iii) single atom incorporated in the framework (right), figure reproduced from [196] with permission

The different metal-support configurations could be influenced by the ways of introducing or fixing the active phase on a pre-existing solid. The metal-supported zeolite catalysts are usually prepared by post-synthesis method (such as impregnation, ion exchange, deposition-precipitation, etc.), which having the advantages of easily controlled dispersion, loading and location of metal species. Meanwhile, metal oxides are produced or aggregated outside of the framework, which result in easy and undesired leaching of active sites in the liquid-phase reactions.

In comparison, the metal-substituted zeolite catalysts are usually prepared by direct synthesis (usually hydrothermal synthesis). In the direct-synthesis method, the condensation of silicon and metal species around the organic micelles occur simultaneously, and it is likely that some of the metal species are trapped in the silica matrix during the formation of the silica support. However, the synthesis itself is a complicated and time-consuming process while the metal-substituted zeolites (especially with high metal loading) prepared via direct synthesis often exhibit morphologies and structures with a poor level of crystallinity or worse

order. Thus, the synthesis of zeolite with heteroatoms in the framework and special morphology poses further challenges in the catalyst preparation step.

Compared to metal nanoparticles, which are generally supported on the external surface of solid supports, localizing metal species within the internal framework of zeolite usually leads to improvements in the catalytic performances [197] because zeolites with heteroatom substituted Si or Al sites in the framework exhibit quite different properties from the conventional aluminosilicate zeolites in aspects of surface acidity, pore structures, particle size and so on. The superior performance of a heteroatom substituted zeolite (sample iii in figure 1.11) over the metal impregnated zeolite catalyst (sample i in figure 1.11) was proved. For example, Yan et al [198] tested the intra-framework Fe (Fe-ZSM-5/PSSF prepared by hydrothermal method) and extra-framework Fe (Fe_2O_3/ZSM-5/PSSF by incipient wetness impregnation) catalysts for the CWPO of phenol in a fixed bed reactor. The results showed that the Fe-ZSM-5/PSSF was far more active than Fe_2O_3/ZSM-5/PSSF for phenol oxidation, as the phenol conversion and TOC conversion after 7 h reached 92% and 46% respectively over framework Fe^{3+} species and < 80%, and < 20%, respectively over supported metal oxides. In addition, the higher stability of framework Fe than extra-framework Fe_2O_3 catalyst was also observed from the Fe leaching of the two catalysts. Furthermore, the higher catalytic activity and stability of the metal-substituted zeolite (sample iii in figure 1.11) over the ion exchanged metal zeolite catalyst (sample ii in figure 1.11) was also reported. For instance, Valkaj [199] prepared Cu/ZSM-5 catalysts by two different methods: by ion-exchange (IE) from the protonic form of commercial ZSM-5 zeolite, and by direct hydrothermal synthesis (DHS). Also, it was evident that the activity of Cu/ZSM-5 catalyst prepared by direct hydrothermal synthesis was higher than in the case when catalyst is prepared by ion exchange method, so was the stability (4.8% for sample prepared by IE method and 3.2% for sample prepared by DHS method).

1.6.2.3 Zeolite catalysts with different macroscopic form

It is worth mentioning that changes of macroscopic parameters of a solid catalyst such as size and shape may also affect the performance of a catalyst in a chemical reaction. That is, besides the need, at industrial level, to uniformly fill up a fixed catalytic bed of a reactor with solid catalyst in the macroscopic forms of powder, granule, pellets sphere, extrudate, coating (figure 1.12). Macroscopic variations are also present in the CWPO process. In this thesis work we also considered powders, pellets and coatings forms.

Figure 1.12. Typical forms of zeolite catalysts, powder (left), pellet (middle) and coating (right) on stainless steel [200]

In a lab scale, zeolites are mostly used in powder form (examples in table 1.6), as in a lab scale batch reactors are more common to use (and they don't involve pressure drop that would be present in a continuous flow reactor and catalytic bed if a fine powder is used). In usual, in a batch reactor, the powder form benefits from a higher surface-to-volume ratio, higher contacting efficiency and lower diffusion resistance. As illustrated in figure 1.13, where the powder catalyst (14.4 μm) presented higher selectivity to CO_2 than the extrudated catalyst (1.3 mm) in a discontinuous stirred-tank reactor due to the enhanced internal diffusion.

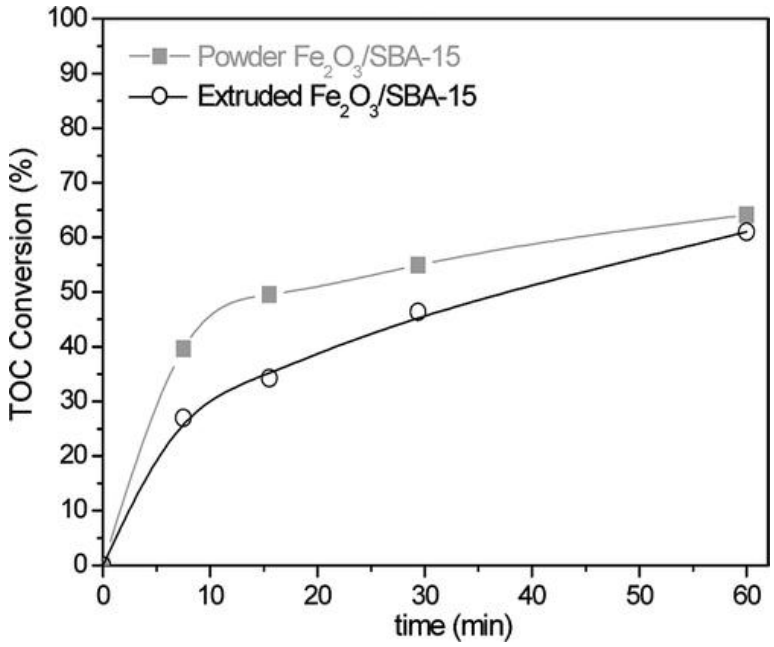

Figure 1.13. Catalytic test over powder and extruded Fe_2O_3/SBA-15 for phenol treatment in a discontinuous stirred-tank reactor. ($[Ph-OH]_0$ = 1 g·L^{-1}; $[H_2O_2]_0$ = 5.1 g·L^{-1}; [cat] = 0.6 g·L^{-1}; T = 80 ^{o}C), figure reproduced from [153] with permission.

By contrast, larger size of zeolites (in pellet form) that can be obtained mechanical pressing, granulation, extrusion, are technically more suitable for engineering applications and scale up, because they are easy to be filtered and recycled. Meanwhile, zeolite pellets offer benefits such as good mechanical properties, low operation cost, low-pressure drop and drawbacks such as high manufacturing cost, easy crushing and abrasion, low contacting efficiency and so on. In this perspective, zeolite coating on a supported foam material would be a highly attractive material for CWPO applications as it would combine the characteristics of different foam materials (porosity, heat conductivity, mechanical strength, chemical stability) with that of different zeolites (porous structure, surface property, hydrothermal stability). In fact the development of these materials is also explored in detail in this thesis (section 5.3 in chapter 5) as it would also represent a novel form of material and with the promise to show better performance than traditional zeolites. For example, Jiang [201] reported the synthesis of Cu-MFI zeolite coating supported on paper-like sintered stainless fibre (PSSF) and its use in the CWPO of phenol in a batch reactor. The coating catalyst exhibited high catalytic activity

with phenol conversion of 100% and H_2O_2 conversion of 99%, respectively. In particular, the coating zeolite presented higher stability over other type of Cu/zeolite catalysts, indicating its potential.

In addition, it should be stressed that the criteria of selection of macroscopic form might not necessarily be identical for different applications. As mentioned above, in batch reactors, where diffusion resistance plays an important role, powder form with small particle size is common while in flow reactors, pellets and coating form that reduce pressure drop efficiently are more viable options. For example, Liu [202] applied the Fe-13X catalyst (column form with a diameter of 1.6 mm) for the CWPO of methyl orange into a batch reactor and a flow reactor, respectively. It was found that the column form of Fe-13X zeolite catalyst showed high activity (methyl orange over 90%) in both reactors and long-term stability in the flow reactor with negligible loss of activity in 3 cycles of reaction.

Overall, great achievements on the CWPO of phenol over zeolite catalysts have been reached so far: 1) High removal efficiency. Owing to the high activity of various metal-doped zeolite catalysts, complete decomposition of phenol was reported (table 1.6). 2) High selectivity. High TOC conversion (CO_2 formation) of over 80% (table 1.6) and almost complete removal of toxic intermediates (e.g. catechol) were widely reported [191,203] when using metal-supported zeolite catalyst at optimal conditions. 3) Mild reaction conditions. The high conversion of phenol over zeolite catalysts at even room temperature and atmospheric pressure was achieved [161,204,205]. 4) Decreased cost: H_2O_2 is one of the important factors that influencing the application of CWPO due to the expensive price. Much effort was made to reduce the cost by increasing the efficiency of H_2O_2 in the oxidation process and huge progress has been made. For example, different H_2O_2 addition modes [115,206] such as in one go (most widely used in a batch reactor), drop by drop in a certain time interval, or in continuous mode were used while the latter two were more effective in terms of H_2O_2 efficiency. 5) Continuous degradation. It was reported in the literature [153,154] that using a

fixed bed reactor in the CWPO of phenol process enabled the treatment of high volume of wastewater in industry continuously.

However, the suitability of a heterogeneous catalyst for an industrial process depends not only on activity and selectivity but also on stability. Catalyst stability can be assessed by measuring activity or selectivity as a function of time, while poor stability of catalyst usually leads to loss of activity thus increase the operating cost. The deactivation behaviour of conventional metal-supported zeolite catalysts in the CWPO of phenol process was reported (as shown in table 1.7) and is a bottleneck for industrial application.

1.6.3 Catalyst deactivation

Catalyst deactivation, the loss of catalytic activity and/or selectivity with time on stream, is a problem of great and continuing concern in the industrial applications of heterogeneous catalysts. The catalyst replacement and process shutdown cost the industry billions of dollars per year [207]. The causes of catalyst deactivation are basically threefold (figure 1.14): chemical (poisoning, leaching, change of catalyst structure), mechanical (fouling, friction/crushing), and thermal (thermal degradation, sintering) [207,208], while in the liquid phase CWPO reaction the deactivation is usually triggered by carbonaceous deposit by polymeric material on the catalyst [209-211], poisoning by impurities in the feed or by reaction by-products, and leaching of active species from the catalyst into the reaction media [212]. It is inevitable that any real catalysts will decay [207,213], while an important distinction that needs to be mentioned between the deactivated catalysts is whether they are reversible or irreversible, renewable or non-renewable. Thus the understanding of the deactivation mechanism is of great importance to enhance the stability of heterogeneous catalyst in the liquid phase reaction and accordingly, design catalyst with high reusability.

In the CWPO literature, catalyst deactivation by leaching is of prime concern. Leaching usually refers to the dissolution of the active sites from the heterogeneous catalyst into the

reaction medium. Unlike other deactivation processes, deactivation of catalysts by metal leaching is usually irreversible and non-renewable [208,215], this is why the study of leaching is so important in liquid-phase reactions. Leaching is obviously an economic as well as environmental problem as it reduces the life of catalysts. Besides, leaching also poses significant challenges to the purification of the downstream effluents since it, in most cases heavy metals, requires additional separation steps.

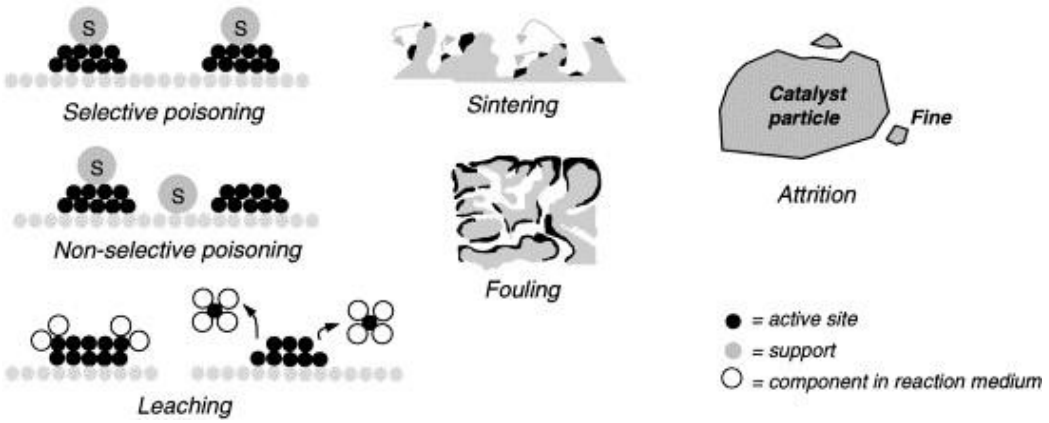

Figure 1.14. Causes of catalyst deactivation in heterogeneous catalysis including poisoning, fouling, thermal degradation, corrosion and leaching (sulfur atoms - solid grey balls marked S, active sites - solid black balls, supports - solid grey balls, reactants - hollow balls). Figure reproduced from [214] with permission.

It follows that an 'ideal' heterogeneous (solid) Fenton catalyst, should not be prone to metal leaching. Unfortunately, most of the catalysts tested so far in the CWPO suffered the loss of active species, as reported in the literature (Table 1.7). As shown, severe leaching, i.e. active metal loss was observed in most cases, with some of the leaching even exceeding 50%, posing significant challenges to the enhancement of the stability of the catalyst. As a result, the catalysts must be regenerated or eventually replaced after one or two cycles of reactions. Though this data in table 1.7 seems discouraging, there are also examples where leaching of catalysts in phenol oxidation has not been observed or conditions for negligible leaching have been found. Thus, it is proved that protecting the catalyst from metal leaching in the CWPO process is possible in theory.

Table 1.7. Metal leaching of various heterogeneous catalysts in phenol CWPO process

No.	catalyst	Initial reactant	M: S	T (°C)	pH_0	time	phenol, H_2O_2, TOC	Leaching	Ref.
1	Cu-Silicalite-1-IE (5.29 wt%, 0.6 g·L^{-1})	1 g·L^{-1} phenol, HP/phenol ratio of 10	1:21	70	NG	2 h	NG, NG, NG	86.9%	[164]
2	Cu/13X (3.6 wt%, 0.5 g·L^{-1})	0.01 M phenol, 0.1 M H_2O_2	1:35	80	NG	3 h	NG, NG 54%	66%	[157]
	Cu/13X (3.7 wt% 0.5 g·L^{-1})	0.01 M phenol, 0.1 M H_2O_2	1:34	80	NG	3 h	NG, NG, 52%	36%	
	Cu/13X (3.4 wt% 0.5 g·L^{-1})	0.01 M phenol, 0.1 M H_2O_2	1:37	80	NG	3 h	NG, NG, 54%	68%	
	Cu/13X (3.6 wt%, 0.5 g·L^{-1})	0.01 M phenol, 0.1 M H_2O_2	1:35	80	NG	3 h	NG, NG, 53%	19%	
3	Fe/AC (4%, 500 mg·L^{-1})	100 mg·L^{-1} phenol, 500 mg·L^{-1} H_2O_2	1:2.94	70	3.0	4 h	100%, 100%, 88%	39% (7.8 mg·L^{-1})	[216]
4	Fe/AC (2%, 500 mg·L^{-1})	0.1 g·L^{-1} phenol, 0.5 g·L^{-1} H_2O_2	1:5.96	50	3	1 h	NG, NG, 86%	25%	[217]
5	Cu-polymer (30%)	1 g·L^{-1} phenol, Ph/H_2O_2 ratio of 1/14	1:14	40	6	4 h	92%, NG, 43%	13% (6.2 mg·L^{-1})	[165]
6	Fe/AC (4%)	100 mg·L^{-1} phenol, 500 mg·L^{-1} H_2O_2	1:2.70	50	3.0	4 h	NG, 96%, 81%	10% (2.2 mg·L^{-1})	[104]
	Fe/AC (4%)	1000 mg·L^{-1} phenol, 5 g·L^{-1} H_2O_2	1:2.93	50	3.0	4 h	NG, 100%, 85%	16% (32.5 mg·L^{-1})	
7	Cu/ZSM-5-IE (2.32-3.52%, 0.1 g·L^{-1})	0.01 M phenol, 0.1 M H_2O_2	1:159-241	NG	NG	3 h	NG, NG, NG	4.8%	[199]
	Cu/ZSM-5-IE (1.62-3.24%, 0.1 g·L^{-1})	0.01 M phenol, 0.1 M H_2O_2	1:173-346	NG	NG	3 h	NG, NG, NG	3.2%	
8	Cu/Al_2O_3 (30%,10.35 g·L^{-1})	1g·L^{-1} phenol, H_2O_2: ph=14	1:0.22	50	NG	3 h	NG NG, NG	1.7%	[218]
9	Fe-TSC-2 (5.63%, 3 g·L^{-1})	100 mg·L^{-1} phenol, 11.8 mM H_2O_2	1:0.35	60	3.0	2.5 h	98%, NG, 66%	1.25% (2.11 mg·L^{-1})	[219]
10	Fe/γ-Al_2O_3 (4%, 1250 mg·L^{-1})	100 mg·L^{-1} phenol, 500 mg·L^{-1} H_2O_2	1:1.2	50	3	8 h	100%, 81%, 78%	1.8% (0.9 mg·L^{-1})	[174]
11	Fe/pillared clays (3.01%, 5 g·L^{-1})	0.5 mM phenol 0.2 mmol·h^{-1} H_2O_2	1:0.93	25	3.7	4 h	NG, NG, 65%	0.13% (0.2 mg·L^{-1})	[151]
12	Fe/pillared clays (4.9%, 10 g·L^{-1})	50 mg·L^{-1} phenol, H_2O_2: ph=1.2	1:0.06	70	3.5	2 h	100%, NG, 78%	0.04% (0.2 mg·L^{-1})	[150]

NG: data not given in the literature.

Other deactivation mechanisms such as carbonaceous deposit were also reported in the phenol oxidation process. For instance, Delgado et al. [220] reported the loss of activity of the Ce-Mn composite catalyst in the oxidation of phenol after reaction time of 50-100 min. The reason for the activity loss was proved as carbonaceous deposits since a thick carbonaceous layer (20 nm) was observed on the surface of the spent catalyst in the TEM image (as shown in figure 1.15). Moreover, the TPO and TPD experiments over the spent catalyst also evidenced the hydrocarbon-like nature of the deposited layer which might be due to the oxidative polymerization of phenol.

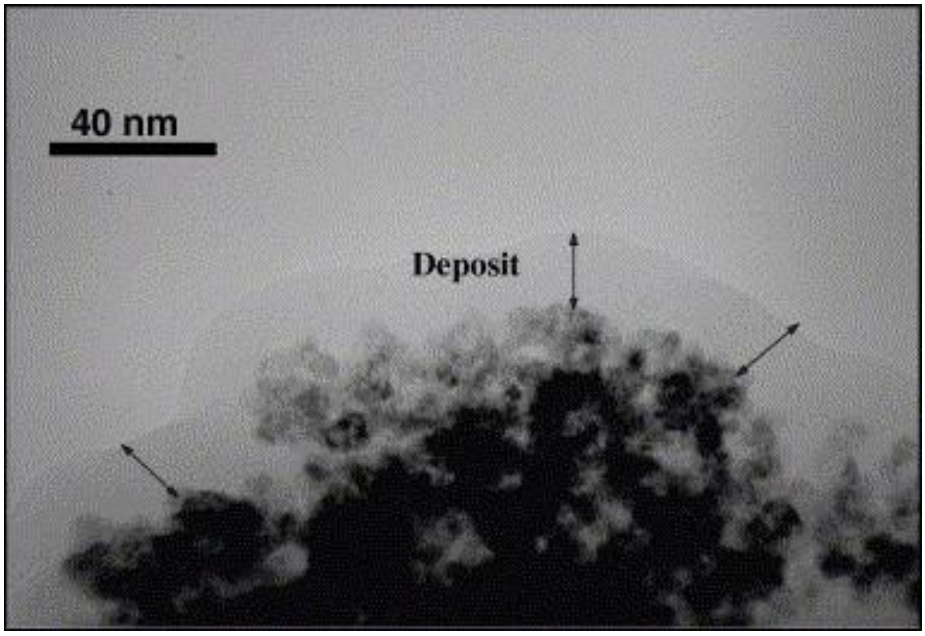

Figure 1.15. TEM image of the used CeMn catalyst after phenol oxidation reaction, where a thick carbonaceous layer (20 nm) is covering the entire sample. Figure reproduced from [220] with permission.

Loss of activity due to carbonaceous deposit is usually reversible by subjecting the catalyst to a calcination step in the presence of air or oxygen to burn the carbonaceous species deposited onto the catalyst surface [215]. As such, the carbonaceous deposit on the Ce-Mn catalyst reported above was fully oxidized to CO_2 and H_2O by calcination above 250 ^oC and after this treatment, the collapsed catalyst recovered its initial catalytic activity, thus

confirming the role of the carbonaceous deposit on the activity loss for phenol elimination. Though it is impossible to avoid catalyst deactivation, regeneration is generally a preferred option than replacement of catalyst from an industrial point of view. Besides, some other similar examples were also reported [221-223].

The loss of activity in the phenol oxidation has been found to occur upon a relatively short time on stream (from minutes to hours) thus it is well accepted that the most important issue in the heterogeneous Fenton process is the development of a heterogeneous catalyst capable of combining activity and long-term stability at a reasonable cost. One of the approaches to prevent or slow catalyst deactivation in this project is to design catalysts with specific properties to minimize these effects.

1.7 Project aims

In view of this background and context, this research project aims to develop an active and stable catalyst for phenol decomposition based on the CWPO technique. The high activity of the catalyst (Cu- and Fe-based catalysts for instance) was widely reported in the literature whereas the stability of the catalyst in the CWPO process is still a challenge. Thus this project would mainly focus on the mechanism of catalyst deactivation in the phenol oxidation process and accordingly, enhance the stability of the prepared catalysts in this liquid phase reaction. Meanwhile, the synthesis and design of zeolite catalysts with different metal-support configurations would also be at the centre of this project to explore whether the metal-substituted zeolite catalyst is a potential solution to the catalyst deactivation issue in the CWPO of phenol reaction.

1.8 References

[1]. Drinking-water, https://www.who.int/news-room/fact-sheets/detail/drinking-water.

[2]. UN World Water Development Report 2021, https://unesdoc.unesco.org/ark:/48223/pf0000375724.

[3]. Drinking-water, https://www.who.int/news-room/fact-sheets/detail/drinking-water.

[4]. UN World Water Development Report 2017, https://www.unwater.org/publications/world-water-development-report-2017/.

[5]. Priority Pollutant List, https://www.epa.gov/sites/production/files/2015-09/documents/priority-pollutant-list-epa.pdf.

[6]. Substance list: National Pollutant Release Inventory, https://www.canada.ca/en/environment-climate-change/services/national-pollutant-release-inventory/substances-list/threshold.html.

[7]. M. Alshabib and S. A. Onaizi, *Sep Purif Technol*, 2019, **219**, 186-207.

[8]. C. I. Nair, K. Jayachandran and S. Shashidhar, *Afr J Biotechnol*, 2008, **7**.

[9]. R. Gingell, J. O'Donoghue, R. J. Staab, I. W. Daly, B. K. Bernard, A. Ranpuria, E. J. Wilkinson, D. Woltering, P. A. Johns and S. B. Montgomery, *Patty's Toxicology*, 2001.

[10]. K. M. Basha, A. Rajendran and V. Thangavelu, *Asian J Exp Biol Sci*, 2010, **1**, 219-234.

[11]. W. Ali, S. K. Rout, S. Guin, A. Modi, A. Banerjee and B. K. Patel, *Adv Synth Catal*, 2015, **357**, 515-522.

[12]. G. Busca, S. Berardinelli, C. Resini and L. Arrighi, *J Hazard Mater*, 2008, **160**, 265-288.

[13]. W. W. Anku, M. A. Mamo and P. P. Govender, *Phenolic compounds-natural sources, importance and applications*, 2017, 419-443.

[14]. A. Krastanov, Z. Alexieva and H. Yemendzhiev, *Eng Life Sci*, 2013, **13**, 76-87.

[15]. B. Lochab, S. Shukla and I. K. Varma, *Rsc Adv*, 2014, **4**, 21712-21752.

[16]. N. Rothman, W. E. Bechtold, S. N. Yin, M. Dosemeci, G. L. Li, Y. Z. Wang, W. C. Griffith, M. T. Smith and R. B. Hayes, *Occup Environ Med*, 1998, **55**, 705-711.

[17]. R. S. Davidson, *J Photoch Photobio B*, 1996, **33**, 3-25.

[18]. Y. Tsuruta, S. Watanabe and H. Inoue, *Anal Biochem*, 1996, **243**, 86-91.

[19]. E. El-Ashtoukhy, Y. A. El-Taweel, O. Abdelwahab and E. M. Nassef, *Int. J. Electrochem. Sci*, 2013, **8**, 1534-1550.

[20]. W. Duan, F. Meng, H. Cui, Y. Lin, G. Wang and J. Wu, *Ecotox Environ Safe*, 2018, **157**, 441-456.

[21]. G. L. Phipps, G. W. Holcombe and J. T. Fiandt, *Bull Environ Contam Toxicol*, 1981, **26**.

[22]. N. C. Saha, F. Bhunia and A. Kaviraj, *B Environ Contam Tox*, 1999, **63**, 195-202.

[23]. H. Babich and D. L. Davis, *Regul Toxicol Pharm*, 1981, **1**, 90-109.

[24]. W. Duan, F. Meng, Y. Lin and G. Wang, *Environ Toxicol Phar*, 2017, **52**, 170-176.

[25]. C. Okumura, O. Miki, Y. Sakamoto and T. Fukami, *J Appl Phycol*, 2018, **30**, 2083-2090.

[26]. S. N. Jarvis, R. C. Straube, A. L. Williams and C. L. Bartlett, *Br Med J (Clin Res Ed)*, 1985, **290**, 1800-1802.

[27]. E. L. Baker, P. J. Landrigan, P. E. Bertozzi, P. H. Field, B. J. Basteyns and H. G. Skinner, *Arch Environ Hea: Int J*, 1978, **33**, 89-94.

[28]. L. G. C. Villegas, N. Mashhadi, M. Chen, D. Mukherjee, K. E. Taylor and N. Biswas, *Curr Pollut Rep*, 2016, **2**, 157-167.

[29]. T. Al-Khalid and M. H. El-Naas, *Crit Rev Env Sci Tec*, 2012, **42**, 1631-1690.

[30]. J. Michałowicz and W. Duda, *Pol J Environ Stud*, 2007, **16**.

[31]. S. Al-Asheh, F. Banat and L. Abu-Aitah, *Sep Purif Technol*, 2003, **33**, 1-10.

[32]. G. Dursun, H. Çiçek and A. Y. Dursun, *J Hazard Mater*, 2005, **125**, 175-182.

[33]. H. Jiang, Y. Tang and Q. Guo, *Sep Sci Technol*, 2003, **38**, 2579-2596.

[34]. C. Yang, Y. Qian, L. Zhang and J. Feng, *Chem Eng J*, 2006, **117**, 179-185.

[35]. A. S. Narang, C. A. Vernoy and G. A. Eadon, *J AOAC*, 1983, **66**, 1330-1334.

[36]. M. T. Galceran and F. J. Santos, *Org Micropollut Aquat Environ*, 1988, 46-51.

[37]. B. Sinha, U. K. Ghosh, N. C. Pradhan and B. Adhikari, *J Appl Polym Sci*, 2006, **101**, 1857-1865.

[38]. X. Hao, M. Pritzker and X. Feng, *J Membrane Sci*, 2009, **335**, 96-102.

[39]. M. A. Al-Obaidi, C. Kara-Zaitri and I. M. Mujtaba, *J water process eng*, 2017, **18**, 20-28.

[40]. A. Mnif, D. Tabassi, M. Ben Sik Ali and B. Hamrouni, *Environ Prog Sustain*, 2015, **34**, 982-989.

[41]. A. Bódalo, E. Gómez, A. M. Hidalgo, M. Gómez, M. D. Murcia and I. López, *Desalination*, 2009, **245**, 680-686.

[42]. R. Kumar and P. Pal, *Water Environ Res*, 2013, **85**, 447-455.

[43]. M. Sulyman, J. Namiesnik and A. Gierak, *Pol J Environ Stud*, 2017, **26**.

[44]. F. A. Banat, B. Al-Bashir, S. Al-Asheh and O. Hayajneh, *Environ Pollut*, 2000, **107**, 391-398.

[45]. M. Djebbar, F. Djafri, M. Bouchekara and A. Djafri, *Appl Water Sci*, 2012, **2**, 77-86.

[46]. S. Mirmohamadsadeghi, T. Kaghazchi, M. Soleimani and N. Asasian, *Appl Clay Sci*, 2012, **59**, 8-12.

[47]. L. Zhu, Y. Deng, J. Zhang and J. Chen, *J Colloid Interf Sci*, 2011, **364**, 462-468.

[48]. X. Zhang, A. Li, Z. Jiang and Q. Zhang, *J Hazard Mater*, 2006, **137**, 1115-1122.

[49]. A. Pacholczyk, A. P. Terzyk, M. Wiśniewski, P. A. Gauden, R. P. Wesołowski, S. Furmaniak, A. Szcześ, E. Chibowski and B. Kruszka, *J Colloid Interf Sci*, 2011, **361**, 288-292.

[50]. N. T. Abdel-Ghani, G. A. El-Chaghaby and F. S. Helal, *J Adv Res*, 2015, **6**, 405-415.

[51]. M. Khalid, G. Joly, A. Renaud and P. Magnoux, *Ind Eng Chem Res*, 2004, **43**, 5275-5280.

[52]. R. I. Yousef, B. El-Eswed and H. Ala A, *Chem Eng J*, 2011, **171**, 1143-1149.

[53]. S. F. Lütke, A. V. Igansi, L. Pegoraro, G. L. Dotto, L. A. A. Pinto and T. R. S. Cadaval, *J Environ Chem Eng*, 2019, **7**, 103396.

[54]. S. Mukherjee, S. Kumar, A. K. Misra and M. Fan, *Chem Eng J*, 2007, **129**, 133-142.

[55]. C. Moreno-Castilla, J. Rivera-Utrilla, J. P. Joly, M. V. López-Ramón, M. A. Ferro-García and F. Carrasco-Marín, *Carbon*, 1995, **33**, 1417-1423.

[56]. S. Chakma and V. S. Moholkar, *Chem Eng J*, 2011, **175**, 356-367.

[57]. A. T. M. Din, B. H. Hameed and A. L. Ahmad, *J Hazard Mater*, 2009, **161**, 1522-1529.

[58]. K. Lin, J. Pan, Y. Chen, R. Cheng and X. Xu, *J Hazard Mater*, 2009, **161**, 231-240.

[59]. L. J. Kennedy, J. J. Vijaya, K. Kayalvizhi and G. Sekaran, *Chem Eng J*, 2007, **132**, 279-287.

[60]. A. Y. Dursun and Ç. S. Kalayci, *J Hazard Mater*, 2005, **123**, 151-157.

[61]. M. Otero, M. Zabkova and A. E. Rodrigues, *Sep Purif Technol*, 2005, **45**, 86-95.

[62]. F. An and B. Gao, *J Hazard Mater*, 2008, **152**, 1186-1191.

[63]. P. S. Thue, M. A. Adebayo, E. C. Lima, J. M. Sieliechi, F. M. Machado, G. L. Dotto, J. C. P. Vaghetti and S. L. P. Dias, *J Mol Liq*, 2016, **223**, 1067-1080.

[64]. A. Rathinam, J. R. Rao and B. U. Nair, *J Taiwan Inst Chem E*, 2011, **42**, 952-956.

[65]. K. Park, M. S. Balathanigaimani, W. Shim, J. Lee and H. Moon, *Micropor Mesopor Mat*, 2010, **127**, 1-8.

[66]. N. Chaudhary and C. Balomajumder, *J Taiwan Inst Chem E*, 2014, **45**, 852-859.

[67]. S. Şenel, A. Kara, G. Alsancak and A. Denizli, *J Hazard Mater*, 2006, **138**, 317-324.

[68]. B. Agarwal, C. Balomajumder and P. K. Thakur, *Chem Eng J*, 2013, **228**, 655-664.

[69]. N. A. S. Amin, J. Akhtar and H. K. Rai, *Chem Eng J*, 2010, **158**, 520-527.

[70]. N. Singh and C. Balomajumder, *J Water Process Eng*, 2016, **9**, 233-245.

[71]. Z. Shi, M. Fang, C. Zhou, Q. Wang and Z. Luo, CDCIEM, IEEE, 2011, 1303-1309.

[72]. N. Messikh, M. H. Samar and L. Messikh, *Desalination*, 2007, **208**, 42-48.

[73]. Z. Li, M. Wu, Z. Jiao, B. Bao and S. Lu, *J Hazard Mater*, 2004, **114**, 111-114.

[74]. C. Yang, S. Yang, Y. Qian, J. Guo and Y. Chen, *Ind Eng Chem Res*, 2013, **52**, 12108-12115.

[75]. J. Xu, W. Duan, X. Zhou and J. Zhou, *J Hazard Mater*, 2006, **131**, 98-102.

[76]. F. Pena-Pereira, I. Lavilla and C. Bendicho, *Spectrochim Acta B*, 2009, **64**, 1-15.

[77]. S. E. Agarry and B. O. Solomon, *Int J Environ Sci & Technol*, 2008, **5**, 223-232.

[78]. A. M. Klibanov, B. N. Alberti, E. D. Morris and L. M. Felshin, *J. Appl. Biochem.;(United States)*, 1980, **2**.

[79]. G. Bayramoğlu and M. Y. Arıca, *J Hazard Mater*, 2008, **156**, 148-155.

[80]. S. Esplugas, J. Gimenez, S. Contreras, E. Pascual and M. Rodríguez, *Water Res*, 2002, **36**, 1034-1042.

[81]. T. Olmez-Hanci and I. Arslan-Alaton, *Chem Eng J*, 2013, **224**, 10-16.

[82]. Q. Guan, X. Huang, J. Liu, J. Gu, R. Miao, Q. Chen and P. Ning, *Chem Eng J*, 2016, **283**, 358-365.

[83]. G. J. DiLeo, M. E. Neff, S. Kim and P. E. Savage, *Energ Fuel*, 2008, **22**, 871-877.

[84]. G. S. Veeresh, P. Kumar and I. Mehrotra, *Water Res*, 2005, **39**, 154-170.

[85]. M. H. El-Naas, S. A. Al-Muhtaseb and S. Makhlouf, *J Hazard Mater*, 2009, **164**, 720-725.

[86]. G. González, G. Herrera, X. Garcı, M. T. A and M. Peña, *Bioresource Technol*, 2001, **80**, 137-142.

[87]. O. Tepe and A. Y. Dursun, *J Hazard Mater*, 2008, **151**, 9-16.

[88]. A. Kumar, S. Kumar and S. Kumar, *Biochem Eng J*, 2005, **22**, 151-159.

[89]. Y. WANG, Y. TIAN, B. HAN, H. ZHAO, J. BI and B. CAI, *J Environ Sci-China*, 2007, **19**, 222-225.

[90]. Y. Jiang, J. Wen, J. Bai, X. Jia and Z. Hu, *J Hazard Mater*, 2007, **147**, 672-676.

[91]. N. K. Pazarlioğlu and A. Telefoncu, *Process Biochem*, 2005, **40**, 1807-1814.

[92]. L. Jiang, Q. Ruan, R. Li and T. Li, *J Basic Microb*, 2013, **53**, 224-230.

[93]. A. Bhattacharya, A. Gupta, A. Kaur and D. Malik, *Appl Microbiol Biot*, 2014, **98**, 9829-9841.

[94]. C. Yang and C. Lee, *Int Biodeter Biodegr*, 2007, **59**, 206-210.

[95]. Y. J. Liu, A. N. Zhang and X. C. Wang, *Biochem Eng J*, 2009, **44**, 187-192.

[96]. V. L. Santos and V. R. Linardi, *Process Biochem*, 2004, **39**, 1001-1006.

[97]. R. Manimekalai and T. Swaminathan, *Bioprocess Eng*, 2000, **22**, 29-33.

[98]. G. Pinto, A. Pollio, L. Previtera and F. Temussi, *Biotechnol Lett*, 2002, **24**, 2047-2051.

[99]. H. Jiang, Y. Fang, Y. Fu and Q. Guo, *J Hazard Mater*, 2003, **101**, 179-190.

[100]. M. Cheng, G. Zeng, D. Huang, C. Lai, P. Xu, C. Zhang and Y. Liu, *Chem Eng J*, 2016, **284**, 582-598.

[101]. X. Li, X. Huang, S. Xi, S. Miao, J. Ding, W. Cai, S. Liu, X. Yang, H. Yang, J. Gao, J. Wang, Y. Huang, T. Zhang and B. Liu, *J Am Chem Soc*, 2018, **140**, 12469-12475.

[102]. S. C. Ameta and R. Ameta, *Advanced oxidation processes for wastewater treatment: emerging green chemical technology*, Academic press, 2018.

[103]. N. H. Phu, T. T. K. Hoa, N. V. Tan, H. V. Thang and P. L. Ha, *Appl Catal B- Environ*, 2001, **34**, 267-275.

[104]. A. Rey, M. Faraldos, J. A. Casas, J. A. Zazo, A. Bahamonde and J. J. Rodríguez, *Appl Catal B-Environ*, 2009, **86**, 69-77.

[105]. S. Heng, P. P. S. Lau, K. L. Yeung, M. Djafer and J. Schrotter, *J Membrane Sci*, 2004, **243**, 69-78.

[106]. S. N. Malik, P. C. Ghosh, A. N. Vaidya and S. N. Mudliar, *J Water Process Eng*, 2020, **35**, 101193.

[107]. A. K. Ray, *Catal Today*, 1998, **44**, 357-368.

[108]. S. H. S. Chan, T. Yeong Wu, J. C. Juan and C. Y. Teh, *J Chem Technol & Biotechnol*, 2011, **86**, 1130-1158.

[109]. F. C. Moreira, R. A. R. Boaventura, E. Brillas and V. J. P. Vilar, *Appl Catal B-Environ*, 2017, **202**, 217-261.

[110]. B. P. Chaplin, *Environ Sci: Proc Imp*, 2014, **16**, 1182-1203.

[111]. M. Magureanu, N. B. Mandache and V. I. Parvulescu, *Water Res*, 2015, **81**, 124-136.

[112]. X. Wang, M. Zhou and X. Jin, *Electrochim Acta*, 2012, **83**, 501-512.

[113]. A. D. Bokare and W. Choi, *J Hazard Mater*, 2014, **275**, 121-135.

[114]. M. Zhang, H. Dong, L. Zhao, D. Wang and D. Meng, *Sci Total Environ*, 2019, **670**, 110-121.

[115]. N. Inchaurrondo, J. Cechini, J. Font and P. Haure, *Appl Catal B-Environ*, 2012, **111-112**, 641-648.

[116]. W. H. Glaze, J. Kang and D. H. Chapin, 1987.

[117]. H. Fenton, *Journal of the Chemical Society, Transactions*, 1894, **65**, 899-910.

[118]. A. Babuponnusami and K. Muthukumar, *J Environ Chem Eng*, 2014, **2**, 557-572.

[119]. Y. Zhu, R. Zhu, Y. Xi, J. Zhu, G. Zhu and H. He, *Appl Catal B-Environ*, 2019, **255**, 117739.

[120]. E. Neyens and J. Baeyens, *J Hazard Mater*, 2003, **98**, 33-50.

[121]. G. Pliego, J. A. Zazo, P. Garcia-Muñoz, M. Munoz, J. A. Casas and J. J. Rodriguez, *Crit Rev Env Sci Tec*, 2015, **45**, 2611-2692.

[122]. X. Zhang, Y. Ding, H. Tang, X. Han, L. Zhu and N. Wang, *Chem Eng J*, 2014, **236**, 251-262.

[123]. S. Hussain, E. Aneggi and D. Goi, *Environ Chem Lett*, 2021, 1-20.

[124]. A. Santos, P. Yustos, A. Quintanilla, S. Rodríguez and F. García-Ochoa, *Appl Catal B-Environ*, 2002, **39**, 97-113.

[125]. A. Santos, P. Yustos, A. Quintanilla and F. García-Ochoa, *Appl Catal B- Environ*, 2004, **53**, 181-194.

[126]. L. F. Liotta, M. Gruttadauria, G. Di Carlo, G. Perrini and V. Librando, *J Hazard Mater*, 2009, **162**, 588-606.

[127]. A. Alejandre, F. Medina, A. Fortuny, P. Salagre and J. E. Sueiras, *Appl Catal B-Environ*, 1998, **16**, 53-67.

[128]. J. A. Zazo, J. A. Casas, A. F. Mohedano, M. A. Gilarranz and J. J. Rodríguez, *Environ Sci Technol*, 2005, **39**, 9295-9302.

[129]. A. Quintanilla, J. A. Casas, A. F. Mohedano and J. J. Rodríguez, *Appl Catal B-Environ*, 2006, **67**, 206-216.

[130]. S. O. Lee, T. Tran, Y. Y. Park, S. J. Kim and M. J. Kim, *Int J Miner Process*, 2006, **80**, 144-152.

[131]. M. Taxiarchou, D. Panias, I. Douni, I. Paspaliaris and A. Kontopoulos, *Hydrometallurgy*, 1997, **46**, 215-227.

[132]. A. Santos, P. Yustos, A. Quintanilla, F. García-Ochoa, J. A. Casas and J. J. Rodríguez, *Environ Sci Technol*, 2004, **38**, 133-138.

[133]. A. Santos, P. Yustos, S. Gomis, G. Ruiz and F. Garcia-Ochoa, *Chem Eng Sci*, 2006, **61**, 2457-2467.

[134]. S. Matavos-Aramyan and M. Moussavi, *Int. J. Environ. Sci. Nat. Resour*, 2017, **2**, 1-18.

[135]. M. M. Arimi, *Progress in Natural Science: Materials International*, 2017, **27**, 275-282.

[136]. J. Hagen, *Industrial catalysis: a practical approach*, John Wiley & Sons, 2015.

[137]. R. A. Van Santen, *Modern heterogeneous catalysis: an introduction*, John Wiley & Sons, 2017.

[138]. F. Wang, H. Xue, Z. Tian, W. Xing and L. Feng, *J Power Sources*, 2018, **375**, 37-42.

[139]. E. Aneggi, A. Trovarelli and D. Goi, *J Environ Chem Eng*, 2017, **5**, 1159-1165.

[140]. C. S. Rodrigues, R. M. Silva, S. A. Carabineiro, F. J. Maldonado-Hódar and L. M. Madeira, *Catalysts*, 2019, **9**, 478.

[141]. T. Hammedi, M. Triki, Z. Ksibi, A. Ghorbel and F. Medina, *J Sol-Gel Sci Techn*, 2015, **76**, 679-685.

[142]. M. J. Kim, M. W. Lee and K. Lee, *Appl Surf Sci*, 2021, **541**, 148409.

[143]. V. Subbaramaiah, V. C. Srivastava and I. D. Mall, *J Hazard Mater*, 2013, **248**, 355-363.

[144]. M. Hachemaoui, C. B. Molina, C. Belver, J. Bedia, A. Mokhtar, R. Hamacha and B. Boukoussa, *Catalysts*, 2021, **11**, 219.

[145]. Q. Zhang, Y. Peng, F. Deng, M. Wang and D. Chen, *Sep Purif Technol*, 2020, **246**, 116890.

[146]. O. P. Taran, A. N. Zagoruiko, A. B. Ayusheev, S. A. Yashnik, R. V. Prihod Ko, Z. R. Ismagilov, V. V. Goncharuk and V. N. Parmon, *Chem Eng J*, 2015, **282**, 108-115.

[147]. J. Carriazo, E. Guélou, J. Barrault, J. M. Tatibouët, R. Molina and S. Moreno, *Water Res*, 2005, **39**, 3891-3899.

[148]. S. G. Peera, T. Maiyalagan, C. Liu, S. Ashmath, T. G. Lee, Z. Jiang and S. Mao, *Int J Hydrogen Energ*, 2021, **46**, 3056-3089.

[149]. R. J. Candal, A. E. Regazzoni and M. A. Blesa, *J Mater Chem*, 1992, **2**, 657-661.

[150]. J. Barrault, J. Tatibouët and N. Papayannakos, *Comptes Rendus de l'Académie des Sciences-Series IIC-Chemistry*, 2000, **3**, 777-783.

[151]. E. Guélou, J. Barrault, J. Fournier and J. Tatibouët, *Appl Catal B-Environ*, 2003, **44**, 1-8.

[152]. J. A. Zazo, J. A. Casas, A. F. Mohedano and J. J. Rodríguez, *Appl Catal B- Environ*, 2006, **65**, 261-268.

[153]. F. Martínez, J. A. Melero, J. Á. Botas, M. I. Pariente and R. Molina, *Ind Eng Chem Res*, 2007, **46**, 4396-4405.

[154]. Y. Yan, S. Jiang and H. Zhang, *Sep Purif Technol*, 2014, **133**, 365-374.

[155]. Y. Yan, X. Wu and H. Zhang, *Sep Purif Technol*, 2016, **171**, 52-61.

[156]. M. N. Timofeeva, Z. Hasan, A. Y. Orlov, V. N. Panchenko, Y. A. Chesalov, I. E. Soshnikov and S. H. Jhung, *Appl Catal B-Environ*, 2011, **107**, 197-204.

[157]. K. M. Valkaj, A. Katovic and S. Zrncevic, *Ind Eng Chem Res*, 2011, **50**, 4390-4397.

[158]. S. Jiang, H. Zhang and Y. Yan, *Catal Commun*, 2015, **71**, 28-31.

[159]. N. Inchaurrondo, J. Cechini, J. Font and P. Haure, *Appl Catal B-Environ*, 2012, **111**, 641-648.

[160]. K. Huang, Y. Xu, L. Wang and D. Wu, *Rsc Adv*, 2015, **5**, 32795-32803.

[161]. S. Valange, Z. Gabelica, M. Abdellaoui, J. M. Clacens and J. Barrault, *Micropor Mesopor Mat*, 1999, **30**, 177-185.

[162]. R. Liou and S. Chen, *J Hazard Mater*, 2009, **172**, 498-506.

[163]. S. Zrnčević and Z. Gomzi, *Ind Eng Chem Res*, 2005, **44**, 6110-6114.

[164]. T. Granato, A. Katovic, K. M. Valkaj, A. Tagarelli and G. Giordano, *J Porous Mat*, 2009, **16**, 227-232.

[165]. I. U. Castro, D. C. Sherrington, A. Fortuny, A. Fabregat, F. Stüber, J. Font and C. Bengoa, *Catal Today*, 2010, **157**, 66-70.

[166]. C. M. Domínguez, A. Quintanilla, J. A. Casas and J. J. Rodriguez, *Chem Eng J*, 2014, **253**, 486-492.

[167]. B. H. D. Son, V. Q. Mai, D. X. Du, N. H. Phong, N. D. Cuong and D. Q. Khieu, *J Porous Mat*, 2017, **24**, 601-611.

[168]. F. Tomul, *Appl Clay Sci*, 2016, **120**, 121-134.

[169]. S. Mnasri-Ghnimi and N. Frini-Srasra, *Korean J Chem Eng*, 2015, **32**, 68-73.

[170]. S. A. Hosseini, M. Davodian and A. R. Abbasian, *J Taiwan Inst Chem E*, 2017, **75**, 97-104.

[171]. S. L. González-Cortés and F. E. Imbert, *Appl Catal A-Gen*, 2013, **452**, 117-131.

[172]. H. Schobert, *Chemistry of fossil fuels and biofuels*, Cambridge University Press, 2013.

[173]. C. Di Luca, P. Massa, R. Fenoglio and F. M. Cabello, *J Chem Technol Biotechnol*, 2014, **89**, 1121-1128.

[174]. P. Bautista, A. F. Mohedano, J. A. Casas, J. A. Zazo and J. J. Rodriguez, , *J Chem Technol Biotechnol*, 2011, **86**, 497-504.

[175]. G. Satishkumar, M. V. Landau, T. Buzaglo, L. Frimet, M. Ferentz, R. Vidruk, F. Wagner, Y. Gal and M. Herskowitz, *Appl Catal B-Environ*, 2013, **138**, 276-284.

[176]. J. A. Melero, G. Calleja, F. Martınez, R. Molina and K. Lázár, *Micropor Mesopor Mat*, 2004, **74**, 11-21.

[177]. M. Ferentz, M. V. Landau, R. Vidruk and M. Herskowitz, *Catal Today*, 2015, **241**, 63-72.

[178]. C. Adán, J. Carbajo, A. Bahamonde, I. Oller, S. Malato and A. Martínez-Arias, *Appl Catal B-Environ*, 2011, **108**, 168-176.

[179]. J. Barrault, C. Bouchoule, K. Echachoui, N. Frini-Srasra, M. Trabelsi and F. Bergaya, *Appl Catal B-Environ*, 1998, **15**, 269-274.

[180]. J. A. Zazo, A. F. Fraile, A. Rey, A. Bahamonde, J. A. Casas and J. J. Rodriguez, *Catal Today*, 2009, **143**, 341-346.

[181]. Y. Yan, S. Jiang and H. Zhang, *Rsc Adv*, 2016, **6**, 3850-3859.

[182]. H. Liang, S. Zhou, Y. Chen, F. Zhou and C. Yan, *J Taiwan Inst Chem E*, 2015, **49**, 105-112.

[183]. J. E. Durán, A. Araya and S. Arguedas, in *International Ozone Association–International UV Association World Congress*, 2013, pp. 22-26.

[184]. E. M. Flanigen, in *Studies in Surface Science and Catalysis*, eds. H. van Bekkum, E. M. Flanigen, P. A. Jacobs and J. C. Jansen, Elsevier, 2001, 11-35.

[185]. E. Koohsaryan and M. Anbia, *Chinese J Catal*, 2016, **37**, 447-467.

[186]. A. Behnam, G. Buck, F. Capacci, A. Checa, F. Di Benedetto, A. Eisenhauer, R. Giere, H. Gies, E. Griesshaber and R. Gunder, *Highlights in Applied Mineralogy*, Walter de Gruyter GmbH & Co KG, 2017.

[187]. S. Salehi and M. Anbia, *J Phys Chem Solids*, 2017, **110**, 116-128.

[188]. J. Weitkamp, *Solid State Ionics*, 2000, **131**, 175-188.

[189]. M. P. Singh, G. S. Baghel, S. J. Titinchi and H. S. Abbo, in *Advanced Catalytic Materials*, Wiley Online Library, 2015, 385-410.

[190]. R. H. Carvalho, M. A. N. D. Lemos, F. Lemos, J. M. S. Cabral and F. R. Ribeiro, *J Mol Catal A-Chem*, 2006, **253**, 170-175.

[191]. G. Calleja, J. A. Melero, F. Martinez and R. Molina, *Water Res*, 2005, **39**, 1741-1750.

[192]. K. M. Valkaj, O. Wittine, K. Margeta, T. Granato, A. Katović and S. Zrnčević, *Pol J Chem Technol*, 2011, **13**, 28-36.

[193]. L. Chen, W. Sun, H. Wei, X. Yang, C. Sun and L. Yu, *Environ Sci Pollut R*, 2021, 1-15.

[194]. A. Cihanoğlu, G. Gündüz and M. Dükkancı, *Appl Catal B-Environ*, 2015, **165**, 687-699.

[195]. O. P. Taran, S. A. Yashnik, A. B. Ayusheev, A. S. Piskun, R. V. Prihod Ko, Z. R. Ismagilov, V. V. Goncharuk and V. N. Parmon, *Appl Catal B-Environ*, 2013, **140-141**, 506-515.

[196]. N. Kosinov, C. Liu, E. J. M. Hensen and E. A. Pidko, *Chem Mater*, 2018, **30**, 3177-3198.

[197]. H. Wang, L. Wang and F. Xiao, *Acs Central Sci*, 2020, **6**, 1685-1697.

[198]. Y. Yang, Y. Yan, H. Zhang and X. Wu, *Sep Purif Technol*, 2020, **237**, 116452.

[199]. K. M. Valkaj, A. Katovic and S. Zrnčević, *J Hazard Mater*, 2007, **144**, 663-667.

[200]. C. Zhou, H. Zhang, Y. Yan and X. Zhang, *Micropor Mesopor Mat*, 2017, **248**, 139-148.

[201]. S. Jiang, H. Zhang and Y. Yan, *Sep Purif Technol*, 2018, **190**, 243-251.

[202]. J. Liu, G. Peng, X. Jing and Z. Yi, *Water Sci Technol*, 2018, **78**, 936-946.

[203]. Q. Wu, X. Hu, P. L. Yue, X. S. Zhao and G. Q. Lu, *Appl Catal B-Environ*, 2001, **32**, 151-156.

[204]. X. Hu, F. L. Lam, L. M. Cheung, K. F. Chan, X. S. Zhao and G. Q. Lu, *Catal Today*, 2001, **68**, 129-133.

[205]. X. Wu, X. Chen, H. Guan, X. Wang and L. Chen, *Catal Commun*, 2014, **51**, 29-32.

[206]. F. Xiao, J. Sun, X. Meng, R. Yu, H. Yuan, J. Xu, T. Song, D. Jiang and R. Xu, *J Catal*, 2001, **199**, 273-281.

[207]. M. D. Argyle and C. H. Bartholomew, *Catalysts*, 2015, **5**, 145-269.

[208]. I. Sádaba, M. L. Granados, A. Riisager and E. Taarning, *Green Chem*, 2015, **17**, 4133-4145.

[209]. C. M. Domínguez, P. Ocón, A. Quintanilla, J. A. Casas and J. J. Rodriguez, *Appl Catal B-Environ*, 2013, **140-141**, 663-670.

[210]. A. Quintanilla, J. L. Diaz De Tuesta, C. Figueruelo, M. Munoz and J. A. Casas, *Catalysts*, 2019, **9**, 518.

[211]. A. Quintanilla, J. Carbajo, J. A. Casas, P. Miranzo, M. I. Osendi and M. Belmonte, *Catal Today*, 2020, **356**, 197-204.

[212]. S. Hamoudi, K. Belkacemi and F. Larachi, *Chem Eng Sci*, 1999, **54**, 3569-3576.

[213]. P. Forzatti and L. Lietti, *Catal Today*, 1999, **52**, 165-181.

[214]. J. A. Moulijn, A. E. van Diepen and F. Kapteijn, *Appl Catal A-Gen*, 2001, **212**, 3-16.

[215]. H. O. Otor, J. B. Steiner, C. García-Sancho and A. C. Alba-Rubio, *Acs Catal*, 2020, **10**, 7630-7656.

[216]. J. A. Zazo, J. A. Casas, A. F. Mohedano and J. J. Rodríguez, *Appl Catal B-Environ*, 2006, **65**, 261-268.

[217]. A. Rey, A. B. Hungria, C. J. Duran-Valle, M. Faraldos, A. Bahamonde, J. A. Casas and J. J. Rodriguez, *Appl Catal B-Environ*, 2016, **181**, 249-259.

[218]. N. S. Inchaurrondo, P. Massa, R. Fenoglio, J. Font and P. Haure, *Chem Eng J*, 2012, **198**, 426-434.

[219]. T. W. Leal, L. A. Lourenço, H. D. L. Brandão, A. Da Silva, S. M. A. G. de Souza and A. A. U. de Souza, *J Hazard Mater*, 2018, **359**, 96-103.

[220]. J. J. Delgado, J. A. Pérez-Omil, J. M. Rodríguez-Izquierdo and M. A. Cauqui, *Catal Commun*, 2006, **7**, 639-643.

[221]. D. Lee, D. Kim, T. Kim, Y. Lee, S. Jeong, N. T. Le, M. Cho and S. D. Henam, *Catal Today*, 2010, **154**, 244-249.

[222]. R. Kouraichi, J. J. Delgado, J. D. López-Castro, M. Stitou, J. M. Rodríguez-Izquierdo and M. A. Cauqui, *Catal Today*, 2010, **154**, 195-201.

[223]. S. Hamoudi, F. Larachi and A. Sayari, *J Catal*, 1998, **177**, 247-258.

Chapter 2. Experimental

2.1 Materials and equipment

2.1.1 Materials and reagents

The materials and chemicals used for catalysts preparation include: copper(II) nitrite hemipentahydrate ($Cu(NO_3)_2{\cdot}2.5H_2O$, 98+%, Acros), iron(III) nitrate nonahydrate ($Fe(NO_3)_3{\cdot}9H_2O$, 99+%, Acros), cobalt(II) chloride ($CoCl_2$, 97%, Sigma Aldrich), manganese (II) nitrate tetrahydrate ($Mn(NO_3)_2{\cdot}4H_2O$, ≥ 97%, Sigma Aldrich), silver (I) nitrate ($AgNO_3$, ≥ 99.8%, Sigma Aldrich), gold(III) chloride trihydrate ($HAuCl_4{\cdot}3H_2O$, ≥ 99%, Honeywell), palladium(II) nitrate hydrate ($Pd(NO_3)_2{\cdot}xH_2O$, 40% Pd, Acros), sodium carbonate (Na_2CO_3, Honeywell), sodium borohydride ($NaBH_4$, ≥ 98.0%, Aldrich), tetraethyl orthosilicate ($Si(OC_2H_5)_4$, 98%, Aldrich), tetrapropylammonium hydroxide ($(CH_3CH_2CH_2)_4N(OH)$, 25% in water, Acros), sodium hydroxide (NaOH, ≥ 98%, VWR international), sodium aluminate ($NaAlO_2$), silicon carbide (SiC, SICAT), sodium silicate solution ($NaSiO_3$, Sigma Aldrich), Hexadecyltrimethylammonium bromide ($CH_3(CH_2)_{15}N(Br)(CH_3)_3$, 99+%, Acros), ethanol (C_2H_5OH, HPLC grade, VWR international), sulfuric acid (H_2SO_4, ≥ 97.5%, Sigma Aldrich), buffer solution (pH 4, pH 7, pH 10, Fisher), ZSM-5 ammonia (425 $m^2{\cdot}g^{-1}$, 23:1 SiO_2: Al_2O_3, Alfa Aesar), Zeolite 13X (< 60 μm, Acros), Zeolite Y hydrogen (730 $m^2{\cdot}g^{-1}$, 5.5:1 SiO_2: Al_2O_3, Alfa Aeser), MCM-41 (SiO_2, Aldrich), SBA-15 (SiO_2, 99%, Aldrich), MCM-48 (SiO_2, 15 μm particle size, 3 nm pore size, Aldrich).

The materials and chemicals used for catalytic tests include: phenol (C_6H_5OH, 99%, Acros), Hydrogen peroxide (H_2O_2, 30 %, VMR International), sulfuric acid (H_2SO_4, ≥ 97.5%, Sigma Aldrich), nitric acid (HNO_3, 68%, VMR International), hydrochloride acid (HCl, 35%,VMR International), sodium oxalate ($Na_2C_2O_4$, ≥ 99.5%, Honeywell).

The materials and chemicals used for analysis include: tests include: phenol (C_6H_5OH, 99%, Acros), hydroquinone ($C_6H_6O_2$, 99.5%, Acros), *p*-benzoquinone ($C_6H_4O_2$, ≥ 99.5%, Sigma Aldrich), catechol ($C_6H_6O_2$, 99+%, Acros), oxalic acid dihydrate ($C_2H_2O_4{\cdot}2H_2O$, ≥ 99.0%,

Sigma Aldrich), acetic acid ($C_2H_4O_2$, 100%, VMR International), formic acid (CH_2O_2, 99%, Acros), malonic acid ($C_3H_4O_4$, ≥ 99.95%, Aldrich), maleic acid ($C_4H_4O_4$, ≥ 99.0%, Sigma Aldrich), fumaric acid ($C_4H_4O_4$, 99+%, Acros), orthophosphoric acid (H_3PO_4, 85%, VWR International), acetonitrile (C_2H_3N, HPLC grade, Fisher), potassium permanganate ($KMnO_4$, 99-100.5%, Fluka), sodium oxalate ($Na_2C_2O_4$, ≥ 99.5%, Honeywell), potassium iodide (KI, 99%, Acros), sodium thiosulfate ($Na_2S_2O_3$, 99%, Fisher), starch (Alfa Aeser), nitric acid (HNO_3, 68%, VMR International), hydrochloride acid (HCl, 35%, VMR International), sodium hydroxide (NaOH, ≥ 98%, VWR international), dimethyl sulfoxide-[D_6] ($(CD_3)_2SO$, 99.8% D, VWR international), chloroform D ($CDCl_3$, 99.80% D, water < 0.01%, VMR International).

2.1.2 Equipment

The equipment used for catalysts preparation is as follows: stirrer hot plate (Asynt), Centrifuge (SCILOGEX D1008 Mini-Centrifuges), drying oven (Genlab Mino 30/F/DIG), muffle oven (Carbolite CWF 11/14), tubular furnace (Carbolite MTF 12/38/250), digital universal oven (UN30, Memmert), autoclave (YZHR-100, Shanghai Yanzheng), pH meter (Accumet AB150, Fisher Science).

The equipment used for catalytic test was as follows: stirrer hot plate (Asynt), alumina block (diameter of 16 cm, custom-made, figure A1 in Appendix A.1), reactor (volume of 100 mL, custom-made, figure A2 in Appendix A.1).

The equipment used for analysis is as follows: centrifuge (SCILOGEX D1008 Mini-Centrifuges), pH meter (Accumet AB150, Fisher Science), UV-vis (PerkinElmer Lambda 35 UV-Vis Spectrometer), ^{1}H-NMR (Bruker Advance III 400 spectrometer), HPLC (Shimadzu Prominence Liquid Chromatograph) equipped with a C18 column (Waters XBridge C18, 4.6×250 mm) and a UV detector (Shimadzu CBM-20A), ICP-OES (Agilent 4500 spectrometer).

2.2 Catalysts preparation

2.2.1 Principle of catalyst preparation

This section briefly describes the basic principles of catalyst preparation, in terms of supported metal nanoparticles and microporous materials, and will mainly focus on a combination of the two (Figure 2.1).

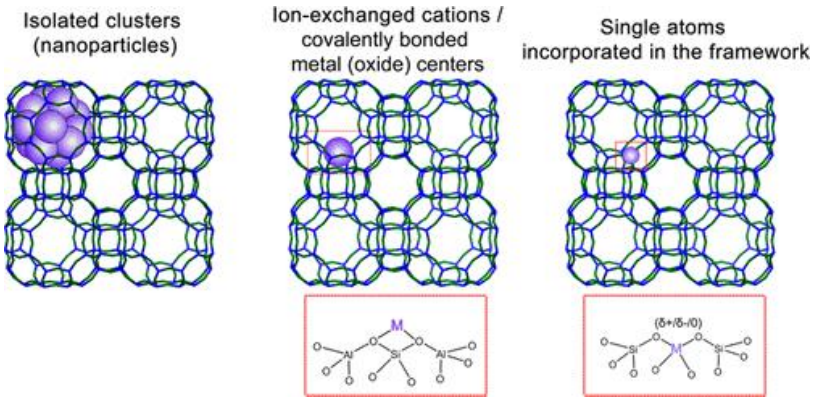

Figure 2.1. Possible zeolite–metal composite configurations: i) isolated metal oxide nanoparticles, ii) ion-exchanged cations stabilized on the AlO_4 tetrahedra, iii) single heteroatoms substituted into the zeolite framework. Figure reproduced from [1] with permission

For catalysts of types (i) and (ii), metal species were doped *after* the synthesis of zeolite support, while for catalyst type (iii), metal species were incorporated simultaneously with the formation of zeolite structure. Each of these composite configurations are characterized by specific chemical, physical, and catalytic properties. Some of the common catalyst preparation techniques, also used in this work, including wet impregnation (WI), deposition-precipitation (DP), ion-exchange (IE), and hydrothermal synthesis (HTS), which are briefly discussed here and further discussed in detail when concerning the specific preparation of materials across this thesis work.

2.2.2 Preparation of metal supported zeolite catalysts

The prepared metal-supported zeolite catalyst was denoted as x% M/support-PM, where x, M and PM represent metal loading, metal species and preparation method respectively. For

example, 1% Cu/ZSM-5-WI is a Cu supported ZSM-5 catalyst prepared by wet impregnation (WI) with an expected metal loading of 1 wt%.

2.2.2.1 Pre-treatment of zeolite

A NH_4-ZSM-5 zeolite precursor was calcined in a muffle oven operating in static air at a temperature of 550 ^oC for 4 h (temperature ramp 20 $^oC \cdot min^{-1}$) to obtain H-ZSM-5.

2.2.2.2 Catalysts preparation by wet impregnation

The desired amount of metal precursor was weighed and dissolved in deionised water (25 mL) to prepare a solution of appropriate concentration to achieve a desired metal loading. Zeolite powder (2 g) was then added into a metal precursor solution under stirring, the resulting slurry was slowly heated up to 80 ^oC with an oil bath and evaporated to dryness. The obtained material was further dried at 120 ^oC for 16 h and calcined in a muffle oven. The calcination processes for different catalysts were as follows: for Cu and Fe, calcination at 550 ^oC for 4 h with the ramping rate of 20 $^oC \cdot min^{-1}$), for Mn and Co, calcination at 500 ^oC for 4 h with the ramping rate of 20 $^oC \cdot min^{-1}$, while for Ag, Au, Pd, calcination at 180 ^oC for 16 h with the ramping rate of 10 $^oC \cdot min^{-1}$.

In order to obtain 1% Cu/ZSM-5-WI catalyst with 1 wt% metal loading, 0.074 g of $Cu(NO_3)_2 \cdot 2.5H_2O$ was dissolved in 25 mL of deionized water and mixed with 2 g of the as-prepared H-ZSM-5 powder under vigorous stirring. The resulting slurry was heated up slowly to 80 ^oC and evaporated to dryness. The solid was then completely dried at 120 ^oC for 16 h and calcined in muffle oven with temperature held at 550 ^oC for 4 h (temperature ramp 20 $^oC \cdot min^{-1}$).

2.2.2.3 Catalyst preparation by deposition-precipitation

In the typical preparation of 1% Cu/ZSM-5-DP catalyst, 2 g of HZSM-5 zeolite powder was stirred in 25 mL of deionized water, and an aqueous copper nitrate solution with 0.074 g of

precursor (dissolved in 10 mL of water) was added dropwise over 5 min. The slurry was then heated to 80 °C with pH adjusted to 10 [2,3] by adding dropwise a saturated Na_2CO_3 solution. After reaching the desired pH the solution was stirred for 4 h. After cooling the slurry was filtered, washed with 2 L of deionized water and dried at 120 °C for 16 h. Then the dried zeolite powder was calcined in muffle oven, with temperature held at 550 °C for 4 h.

2.2.2.4 Catalyst preparation by ion exchange

In the typical preparation of Cu/ZSM-5-IE catalyst, 2 g of HZSM-5 zeolite powder obtained from NH_4-ZSM-5 was added into 25 mL of aqueous copper nitrate solution (1 M) under stirring. The resulting slurry was heated in a reflux condenser at 95 °C for 24 h. After cooling, the slurry was filtered and the solid was washed with 1 L of deionized water. The material obtained was dried at 120 °C for 16 h and afterwards calcined in muffle oven, with temperature held at 550 °C for 4 h.

2.2.2.5 Catalyst reduction

The 1% Cu/ZSM-5-WI catalyst was reduced by using two distinct procedures by means of H_2 or $NaBH_4$. In a typical process, 0.5 g of the Cu/ZSM-5-WI catalyst was reduced under flow of H_2/N_2 (5%/95% v/v) at 300 °C for 2 h in a tubular furnace [4-7]. Alternatively 0.5 g of Cu/ZSM-5-WI catalyst was dispersed into 20 mL of 0.1 M aqueous solution containing $NaBH_4$ under stirring. The reduction was considered completed when no more hydrogen evolution was observed [8]. The catalyst was then filtered, washed using 2 L of deionized water and dried under vacuum suction filtration using a Schlenk line at room temperature for 48 h.

2.2.3 Synthesis of metal substituted ZSM-5 catalysts

The ZSM-5 catalyst prepared by hydrothermal synthesis was denoted as M-ZSM-5-HTS (Si/M), where M, HTS and Si/M represent metal species, synthesis method (hydrothermal synthesis, HTS) and Si to metal ratio, respectively.

2.2.3.1 Metal substituted ZSM-5 catalysts

The ZSM-5 zeolite catalyst was prepared by hydrothermal synthesis from a zeolite synthesis reaction mixture having the molar ratios 1TEOS: 0.112TPAOH: x $NaAlO_2$: 111H_2O [9,10], where x varies with the Si/Al ratio of the prepared catalyst. In the synthesis of Cu- or Fe-substituted ZSM-5, the metal precursor, sodium aluminate, was replaced by copper nitrate and iron nitrate, respectively.

In the typical synthesis of Fe-ZSM-5-HTS(80), 2.46 g of the organic template (25% TPAOH) and 5.63 g of silica source (TEOS) were dissolved in 50 mL deionized water under continuous stirring, followed by dropwise addition of 4 mL of Fe nitrate solution which containing 0.136 g $Fe(NO_3)_3 \cdot 9H_2O$. The mixture solution was aged 24 h at room temperature to assure the complete hydrolysis of TEOS. The resultant clear synthesis solution was then transferred into a 100 mL Teflon lined autoclave and treated hydrothermally at 150 °C for 48 h. The crystalline material was collected from the bottom of the autoclave and then washed with 1 L of deionized water. The as-synthesized material was dried overnight in an oven at 120 ^oC and calcined at 550 ^oC in static air for 4 h with ramping rate of 5 $^oC \cdot min^{-1}$ to remove the organic template.

2.2.3.2 ZSM-5 coating supported SiC catalysts

The ZSM-5 coating was prepared on the surface of SiC by using secondary growth process following the protocol developing by Yan's group [9,10], which involves a three step procedure.

Step 1: Pre-calcination of SiC

SiC extrudates (diameter 3 mm, 30 PPI, BET surface area 25 $m^2 \cdot g^{-1}$, microporous surface area < 5 $m^2 \cdot g^{-1}$, pore volume 0.55 $cc \cdot g^{-1}$, information from supplier [11]) were calcined in air at 900 ^oC for 4 h to clean and create an oxide layer on the surface.

Step 2: Seeding of SiC

The silicalite-1 seeds were prepared by hydrothermal synthesis from a mixture solution with the molar ratio: 9TPAOH: 25TEOS: 500H_2O: 100C_2H_5OH [9]. Typically, 14 g of template (25% TPAOH solution), 10 g of silica source (TEOS), and 11.2 mL of ethanol were added dropwise to 17 mL of deionized water under stirring. The mixture solution was aged 24 h and treated hydrothermally in a 100 mL Teflon lined autoclave at 100 °C for 24 h. The mixture solution was centrifuged for 4 h, the obtained precipitate was washed five times with deionised water to achieve a neutral pH and then dried overnight at 120 °C in an oven. 2 g of the pre-calcined SiC extrudates were dip-coated with 4 mL of the silicalite-1 in ethanol solution (1 wt%) and then dried overnight in an oven at 120 °C to adsorb silicalite-1 seeds on the surface of the SiC extrudates.

Step 3: Growth of ZSM-5 coating on SiC

The seeded SiC extrudates obtained from step 2, together with 10 mL of the synthesis solution prepared with the same method described in section 2.2.2.1, were transferred to a 100 mL Teflon lined autoclave. The synthesis was conducted in an oven at 150 °C for 48 h for the secondary growth of silicalite-1 seeds into ZSM-5 crystals. The obtained material was filtered, washed, dried and calcined in the same manner as described in 2.2.2.1.

2.2.3.3 Acid treatment of metal substituted ZSM-5 zeolite catalysts

Batches of 1 g of the prepared metal substituted ZSM-5 catalysts, either in powder form or pellet form, were washed with 50 mL of HCl solution (1 M) at 80 ^oC under stirring for 24 h to remove the metal species deposited on zeolite surface (the principle the formation of soluble MCl_x species) Then the catalysts were filtered, washed with 2 L of deionized water and dried at 120 ^oC for 16 h.

2.2.4 Synthesis of metal substituted MCM-48 catalysts

2.2.4.1 Synthesis of MCM-48

The MCM-48 catalyst was prepared by hydrothermal synthesis from a mixture with molar composition of SiO_2: CTAB: ethanol: H_2O: H_2SO_4 = 1: 0.2: 4.3: 83: 0.1.

In a typical synthesis of MCM-48, 1.64 mL of sodium silicate was added dropwise into 10 mL of deionized water to prepare a solution denoted as 'solution A'. Then, 0.728 g of the organic template (CTAB) was dissolved in a co-solvent which is composing of 2.5 mL ethanol and 3 mL H_2O, to prepare a solution denoted as 'solution B'. This solution B was then added into solution A dropwise under continuous stirring then 0.5 mL of 2 M H_2SO_4 was added into the mixture. The mixture was aged for 3 h and then transferred into an autoclave for hydrothermal synthesis at 110 ^oC for 36 h. The obtained solid was washed with 1 L of deionized water and dried overnight in an oven at 120 ^oC. The as synthesized catalyst was calcined at 550 ^oC in static air for 6 h with a ramping rate of 5 $^oC \cdot min^{-1}$ to remove the template.

2.2.4.2 Synthesis of Cu-MCM-48 catalysts

Cu-MCM-48 catalysts were prepared by hydrothermal synthesis from a mixture with molar composition of SiO_2: $Cu(NO_3)_2$: CTAB: ethanol: H_2O: H_2SO_4=1: a: b: 4.3: c: d, where a varies from 0.0073 to 0.0292, b from 0.05 to 0.2, c from 83 to 332 and d from 0.05 to 0.3. Likewise, the MCM-48 catalyst prepared by hydrothermal synthesis was denoted as M-MCM-48-HTS(Si/M) as well, where M, HTS and Si/M represent metal species, synthesis method (hydrothermal synthesis, HTS) and Si to metal ratio, respectively.

In a typical synthesis of Cu-MCM-48-HTS(137), 1.64 mL of the silica source (sodium silicate) was added dropwise into 8 mL of deionized water. Then 0.017 g of $Cu(NO_3)_2 \cdot 2.5H_2O$ was dissolved in 2 mL of water and added into the solution to prepare solvent A. 0.728 g of the organic template (CTAB) was dissolved in a co-solvent which composed of 2.5 mL ethanol

and 3 mL H_2O, to prepare solution B. The solution B was added into solution A dropwise under continuous stirring then 0.5 mL of 2 M H_2SO_4 was added into the mixture. The mixture was aged for 3 h and then transferred into an autoclave for hydrothermal synthesis at 110 ^oC for 36 h. The obtained solid was washed with 1 L of deionized water and dried overnight in an oven at 120 ^oC. The as-synthesized catalyst was calcined at 550 ^oC for 6 h with ramping rate of 5 $^oC \cdot min^{-1}$ to remove the template.

2.2.4.3 Acid treatment of Cu substituted MCM-48 catalysts

Each 0.1 g of the prepared Cu-MCM-48 catalysts were washed with 1 mL of *aqua regia* (volume ratio HNO_3: HCl = 1:3) and left overnight, to leach the metal supported on the surface of zeolite. Then the catalysts were filtered, washed with 2 L of deionized water and dried at 120 ^oC for 16 h.

2.3 Catalysts characterization

2.3.1 X-ray diffraction (XRD)

Powder XRD patterns were collected by using a Bruker D8 Advance equipped with a LynxEye detector. The instrument was operated at 40 kV and 40 mA with CuKα radiation as X-ray source. Mesoporous materials (MCM-41 and MCM-48) were analysed in a 2θ range from 1° to 30° with a scan time of 34 min and incident arm aperture of 0.1^o. While for microporous (zeolites ZSM-5 and Y) and metal oxide samples were analysed in the 2θ range from 10° to 60° with a scan time of 71 min and incident arm aperture of 0.3^o. A time per step of 1.4 s and a diffraction arm aperture of 9.5 mm was used for all the samples. Analysis of the diffraction patterns was carried out using X'Pert HighScore Plus software.

The relative crystallinity (RC) of ZSM-5 zeolite was calculated using Eq. 2.1 [12,13]:

$$\mathrm{RC},100\% = \frac{I}{I_{ref}} \times 100\% \quad \text{(Eq. 2.1)}$$

Where I is the area of a specific peak between 2θ of 22.5–25° of a target material, and I_{ref} is for a reference sample of the same material at the same 2θ range.

The particle sizes of metal oxides on the surface of zeolites were calculated by Scherrer's equation (Eq. 2.2) [14-16]:

$$\tau = \frac{K\lambda}{\beta \cos\theta} \quad \text{(Eq. 2.2)}$$

Where τ is the particle size; K is a dimensionless shape factor, with a typical value of 0.9; λ is the X-ray wavelength with value equivalent to 0.15406 nm; β is the line broadening at half the maximum intensity (or full width at half maximum, FWHM); θ is the Bragg angle.

The d-spacing of mesoporous zeolites was calculated based on the Bragg's law, which was exhibited as equation 2.3 [17-19]:

$$d = \frac{\lambda}{2\sin\theta} \quad \text{(Eq. 2.3)}$$

Where θ is the diffraction angle of peak and λ is the wavelength (λ = 0.15406 nm).

The unit cell parameter (a_0) of MCM-48 sample was calculated with equation 2.4 [20-22]:

$$a_0 = d(\mathrm{hkl})\sqrt{(h^2 + k^2 + l^2)} \quad \text{(Eq. 2.4)}$$

For d(2 1 1) plane, the a_0 was calculated as follows：

$$a_0 = d(211)\sqrt{(2^2 + 1^2 + 1^2)} = d(211)\sqrt{6} \quad \text{(Eq. 2.5)}$$

2.3.2 Porosimetry and BET surface area

BET analysis was conducted on a Micromeritics 3Flex Gas Sorption System with liquid nitrogen at 77 K. Sample was degassed at 120 – 180 °C for 24 h before analysis.

The wall thickness (W_t) of the synthesized MCM-48 samples was calculated using the XRD and porosimetry data based on equation 2.6 [22-24]:

$$W_t = \frac{a_0}{3.092} - \frac{D_p}{2} \qquad \text{(Eq. 2.6)}$$

Where 3.092 is a constant representing the minimal surface area for the MCM-48 space group and D_p is pore diameter of the sample.

2.3.3 Transmission electron microscopy (TEM)

Transmission electron microscopy was performed on Hitachi HF5000 in a scanning transmission electron microscopy mode at an accelerating voltage of 200kV.

2.3.4 X-ray photoelectron spectroscopy (XPS)

X-ray photoelectron spectroscopy (XPS) was performed on a Thermo Fisher Scientific K-alpha+ spectrometer. Samples were analysed using a micro-focused monochromatic Al x-ray source (72 W) using the '400-micron spot' mode, which provides an analysis defining elliptical x-ray spot of ca. 400 x 600 microns. Data was recorded at pass energies of 150 eV for survey scans and 40 eV for high resolution scan with 1 eV and 0.1 eV step sizes respectively. Charge neutralisation of the sample was achieved using a combination of both low energy electrons and argon ions.

Data analysis was performed in CasaXPS v2.3.24 after calibrating the data to the lowest C(1s) component taken to have a value of 284.8 eV. Quantification was made using a Shirley type background and Scofield cross sections, with an electron energy dependence of -0.6.

2.3.5 Attenuated total reflectance - Fourier transform infrared (ATR-FTIR)

ATR-FTIR analysis was conducted using a Bruker ALPHA-T spectrometer fitted with an ALPHA-P platinum ATR scanned between 450-4000 cm^{-1} over 20 scans. The technique was mainly used to 1) detect the presence of the organic template (such as CTAB) within the

synthesized zeolite samples to study the conditions of template removal and 2) explore the M-O bond in the zeolite structure to evidence the incorporation of metal into the zeolite framework.

2.3.6 Inductively coupled plasma optical emission spectroscopy (ICP-OES)

The actual metal loading of catalyst was tested by ICP-OES using an Agilent 4500 instrument via appropriate calibration curve. The catalyst (0.1 g) was digested in 1 mL of *aqua regia* (volume ratio HNO_3: HCl = 1:3) and left overnight, to leach the doped metal. Prior to analysis, the mixture was diluted with deionized water and adjusted to pH around 3 with NaOH. 5 mL of the supernatant was submitted for ICP analysis.

2.4 Catalytic tests

In order to conduct catalytic tests, a custom-made reaction setup was designed and the temperature of the reaction mixture heated by the reaction setup was calibrated, as displayed and described in Appendix A.1 and Appendix A.2, respectively.

2.4.1 Oxidation of phenol

A stock solution of phenol was prepared by dissolving the desired amount of solid reagent in deionized water and storing it in the dark. The catalytic tests for phenol oxidation were carried out in a custom-made 100 mL stoppered glass batch reactor at a desired temperature and stirring rate (see figure A1 and figure A2 in Appendix A.1). A known amount of catalyst, (typical value between 0.03 and 0.1 mg) together with a volume of 50 mL phenol aqueous solution were placed into the glass reactor and heated to controlled temperature using a Asynt stirrer-hotplate with heating rate of 200 $^{o}C \cdot min^{-1}$ via an aluminium block at atmospheric pressure. Upon stabilization at the desired temperature, a known amount of H_2O_2 was added into the solution to start the reaction. The reaction was quenched after reaction using an ice bath to ensure a constant and reproducible reaction time, while for kinetic test, samples were withdrawn from the reactor at intervals of 20 min in the first hour and with interval of 1 hour in

the last three hours. The reaction mixture was centrifuged to separate the suspended solid catalyst, the supernatant solution was then collected for analysis directly while the used catalyst, after washing with deionized water and drying at 120 ^{o}C overnight, was collected for further characterisation and/or next batch of reaction.

In a typical experiment, a certain amount of solid catalyst (0.1 g of 1% Cu/ZSM-5-WI catalyst with M:S ratio of 34) and 50 mL of phenol (1000 mg·L^{-1}) were placed into the reactor and heated to 80 ^{o}C (set temperature from calibration 83 ^{o}C - see figure A3 in appendix A.2). 758 µL of H_2O_2 (30% (w/w) with a stoichiometric ratio of phenol and H_2O_2 of 1:14 was added into the reaction mixture to start the reaction after the set temperature stabilizing at 83 ^{o}C for 10 min. The reaction was conducted for 4 h under continuous stirring rate of 500 rpm and then quenched with ice-water bath.

A stoichiometric ratio of phenol to H_2O_2 was set as 1:14 for complete oxidation of phenol to CO_2 and H_2O, as shown in Eq. 2.7.

$$C_6H_6O + 14\ H_2O_2 = 6\ CO_2 + 17\ H_2O \qquad \text{(Eq. 2.7)}$$

2.4.2 Homogeneous contribution tests

Homogeneous tests were carried out in two ways. In the first method [25], the aim was to establish whether small amounts of ions leached from the heterogeneous catalysts were responsible for the observed catalytic activity. After the wet oxidation with hydrogen peroxide the zeolite was filtered at the temperature of the catalytic tests, in order to prevent the possible re-adsorption of the leached iron during the cooling of the solution. The substrate and H_2O_2 were then added to the solution to adjust their concentrations to the same as before the catalytic tests (typically 1000 mg·L^{-1} and 5600 mg·L^{-1} respectively). The conversion of phenol was then measured at the same temperature of the catalytic tests as a function of time, but in the absence of the solid zeolite. If dissolved ions were responsible for the catalytic behaviour, a reactivity similar to that shown in the presence of the zeolite would be expected.

The second method to check the catalytic contribution of the leached metal from the zeolite involved the catalytic test using homogeneous catalyst directly. 50 mL of the mixture solution containing 1 $g \cdot L^{-1}$ of phenol and metal ions (such as Cu^{2+} from $Cu(NO_3)_2$ and Fe^{3+} from $Fe(NO_3)_3$) with concentration corresponding to that of leached metal was prepared and heated to 80 ^oC. After stabilizing for 10 min, H_2O_2 was added to the solution to start the reaction. The catalytic results of the reaction were analysed and compared with that using heterogeneous catalyst.

2.4.3 Reusability tests of catalysts

The reusability tests of catalyst in successive (sequential) reaction runs were conducted by recovering catalyst after each run of reaction and then using it for next cycle without regeneration. The recovery process of catalyst was as follows: the catalyst was filtered immediately after the first cycle of reaction at a low vacuum condition, then the catalyst was completely washed with deionized water (2 L of water per 1 g of catalyst) and dried overnight at 120 ^oC. Prior to its use in the next run of the catalytic test, the recovered catalyst was weighed and the same amount of catalyst as that used in the first run was used to ensure the error caused by the loss of catalyst in each run of reaction. The process was repeated in the same manner till the last reaction run.

2.4.4 Regeneration of catalysts

The catalyst was recovered by hot filtration from the solution after the catalytic test, then washed with deionized water, dried at 120 ^oC overnight and then calcined in a muffle oven to remove any organic species remaining on the catalyst. The ZSM-5 catalysts were regenerated by calcination at 550 ^oC in static air for 4 h with ramping rate of 20 $^oC \cdot min^{-1}$ while the MCM-48 catalysts were regenerated by calcination at 550 ^oC for 6 h with ramping rate of 5 $^oC \cdot min^{-1}$.

2.5 Chemical analysis for the characterization of the reaction mixtures

The catalytic performance of a catalyst in the CWPO of phenol was mainly characterized by phenol conversion, intermediates distribution, CO_2 formation, H_2O_2 consumption and metal leaching, respectively. The phenol conversion, intermediates distribution and CO_2 formation were calculated based on the HPLC results (details see Appendix A.6.3) while the calculation of H_2O_2 is described in detail in Appendix A.5. The formule for calculation of these values are given briefly here:

The phenol conversion ($X_{phenol,\%}$) was calculated as Eq. 2.8:

$$X_{\text{phenol},\%} = \frac{C_{0,\text{ phenol}} - C_{\text{f, phenol}}}{C_{0,\text{ phenol}}} \times 100\% \qquad \text{(Eq. 2.8)}$$

Where $C_{0,phenol}$ ($mol \cdot L^{-1}$) and $C_{f,phenol}$ ($mol \cdot L^{-1}$) represent the initial (time 0) and final concentration of phenol in the reaction mixture. Phenol concentration was analysed by HPLC, see Appendix A.6.3.

The carbon mass balance (CMB) was calculated as:

$$CMB,\% = \frac{\sum n_{f,i} \times N_{C,i}}{n_{0,phenol} \times N_{C,phenol}} \times 100\% \qquad \text{(Eq. 2.9)}$$

Where $n_{f,i}$ is the moles of intermediates (includes phenol) remained in the reaction mixture after reaction, $N_{C,i}$ is the number of C atoms in each intermediates (includes phenol) molecule, $n_{0,phenol}$ is the number of moles of initial phenol in water, $N_{C,phenol}$ is the number of C atoms in phenol molecule. Phenol and intermediates concentrations were analysed by HPLC, see Appendix A.6.3.

The CO_2 formation ($X_{CO2,\%}$) was calculated by Eq. 2.10:

$$X_{CO_2,\%} = (1 - CMB) \times 100\% \qquad \text{(Eq. 2.10)}$$

The H_2O_2 consumption ($X_{H2O2,\%}$) was calculated by Eq. 2.11:

$$X_{H_2O_2,\%} = \frac{C_{0,H_2O_2} - C_{f,H_2O_2}}{C_{0,H_2O_2}} \times 100\% \qquad \text{(Eq. 2.11)}$$

Where $C_{0,H2O2}$ ($mol \cdot L^{-1}$) and $C_{f,H2O2}$ ($mol \cdot L^{-1}$) represent the initial and final concentration of H_2O_2 in the reaction mixture. The concentration of the initial and final concentration of H_2O_2 in the reaction mixture were determined by iodometry titration (see Appendix A.5.2).

The metal leaching ($X_{leaching,\%}$) was calculated by Eq. 2.12:

$$X_{leaching,\%} = \frac{C_{metal,leached}}{C_{metal,total}} \times 100\% \qquad \text{(Eq. 2.12)}$$

Where $C_{metal,leached}$ ($mg \cdot L^{-1}$) and $C_{metal,total}$ ($mg \cdot L^{-1}$) represent the metal concentration detected in the reaction mixture after reaction and the total concentration of metal used in the reaction, respectively. The concentration of metal in the reaction mixture was determined using ICP-OES (see section 2.5.1 in chapter 2).

2.5.1 Determination of phenol and intermediates

The qualitative and quantitative analysis of the reaction mixture is a challenging task due to the similar properties amongst the tens of potential products during oxidation and the low concentration of some components (see section 3.2 in chapter 3). Hence several methods including UV-vis, HNMR and HPLC were tried to determine the phenol and intermediates in the reaction mixture (details see in Appendix A.6). HPLC was used as the main technique for intermediates analysis in this project due to the capability of determining all the potential products.

The HPLC analysis conditions were as follows: the sample mixture after filtration was analysed by HPLC equipped with a UV detector, using a Waters XBridge C18 column as stationary phase, orthophosphoric acid solution (0.1% (v/v)) as well as acetonitrile as dual mobile phases. The flow rate was set as 1 $mL \cdot min^{-1}$ and a gradient elution program was as

follows: 2% of acetonitrile from 0-5 min, 2% of acetonitrile at 5 min to 70% at 20 min, 2 % of acetonitrile from 20.1 min - 30 min. A volume of 5 µL samples was injected into the sampling system and analysed with a UV detector at different wavelengths (phenol at 270 nm, other intermediates at 200 nm). The calibration curves of phenol (figure 3.4 in chapter 3) and intermediates (Appendix A.6.3) were reported.

2.5.2 Determination of H_2O_2

Two methods, potassium permanganate and iodometry titration, were tried to determine the concentration of H_2O_2 in this project (details see Appendix A.5). The iodometry titration was selected as it is more appropriate in this reaction system, the typical titration process is as follows:

5 mL of diluted reaction mixture solution (with dilution ratio of 100), 3 mL KI (100 $g \cdot L^{-1}$) and 1 mL H_2SO_4 (10%, m/m) was pipetted into the iodine flask, the mixture was then placed in a dark place for 10 min [26] till a yellow solution was obtained. The sample solution was titrated with $Na_2S_2O_3$ (0.002 $mol \cdot L^{-1}$) till the solution becomes pale yellow. 1 mL starch solution (10 $g \cdot L^{-1}$) was added to indicate the colour change (from pale yellow to blue). More $Na_2S_2O_3$ (0.002 $mol \cdot L^{-1}$) was added till the blue colour disappeared. The volume (V_4) of $Na_2S_2O_3$ solution at the end point of titration was recorded, then calculate the concentration of H_2O_2 following the formula (Eq. 2.13):

$$C_{H_2O_2} = \frac{1}{2} \times \frac{C_{Na_2S_2O_3} \times V_4}{V_{H_2O_2}} \times D_2 = 10 \times C_{Na_2S_2O_3} \times V_4 \qquad \text{(Eq. 2.13)}$$

Where $C_{Na2S2O3}$ ($mol \cdot L^{-1}$) and V_4 (mL) represent the concentration and the volume of $Na_2S_2O_3$ solution, while V_{H2O2} (mL) and D_2 (=100) are volume and the dilution ratio of H_2O_2 solution (or reaction mixture), respectively. The determination of H_2O_2 and the calculation of H_2O_2 consumption by iodometry titration were reported in Appendix A.5.2 in detail.

2.5.3 Determination of metal leaching

The metal leaching of catalyst during the reaction was tested by ICP-OES using an Agilent 4500 instrument which was calibrated up to 10 parts per billion (ppb) using standards prepared by dilution from stock solutions containing 1000 parts per million (ppm) of metal standards. The concentrations of metal ions in the samples were calculated against a calibration graph. For the leaching tests, sample of the reaction mixture (5 mL) was taken after the reaction.

2.6 References

[1]. N. Kosinov, C. Liu, E. J. M. Hensen and E. A. Pidko, *Chem Mater*, 2018, **30**, 3177-3198.

[2]. Z. Huang, F. Cui, J. Xue, J. Zuo, J. Chen and C. Xia, *Catal Today*, 2012, **183**, 42-51.

[3]. Q. Xin, A. Papavasiliou, N. Boukos, A. Glisenti, J. P. H. Li, Y. Yang, C. J. Philippopoulos, E. Poulakis, F. K. Katsaros and V. Meynen, *Appl Catal B-Environ*, 2018, **223**, 103-115.

[4]. J. Y. Yan, W. M. H. Sachtler and H. H. Kung, *Catal Today*, 1997, **33**, 279-290.

[5]. J. Y. Kim, J. A. Rodriguez, J. C. Hanson, A. I. Frenkel and P. L. Lee, *J Am Chem Soc*, 2003, **125**, 10684-10692.

[6]. Z. Xiao, X. Wang, J. Xiu, Y. Wang, C. T. Williams and C. Liang, *Catal Today*, 2014, **234**, 200-207.

[7]. L. Delannoy, G. Thrimurthulu, P. S. Reddy, C. Méthivier, J. Nelayah, B. M. Reddy, C. Ricolleau and C. Louis, *Phys Chem Chem Phys*, 2014, **16**, 26514-26527.

[8]. M. Zahmakıran, F. Durap and S. Özkar, *Int J Hydrogen Energ*, 2010, **35**, 187-197.

[9]. H. Chen, H. Zhang and Y. Yan, *Chem Eng J*, 2012, **209**, 372-378.

[10]. S. Jiang, H. Zhang, Y. Yan and X. Zhang, *Micropor Mesopor Mat*, 2017, **240**, 108-116.

[11]. beta SiC catalyst supports SDS, https://f7de78fd-3a1d-48c1-a143-b2a07048f31b.filesusr.com/ugd/8aa046_f81cba0fafb94938b6a49dc4ed1bcfdf.pdf.

[12]. M. H. Nada and S. C. Larsen, *Micropor Mesopor Mat*, 2017, **239**, 444-452.

[13]. R. M. Mohamed, H. M. Aly, M. F. El-Shahat and I. A. Ibrahim, *Micropor Mesopor Mat*, 2005, **79**, 7-12.

[14]. U. Holzwarth and N. Gibson, *Nat Nanotechnol*, 2011, **6**, 534.

[15]. A. Monshi, M. R. Foroughi and M. R. Monshi, *World J Nano Sci Eng*, 2012, **2**, 154-160.

[16]. J. Hargreaves, *Catal Struct React*, 2016, **2**, 33-37.

[17]. F. Chen, F. Song and Q. Li, *Micropor Mesopor Mat*, 1999, **29**, 305-310.

[18]. A. M. Doyle, E. Ahmed and B. K. Hodnett, *Catal Today*, 2006, **116**, 50-55.

[19]. F. Tavakoli, M. Mamaghani and M. Sheykhan, *Appl Organomet Chem*, 2019, **33**, e5083.

[20]. W. Zhao, Q. Li, L. Wang, J. Chu, J. Qu, S. Li and T. Qi, *Langmuir*, 2010, **26**, 6982-6988.

[21]. V. Zeleňák, D. Halamová, M. Almáši, L. Žid, A. Zeleňáková and O. Kapusta, *Appl Surf Sci*, 2018, **443**, 525-534.

[22]. O. Collart, P. Van Der Voort, E. F. Vansant, D. Desplantier, A. Galarneau, F. Di Renzo and F. Fajula, *J Phys Chem B*, 2001, **105**, 12771-12777.

[23]. U. S. Taralkar, M. W. Kasture and P. N. Joshi, *J Phys Chem Solids*, 2008, **69**, 2075-2081.

[24]. D. Zhao, S. Budhi, A. Rodriguez and R. T. Koodali, *Int J Hydrogen Energ*, 2010, **35**, 5276-5283.

[25]. G. Centi, S. Perathoner, T. Torre and M. G. Verduna, *Catal Today*, 2000, **55**, 61-69.

[26]. Y. Pan, H. Xie, X. Tan, L. Liu and C. F. Zheng, *Physical Testing and Chemical Analysis Part B Chemical Analysis*, 2003, **39**, 404-405.

Chapter 3. Method development for the characterization of reaction mixtures

3.1 Overview

As well established in literature [1-7], organic pollutants in wastewater which are degraded by using the CWPO process are not directly oxidized to CO_2 and water in a single step, but this process involves the formation of a set of intermediates. Widely reported intermediates that are formed during the phenol oxidation process include aromatic compounds such as hydroquinone and organic acids such as acetic acid and formic acid, though specific intermediates and their relative amounts may vary by changing the reaction conditions [2,5,7,8]. As a consequence, the characterization of intermediates during the phenol oxidation process is indispensable because the objective of this project is not only to remove phenol but to obtain an effluent of low toxicity and high biodegradability. In fact, any abatement of pollutant process, would make little point if the degradation products of the substrate would be more toxic that the starting material which would then require further treatments. For example, some aromatic intermediates, hydroquinone and catechol, are reported to present even higher toxicity than phenol [9-12], thus have to be completely removed in the reaction process to assure a high treatment efficiency of water. On the other hand, metal oxide catalysts may suffer deactivation during the oxidation process as a consequence to being in contact with hot acid (>50 ^{o}C for instance) aqueous solution [13]. As a consequence, an accurate analysis of those acids, such as oxalic acid and acetic acid, is of significance for the study of the catalyst stability. Thus, the identification and quantification of the product distribution of the reaction mixture in the phenol oxidation reaction is not only one of the criteria to evaluate the performance of a catalyst in the efficiency of water treatment but it is very relevant in the catalyst design.

Many established analytical techniques, such as ultraviolet-visible spectrophotometry (UV-vis) [3], ion chromatography (IC) [14,15], gas chromatography (GC) [16-18] and high-performance liquid chromatography (HPLC) [19-23] have been developed for the analysis of degradation products from phenol oxidation, and among these methods, HPLC is

probably the most effective method due to easy operation, wide applicability, high reproducibility and low detection limit. However, the simultaneous determination of phenol and all the intermediates using HPLC is still a challenging task because of the relatively large number of intermediates (>15), as well as the similarity on their physico-chemical properties, which makes their chromatographic separation challenging. Most of the reported intermediates determination methods involve combination of various techniques (HPLC and IC, or GC, UV-vis and HPLC) [3,7,14,24,25] or HPLC columns [5,26,27], often resulting in costly and time-consuming analysis. For example, Zazo and coworkers [7] applied HPLC and IC to determine aromatic intermediates and short chain acids, respectivel, while Quintanilla et al. [5] used HPLC equipped with two chromatographic columns for determination of aromatic compounds and organic acids, respectively. Despite these advances, the fast and simultaneous determination of phenol and all the intermediates with an effective HPLC analysis method is rarely reported.

Therefore, part of the aims of this research work were to: 1) confirm and identify all, or the highest possible number, of the potential intermediates formed in the phenol oxidation process, 2) obtain an effective HPLC analysis method for the simultaneous determination of phenol and all the expected intermediates rapidly (< 30 min) both qualitatively and quantitatively, 3) verify the feasibility of using the obtained data to reflect the extent of the reaction and evaluate the catalytic performance of catalysts in terms of conversion and selectivity, 4) obtain data for the calculation of carbon mass balance and H_2O_2 efficiency.

3.2 Analysis of phenol and intermediates

Five steps were used to develop an analysis method for the determination of phenol and intermediates in the reaction mixture in this research: i) prepare an expected list of all the possible intermediates in phenol oxidation based on current literature, ii) develop analysis methods to determine phenol and the expected intermediates, by preparing a set of standard solutions, mimicking an expected set of reaction mixtures, iii) confirm the effectiveness of the

analysis method in the characterization of actual reaction mixtures, iv) quantitatively analyse the concentration of phenol and all the quoted intermediates in the reaction mixture by external standard method and v) validate the analysis method by the consistency of the carbon concentration from carbon mass balance (CMB) and total organic carbon (TOC) in water. In this section, more efforts are put on the steps i), ii), iii) and iv) while the step v) is discussed in section 3.3.

3.2.1 Expected intermediates

Though the decomposition of phenol to CO_2 and H_2O has been developed over a number of years, the actual details of this oxidation route is still an open question due to the diversity of intermediates and its dependence on reaction condition (as discussed in section 1.5.2). The various phenol oxidation routes that have been reported so far [1,2,5,7,10,28] were proposed based on clearly identified intermediates, while the identification of intermediates themselves somehow depends on effective determination techniques. On the other hand, the composition of reaction mixtures can also change by changing reaction conditions such as using different catalysts. However, all the oxidation routes suggested so far, consider the hydroxylation of phenol to hydroquinone and catechol as the first step in two parallel reactions, followed by oxidation of the dihydroxyl benzenes to benzoquinones, while the quinone intermediates would be further decomposed to short-chain acids such as acetic acid and formic acid, and then to CO_2 and water. Furthermore, it is widely accepted that the final products of phenol oxidation were some acids resistant to further oxidation like acetic acid, formic acid, and CO_2. Against this background, though the identified intermediates in different oxidation routes were not fully the same as each other, most of the likely reaction intermediates could still be predicted on the basis of oxidation routes proposed in the literature.

A summary of the intermediates reported in the literature is listed in table 3.1. Species like: hydroquinone, *p*-benzoquinone, catechol, formic acid, maleic acid, oxalic acid, and acetic

acid, were identified in most of the current literature, while other intermediates like malonic acid and fumaric acid, were occasionally reported. In comparison, the formation of resorcinol, succinic acid, muconic acid, and acrylic acid was less frequently investigated. Therefore, the main intermediates which are predicted to be formed in the CWPO process, based on their frequency to be reported in the following 12 papers (in table 3.1), include hydroquinone, *p*-benzoquinone, catechol, acetic acid, formic acid, oxalic acid, malonic acid, maleic acid, and fumaric acid.

Table 3.1. Lists of intermediates identified in reaction mixtures after phenol oxidation over different catalysts reported in the literature

Intermediates	Catalyst	oxalic acid	formic acid	malonic acid	acetic acid	maleic acid	fumaric acid	succinic acid	acrylic acid	muconic acid	HQ	PBQ	CAT	OBQ	RES	Ref
Identified (√) or not identified (×) in the literature	Cu-0803T	√	×	×	×	√	×	×	×	×	√	×	√	×	×	[29]
	Pt/CeO_2	√	√	√	√	√	×	×	√	√	√	√	√	√	√	[30]
	Cu/Al_2O_3	×	×	×	×	×	×	×	×	×	√	√	√	√	×	[28]
	Cu-0203T	√	√	√	√	√	√	×	×	×	√	√	√	×	×	[2]
	Fe^{2+}	√	√	√	√	√	√	×	×	√	√	√	√	√	√	[7]
	Cu-Ni-Al hydrotalcite	√	√	×	×	√	×	×	×	×	√	√	×	×	×	[3]
	AC	√	√	√	√	√	×	×	×	×	√	√	√	×	√	[15]
	Carbon	√	√	√	√	√	√	×	×	×	√	√	×	×	×	[31]
	CNT	×	×	×	×	×	×	×	×	×	√	√	√	×	√	[32]
	Ti/SnO_2-Sb_2O_4	√	√	√	√	√	×	√	×	×	×	√	×	×	×	[33]
	Fe-D, Cu-Z, Co-CX	√	√	×	√	√	√	×	×	×	√	√	√	√	×	[4]
	not reported	×	×	×	√	×	×	×	×	×	√	√	√	√	×	[6]

3.2.2 Analysis of phenol and intermediates in standard solution by HPLC

The analysis method for the determination of phenol and the expected intermediates was developed by means of UV-vis (see Appendix A.6.1), NMR (see Appendix A.6.2), and HPLC (discussed below). Among them, the UV-vis and NMR are of limited use since they are only capable of determining part of the intermediates, while the HPLC method was discussed in this section as the main technique for phenol and intermediates analysis.

HPLC is frequently used to separate, identify, and quantify different components in a mixture and so is a potential analytical method for the quantification of phenol and its intermediates in the reaction mixture. In principle, each component in the mobile phase (a solvent that carries the sample through the column [34]) interacts slightly differently with the stationary phase (the immobile phase responsible for retaining the sample component in the column [34]), causing different time spent by the different component in the liquid phase, which in turn will translate to a different total time for each component to flow out the column. This time is known as retention time (t_R, defined as the time between the sample injection and the peak maximum, as calculated by Eq.3.1 [34,35]).

$$t_R = t_R' + t_M \qquad \text{(Eq.3.1)}$$

Thus the retention time is the total time the solute spends in the stationary phase (t_R') and in the mobile phase (t_M).

In addition, a high resolution (R_s, defined as the quality of separation or the ability of the column to resolve two components into two separate peaks, as calculated by Eq. 3.2 [35,36]) of peaks in the HPLC chromatogram has also to be satisfied to charaterize a good analysis method.

$$R_s = \frac{2(t_{R2} - t_{R1})}{w_2 + w_1} \qquad \text{(Eq.3.2)}$$

Here t_{R1} and t_{R2} are the retention times of the first and the second adjacent peaks and w_1 and w_2 are the width at the base of the two chromatographic peaks.

Overall, the chromatographic separation of the intermediates is the result of different interactions of each component in the mobile phase with the stationary phase. The compound that presents the weakest interaction with the stationary phase elutes first, while the component that has a strong interaction with the stationary phase has also a longer retention time. Thus, each component in the mixture can be qualitatively analysed by its retention time. Meanwhile, the detector generates a signal proportional to the amount of sample component emerging from the column, hence allowing for quantitative analysis of the sample components.

In order to develop an HPLC analysis method for the quantification and separation of phenol and the above expected intermediates, a Shimadzu HPLC equipped with a UV detector and a C18 column (chain length (octadecyl) of alkyl bonded phase) was used. A standard solution of the mixture was prepared by mixing individual stock solutions of phenol and other 9 expected intermediates. The HPLC chromatogram of the standard solution is shown in figure 3.1. As can be seen, the separation of phenol and these expected intermediates is achieved under the analysis condition (see figure 3.1) since the HPLC chromatogram of each known standard compound in the mixture solution can be clearly identified from the retention times. The elution order of those compounds is (shown in table 3.2): oxalic acid (2.6 ± 0.1 min), formic acid (3.1 ± 0.1 min), malonic acid (3.8 ± 0.1 min), acetic acid (4.4 ± 0.1 min), maleic acid (5.1 ± 0.1 min), fumaric acid (6.1 ± 0.1 min), hydroquinone (8.9 ± 0.2 min), *p*-benzoquinone (12.1 ± 0.1 min), catechol (13.2 ± 0.1 min) and phenol (16.0 ± 0.1 min). Though a small tailing is observed in the peak of maleic acid, the peaks of all the other compounds presented a Gaussian profile. It indicated that a good resolution ($R_s \geq 1$) of all of the relative compounds in the reaction solution was achieved, especially the aromatic compounds that showed long time interval with other substances ($R_s > 4$). As can be seen from table 3.1, the separation of phenol and all the expected intermediates per sample is achieved in merely 20 min, thus showing a highly efficient analysis method.

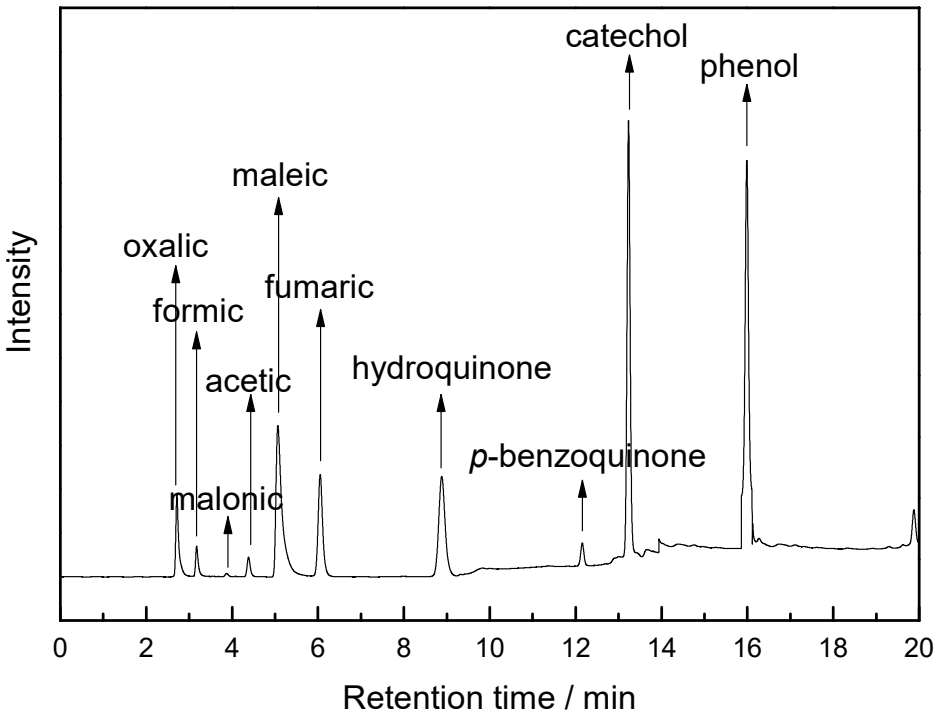

Figure 3.1. HPLC chromatogram of mixed standard solution (analysis condition: H_3PO_4 solution (0.1% (v/v)) and acetonitrile as dual mobile phases with acetonitrile percentage of 2% from 0-5 min, 2%- 70% from 5-20 min, 2 % from 20.1-30 min, injection volume 5 µL, wavelength 200 nm)

Therefore, a comprehensive and rapid analysis method for the simultaneous determination of phenol and 9 expected intermediates in the mixed standard solution was obtained by HPLC.

3.2.3 Analysis of phenol and intermediates in reaction mixture by HPLC

Though phenol and all the expected intermediates were detected and resolved by the HPLC analysis method, this was obtained by means of standards; it is necessary to confirm if the expected intermediates well replicate the actual reaction mixture and intermediates in the reaction process. In this case, a series of HPLC chromatograms of a reaction mixture sample were collected at the same analysis condition (a representative example is shown in figure 3.2) and compared with that of the standard solution. The identification of the intermediates formed in the actual phenol oxidation process was performed by comparison of retention

times of the components in standard mixture solution with those of the intermediates in actual reaction mixture.

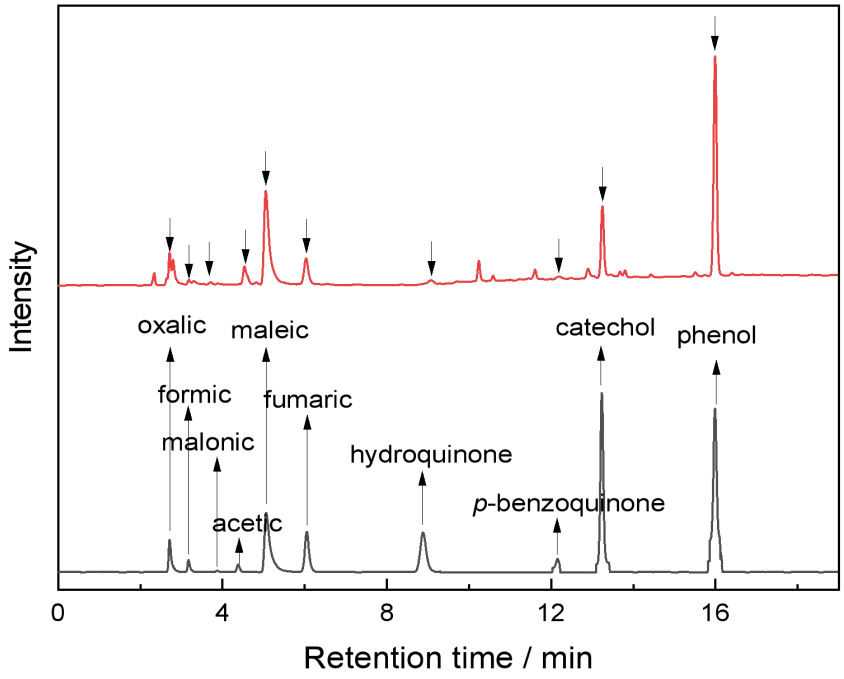

Figure 3.2. Comparison of HPLC chromatograms of standard solution (in black) and example reaction mixture (in red) (reaction condition: 0.1 g 1% Cu/ZSM-5-WI, 50 mL of 2 $g \cdot L^{-1}$ phenol, phenol: H_2O_2 =1: 14, P = endogenous, 80 °C, 40 min, 500 rpm)

As can be seen in figure 3.2 and table 3.2, the peaks of phenol and all the expected intermediates were well matched by comparison of their retention times with that of standards, indicating the formation of all those intermediates in a real reaction. However, the peak of unreacted H_2O_2 partly overlapped with the peak of oxalic acid therefore an additional deconvolution step is required to determine the concentration. It is noteworthy that, in comparison with the HPLC chromatogram of standard solution, there are also some small and unknown peaks observed in the chromatogram of the reaction mixture, such as the peaks at 10.3 min and 11.6 min, which were probably caused by the formation of muconic acid and resorcinol, as listed in table 3.1.

Table 3.2. Retention times of phenol and the expected intermediates in mixed standards solution and in actual reaction mixture (reaction condition: 0.1 g 1% Cu/ZSM-5-WI, 50 mL of 2 $g \cdot L^{-1}$ phenol, phenol: H_2O_2 =1: 14, P = endogenous, 80 ^oC, 40 min, 500 rpm)

Component	Retention time in mixed standards solution / min	Retention time in actual reaction mixture / min
Oxalic acid	2.6 ± 0.1	2.6 ± 0.1
H_2O_2	--	2.7 ± 0.1
Formic acid	3.1 ± 0.1	3.1 ± 0.1
Malonic acid	3.8 ± 0.1	3.8 ± 0.1
Acetic acid	4.4 ± 0.1	4.4 ± 0.1
Maleic acid	5.1 ± 0.1	5.1 ± 0.1
Fumaric acid	6.1 ± 0.1	6.1 ± 0.1
hydroquinone	8.9 ± 0.2	8.9 ± 0.2
p-benzoquinone	12.2 ± 0.1	12.2 ± 0.1
Catechol	13.2 ± 0.1	13.2 ± 0.1
phenol	16.0 ± 0.1	16.0 ± 0.1

3.2.4 Quantitative analysis of phenol and intermediates by HPLC

In addition to the qualitative analysis of expected intermediates, the quantitative analysis is also fundamental to gather information on the catalytic activity in terms of phenol conversion and selectivity to intermediates, and particularly in this thesis work where CO_2 is indirectly quantified by carbon mass balance determination. The quantification of the various compounds in the reaction mixture was obtained by means of calibration curves. The calibration curve of phenol is reported in this section as an example to show how quantification of phenol proceeded in this project while the calibration curves of other intermediates were obtained with the same method and shown in Appendix A.6.3. The phenol standard solutions were prepared covering a range of 200 to 1000 mg L^{-1}, and

analysed via HPLC. The preparation and determination process were repeated for three times to obtain the error of the determination method. The peak areas of phenol solutions were measured as response signals at detector wavelength of 270 nm rather than 200 nm, while the latter is the wavelength for the determination of other intermediates. The organic acids formed during the phenol decomposition process do not show any absorption band in the UV spectra (in figure A13 in Appendix A.6.1) in the range of 200 nm - 700 nm but have maximal absorbance at 200 nm, at which acids presented the strongest signal and could be identified at low concentrations. Unlike those acids, aromatic compounds usually have absorption bands in the UV spectra owing to the conjugated double bonds of benzene ring. For example, phenol has two main absorption bands in the UV spectra (in figure A11 in Appendix A.6.1), one is at 210 nm and the other is at 270 nm, resulting from the conjugated double bonds of benzene ring as well as hydroxyl ·OH and conjugated double bond of benzene ring, respectively. In general, the peak at maximum absorption wavelength of 270 nm is regarded as the characteristic absorption peak of phenol and the optimal wavelength for quantification analysis. Peak areas were plotted versus phenol concentrations to obtain a calibration curve. A linear regression y = a + b*x was used to fit the data to the formula, and the correlation coefficient, R, was calculated using OriginLab software.

The retention time of phenol in HPLC chromatogram was at 16 ± 0.1 min and the peak height and peak area increase proportionally with the increase of the phenol concentration, as shown in figure 3.3. In the range of 200 - 1000 $mg \cdot L^{-1}$ the correlation coefficient was very close to 1 (0.99996), indicating that the linear regression fits the data very well. Other 9 intermediates could be quantitatively determined in the same way at different wavelength and all compounds presented straight-line fits in the concentration range. The calibration curves of other 9 intermediates were plotted and showed in Appendix A.6.3. Therefore, a method for fast qualitative and quantitative analysis of phenol and 9 intermediates were acquired by HPLC technique.

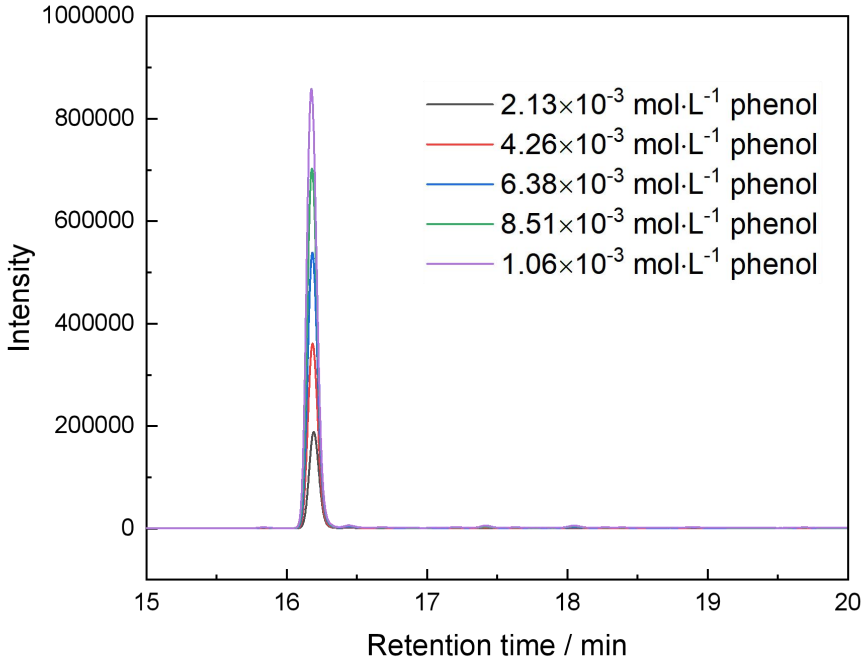

Figure 3.3. HPLC chromatograms of phenol solutions in the range of 2.13×10^{-3} – 1.06×10^{-2} mol·L^{-1} (200 mg·L^{-1} to 1000 mg·L^{-1})

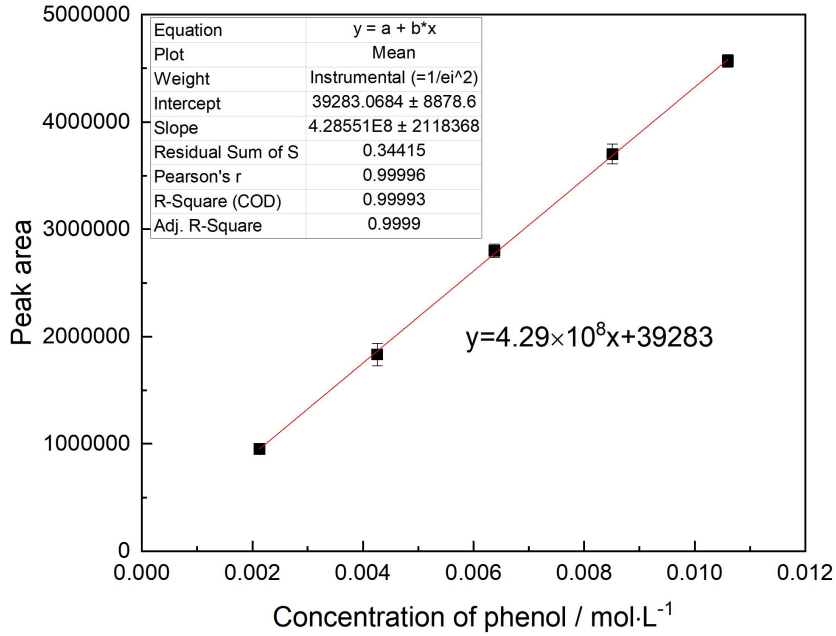

Figure 3.4. Calibration curve of phenol solutions with concentrations ranging from 2.13×10^{-3} to1.06×10^{-2} mol·L^{-1} (200 mg·L^{-1} to 1000 mg·L^{-1})

3.3 Carbon mass balance and CO_2 formation

CO_2 formation (discussed in section 3.3.2) is an important parameter used to evaluate the mineralization efficiency of pollutant in the CWPO of phenol reaction. In this project, the CO_2 formation calculation is based on the carbon mass balance (CMB, discussed in section 3.3.2) which requires the qualitative and quantitative determination of *all* the intermediates formed in the reaction process. However, as discussed in section 3.2, though phenol and 9 components based on the expected intermediates were determined, there are still some intermediates that are not identified, as suggested by the unknown peaks in the HPLC chromatogram of the reaction mixture in figure 3.2. Therefore three steps are used to assess if these unknown intermediates have significant influences on the calculation of CO_2 formation: 1) select a set of reaction mixtures obtained at different reaction times and determine their concentrations of phenol and the identified intermediates, 2) calculate the CMB and CO_2 formation of these reaction mixtures based on the concentrations of phenol and identified intermediates, 3) compare the calculated CO_2 formation with the TOC conversion (set as reference, discussed in section 3.3.3) of the reaction mixtures to assess the error of the HPLC analysis method.

3.3.1 Intermediates distribution

The intermediate distribution is one of the parameters indicating the efficiency of catalyst in CWPO of phenol as it not only reflects the extent of reaction and selectivity of catalyst to different intermediates, but acts as an important evidence of the oxidation route and the design of improved catalyst. The evolution of the concentration of phenol and the identified intermediates are reported as a function of reaction time (table 3.3). As shown, phenol was decomposed (> 99%) quickly (< 1 h). Besides phenol, the nine reaction intermediates were all detected in the aqueous phase. The distribution of these intermediates can typically be subdivided in three stages: (i) intermediates formation, (ii) a maximum of intermediates concentration, and (iii) consumption of the intermediate and decrease of its concentration. Among the intermediates that have been identified, the aromatic compounds (hydroquinone,

p-benzoquinone and catechol) formed simultaneously with the decomposition of phenol and their concentrations reached a maximum after ca. 40 min of reaction time. Afterwards the aromatic intermediates were further oxidized, leading to the formation of an array of acids. Among these, short-chain acids like acetic acid and formic acid were much higher than other acids while only traces of fumaric acid were identified. The main intermediates in phenol oxidation process, in terms of maximum concentration level in the reaction mixture, were hydroquinone, *p*-benzoquinone, catechol, acetic acid and formic acid. However it should be underlined that the concentrations versus time of these main intermediates (as well as of any other intermediate) are strongly dependent from the experimental conditions such as: temperature, initial phenol concentration, M:S ratio and H_2O_2 dosage. Furthermore, the only intermediates remained in the reaction mixture after 4 h were some recalcitrant and biodegradable acids (such as acetic acid and formic acid) which could be easily degraded by a biological method such as activated sludge.

3.3.2 Calculation of carbon mass balance and CO_2 formation

Carbon mass balance (CMB) was defined as the ratio between the number of moles of carbon in the products, $n_{C,P}$, and the number of moles of carbon in the reactants, $n_{C,R}$, (Eq 3.3):

$$CMB = \frac{n_{C,P}}{n_{C,R}} \qquad \text{(Eq. 3.3)}$$

Or if expressed as percentage (Eq 3.4):

$$CMB,\% = \frac{n_{C,P}}{n_{C,R}} \times 100\% \qquad \text{(Eq. 3.4)}$$

For our specific case, the number of moles of carbon in products, $n_{C,R}$, originates from phenol and intermediates in the reaction mixture after reaction, therefore, it can be calculated as follows (Eq 3.5):

$$n_{C,P} = \sum n_{f,i} \times N_{C,i} \qquad \text{(Eq. 3.5)}$$

Where $n_{f,i}$ is the moles of intermediates and products (as well as unreacted phenol) present in the reaction mixture at the end of the reaction, $n_{C,i}$ is the number of C atoms in each intermediates (including unreacted phenol) molecule.

While the number of moles of carbon in reactants, $n_{C,R}$, originating from initial pollutant in water, can be calculated as follows (Eq 3.6):

$$n_{C,R} = n_{i,phenol} \times N_{C,phenol} \quad \text{(Eq. 3.6)}$$

Where $n_{i,phenol}$ is the number of moles of initial phenol in water, $n_{C,phenol}$ is the number of C atoms in phenol molecule.

Another parameter, CO_2 formation, defined as the difference of molar percentage of total organic carbon between the initial and the final reaction organic products in the aqueous phase, was calculated as follows (Eq. 3.7):

$$CO_2 \text{formation},\% = (1 - \text{CMB}) \times 100\% \quad \text{(Eq. 3.7)}$$

A typical example about the calculation of CMB and CO_2 formation over the Cu/ZSM-5 catalyst after 4 h was shown below based on the above equations (Eq. 3.3-3.7).

The number of moles of carbon in reactants, $n_{C,R}$, originating from initial phenol (1 $g \cdot L^{-1}$, 50 mL) in water:

$$n_{C,R} = (1/94) \times 0.05 \times 6 = 3.2 \times 10^{-3} mol \quad \text{(Eq. 3.8)}$$

Where the number of moles of carbon in products, $n_{C,R}$, originates from phenol and intermediates in the reaction mixture after 4 h (concentrations listed in table 3.3), thus

$$
\begin{aligned}
n_{C,P} &= n_{f,phenol} \times N_{C,phenol} + n_{f,hydroquinone} \times N_{C,hydroquinone} + n_{f,p-benzoquinone} \times N_{C,p-benzoquinone} \\
&+ n_{f,catechol} \times N_{C,catechol} + n_{f,oxalic} \times N_{C,oxalic} + n_{f,formic} \times N_{C,formic} + n_{f,\mathrm{malonic}} \times N_{C,malonic} \\
&+ n_{f,acetic} \times N_{C,acetic} + n_{f,maleic} \times N_{C,maleic} + n_{f,fumaric} \times N_{C,fumaric} \\
&= (3.1\times10^{-5}\times6 + 4.4\times10^{-6}\times6 + 1.1\times10^{-5}\times6 + 4.0\times10^{-6}\times6 + 6.0\times10^{-4}\times2 \\
&+ 5.8\times10^{-3}\times1 + 9.2\times10^{-4}\times3 + 2.3\times10^{-3}\times2 + 2.9\times10^{-5}\times4 + 1.6\times10^{-5}\times4)\times0.05 \\
&= 7.5\times10^{-4}\,\mathrm{mol}
\end{aligned}
\qquad \text{(Eq. 3.9)}
$$

In that case, the CMB can be calculated as follows:

$$CMB,\% = \frac{7.5\times10^{-4}}{3.2\times10^{-3}}\times100\% = 23\% \qquad \text{(Eq. 3.10)}$$

It is indicated that the total contribution of all the identified organics in reaction mixture after 4 h, did not exceed 25% of the carbon balance, indicating that most of the organic carbon may be oxidized to CO_2, where the CO_2 formation was calculated as below:

$$CO_2\text{formation},\% = (1-0.23)\times100\% = 77\% \qquad \text{(Eq. 3.11)}$$

The CO_2 formation over the Cu/ZSM-5 catalyst after 4 h was approximately 77%, which highlighted that about three quarters of carbon in the aqueous phase was decomposed completely and the majority discharged into the atmosphere in the form of CO_2. The high CO_2 formation suggested the high pollutant removal efficiency over the Cu catalyst in the CWPO process, which is an excellent result for a catalyst that is not optimized yet, and used as an example for our calculations. However, the further decomposition of those acids to achieve higher or even complete CO_2 formation is theoretically feasible if the reaction time is sufficiently long and/or a catalyst is active enough (discussed in chapter 4), while the complete CO_2 will undoubtedly increase the possibility of the application and exploitation of CWPO of phenol in industry.

Table 3.3. Concentration of intermediates in the example reaction mixture over 1% Cu/ZSM-5-WI in 4 h (M: S of 1: 100, 50 mL of 1 $g \cdot L^{-1}$ phenol, phenol: H_2O_2 of 1: 14,P = endogenous, 80 ^oC, 500 rpm)

Component (molecular formula)	Reaction time					
	20 min	**40 min**	**1 h**	**2 h**	**3 h**	**4 h**
Phenol (C_6H_6O)	7.8×10^{-3}	1.5×10^{-3}	2.4×10^{-4}	3.9×10^{-5}	3.1×10^{-5}	0
Hydroquinone ($C_6H_6O_2$)	4.3×10^{-6}	1.4×10^{-5}	2.0×10^{-5}	6.9×10^{-6}	4.4×10^{-6}	3.6×10^{-6}
p-benzoquinone ($C_6H_4O_2$)	2.5×10^{-5}	3.0×10^{-5}	6.5×10^{-5}	1.5×10^{-5}	1.1×10^{-5}	8.0×10^{-6}
Catechol ($C_6H_6O_2$)	6.5×10^{-5}	4.3×10^{-5}	1.2×10^{-5}	9.0×10^{-6}	4.0×10^{-6}	0
Oxalic acid ($C_2H_2O_4$)	1.3×10^{-4}	3.8×10^{-4}	5.1×10^{-4}	6.1×10^{-4}	6.0×10^{-4}	5.7×10^{-4}
Formic acid (CH_2O_2)	1.4×10^{-3}	3.4×10^{-3}	5.1×10^{-3}	7.0×10^{-3}	5.8×10^{-3}	4.2×10^{-3}
Malonic acid ($C_3H_4O_4$)	4.0×10^{-4}	6.5×10^{-4}	7.3×10^{-4}	8.2×10^{-4}	9.2×10^{-4}	7.5×10^{-4}
Acetic acid ($C_2H_4O_2$)	5.2×10^{-3}	1.5×10^{-2}	1.6×10^{-2}	4.9×10^{-3}	2.3×10^{-3}	4.0×10^{-3}
Maleic acid ($C_4H_4O_4$)	8.1×10^{-5}	4.6×10^{-4}	4.0×10^{-4}	8.7×10^{-5}	2.9×10^{-5}	6.4×10^{-6}
Fumaric acid ($C_4H_4O_4$)	4.8×10^{-5}	1.5×10^{-4}	1.3×10^{-4}	5.3×10^{-5}	1.6×10^{-5}	9.3×10^{-6}
Calculation based on phenol and intermediates concentrations						
Total amount of carbon / mol[a]	3.0×10^{-3}	2.4×10^{-3}	2.2×10^{-3}	1.1×10^{-3}	7.5×10^{-4}	7.5×10^{-4}
Carbon mass balance[b]	94%	75%	70%	34%	23%	23%
CO_2 formation[c]	6%	25%	30%	66%	77%	77%

[a] calculated by Eq. 3.5, [b] calculated by Eq. 3.4, [c] calculated by Eq. 3.7.

3.3.3 Validation of carbon mass balance with total organic carbon concentration

Total organic carbon (TOC), is defined as the absolute sum of organically bound carbon present in water, either dissolved or connected to suspended matter, and it is playing a key role in the assessment of the efficiency of a wastewater purification process [37,38]. Lower TOC concentration usually indicates the higher water cleanliness. For example, the concentrations of total organic carbon about 2.0 $mg \cdot L^{-1}$ in surface water and 1.5 $mg \cdot L^{-1}$ in deep water in the Northwest Atlantic were reported [39], while China sets TOC concentration of no more than 20 $mg \cdot L^{-1}$ as class-I criteria of the Integrated Wastewater Discharge Standard (GB 8978-1996) [40].

Usually, TOC analysis are performed on a TOC analyser where the TOC measurement is achieved by indirect method, namely, the TOC content is obtained by subtraction of the total inorganic carbon (TIC) content from the total carbon (TC) content, as expressed in Eq.3.8:

$$TOC = TC - TIC \quad \text{(Eq.3.8)}$$

The flow chart of the process for the determination of TOC is shown in figure 3.5 [41]. As can be seen, the TIC components are removed from the raw sample by acidification with aqueous H_3PO_4 (to pH 2-3 [38]) or sparging with gas (such as carbon-free air or nitrogen). Then the carbon remaining in the sample is converted to an identifiable form to determine total organic carbon, and the result is generally referred to as TOC. Usually, the TOC completely converts into CO_2 through a combustion furnace, which is filled with an oxidation catalyst and heated to 680 ^oC [38]. A carrier gas flows to the combustion tube and carries the generated CO_2 from the combustion tube to a non-dispersive infrared (NDIR) detector. Sensitive to the absorption frequency of CO_2 (2346 cm^{-1}) the NDIR generates a non-linear signal that is proportional to the instantaneous concentration of CO_2 in the carrier gas [38].

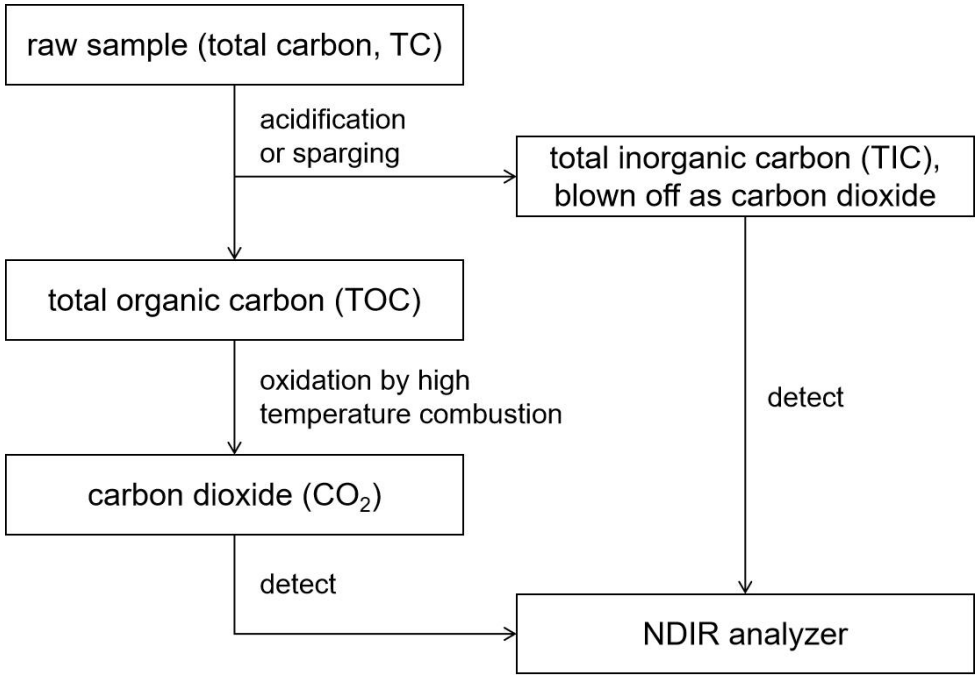

Figure 3.5. Flow chart of the process for the determination of total organic carbon (TOC) in an aqueous liquid sample [41]. Total inorganic carbon (TIC) is removed from the sample by acidification or sparging so dissolved CO_2 is not detected.

However, though it is widely used as an effective method for TOC measurement, TOC analysis is very lengthy (up to a few days for less than 10 samples) and costly (unavailable in our department) thus this would be completely unfeasible in our project. As such this study relied on HPLC data, but TOC data for a small set of samples was used to validate the method.

For validation purposes, the values obtained by the above two methods should be consistent with each other, when the qualitative and quantitative analysis of phenol and intermediates are accurate and meanwhile, no significant amounts of other organic intermediates, except for those expected, are produced in the oxidation process. To evaluate the error between the TOC-calculated (by HPLC) and the TOC-detected (by TOC analyser), the total amount of organic carbon from phenol and all the intermediates in the reaction mixture obtained at

different reaction times (in table 3.3) were calculated and compared with the TOC measured by TOC analyser, as plotted in figure 3.6.

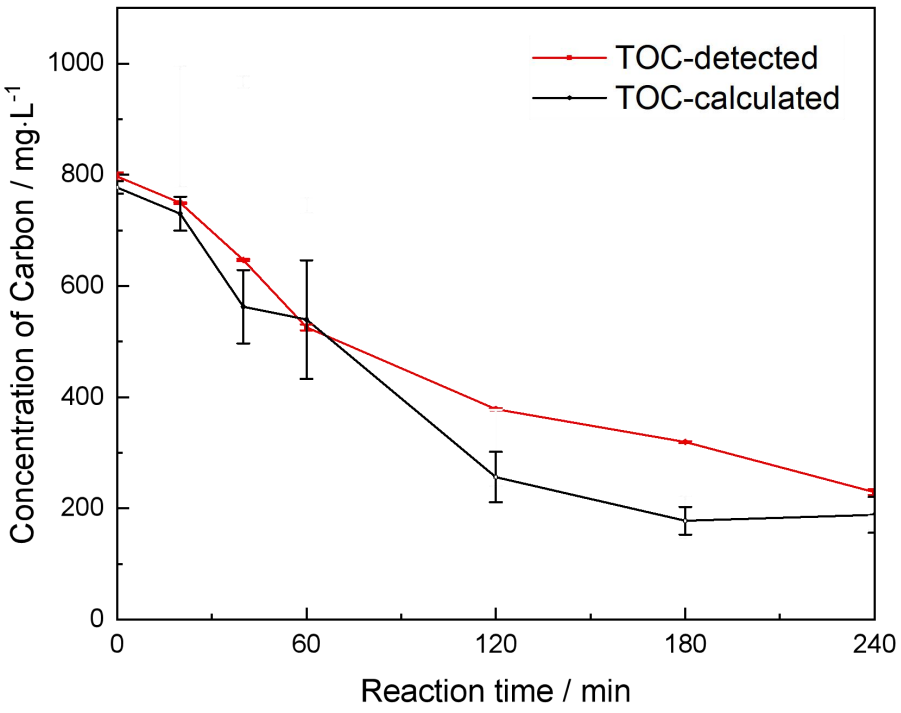

Figure 3.6. Comparison of the TOC calculated from HPLC (in black line) with the TOC detected by TOC analyser (in red line) in the same reaction mixtures (1% Cu/ZSM-5-WI catalyst, M: S of 1: 100, 50 mL of 1 g·L^{-1} phenol, phenol: H_2O_2 of 1: 14,P = endogenous, 80 ^{o}C, 500 rpm)

As shown, the total organic carbon, whatever the determination methods, decreased with reaction time, which is consistent with the trend of phenol and intermediates distribution showed in figure 3.6. Besides, in the first 1 h, the TOC-calculated was fully consistent with the TOC-detected, while at 2-3 h, the TOC-calculated was somewhat lower than the TOC-detected possibly due to the formation of some unidentified acid intermediates, which supports the conclusion of figure 3.2. In particular, the TOC-calculated is close to the TOC-detected in 4 h, suggesting that most of the final intermediates that remained in the reaction mixture have been identified by the HPLC analysis method. Meanwhile, it also indicates that the difference at 2-3 h may be caused by some unidentified C3-C4 acids (such

as acrylic acid and succinic acid) that can be further degradable to detectable acetic acid and formic acid, leading to the similar results of the TOC-calculated and the TOC-detected at 4 h. Overall, the results obtained from both methods, though not completely coincident, gave acceptable deviations, which confirmed that most of the intermediates were detected in the reaction mixture and the determination method was accurate. The fairly good agreement between the two methods made it acceptable to use the TOC-calculated, replacing the TOC-detected, as an effective parameter in this project to assess organic removal rate and estimate CO_2 formation.

3.4 Conclusions

A rapid and efficient HPLC analysis method was established to simultaneously determine phenol and nine of the identified and important intermediates in actual reaction mixture including hydroquinone, *p*-benzoquinone, catechol, acetic acid, formic acid, oxalic acid, malonic acid, maleic acid and fumaric acid. The characterization of phenol and intermediates distribution by the proposed HPLC analysis method is indispensable to acknowledge the route and extent of phenol oxidation, and furthermore, to acquire reaction mixture with low toxicity and high biodegradability. Meanwhile, by monitoring the intermediates distribution in the reaction mixture, data support such as CO_2 formation could be provided to evaluate the performance of catalysts and guide the selection and design of catalysts with the aim of industrial application of the CWPO of phenol. It is noted that though some of the unidentified compounds in the reaction mixture may induce an error to the overall carbon mass balance and CO_2 formation calculation, the error was acceptable. In summary, the qualitative and quantitative analysis of phenol and intermediates laid solid foundation for the investigation of the phenol oxidation research on which this project is focused.

3.5 References

[1]. L. F. Liotta, M. Gruttadauria, G. Di Carlo, G. Perrini and V. Librando, *J Hazard Mater*, 2009, **162**, 588-606.

[2]. A. Santos, P. Yustos, A. Quintanilla, S. Rodríguez and F. García-Ochoa, *Appl Catal B-Environ*, 2002, **39**, 97-113.

[3]. S. Zhou, Z. Qian, T. Sun, J. Xu and C. Xia, *Appl Clay Sci*, 2011, **53**, 627-633.

[4]. R. Pleşa Chicinaş, E. Gál, H. Bedelean, M. Darabantu and A. Măicăneanu, *Sep Purif Technol*, 2018, **197**, 36-46.

[5]. A. Quintanilla, J. A. Casas, A. F. Mohedano and J. J. Rodríguez, *Appl Catal B-Environ*, 2006, **67**, 206-216.

[6]. J. Levec and A. Pintar, *Catal Today*, 1995, **24**, 51-58.

[7]. J. A. Zazo, J. A. Casas, A. F. Mohedano, M. A. Gilarranz and J. J. Rodríguez, *Environ Sci Technol*, 2005, **39**, 9295-9302.

[8]. A. Santos, P. Yustos, A. Quintanilla and F. García-Ochoa, *Appl Catal B-Environ*, 2004, **53**, 181-194.

[9]. A. Santos, P. Yustos, A. Quintanilla, F. García-Ochoa, J. A. Casas and J. J. Rodríguez, *Environ Sci Technol*, 2004, **38**, 133-138.

[10]. A. Santos, P. Yustos, S. Gomis, G. Ruiz and F. Garcia-Ochoa, *Chem Eng Sci*, 2006, **61**, 2457-2467.

[11]. M. S. Yalfani, S. Contreras, F. Medina and J. Sueiras, *Appl Catal B-Environ*, 2009, **89**, 519-526.

[12]. Y. Lin, C. Liang and J. Chen, *Chemosphere*, 2011, **82**, 1168-1172.

[13]. A. Santos, P. Yustos, A. Quintanilla, G. Ruiz and F. Garcia-Ochoa, *Appl Catal B-Environ*, 2005, **61**, 323-333.

[14]. C. Adán, A. Martínez-Arias, S. Malato and A. Bahamonde, *Appl Catal B-Environ*, 2009, **93**, 96-105.

[15]. C. M. Domínguez, P. Ocón, A. Quintanilla, J. A. Casas and J. J. Rodriguez, *Appl Catal B-Environ*, 2013, **140-141**, 663-670.

[16]. V. Peings, J. Frayret and T. Pigot, *J Environ Manage*, 2015, **157**, 287-296.

[17]. J. M. Britto, S. B. D. Oliveira, D. Rabelo and M. D. C. Rangel, *Catal Today*, 2008, **133-135**, 582-587.

[18]. E. B. Azevedo, F. R. D. A. Neto and M. Dezotti, *Appl Catal B-Environ*, 2004, **54**, 165-173.

[19]. A. Shimizu, M. Tokumura, K. Nakajima and Y. Kawase, *J Hazard Mater*, 2012, **201-202**, 60-67.

[20]. O. Osegueda, A. Dafinov, J. Llorca, F. Medina and J. Sueiras, *Chem Eng J*, 2015, **262**, 344-355.

[21]. J. A. Melero, G. Calleja, F. Martínez, R. Molina and M. I. Pariente, *Chem Eng J*, 2007, **131**, 245-256.

[22]. J. Guo and M. Al-Dahhan, *Ind Eng Chem Res*, 2003, **42**, 2450-2460.

[23]. A. Xu, M. Yang, R. Qiao, H. Du and C. Sun, *J Hazard Mater*, 2007, **147**, 449-456.

[24]. M. Stoyanova, S. Christoskova and M. Georgieva, *Appl Catal A-Gen*, 2003, **249**, 295-302.

[25]. A. Rey, M. Faraldos, J. A. Casas, J. A. Zazo, A. Bahamonde and J. J. Rodríguez, *Appl Catal B-Environ*, 2009, **86**, 69-77.

[26]. F. Tomul, *Appl Clay Sci*, 2016, **120**, 121-134.

[27]. B. Boye, E. Brillas, A. Buso, G. Farnia, C. Flox, M. Giomo and G. Sandonà, *Electrochim Acta*, 2006, **52**, 256-262.

[28]. A. Alejandre, F. Medina, A. Fortuny, P. Salagre *Appl Catal B-Environ*, 1998, **16**, 53-67.

[29]. H. Ohta, S. Goto and H. Teshima, *Ind Eng Chem Fundam*, 1980, **19**, 180-185.

[30]. D. Duprez, F. Delanoe, J. Barbier Jr, P. Isnard and G. Blanchard, *Catal Today*, 1996, **29**, 317-322.

[31]. J. Wang, W. Fu, X. He, S. Yang and W. Zhu, *J Environ Sci-China*, 2014, **26**, 1741-1749.

[32]. M. T. Pinho, H. T. Gomes, R. S. Ribeiro, J. L. Faria and A. M. T. Silva, *Appl Catal B-Environ*, 2015, **165**, 706-714.

[33]. M. Loloi, A. Rezaee, M. Aliofkhazraei and A. S. Rouhaghdam, *Environ Sci Pollut R*, 2016, **23**, 19735-19743.

[34]. M. W. Dong, *Modern HPLC for practicing scientists*, John Wiley & Sons, 2006.

[35]. Y. V. Kazakevich and R. Lobrutto, *HPLC for pharmaceutical scientists*, John Wiley & Sons, 2007.

[36]. L. R. Snyder, J. J. Kirkland and J. L. Glajch, *Practical HPLC method development*, John Wiley & Sons, 2012.

[37]. I. Bisutti, I. Hilke and M. Raessler, *TrAC Trend Anal Chem*, 2004, **23**, 716-726.

[38]. D. Florescu, A. M. Iordache, D. Costinel, E. Horj, R. E. Ionete and M. Culea, *Rom. Journ. Phys*, 2013, **58**, 211-219.

[39]. D. C. Gordon and W. H. Sutcliffe, *Mar Chem*, 1973, **1**, 231-244.

[40]. Y. Wang, S. Wang, Y. Guo, D. Xu, Y. Gong, X. Tang and H. Ma, *Ind Eng Chem Res*, 2012, **51**, 16573-16579.

[41]. E. T. Urbansky, *J Environ Monitor*, 2001, **3**, 102-112.

Chapter 4. Preparation of Cu supported ZSM-5 catalysts for the CWPO of phenol

4.1 Overview

Phenol has high toxicity [1,2], low biodegradability [3,4] as well as high prevalence in industry, thus its thorough abatement using CWPO is of importance in both academic research and for environmental quality control for industrial production. The stability in the CWPO process is key point for the evaluation of the performance of a catalyst [5,6]. In fact, the deactivation of a catalyst is still a bottleneck for the scale-up of conventional metal-supported heterogeneous catalysts for industrial applications [7,8]. For example, the loss of activity of the heterogeneous catalysts in the CWPO process due to the leaching of active component caused by acid (especially oxalic acid like in our case) has been reported [9,10].

Therefore, part of the objectives of this chapter are to: 1) explore the activity of different metal species and supports in phenol degradation to obtain high-efficient catalysts, 2) assess the activity of the Cu/ZSM-5 catalyst comprehensively in the CWPO of phenol reaction in terms of phenol conversion, H_2O_2 consumption and efficiency, intermediates distribution and CO_2 formation, 3) study the stability of Cu/ZSM-5 catalysts from the perspective of metal leaching and the investigate the causes of metal leaching in the CWPO of phenol, 4) identify and assess preparation methods aimed to improve the stability of Cu/ZSM-5 catalysts, and 5) test and quantify the homogeneous contribution of the metal ions that leaching from the catalyst surface to phenol decomposition. Although all of these points are important, we would like to draw the attention to the latter as it is often neglected even in literature [11-13].

4.2 Activity of different metal doped catalysts in the CWPO of phenol

4.2.1 Activity of different metal dopants

Active species which play a catalytic role in the formation of ·OH radicals to decompose pollutant molecules, are the decisive factors influencing the performance of a catalyst in the CWPO of phenol reaction. Hence, the major criteria for the selection of active metals are high catalytic activity in phenol abatement and high selectivity towards the desired products

(organic acids and CO_2). As discussed in chapter 1, some metal species that show two oxidation states (for example Fe^{3+}/Fe^{2+}, Cu^{2+}/Cu^{+}) are capable of decomposing H_2O_2 to ·OH radicals, which are therefore potential metal dopants in the CWPO process. Thus in this project, different metal species, including both earth-abundant transition metals and noble metals like: Cu, Fe, Co, Mn, and Au doped zeolite catalysts were prepared by wet impregnation (WI) method, and were tested in phenol oxidation reaction with M: S ratio of 1: 100. In addition, Ag [14-16] and Pd [17,18] as reported, were also active in the CWPO process since a redox cycle like Ag^{+}/Ag^{0} is also able to convert H_2O_2 to ·OH radicals [15], therefore they were also tested.

Table 4.1. Activity of different metal doped ZSM-5 catalysts in the CWPO of phenol (50 mL of 1 $g \cdot L^{-1}$ phenol, M:S = 1:100, phenol: H_2O_2 = 1:14, P = endogenous, 80 ^{o}C, 4 h, 500 rpm). All metal loading were 1wt%.

Catalyst	Phenol conversion	H_2O_2 consumption	CO_2 formation*
No catalyst	4%	7%	0%
1% Cu/ZSM-5-WI	100%	76%	61%
1% Fe/ZSM-5-WI	100%	91%	76%
1% Co/ZSM-5-WI	37%	16%	0%
1% Mn/ZSM-5-WI	37%	13%	0%
1% Ag/ZSM-5-WI	40%	26%	0%
1% Au/ZSM-5-WI	58%	46%	12%
1% Pd/ZSM-5-WI	40%	41%	6%

*the CO_2 formation was calculated by Eq. 3.7, based on the determination of phenol and intermediates of the reaction mixtures. The HPLC chromatogram of the reaction mixtures over the above catalysts were shown in Appendix A.7 (figure A26).

The activity of the above catalysts in phenol decomposition was evaluated by phenol conversion, H_2O_2 consumption and CO_2 formation. In comparison with a blank test in the

presence of H_2O_2 (phenol conversion of 4%), all those catalysts were active in phenol decomposition as the phenol conversions (>30%) were relatively higher when catalysts were involved, as shown in table 4.1. Among those catalysts, Co, Mn and Ag metal doped zeolites had weak activities with phenol conversion of approximately 40% and CO_2 formation of near 0%. By contrast, the Cu and Fe supported catalysts presented the highest activities with high phenol conversions (100%), high H_2O_2 consumption (>70%) and high CO_2 formations (>60%), the Fe catalyst presented even slightly higher activity due to its higher CO_2 formation when the phenol consumption over the two catalysts both maintained 100%. The high activity over Fe and Cu catalyst is because of the formation of Fenton or Fenton-like reagent when Fe ions or Cu ions involved. In the classical Fenton reaction [19-21], the ferrous ions (Fe^{2+}) catalyse the decomposition of H_2O_2 via Eq. 4.1, resulting in the generation of ·OH radicals, while the formed ferric ions (Fe^{3+}) can be reduced through Eq. 4.2.

$Fe^{2+} + H_2O_2 \rightarrow Fe^{3+} + HO\cdot + OH^-$ (Eq. 4.1)

$Fe^{3+} + H_2O_2 \rightarrow Fe^{2+} + HOO\cdot + H^+$ (Eq. 4.2)

Similarly, a Fenton-like reaction involving Cu^+/Cu^{2+} and H_2O_2 also produced hydroxyl radicals through Eq. 4.3 and Eq. 4.4. [21,22].

$Cu^+ + H_2O_2 \rightarrow Cu^{2+} + HO\cdot + HO^-$ (Eq. 4.3)

$Cu^{2+} + H_2O_2 \rightarrow Cu^+ + HOO\cdot + H^+$ (Eq. 4.4)

The $M^{n+}/M^{(n+1)+}$ cycle ensures the generation of ·OH radicals, which are very reactive and 'engaged' in the oxidation of phenol, as shown in Eq. 4.5 [20].

$C_6H_5OH + \cdot OH \rightarrow H_2O + C_6H_5O\cdot \rightarrow$ further oxidation (Eq. 4.5)

Phenol and intermediates from this initial step were further decomposed to form short-chain acids and CO_2 under the attack of ·OH radicals, as described above. Thus, the catalysts with Cu or Fe as active species were ideal options in the CWPO of phenol due to their excellent performances. The Au and Pd catalysts showed uncompetitive activity in phenol and H_2O_2 decomposition possibly due to their strong dependence on the reaction conditions such as

metal loading and particle size of metal oxides [23], which together with the higher cost makes them lower-priority candidates in this project.

4.2.2 Activity of different supports

Zeolites are one of the widely used supports in the CWPO of phenol reaction [24-27], owing to the uniform and reproducible pore size, large specific surface area, and the possibility to incorporate transition metal ions into their framework [28-31]. An array of seven zeolites, selected by considering different physicochemical properties such pore size and acidity, including: microporous HZSM-5, NH_4ZSM-5, 13X, HY, mesoporous MCM-41, MCM-48 and SBA-15, regarding their pore sizes, or aluminosilicate (HZSM-5, NH_4ZSM-5, 13X, HY) and silica (MCM-41, MCM-48 and SBA-15) according to their composition, were studied, as shown in table 4.2. It can be seen that all the undoped zeolites, used afterwards as supports presented slight activity in phenol oxidation with phenol conversion of 10-30% in comparison with the blank test whose phenol conversion was 4% (in table 4.2), which might be attributed to the different acidity and/or the large surface area (in table 4.2) of these supports [32]. Though the difference in the activities of the six zeolite supports was observed, it is indicated that the zeolite support, if in the absence of metal dopant active species, had low activity in decomposing H_2O_2 to radicals. In fact, all these porous materials were capable of a complete phenol decomposition to intermediates and/or CO_2 after being impregnated with Cu, as shown in table 4.2, indicating the potential of catalysts that combine Cu with zeolites as support. Among the aforementioned zeolites, HZSM-5 and MCM-48, which showed higher phenol conversion were mainly investigated in this research as representatives of micro- and mesoporous zeolites, respectively.

Table 4.2. Activity of different undoped zeolite supports in the CWPO of phenol (50 mL of 1 $g \cdot L^{-1}$ phenol, catalyst loading of 2 $g \cdot L^{-1}$, phenol: H_2O_2 molar of 1: 14, 500 rpm, P = endogenous, 80 ^oC, 4 h)

Support	Si/Al ratio[a]	Surface area[b]	Phenol conversion[c]	Cu doped catalyst	Phenol conversion[d]
HZSM-5	46: 1	425 $m^2 \cdot g^{-1}$	30%	1% Cu/HZSM-5-WI	100%
NH_4ZSM-5	46: 1	425 $m^2 \cdot g^{-1}$	8%	1% Cu/NH_4ZSM-5-WI	100%
13X	1.2: 1	Not available	14%	1% Cu/13X-WI	100%
HY	11: 1	730 $m^2 \cdot g^{-1}$	12%	1% Cu/HY-WI	100%
MCM-41	1: 0	~1000 $m^2 \cdot g^{-1}$	19%	1% Cu/MCM-41-WI	100%
MCM-48	1: 0	1435 $m^2 \cdot g^{-1}$	20%	1% Cu/MCM-48-WI	100%
SBA-15	1: 0	750-1000 $m^2 \cdot g^{-1}$ *	8%	1% Cu/SBA-15-WI	100%

Notes: [a] data from supplier, [b] data from supplier, [c] phenol conversion over blank support, [d] phenol conversion over Cu impregnated support, * data from literature [33].

4.3 Activity of Cu/ZSM-5 catalyst in the CWPO of phenol

Activity, a key parameter for evaluation of the catalytic performance of a catalyst in a chemical reaction is sometimes a comprehensive reflection of reaction results rather than merely defined by conversion of the target reactant. In addition to phenol conversion, other parameters such as H_2O_2 consumption, and CO_2 formation are all presented in this project, to thoroughly assess the activity of the catalysts in the CWPO of phenol reaction. Prior to fully confirm the potential of the active species (Cu and Fe) doped zeolite (ZSM-5 and MCM-48) catalysts in phenol oxidation, the activity of Cu/ZSM-5, the most potential catalysts tested so far, was thoroughly investigated owing to the high CO_2 formation (61%) under an incomplete consumption of H_2O_2 (76%), as displayed in table 4.1.

4.3.1 Control tests in 12 h

The kinetics of phenol decomposition by considering: no catalyst, HZSM-5 only as a catalyst, and doped Cu/ZSM-5 over a 12 h reaction time, were investigated (figure 4.1-4.6). The results indicate the necessity of a Cu doped material to detect a high conversion of phenol. The catalytic tests were carried out in a batch reactor with an initial phenol concentration of 1 $g \cdot L^{-1}$, phenol: H_2O_2 molar ratio of 1:14 and a reaction temperature of 80 ^oC.

4.3.1.1 Effects of hydrothermal condition on the decomposition of H_2O_2 and phenol

Prior to the catalytic test of the Cu/ZSM-5 catalyst, the study of the hydrothermal stability of phenol and H_2O_2 was carried out in order to obtain insights into their decomposition mechanisms for catalyst development. In this section, the tolerance of phenol and H_2O_2 to hydrothermal conditions (80 ^oC), in the form of phenol conversion and H_2O_2 consumption respectively, was assessed.

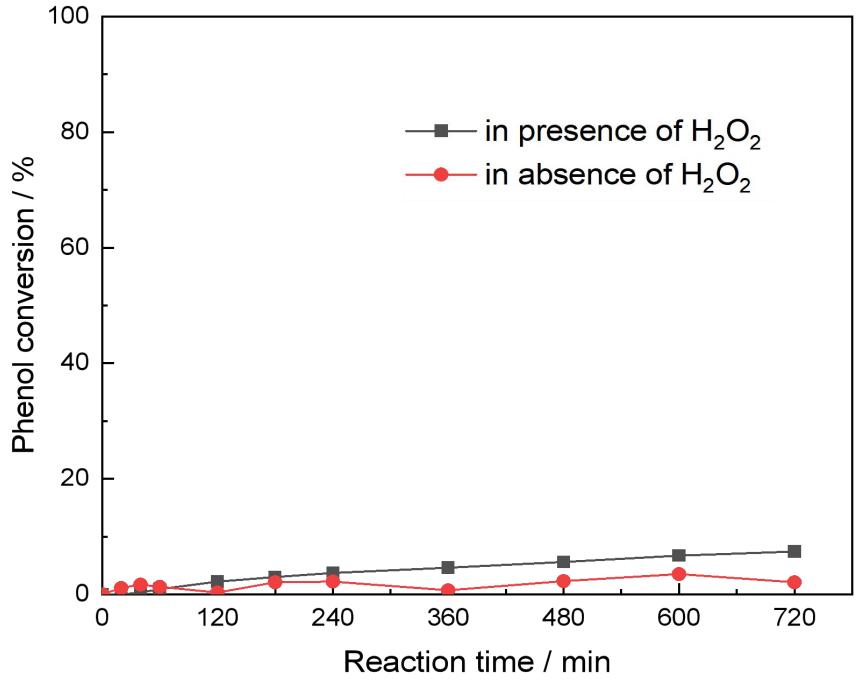

Figure 4.1. Control test for phenol decomposotion in the absence of any catalyst: a) in presence of H_2O_2, black line and b) in absence of H_2O_2, red line (50 mL solution, phenol concentration of 1 $g \cdot L^{-1}$, H_2O_2: phenol of 14, P = endogenous, 80 °C, 500 rpm). Addition of H_2O_2 made no difference in the phenol conversion when no catalyst was used in the reaction.

As shown in figure 4.1, the phenol conversion was only 2% (mol%) after 12 h of reaction in the absence of catalyst and H_2O_2, indicating the difficulty of removing phenol from water by heating, or conversely the stability of phenol at such conditions. In addition, the phenol conversion increased to only 8% over 12 h even in the presence of H_2O_2, suggesting that though slightly improved the phenol removal efficiency, the addition of H_2O_2 had a negligible effect on the contaminant abatement.

Compared to phenol, H_2O_2 was more prone to decomposition under the hydrothermal conditions, as illustrated in figure 4.2. The H_2O_2 consumption reached around 13% in 12 h without catalyst and phenol, indicating the slight degradation of H_2O_2 at temperature of 80 °C.

Besides, the value was almost invariable (15%) when phenol was used in the reaction, showing that the decomposition of H_2O_2 and phenol occurred almost independently and few ·OH radicals were formed when no effective catalyst involved.

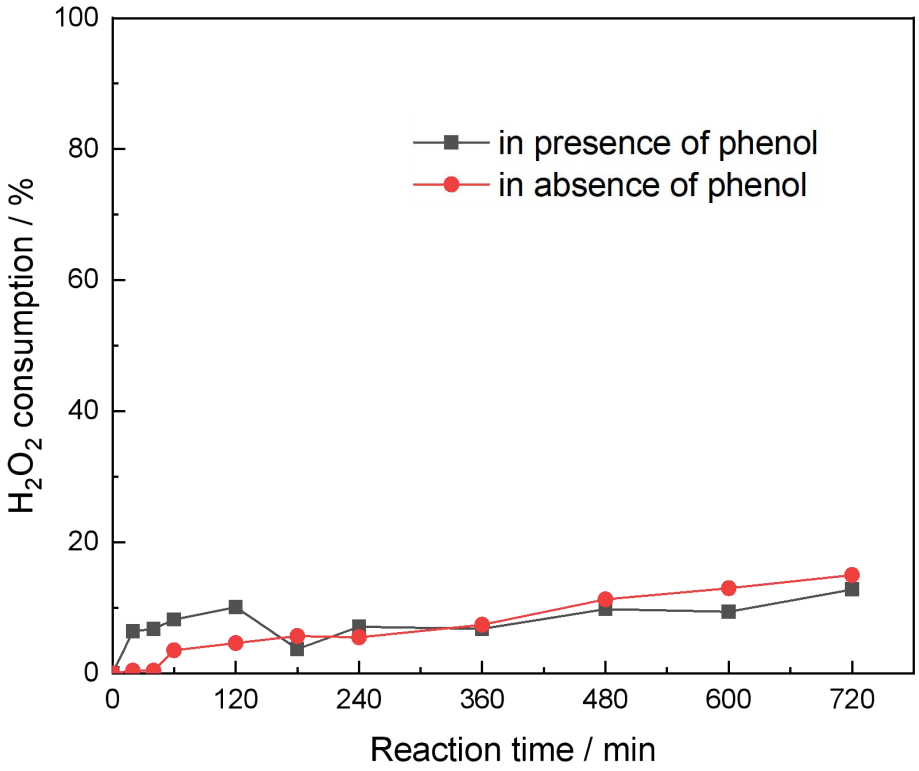

Figure 4.2. Control test for H_2O_2 decomposition in the absence of any catalyst: a) in presence of phenol, black line and b) in absence of phenol, red line (50 mL solution, phenol concentration of 1 $g \cdot L^{-1}$, H_2O_2: phenol of 14, P = endogenous, 80 ºC, 500 rpm). The H_2O_2 consumption kept almost the same whether with or without phenol when no catalyst was used in the reaction. The decrease of H_2O_2 consumption at 180 ºC in the presence of phenol was due to experimental error.

Furthermore, the CO_2 formation was close to 0% after 12 h, leading to low H_2O_2 efficiency (8%, in table 4.3) and suggesting that most of the consumed H_2O_2 was hydrothermally decomposed to H_2O and O_2, rather than active radicals ·OH. In addition, the molar sum of aromatic compounds (hydroquinone, *p*-benzoquinone, catechol) which reflected the toxic level of the reaction mixture reached approximately 7.3×10^{-4} $mol \cdot L^{-1}$ (table 4.3, compared to

7% initial mol of PhOH at the start of the reaction) while the molar sum of acids intermediates (acetic, formic, malonic, maleic, fumaric acid) maintained very low concentration (2.0×10^{-4} mol·L^{-1}, table 4.3) during the reaction, which indicated that after 12 h, the main organic components of the reaction mixture were phenol (majority) and aromatic intermediates (minority). Based on the above analysis results, the blank test with no presence of catalyst, had negligible activity in phenol oxidation reaction as the phenol conversion, H_2O_2 consumption and efficiency, CO_2 formation were all very low. More importantly, though small amount of phenol was oxidized, the main oxidation products were aromatic compounds rather than organic acids and CO_2, which means that the outflow was even more toxic than the initial reactant solution. As a consequence a catalyst is necessary to carry out this decomposition reaction efficiently and in a viable manner.

4.3.1.2 Effects of zeolite support on the decomposition of H_2O_2 and phenol

Compared to the blank test, undoped HZSM-5 zeolite used as a catalyst presented higher activity in the CWPO of phenol with the phenol conversion (figure 4.3) and H_2O_2 consumption (figure 4.4) gradually going up to 57% and 62% respectively in 12 h in the presence of an oxidant. The low phenol conversion (4%) using HZSM-5 catalyst in the absence of H_2O_2, as a control test, indicated that the 57% of phenol conversion was due to the capability of the porous support of decomposing H_2O_2 to active radicals. Besides, significant CO_2 formation (30%), and the H_2O_2 efficiency (52%, in table 4.3) were also observed. It is implied that at least half of the consumed H_2O_2 worked in the degradation of organic compounds in the form of active radicals, though another half of it still decomposed to O_2. With the decomposition of H_2O_2, a proportion of phenol decomposed to aromatic compounds then further to organic acids and CO_2. The final sum of aromatic compounds (9.8×10^{-4} mol·L^{-1}, table 4.3) still accounted for 9% (table 4.3) of the total amount of aromatics (1.1×10^{-2} mol·L^{-1} phenol at the beginning of reaction).

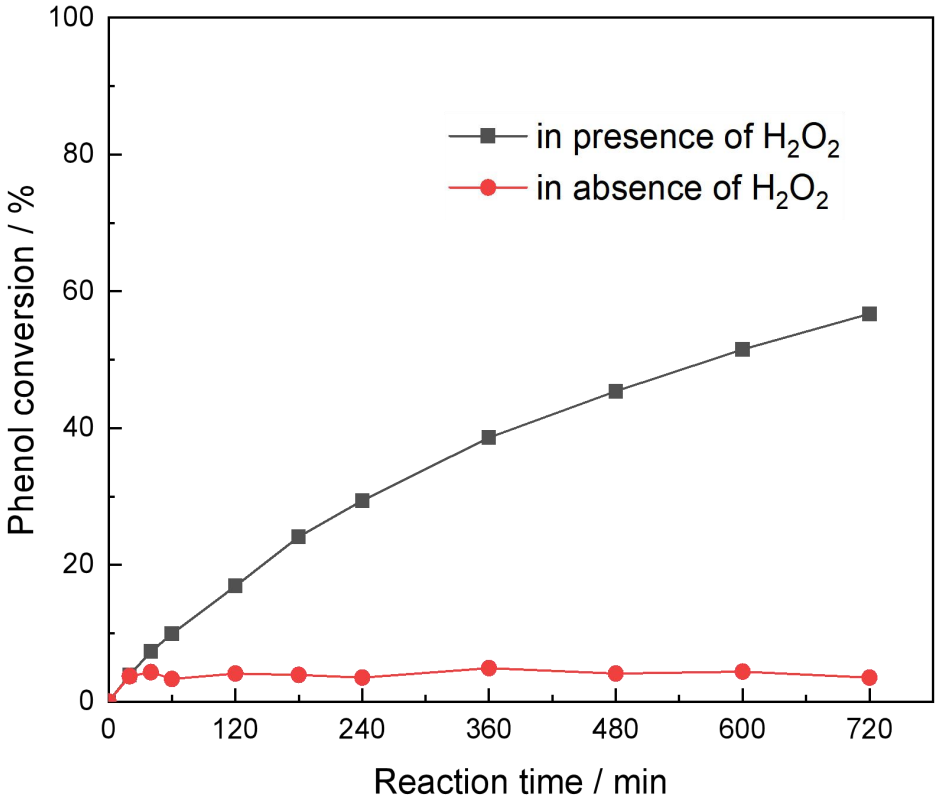

Figure 4.3. Control test for phenol decomposition using undoped HZSM-5 support as a catalyst: a) in presence of H_2O_2, black line and b) in absence of H_2O_2, red line (0.1 g HZSM-5, 50 mL 1 $g \cdot L^{-1}$ phenol, H_2O_2: phenol = 14, P = endogenous, 80 °C, 500 rpm). Phenol conversions in the H_2O_2/HZSM-5 system were much higher than in the HZSM-5 system, indicating the importance of oxidant (H_2O_2) in the phenol decomposition.

The other control test, as shown in figure 4.4, indicated that the H_2O_2 consumption of HZSM-5 in the absence of phenol (86%) was higher than that in the presence of phenol (62%), implying that more H_2O_2 was consumed when no pollutant existing in the solution. The reason for the difference might be that, when there is no phenol in the solution, all the radicals formed due to the decomposition of H_2O_2 react directly with each other to form O_2 (chain termination steps). By contrast, the reactions of radicals with reactants (chain propagation steps) and with radicals (chain termination steps) both occurred when phenol was in the

solution, while the former reaction also produces radicals (such as ·OOH) that can be reduced to H_2O_2 [34].

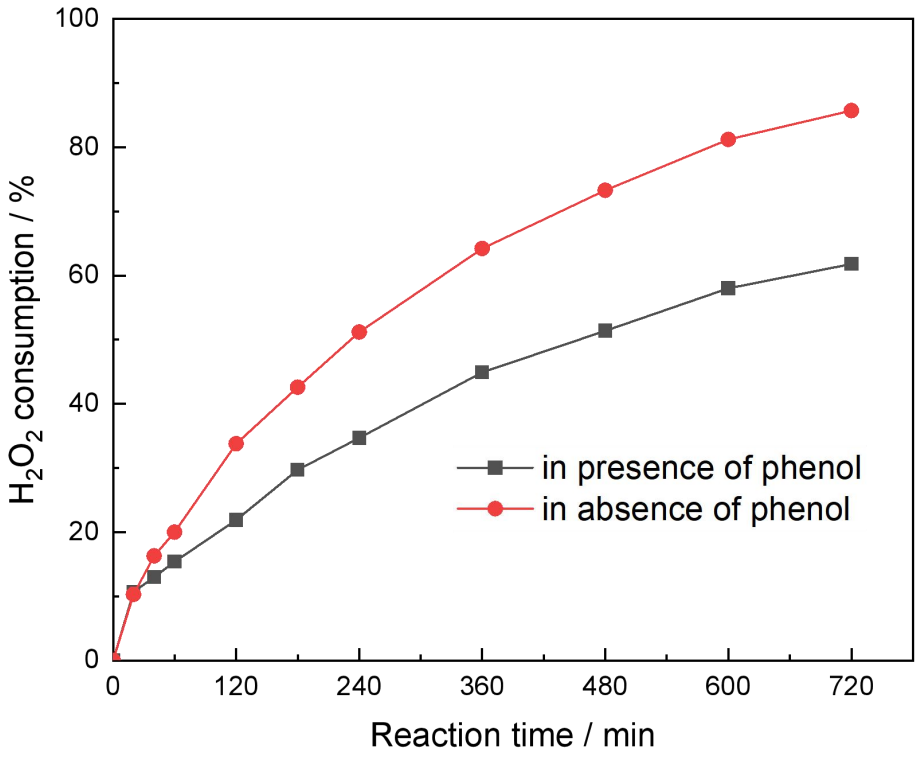

Figure 4.4. Control test for H_2O_2 decomposition using undoped HZSM-5 support as a catalyst: a) in presence of phenol, black line, and b) in absence of phenol, red line (0.1 g HZSM-5, 50 mL 1 $g \cdot L^{-1}$ phenol, H_2O_2: phenol = 14, P = endogenous, 80 °C, 500 rpm). More H_2O_2 was consumed in the H_2O_2/HZSM-5 system than in the phenol/H_2O_2/HZSM-5 system.

Overall, the HZSM-5 catalyst was active in phenol decomposition but had unsatisfactory performance with incomplete phenol conversion, moderate H_2O_2 consumption/efficiency and CO_2 formation, as well as inadequate oxidation of aromatic intermediates.

4.3.1.3 Effects of the Cu/ZSM-5 catalyst on the decomposition of H_2O_2 and phenol

The activity of HZSM-5 was greatly enhanced after being doped with Cu. In this case a wetness impregnation protocol was initially investigated. A 1wt% Cu/ZSM-5-WI catalyst

presented very high activity and efficiency in the CWPO of phenol with the phenol conversion and H_2O_2 consumption rapidly reaching 99% and 63% respectively in merely 40 min (in figure 4.5), while the undoped HZSM-5 had a much lower activity with phenol conversion and H_2O_2 consumption of only 7% and 13% at 40 min (in figure 4.3 and figure 4.4), respectively. Complete phenol conversion and H_2O_2 consumption (figure 4.5 and figure 4.6), when using 1% Cu/ZSM-5-WI as catalyst, were achieved at 1 h and 10 h, respectively, suggesting that H_2O_2 are used not only for the decomposition of phenol to intermediates (aromatics and acids) but also for the degradation of intermediates to organic acids and CO_2. It indicated that the toxic intermediates were formed with the decomposition of phenol, and then oxidized to acids and CO_2 with a continuous consumption of H_2O_2 (figure 4.5), and a negligible amount of aromatic compounds (3.4×10^{-5} mol·L^{-1}, 0.3% of the initial amount) was detected after 12 h (table 4.3). Meanwhile, the amount of acids intermediates were also very low as most of them degraded to CO_2 and only a small proportion of them (3.3×10^{-3} mol·L^{-1}, table 4.3) remained in the solution after reaction. As a consequence, the main organic constituents in the reaction mixture after reaction with the Cu doped ZSM-5 catalyst for 12 h, were organic acids only, indicating the high efficiency of the catalyst in aromatic pollutant removal from water. What's noteworthy is that the Cu/ZSM-5 presented superior activity in the removal of phenol not only because of faster phenol and H_2O_2 decomposition but also higher efficiency of H_2O_2 utilization. As displayed in table 4.3, the H_2O_2 efficiency in the absence of a catalyst and by using HZSM-5 as a catalyst was 8% and 52% respectively, much lower than that over the Cu catalyst (90%), implying the excellent performance of Cu catalyst in the generation of ·OH radicals.

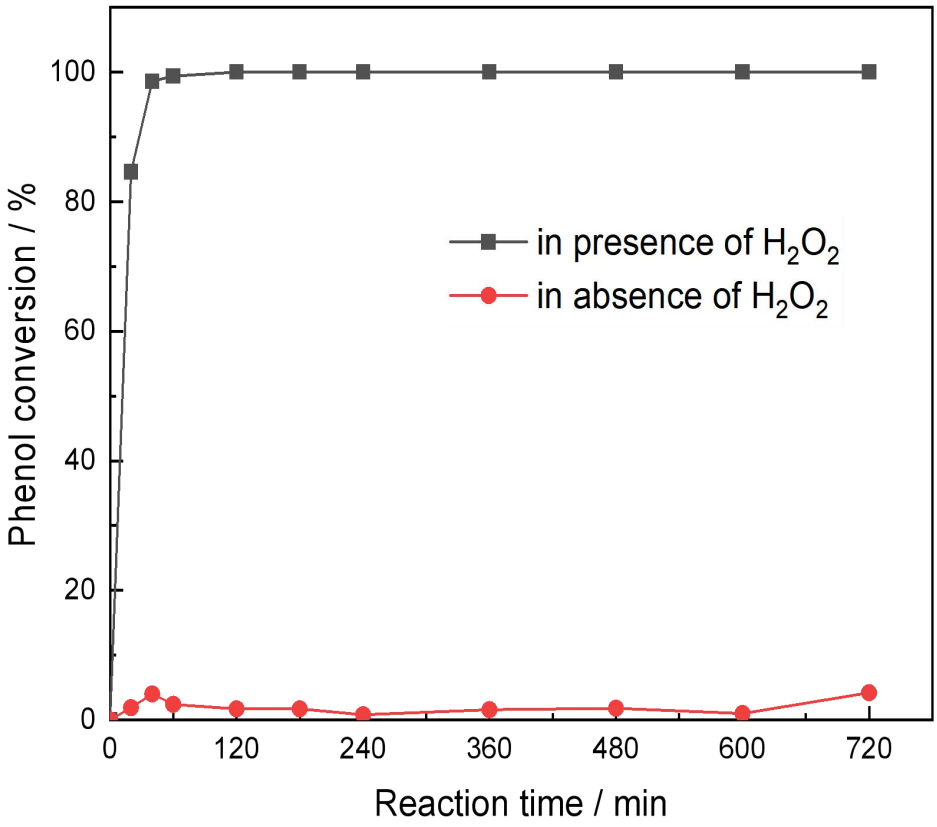

Figure 4.5. Control test for CWPO using Cu/ZSM-5-WI catalyst. Phenol conversion: a) in presence of H_2O_2, black line, and b) in absence of H_2O_2, red line (0.1 g Cu/ZSM-5-WI, 50 mL 1 $g \cdot L^{-1}$ phenol, H_2O_2: phenol of 14, P = endogenous, 80 ºC, 500 rpm). Phenol decomposed completely to intermediates and CO_2 in the presence of H_2O_2 while the phenol conversion was very low when no H_2O_2 used, if Cu/ZSM-5 catalyst was used, suggesting the positive effects of H_2O_2 on phenol decomposition in a system with active catalyst.

In this context and with our methods, control tests were carried out to assess the actual need of H_2O_2 as primary oxidant (figure 4.6): the phenol conversion (4%) over the Cu/ZSM-5 catalyst was as low as that over HZSM-5 and no catalyst, just due to the absence of H_2O_2. The other control test, as can be seen in figure 4.6, reminded of the high capability of the Cu catalyst of H_2O_2 decomposition to free radicals, which reacted with themselves and as a

result to generate O_2 (as shown in Eq. 1.8 - Eq. 1.13) due to the absence of substrate (phenol) in the reaction media.

From all the above control tests, it is thus confirmed that both H_2O_2 and active catalyst were indispensable in the decomposition of phenol and the high activity of Cu/ZSM-5 catalyst by using H_2O_2 as oxidant, to simultaneously achieve: high phenol conversion, high H_2O_2 consumption and efficiency, and large extend of phenol degradation to CO_2.

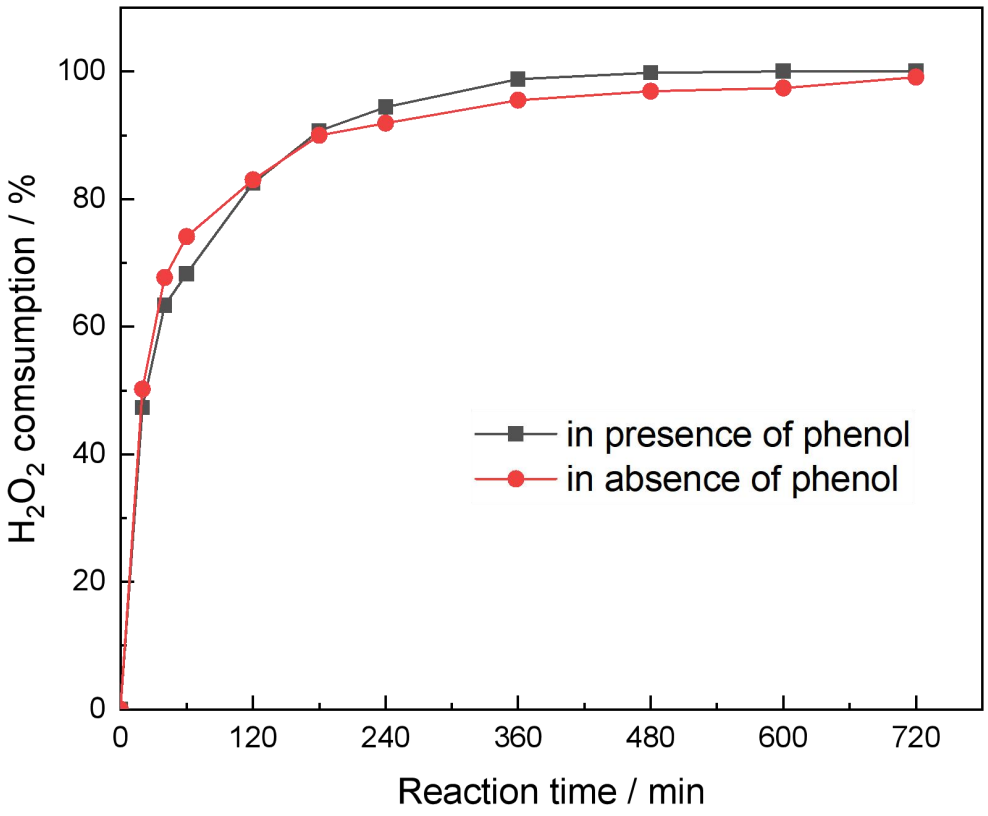

Figure 4.6. Control test for CWPO using Cu/ZSM-5-WI catalyst. H_2O_2 consumption: a) in presence of phenol, black line, b) in absence of phenol, red line (0.1 g Cu/ZSM-5-WI, 50 mL 1 $g \cdot L^{-1}$ phenol, H_2O_2: phenol of 14, P = endogenous, 80 ºC, 500 rpm). H_2O_2 was consumed rapidly when Cu/ZSM-5-WI catalyst was used, regardless of with or without phenol.

Table 4.3. Catalytic results over different reaction systems **in 12 h**. High phenol conversion needs both catalyst and H_2O_2, whereas H_2O_2 consumption needs catalyst only. To obtain high H_2O_2 efficiency, an additional active catalyst such as Cu/ZSM-5 is required in the phenol/H_2O_2 reaction system.

Catalyst	Reactants	**Phenol conversion**	Sum of aromatic compounds[a] (% of the total amount)[b]	Sum of acids	CO_2 formation[c]	**H_2O_2 consumption**	**H_2O_2 efficiency (η)***
Blank test (no catalyst)	Phenol + H_2O_2	**8%**	7.3×10^{-4} mol·L^{-1} (7%)	2.0×10^{-4} mol·L^{-1}	1%	**13%**	**8%**
	Phenol	**2%**	5.7×10^{-6} mol·L^{-1} (0%)	1.3×10^{-5} mol·L^{-1}	0%	**--**	**--**
	H_2O_2	**--**	--	--	--	**15%**	**--**
HZSM-5	Phenol + H_2O_2	**57%**	9.8×10^{-4} mol·L^{-1} (9%)	5.8×10^{-3} mol·L^{-1}	30%	**62%**	**52%**
	Phenol	**4%**	2.6×10^{-5} mol·L^{-1} (0.2%)	4.2×10^{-4} mol·L^{-1}	2%	**--**	**--**
	H_2O_2	**--**	--	--	--	**86%**	**--**
1% Cu/ZSM-5-WI	Phenol + H_2O_2	**100%**	3.4×10^{-5} mol·L^{-1} (0.3%)	3.3×10^{-3} mol·L^{-1}	90%	**100%**	**90%**
	Phenol	**4%**	6.0×10^{-6} mol·L^{-1} (0%)	1.3×10^{-3} mol·L^{-1}	1%	**--**	**--**
	H_2O_2	**--**	--	--	--	**99%**	**--**

a - the sum of hydroquinone, *p*-benzoquinone and catechol in mole, b - the ratio of the aromatic intermediates to the amount of phenol at the beginning of reaction (1.1×10^{-2} mol·L^{-1}), c - CO_2 formation calculated from CMB, *η - the percentage of H_2O_2 decomposed to ·OH radicals used for phenol/intermediates degradation, calculated by Eq. 4.6 [13,35-41]: H_2O_2 efficiency = (CO_2 formation, 100%) / (H_2O_2 consumption, 100%)

Table 4.4. Catalytic results over different reaction systems **in 4 h**. The H_2O_2 efficiency (95%) in 4 h was higher than that in 12 h (90%) indicating a long reaction time (12 h) is not necessary when Cu/ZSM-5 was used as catalyst in the CWPO of phenol.

Catalyst	Reactants	**Phenol conversion**	Sum of aromatic compounds[a] (% of the total amount)[b]	Sum of acids	CO_2 formation[c]	**H_2O_2 consumption**	**H_2O_2 efficiency (η)***
Blank test (no catalyst)	Phenol + H_2O_2	**4%**	4.3×10^{-4} mol·L^{-1} (4%)	3.0×10^{-5} mol·L^{-1}	0%	**7%**	**0%**
	Phenol	**2%**	2.5×10^{-4} mol·L^{-1} (2%)	3.7×10^{-4} mol·L^{-1}	0%	**--**	**--**
	H_2O_2	**--**	--	--	--	**5%**	**--**
HZSM-5	Phenol + H_2O_2	**30%**	1.8×10^{-4} mol·L^{-1} (2%)	3.0×10^{-3} mol·L^{-1}	13%	**35%**	**37%**
	Phenol	**4%**	2.6×10^{-5} mol·L^{-1} (0.2%)	9.5×10^{-4} mol·L^{-1}	1%	**--**	**--**
	H_2O_2	**--**	--	--	--	**51%**	**--**
1% Cu/ZSM-5-WI	Phenol + H_2O_2	**100%**	4.3×10^{-5} mol·L^{-1} (0.3%)	3.8×10^{-3} mol·L^{-1}	89%	**94%**	**95%**
	Phenol	**1%**	3.1×10^{-6} mol·L^{-1} (0%)	6.8×10^{-4} mol·L^{-1}	0%	**--**	**--**
	H_2O_2	**--**	--	--	--	**92%**	**--**

a - the sum of hydroquinone, *p*-benzoquinone and catechol in mole, b - the ratio of the aromatic intermediates to the amount of phenol at the beginning of reaction (1.1×10^{-2} mol·L^{-1}), c - CO_2 formation calculated from CMB, *η - the percentage of H_2O_2 decomposed to ·OH radicals used for phenol/intermediates degradation, calculated by Eq. 4.6 [13,35-41]: H_2O_2 efficiency = (CO_2 formation, 100%) / (H_2O_2 consumption, 100%)

4.3.2 Activity of Cu/ZSM-5 catalyst in the CWPO of phenol

4.3.2.1 Effects of reaction time on the activity of Cu/ZSM-5 catalyst

Owing to the HPLC analysis method we developed that allowing to identify large numbers of intermediates, the aromatic compounds and organic acid were discussed in the form of molar sum rather than the distribution of the specific intermediates in the reaction mixture in the above section, to simplify the analysis of results. In addition, the reaction time (12 h) was unnecessarily long for the reaction using 1% Cu/ZSM-5-WI catalyst, as the phenol conversion, H_2O_2 consumption, CO_2 formation, and intermediates concentration reached a plateau after 4 h (figure 4.7 and table 4.4). Furthermore, the H_2O_2 efficiency even decreased from 95% in 4 h (table 4.4) to 90% in 12 h (table 4.3), which is due to the decomposition of unreacted H_2O_2 to O_2 when substrates were almost removed in the reaction mixture. As a consequence, a reaction time of 4 h was considered more appropriate for all the reactions carried out in this project. In this section, the activity of 1% Cu/ZSM-5-WI in 4 h is comprehensively discussed, including the phenol conversion, H_2O_2 consumption, CO_2 formation and the distribution of each intermediate.

As shown in figure 4.7a, the phenol conversion, H_2O_2 consumption and CO_2 formation increased with reaction time, and reached 100%, 94% and 90% respectively after 4 h, highlighting the high efficiency of the Cu catalyst. Besides, the aromatic compounds, including hydroquinone, *p*-benzoquinone and catechol, though all largely produced at 20 min with the degradation of phenol, were further decomposed within 2 h. Whereas acids such as acetic acid and formic acid were formed after the decomposition of the aromatic compounds and further oxidized. All the intermediates maintained at low concentrations (figure 4.7b and 4.7c) and the sum of aromatics kept at 4.3×10^{-5} mol·L^{-1} (equivalent to 0.3% of the total aromatics, see table 4.4) after 4 h of oxidation, indicating that the reaction time of 4 h is enough for the purification of the phenol-containing water to that of harmless as it is close the discharge limit (1 ppm [42]).

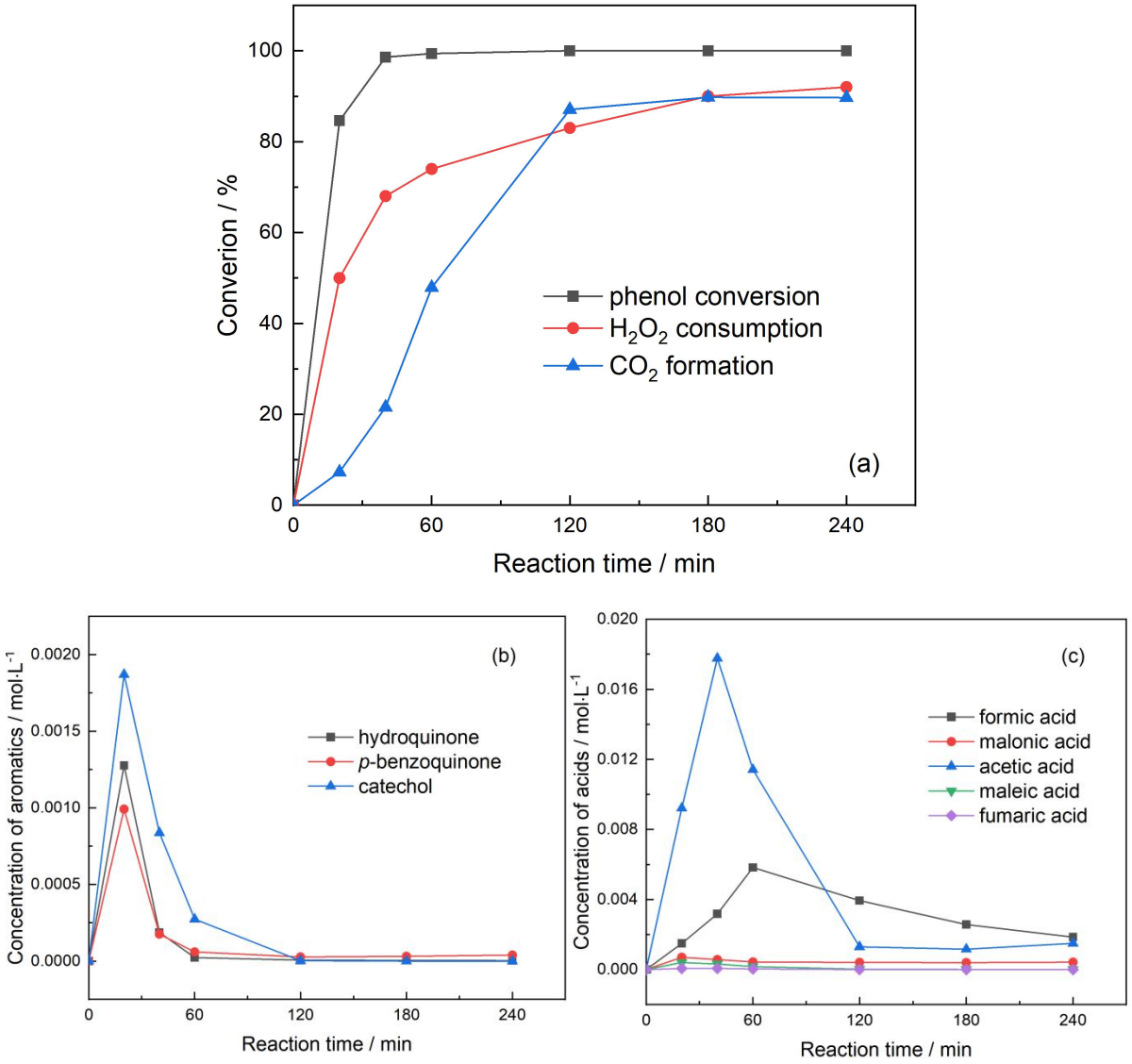

Figure 4.7. a) Phenol conversion, H_2O_2 consumption, CO_2 formation, b) aromatic compounds distribution and c) organic acids distribution in 4 h over 1% Cu/ZSM-5-WI catalyst (0.1 g catalyst, 50 mL 1 g·L^{-1} of phenol, H_2O_2: phenol molar ratio of 14, P = endogenous, 80 ^{o}C, 500 rpm)

4.3.2.2 Effects of stirring speed on the activity of Cu/ZSM-5 catalyst

The stirring speed affects the reaction efficiency as it to some extent determines the external diffusion of reagents (and products) within the aqueous phase reaction. It is well known that the uniform distribution of a solid catalyst in the reaction mixture as well as the diffusion of reactant from the liquid phase to the surface of the catalyst are crucial for the improvement of mass transfer in a heterogeneous liquid phase reaction. A low stirring rate may cause a solid

catalyst to behave like a precipitate sitting at the bottom of a reaction flask, as well as to potentially lead to low contacting efficiency between catalyst and reactants, hence leading to a decrease of catalytic activity of catalyst. To optimize the decomposition rate of the pollutant, the activity of Cu/ZSM-5 catalyst with various stirring rates (200 to 500 rpm) was studied.

Changing the stirring rate within the range of 200 to 500 rpm gave almost identical phenol conversions and CO_2 formations within the experimental error, as shown in figure 4.8, indicating that effects of the external diffusion limitation (or diffusion regime) was insignificant within the ranges we investigated. In this case, stirring speeds ranging from 200 rpm to 500 rpm are all acceptable and in this project, we mainly use 500 rpm.

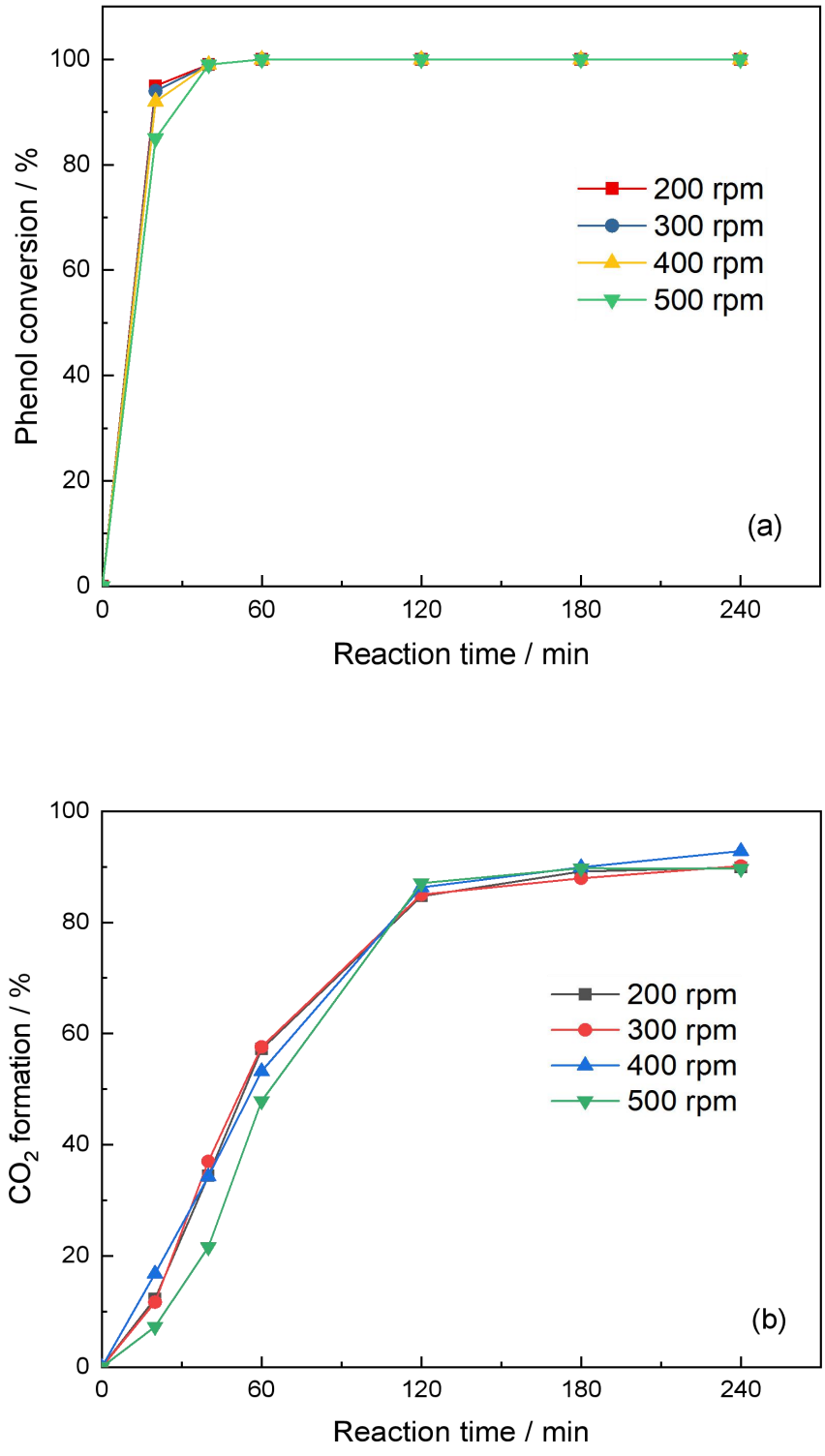

Figure 4.8. Activity of 1% Cu/ZSM-5-WI catalyst in the CWPO of phenol under different stirring rate: a) phenol conversion, b) CO_2 formation (50 mL 1 $g \cdot L^{-1}$ of phenol, H_2O_2: phenol of 14, initial pH of 6, M: S of 1: 30, P = endogenous, 80 ºC, 500 rpm)

4.3.2.3 Effect of initial pH on the phenol conversion and H_2O_2 decomposition over Cu/ZSM-5 catalyst

As discussed in chapter 1, the pH of the reaction mixture is one of the limiting factors influencing the application of Fenton reagent as the formation of ·OH radicals requires narrow pH range (3-5). As the principle may remain the same even alternating the homogeneous Fenton catalyst to a heterogeneous Fenton-like catalyst, thus the catalytic performances of Cu/ZSM-5 catalyst under various initial pH range was investigated by changing the acidity of the initial phenol solution with nitric acid (nitric acid was selected as Cl^- and SO_4^{2-} may affect the rate of H_2O_2 decomposition in Fenton reaction [43]).

No significant changes of activity were observed when the initial pH was not adjusted (actual pH of 5-6) or adjusted to ≥ 3 (figure 4.9), since the phenol conversion and H_2O_2 consumption remained constant. In view of this, the heterogeneous Cu catalyst could be applied in the CWPO process at pH range as wide as (or even wider than) classical Fenton reagent. Furthermore, it is also clear that the activity of the catalyst decreased considerably at an initial pH of 2. As can be seen, the phenol conversion and H_2O_2 consumption increased slowly to 67% and 61%, respectively in 4 h, exhibiting an overall activity only slightly higher than undoped HZSM-5 but just at the same level as that using much lower M: S ratio (1:1600, as shown in figure 4.11, discussed later). This is because that at pH below 2.5, the decomposition efficiency of phenol decreases due to the slow formation ·OH radicals/the scavenging effect of ·OH by hydrogen protons and the formation of stable $[H_3O_2]^+$ in the presence of high concentrations of H^+ which make H_2O_2 more stable, as discussed in section 1.5.3.

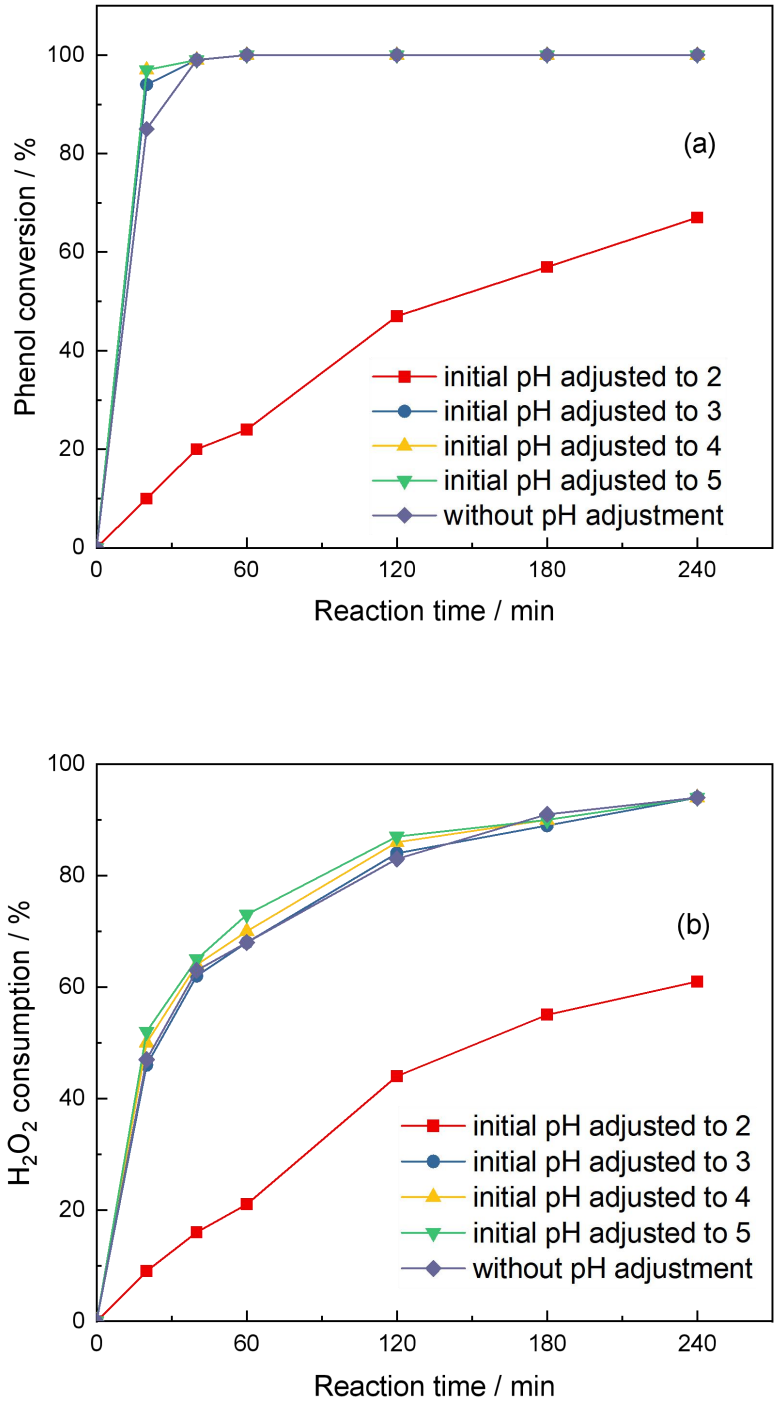

Figure 4.9. a) Phenol conversion and b) H_2O_2 consumption using 1% Cu/ZSM-5-WI catalyst in the CWPO of phenol under different initial pH (50 mL 1 g·L^{-1} of phenol, H_2O_2: phenol of 14, M: S of 1: 30, P = endogenous, 80 ºC, 500 rpm). The activity of the catalyst, in terms of phenol conversion and H_2O_2 consumption, decreased significantly when adjusting the initial pH to 2.

This result was interpreted as the scavenging effect of ·OH by protons, and the formation of stable oxonium ion $[H_3O_2]^+$ [44] originating from H_2O_2 in the presence of high concentrations of H^+, As a consequence, the oxonium ions make hydrogen peroxide more stable and reduce its reactivity with Cu catalyst. Therefore, a pH of 6 without any adjustment was adopted in this project for simple operation and high efficiency. Furthermore, it could be reasonably deduced that the formation of organic acids may result in a decrease in the activity of a catalyst in the reaction when the pH of the reaction mixture declines below pH 3 [44-46]. Acetic acid, formic acid, and oxalic acid are the main acid intermediates in the reaction process from the perspective of the concentration (as proved in figure 4.7) and are more likely to cause a significant decrease in the pH of the reaction mixture.

Besides, the influence of anion, nitrate (NO_3^-), needs to be eliminated as it may act as an oxidant [47,48] and affect the catalytic result. Thus the activity of the catalyst in acidic solutions adjusted by different acids (hydrochloric acid HCl, sulfuric acid H_2SO_4, and oxalic acid $H_2C_2O_4$) was further investigated to prove the decreased activity is due to the effects of pH. The catalytic performances, in terms of phenol conversion in the four tests in figure 4.10 were different, especially the phenol conversion using oxalic acid was less than 20%, this is probably because oxalic acid itself is an organic compound that can be oxidized in the CWPO process [49], thus it forms competitive reaction with phenol and/or because that oxalic acid can be used as a natural antioxidant in the Cu^{2+}/H_2O_2 system [50]. The phenol conversion in solution of HCl was higher than in other acids, which is probably because the radical formation in the CWPO process was affected in the presence of Cl^- [51]. Though the phenol conversions varied in the presence of different anions, they all maintained at lower than 60% after 4 h when the initial pH of the phenol solution was adjusted to 2, as shown in figure 4.10, which proved the negative effects of low pH (< 3) on the activity of Cu/ZSM-5 catalyst in the CWPO of phenol process.

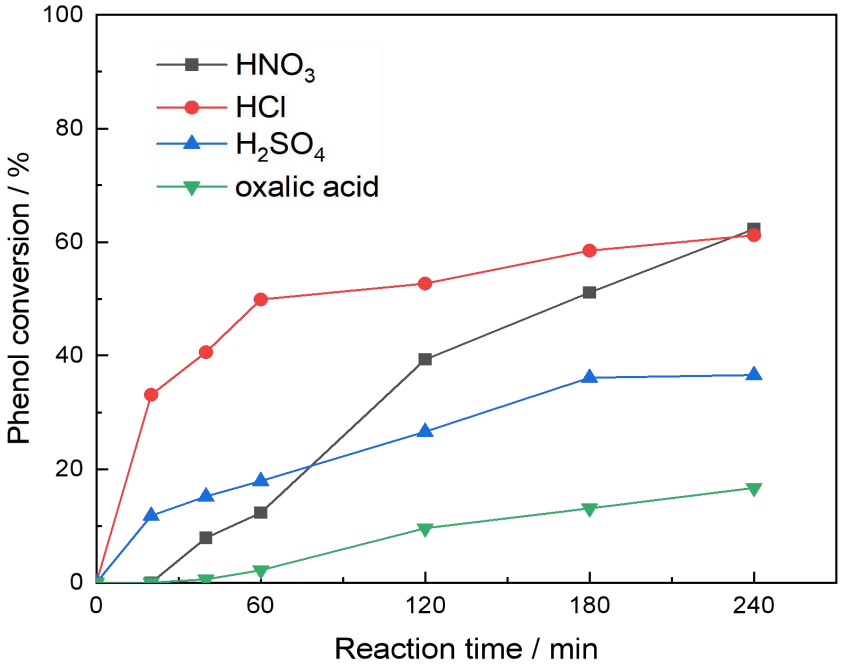

Figure 4.10. Activity of 1% Cu/ZSM-5-WI catalyst with initial pH of 2, pH adjusted by nitric acid (HNO_3), hydrochloric acid (HCl), sulfuric acid (H_2SO_4) and oxalic acid ($H_2C_2O_4$) (50 mL 1 $g \cdot L^{-1}$ of phenol, H_2O_2: phenol of 14, M: S = 1: 30, P = endogenous, 80 °C, 500 rpm). The phenol conversions were < 60% when the initial pH was adjusted to 2 no matter what acid was used.

4.3.2.4 Effects of metal to substrate ratio on the phenol conversion and CO_2 formation over Cu/ZSM-5 catalyst

The search for optimal M:S ratio is essential for several reasons: 1) increasing the M:S ratio within a certain range sometimes translates to an increasing of reaction rate (and in turn diagnostic of a reaction not affected by external diffusion limitations), 2) the use of an excess of catalyst results in waste of materials. The M:S ratio varying from 1:3200 to 1:30 showed significantly different results in the CWPO of phenol (figure 4.11). As can be seen, the phenol conversion, though less than 100%, increased with the increase of the amount of catalyst at the M: S ratio lower than 1:200, suggesting that the reaction is under kinetic regimes whereas the external diffusion limitation effects (mass transfer) are negligible. Increasing the M: S ratio from 1: 100 to 1: 30 led to constant phenol conversions (100%), which could be due to: (i)

diffusion limitation present or (ii) the conversion is already at maximum. The former reason is denied since the increase of CO_2 formation from 59% (at M:S of 1:100) to 89% (at M:S of 1:30) was observed, indicating the few effects of the external diffusion limitation. Further increasing M: S ratio to 1: 10, the plateau of phenol conversion, CO_2 formation as well as intermediates (both acids and aromatics) concentration were shown, indicating that it reached an external diffusion limitation and should not be considered. To summarise the reaction is under kinetic regime and is not affected by diffusion limitation at M: S ratio from 1:3200 to 1:30, while within this range, the M: S ratio of 1:30 led to the satisfactory catalytic results with high phenol concentration (100%), high CO_2 formation (90%), complete removal of aromatic compounds and low acids concentration (0.0038 mol·L^{-1}) thus was used in this project.

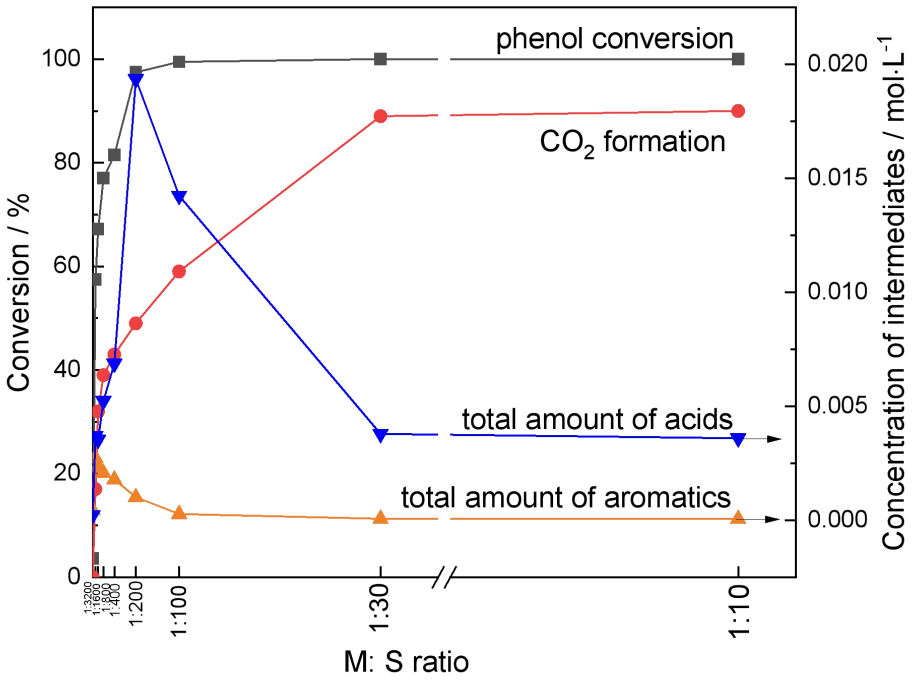

Figure 4.11. Activity of 1% Cu/ZSM-5-WI catalyst in phenol oxidation with different M: S ratio: phenol conversion in black, CO_2 formation in red, total aromatics in orange, total acids in blue (50 mL 1 g·L^{-1} of phenol, H_2O_2: phenol of 14, 4 h, 500 rpm, initial pH of 6, P = endogenous, 80 °C, 500 rpm). The reaction was under kinetic regimes and the external diffusion limitation effects (mass transfer) were negligible when M: S ratio ranging from 1:3200 to 1:30.

Overall, complete phenol conversion, high H_2O_2 consumption and CO_2 formation, thorough oxidation of toxic aromatic intermediates were obtained. Thus indicating the achievement of high water purification efficiency from the aspect of low toxicity and high biodegradability with the Cu/ZSM-5 catalyst under the experimental conditions (time of 4 h, stirring rate of 500 ppm, initial pH of 6 and M: S molar ratio of 1: 30).

4.4 Stability of Cu/ZSM-5 catalyst in the CWPO of phenol

In addition to activity, stability is also a well-recognized parameter to evaluate the performance of catalysts in a chemical reaction. In fact a stable catalyst implies a higher durability in the long term and as such a platform for scale up or continuous usage (for example from a batch reactor to a plug flow reactor). A stable catalyst is supposed to exhibit steady activity throughout its lifetime, or can be easily regenerated to the initial activity level [52,53]. However, some behaviour such as severe active metal leaching in solution (in our case aqueous conditions), would damage the longevity of heterogeneous catalyst and consequently cause irreversible catalyst deactivation, leading to an increase in the cost for the water purification process or even an abandoning of catalysts. Therefore, the evaluation and enhancement of the stability of heterogeneous Cu catalyst in phenol oxidation is of the foremost importance after the confirmation of the high activity.

4.4.1 Stability of 1% Cu/ZSM-5 catalyst in the CWPO of phenol

Table 4.5. Leaching of 1% Cu/ZSM-5 catalyst in phenol oxidation reaction (tested by ICP-OES)

Reaction media	Cu concentration in solution	Cu leaching
In water (80 ^oC, 4 h)	0.12 $mg \cdot L^{-1}$	<1%
In reaction (80 ^oC, 4 h)	14 $mg \cdot L^{-1}$	81%

The stability of prepared catalysts, in this research, was characterized by the concentration of active metal in the aqueous phase. The concentration of active species that passed from the catalyst to the reaction medium during the reaction, as well as the actual concentration of

active species that doped on the zeolite were measured by ICP-OES (see 2.5.3 in Experimental). The ratio of the obtained results is known as leaching (%), as expressed in Eq. 4.7.

$$\text{Metal leaching} = \frac{\text{concentration of leached metal}}{\text{total concentration of metal used in a reaction}} \times 100\% \qquad \text{(Eq. 4.7)}$$

The higher the leaching, the lower the stability of catalyst and the higher the toxicity of the leached metal to the environment. In usual, a 50% loss may quickly make the catalyst nonreusable while metal leaching over 1.3 ppm threatens the safety of drinking water [54,55]. In that case, catalyst with low leaching and high stability is required in this project. The Cu leaching of Cu/ZSM-5-WI catalyst after an actual reaction in the phenol oxidation for 4 h was compared with that in water without any substrate, in order to test if any leaching was present at all (given our WI preparation method), and if leaching was presented, this was the result of the reaction/reaction products or of the reaction media. As it can be seen (table 4.5), the leaching of the heterogeneous Cu catalyst in water was negligible since only 0.12 ppm Cu (corresponding to <1% Cu leaching) was detected in the aqueous phase after 4 h, suggesting the high stability of the impregnated catalyst in hot aqueous condition. In comparison, the Cu/ZSM-5 catalyst had low stability in phenol oxidation as over 80% of Cu (14 ppm of Cu in solution) leaching from the surface of the catalyst to the reaction mixture. The high Cu leaching not only highlighted the low reusability of the catalyst, but resulted in secondary contamination due to the Cu concentration far more exceeding the permissible limit of Cu (1.3 ppm in drinking water [54,55]).

4.4.2 Causes of metal leaching in phenol oxidation reaction

The metal leaching from a heterogeneous catalyst in the CWPO process may threaten water safety as discussed above. Furthermore, it also hampers the development of heterogeneous catalyst in the CWPO process. In this case, a better understanding of the origin of metal leaching is helpful for both the design of stable catalyst and the regeneration of a deactivated

catalyst. In the following sections (4.4.2.1-4.4.2.7), all the factors that probably lead to metal leaching of heterogeneous catalyst in the CWPO process were systematically investigated.

4.4.2.1 pH

Metal oxides (such as CuO [56,57], Fe_2O_3 [58,59], Co_3O_4 [60,61]) are vulnerable to leaching in acidic conditions. Therefore, the investigation on the effects of pH on Cu leaching of catalyst is necessary as the formation of acid intermediates such as acetic acid and formic acid is unavoidable in the phenol degradation reaction [11,62], which results in a decrease of the pH of the aqueous reaction mixture from being neutral to markedly acidic (pH around 3). In this context, the Cu leaching of Cu/ZSM-5-IE catalyst in different acidic solutions, for which the pH was decreased by using different inorganic acids were tested.

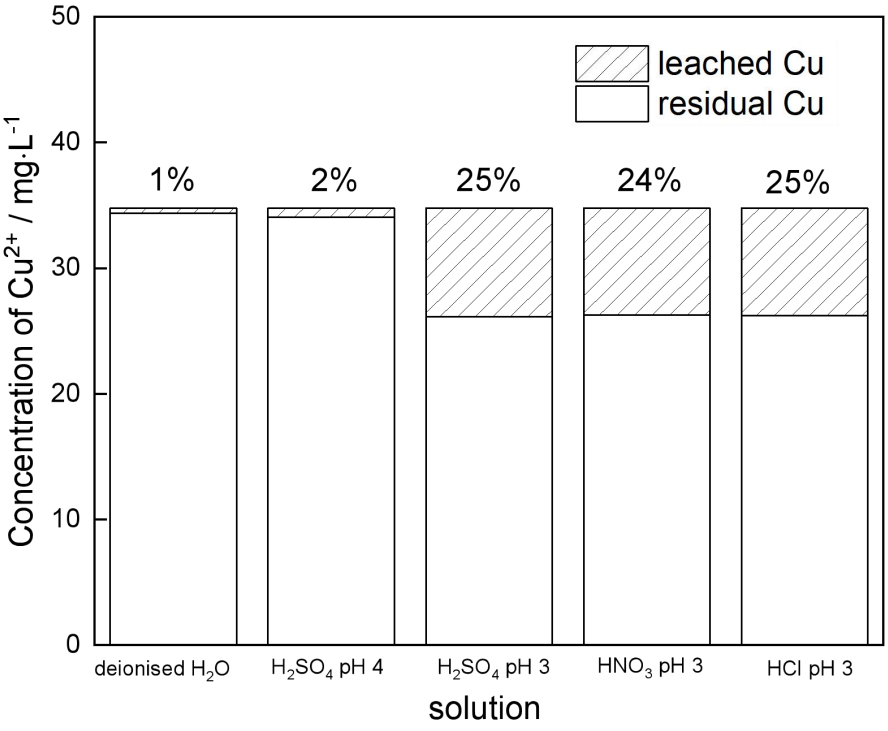

Figure 4.12. Leaching of Cu/ZSM-5-IE catalyst in different inorganic acid solutions (50 mL solution, 0,1 g catalyst, P = endogenous, 80 °C, 4 h, 500 rpm). Cu leaching increased with the decrease of pH and it was significant at pH 3.

Three common inorganic acids, HCl, HNO_3, H_2SO_4 were used in this section to adjust the pH of the solution as the anions of inorganic acids may also affect the metal leaching [63]. For example, it is reported in the literature that temperature (30-50 ^oC, whereas in our case 80 ^oC is used) has a significant effect on the acceleration of copper dissolution with HNO_3 followed by H_2SO_4 while has a weak effect on the dissolution of copper with HCl.

The solutions with desired pH value were prepared by firstly calculating the expected $[H^+]$ concentration according to their desired pH, and then by confirming the actual pH value via a pH meter. As shown in figure 4.12, the metal leaching of catalyst increased with the decrease of pH of the acid solution, which was especially significant when pH of solution lower than 4, as consistent with that reported in the literature [9]. In a typical reaction in this project, the lowest pH of reaction mixture can reach below 3 (2.7 for instance) when an active catalyst such as Cu/ZSM-5 is used, indicating pH change *is* one of the reasons of catalyst deactivation. In addition, the anions Cl^-, NO_3^-, SO_4^{2-} had no obvious effects on the Cu leaching as the metal concentrations in HCl, HNO_3 and H_2SO_4 solutions were at the same level when pH kept constant. As the metal leaching at pH higher than 4 was negligible, it would seem reasonable to deduce that by adjusting the pH of the reaction mixture to above 4 (for example with an alkaline solution such as Na_2CO_3) during the reaction, might be helpful to reduce Cu leaching.

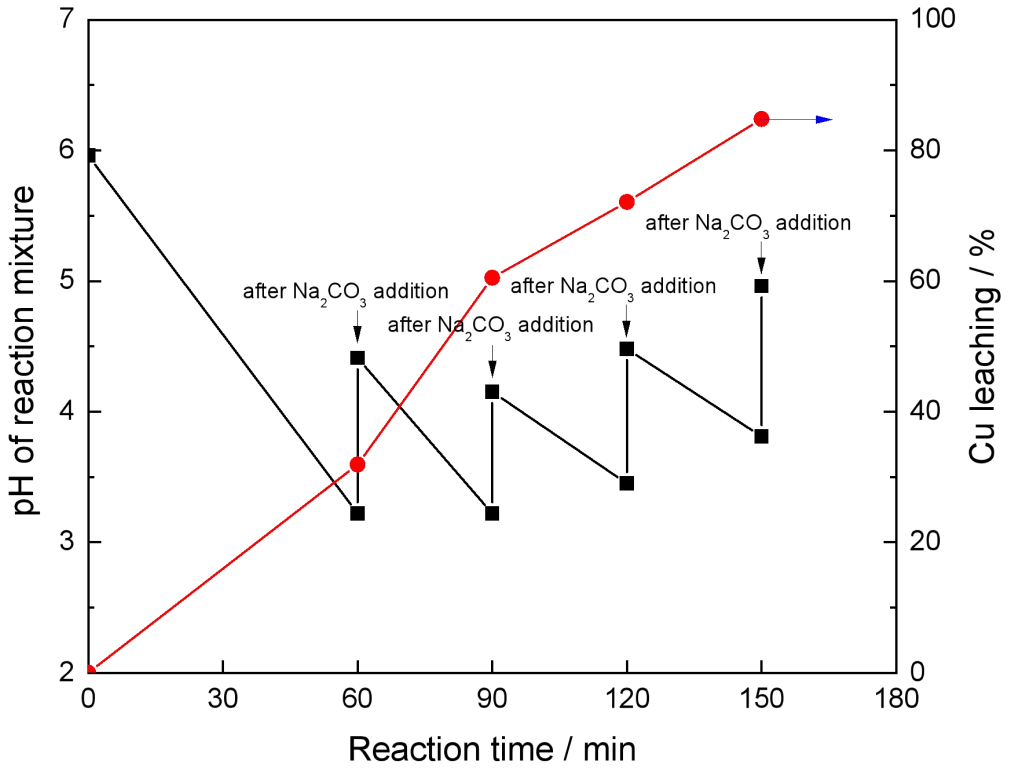

Figure 4.13. The effects of pH adjustment (black line) of reaction mixture on metal leaching (red line) of the Cu/ZSM-5-IE catalyst (50 mL solution, 0,1 g catalyst, P = endogenous, 50 °C, 4 h, 500 rpm). The Cu leaching kept growing with reaction time though the pH of the reaction mixture was maintained 3-5, indicating the pH is not the only reason for metal leaching.

To verify the effects of pH adjustment on the catalyst stability, the metal leaching of Cu/ZSM-5-IE catalyst in the phenol oxidation reaction was monitored when pH of the reaction mixture being adjusted by Na_2CO_3 solution. The pH of the reaction mixture was adjusted with Na_2CO_3 solution (2.5×10^{-2} mol·L^{-1}) every half hour and for each time the volume of the Na_2CO_3 solution was controlled within 0.1-0.2 mL to minimize the effects of the volume change of reaction mixture (initial solution of 50 mL) on the determination of Cu ions. On the other hand, the pH of the reaction was maintained within the range of 3-5 for several reasons: 1) the metal leaching of less than 25% (see figure 4.12) can be expected at pH above 3 if pH is the only factor influencing metal leaching, 2) the pH range 3-6 is within the optimal reaction

conditions which would not significantly affect the activity of Cu/ZSM-5 catalyst (as shown in figure 4.9), 3) it is reported that Cu tended to precipitate by carbonate (CO_3^{2-}) at pH > 6.4 [64] thus pH at 3-5 may avoid the Cu leaching promoted by Na_2CO_3. The results are shown in figure 4.13. For a pH of the reaction mixture decreasing from around 6 to 3.2 in 1 h, a Cu leaching of 32% was observed, which was slightly higher than that in inorganic acid solutions with pH of 3.0 for 4 h. It suggested that pH change might not the only reason for Cu leaching. Besides, the Cu leaching increased gradually with time to > 80% after 4 h, even though the pH of the reaction mixture was maintained at 3-5, suggesting that 1) pH decrease is not the only reason for metal leaching and 2) pH adjustmenthas little help to improve catalyst stability in the CWPO of phenol.

4.4.2.2 H_2O_2

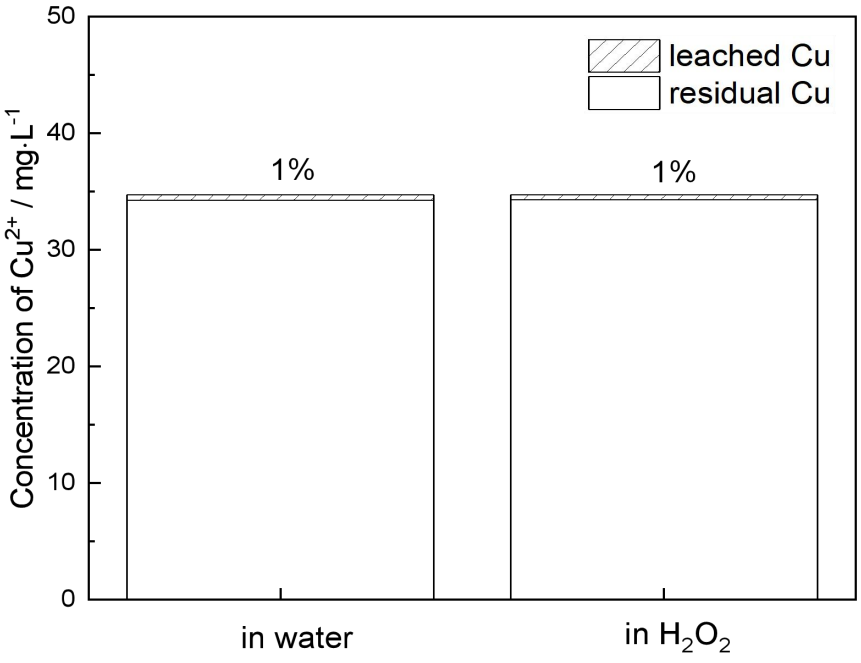

Figure 4.14. Leaching of Cu/ZSM-5-IE catalyst in H_2O and H_2O_2 solutions tested by ICP-OES (0.1 g catalyst, 50 mL of solution, P = endogenous, 80 ^oC, 4 h, 500 rpm). Cu leaching maintained constant with or without addition of H_2O_2.

It is reported in some literature that the hydrogen peroxide may also contribute to the metal leaching in the CWPO of phenol [65]. However, the leaching of Cu in H_2O_2 solution (0.40 ppm, 1% of loss) was as low as that in water (0.44 ppm, 1% of loss), as shown in figure 4.14, which suggested that the influence of the H_2O_2 on the catalyst deactivation is insignificant for this catalyst and under reaction conditions and as such it can be neglected.

4.4.2.3 Reaction time

Exposure of the catalyst to a reaction mixture at low pH in a batch reactor for long time may impair the longevity of catalyst, as mentioned in literature [66,67]. Therefore, the effect of reaction time (or contact time) [68] on the stability of catalyst in the phenol degradation process was investigated. In our case the major investigation tool for the effect of this parameter was ICP-OES for the detection of Cu and the determination of its concentration in the reaction mixture at different times. As shown in figure 4.15, Cu transferred rapidly in the reaction mixture with the highest Cu leaching (85%, 30 ppm) observed at 20 min. Based on these data, it would be impossible to improve the stability of this catalyst in a batch reactor, and meanwhile maintain the activity. Conversely by reducing the reaction time would not be a viable option either, as reaction time longer than 20 min would be necessary for the complete decomposition of phenol and aromatic intermediates. On the other hand, the curves of Cu leaching and phenol conversion showed similar trends, suggesting that the formation of intermediates (acids capable to form complexes with Cu) might be the main cause of leaching (discussed below, see section 4.4.2.6).

Interestingly the Cu concentration detected in the reaction media reached a peak at 20 min (85%, 30 ppm) and kept constant till 1 h, indicating that the metal species transferred from the surface of the catalyst into the reaction mixture rapidly. Afterward, it decreased gradually to 55% (19 ppm) at 4 h. This means 35% of the leached Cu ‘disappeared’ from the solution. This effect has been reported in the literature and and the possible explanations given in the

literature were the formation/precipitation of copper oxalate [69] and/or re-adsorption of Cu by the zeolite support [64-66].

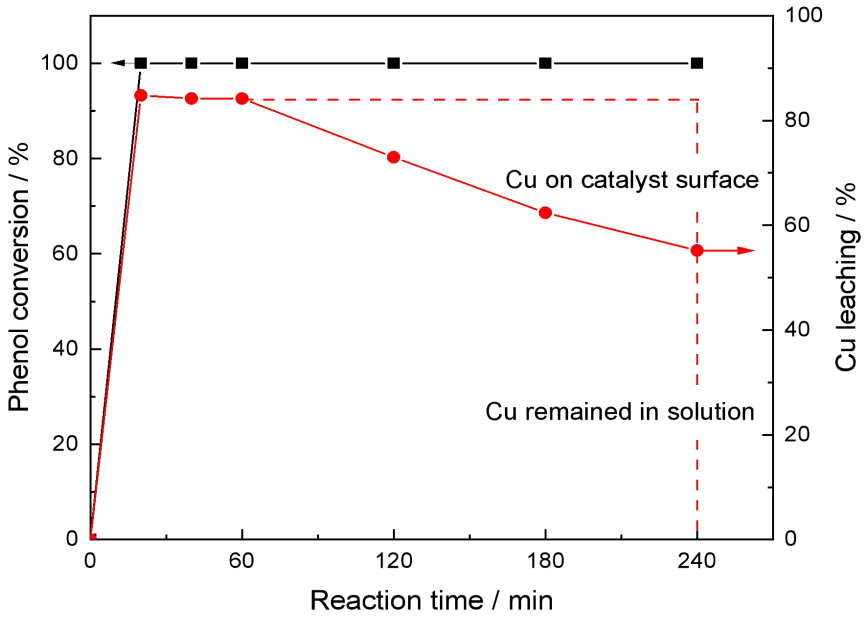

Figure 4.15. Leaching of Cu/ZSM-5-IE catalyst in phenol oxidation reaction with time in a batch reactor: phenol conversion in black and Cu leaching in red (0.1 g Cu/ZSM-5-IE catalyst, 50 mL 1 $g \cdot L^{-1}$ phenol solution, phenol: H_2O_2 = 1: 14, P = endogenous, 80 °C, 4 h, 500 rpm). The leaching reached peak value at 20 min and decreased with time after 1 h, suggesting that Cu leaching occurred rapidly in the reaction and whereas part of the leached Cu ions went back onto the zeolite after 1 h.

To explain why the Cu concentration detected in the reaction mixture was decreasing after 1 h, a series of tests were conducted. Firstly, in order to assess if this was the result of the formation of Cu/oxalate precipitates, a series of Cu concentrations as a function of oxalic acid concentrations were plotted (Figure 4.16). In those tests, an array of Cu nitrate ($Cu(NO_3)_2$) and oxalic acid ($H_2C_2O_4$) mixed solutions were prepared; and stirred at 80 °C for 4 h to mimic the actual reaction conditions. The Cu concentration in each mixed solution was fixed at 30 ppm, namely, the maximal Cu concentration detected in the reaction mixture when using Cu/ZSM-5-IE catalyst, whereas the oxalic acid concentrations varying from 0 to 250 $mg \cdot L^{-1}$

(2.8×10^{-3} mol·L^{-1}, corresponding to 26% selectivity of phenol to oxalic acid and far higher than the solubility of Cu oxalate, 1.6×10^{-4} mol·L^{-1} [70]). As shown in figure 4.16, the Cu concentrations maintained stable with the increase of oxalic acid concentration, indicating that Cu oxalate formation, at least at these concentration ranges, is not the reason for the decreased Cu concentration in an actual reaction. It is concluded that Cu oxalate precipitate occurred but the grain size of the precipitates was so small and completely dispersed in the aqueous media thus they could be atomized by ICP-OES.

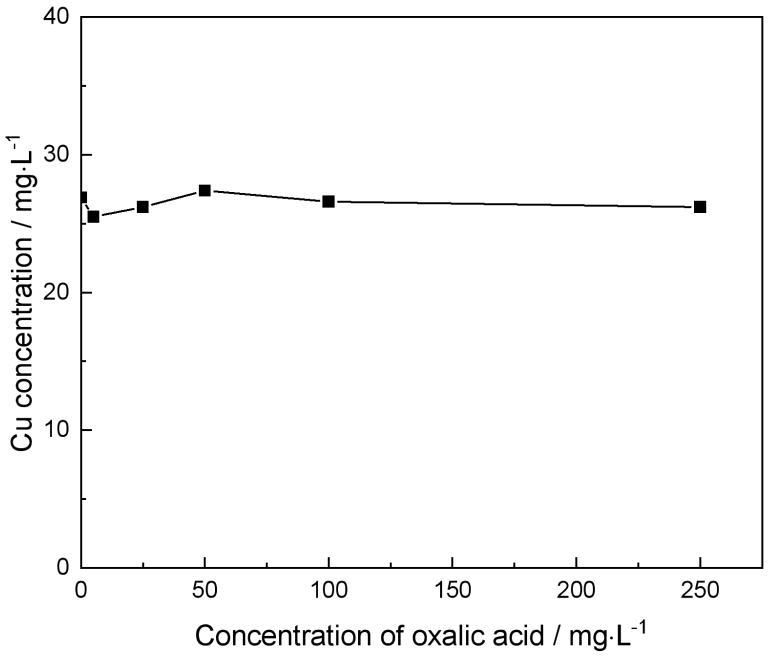

Figure 4.16. Cu concentration ($Cu(NO_3)_3$ as precursor) with function of oxalic acid concentration (50 mL solution, P = endogenous, 80 °C, 4 h, 500 rpm). The Cu concentration determined by ICP-OES maintained stable in the solution with oxalic acid concentrations ≤ 250 mg·L^{-1}.

Secondly, to assess the effect of a possible re-incorporation of Cu within the zeolite [71-73], two tests were conducted: 1) the leaching behaviour of Cu supported nonporous SiO_2 catalyst in the CWPO of phenol reaction, 2) the change of Cu concentrations with time in deionized water with the presence of HZSM-5. For the former test, the result is shown in figure 4.17, the phenol conversion reached over 90% in 20 min and meanwhile, the Cu

leaching (80%, 16 mg·L^{-1}) maintained high and stable throughout the reaction. The decrease of Cu ions with reaction time after 1 h in the reaction mixture was not observed, which is different from the data in figure 4.15, possibly because nonporous silica has weak adsorption capability of Cu ions [74].

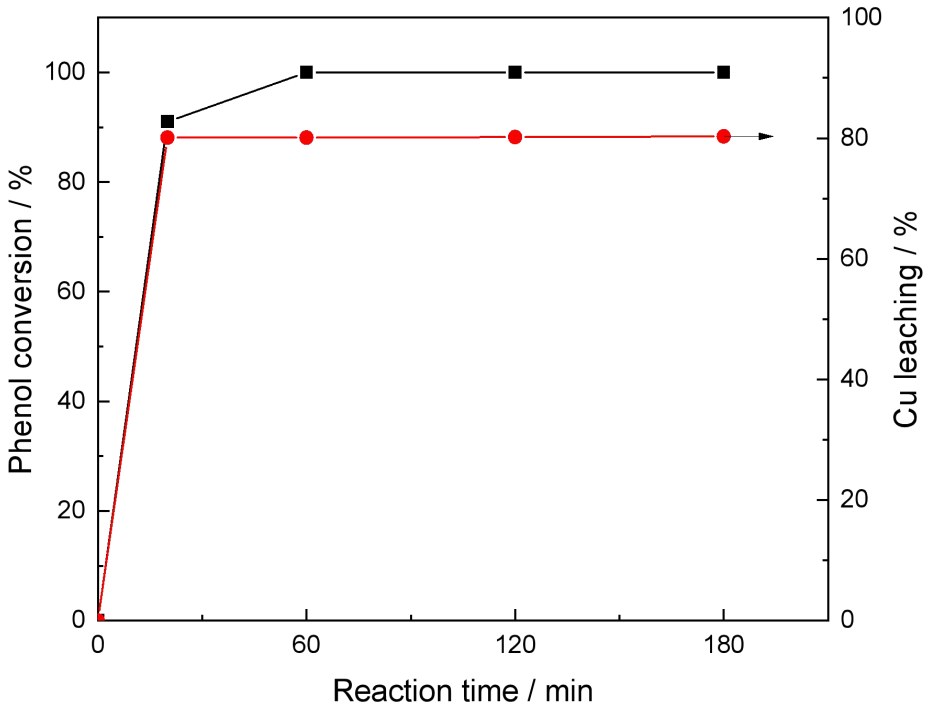

Figure 4.17. Cu leaching of 1% Cu/SiO_2-WI in the CWPO of phenol with time: phenol conversion in black and Cu leaching in red (0.1 g Cu/SiO_2-WI catalyst, 50 mL 1 g·L^{-1} phenol solution, phenol: H_2O_2 = 1: 14, P = endogenous, 80 °C, 500 rpm). The Cu leaching maintained stable after the first hour possibly due to the weak adsorption capability of nonporous silica to Cu ions.

In comparison, the effects of zeolite support on the adsorption of Cu ions in aqueous solutions were presented in figure 4.18. The Cu concentration was monitored in solution containing 0.1 g of HZSM-5, while the same reaction conditions kept same as that using Cu/ZSM-5-IE catalyst. If HZSM-5 adsorbs Cu under the experimental condition (50 mL of 30 ppm Cu solution, 0.1 g HZSM-5, 80 °C, 4 h), Cu concentration lower than the initial value (30 ppm) would be detected. The Cu concentrations versus reaction time were presented in

figure 4.18. As shown, the Cu concentration (initial concentration of 30 ppm), as expected, decreased greatly from 20 min and maintained at lower concentration (around 10 $mg \cdot L^{-1}$) than the initial value (27 $mg \cdot L^{-1}$), suggesting the adsorption ability of the HZSM-5 zeolite in the condition.

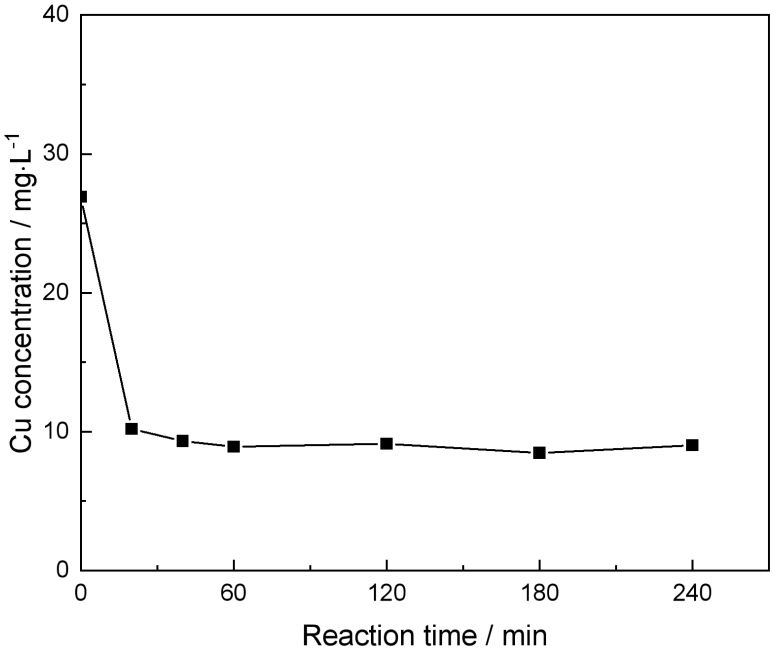

Figure 4.18. Change of Cu concentration with reaction time in the mixture solution of HZSM-5 and Cu nitrate (0.1 g of HZSM-5, 50 mL of solution, 80 °C, 500 rpm). The Cu concentration decreased in the solution with presence of HZSM-5 due to the adsorption of Cu ions onto HZSM-5 zeolite.

To sum up, the reason of the decreased Cu concentration in reaction mixture was due to the re-adsorption of leached Cu ions by ZSM-5 zeolite.

4.4.2.4 Reaction temperature

A hydrothermal environment may also affect the leaching behaviour of metal oxide catalysts [75-77]. As shown in figure 4.19, Cu leached out much more slowly with time at temperature of 50 °C in comparison with that at 80 °C. However, the Cu leaching of Cu/ZSM-5 catalyst in

the reaction process, whether at temperature of 80 °C or 50 °C, rose simultaneously with the phenol conversion and reached approximately 80% when complete phenol conversions were obtained. It suggested that decreasing the reaction temperature slowed down the Cu leaching process through decreasing the phenol degradation efficiency or slowing acid formation but did not change the final leaching. In addition, it is also implied that the improvement of the stability of catalyst by decreasing reaction temperature is unfeasible as it sacrificed the phenol removal efficiency. Also, temperature affected the stability of catalyst possibly through the formation of intermediates, which might be the true and main reason of Cu leaching (discussed below).

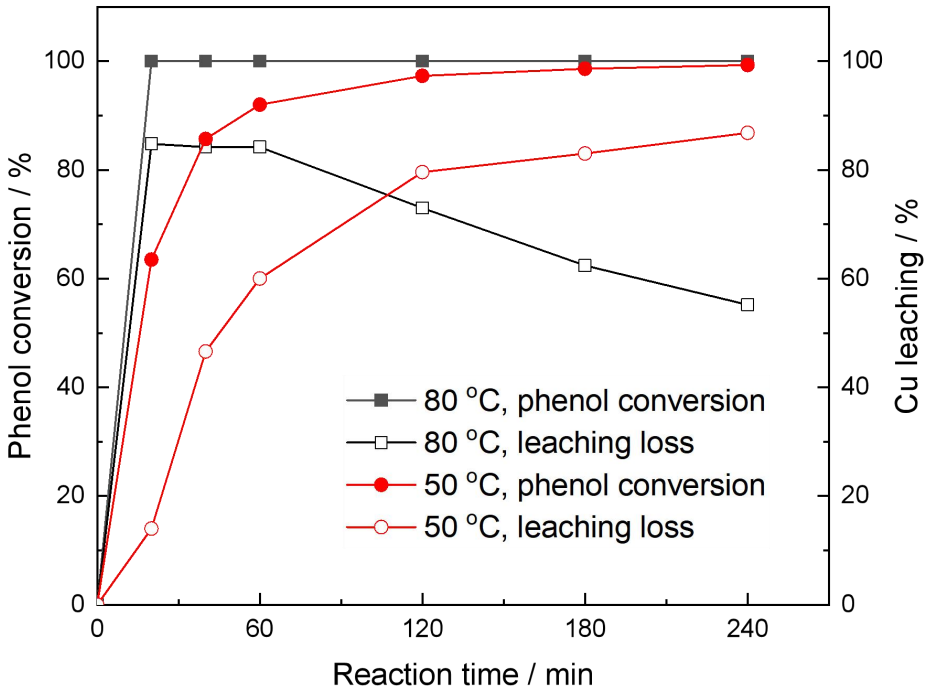

Figure 4.19. Leaching of Cu/ZSM-5-IE catalyst with reaction time at different temperatures (0.1 g Cu/ZSM-5-IE catalyst, 50 mL 1 g·L^{-1} phenol solution, phenol: H_2O_2 = 1: 14, P = endogenous, 4 h, 500 rpm). Decreasing the reaction temperature slowed down the Cu leaching process by decreasing the phenol degradation efficiency or slowering acid formation but did not change the final leaching.

4.4.2.5 M: S ratio

The effect of the M: S ratio (metal to substrate ratio, where metal in this section refers to Cu) on the leaching was also studied. As shown, changing the M: S ratio, from the trend of phenol conversion and Cu leaching in figure 4.20, had big influence on the phenol decomposition efficiency while less effects on the stability. As it can be seen, when the M: S ratio decreased to 1: 200 the Cu leaching increased gradually with time and finally reached 70% at 2 h, while at M: S ratio of 1: 20 the leaching reached 84% at 20 min. However, whether the M: S ratio was high or low, the final leaching maintained as high as over 70% when the phenol conversion reaching 100%, which emphasized once more that the intermediates (discussed below) capable of forming Cu complexes are most likely reasons for metal leaching rather than reaction conditions.

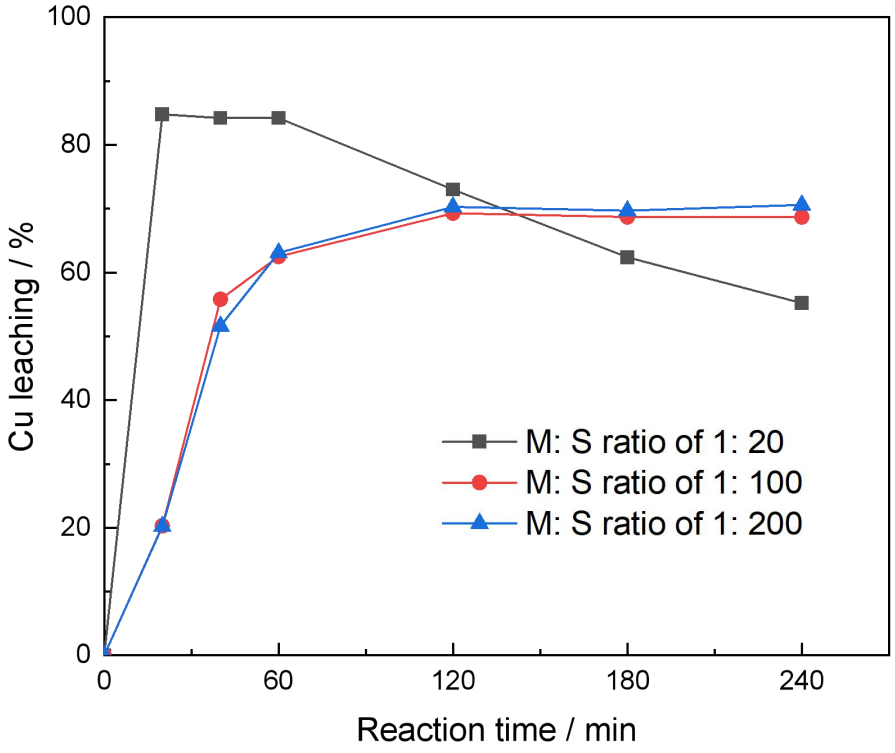

Figure 4.20. Phenol conversion and Cu leaching over Cu/ZSM-5-IE catalyst in the CWPO of phenol with different M: S ratio (0.1 g Cu/ZSM-5-IE catalyst, 50 mL 1 g·L^{-1} phenol solution, phenol: H_2O_2 = 1: 14, P = endogenous, 80 °C, 500 rpm)

4.4.2.6 Formation of intermediates

The physicochemical properties of the various intermediates that are formed in the phenol decomposition process, such as hydroquinone and acetic acid, are quite different, thus they may result in a different influence on the metal leaching of Cu in solution. In order to investigate the effects of the formation of aromatic and acid intermediates in the reaction process on the catalyst stability, the Cu leaching of catalyst in solution of each of the intermediate was studied. The reaction conditions were the same as those heterogeneous reaction except that the initial reactant solution was pure intermediates solution but in the absence of H_2O_2.

Table 4.6. Physicochemical properties of the intermediates. The pKa values of the intermediates are correlated to the ability of these intermediates of leaching metal into the liquid phase.

Organic compound	Formula	pKa_1
hydroquinone	C_6H_4-1,4-$(OH)_2$	9.96
p-benzoquinone	$C_6H_4(=O)_2$	--
catechol	C_6H_4-1,2-$(OH)_2$	9.45
acetic acid	CH_3COOH	4.76
formic acid	HCOOH	3.75
malonic acid	$HOOCCH_2COOH$	2.85
maleic acid	HOOCCH=CHCOOH	1.95
oxalic acid	HOOC-COOH	1.25

The presence of aromatic compounds had no obvious effects on the stability of the catalyst. As shown in figure 4.21, the Cu concentrations in hydroquinone (5%, 1.8 ppm) and catechol (3%, 1.0 ppm) solutions were roughly matched up with that in water (1%, 0.44 ppm), suggesting that the formation of hydroquinone and catechol during the CWPO process would not aggravate Cu leaching seriously. The Cu leaching in those solutions could be explained by their properties, as shown in table 4.6, as the hydroquinone (pKa_1=9.96) solution and

catechol (pKa_1=9.45) solution presented weak acidic, which are insufficient to attack any Cu/CuO_x to a significant extent. Conversely there aren't known or established complexes of Cu with these compounds as ligands. While *p*-benzoquinone had almost no influence on the leaching behaviour of catalyst when the Cu leaching in *p*-benzoquinone solution (2%, 0.68 ppm) was close to that in water (1%, 0.44 ppm).

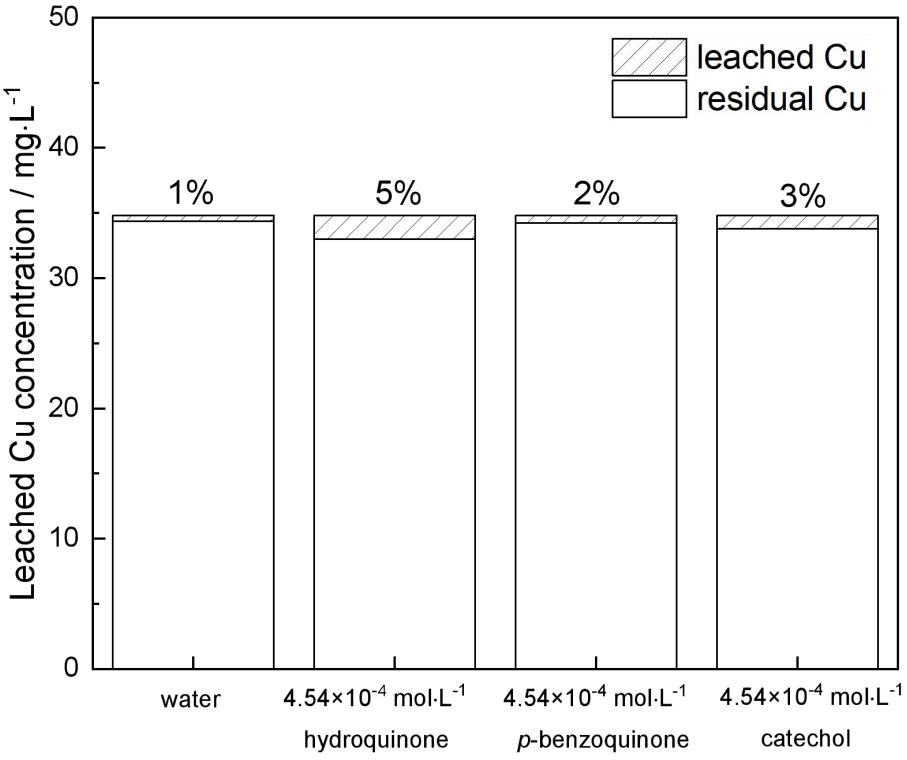

Figure 4.21. Leaching of Cu/ZSM-5-IE catalyst in aromatic intermediates solution of a) hydroquinone, b) *p*-benzoquinone, c) catechol (0.1 g Cu/ZSM-5-IE catalyst, 50 mL solution, P = endogenous, 80 °C, 4 h, 500 rpm)

By contrast, the formation of short-chain organic acids strongly impaired the stability of metal supported catalyst [39]. To eliminate the influence of changes in pH, the leaching tests in solutions of acid intermediates were all studied at pH 3, and the Cu concentrations in those acid solutions were detected by ICP-OES and compared with that in H_2SO_4 solution at the same pH level. As it can be seen in figure 4.22, the Cu concentrations in the above organic

acid solutions (30-75%, 10-25 ppm) were higher than in the inorganic acid solution (25%, 8.6 ppm), indicating that except pH, other factors were also related to metal loss, for example, the dissociation constant and anions. All those organic acids are weak electrolytes in water, therefore they dissociate more H^+ to maintain the dissociation equilibrium after the consumption of some H^+ in the dissolution of CuO (which is formed on the surface of the zeolite after calcination), and as a result, leading to higher leaching. Meanwhile, the most severe leaching of Cu in the organic acid solutions was, oxalic acid (pKa_1=1.25), malonic acid (pKa_1=2.85), formic acid (pKa=3.75), acetic acid (pKa_1=4.76) and maleic acid (pKa_1=1.95), in this same order. The order of leaching in these acids roughly matched up with their dissociation constant (in table 4.6), except in maleic acid which might be caused by experimental error, or most likely the sequence also matches the capability of the anionic form of the acid to act as a ligand to Cu^{2+} ions and form complexes capable to bring Cu in solutions. In fact there are known complexes of Cu^{2+} and oxalic acid [70,78]. Besides, the Cu leaching in organic acid solutions including acetic, formic, maleic and malonic acid, though fluctuating between 30% to 36% (10-13 ppm of Cu), was only slightly higher than that in inorganic acid (25%, 8.6 ppm). However, the Cu leaching in oxalic acid solution (74%, 26 ppm) almost tripled that in H_2SO_4 solution (25%, 8.6 ppm), indicating the formation of oxalic acid was the most important reason for leaching. The net result could then be the combination of two factors: H^+ species that attach CuO to form Cu^{2+} which is further leached by the formation complexes with R-COO- species.

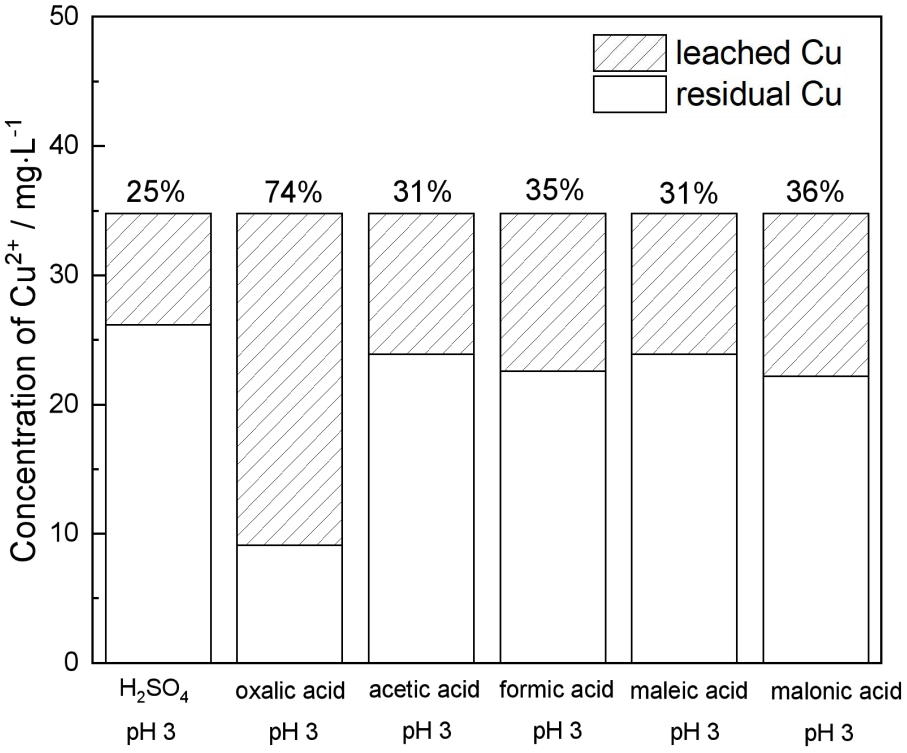

Figure 4.22. leaching of Cu/ZSM-5-IE catalyst in a) aromatic and b) organic acid intermediates solutions (0.1 g Cu/ZSM-5-IE catalyst, 50 mL solution, P = endogenous, 80 ^{o}C, 4 h, 500 rpm)

Overall, the formation of all those identified acid intermediates aggravated metal leaching of Cu catalyst to a major or to a minor extent. Among those intermediates, the formation of oxalic acid during the oxidation reaction triggered the most severe copper leaching. To improve the stability of Cu catalyst, the following options could be considered: a) develop Cu catalyst with high tolerance to oxalic acid, which could involve some form of coating to protect the metal (although this could also preclude catalytic activity), or b) have a catalyst that decreases the selectivity to oxalic acid or c) a catalyst that consumes any oxalic acid that is formed to CO_2 and water in a fast process.

4.4.2.7 Effects of oxalic acid and oxalate

To further study the effects of oxalic acid on the stability of Cu catalyst in aqueous solution and explain why oxalic acid caused far more severe leaching than other acids, the leaching of Cu catalyst in oxalic acid solutions with concentrations ranging from 5×10^{-5} mol·L^{-1} to 8.0×10^{-4} mol·L^{-1} (namely, 4.5 mg·L^{-1} to 72 mg·L^{-1}) were tested and characterized by ICP-OES. As shown in figure 4.23a, Cu was detected at 0 min in solution of oxalic acid regardless of the concentration, which stated that Cu catalyst suffered extraction once in contact with the oxalic acid solution. The result was consistent with the conclusion obtained from figure 4.15 (reaction time). Against this background, improving the stability of Cu catalyst by removing oxalic acid in the reaction process is too challenging to be applicable, because long reaction time (several hours) from the formation to the removal of oxalic acid is required [79,80]. Besides, the Cu concentration was kept constant with time in oxalic acid solution with specific concentration but varied with oxalic acid concentration, which implies that the amount of leached Cu probably depended on the concentration of oxalic acid. Thus, the correlation between concentration of oxalic acid and Cu leaching was studied, as plotted in figure 4.23b. The Cu concentrations in the figure were obtained from the mean values of the leached Cu detected in each oxalic acid solution to assure the accuracy. As displayed, a linear regression was used to fit the data and a function of $y = 1.07\times10^{-5} + 0.52x$ was obtained. As it can be seen, the intercept was compatible with zero, whereas the slope was compatible to a 1:2 ratio, indicating that every two moles of oxalic acid leached out 1 mole of Cu ions, as for a $[Cu(C_2O_4)_2]^{2-}$ [70] complex thus the complexation of copper oxalate might be the direct reason of leaching.

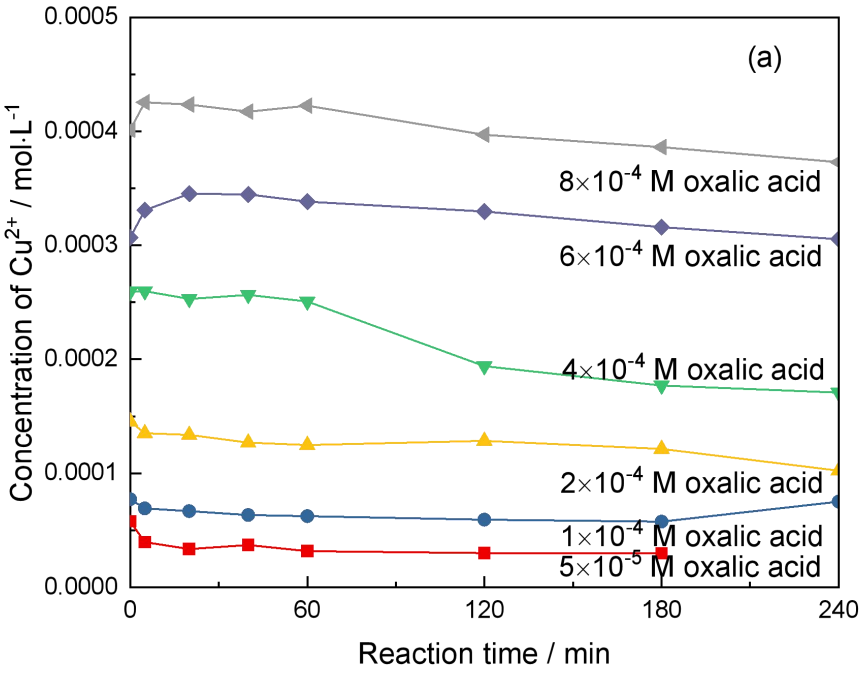

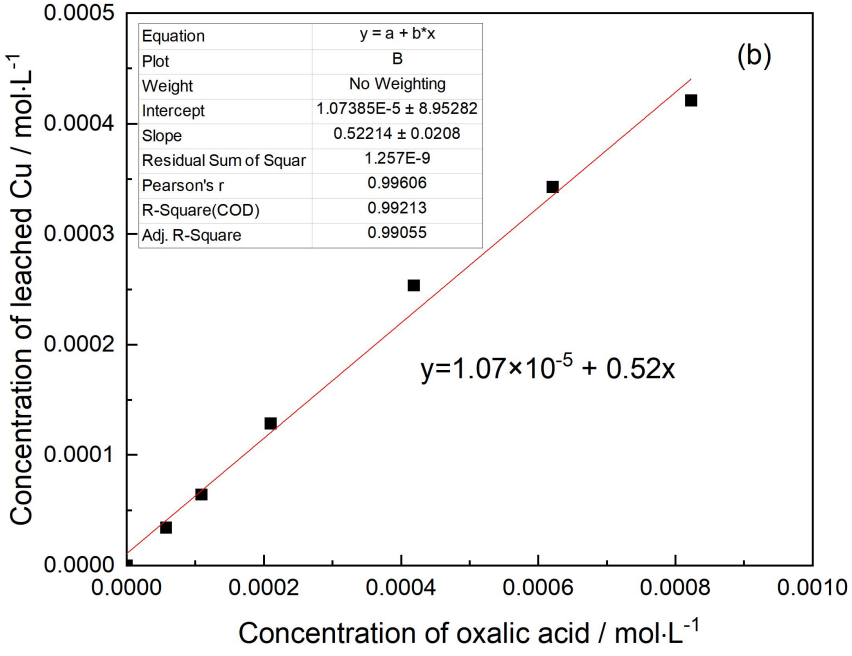

Figure 4.23. a) Concentration of leached Cu from Cu/ZSM-5-IE catalyst with time in oxalic acid solutions and b) linear relation of leached Cu concentration with oxalic acid concentration (0.1 g catalyst, 50 mL oxalic acid solution, P = endogenous, 80 °C, 4 h, 500 rpm)

The severe metal leaching caused by oxalic acid, though proved, was attributed to the combined effects of an acid attack by H^+ and a complexation effect by the oxalate. To investigate the effect of oxalate straightforwardly, the Cu leaching of catalyst in sodium oxalate solutions with concentrations of 5.0×10^{-5} mol·L^{-1} to 8.0×10^{-4} mol·L^{-1} was also detected. In this test, the Cu leaching from Cu/ZSM-5 in sodium oxalate solution was completely due to the effect of oxalate as the interference of pH was completely eliminated owing to the weak alkalinity of the sodium oxalate solution. As observed in figure 4.24a, like that in oxalic acid solution, the Cu concentration in specific sodium oxalate solution also kept constant from 0 min to 4 h and varied with concentration of oxalate. Likewise, the Cu leaching with function of the concentration of sodium oxalate was plotted in figure 4.24b and a linear function of $y = 4.00\times10^{-6} + 0.50x$ was obtained with the intercept compatible with zero. The two series of tests as shown in figure 4.23b and figure 4.24b, from the perspective of linear regressions, were almost the same. which proved again that the pH adjustment of the reaction mixture during the phenol oxidation process would make little improvement of the catalyst stability as long as oxalic acid was produced in the phenol oxidation reaction. Last but not least, the leached Cu to oxalate ratio was 0.5, corresponding to a bivalent Cu-oxalate complex, which suggested the complexation of oxalate to copper was the reason of Cu leaching and the formula of the complex might be $Cu(C_2O_4)_2^{2-}$ [70].

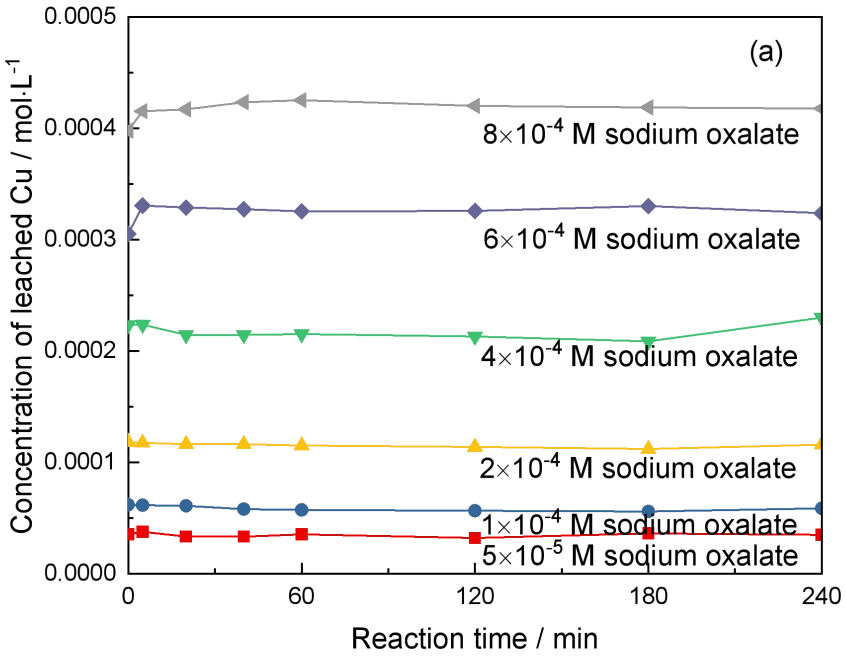

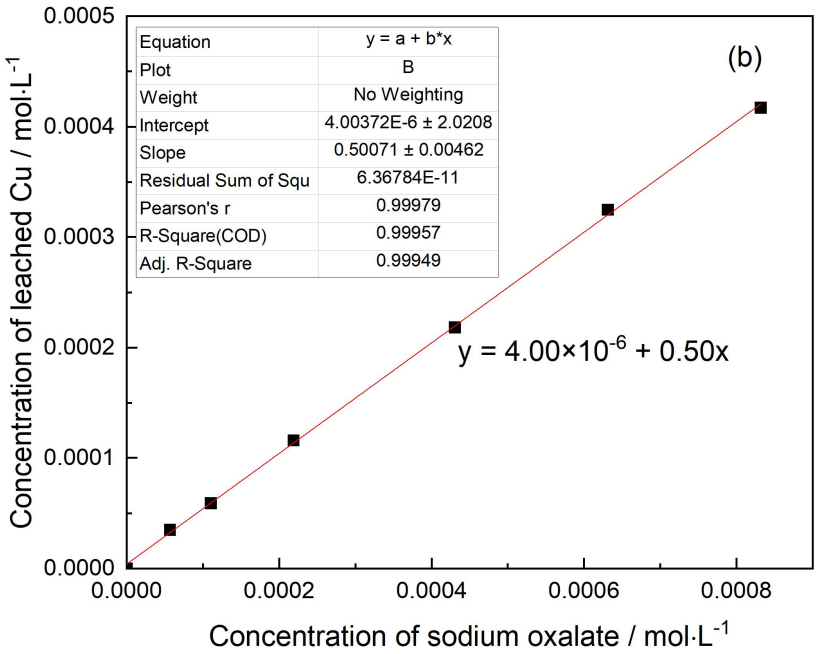

Figure 4.24. a) Concentration of leached Cu from Cu/ZSM-5-IE catalyst with time in sodium oxalate solutions and b) linear relation of leached Cu concentration with sodium oxalate concentration (0.1 g catalyst, 50 mL sodium oxalate solution, P = endogenous, 80 °C, 4 h, 500 rpm)

To sum up, the reaction conditions such as reaction time, temperature and M: S ratio affected the *rate* of Cu leaching, but had almost no influence on the final leaching. The main reason for Cu leaching is the formation of intermediates during the reaction process, especially the formation of oxalic acid.

4.5 Improvements of the stability of Cu/ZSM-5 catalyst

Even if the Cu/ZSM5 catalyst presented high activity for phenol abatement, it suffered from deactivation caused by metal leaching in an aqueous solution. From the data and data analysis reported so far (see sections 4.4.2.1-4.4.2.5) any pH adjustment and changes in reaction parameters like temperature, reaction time, M: S ratio, were of little help to minimize this experimental challenge. Thus, to reduce the leaching of the Cu doped zeolite catalyst in phenol oxidation reaction at the very root, more efforts should be put on 1) minimizing (ideally prohibiting) the formation of oxalic acid during the reaction, 2) getting rid of the oxalic acid once it is formed during the CWPO process, or 3) developing novel Cu catalyst with high tolerance to oxalic acid. The first solution is unlikely to be feasible because oxalic acid is one of the main products of the ring-opening reaction of aromatic intermediates [69], whereas to obtain a low toxic effluent, the further oxidation of aromatic intermediates to oxalic acid is almost indispensable. The second solution requires a rapid and efficient method for the removal of oxalic acid, however, the CWPO method itself seems not an effective option in the degradation of oxalic acid because this acid is quite refractory in the CWPO process, as reported in the literature [49,81]. In this case, the combined use of CWPO with other techniques such as ozonation [79,80,82,83] and/or photocatalytic degradation [84-86] is necessary to achieve a fast removal of oxalic acid, which is not adopted as the first option in this project due to the increased difficulty and cost and will be discussed in the future work (see chapter 8). Therefore, in this project, we mainly focused on the last solution, namely, exploiting Cu catalyst with possibly high resistance to oxalic acid, as discussed below.

4.5.1 Characterization of metal doped ZSM-5 catalysts

As discussed, the key to obtaining an effective and stable catalyst is the development of catalysts with high resistance to oxalic acid, whereas important efforts have been focused on seeking for appropriate catalyst preparation method [87,88], adjusting the oxidation state of the metal oxide [89,90], chemical modification [91,92], and so on. Against this background, the initial test is started from the catalysts prepared by different preparation methods (WI, IE, and DP) and catalyst with chemical reduction (Cu^{+} or Cu^{0} catalyst) in this section, to study whether the different metal-support interactions and the reduced metal help reduce metal leaching from Cu/ZSM-5 catalysts in the CWPO process. It is supposed that the preparation method may affect the size of metal oxide, metal dispersion, metal loading, morphology property of the catalysts which may in turn influence the performance of catalyst in a reaction, while the chemical reduction process is widely used to change the oxidation state of metal oxide on the surface of catalyst. Therefore, the catalysts prepared by different preparation methods (WI, IE, and DP) and that treated by chemical reduction (H_2 reduction and $NaBH_4$ reduction) were characterized by an array of techniques prior to the catalytic test to study their physicochemical properties.

4.5.1.1 X-ray diffraction (XRD)

To characterize the crystalline structure of the prepared catalysts, XRD patterns of different Cu doped zeolite catalysts were collected. As shown in figure 4.25, all the Cu/ZSM-5 catalysts presented diffraction peaks of crystalline structure of ZSM-5 zeolite with 2θ of 7-9^{o} and 23-25^{o}. Diffraction peaks for CuO facets (1 1 0), (0 0 2), (1 1 1), (-2 0 2), (0 2 0), (2 0 2) are expected at 32.6, 35.5, 38.7, 48.8, 53.5 and 58.2^{o} 2θ respectively [93,94]. However no diffractions for Cu oxide were detected, which could be because of either [95]: (i) a particle size of below 4–5 nm, (ii) a thin layered metal structure or (iii) highly dispersed metal species with less 5% loading.

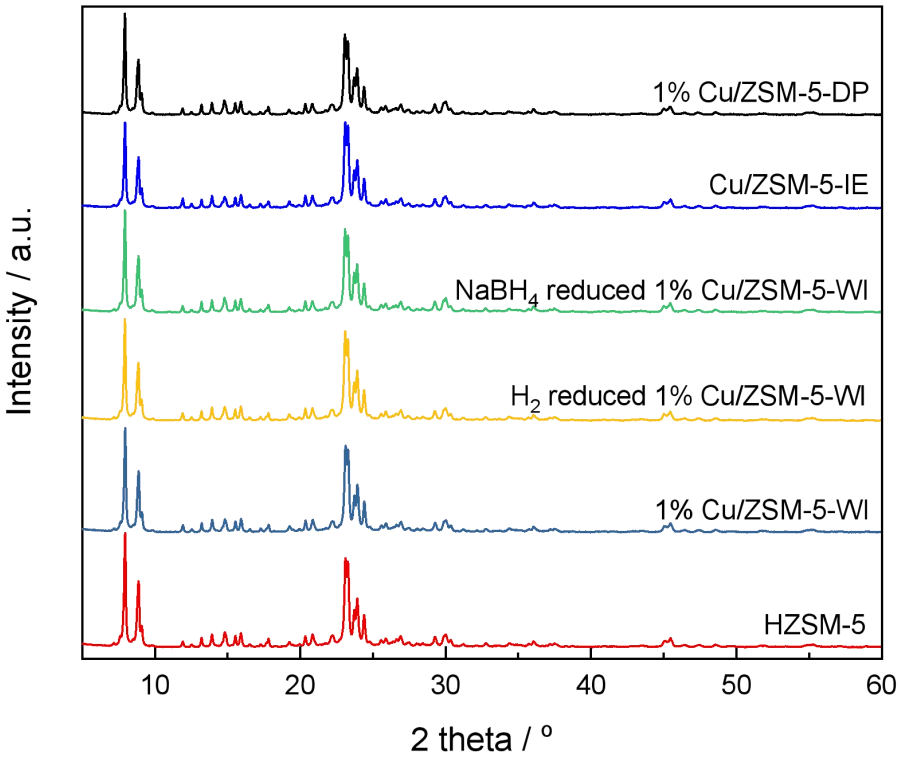

Figure 4.25. XRD patterns of different ZSM-5 zeolite catalysts. No CuO was detected in these XRD patterns. Facets typical for ZSM-5 zeolite were detected for all samples.

Table 4.7. Parameters of unit cell of the Cu doped zeolite catalysts, compared to undoped HZSM-5. The expansion or contraction (ΔV/V, caculated by Eq. 4.8) of the doped material is referred to as the undoped material, where the sign (+) stands for an expansion and the sign (-) stands for a contraction with respect to the undoped zeolite.

Catalyst	Unit cell parameters[a]							Expansion or contraction
	a (Å)	*b* (Å)	*c* (Å)	α (º)	β (º)	γ (º)	V (Å^3)	
HZSM-5	20.110 ± 0.011	19.947 ± 0.010	13.433 ± 0.011	90.00 ± 0.07	90.00 ± 0.08	90.00 ± 0.09	5388 ± 6	--
1% Cu/ZSM-5-WI	20.120 ± 0.013	19.954 ± 0.012	13.432 ± 0.013	90.00 ± 0.09	90.00 ± 0.10	90.00 ± 0.11	5392 ± 7	– 0.07%
Cu/ZSM-5-IE	20.086 ± 0.009	19.939 ± 0.008	13.402 ± 0.007	90.00 ± 0.05	90.00 ± 0.05	90.00 ± 0.05	5367 ± 5	- 0.4%
1% Cu/ZSM-5-DP	20.149 ± 0.014	19.957 ± 0.012	13.434 ± 0.015	90.00 ± 0.10	90.00 ± 0.11	90.00 ± 0.12	5402 ± 8	– 0.3%

The expansion or contraction of the unit cell is calculated with Eq.4.8: $\exp ansion / contraction, 100\% = \frac{V_{sample} - V_{HZSM-5}}{V_{HZSM-5}} \times 100$

a - unit cell parameters were obtained from X'pert Highscore software.

In order to know the metal-zeolite interactions, it is necessary to know, apart from the structure and bulk chemical composition, the unit cell parameter (acquired from the XRD data) of Cu supported zeolite catalysts prepared by different preparation methods. Various studies have shown that metal incorporated zeolites prepared by different methods may deposit metal on the surface of zeolite or trap metal into the framework of catalyst, while the two forms of metal-zeolite interactions lead to a different performance of catalysts to leaching [25,96]. The substitution of metal into the zeolite matrix replacing Al sites is usually evidenced by the expansion or contraction of the unit cell depending on the larger/smaller size of the metal (in our case, Cu) than Al, while the percentage of expansion/contraction is to some extent related to the number of incorporated metal atoms [97]. Owing to the larger size of the copper relative to aluminium, volume expansion of the unit cell is one indicator of successful incorporation of that metal into the structural sites [98]. However, no expansions of unit cell were observed within those Cu catalysts showed in table 4.7, indicating that Cu species of the catalysts prepared by WI, IE and DP methods were all supported on the surface or in the pore/channel of those zeolite catalysts rather than embedded into the framework.

4.5.1.2 Porosimetry

Low-temperature nitrogen adsorption isotherms are used for assessing the pore structure of the ZSM-5 zeolite after immobolization of Cu by different techniques (WI, IE, and DP). The N_2 adsorption-desorption isotherms of all the samples, as can be seen in figure 4.26, presented a typical type I isotherms with a hysteresis loop at a high relative pressure (0.4-1.0) as defined by International Union of Pure and Applied Chemistry (IUPAC) classification. The sharp increase of volume adsorbed at low relative pressure (< 0.1) was mainly due to the volume filling of micropores, whereas the gradually increase of volume adsorbed with the increase of the relative pressures was caused by the multilayer adsorption [99]. The specific surface areas (S_{BET}) of the samples were calculated from adsorption branches at low relative pressures (<0.3) using the BET (Brunauer-Emmett-Teller) method, while the micropore area (S_{micro}), external surface area (S_{ext}), and micropore volume (V_{micro}) were calculated using the

t-plot method, as listed in table 4.8. As shown, the BET-surface area of the HZSM-5 catalyst reached 408 $m^2 \cdot g^{-1}$, however, it decreased after Cu incorporation (348-380 $m^2 \cdot g^{-1}$), the possible reason is that pore blockage occurred when immobilizing Cu oxide on ZSM-5 zeolite, which is consistent with literature data [100-102] and meanwhile, was proved by the decreased micropore area (S_{micro}) and micropore volume (V_{micro}), as displayed in table 4.8. In addition, a significant hysteresis loop known as symbol of hierarchical porous system [103], was observed in the isotherms of all the samples.

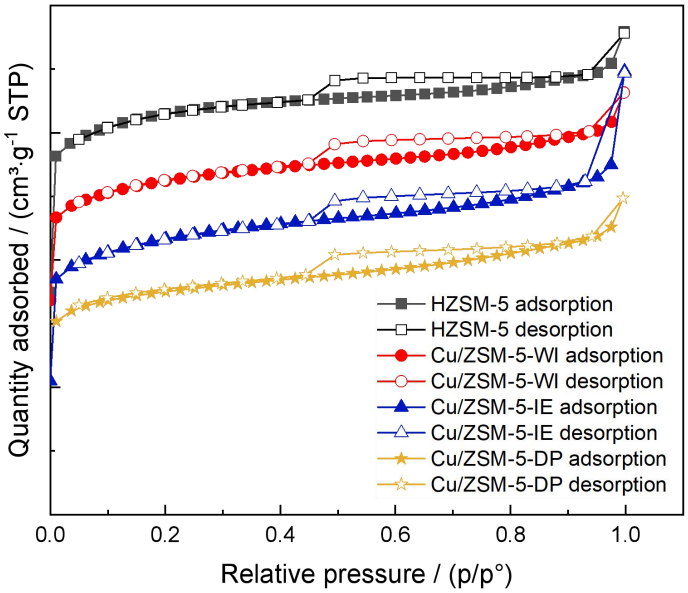

Figure 4.26. N_2 adsorption–desorption isotherms of the Cu/ZSM-5 catalysts prepared by different methods

Table 4.8. Porosimetry data of the Cu/ZSM-5 catalysts prepared by different methods

Sample name	S_{BET}[a] ($m^2 \cdot g^{-1}$)	S_{micro}[b] ($m^2 \cdot g^{-1}$)	S_{ext}[b] ($m^2 \cdot g^{-1}$)	V_{total} ($cm^3 \cdot g^{-1}$)	V_{micro}[b] ($cm^3 \cdot g^{-1}$)
HZSM-5	408	375	33	0.191	0.153
1% Cu/ZSM-5-WI	380	339	42	0.184	0.138
Cu/ZSM-5-IE	380	335	45	0.199	0.137
1% Cu/ZSM-5-DP	348	308	40	0.172	0.125

a - determined using BET method.

b - determined using t-plot method.

4.5.1.3 Inductively coupled plasma – optical emission spectroscopy (ICP-OES)

Table 4.9. Loading of Cu catalysts prepared by different methods tested by ICP-OES

Catalyst	Cu leaching per 0.1 g of catalyst in *aqua regia* solution	Actual Cu loading
1% Cu/ZSM-5-WI	16 $mg \cdot L^{-1}$	0.82%
1% Cu/ZSM-5-DP	16 $mg \cdot L^{-1}$	0.78%
Cu/ZSM-5-IE	35 $mg \cdot L^{-1}$	1.7%

Metal loading is one of the significant physical properties to characterize catalyst as it has great influence on the decomposition of H_2O_2 and phenol [32]. In principle, the higher actual loading of a catalyst, the more active species involved in reaction when the same dosage of catalyst used, thus the higher activity could be expected. The actual metal loading of the three catalysts prepared by WI, DP and IE methods was tested by ICP-OES after soaking the catalysts in *aqua regia* for 24 under continuous stirring to assure all Cu ions were leached out from the catalyst. Prior to analysis, the solutions were diluted and the pH of the solutions were adjusted by NaOH solution to a pH of ca.3. The Cu concentrations in the solutions determined by ICP-OES were listed in table 4.9. As displayed, the metal loading of the Cu catalysts prepared by WI, IE and DP methods were 0.82%, 1.7% and 0.78%, respectively.

4.5.1.4 X-ray photoelectron spectroscopy (XPS)

The XPS spectra were collected to identify the oxidation states of Cu on the ZSM-5 zeolite catalysts after chemical reduction. CuO is usually characterized by the satellite peaks at around 10 eV higher binding energy (BE) than the main 2p1/2 and 2p3/2 peaks, which are absent in the spectra for Cu_2O or Cu [104-106], meanwhile the peaks of CuO are broader than that of the Cu_2O and metallic Cu which is attributed to its shake up process [104]. The Cu_2O and Cu^0 can not be distinguished using Cu2p since the BEs of Cu^+ generally overlap with those of Cu^0 in the Cu 2p spectra [105]. Figure 4.27 depicted the Cu2p spectra of the Cu/ZSM-5-WI catalyst and the reduced catalysts, respectively. As it can be seen in the spectra of Cu/ZSM-5-WI sample, a weak broad Cu 2p3/2 peak at 933.3 eV (in agreement

with NIST-XPS database) was observed which is because that very little surface Cu was deposited on the surface of ZSM-5 catalyst. In addition, the satellite peak was not observed neither, which might be because it was too weak to be detected since it usually displays peak even less intense than the main peak.

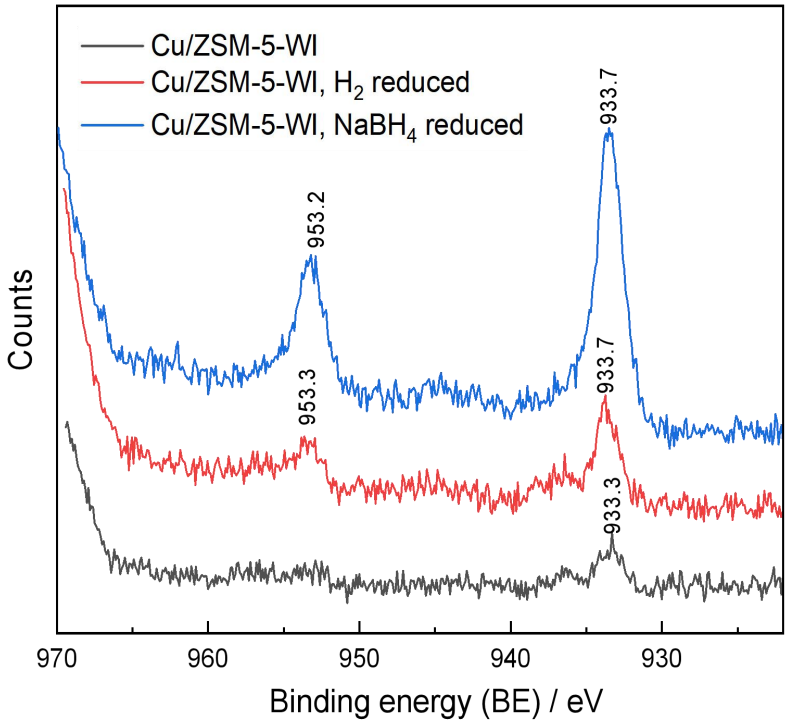

Figure 4.27. XPS spectra of Cu2p of a) 1% Cu/ZSM-5-WI, b) H_2 reduced 1% Cu/ZSM-5-WI and c) $NaBH_4$ reduced 1% Cu/ZSM-5-WI

The Cu2p of the H_2 reduced catalyst (figure 4.27) presented main peaks at 933.7 eV and 953.3 eV (without obvious shift in the binding energy in comparison with the Cu/ZSM-5 sample), which was indicative of the majority of pure CuO particles. This suggested that very little surface reduction occurred under hydrogen even up to 300 °C. The resistance of dispersed CuO clusters to reduction may be related to the lower intrinsic surface energies of metal oxides versus metals, and thus preferential stabilization of small CuO particles over their Cu analogues, as reported in the literature [107]. Moreover, the H_2 reduced catalyst

displayed a more intense peak than that without reduction, which would be explained by a decrease in the Cu particle size because XPS is a surface technique and the signal is a function of the surface to bulk atoms ratio [108], the percentage of Cu detected on the surface of H_2 reduced ZSM-5 catalyst is also slightly higher (table 4.10). In comparison, the shift in the Cu 2p3/2 peaks at 933.7 eV was not observed in spectra of the $NaBH_4$ reduced catalyst neither. However, the $NaBH_4$ reduced catalyst exhibited much sharper main peaks at Cu2p3/2 of 933.7 eV and Cu2p1/2 of 953.2 eV whereas the shakeup satellite peaks were not detected, which may imply the partly reduction of CuO to Cu_2O and/or Cu^0 species.

Overall, it is concluded that the expected H_2 reduction process enhanced the metal dispersion of the Cu/ZSM-5 zeolite and did not convert CuO to Cu_2O and/or Cu^0; in contrast the $NaBH_4$ reduction is more efficient at reducing CuO on the surface of ZSM-5 catalyst to Cu^0 and/or Cu_2O.

Table 4.10. Surface composition of Cu/ZSM-5-WI catalysts with chemical reduction, determined by XPS

Catalyst	Elemental composition / %				
	Al 2p	C 1s	Cu 2p 3/2	O 1s	Si 2p
1% Cu/ZSM-5-WI	2.83	1.70	0.06	61.58	33.84
1% Cu/ZSM-5-WI, H_2 reduced	2.88	1.89	0.12	61.79	33.31
1% Cu/ZSM-5-WI, $NaBH_4$ reduced	3.72	2.83	0.40	60.43	32.62

4.5.2 Activity and stability of Cu/ZSM-5 catalysts with chemical reduction

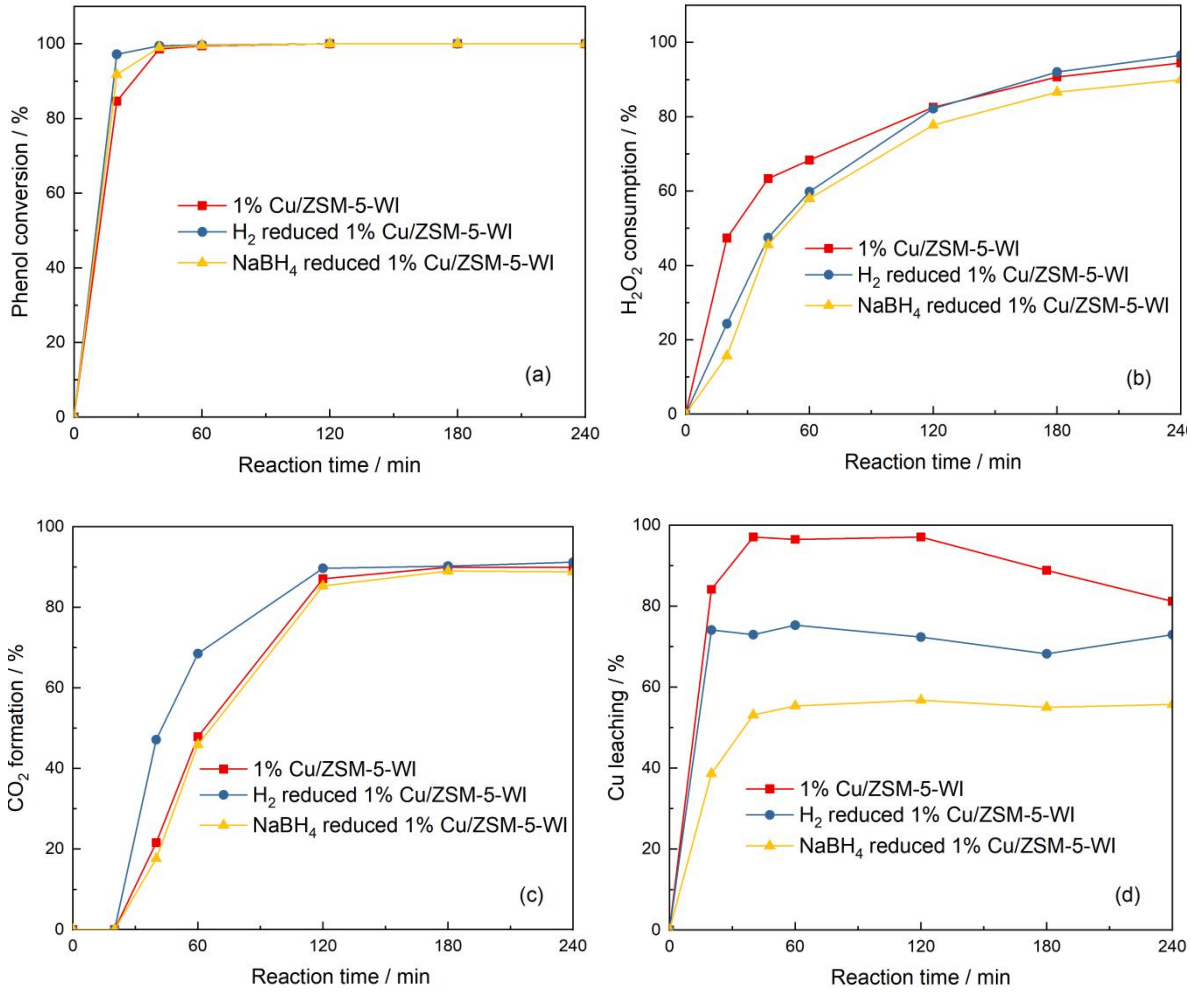

Figure 4.28. a) Phenol conversion, b) H_2O_2 consumption, c) CO_2 formation, d) Cu leaching over i) 1% Cu/ZSM-5-WI, ii) H_2 reduced 1% Cu/ZSM-5-WI and iii) $NaBH_4$ reduced 1% Cu/ZSM-5-WI in the CWPO of phenol with time (0.1 g catalyst, 50 mL 1 $g \cdot L^{-1}$ phenol solution, phenol: H_2O_2 = 1: 14, P = endogenous, 80 °C, 4 h, 500 rpm). The Cu/ZSM-5 catalysts with chemical reduction presented lower metal leaching while their activities were almost identical.

It is widely accepted the reduction treatment has a significant influence upon the catalyst stability [90] whereas the reduced metal (i.e. oxidation state 0) presents higher resistance to acids than their metal oxides counterpart therefore may contribute to an enhanced stability in treated phenolic solution, and the catalyst leaching could be suppressed with the reduced Cu catalysts under this background. In this context, the activity and stability over the chemical reduced catalysts were investigated, as exhibited in figure 4.28. It is evident from figure

4.28a-c that the chemical reduction had little effects on the activity of Cu/ZSM-5 catalysts as the phenol conversions, H_2O_2 consumption and CO_2 formations using the catalysts with reduction keeping similar with that using the catalyst without reduction. This can be explained that the reduced Cu^0 is also active in the decomposition of H_2O_2 to generate ·OH radicals, as exhibited in Eq. 4.9 and Eq. 4.10 [109]:

$Cu^0 + H_2O_2 \rightarrow Cu^+ + OH^- + \cdot OH$ (Eq. 4.9)

$Cu^+ + H_2O_2 \rightarrow Cu^{2+} + OH^- + \cdot OH$ (Eq. 4.10)

Hence, phenol was decomposed under the attack of ·OH radicals as described in Eq. 4.5. Nevertheless, and despite this chemical treatment, the reduced 1% Cu/ZSM-5-WI catalysts still suffered severe leaching (around 70% for H_2 reduced and 50% for $NaBH_4$ reduced, in figure 4.28d), though lower than that without chemical reduction, with over 50% of Cu leaching into the reaction mixture. This is probably resulting from the corrosive dissolution of reduced Cu and the concurrent reduction of oxygen [110].

4.5.3 Activity and stability of catalysts prepared by different preparation methods (WI, IE and DP)

Catalysts prepared by different methods usually present different properties such as different metal dispersion/distribution and metal size, which finally influence the performance of catalyst in chemical reaction [111-114]. In this study, the activity and stability of catalysts prepared by wet impregnation (WI), ion exchange (IE) and deposition-precipitation (DP) method were investigated and compared (in figure 4.29). The three Cu/ZSM-5 catalysts prepared by different methods presented similar trends in phenol conversions, both per time and maximum value, as well as for H_2O_2 consumption and CO_2 formations, amongst the Cu/ZSM-5-IE catalyst showed slightly higher activity. As determined by ICP-OES, the Cu-loading in the IE catalyst was slightly higher (1.7%) than WI and DP catalyst (0.82% and 0.78% respectively), which may explain the observed trends. Based on these small differences in catalytic activity, however, can also be a consequence of the circumstance that the activity of Cu catalyst was so high that changing preparation method would not apparently

affect the performance. Furthermore, it is observed in figure 4.29d that the Cu leaching for the three above-mentioned catalysts all reached at least 80% after 40 min, implying the poor stability of the Cu/ZSM-5 catalysts. To explain these similarities, we speculate that the Cu species on the Cu/ZSM-5 catalysts prepared by WI, IE and DP methods are mainly extra-framework rather than intra-framework Cu. Meanwhile, the Cu concentrations determined in the reaction mixture, over all the three catalysts, went down gradually with reaction time after 1 h owing to the re-adsorption of Cu ions onto the zeolite support.

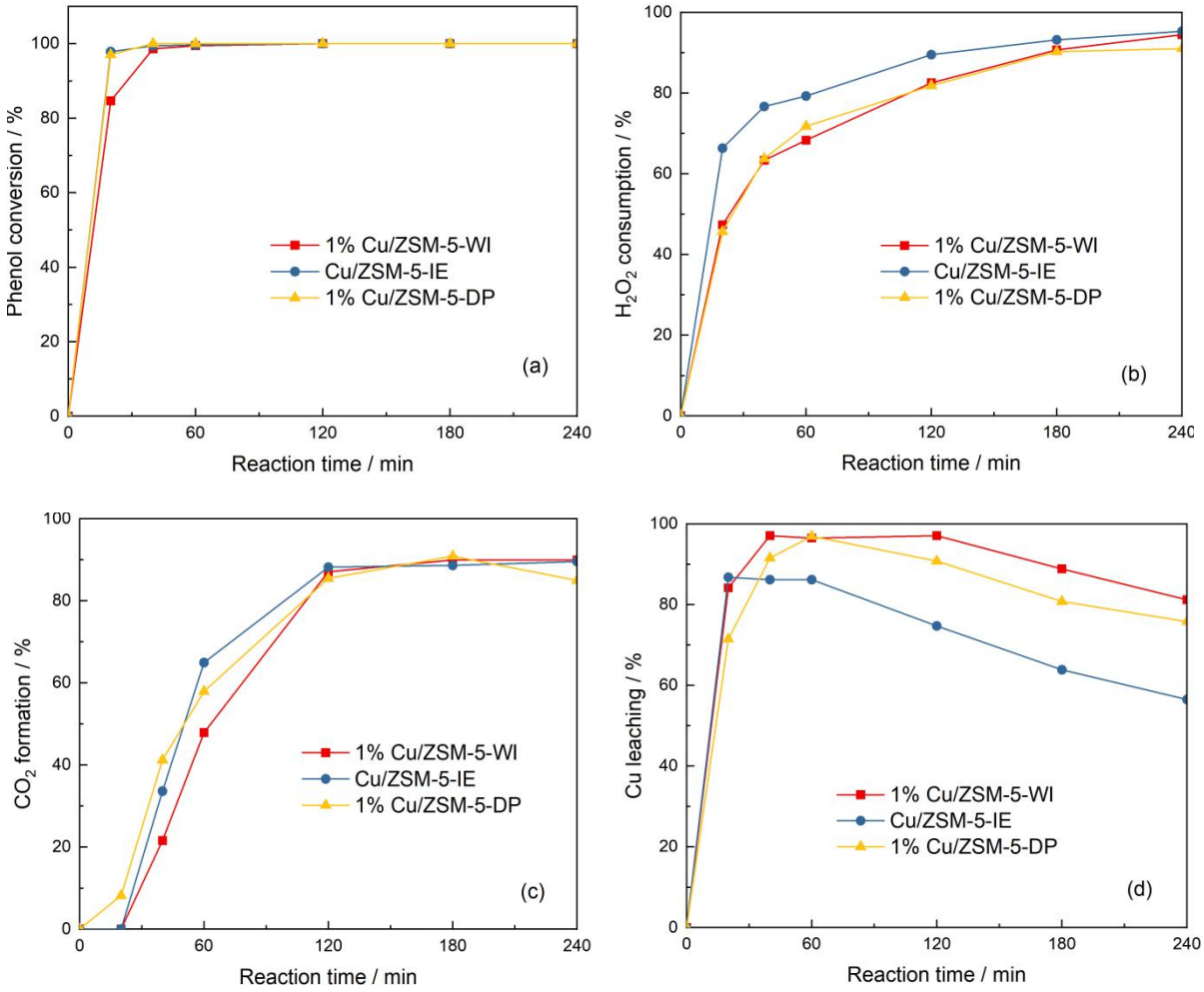

Figure 4.29. a) Phenol conversion, b) H_2O_2 assumption, c) CO_2 conversion, d) Cu leaching over i) 1% Cu/ZSM-5-WI, ii) Cu/ZSM-5-IE and iii) 1% Cu/ZSM-5-DP in the CWPO of phenol with time (0.1 g catalyst, 50 mL 1 g·L^{-1} phenol solution, phenol: H_2O_2 = 1: 14, P = endogenous, 80 °C, 4 h, 500 rpm). No obvious differences in the activity and stability of the WI, IE and DP catalysts were observed as the phenol conversion, H_2O_2 consumption, CO_2 formation and Cu leaching over the three catalysts were almost constant.

Overall, it is confirmed that the Cu/ZSM-5 catalysts, regardless of with or without chemical reduction, regardless of the preparation methods, had high activity in the CWPO of phenol reaction, but with a large leaching of Cu in solution which would prompt the question on a homogeneous contribution of Cu^{2+} in solution (see section 4.6 below) to the phenol decomposition versus a heterogeneous contribution. Unfortunately, substantial improvements of catalyst stability were not observed on those catalysts as their Cu leaching was still significant.

4.6 Homogeneous contribution of leached Cu

It was reported in previous literature [38,115] that metal leaching from the heterogeneous catalyst may, as homogeneous catalyst, contribute to phenol decomposition in the reaction, and therefore shift the reaction from being heterogeneous to homogeneous catalysis. Due to large proportion of Cu leaching that we've observed, the CWPO of phenol reaction could be either heterogeneous, homogeneous or combination of heterogeneous and homogeneous catalysis. To address this important research question, a systematic evaluation on the contribution of Cu in solution and in turn the leached Cu was carried out.

4.6.1 Catalytic activity of homogeneous Cu catalyst in phenol oxidation

To confirm the activity of the homogeneous Cu catalyst in solution, a series of reactions were performed using Cu^{2+} (copper nitrate as precursor) with different concentrations under the same reaction conditions as those heterogeneous experiments. As shown in figure 4.30, 'homogeneous Cu catalyst' that is $Cu(NO_3)_2 \cdot 2.5H_2O$ dissolved in solution, was extremely active in the CWPO of phenol as the phenol conversion, H_2O_2 consumption and CO_2 formation increased rapidly with the growth of Cu^{2+} concentration (and incidentally also showing the tests were carried out under kinetic regime). The homogeneous Cu catalyst ($Cu(NO_3)_2$) presented high phenol oxidation capability even at low concentrations, since phenol conversion (30%) with merely 0.04 $mg \cdot L^{-1}$ of Cu^{2+} (corresponding to M: S of 1:17000 and relevant loss of 0.25%) was achieved at 80 ^oC in 4 h. Besides, complete phenol

conversion was achieved when the concentration of homogeneous Cu^{2+} was above 5 mg·L^{-1} (corresponding to M: S of 1:136 and relevant loss of 31%). That is to say, complete phenol conversion could all be achieved with the leached Cu, since the Cu leaching of all the heterogeneous Cu/ZSM-5 catalysts in this study so far was over 10 mg·L^{-1}. Therefore, the homogeneous contribution of leached Cu was a significant contributor to the observed catalytic activity.

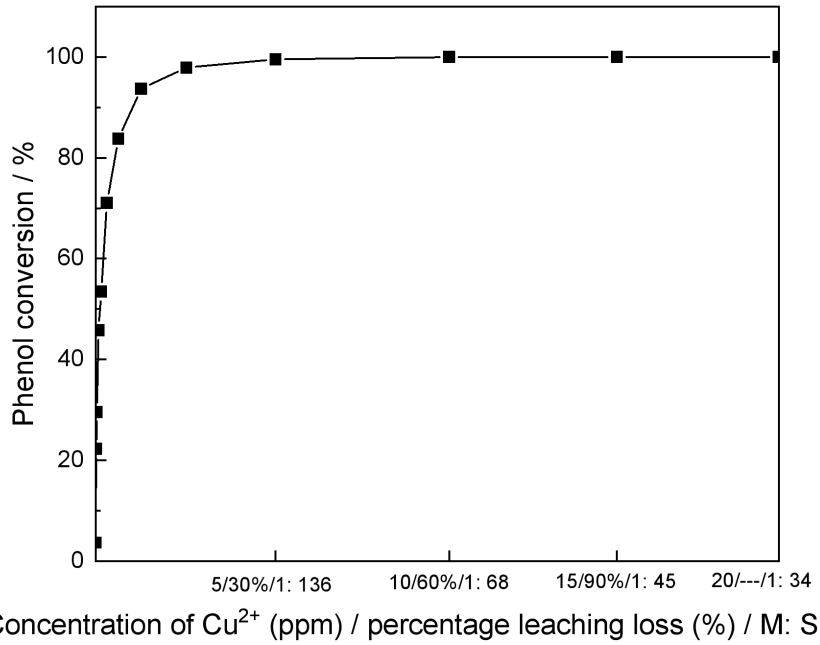

Figure 4.30. Catalytic activity of homogeneous Cu catalysts in the CWPO of phenol ($Cu(NO_3)_2$ as precursor, 50 mL 1 g·L^{-1} phenol, phenol: H_2O_2 of 1:14, P = endogenous, 80 °C, 4 h, 500 rpm)

4.6.2 Homogeneous contribution of leached metal in phenol oxidation

The three most widely used methods for a comprehensive assessment of the homogeneous contribution of metal leaching in heterogeneous catalyst are summarized from the literature [38,71,116-121] here and they are: 1) Metal ion test. This is to test the activity of the homogeneous catalyst (metal salt) with the concentration of metal ions equivalent to the leaching in the reaction. 2) Hot filtration test. In this method the solid catalyst is removed from the reaction mixture by filtration soon after reaction started (5-20 min), and the filtrate is

monitored for continued activity. 3) Final filtrate test. The solid catalyst is removed after the reaction is completed and the concentrations of reactants are compensated to their initial value; then any activity present in the final filtrate is monitored in the next run of reaction. In these homogeneous contribution tests, the 1% Cu/ZSM-5-WI catalyst was used as example as it suffered the highest leaching among all of the Cu catalysts tested so far (figure 4.28d and figure 4.29d).

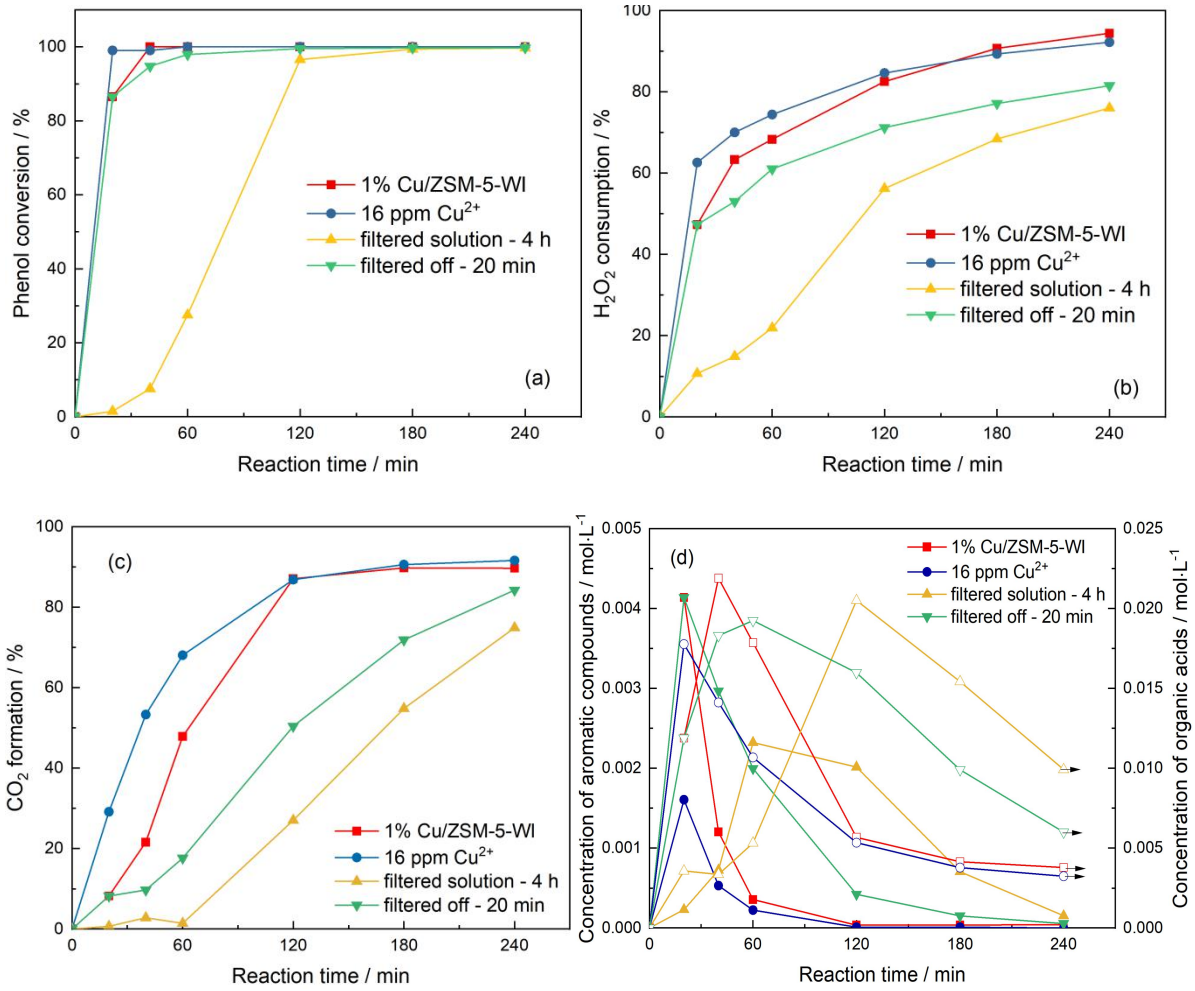

Figure 4.31. a) phenol conversion and b) H_2O_2 consumption, c) CO_2 formation and d) intermediates distribution over i) 1% Cu/ZSM-5-WI catalysts, ii) 16 ppm of Cu^{2+}, iii) filtered solution - 4 h, iv) filtered off - 20 min (0.1 g 1% Cu/ZSM-5-WI catalyst, 50 mL 1 $g \cdot L^{-1}$ phenol solution, phenol: H_2O_2 = 1: 14, P = endogenous, 80 ºC, 4 h, 500 rpm). The activity of the 1% Cu/ZSM-5-WI catalyst gave identical results to the two control tests (metal ion test and hot filtration test) and was higher than the final filtrate test, indicating that the catalysis was a result of both contributions of heterogeneous and homogenous catalysis.

Firstly, the metal ion test performed with 16 ppm of Cu^{2+} ($Cu(NO_3)_2$ as precursor) that corresponding to the highest Cu concentration detected in the reaction mixture using 1% Cu/ZSM-5-WI catalyst was studied. The phenol conversion and H_2O_2 consumption with 16 ppm of Cu^{2+} catalyst were as high as that with the 1% Cu/ZSM-5-WI catalyst (figure 4.31a and 4.31b), suggesting that the phenol decomposition might completely originate from the effect of leached metal, and therefore in practical terms homogeneous catalysis. However, as stated by Inchaurrondo and his co-workers [117], the homogeneous contribution was clearly overestimated in the metal ion test, since the homogeneous catalytic contribution resulted from the leached metal ion in a batch reactor depended on both time and reaction conditions. Thus using Cu^{2+} (from $Cu(NO_3)_2$) directly as an alternative to leached Cu to investigate the homogeneous contribution of Cu/ZSM-5 catalyst in phenol decomposition is still controversial. At first, the first step of this reaction process is the decomposition of H_2O_2 to ·OH radicals in the presence of heterogeneous Cu on ZSM-5 catalyst, then the phenol was decomposed under the attack of radicals, thus the contribution of heterogeneous catalyst is incontrovertible at the beginning of reaction. Secondly, in the catalytic reaction with 1% Cu/ZSM-5-WI, the Cu ions leached into the solution gradually and reached the peak concentration at 20 min, during this period, the phenol conversion (85% at 20 min) was attributed to both heterogeneous catalyst and leached Cu. Thirdly, the start time of Cu leaching also matters. As discussed in section 4.4.2.7 the main cause of Cu leaching is the formation of oxalic acid, that is to say, the Cu leaching occurred after phenol decomposition and oxalic acid formation. Therefore, the phenol decomposition occurred by means of ·OH radicals from H_2O_2, which was triggered by heterogeneous Cu catalyst and enhanced by the leached Cu, namely, homogeneous catalyst. On the other hand, the Cu^{2+} ions presented higher selectivity to CO_2 and organic acid and lower selectivity to aromatic intermediates especially within the first 1 h, as suggested by the higher CO_2 formation (figure 4.31c) and the lower total concentration of aromatic compounds (figure 4.31d), respectively. This is because of the higher activity of homogeneous catalyst than heterogeneous catalyst owing to its higher diffusion efficiency.

In order to prove that the performance of leached metal differs from that of Cu^{2+} catalyst derived from Cu nitrate, either in terms of H_2O_2 decomposition efficiency or product distribution, the catalytic activity of the filtrates obtained from different stage of the reaction over 1% Cu/ZSM-5-WI were investigated and compared with that of the Cu^{2+} catalyst. The reaction mixtures after 20 min (hot filtration test) and 4 h (final filtrate test) of reaction using 1% Cu/ZSM-5-WI as catalyst, after being filtered in hot conditions to remove the solid catalyst, were denoted as 'filtered off – 20 min' and 'filtered solution – 4 h', respectively. Thereafter, the test over 'filtered-off – 20 min' filtrate was carried out immediately after filtration to mimic the reaction condition of 1% Cu/ZSM-5-WI catalyst from 20 min to 4 h while without the influence of heterogeneous catalysis. As shown, the increasing phenol conversion and H_2O_2 consumption from 20 min proved that the leached Cu was active. The overall activity (phenol conversion, H_2O_2 consumption, CO_2 formation and intermediates distribution) over the filtrate were slightly lower than that over 1% Cu/ZSM-5-WI, which might be explained by several reasons: 1) the decreased M: S ratio after 20 min. The total amount of active species reduced as there were still metal species deposit on the solid catalyst zeolite, since the Cu leaching at 20 min was 84% rather than 100%. 2) The absence of ZSM-5. The results in figure 4.3 and figure 4.4 suggested the capability of zeolite support ZSM-5 of decomposing H_2O_2 to ·OH radical and degrading phenol, thus the activity might be affected when it was removed. 3) The fluctuation of temperature. Though the hot filtration was completed within 1-2 min, the temperature of the reaction mixture decreased when it was filtered and transferred between glassware, considering the volume of reaction mixture (50 mL). Whereas the temperature has significant influence on the decomposition rate of phenol (as proved in figure 4.19).

In comparison with 'filtered-off – 20 min' filtrate, in the 'filtered solution – 4 h' solution, there were only Cu ions, organic acids as well as Cu-acids complexes remained since phenol and aromatic compounds were all removed and 94% of H_2O_2 was consumed, as evidenced in figure 4.7. In this kind of test, phenol and hydrogen peroxide were further added into the filtrates to return them to the initial concentrations to start a new reaction, to investigate the

activity and homogeneous contribution of the leached Cu ions and Cu-acid complexes. If copper ions leached from Cu/ZSM-5 are active and dominate the reaction, a homogeneous reaction would occur and phenol decomposition as fast as that using 1% Cu/ZSM-5-WI would be observed. However, as shown in figure 4.31, the filtered solution presented very low activity in the first 1 h, and complete phenol conversion (figure 4.31a) was achieved in 3 h, taking much longer time than that over 1% Cu/ZSM-5-WI (40 min). The long induction period (more than 20 min) over filtered solution could be explained by the reduced activity of Cu catalyst due to the complexation with acids intermediates, most likely oxalate, and the initial pH (around 2.7) also influenced the reduced the activity, which is in agreement with the results shown in figure 4.9 and figure 4.10. It also proved the heterogeneous contribution of 1% Cu/ZSM-5-WI as no induction period was observed in its catalytic reaction. The H_2O_2 consumption (figure 4.31b), CO_2 formation (figure 4.31c) and intermediates distribution (figure 4.31d) explained the same results. The results supported Inchaurrondo's conclusion that copper-acid complexes had lower activity than homogeneous Cu^{2+} catalyst [117].

To sum up, by combining all of the three control tests on the activity of leached species, it can be concluded that the catalytic activity for Cu/ZSM5 is result of two contributions: a heterogeneous and a homogeneous component. From the above analysis, the phenol oxidation reaction was initiated by a heterogeneous route and the overall activity of the Cu/ZSM-5 catalysts was due to both heterogeneous and homogeneous catalysis.

4.7 Conclusions

It is concluded in this chapter:

1) Cu and Fe were ideal catalyst in the CWPO of phenol, as they were more active than other tested metal species (Co, Mn, Ag, Au Pd). The six commercial zeolites (HZSM-5, NH_4ZSM-5, 13X, HY, MCM-41, SBA-15) all showed weak activity and were potential catalyst supports in phenol oxidation.

2) In comparison with blank test and HZSM-5, the Cu doped ZSM-5 catalyst presented the highest activity in phenol oxidation, not only in the form of high phenol conversion, but also high H_2O_2 consumption/efficiency, high purification from aromatic intermediates and high CO_2 formation. The final products remaining in the reaction mixture after reaction using Cu/ZSM-5 catalyst were low-toxic organic acids such as acetic, formic and oxalic acid.

3) The Cu/ZSM-5 catalyst presented poor stability in the CWPO of phenol process due to the high metal leaching. The Cu leaching was influenced by various factors. On the one hand, the reaction parameters like temperature and M: S ratio, on the other and, the decomposition of phenol itself, for example, the products of phenol decomposition and the pH change caused by the formation of those products. However, the main reason of catalyst deactivation was the formation of intermediates, especially oxalic acid, which complexing with Cu with Cu to oxalate ratio of 1: 2 to form $Cu(C_2O_4)_2^{2-}$.

4) Chemical reduction or preparation of catalyst by different methods had little positive effects on the improvement of the stability of Cu/ZSM-5 catalysts.

5) The leached metal from the catalyst surface to solution, as homogeneous catalyst, played catalytic role in the CWPO reaction. The homogeneous contribution was significant due to the large proportion of metal leaching, making the phenol decomposition a combined heterogeneous and homogeneous reaction.

4.8 References

[1]. N. C. Saha, F. Bhunia and A. Kaviraj, *B Environ Contam Tox*, 1999, **63**, 195-202.

[2]. H. H. Fang and O. Chan, *Water Res*, 1997, **31**, 2229-2242.

[3]. O. A. O'Connor and L. Y. Young, *Environ Toxicol Chem*, 1989, **8**, 853-862.

[4]. C. Vassilakis, A. Pantidou, E. Psillakis, N. Kalogerakis and D. Mantzavinos, *Water Res*, 2004, **38**, 3110-3118.

[5]. J. Regalbuto, *Catalyst preparation: science and engineering*, CRC press, 2016.

[6]. M. Benaglia and A. Puglisi, *Catalyst immobilization: methods and applications*, John Wiley & Sons, 2019.

[7]. M. D. Argyle and C. H. Bartholomew, *Catalysts*, 2015, **5**, 145-269.

[8]. C. Hammond, *Green Chem*, 2017, **19**, 2711-2728.

[9]. A. Santos, P. Yustos, A. Quintanilla, G. Ruiz and F. Garcia-Ochoa, *Appl Catal B-Environ*, 2005, **61**, 323-333.

[10]. P. Brussino, M. S. Gross, E. D. Banús and M. A. Ulla, *Chem Eng Process*, 2019, **146**, 107686.

[11]. A. Rey, M. Faraldos, J. A. Casas, J. A. Zazo, A. Bahamonde and J. J. Rodríguez, *Appl Catal B-Environ*, 2009, **86**, 69-77.

[12]. A. Quintanilla, J. A. Casas and J. J. Rodriguez, *Appl Catal B-Environ*, 2010, **93**, 339-345.

[13]. C. M. Domínguez, P. Ocón, A. Quintanilla, J. A. Casas and J. J. Rodriguez, *Appl Catal B-Environ*, 2014, **144**, 599-606.

[14]. F. Tomul, F. Turgut Basoglu and H. Canbay, *Appl Surf Sci*, 2016, **360**, 579-593.

[15]. E. Aneggi, A. Trovarelli and D. Goi, *J Environ Chem Eng*, 2017, **5**, 1159-1165.

[16]. G. Zhao, H. Liang, H. Xu, C. Li, Q. Tan and D. Zhang, *Rsc Adv*, 2021, **11**, 15959-15968.

[17]. W. Xie, C. Song, W. Ren, J. Zhang, L. Chen and J. Sun, *Chemosphere*, 2021, **274**, 129654.

[18]. H. Niu, Y. Zheng, S. Wang, L. Zhao, S. Yang and Y. Cai, *J Hazard Mater*, 2018, **346**, 174-183.

[19]. A. D. Bokare and W. Choi, *J Hazard Mater*, 2014, **275**, 121-135.

[20]. M. Cheng, C. Lai, Y. Liu, G. Zeng, D. Huang, C. Zhang, L. Qin, L. Hu, C. Zhou and W. Xiong, *Coordin Chem Rev*, 2018, **368**, 80-92.

[21]. X. Zhang, Y. Ding, H. Tang, X. Han, L. Zhu and N. Wang, *Chem Eng J*, 2014, **236**, 251-262.

[22]. Y. Sheng, Y. Sun, J. Xu, J. Zhang and Y. Han, *Aiche J*, 2018, **64**, 538-549.

[23]. C. S. Rodrigues, R. M. Silva, S. A. Carabineiro, F. J. Maldonado-Hódar and L. M. Madeira, *Catalysts*, 2019, **9**, 478.

[24]. O. P. Taran, A. N. Zagoruiko, A. B. Ayusheev, S. A. Yashnik, R. V. Prihod Ko, Z. R. Ismagilov, V. V. Goncharuk and V. N. Parmon, *Chem Eng J*, 2015, **282**, 108-115.

[25]. K. M. Valkaj, A. Katovic and S. Zrnčević, *J Hazard Mater*, 2007, **144**, 663-667.

[26]. M. J. Kim, M. W. Lee and K. Lee, *Appl Surf Sci*, 2021, **541**, 148409.

[27]. A. Filiz and S. BALCI, *Gazi U J Sci*, 2019, **32**, 91-102.

[28]. I. O. Ali, A. M. Ali, S. M. Shabaan and K. S. El-Nasser, *J Photoch Photobio A*, 2009, **204**, 25-31.

[29]. S. Yuvaraj, M. Palanichamy and V. Krishnasamy, *Chem Commun*, 1996, 2707-2708.

[30]. K. Schumacher, C. D. F. V. Hohenesche, K. K. Unger, R. Ulrich, A. D. Chesne, U. Wiesner and H. W. Spiess, *Adv Mater*, 1999, **11**, 1194-1198.

[31]. S. Gontier and A. Tuel, *J Catal*, 1995, **157**, 124-132.

[32]. C. M. Domínguez, A. Quintanilla, P. Ocón, J. A. Casas and J. J. Rodriguez, *Carbon*, 2013, **60**, 76-83.

[33]. Y. Li, Z. Feng, Y. Lian, K. Sun, L. Zhang, G. Jia, Q. Yang and C. Li, *Micropor Mesopor Mat*, 2005, **84**, 41-49.

[34]. Y. Zhu, R. Zhu, Y. Xi, J. Zhu, G. Zhu and H. He, *Appl Catal B-Environ*, 2019, **255**, 117739.

[35]. R. S. Ribeiro, A. M. Silva, J. L. Figueiredo, J. L. Faria and H. T. Gomes, *Catal Today*, 2017, **296**, 66-75.

[36]. M. T. Pinho, H. T. Gomes, R. S. Ribeiro, J. L. Faria and A. M. T. Silva, *Appl Catal B-Environ*, 2015, **165**, 706-714.

[37]. K. M. Valkaj, O. Wittine, K. Margeta, T. Granato, A. Katović and S. Zrnčević, *Pol J Chem Technol*, 2011, **13**, 28-36.

[38]. G. Calleja, J. A. Melero, F. Martinez and R. Molina, *Water Res*, 2005, **39**, 1741-1750.

[39]. A. Rey, M. Faraldos, J. A. Casas, J. A. Zazo, A. Bahamonde and J. J. Rodríguez, *Appl Catal B-Environ*, 2009, **86**, 69-77.

[40]. M. Munoz, Z. M. de Pedro, J. A. Casas and J. J. Rodriguez, *Chem Eng J*, 2013, **228**, 646-654.

[41]. J. D. de Tuesta, A. Quintanilla, J. A. Casas and J. J. Rodriguez, *Appl Catal B-Environ*, 2017, **209**, 701-710.

[42]. E. El-Ashtoukhy, Y. A. El-Taweel, O. Abdelwahab and E. M. Nassef, *Int. J. Electrochem. Sci*, 2013, **8**, 1534-1550.

[43]. G. L. Truong, J. D. Laat and B. Legube, *Water Res*, 2004, **38**, 2384-2394.

[44]. A. Babuponnusami and K. Muthukumar, *J Environ Chem Eng*, 2014, **2**, 557-572.

[45]. Y. S. Jung, W. T. Lim, J. Y. Park and Y. H. Kim, *Environ Technol*, 2009, **30**, 183-190.

[46]. A. Babuponnusami and K. Muthukumar, *Sep Purif Technol*, 2012, **98**, 130-135.

[47]. C. Fang, B. Min and I. Angelidaki, *Appl Biochem Biotech*, 2011, **164**, 464-474.

[48]. M. S. Waring and J. R. Wells, *Atmos Environ*, 2015, **106**, 382-391.

[49]. N. Gokulakrishnan, A. Pandurangan and P. K. Sinha, *Ind Eng Chem Res*, 2009, **48**, 1556-1561.

[50]. T. Kayashima and T. Katayama, *Biochim Biophys Acta Gen Subj*, 2002, **1573**, 1-3.

[51]. S. Zhou, C. Zhang, R. Xu, C. Gu, Z. Song and M. Xu, *Water Sci Technol*, 2016, **73**, 1025-1032.

[52]. E. Rytter and A. Holmen, *Catalysts*, 2015, **5**, 478-499.

[53]. I. Song, H. Lee, S. W. Jeon, I. A. Ibrahim, J. Kim, Y. Byun, D. J. Koh, J. W. Han and D. H. Kim, *Nat Commun*, 2021, **12**, 1-9.

[54]. B. High, D. Bruce and M. M. Richter, *Anal Chim Acta*, 2001, **449**, 17-22.

[55]. United States Environmental Protection Agency Consumer Fact Sheet on Copper, 2001.

[56]. R. M. Saleh, J. M. Abd El Kader, A. A. El Hosary and A. M. Shams El Din, *J Electroanal Chem Interfacial Electrochem*, 1975, **62**, 297-310.

[57]. C. K. Ko and W. G. Lee, *Surf Interface Anal*, 2010, **42**, 1128-1130.

[58]. S. O. Lee, T. Tran, B. H. Jung, S. J. Kim and M. J. Kim, *Hydrometallurgy*, 2007, **87**, 91-99.

[59]. D. Panias, M. Taxiarchou, I. Paspaliaris and A. Kontopoulos, *Hydrometallurgy*, 1996, **42**, 257-265.

[60]. R. C. Hubli, J. Mittra and A. K. Suri, *Hydrometallurgy*, 1997, **44**, 125-134.

[61]. E. A. Yakusheva, I. G. Gorichev, T. K. Atanasyan and Y. A. Lainer, *Russian Metallurgy (Metally)*, 2010, **2010**, 18-23.

[62]. J. A. Zazo, J. A. Casas, A. F. Mohedano, M. A. Gilarranz and J. J. Rodríguez, *Environ Sci Technol*, 2005, **39**, 9295-9302.

[63]. H. Majima, Y. Awakura, T. Yazaki and Y. Chikamori, *Metall Trans B*, 1980, **11**, 209-214.

[64]. W. F. Pickering, *Water, Air, and Soil Pollution*, 1983, **20**, 299-309.

[65]. I. U. Castro, D. C. Sherrington, A. Fortuny, A. Fabregat, F. Stüber, J. Font and C. Bengoa, *Catal Today*, 2010, **157**, 66-70.

[66]. Y. Yan, S. Jiang, H. Zhang and X. Zhang, *Chem Eng J*, 2015, **259**, 243-251.

[67]. N. Habbache, N. Alane, S. Djerad and L. Tifouti, *Chem Eng J*, 2009, **152**, 503-508.

[68]. E. B. Nauman, *Residence time distributions*, Wiley, 2003.

[69]. A. Santos, P. Yustos, A. Quintanilla, S. Rodríguez and F. García-Ochoa, *Appl Catal B-Environ*, 2002, **39**, 97-113.

[70]. A. McAuley and G. H. Nancollas, *Trans Faraday Soc*, 1960, **56**, 1165-1171.

[71]. N. Crowther and F. Larachi, *Appl Catal B-Environ*, 2003, **46**, 293-305.

[72]. C. Adán, J. Carbajo, A. Bahamonde, I. Oller, S. Malato and A. Martínez-Arias, *Appl Catal B-Environ*, 2011, **108**, 168-176.

[73]. J. Chen and L. Zhu, *J Hazard Mater*, 2011, **185**, 1477-1481.

[74]. G. C. Bye, M. McEvoy and M. A. Malati, *J Chem Technol Biot*, 1982, **32**, 781-789.

[75]. I. Sádaba, M. L. Granados, A. Riisager and E. Taarning, *Green Chem*, 2015, **17**, 4133-4145.

[76]. S. E. Ziemniak, M. E. Jones and K. Combs, *J Solution Chem*, 1992, **21**, 179-200.

[77]. D. Bingöl and M. Canbazoğlu, *Hydrometallurgy*, 2004, **72**, 159-165.

[78]. Y. FAN, C. ZHANG, J. ZHAN and J. WU, *T Nonferr Metal Soc*, 2008, **18**, 454-458.

[79]. F. J. Beltrán, F. J. Rivas, L. A. Fernández, P. M. Álvarez and R. Montero-de-Espinosa, *Ind Eng Chem Res*, 2002, **41**, 6510-6517.

[80]. Y. Huang, Y. Sun, Z. Xu, M. Luo, C. Zhu and L. Li, *Sci Total Environ*, 2017, **575**, 50-57.

[81]. J. A. Zazo, A. F. Fraile, A. Rey, A. Bahamonde, J. A. Casas and J. J. Rodriguez, *Catal Today*, 2009, **143**, 341-346.

[82]. G. Wen, Z. Pan, J. Ma, Z. Liu, L. Zhao and J. Li, *J Hazard Mater*, 2012, **239**, 381-388.

[83]. F. J. Beltran, F. J. Rivas and R. Montero-de-Espinosa, *Appl Catal B-Environ*, 2004, **47**, 101-109.

[84]. M. M. Kosanić, *J Photochem Photobio A-Chem*, 1998, **119**, 119-122.

[85]. T. A. McMurray, J. A. Byrne, P. Dunlop, J. Winkelman, B. R. Eggins and E. T. McAdams, *Appl Catal B-Environ*, 2004, **262**, 105-110.

[86]. E. Szabó-Bárdos, H. Czili and A. Horváth, *J Photochem Photobio A-Chem*, 2003, **154**, 195-201.

[87]. L. Xiang, S. Royer, H. Zhang, J. M. Tatibouët, J. Barrault and S. Valange, *J Hazard Mater*, 2009, **172**, 1175-1184.

[88]. I. F. Mena, E. Diaz, I. Moreno-Andrade, J. J. Rodriguez and A. F. Mohedano, *J Environ Chem Eng*, 2018, **6**, 6444-6450.

[89]. M. Munoz, Z. M. de Pedro, N. Menendez, J. A. Casas and J. J. Rodriguez, *Appl Catal B-Environ*, 2013, **136-137**, 218-224.

[90]. P. García-Muñoz, G. Pliego, J. A. Zazo, B. Barbero, A. Bahamonde and J. A. Casas, *Chem Eng J*, 2017, **318**, 89-94.

[91]. M. Martin-Martinez, B. F. Machado, P. Serp, S. Morales-Torres, A. M. T. Silva, J. L. Figueiredo, J. L. Faria and H. T. Gomes, *Catal Today*, 2020, **357**, 332-340.

[92]. K. M. Valkaj, A. Katovic and S. Zrncevic, *Ind Eng Chem Res*, 2011, **50**, 4390-4397.

[93]. S. C. Ray, *Sol Energ Mat Sol C*, 2001, **68**, 307-312.

[94]. H. Wu, X. Wei, M. Shao, J. Gu and M. Qu, *Chem Phys Lett*, 2002, **364**, 152-156.

[95]. J. O. Weston, H. Miyamura, T. Yasukawa, D. Sutarma, C. A. Baker, P. K. Singh, M. Bravo-Sanchez, N. Sano, P. J. Cumpson and Y. Ryabenkova, *Catal Sci Technol*, 2017, **7**, 3985-3998.

[96]. Y. Yang, Y. Yan, H. Zhang and X. Wu, *Sep Purif Technol*, 2020, **237**, 116452.

[97]. A. Cichocki, J. Datka, A. Olech, Z. Piwowarska and M. Michalik, *J Chem Soc, Faraday Trans*, 1990, **86**, 753-756.

[98]. R. Szostak, V. Nair and T. L. Thomas, *J. Chem. Soc., Faraday Trans. 1*, 1987, **83**, 487-494.

[99]. Y. Yan, S. Jiang and H. Zhang, *Sep Purif Technol*, 2014, **133**, 365-374.

[100]. R. Alotaibi, F. Alenazey, F. Alotaibi, N. Wei, A. Al-Fatesh and A. Fakeeha, *Appl Petrochem Res*, 2015, **5**, 329-337.

[101]. E. F. Iliopoulou, S. D. Stefanidis, K. G. Kalogiannis, A. Delimitis, A. A. Lappas and K. S. Triantafyllidis, *Appl Catal B-Environ*, 2012, **127**, 281-290.

[102]. G. Qi and R. T. Yang, *Appl Catal B-Environ*, 2005, **60**, 13-22.

[103]. L. Dai, Y. Wang, Y. Liu, R. Ruan, D. Duan, Y. Zhao, Z. Yu and L. Jiang, *Bioresource Technol*, 2019, **272**, 407-414.

[104]. S. Poulston, P. M. Parlett, P. Stone and M. Bowker, *Surf Interface Anal*, 1996, **24**, 811-820.

[105]. A. Corma, A. Palomares and F. Márquez, *J Catal*, 1997, **170**, 132-139.

[106]. J. P. Espinós, J. Morales, A. Barranco, A. Caballero, J. P. Holgado and A. R. González-Elipe, *J Phys Chem B*, 2002, **106**, 6921-6929.

[107]. E. B. Fox, A. F. Lee, K. Wilson and C. Song, *Top Catal*, 2008, **49**, 89-96.

[108]. M. Conte, C. J. Davies, D. J. Morgan, T. E. Davies, D. J. Elias, A. F. Carley, P. Johnston and G. J. Hutchings, *J Catal*, 2013, **297**, 128-136.

[109]. J. Xu, W. Wang, E. Gao, J. Ren and L. Wang, *Catal Commun*, 2011, **12**, 834-838.

[110]. G. Wen, S. Wang, J. Ma, T. Huang, Z. Liu, L. Zhao and J. Xu, *J Hazard Mater*, 2014, **275**, 193-199.

[111]. Y. Huang, J. A. Schwarz, J. R. Diehl and J. P. Baltrus, *Appl catal*, 1988, **36**, 163-175.

[112]. A. Infantes-Molina, C. Moreno-León, B. Pawelec, J. L. G. Fierro, E. Rodríguez-Castellón and A. Jiménez-López, *Appl Catal B-Environ*, 2012, **113-114**, 87-99.

[113]. G. Lee, Y. Jeong, B. Kim, J. S. Han, H. Jeong, H. B. Na and J. C. Jung, *Catal Commun*, 2015, **67**, 40-44.

[114]. C. Wang, D. van der Vliet, K. Chang, H. You, D. Strmcnik, J. A. Schlueter, N. M. Markovic and V. R. Stamenkovic, *J Phys Chem C*, 2009, **113**, 19365-19368.

[115]. J. F. Barona, D. F. Morales, L. F. González-Bahamón, C. Pulgarín and L. N. Benítez, *Appl Catal B-Environ*, 2015, **165**, 620-627.

[116]. H. Gruber-Wölfler, P. F. Radaschitz, P. W. Feenstra, W. Haas and J. G. Khinast, *J Catal*, 2012, **286**, 30-40.

[117]. N. S. Inchaurrondo, P. Massa, R. Fenoglio, J. Font and P. Haure, *Chem Eng J*, 2012, **198**, 426-434.

[118]. K. Maduna Valkaj, A. Katovic, V. Tomašic and S. Zrncevic, *Chem Eng Technol*, 2008, **31**, 398-403.

[119]. D. Q. Khieu, D. T. Quang, T. Dai Lam, N. H. Phu, J. H. Lee and J. S. Kim, *J Incl Phenom Macro*, 2009, **65**, 73-81.

[120]. A. Moncayo-Lasso, R. A. Torres-Palma, J. Kiwi, N. Benítez and C. Pulgarin, *Appl Catal B-Environ*, 2008, **84**, 577-583.

[121]. J. A. Melero, G. Calleja, F. Martínez, R. Molina and M. I. Pariente, *Chem Eng J*, 2007, **131**, 245-256.

Chapter 5. Activity and stability of metal substituted ZSM-5 catalyst in the CWPO of phenol

5.1 Overview

The wide application of CWPO for the abatement of pollutants in wastewater requires heterogeneous catalysts which are not only active but stable, since the activity and stability are key factors in evaluating the effectiveness and feasibility of a heterogeneous catalyst in industry, or more in general for scale up or exploitation. However, most of the supported Cu and Fe catalysts reported in the CWPO of phenol reaction so far [1-4], although highly efficient for the removal of phenol, suffer irreversible deactivation due to metal leaching in the reaction phase. The leached metal, not only hinders the prospect of practical application of heterogeneous catalyst in the CWPO process, but introduces secondary pollution to the reaction mixture. Hence, the improvement of the stability of metal doped heterogeneous catalysts for the phenol oxidation reaction is the first task to tackle after highly active catalysts have been confirmed or identified.

Three common solutions are summarized and accepted in literature to prevent or minimize metal leaching from heterogeneous catalyst in aqueous phase reaction [5]: (i) optimization of reaction conditions, (ii) replacement of catalyst and (iii) change of reaction type from liquid phase to gas phase. Among the above solutions, the optimization of reaction parameters has often a limited applicability, in the sense it makes only limited improvement in the catalyst stability, as proved in Chapter 4 (section 4.4). Whereas the third option is inapplicable for wastewater treatment processes. The second one appears like the only solution, and some successful examples have been reported by replacing routine catalysts (such as metal impregnated catalysts) with catalysts with unique properties (such as catalysts with metal introduced into matrix of support or catalysts with chemical modification). However, within those successful cases [6,7], most research focused on the surface modification of metal-supported catalyst such as pre-treatment of catalyst, acid washing, calcination conditions and so on, while metal leaching still occurs on catalyst after modification. This is

because that for metal-supported catalyst, most of the active species are retained to the support only by weak Van der Waals bonds [8] and readily dissolved when exposed to the reaction mixtures [9]. The investigation into more stable metal doped heterogeneous catalysts is therefore still a challenge.

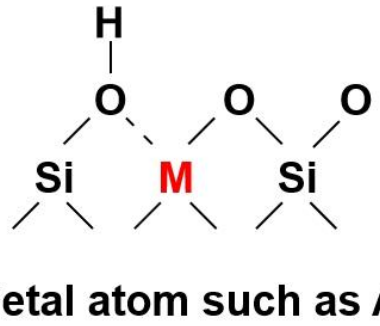

M = Metal atom such as Al, Fe

Figure 5.1. Schematic diagram of metal substitution into the framework of zeolite.

Considering the strong complexation of oxalate to metal ions (as shown in section 4.4.2.7), the design of catalyst with heteroatoms substitution into framework positions of high silica zeolites and silicates (figure 5.1) seems to be a more efficient solution to the metal leaching as the coordination environment of the metal atoms has high stability and inherent resistance to leaching [10]. Besides, substituted transition metal ions have outstanding catalytic behaviour in the oxidation of organic compounds as they provide highly dispersed metal elements within zeolite structure. A series of metal atoms, Ti [11,12], V [13,14], Cr [15,16], Mn [17,18], Fe [19,20] and Ga [21,22] for example, were reported to be successfully incorporated into the framework of zeolite to obtain modified catalysts with enhanced catalytic activity and leaching resistance. As reported [19], Fe-ZSM-5 catalyst with Si/Fe ratio of 120 was prepared by hydrothermal synthesis via introducing Fe atoms into the ZSM-5 matrix and it presented extraordinary performance in phenol oxidation with complete phenol conversion and low leaching (< 0.40 $mg \cdot L^{-1}$) in 7 h. Moreover, Fe substituted MCM-41 prepared by sol-gel process also had high stability in phenol oxidation reaction in the CWPO process with only 6% of metal leached to the reaction mixture in 3 h [23].

Thus, the aims of this chapter are to discuss and describe: 1) the synthesis of metal incorporated ZSM-5 catalyst by hydrothermal synthesis, 2) the activity and stability of the metal substituted zeolite catalyst in the CWPO of phenol reaction, and 3) an assessment of the homogeneous contribution of the metal ion that leaches from the metal substituted zeolite catalyst in the CWPO of phenol reaction, 4) a comparison of the activity and stability of the metal substituted zeolite catalyst in the form of powder and coating, respectively.

5.2 Activity and stability of Fe substituted ZSM-5 catalyst in CWPO of phenol

As discussed in the section 4.2.1 (table 4.1) in the last chapter, both Cu and Fe catalysts were active for phenol decomposition in the presence of H_2O_2. In most of the reports involving heteroatom incorporated zeolites, the iron-containing catalyst is more frequently studied and well-developed than the copper-containing catalyst due to its more steady catalytic performance, more facile and controllable preparation routes. Many pieces of research [20,24,25] evidenced that the Fe atoms could be incorporated into the framework of ZSM-5 by hydrothermal synthesis, while fewer papers [26,27] were found on the successful synthesis of Cu substituted catalyst. In theory, the incorporation of trivalent iron into tetravalent silicate matrixes is much easier than that of bivalent copper as Fe atoms favour the formation of tetrahedra due to their suitable T-O bond and T-O-T angles that can stabilize these building units [28] while this is vital for forming isolated redox centres and generating Lewis and Brønsted acid sites [20] of the catalyst. In other words, the capability of metal species of incorporating into the matrix decides the performance of the metal-substituted zeolite catalyst. Therefore, a quick assessment of whether the metal-substituted zeolite catalyst a good way forward to solve, or at least to minimize, the metal leaching could be made when using Fe-ZSM-5 zeolite as benchmark. This approach is feasible after the high stability of Fe-ZSM-5 was confirmed, otherwise alternative solutions have to be considered. Against this background, the Fe-ZSM-5 catalyst, rather than Cu-ZSM-5, was preferentially prepared by hydrothermal synthesis and then tested in the CWPO of phenol reaction.

5.2.1 Synthesis and characterization of Fe substituted ZSM-5 catalyst

The Fe-ZSM-5 catalyst was prepared by hydrothermal synthesis following the protocol from Zhang's group [29]. In this protocol, a zeolite was prepared using an alkaline synthesis gel with TEOS (tetraethyl orthosilicate, $Si(OC_2H_5)_4$) as silica source, Fe nitrate ($Fe(NO_3)_3$) as metal precursor and TPAOH (tetrapropylammonium hydroxide, $(CH_3CH_2CH_2)_4N(OH)$) as template. The white powder at the bottom of a synthesis liner after hydrothermal treatment was yielded as product after calcination. The synthesized catalysts are denoted as M-ZSM-5-HTS(x), where M refers to metal species, HTS is the preparation method (hydrothermal synthesis) and x represents Si/Metal ratio, for example, the Fe-ZSM-5-HTS(80) is Fe incorporated ZSM-5 prepared by hydrothermal synthesis with Si/Fe ratio of 80.

5.2.1.1 XRD

Both commercial HZSM-5 (Si/Al of 46) and ZSM-5 prepared by hydrothermal synthesis (Si/Al of 80 in synthesis gel) were used as blank control in this section. Figure 5.2 showed XRD patterns of these samples. As it can be seen, similar to the commercial HZSM-5, the synthesized HZSM-5 showed intense and characteristic peaks at 7.9°, 8.8°, 23.1°, 24.0° and 24.5°, 2θ that corresponding to the (011), (020), (051), (303) and (313) facets as according to the JCPDS database (entry 42-0024), indicating the successful synthesis of zeolite with MFI (Mordenite Framework Inverted zeolites, framework code used to distinguish different zeolite structures) structure. Besides, the synthesized ZSM-5 was highly crystalline with a relative crystallinity (RC) of 99.6% (table 5.1), defined as the ratio of integrated peak area between 2θ of 22.5–25° of the synthesized ZSM-5 samples to the integrated peak area of the reference ZSM-5 (commercial, RC of 100%), as shown in Eq. 5.1 [30,31],

$$\text{relative crystallinity (RC)},100\% = \frac{I}{I_{ref}} \times 100\% \qquad \text{(Eq. 5.1)}$$

Where I is the area of a specific peak of a target material, and I_{ref} is for a commercial sample of the same material.

The Fe-ZSM-5 catalyst was prepared under the same condition as the ZSM-5 (synthesized) except for replacing the Al precursor with Fe precursor. All the characteristic peaks were observed, as can be seen in figure 5.2, suggesting that the addition of Fe nitrate did not affect the formation of the MFI structure. However, peaks expected at 24.20, 33.23, 35.68, 40.92, 49.54, 54.16, and 57.70° 2θ attributable to the (012), (104), (110), (113), (024), (116), and (018) reflections, characteristic of pure α-Fe_2O_3 [32] were not observed in the XRD pattern of the synthesized Fe catalyst, which could be due to the small size of metal oxide particles, and/or highly dispersed metal species with less 5% loading. Furthermore, the high relative crystallinity (94.7%, in table 5.1) of Fe-ZSM-5-HTS(80) also implied that the zeolite had a well defined crystallined structure. In addition, the volume of the unit cell of the Fe substituted ZSM-5 catalyst was slightly higher (0.4% of volume expansion, table 5.1) than the pure silica counterpart (synthesized ZSM-5), which is due to the distortion of the tetrahedra caused by the substitution of Fe. The expansion of the unit cell evidenced that part of the Fe atoms were incorporated into the framework of zeolite.

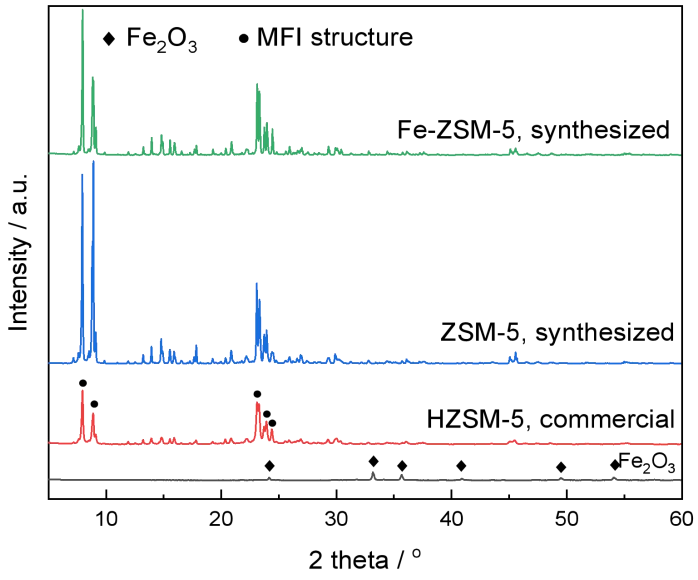

Figure 5.2. XRD patterns of a) commercial HZSM-5, b) synthesized ZSM-5, c) Fe-ZSM-5-HTS and d) commercial Fe_2O_3 (where black dots ● represent characteristic peaks of MFI structure and black rhombi ◆ stand for peaks of Fe_2O_3)

Table 5.1. Parameters of unit cell of the Cu doped zeolite catalysts. The expansion or contraction (ΔV/V, caculated by Eq. 5.3) of the synthesized metal incorporated materials is referred to as the undoped material (silicalite-1), where the sign (+) stands for an expansion and the sign (-) stands for a contraction with respect to the undoped zeolite.

Catalyst	Relative crystallinity[a]	Unit cell parameters[b]							Expansion or contraction[d]
		a (Å)	*b* (Å)	*c* (Å)	α (°)	β (°)	γ (°)	V[c] (Å^3)	
Pure silica ZSM-5 (silicalite-1)	99.6%	20.029 ± 0.007	19.894 ± 0.006	13.386 ± 0.007	90.00 ± 0.07	90.00 ± 0.08	90.00 ± 0.09	5334 ± 13	--
Fe-ZSM-5-HTS(80)	94.7%	20.088 ± 0.002	19.902 ± 0.002	13.396 ± 0.002	90.00 ± 0.07	90.00 ± 0.08	90.00 ± 0.09	5356 ± 1	0.4%
Fe-ZSM-5-HTS(80)-HCl, used	91.1%	20.091 ± 0.002	19.902 ± 0.002	13.397 ± 0.002	90.00 ± 0.07	90.00 ± 0.08	90.00 ± 0.09	5357 ± 1	0.4%
Fe-ZSM-5/SiC(80)	--	20.076 ± 0.008	19.898 ± 0.007	13.388 ± 0.00	90.00 ± 0.07	90.00 ± 0.08	90.00 ± 0.09	5348 ± 5	0.3%
Cu-ZSM-5-HTS(80)	98.6%	20.092 ± 0.003	19.882 ± 0.003	13.398 ± 0.003	90.00 ± 0.07	90.00 ± 0.08	90.00 ± 0.09	5352 ± 2	0.3%
Cu-ZSM-5/SiC(80)	--	20.082 ± 0.013	19.886 ± 0.012	13.399 ± 0.012	90.00 ± 0.07	90.00 ± 0.08	90.00 ± 0.09	5351 ± 7	0.3%

a - calculated by Eq. 5.1.

b - unit cell parameters obtained from X'pert Highscore software.

c - volume of unit cell, calculated by Eq.5.2: V=a*b*c

d - calculated by Eq. 5.3 $\exp ansion / contraction,100\% = \frac{V_{sample} - V_{HZSM-5}}{V_{HZSM-5}} \times 100$

5.2.1.2 BET

The N_2 adsorption-desorption isotherms of the commercial HZSM-5 and the synthesized Fe-ZSM-5-HTS(80) samples, as can be seen in figure 5.3, presented typical type I isotherms (by IUPAC classification) which are given by microporous solids having relatively small external surfaces [33]. The steep uptake at very low p/p^0 is due to enhanced adsorbent-adsorptive interactions in narrow micropores, resulting in micropore filling at very low p/p^0 [33]. In addition, the synthesized Fe-ZSM-5-HTS(80) exhibited a high-quality microporous structure with the BET surface area (394 $m^2 \cdot g^{-1}$), micropore area (368 $m^2 \cdot g^{-1}$) and micropore volume (0.17 $cm^3 \cdot g^{-1}$) listed in table 5.2, which are almost identical with that of the reference sample HZSM-5 (408 $m^2 \cdot g^{-1}$, 375 $m^2 \cdot g^{-1}$, 0.153 $cm^3 \cdot g^{-1}$, respectively). Thus it was indicated that the Fe-ZSM-5-HTS(80) with microporous structure was synthesized successfully. From these data it is also possible to infer that Fe-ZSM-5/SiC(80) (see section 5.3.2.2) was indeed coated on SiC because surface area and micropore volume of the material are indeed similar to those of SiC, although an excess of SiC is likely to have been deposited and the surface area of ZSM-5 has been completely lost.

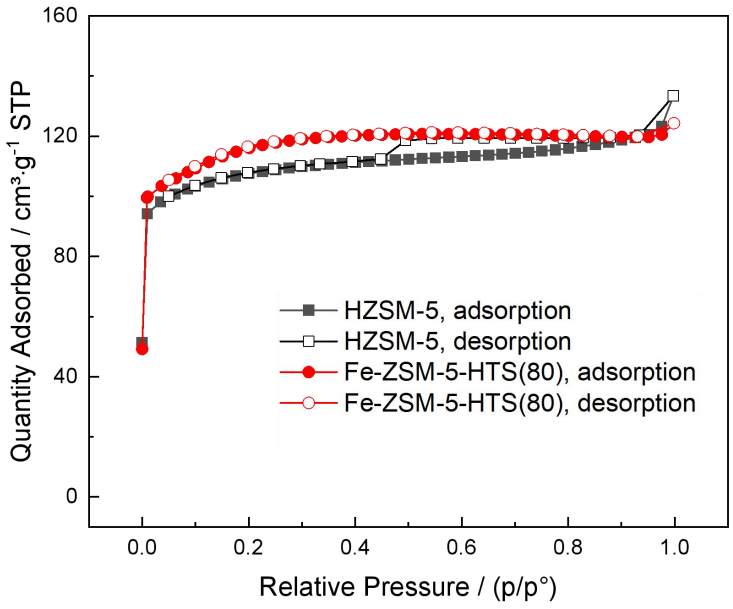

Figure 5.3. Adsorption-desorption isotherms of HZSM-5, commercial and Fe-ZSM-5-HTS(80), synthesized

Table 5.2. Pore parameters of different catalysts

Sample name	S_{BET}[a] ($m^2 \cdot g^{-1}$)	S_{micro}[b] ($m^2 \cdot g^{-1}$)	S_{ext}[b] ($m^2 \cdot g^{-1}$)	V_{total} ($cm^3 \cdot g^{-1}$)	V_{micro}[b] ($cm^3 \cdot g^{-1}$)
HZSM-5, commercial	408	375	33	0.191	0.153
Fe-ZSM-5-HTS(80), synthesized	394	368	26	0.187	0.171
SiC, commercial	27	5	22	0.092	0.002
Fe-ZSM-5/SiC(80), synthesized	21	16	5	0.024	0.007

a - determined using BET method.

b - determined using t-plot method.

5.2.1.3 ATR-FTIR

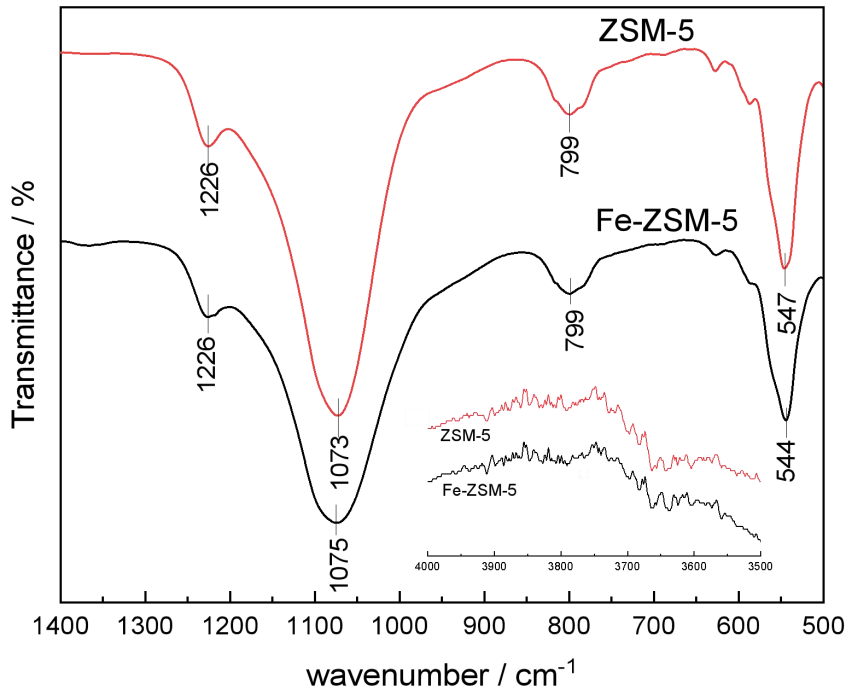

Figure 5.4. IR spectra of ZSM-5 and Fe-ZSM-5-HTS (Si/Fe of 80) prepared by hydrothermal synthesis. The features of Fe incorporating into the framework into the zeolite structure were not observed.

The ATR-FTIR spectra of ZSM-5 and Fe-ZSM-5 zeolites prepared by hydrothermal synthesis were depicted in figure 5.4 for the range of 1500-500 cm^{-1}. The typical IR spectrum of a ZSM-5 zeolite featured bands at around 550, 800, 1100 and 1225 cm^{-1} with characteristic of TO_4 (T = Si or Al) tetrahedron units. The absorption bands at approximately 1225 and 1100 cm^{-1} correspond to TO_4 asymmetric stretching vibration, while the bands at about 800 and 550 cm^{-1} are assigned to TO_4 symmetric stretching, double ring and bending vibrations, respectively [24,34-36]. Both synthesized samples presented the bands characterizing skeletal vibrations of MFI zeolite structure, indicating the successful synthesis of ZSM-5 with high crystallinity. However, the features of Fe incorporating into the framework into the zeolite structure were not observed in these spectra. As reported in the literature, the incorporation of Fe species inside ZSM-5 zeolite channels would lead to the shift of absorption bands at 1225 and 1100 cm^{-1} to lower wavenumbers because the Fe-O bond is longer than the Al-O bond and atomic weight of Fe>Al [24,37]. On the other hand, The band at around 3620 cm^{-1} associated with Fe-OH was not found as well, which is possibly due to the very low percentage of Fe incorporation, and as such a lack of direct detection.

5.2.1.4 ICP-OES

Table 5.3. Metal loading of the synthesized Fe-ZSM-5-HTS catalyst tested by ICP-OES

Catalyst	Loading of supported Fe	Loading of substituted Fe	Total Fe loading
Fe-ZSM-5-HTS(80)	0.11%	1.5%	1.6%

Although the theoretical loading was around 1 wt% when Si/Fe ratio of 80 was designed in the synthesis gel, the actual loading of the Fe-ZSM-5 catalyst is uncontrollable. Hence the actual loading of the Fe substituted ZSM-5 catalyst was determined by ICP-OES. Unlike post-impregnated Fe catalyst with metal almost supported on the surface of the support, hydrothermal synthesized catalyst has both metal species supported on the surface and metal species incorporated into the framework. The loading of supported Fe was obtained by testing the leached Fe concentration of the Fe-ZSM-5-HTS catalyst that was treated by 1 M

of HCl solution for 24 h at 80 °C. The substituted Fe species that remained in the Fe-ZSM-5-HTS catalyst after HCl washing, was tested by further digesting of the solid with HF acid solution. As shown in table 5.3, the loading of supported Fe was 0.11 wt%, while the loading of substituted Fe reached 1.5 wt%, indicating that most of the Fe was incorporated into the framework of the zeolite.

From the above analysis, it is deduced that the synthesis of Fe-ZSM-5-HTS was successful and most of the Fe atoms were incorporated into the framework of the catalyst.

5.2.2 Catalytic activity of Fe substituted ZSM-5 catalyst

The catalytic performance of the Fe-ZSM-5 was presented in the form of activity and stability. The activity, as discussed in the last chapter, was defined by means of an array of parameters: phenol conversion, H_2O_2 consumption, and CO_2 formation, as well as the selectivity of the distribution of intermediates. The stability of the catalyst instead was quantified as Fe leaching and reusability. The reusability was evaluated by testing the sample catalyst in successive runs of reactions (≥ 5 runs). For our scopes, a material with both low leaching (such as < 5%) and high reusability (100% phenol conversion in at least 5 runs) was regarded as a stable catalyst.

5.2.2.1 Control tests - activity of iron-free ZSM-5 catalysts

In order to assess the catalytic activity of the Fe substituted zeolite catalyst, the performance of blank test and the iron-free ZSM-5 were studied, as they may also contribute to phenol decomposition. Only 4% of phenol decomposed under our reaction conditions (T = 80 °C, t = 4 h, P = endogenous, oxidant H_2O_2), when no catalysts used, as shown in figure 5.5. In comparison with no catalyst, the phenol conversion increased to 18% when using synthesized HZSM-5 as catalyst, indicating the activity of the iron-free ZSM-5 zeolite in phenol degradation which might be due to the correlation between the surface acidity and catalytic activity [38,39]. On the other hand, the phenol conversion over the synthesized

ZSM-5 was slightly lower than that over commercial HZSM-5 (30%) after 4 h which is probably because of the weaker acidity of the zeolite. The Si/Al ratio, as reported, affects catalytic activity of catalyst in phenol oxidation through the Brønsted acid sites [40,41], while the Si/Al ratio of the synthesized and the commercial zeolite is 80 and 46, respectively. The results of the control tests confirmed again that the incorporation of active species into ZSM-5 zeolite is necessary to increase the activity of the catalyst in the CWPO process.

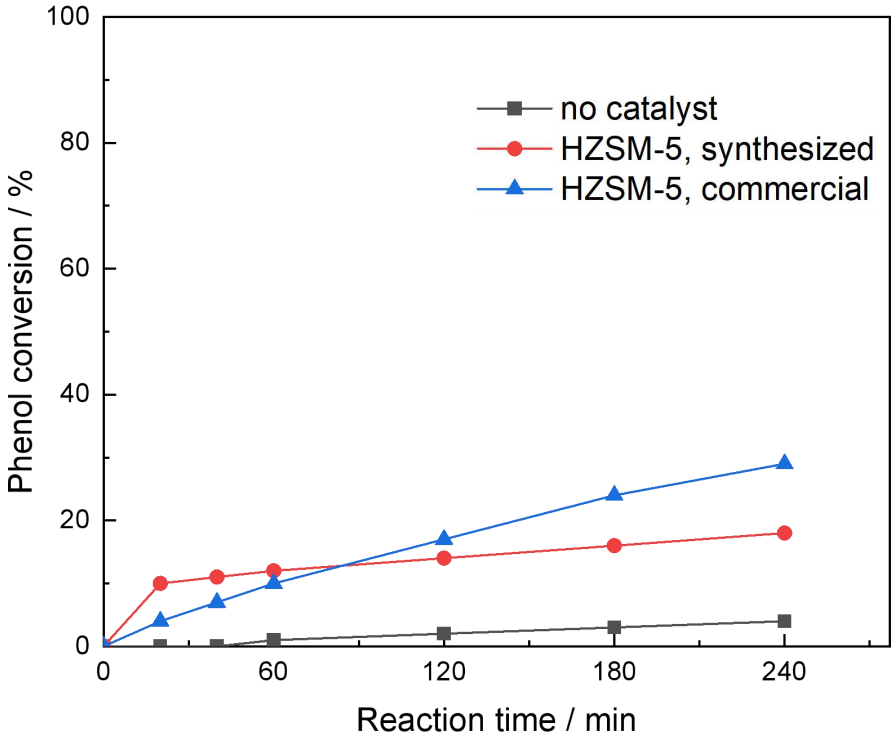

Figure 5.5. Phenol conversion over a) blank test without catalyst, b) commercial HZSM-5 catalyst and c) synthesized ZSM-5 catalyst in the CWPO process (2 $g \cdot L^{-1}$ catalyst, 50 mL solution 1 $g \cdot L^{-1}$ phenol, phenol: H_2O_2 of 1: 14, P = endogenous, 80 ^oC, 500 rpm)

5.2.2.2 Activity, stability and reusability of Fe-ZSM-5-HTS

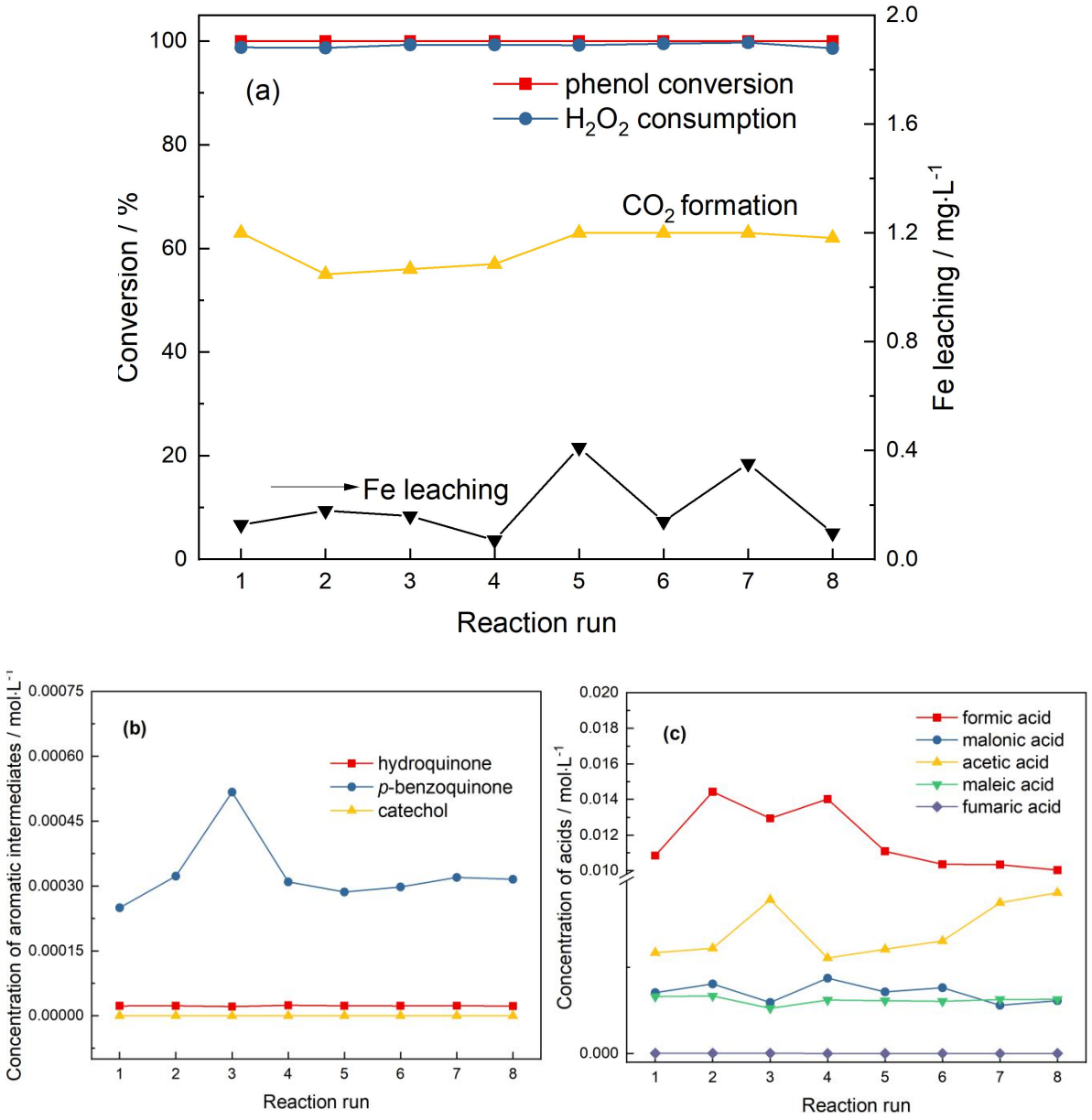

Figure 5.6. a) Phenol conversion, CO_2 formation and Fe leaching b) aromatic intermediates distribution, c) organic acids distribution in the CWPO of phenol using Fe-ZSM-5-HTS(80) in 8 runs of reaction (0.2 g of catalyst, 50 mL of 1 g·L^{-1} phenol, phenol: H_2O_2 of 1: 14, 80 ºC, 500 rpm)

From the catalytic results of first run of reaction (figure 5.6(a)), it is clear that the Fe-ZSM-5-HTS(80) catalyst presented high activity in the CWPO of phenol with phenol conversion of 100% in 4 h, much higher than that of the iron-free ZSM-5 (18%), indicating the high activity of the heterogeneous catalyst. Additionally, the high H_2O_2 consumption (99%)

and high CO_2 conversion (63%) all reflected the high activity of the Fe catalyst in phenol oxidation. Furthermore, the aromatic compounds, hydroquinone and catechol were almost removed after 4 h of reaction, while *p*-benzoquinone, though remaining in the reaction mixtures, had very low concentration (less than 3.0×10^{-4} mol·L^{-1}, figure 5.6(b)). By contrast, the concentration of acid intermediates (figure 5.6(c)), except fumaric acid (0.58 mg·L^{-1}, 5.0×10^{-6} mol·L^{-1}), was maintained high after reaction with acetic acid, malonic acid and maleic acid of approximately 70 mg·L^{-1} (1.2×10^{-3} mol·L^{-1}), 73 mg·L^{-1} (7.1×10^{-4} mol·L^{-1}) and 76 mg·L^{-1} (6.6×10^{-4} mol·L^{-1}), respectively, the concentration of formic acid even reached 500 mg·L^{-1} (1.1×10^{-2} mol·L^{-1}). Based on these data, we can consider Fe-ZSM-5-HTS(80) a highly efficient catalyst in phenol degradation since an effluent of low toxicity could be obtained with the catalyst.

More importantly, a stable catalyst was obtained for the first time in this project. Firstly, the Fe leaching of the catalyst was negligible throughout up to 8 runs of reactions with a Fe concentration in solution ranging only from 0.070 mg·L^{-1} to 0.41 mg·L^{-1} (figure 5.6(a)). Furthermore, the reusability of the catalyst was also high. As it can be seen, the catalytic activity of the catalyst kept constant for 8 runs of reactions as the phenol conversion, H_2O_2 consumption and efficiency, and CO_2 formation all remained steady, while the concentration of intermediates in the reaction mixtures, kept roughly stable in the 8 runs of reactions. Thus meaning that the catalyst has good reusability even without any regeneration process. Thus, the high activity and stability of the Fe-ZSM-5-HTS(80) catalyst was confirmed.

5.2.2.3 Effect of leached Fe on the decomposition of phenol

Although the Fe leaching from the Fe-ZSM-5-HTS(80) catalyst was numerically low (0.07-0.41 mg·L^{-1}, figure 5.6(a)), control tests by using iron nitrate ($Fe(NO_3)_3$) precursor were carried out to assess the effect of any leached Fe species was indeed negligible and as such the reaction truly heterogeneously catalysed.

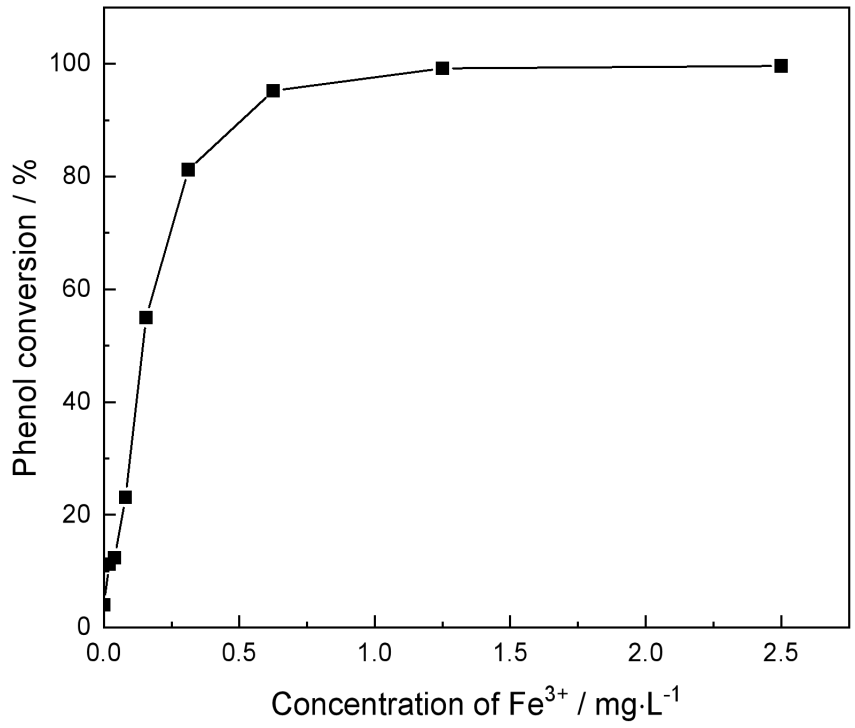

Figure 5.7. Activity of homogeneous Fe^{3+} (Fe nitrate ($Fe(NO_3)_3$) as precursor) with different concentrations in CWPO of phenol (50 mL 1 $g \cdot L^{-1}$ phenol, phenol: H_2O_2 of 1: 14, 80 ^oC, 4 h, 500 rpm)

The catalytic activity of Fe^{3+} from a $Fe(NO_3)_3 \cdot 9H_2O$ precursor at different concentrations was investigated. As shown in figure 5.7, just like the homogeneous Cu catalyst (in figure 4.30), the homogeneous Fe catalyst also presented high activity even at low concentrations (2.0 $mg \cdot L^{-1}$). However, when the concentration of Fe^{3+} was 0.080 $mg \cdot L^{-1}$, that is in the same range as that of Fe leaching from Fe-ZSM-5-HTS(80) catalyst, phenol conversion was only 23%. For complete phenol conversion to be obtained, homogeneous Fe^{3+} concentration of at least 2.5 $mg \cdot L^{-1}$ was required, which was much higher than the maximal Fe leaching detected in the reaction mixture using the Fe-ZSM-5-HTS(80) catalyst. Hence, it is deduced that the phenol decomposition did not result from the homogeneous contribution.

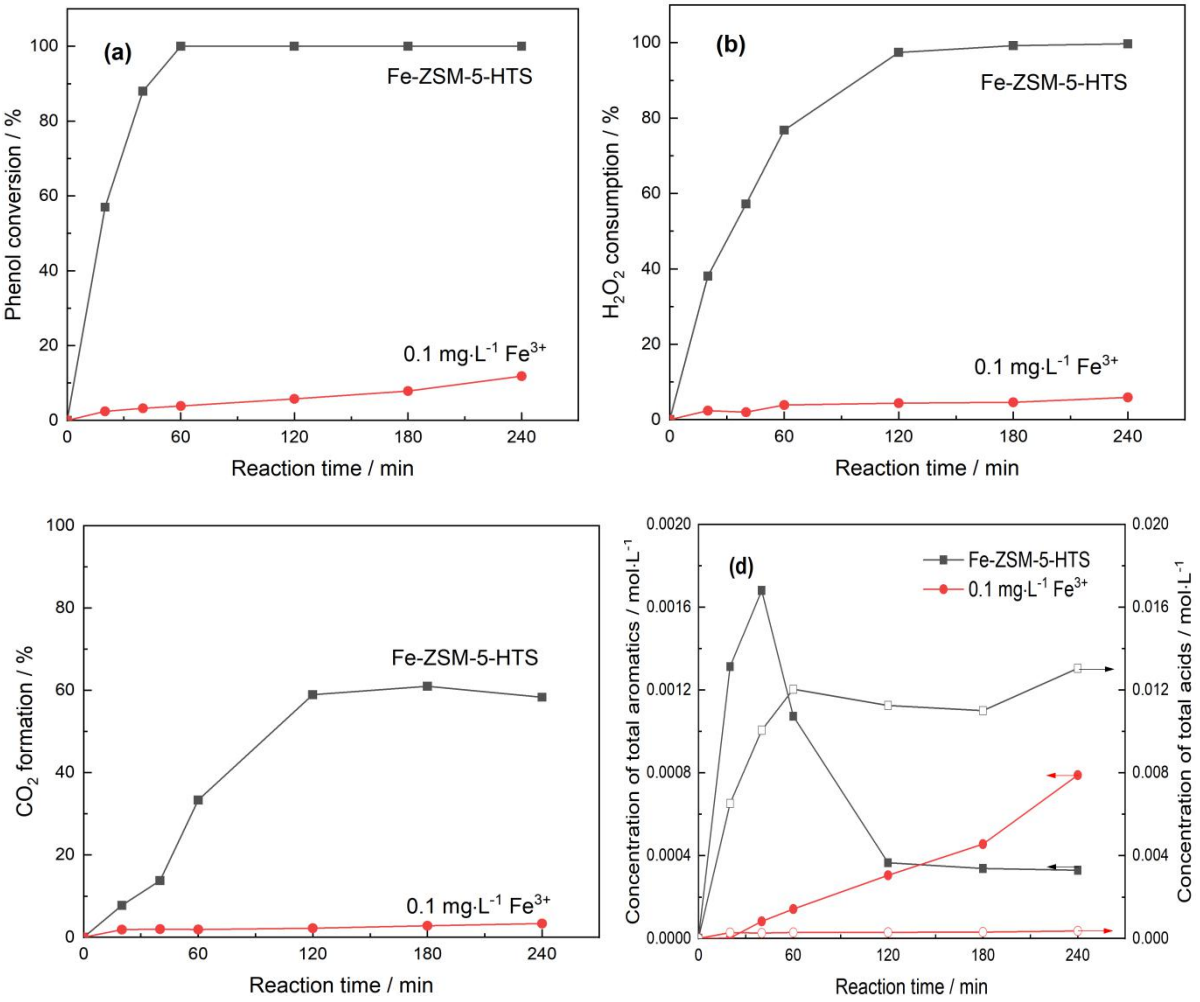

Figure 5.8. The activity of the Fe-ZSM-5-HTS catalyst and the Fe^{3+} catalyst with concentration equivalent to the metal leaching (0.1 mg·L^{-1}) of Fe-ZSM-5-HTS in the 8th run of reaction, a) phenol conversion, b) H_2O_2 consumption, 3) CO_2 formation and d) intermediates concentration (50 mL 1 g·L^{-1} phenol, phenol: H_2O_2 of 1: 14, 80 ^{o}C, 4 h, 500 rpm)

In order to further defend the above conclusion, the kinetics of phenol decomposition over Fe-ZSM-5-HTS(80) in the 8th run of reaction was tested (figure 5.8). The results were compared with that using homogeneous Fe^{3+} catalyst ($Fe(NO_3)_3 \cdot 9H_2O$ as precursor) with the concentration of 0.10 mg·L^{-1}, which corresponding to the Fe leaching (0.10 mg·L^{-1}) of the Fe substituted zeolite catalyst in the 8th run of reaction. As exhibited in figure 5.8(a), the Fe-ZSM-5-HTS(80) catalyst showed good performance in phenol degradation as complete phenol conversion was reached at merely 1 h, while the homogeneous Fe^{3+} catalyst had

phenol conversion of only 4% at the same reaction time. Thus, the actual phenol decomposition efficiency of the Fe-ZSM-5-HTS(80) was more than 25 times higher than that of homogeneous catalyst in 1 h. Even after 4 h, the phenol conversion over 0.10 $mg \cdot L^{-1}$ of Fe^{3+} was only 12%.

On the other hand, the H_2O_2 consumption (figure 5.8(b)) and CO_2 formation (figure 5.8(c)) using Fe-ZSM-5-HTS catalyst reached 100% and 60% respectively after 4 h, indicating the strong ability of the catalyst of generating hydroxyl radicals and decomposing phenol to CO_2. In comparison, the homogeneous Fe catalyst had a far lower activity with the H_2O_2 consumption and CO_2 formation of merely 6% and 3%, respectively. Furthermore, the toxic intermediates (aromatic compounds, figure 5.8(d)) were almost removed with the Fe substituted catalyst as the final concentration kept low (below 4.0×10^{-4} $mol \cdot L^{-1}$, corresponding to 3.7% of initial phenol concentration), whereas a high concentration of nontoxic acids (1.3×10^{-2} $mol \cdot L^{-1}$) remained in the reaction mixture. As a result, the heterogeneous Fe-ZSM-5 catalyst presented an activity that was much greater than the homogeneous - leached – counterpart; the homogeneous contribution of the leached Fe was insignificant and the phenol decomposition on Fe-ZSM-5-HTS(80) was a heterogeneous reaction.

Overall, the Fe substituted ZSM-5 catalyst was not only active but also stable for the CWPO of phenol and it is an ideal heterogeneous catalyst, which is in agreement with the literature [42,43]. It is therefore used as a benchmark in this project to evaluate the performance of other potential catalysts.

5.3 Activity and stability of Fe substituted ZSM-5 coated SiC catalyst in the CWPO of phenol

Zeolite coating on macro foam material is recently emerging as a novel form of catalyst with combined properties of porous zeolite catalyst (e.g. uniform porous structure, unique surface

property) and foam material (e.g. high porosity, high heat conductivity and low diffusion resistance) and was widely studied in liquid phase reactions [19,44-47].

5.3.1 Preparation of ZSM-5 coated SiC catalyst

Preparation of MFI coating was recently reported [48-50] and can be broadly classified into two categories: in situ preparation and secondary (or seeded) growth. In the in situ technique, the synthesis of zeolite coating follows the same method as the synthesis of zeolite powder, namely, the support surface is directly contacted with an alkaline synthesis gel and subjected to hydrothermal conditions [51,52]. However, by this method, the growth of zeolite coating occurs almost concurrently with the crystals nucleation in the hydrothermal process, but thus allowing for the undesirable formation of a non-uniformly oriented MFI layer. Whereas in the secondary growth method, the nucleation of crystals is separated from the zeolite growth through an additional seeding step [30,53]. In this method, a suitable support is coated by a layer of nanosized zeolite seed crystals followed by the secondary growth of these zeolite crystals to a continuous coating on the support surface during a hydrothermal process [54,55]. Though additional steps are required, this secondary growth method is attracting wide attention, since it offers greater flexibility in controlling the orientation of the zeolite crystals and the microstructure of the zeolite coating.

The ZSM-5 coating supported SiC catalyst was prepared by secondary growth method following a protocol from Fan's group [30,56]. In this protocol, the synthesis includes pre-treatment of SiC foam, support of seeding, and growth of coating.

5.3.1.1 Pre-treatment of SiC

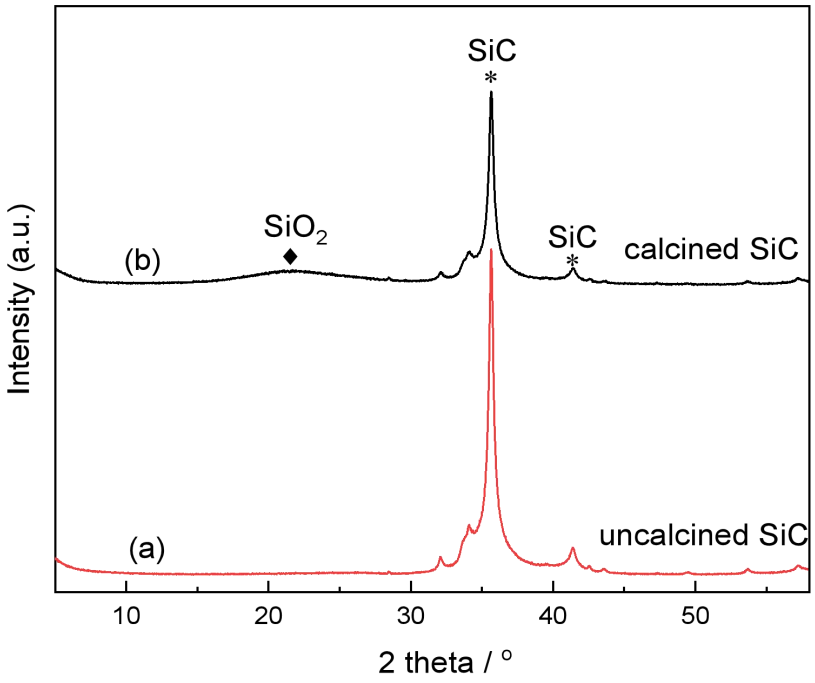

Figure 5.9. XRD patterns of a) SiC, b) pre-calcined SiC (900 °C, 4 h), the layer of amorphous SiO_2 was visible in 20-30°, 2θ after pre-treatment, marked by the black rhombic symbol

Prior to the seeding process, the pre-calcination of SiC (as received) is an important step to remove the impurity and contaminants on the surface and to assure the successful growth of coating on the SiC. The XRD patterns of SiC before and after calcination at 900 °C were showed in figure 5.9. As exhibited, the SiC was characterized by the two main reflection peaks at 2θ of 35.6 and 41.4° assigned to 111 and 200 planes, respectively [57,58]. It is reported that a thin layer of SiO_2 would be formed on the surface of SiC extrudates after calcination at high temperature in air, as displayed in Eq. 5.4.

$$SiC\,(s) + 3/2\,O_2\,(g) = SiO_2\,(s) + CO\,(g) \quad \text{(Eq. 5.4)}$$

The conversion of surface SiC substrate to the thin SiO_2 layer was confirmed by a weight gain (by ca. 10%) of SiC extrudates after calcination, as the molecular weight of SiO_2 (60.08

$g \cdot mol^{-1}$) is higher than SiC (40.11 $g \cdot mol^{-1}$). On the other hand, XRD pattern of the calcined SiC also showed the formation of SiO_2 layer as a broad peak at approximately 2θ of 21.7° appeared after calcination, which is the characteristic diffraction pattern of the amorphous SiO_2 phase [59] and/or as a thin layer.

The silica layer plays several important roles in the synthesis of ZSM-5 coating on SiC extrudates. Seeds powder was more likely to be anchored on the surface of SiO_2 rather than SiC, which led to the more stable growth of coating, because the presence of the thin SiO_2 layer ensures a strong interaction between the support and the seed gel [60,61]. In principle, the SiO_2 layer on the surface has intrinsic hydroxyl groups (silanols) in an aqueous solution, which is able to hydrate with silicalite-1 seeds, hence leading to the formation of siloxanes with strong Si-O bonds [30]. The formation of Si-O bonds is vital for bonding the zeolite seed crystals to the substrate.

5.3.1.2 Seeds preparation

The effects of the seeding process include [62,63]: (a) increase the crystallization rate and reduce the synthesis time, (b) suppress the formation of undesired crystal phases, (c) control the zeolite particle size, and (d) enable the intergrowth of zeolite films on functional surfaces. ZSM-5, ZSM-8, ZSM-11 and silicalite-1 and some other zeolite species were proved potential crystalline seeds in the synthesis of ZSM-5 [62-65]. Among them, silicalite-1 is the most widely used seed candidate as it is well reproduced and simply synthesized even for mass production. Meanwhile, it can be stored and stabilized for a long time and the particle size distribution is perfectly controlled. Furthermore, the silicalite-1 seed presented a typical MFI structure, as can be seen in figure 5.10. Silicalite-1 is pure silica MFI zeolite and consists of eight 5-membered oxygen rings, the similarity of its framework and building unit with ZSM-5 made it an appropriate seed crystal in the synthesis of ZSM-5 coating.

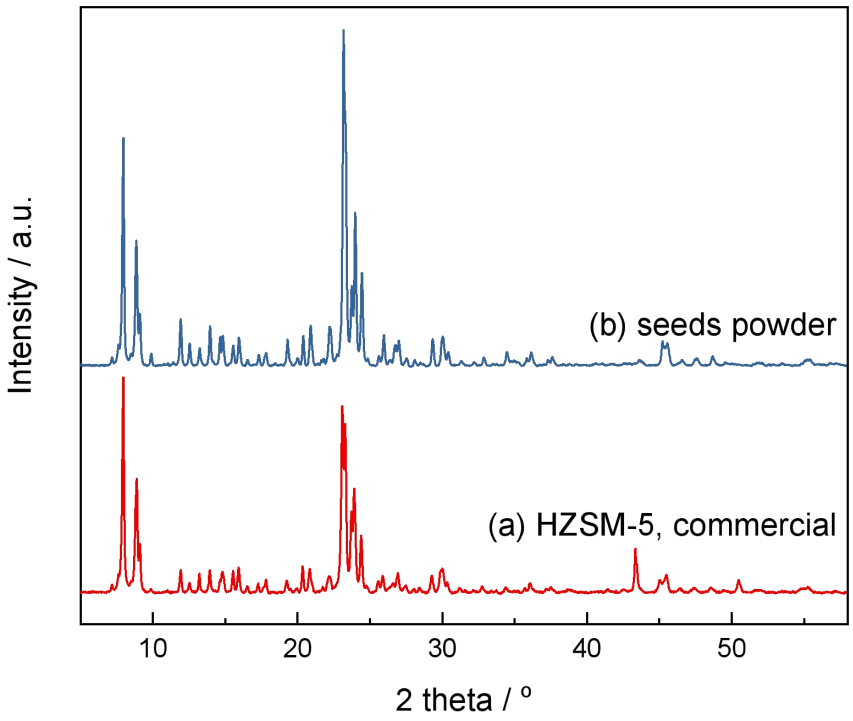

Figure 5.10. XRD patterns of a) HZSM-5 powder and b) seeds powder

5.3.1.3 Growth of coating

The ZSM-5 coating was synthesized on a seeded SiC foam: firstly, the pre-calcined SiC extrudates were dip-coated with the silicalite-1 seed in ethanol solution (1 wt.%) and then dried in an oven at 120 ºC to assure the pre-deposition of a seed layer of zeolite crystals on the support surface. Then the seeded SiC extrudates, together with the synthesis gel, were transferred to Teflon liner for the further growth of silicalite-1 seeds into ZSM-5 coating.

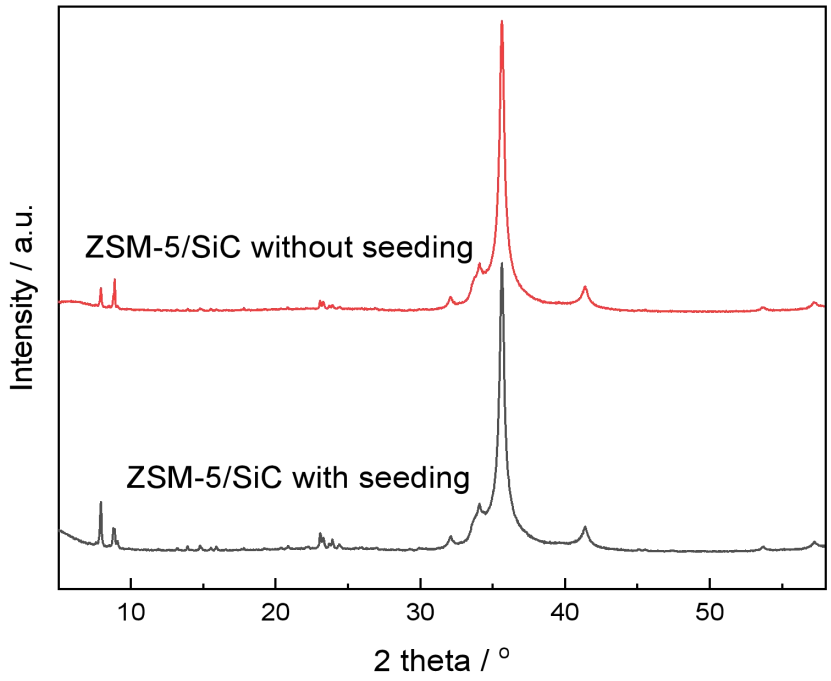

Figure 5.11. XRD patterns of ZSM-5/SiC with and without seeding step

The effectiveness of the growth of ZSM-5 coating was established by two parameters: XRD pattern and weight gain after synthesis. It is clear in figure 5.11 that well-developed MFI coating with the characteristic peaks at 7-9° and 22-25° were nucleated and grew on the calcined SiC extrudates after secondary growth regardless of with or without the seeding process, indicating the success of preparation of zeolite coating. On the other hand, it was also found that the seeding process is crucial to allow a more effective synthesis of ZSM-5 coatings on SiC substrate from the perspective of yield, as only 2 wt% of ZSM-5 coating was produced on the surface of unseeded SiC, while 8 wt% of ZSM-5 coating was formed on the seeded SiC. In addition, the intensities of the characteristic peaks of the ZSM-5 structure in the XRD patterns of two ZSM-5/SiC samples also indicated more coating was formed on the surface of seeded SiC. The necessity of the seeding process (or the secondary growth method) is evidenced as it increased the crystallization rate greatly.

5.3.2 Characterization of Fe-ZSM-5/SiC extrudates catalyst

5.3.2.1 XRD

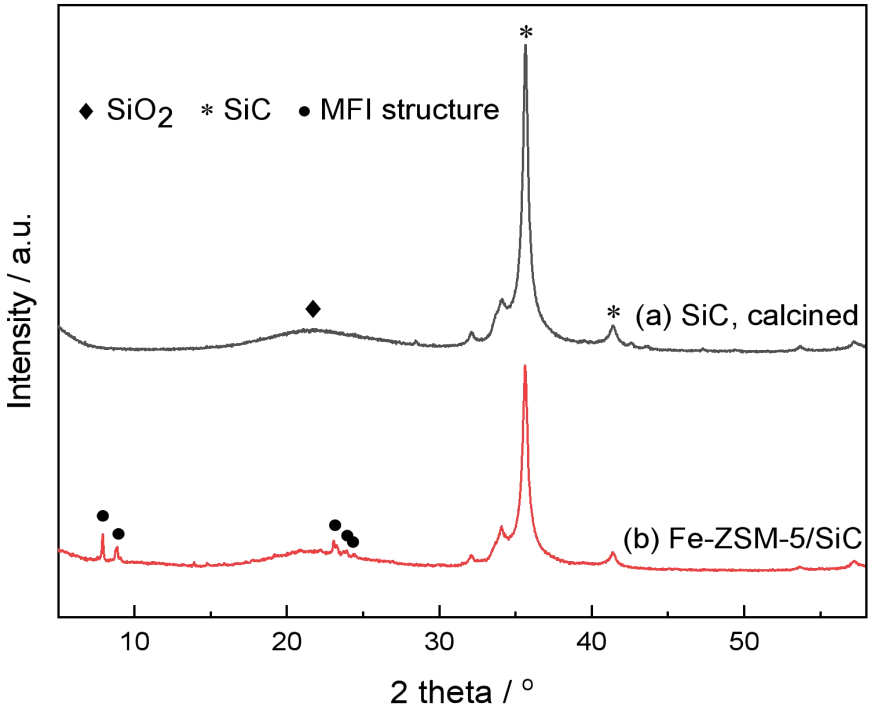

Figure 5.12. XRD patterns of a) calcined SiC and b) Fe-ZSM-5/SiC

The XRD pattern (in figure 5.12) suggested that the Fe-ZSM-5(80) coating grew up on the surface of SiC extrudates after the hydrothermal treatment as the characteristic peaks of MFI zeolite at 2θ of 7-9º and 22-25º were all observed.

5.3.2.2 BET

The N_2 adsorption-desorption isotherms of the SiC and the Fe-ZSM-5/SiC samples, as can be seen in figure 5.13, showed typical type III isotherms which are given by the nonporous or macroporous materials with weak adsorbate-adsorbent interactions [66,67]. As it can be seen in table 5.2 the SiC showed low BET surface area (27 $m^2 \cdot g^{-1}$) and low micropore area (5 $m^2 \cdot g^{-1}$) and low micropore volume (0.002 $cm^3 \cdot g^{-1}$), which is consistent with the information

given by the supplier [68]. Whereas the Fe-ZSM-5/SiC also displayed a low BET surface area (21 $m^2 \cdot g^{-1}$), it had increased micropore area (16 $m^2 \cdot g^{-1}$) and micropore volume (0.007 $cm^3 \cdot g^{-1}$) in comparison with the SiC, which might be due to the growth of the ZSM-5 coating.

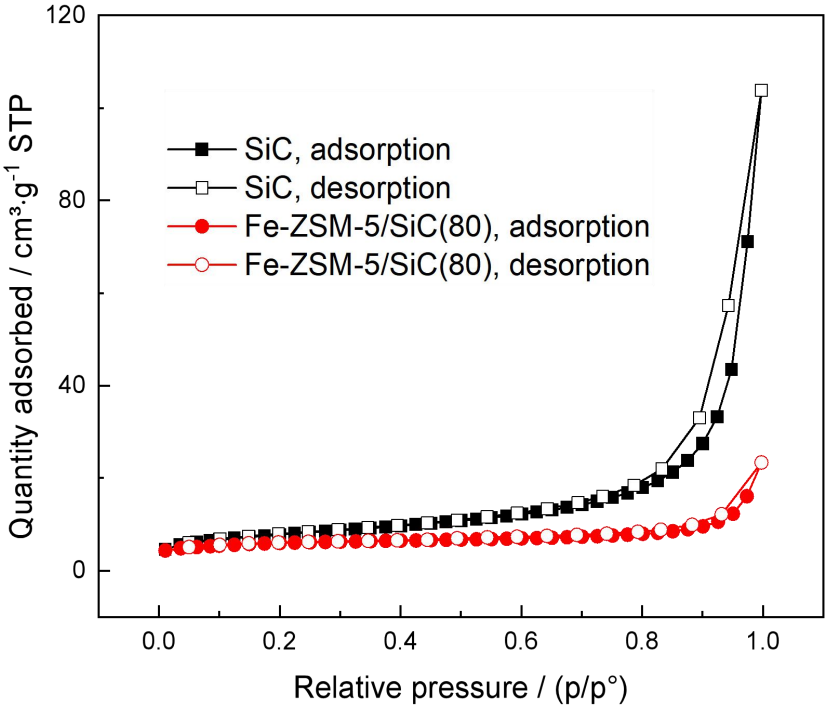

Figure 5.13. Adsorption-desorption isotherms of SiC and Fe-ZSM-5/SiC

5.3.3 Catalytic activity and stability of Fe-ZSM-5/SiC extrudates catalyst

5.3.3.1 Control tests - activity of SiC and ZSM-5/SiC

The catalytic role of SiC in phenol degradation has to be studied to understand the activity of zeolite coating. As shown in figure 5.14, the calcined SiC extrudates were almost inactive in phenol decomposition with the phenol conversion in 4 h on the support of only 7%, almost comparable with that of no catalyst (4%). The ZSM-5 coating supported SiC catalyst (without metal substitution), in comparison with the other two materials, had phenol conversion of 20% after 4 h of reaction due to the effect of the zeolite coating. Furthermore, the Fe leaching of the ZSM-5/SiC catalyst in the CWPO process was less than 0.002 $mg \cdot L^{-1}$ after 4 h of reaction, indicating that the impurity of the SiC extrudates (the SiC extrudates contain trace amount of

Fe and Al thus the Fe leaching from the impurity of the SiC is detected) had no influence on the phenol decomposition.

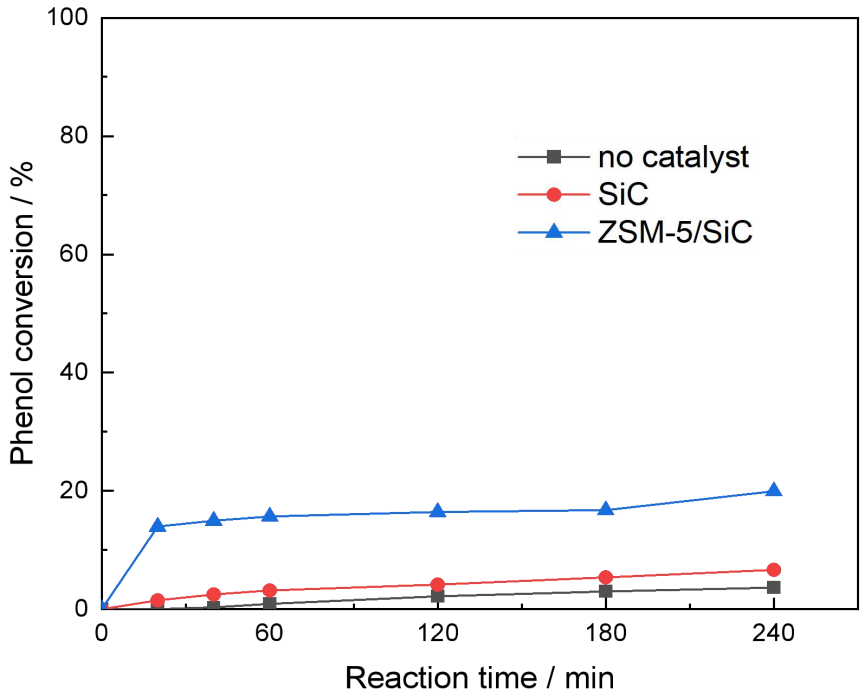

Figure 5.14. Phenol conversion over a) blank test using no catalyst, b) pre-calcined SiC and c) ZSM-5/SiC in the CWPO process (2 g catalyst, 50 mL 1 g·L^{-1} phenol, phenol: H_2O_2 of 1: 14, 80 ^{o}C, 500 rpm)

5.3.3.2 Activity, stability and reusability of Fe-ZSM-5/SiC extrudates catalyst

It is clear that the activity of the FeZSM-5/SiC originates from Fe that is incorporated into the coating, due to the the negligible activity of the SiC support and the iron-free ZSM-5/SiC. As shown in figure 5.15(a), the Fe-ZSM-5/SiC(80) catalyst was active in the CWPO of phenol as the phenol conversion (75%), H_2O_2 consumption (99%) and CO_2 conversion (31%) in the first run of reaction were much higher than that over ZSM-5/SiC, indicating that the introduction of Fe into the catalysts improved the activity efficiently. However, the coated catalyst was far less active than its powder form (Fe-ZSM-5-HTS), not only because of the lower phenol removal efficiency but the lower selectivity to organic acids and CO_2. For example, a

proportion of aromatic intermediates (total aromatic compounds of 1.4×10^{-3} mol·L^{-1}, 14% of initial concentration) remained in the reaction mixture after the reaction (figure 5.15(c)), which is still harmful to the environment. The higher resistance to diffusion, and in turn mass transfer, may explain the lower activity of the coating catalyst. Hence, using the coating form of catalyst in a fixed bed reactor instead of in a batch reaction may be a better option to exploit these materials.

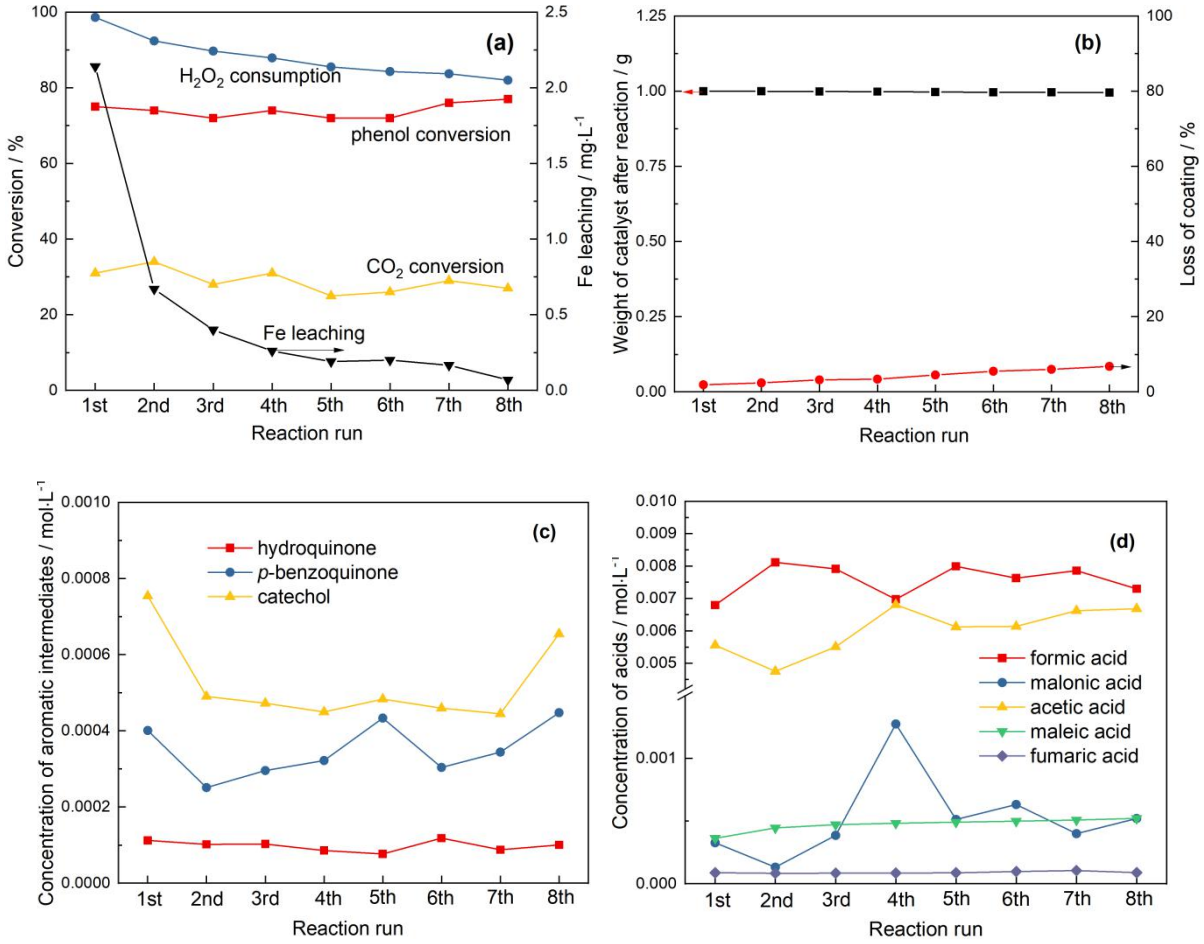

Figure 5.15. a) phenol conversion, H_2O_2 consumption, CO_2 formation and Fe leaching, b) weight loss of coating, c) aromatic intermediates and d) acid intermediates distributionwhen using FeZSM-5/SiC(80) in the CWPO of phenol for 8 runs of reaction (50 mL 1 g·L^{-1} phenol solution, phenol: H_2O_2 = 1: 14, 80 ºC, 4 h, 500 rpm)

The stability of the catalyst was as high as the powder catalyst, as indicated by the low Fe leaching and the steady performance of the catalyst. On the one hand, the Fe leaching (figure

5.15(a)), though reaching 2.0 $mg \cdot L^{-1}$ in the first run, decreased drastically with reaction runs and maintained a very low concentration (below 0.20 $mg \cdot L^{-1}$) from the 4th run of reaction onwards. On the other hand, the Fe-ZSM-5/SiC(80) foam catalyst showed an almost constant performances in the successive 8 runs of reactions with the phenol conversion and CO_2 conversion maintaining at around 75% and 30%, respectively. The concentration of the intermediates also fluctuated just within a narrow range.

One more of the outstanding advantages of the foam materials, the fastness of the coating, also proved the stability of the new form of catalyst. In this project, the fastness of the coating was reflected by the minimal weight loss of the coating layer in the reactions, whereas the weight of the Fe-ZSM-5/SiC extrudates decreased only by 7% of the coating (< 1% of the gross weight, figure 5.15(b)) after 8 runs of reactions under continuous stirring (500 rpm), implying the potential of the new form of catalyst in actual application.

5.3.3.3 Effect of leached Fe on the decomposition of phenol

Likewise, to further confirm that the activity of the catalyst did not originate from leached Fe, the activity of homogeneous Fe^{3+} catalyst ($Fe(NO_3)_3$ as precursor) with concentration equivalent to the Fe leaching of the 8th run of reaction (0.070 $mg \cdot L^{-1}$) was tested and compared with the activity of the Fe-ZSM-5/SiC extrudates in that reaction run, thus the effects of the homogeneous contribution of leached Fe could be mimicked. As shown in figure 5.16(a), after 4 h of reaction, the activity of the heterogeneous catalyst with phenol conversion of 78% was an order of magnitude higher than the homogeneous catalyst with phenol conversion of only 7%, which proved again that the phenol decomposition on Fe-ZSM-5/SiC catalyst was mainly attributed to heterogeneous reaction. Moreover, the huge difference of H_2O_2 consumption (figure 5.16(b)), CO_2 formation (figure 5.16(a)) and intermediates concentrations (figure 5.16(d)) between the activity of coating catalyst and that of homogeneous catalyst implied the same conclusion.

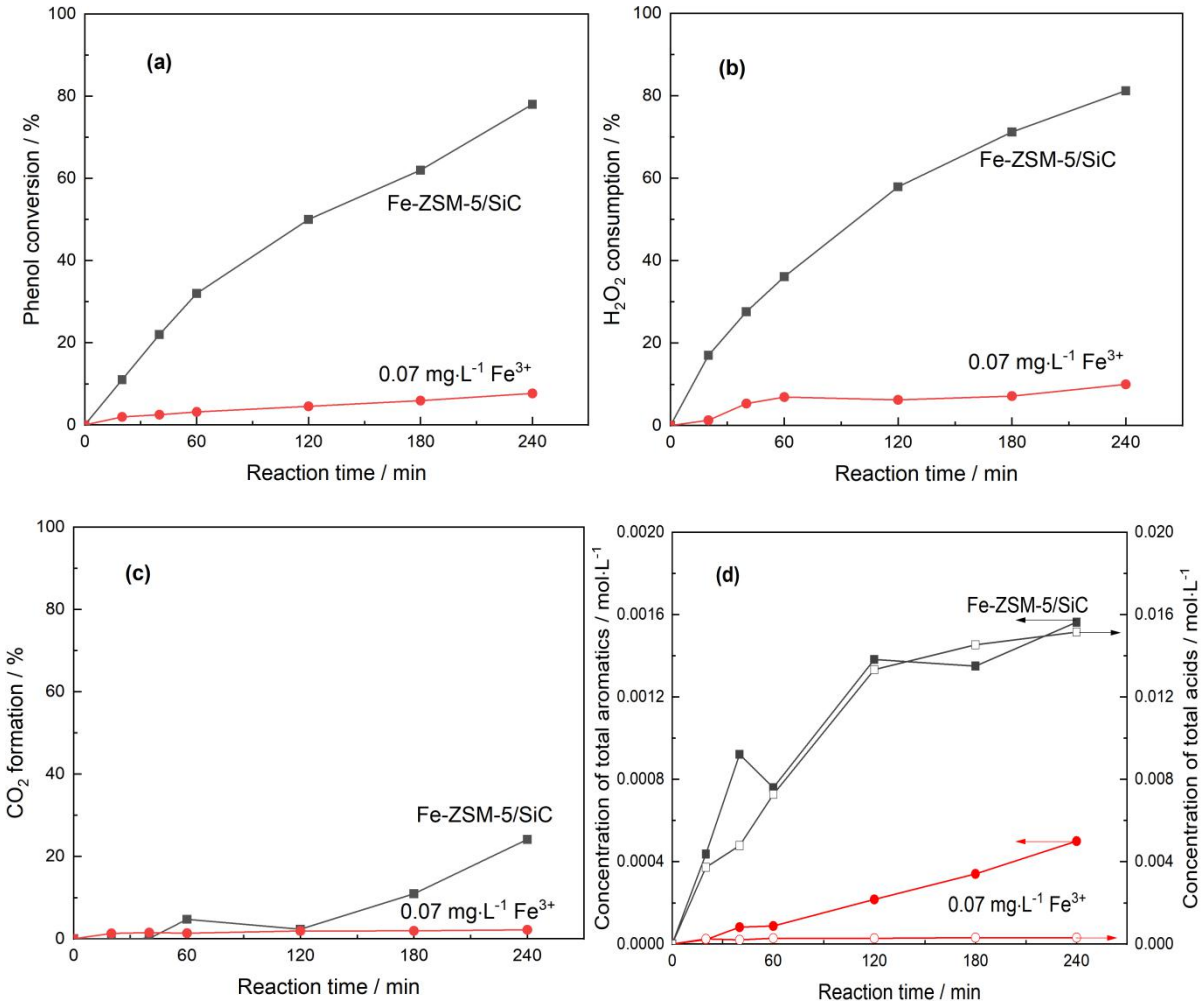

Figure 5.16. The activity of the Fe-ZSM-5-HTS catalyst and the Fe^{3+} with concentration equivalent to the metal leaching of Fe-ZSM-5-HTS (0.070 $mg \cdot L^{-1}$) in the CWPO of phenol in the 8th run of reaction, a) phenol conversion, b) H_2O_2 consumption, 3) CO_2 formation and d) intermediates concentration (50 mL 1 $g \cdot L^{-1}$ phenol solution, phenol: H_2O_2 = 1: 14, 80 °C, 4 h, 500 rpm)

To sum up, the Fe-ZSM-5 coating supported catalyst was synthesized by secondary growth method. The synthesized coating materials presented high and stable performances in the phenol oxidation reaction, as a promising heterogeneous catalyst, and as such capable of providing a robust platform for the synthesis and development of Cu based catalyst based on the same principles.

5.4 Activity and stability of Cu-ZSM-5/SiC extrudates catalyst in the CWPO of phenol

Since the Fe-ZSM-5 catalyst presented desirable performances, and it was confirmed that the metal substituted zeolite catalyst can be a good solution to the catalyst deactivation in the CWPO of phenol, thus a Cu-ZSM-5/SiC catalyst was also prepared and tested.

5.4.1 Synthesis and characterization of Cu-ZSM-5-HTS and Cu-ZSM-5/SiC catalysts

Cu-ZSM-5 catalysts, both powder form and coating form, were prepared in the same way as preparing the Fe counterpart except for varying metal precursors.

5.4.1.1 XRD

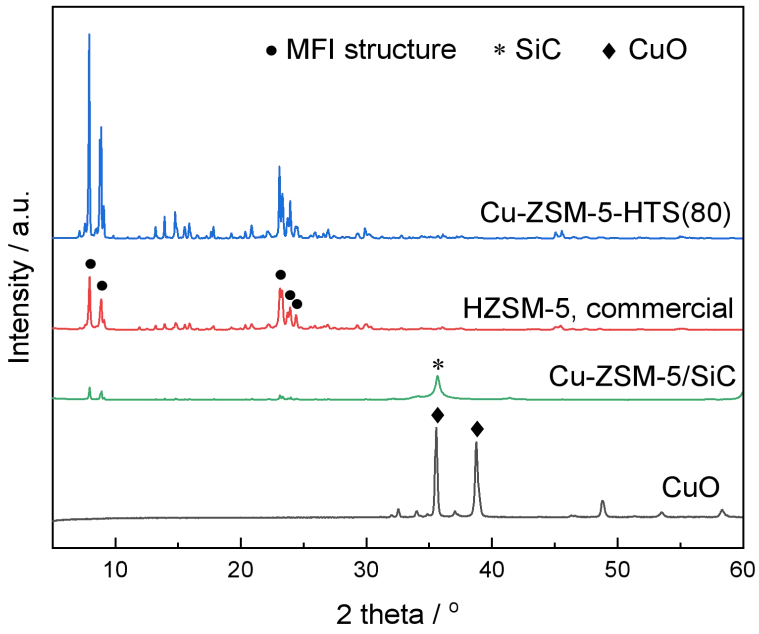

Figure 5.17. XRD patterns of a) commercial CuO, b) Cu-ZSM-5-HTS(80) c) Cu-ZSM-5-HTS(80) and d) Cu-ZSM-5/SiC

Like in the case of Fe-ZSM-5 catalyst, the XRD pattern of Cu-ZSM-5 (figure 5.17) also presented MFI structure as the two characteristic peaks at 2θ of 7-9° and three peaks at 22-25° were all observed. In addition, the main characteristic peaks of Cu oxide at 2θ of 32.6,

35.5, 38.7, 48.8, 53.5 and 58.2º that corresponding to the crystal planes of (1 1 0), (0 0 2), (1 1 1), (-2 0 2), (0 2 0), (2 0 2) [69,70] were not found in the XRD pattern. Furthermore, in comparison with the commercial ZSM-5 (reference), the crystallinity (98.6%, table 5.1) of the synthesized Cu catalyst implied that the ZSM-5 zeolite was also well-crystallized whereas the unit cell parameters indicated that some Cu atoms may be incorporated into the framework as the expansion of unit cell volume (0.3%) was observed. The patterns also indicated that the Cu-ZSM-5 zeolite coating grew successfully on the surface of SiC extrudates.

5.4.2 Catalytic activity of Cu-ZSM-5/SiC catalyst

5.4.2.1 Activity, stability and reusability of Cu-ZSM-5/SiC catalyst

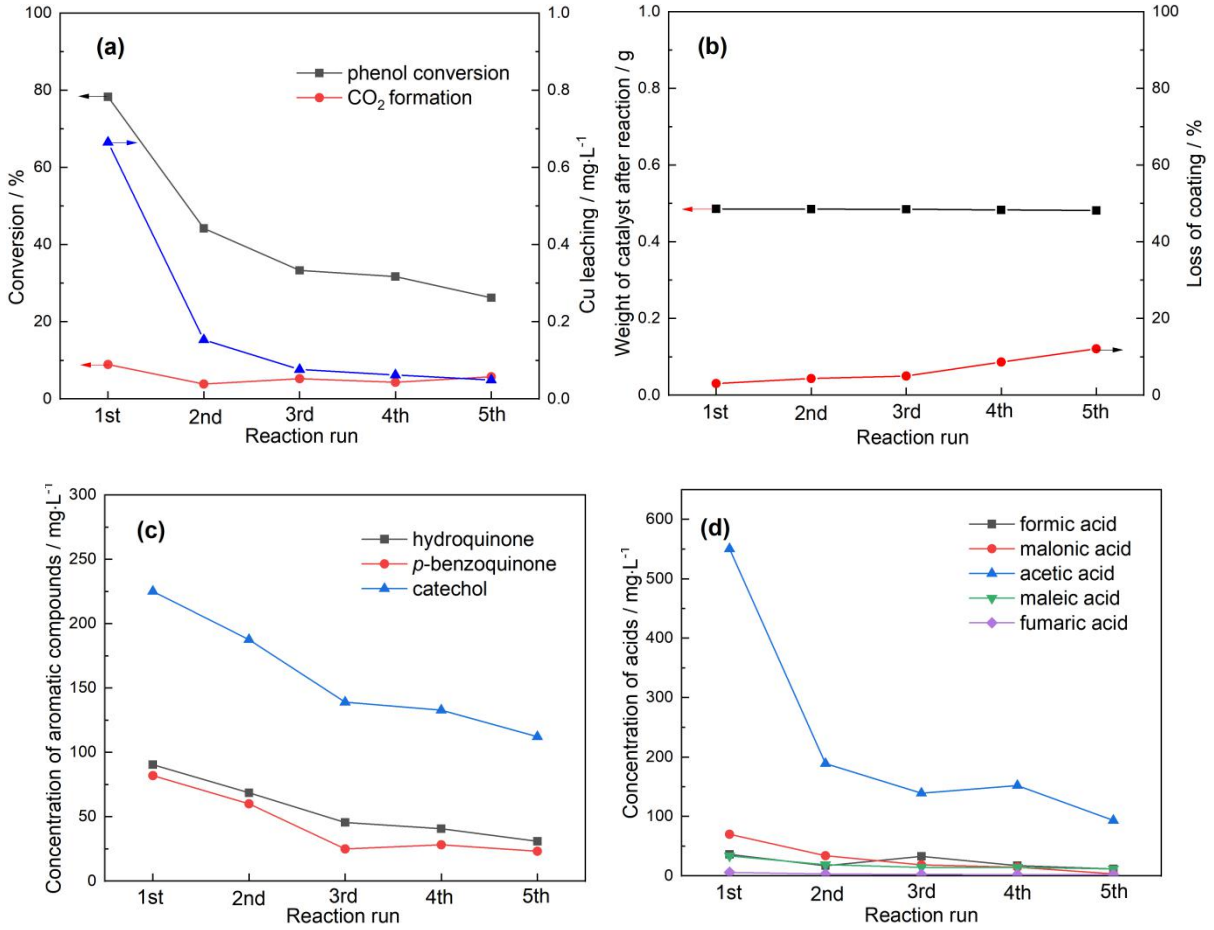

Figure 5.18. a) Phenol conversion, CO_2 formation and Cu leaching, b) weight loss of coating, c) aromatic compounds distribution and d) acid intermediates distribution when using Cu-ZSM-5/SiC(80) in the CWPO of phenol for 5 runs of reaction (50 mL 1 g·L^{-1} phenol, phenol: H_2O_2 = 1: 14, 80 ºC, 4 h, 500 rpm)

The Cu substituted ZSM-5 catalyst presented higher activity in phenol degradation in comparison with ZSM-5/SiC, especially in the first run of reaction when the phenol conversion reached 78%, suggesting the contribution of metal species. However, as it can also be seen in figure 5.18(a), the CO_2 formation in the first run was only 9%, while the concentration of aromatic compounds remained high in the reaction mixture without being completely oxidized to acids and CO_2, which stating that the performance of the Cu catalyst was unsatisfactory when compared with that of Fe catalyst prepared under the same condition.

On the other hand, the stability of the Cu-ZSM-5/SiC catalyst also failed to meet the expectations. As can be seen, only trace metal leaching was detected in the reaction mixture after each run of reaction, with the concentration decreasing from 0.67 $mg \cdot L^{-1}$ in the first run to 0.050 $mg \cdot L^{-1}$ in the 5th run (figure 5.18(a)). However, with the number of reaction runs, the phenol conversion and CO_2 formation also decreased greatly to 26% and 5% respectively, which was at the same level as the ZSM-5/SiC catalyst, indicating that the Cu catalyst almost deactivated. The low stability of the Cu-ZSM-5/SiC might be due to the failure of Cu remaining in the tetrahedra.

Meanwhile, the trend of the phenol conversion in successive 5 runs matched up with that of metal leaching, leading to the hypothesis that the phenol conversion was probably attributed to the homogeneous contribution of leached metal in the solution.

5.4.2.2 Homogeneous reaction contribution

The catalytic role of the leached Cu from Cu-ZSM-5/SiC catalyst, though the metal leaching was low (0.049-0.66 $mg \cdot L^{-1}$), was still necessary to be investigated in this research. To reflect the effects of the leached Cu ions in phenol decomposition intuitively, the phenol conversions over Cu-ZSM-5-HTS(80) in five reaction runs versus metal leaching was plotted and compared with the phenol conversions over homogeneous Cu^{2+} catalyst (Cu nitrate as precursor) with different concentrations, as shown in figure 5.19.

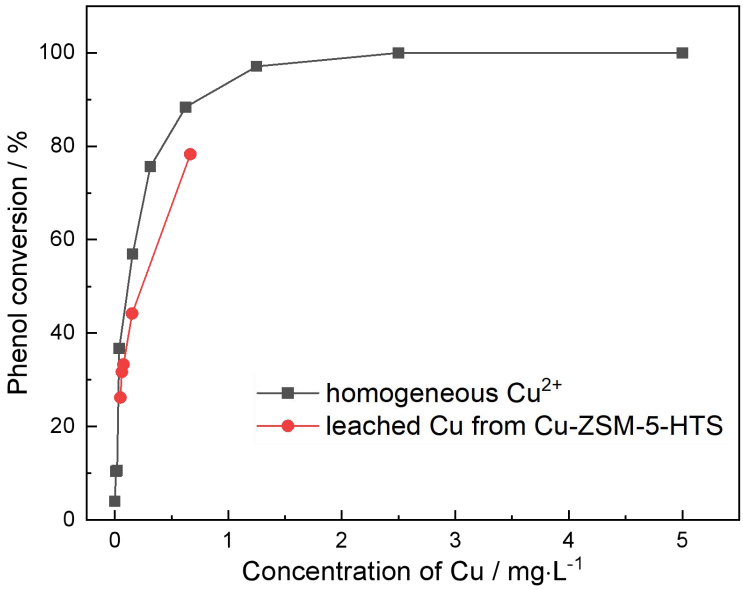

Figure 5.19. Phenol conversion with Cu concentration in reaction mixture with Cu derived from a) homogeneous $Cu(NO_3)_2$ catalysts and b) Cu leaching of Cu-ZSM-5-HTS catalyst (50 mL 1 $g \cdot L^{-1}$ phenol solution, phenol: H_2O_2 = 1: 14, 80 °C, 4 h, 500 rpm)

It can be seen that the phenol conversions on Cu-ZSM-5/SiC catalyst in five runs roughly matched with that on the homogeneous Cu catalysts whose concentration corresponding to Cu leaching, suggesting that the significant homogeneous contribution of the leached metal. Therefore, the Cu-ZSM-5/SiC catalyst, just like other Cu/ZSM-5 catalysts mentioned in chapter 4, presented low stability in the CWPO process, and the leached metal made a great contribution to the phenol oxidation reaction.

Overall, the Cu-ZSM-5-HTS powder catalyst and the Cu-ZSM-5 coating catalyst were both suffessfully synthesized following hydrothermal synthesis and secondary growth method, respectively. However, the Cu-ZSM-5/SiC catalyst, unlike its Fe substituted counterpart, failed to present steady performance in the CWPO process possibly due to the likely failure of Cu substitution. In that case, the preparation of a more sustainable Cu catalyst is still challenging.

5.5 Conclusions

Metal-substituted ZSM-5 zeolite catalysts were prepared by hydrothermal synthesis. The XRD patterns showed that the synthesized metal-free, Fe-substituted and Cu-substituted ZSM-5 all exhibited classical MFI structure and high crystallinity. Evidence of metal substituted into the framework of zeolite is the expansion of the unit cell of Fe-ZSM-5 (0.4%) caused by the distortion of tetrahedra and the loading of substituted Fe (1.5wt%). Metal-substituted zeolite catalyst is proved one of the effective solutions to the catalyst deactivation problem in the CWPO of phenol process caused by severe metal leaching as the Fe-ZSM-5 catalyst displayed both high activity and high stability in the phenol decomposition process. On the one hand, high performances such as complete phenol conversion and H_2O_2 consumption, low selectivity to aromatic intermediates (around 5%) and high CO_2 conversion (60%) were observed when using Fe-ZSM-5 as catalyst. On the other hand, the Fe-ZSM-5-HTS catalyst exhibited negligible (0.2 $mg \cdot L^{-1}$) metal leaching and meanwhile, suffered no loss of activity in the successive runs of reactions. The coating form of zeolite, though exhibiting steady performance in the phenol oxidation reaction, presented slightly lower activity than the powder form of catalyst in the batch reactor because of the high diffusion resistance. However, the Cu-substituted ZSM-5 catalyst that prepared under the same conditions presented activity and stability much lower than the Fe-substituted zeolite with unsatisfactory phenol conversion, H_2O_2 consumption, aromatic compounds selectivity and CO_2 formation, which may be caused by the failure of Cu incorporation into the tetrahedral framework of zeolite.

5.6 References

[1]. K. M. Valkaj, A. Katovic and S. Zrncevic, *Ind Eng Chem Res*, 2011, **50**, 4390-4397.

[2]. T. Granato, A. Katovic, K. M. Valkaj, A. Tagarelli and G. Giordano, *J Porous Mat*, 2009, **16**, 227-232.

[3]. J. A. Zazo, J. A. Casas, A. F. Mohedano and J. J. Rodríguez, *Appl Catal B-Environ*, 2006, **65**, 261-268.

[4]. A. Rey, A. B. Hungria, C. J. Duran-Valle, M. Faraldos, A. Bahamonde, J. A. Casas and J. J. Rodriguez, *Appl Catal B-Environ*, 2016, **181**, 249-259.

[5]. I. Sádaba, M. L. Granados, A. Riisager and E. Taarning, *Green Chem*, 2015, **17**, 4133-4145.

[6]. Y. Yan, S. Jiang and H. Zhang, *Sep Purif Technol*, 2014, **133**, 365-374.

[7]. J. A. Zazo, J. Bedia, C. M. Fierro, G. Pliego, J. A. Casas and J. J. Rodriguez, *Catal Today*, 2012, **187**, 115-121.

[8]. J. Haber, J. H. Block and B. Delmon, *Pure Appl Chem*, 1995, **67**, 1257-1306.

[9]. L. Xiang, S. Royer, H. Zhang, J. M. Tatibouët, J. Barrault and S. Valange, *J Hazard Mater*, 2009, **172**, 1175-1184.

[10]. N. Kosinov, C. Liu, E. J. M. Hensen and E. A. Pidko, *Chem Mater*, 2018, **30**, 3177-3198.

[11]. L. Chen, Y. M. Wang and M. He, *Mater Res Bull*, 2011, **46**, 698-701.

[12]. T. Tatsumi and N. Jappar, *J Phys Chem B*, 1998, **102**, 7126-7131.

[13]. S. Chien, J. Ho and S. Mon, *Zeolites*, 1997, **18**, 182-187.

[14]. M. Anpo, S. Higashimoto, M. Matsuoka, N. Zhanpeisov, Y. Shioya, S. Dzwigaj and M. Che, *Catal Today*, 2003, **78**, 211-217.

[15]. Y. Wang, Y. Ohishi, T. Shishido, Q. Zhang, W. Yang, Q. Guo, H. Wan and K. Takehira, *J Catal*, 2003, **220**, 347-357.

[16]. S. C. Laha, G. Kamalakar and R. Gläser, *Micropor Mesopor Mat*, 2006, **90**, 45-52.

[17]. Y. Meng, H. C. Genuino, C. Kuo, H. Huang, S. Chen, L. Zhang, A. Rossi and S. L. Suib, *J Am Chem Soc*, 2013, **135**, 8594-8605.

[18]. Z. He, J. Wu, B. Gao and H. He, *ACS Appl Mater Inter*, 2015, **7**, 2424-2432.

[19]. Y. Yang, Y. Yan, H. Zhang and X. Wu, *Sep Purif Technol*, 2020, **237**, 116452.

[20]. J. Li, P. Miao, Z. Li, T. He, D. Han, J. Wu, Z. Wang and J. Wu, *Energ Convers Manage*, 2015, **93**, 259-266.

[21]. M. Yabushita, M. Yoshida, F. Muto, M. Horie, Y. Kunitake, T. Nishitoba, S. Maki, K. Kanie, T. Yokoi and A. Muramatsu, *Mol Catal*, 2019, **478**, 110579.

[22]. V. R. Choudhary, A. K. Kinage and A. A. Belhekar, *Zeolites*, 1997, **18**, 274-277.

[23]. N. Crowther and F. Larachi, *Appl Catal B-Environ*, 2003, **46**, 293-305.

[24]. I. O. Ali, A. M. Ali, S. M. Shabaan and K. S. El-Nasser, *J Photoch Photobio A*, 2009, **204**, 25-31.

[25]. Y. S. Ko, H. T. Jang and W. S. Ahn, *Korean J Chem Eng*, 2008, **25**, 1286-1291.

[26]. H. Jiang, B. Guan, H. Lin and Z. Huang, *Fuel*, 2019, **255**, 115587.

[27]. O. P. Taran, S. A. Yashnik, A. B. Ayusheev, A. S. Piskun, R. V. Prihod Ko, Z. R. Ismagilov, V. V. Goncharuk and V. N. Parmon, *Appl Catal B-Environ*, 2013, **140-141**, 506-515.

[28]. J. Li, A. Corma and J. Yu, *Chem Soc Rev*, 2015, **44**, 7112-7127.

[29]. Y. Yan, S. Jiang and H. Zhang, *Rsc Adv*, 2016, **6**, 3850-3859.

[30]. X. Ou, S. Xu, J. M. Warnett, S. M. Holmes, A. Zaheer, A. A. Garforth, M. A. Williams, Y. Jiao and X. Fan, *Chem Eng J*, 2017, **312**, 1-9.

[31]. M. H. Nada and S. C. Larsen, *Micropor Mesopor Mat*, 2017, **239**, 444-452.

[32]. O. A. Bulavchenko, Z. S. Vinokurov, A. A. Saraev, A. M. Tsapina, A. L. Trigub, E. Y. Gerasimov, A. Y. Gladky, A. V. Fedorov, V. A. Yakovlev and V. V. Kaichev, *Inorg Chem*, 2019, **58**, 4842-4850.

[33]. M. Thommes, K. Kaneko, A. V. Neimark, J. P. Olivier, F. Rodriguez-Reinoso, J. Rouquerol and K. S. Sing, *Pure Appl Chem*, 2015, **87**, 1051-1069.

[34]. Y. Cheng, L. Wang, J. Li, Y. Yang and X. Sun, *Mater Lett*, 2005, **59**, 3427-3430.

[35]. I. Othman Ali, A. M. Hassan, S. M. Shaaban and K. S. Soliman, *Sep Purif Technol*, 2011, **83**, 38-44.

[36]. Y. Xia and R. Mokaya, *J Mater Chem*, 2004, **14**, 863-870.

[37]. Y. Chen, C. Li, X. Chen, Y. Liu, C. Tsang and C. Liang, *Ind Eng Chem Res*, 2018, **57**, 13721-13730.

[38]. Y. Yu, Y. Sun, Y. Zhou, A. Xu, Y. Xu, F. Huang and Y. Zhang, *J Colloid Interf Sci*, 2021, **597**, 84-93.

[39]. H. T. Gomes, S. M. Miranda, M. J. Sampaio, A. M. T. Silva and J. L. Faria, *Catal Today*, 2010, **151**, 153-158.

[40]. L. Shirazi, E. Jamshidi and M. R. Ghasemi, *Cryst Res Technol*, 2008, **43**, 1300-1306.

[41]. P. L. Benito, A. G. Gayubo, A. T. Aguayo, M. Olazar and J. Bilbao, *J Chem Tech Biotechnol*, 1996, **66**, 183-191.

[42]. K. Fajerwerg and H. Debellefontaine, *Appl Catal B-Environ*, 1996, **10**, L229-L235.

[43]. S. Jiang, H. Zhang, Y. Yan and X. Zhang, *Rsc Adv*, 2015, **5**, 41269-41277.

[44]. X. Ou, F. Pilitsis, Y. Jiao, Y. Zhang, S. Xu, M. Jennings, Y. Yang, S. R. Taylor, A. Garforth and H. Zhang, *Chem Eng J*, 2019, **362**, 53-62.

[45]. Y. Jiao, S. Xu, C. Jiang, M. Perdjon, X. Fan and J. Zhang, *Appl Catal A-Gen*, 2018, **559**, 1-9.

[46]. K. Okada, K. Kuboyama, T. Takei, Y. Kameshima, A. Yasumori and M. Yoshimura, *Micropor Mesopor Mat*, 2000, **37**, 99-105.

[47]. M. N. Katariya, A. K. Jana and P. A. Parikh, *J Ind Eng Chem*, 2013, **19**, 286-291.

[48]. D. He, H. Zhang and Y. Yan, *Rsc Adv*, 2017, **7**, 47435-47447.

[49]. G. Li, S. Ma, F. Ye, L. Zhou, Y. Wang, X. Lang and S. Fan, *Ind Eng Chem Res*, 2021, **60**, 1799-1807.

[50]. H. Schneider, L. K. Schindel, L. B. Gomes, I. C. Tessaro and N. R. Marcilio, *Curr Res Green Sus Chem*, 2021, **4**, 100049.

[51]. J. Guo and Z. Ji, *Colloids and Surfaces A: Physicochem Eng Aspects*, 2020, **595**, 124727.

[52]. Y. Yan, M. E. Davis and G. R. Gavalas, *Ind Eng Chem Res*, 1995, **34**, 1652-1661.

[53]. H. Chen, H. Zhang and Y. Yan, *Chem Eng J*, 2012, **209**, 372-378.

[54]. G. Li, E. Kikuchi and M. Matsukata, *Micropor Mesopor Mat*, 2003, **62**, 211-220.

[55]. J. Choi, S. Ghosh, Z. Lai and M. Tsapatsis, *Angew Chem Int Edit*, 2006, **45**, 1154-1158.

[56]. X. Ou, F. Pilitsis, N. Xu, S. R. Taylor, J. Warren, A. Garforth, J. Zhang, C. Hardacre, Y. Jiao and X. Fan, *Catal Today*, 2020, **356**, 631-640.

[57]. R. J. Iwanowski, K. Fronc, W. Paszkowicz and M. Heinonen, *J Alloy Compd*, 1999, **286**, 143-147.

[58]. V. V. Pujar and J. D. Cawley, *J Am Ceram Soc*, 1995, **78**, 774-782.

[59]. S. Musić, N. Filipović-Vinceković and L. Sekovanić, *Braz J Chem Eng*, 2011, **28**, 89-94.

[60]. Y. Liu, S. Podila, D. L. Nguyen, D. Edouard, P. Nguyen, C. Pham, M. J. Ledoux and C. Pham-Huu, *Appl Catal A-Gen*, 2011, **409-410**, 113-121.

[61]. S. Ivanova, B. Louis, B. Madani, J. P. Tessonnier, M. J. Ledoux and C. Pham-Huu, *J Phys Chem C*, 2007, **111**, 4368-4374.

[62]. A. Javdani, J. Ahmadpour and F. Yaripour, *Micropor Mesopor Mat*, 2019, **284**, 443-458.

[63]. G. Majano, A. Darwiche, S. Mintova and V. Valtchev, *Ind Eng Chem Res*, 2009, **48**, 7084-7091.

[64]. X. Wang, H. Chen, F. Meng, F. Gao, C. Sun, L. Sun, S. Wang, L. Wang and Y. Wang, *Micropor Mesopor Mat*, 2017, **243**, 271-280.

[65]. S. Choi, D. S. Park, S. J. Kim, D. H. Choo, Y. K. Park, C. W. Lee, H. Y. Kim, W. C. Choi, N. Y. Kang and B. S. Song, Google Patents, 2014.

[66]. M. D. Donohue and G. L. Aranovich, *Adv Colloid Interfac*, 1998, **76**, 137-152.

[67]. M. D. Donohue and G. L. Aranovich, *Fluid Phase Equilibr*, 1999, **158-160**, 557-563.

[68]. beta SiC catalyst supports SDS, https://f7de78fd-3a1d-48c1-a143-b2a07048f31b.filesusr.com/ugd/8aa046_f81cba0fafb94938b6a49dc4ed1bcfdf.pdf.

[69]. S. C. Ray, *Sol Energ Mat Sol C*, 2001, **68**, 307-312.

[70]. H. Wu, X. Wei, M. Shao, J. Gu and M. Qu, *Chem Phys Lett*, 2002, **364**, 152-156.

Chapter 6. Synthesis of Cu-MCM-48 catalysts with heteroatoms incorporated into the silica framework

6.1 Overview

The insertion of an active metal into the framework of a zeolite, was proved one of the efficient solutions to the metal leaching of catalyst in the heterogeneous Fenton or Fenton-like reaction (see section 5.2 and 5.3 in chapter 5). However, the difficulty of Cu substitution into the framework of MFI zeolite prompted a search for other potential materials which are more prone for metal substitution into silica framework. In recent years, mesoporous silica materials with an adjustable pore size (1.5–30 nm), tailorable interior surfaces, and large unit cell, are potential hosts to incorporate metal species [1-3].

The synthesis of a new family of mesoporous molecular sieves with regular and constant pore diameters from 2 to 10 nm, designated as M41S, was reported in 1992 by researchers at Mobil Oil Corporation [4,5]. Among the members of the M41S family, MCM-41 and MCM-48 have received particular attention due to their large pore volume, high specific surface area, ordered pore structure array and narrow pore size distribution [6-9], and are widely used as catalysts support and adsorbent materials. Compared to two-dimensional MCM-41 with hexagonal symmetry, MCM-48 mesoporous silica with three-dimensional cubic space group is preferred in catalytic reactions (such as photocatalytic reduction of CO_2 [10], ethylbenzene oxidation [11]) from a diffusional and catalytic point of view. The MCM-48 molecular sieve consists of two interpenetrating continuous networks of chiral channels, these enantiomeric pairs of porous channels are known to be separated by an inorganic wall that follows exactly the gyroid infinite periodic minimal surface [12,13]. The three-dimensional channel network provides a highly opened porous host with easy and direct access for guest species, thus facilitating more efficient mass transfer and diffusion throughout the pore channels [8,9,14]. On the other hand, the open pore structure increases the number of interactions between reagents and catalytic sites, resulting in higher activity.

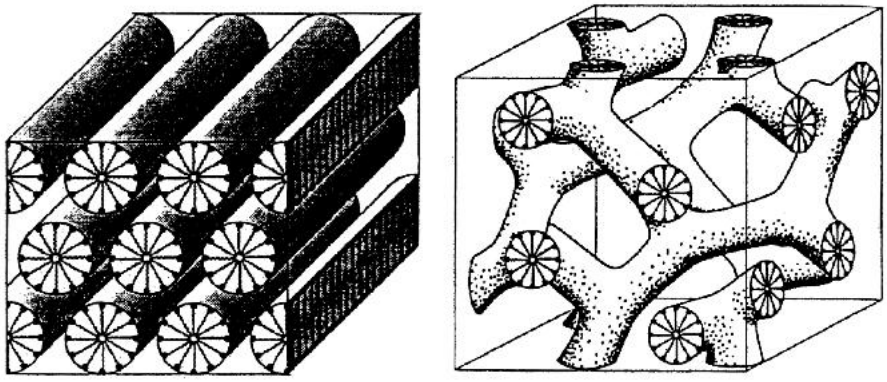

Figure 6.1. Structure of MCM-41 (left) and MCM-48 (right), figures reused with permission from literature [7], American Chemical Society.

However, less attention has been paid to the synthesis of MCM-48, compared with plentiful studies on MCM-41, probably due to the difficulty of the synthesis as it is an intermediate stage formed during the transformation of hexagonal phases into the lamellar phase [15-21]. Usually, mesoporous MCM-48 is prepared by hydrothermal synthesis under very demanding conditions such as strong alkali synthesis media [9,15], high concentration of surfactants [9,22], the addition of a co-solvent [13,23], and delicated, specific, hydrothermal conditions [18,23]. Just minor variations of the synthesis factors may lead to the absence of the cubic mesoporous structure. Even more challenging, is the preparation of cubic MCM-48 catalyst with the isomorphous substitution of heteroatoms into silicate framework during the hydrothermal synthesis process. This is because the desired mesostructure and morphology of the material may be further destroyed by the introduction of metal ions [24-26]. To the best of our knowledge, there aren't reports on the synthesis of Cu substituted MCM-48 with aim of systematically increasing the percentage of heteroatoms into the framework, and this chapter will be focused on this particular area of research.

In this chapter, the investigations are mainly focused on 1) preparation of Cu substituted MCM-48 by hydrothermal synthesis, 2) characterization of the synthesized materials and 3)

optimization of the synthesis conditions of Cu-MCM-48, with the aim of high ordering degree, high metal incorporation and high yield.

6.2 Synthesis of Cu-MCM-48

Byrappa and Yoshimura [27] described the hydrothermal synthesis as any heterogeneous chemical reaction in the presence of a solvent (whether aqueous or non-aqueous) above room temperature and at pressure greater than 1 atm in a closed system. The preparation of amorphous silica by hydrothermal synthesis is very complex because the system is affected by a large number of parameters, such as the composition of the gel, pH, water content, hydrothermal synthesis temperature, synthesis and aging time, stirring, concentration gradients. To unravel the effects of these parameters on the synthesis of mesoporous MCM-48 is crucial to increase the yields of these synthesis and for the understanding of the mechanisms.

In this project, Cu-MCM-48 mesoporous silicas were prepared by using a hydrothermal synthesis method with sodium silicate (water glass, Na_2SiO_3) as Si source, Cu nitrate ($Cu(NO_3)_2$) as Cu precursor, CTAB ($C_{19}H_{42}NBr$) as organic template, water and ethanol (C_2H_6O) as co-solvents and sulfuric acid (H_2SO_4) for pH adjustment. The synthesis process consists of five steps (see figure 6.2), the solid materials obtained after each synthesis steps were collected and tested via XRD to investigate the effects of each preparation steps and to study the mechanism of MCM-48 formation.

The sample taken after each step was filtered, washed with deionized water and dried overnight to obtain solid material. The obtained solids were analysed and gave the XRD patterns as shown in figure 6.2.

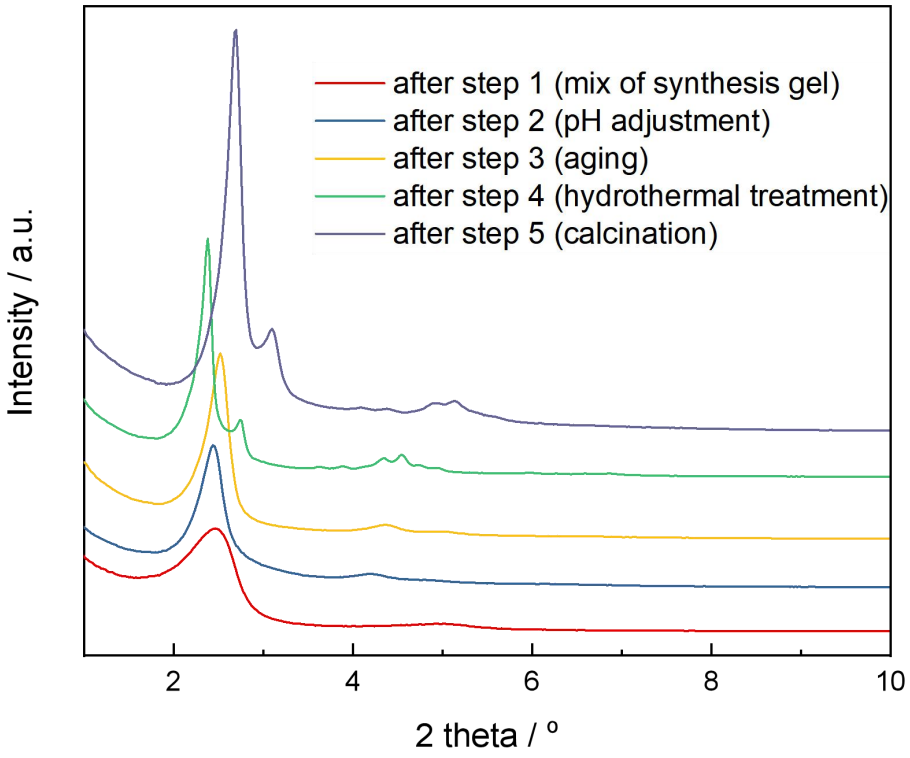

Figure 6.2. XRD patterns of synthesized Cu-MCM-48 samples collected from different steps (synthesis condition: Si: Cu: CTAB: ethanol: H_2O: H_2SO_4=1: 0.0073: 0.2: 4.3: 83: 0.1, aging time 3 h, hydrothermal synthesis temperature 110 °C, synthesis time 36 h, calcination at 550 °C 6 h)

As shown, a broad peak with low intensity at 2θ of 2-3° was observed in the pattern of sample collected in step 1, which is assigned to the MCM-41 analogue (or an intermediate state of mesoporous material), as reported in the literature [28,29]. It also indicates that simply mixing all the reactants at room temperature would not form defined, mesoporous material, though an initial precipitate was obtained. After blending all the reactants, the pH of the mixture gel was adjusted by diluted H_2SO_4 solution (2 M) under continuous stirring, while the synthesis gel was sampled immediately after the pH was adjusted to the desired value. The solid material obtained at this step presented a sharper and narrower peak at 2-3°, suggesting the formation of a more ordered MCM-41 analogue. If aging the synthesis gel for 3 h via constant stirring (stirring rate of 500 rpm) at room temperature, instead of sampling it immediately, the

material with some preliminary features of MCM-41 became the main product, as shown by the yellow line in figure 6.2. The phenomenon shows that the formation of MCM-41 could be achieved at room temperature, suggesting an apparent simplicity of synthesis of hexagonal structure.

After hydrothermal treatment at 110 ^{o}C for 36 h at step 4, the phase of the obtained solid transformed from hexagonal MCM-41 to cubic MCM-48, as the material exhibited the typical Bragg reflections of cubic structure with six characteristic peaks at 2θ of 2-5^{o} (figure 6.2), especially the high (211) and its adjacent smaller (220) reflection in the range of 2-3^{o}. Upon calcination at 550 ^{o}C for 6 h, the sample showed a broader and yet more intense diffraction peaks compared to the as-synthesized sample, indicating the high thermal stability of the material and the great improvement of the pore orderings through surfactant removal. On the other hand, the XRD patterns of the calcined samples shifted to a higher angle. Meanwhile, the d-spacing (d_{211}, introduced in section 6.3.1) of the samples decreased from 3.71 nm to 3.27 nm and the corresponding cubic unit cell parameter (a_0, introduced in section 6.3.1) contracted from 9.09 nm to 8.01 nm after calcination (in table 6.1), implying the occurrence of the lattice contraction due to the condensation of silanol groups on the wall after the removal of the surfactant.

6.3 Characterization of the Cu-MCM-48

6.3.1 XRD

MCM-48 was synthesized at the same conditions as the Cu-MCM-48 except for the addition of metal precursor ($Cu(NO_3)_2$). The synthesized MCM-48 presented typical mesoporous MCM-48 structure, as a strong (211) peak centred at about 2θ of 2.7^{o} and a minor peak at 2θ of 3.1^{o}, corresponding to (220) plane, were all clearly observed in figure 6.3. The presence of all the above characteristic peaks of MCM-48 confirming the formation of the cubic mesoporous framework with uniform order, while the absence of other interferences proves that MCM-48 formed with high phase purity.

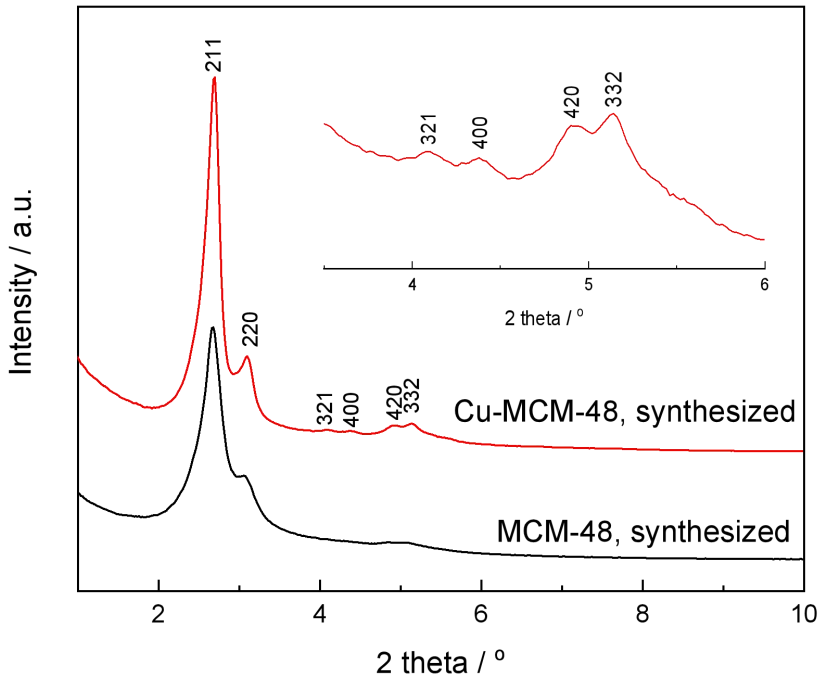

Figure 6.3. XRD patterns of synthesized MCM-48 and Cu-MCM-48 (synthesis condition: Si: Cu: CTAB: ethanol: H_2O: H_2SO_4=1: 0 (or 0.0073): 0.2: 4.3: 83: 0.1, aging time 3 h, hydrothermal synthesis temperature 110 °C, synthesis time 36 h)

After metal incorporation, the Cu-MCM-48 retained all the obvious diffraction peaks, which illustrated that the introduction of metal precursor did not destroy the highly ordered cubic mesoporous structure. However, except for the appearance of the (211) and (220) characteristic peaks, the differences in the shape and position of XRD peaks and their relative intensities that correspond with changes in the synthesis conditions also indicate a variation of structural properties and sample quality. As shown, the intensities of the peaks were even higher, which is probably due to the positive effects of the ions (salt effect) on the wall thickness of the structure [2,30,31]. Additionally, other characteristic peaks assigned to (321), (400), (420) and (332) planes were also observed [15,32,33], which also suggested the higher regularity of the material compared with the undoped counterpart.

In addition to the ordered structure and the regularity of the silicate framework, the metal incorporation is also a significant factor in this study as it decides the activity and stability of the synthesized material in the CWPO of phenol. In principle, the d-spacing of (211) plane and the corresponding unit cell parameter, a_0 (the centre-to-centre pore distance) of MCM-48 samples are used as evidence of metal incorporation, while the two indexes are obtained from the XRD of samples. The d-spacing was calculated using the Bragg's law, as exhibited in equation 6.1 [34-36]:

$$\mathrm{d\_}spacing = \frac{\lambda}{2\sin\theta} \qquad \text{(Eq. 6.1)}$$

Where θ is the diffraction angle of peak and λ is wavelength (λ = 0.154 nm).

The unit cell parameter was calculated with equation 6.2 and 6.3 [7,8,16,37,38]

$$a_0 = d(\mathrm{hkl})\sqrt{(h^2 + k^2 + l^2)} \qquad \text{(Eq. 6.2)}$$

For d(2 1 1) plane, the a_0 was calculated as follows,

$$a_0 = d(211)\sqrt{(2^2 + 1^2 + 1^2)} = d(211)\sqrt{6} \qquad \text{(Eq. 6.3)}$$

Table 6.1. Properties of the synthesized MCM-48 catalysts

catalyst	2θ of (211) plane [a]	d(211) [b]	a_0 (nm) [c]
MCM-48, calcined	2.68°	3.29	8.06
Cu-MCM-48, calcined	2.70°	3.27	8.01
Cu-MCM-48 as-synthesized	2.38°	3.71	9.09

a - data from XRD; b - calculated by Eq. 6.1 ;c - calculated by Eq. 6.3.

Both the d-spacing and a_0 were represented by the peak shift of the sample (with blank MCM-48 as reference) in the XRD pattern. In general, a peak shift to a lower 2θ correlates to an increase of the interplanar distance, as a consequence of an increase in the number of heteroatoms into the silicate framework, leading to the increase of d-spacing and unit cell parameter (a_0). This can be explained in terms of the longer M–O bond distance than the

Si–O bond which caused by the replacement of Si atom (ionic radius = 40 pm [39]) by a larger Cu atom (ionic radius = 71 pm [40]). In other words, the substitution of large-radius transition metal ions (larger than Si) into the silicate matrix causes an enlargement of the cubic unit cell, which can be considered as evidence for the incorporation of copper into the matrix [41-47].

As shown in table 6.1, no obvious peak shift toward smaller 2θ value was noticed after the introduction of metal precursor, and the d-spacing of (211) plane and the corresponding unit cell parameter a_0 also maintained constant. Thus it was indicated that though structure of MCM-48 was formed, few Cu species were substituted into the silica framework. It is also worth noting that except for metal incorporation, calcination process can also lead to the change of unit cell, as reported in [48]. Hence, the calcination process must be kept the same when the unit cells of samples were compared, as what we did in this project.

6.3.2 Porosimetry and BET surface area

Low-temperature nitrogen adsorption isotherms are used for assessing the quality of the synthesized mesoporous material. N_2 adsorption-desorption isotherms of as synthesized MCM-48 and Cu-MCM-48 at 77 K (figure 6.4a) were typical type IV isotherms as defined by International Union of Pure and Applied Chemistry (IUPAC) classification, which were diagnostic of highly ordered mesoporous materials, and consistent with the kind of materials that we have synthesized. Furthermore, a sharp increase in the volume of N_2 adsorbed at a relative pressure of p/p^0 of 0.2-0.3, which is corresponding to capillary condensation within uniform mesopores [15], was observed. The steepness of the capillary condensation step reflected the uniformity of pore channels and their narrow size distribution, which is in agreement with data observed in the XRD pattern (figure 6.3). Besides, the isotherms obtained on the two samples were reversible and no defined hysteresis loop in the adsorption and desorption cycles upon pore condensation were observed, which can be attributed to the small size of the particles [15]. Furthermore, the adsorbed amount of N_2 decreased after metal substitution, causing a reduction in surface area and pore volume, as listed in table 6.2.

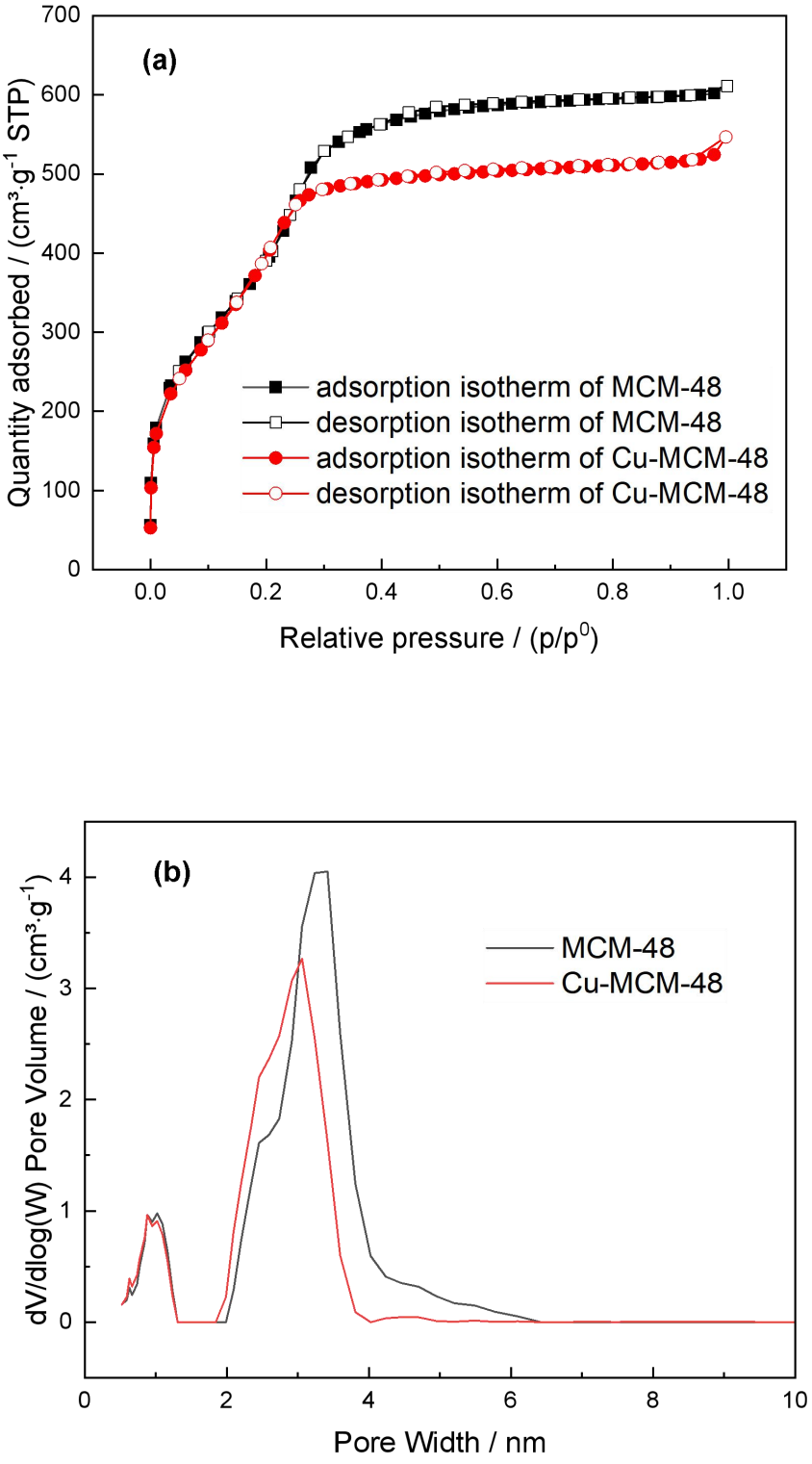

Figure 6.4. a) N_2 adsorption-desorption isotherms and b) pore distribution of the synthesized mesoporous Cu-MCM-48 (synthesis condition: Si: Cu: CTAB: ethanol: H_2O: H_2SO_4=1: 0.0073: 0.2: 4.3: 83: 0.1, aging time 3 h, hydrothermal synthesis temperature110 ^oC, synthesis time 36 h)

The BJH plot of the derivative of the pore volume per unit weight with respect to the pore diameter versus the pore width was shown in Figure 6.4b. The narrow and sharp pore size distribution curves indicated a uniform mesoporosity of the synthesized materials. As shown in table 6.2, the average pore diameters of MCM-48 and Cu-MCM-48 of 2.59 nm and 2.66 nm were observed, indicating that the synthesized samples are mesoporous (2 nm-50 nm) materials.

Table 6.2. Porosimetry data of synthesized materials

Sample name	S_{BET}[a] ($m^2 \cdot g^{-1}$)	V_p[b] ($cm^3 \cdot g^{-1}$)	D_p[a] (nm)	W_t (nm)
CM-1* (MCM-48)	1435	1.06	2.59	1.31
CM-23* (Cu-MCM-48)	1219	0.67	2.66	1.26
CM-16* (Cu-MCM-41)	1019	1.07	3.73	---
CM-12* (Cu-MCM-48)	1338	1.05	2.55	1.30

a - determined using BET method.

b - determined using BJH method.

* - catalyst number see table 6.5.

Additionally, the low-temperature nitrogen adsorption isotherms also enable the calculation of the specific surface area, pore volume, and mesopore size distribution and accordingly, wall thickness, as displayed in table 6.2. Usually, the reduction in the pore diameter, pore surface, and pore volume corresponds to the blockage of mesopores by metal oxides whereas no significant differences between the two samples were observed in table 6.2, for example, the BET specific surface area of the pure silica MCM-48 and the Cu incorporated MCM-48 kept at 1435 $m^2 \cdot g^{-1}$ and 1219 $m^2 \cdot g^{-1}$, respectively. This shows that the introduction of metal species into the silica matrix did not alter or harm the pore characteristics of the MCM-48 materials apparently. Besides, the wall thickness (W_t) of the samples that calculated using the XRD and porosimetry data were also summarized in table 6.2, the formula for the pore wall thickness calculation was based on equation 6.4 [7,16,37,42,49]

$$W_t = \frac{a_0}{3.092} - \frac{D_p}{2} \qquad \text{(Eq. 6.4)}$$

Where 3.092 is a constant representing the minimal surface area for the MCM-48 space group and D_p is on behalf of pore diameter of the sample.

The wall thickness of the MCM-48 and the Cu-MCM-48 sample were 1.31 and 1.26 nm respectively, which are close to those reported in the literature (1.0-1.4 nm [50], 1.2-1.9 nm [51]).

6.3.3 TEM

TEM investigation can provide the direct observation of the morphology and distribution of metal oxide particles in the MCM-48. TEM micrographs of a Cu-MCM-48 sample prepared by hydrothermal synthesis were shown in Figure 6.5. It is possible to observe Cu-MCM-48 particles with well-defined edges and a spherical shape (Fig 6.5a), and a well-ordered structure was clearly defined (figure 6.5b), indicating the high quality of the synthesized material. The actual shape and structure of the channels which are typical for MCM-48, were also detected (figure 6.5c) which well matched with the MCM-48 micrographs reported in the literature [7,15,52]. It is also relevant to point out that the image in figure 6.5c showed a well-defined hexagonal arrangement, along the plane direction a very regular pattern without irregularities is observed, while the regularity of the material (figure 6.5d) indicated the formation and presence of a uniform channel system. Besides, no distortion was exhibited over the sample, suggesting that the isomorphous substitution of Cu atoms into the silica has little influence on the morphology and the integrity of the pore structure of the MCM-48 framework, which is in good agreement with the results of XRD and N_2 adsorption-desorption. Even more, no extra phases of CuO particles were detected from this TEM analysis, indicating the high dispersion of copper in the MCM-48 matrix.

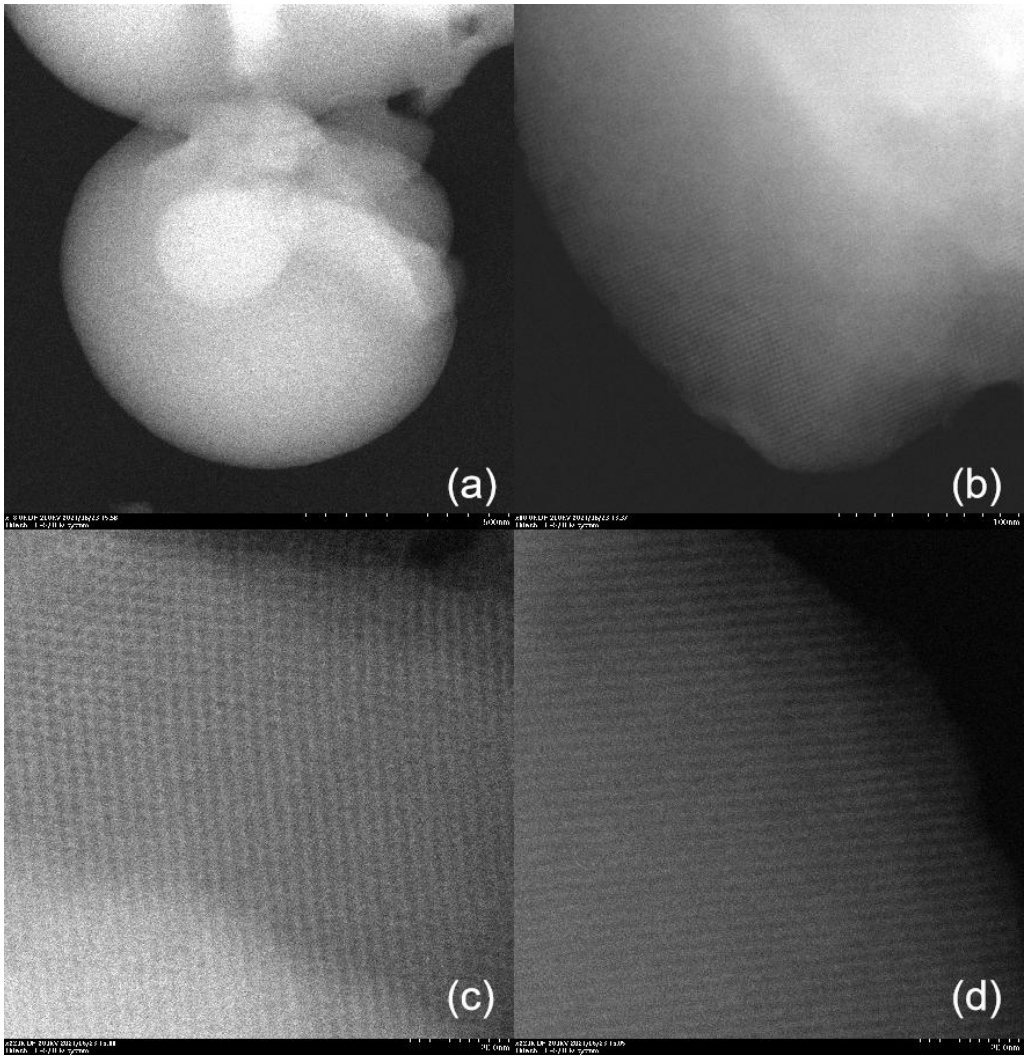

Figure 6.5. TEM micrographs of Cu-MCM-48 (magnification from (a) to (d): ×18k, ×80k, ×220k, ×220k) (synthesis condition: Si: Cu: CTAB: ethanol: H_2O: H_2SO_4 = 1: 0.0073: 0.2: 4.3: 83: 0.1, aging time 3 h, hydrothermal synthesis temperature 110 ^oC, synthesis time 36 h)

6.3.4 ATR-FTIR

Infrared spectra of the as-synthesized and calcined Cu-MCM-48 in the region of 500 - 4000 cm^{-1} were collected (Figure 6.6). As it can be seen, the as-synthesized sample exhibited intense absorption bands at around 2926 and 2854 cm^{-1} which are corresponding to asymmetric and symmetric stretching of the surfactant molecules (CTAB, $C_{19}H_{42}BrN$), while the band at 1470 cm^{-1} is due to the C-H bending vibrations of the surfactant [53]. These characteristic bands disappeared in the spectrum of the calcined sample, thus proving the complete removal of organic template after calcination at 550 ^oC for 6 h.

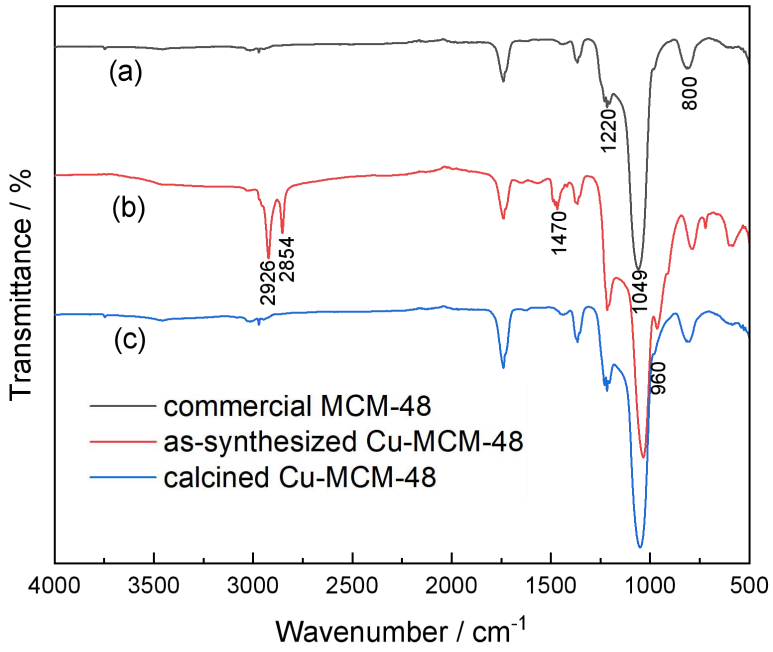

Figure 6.6. FT-IR spectrum of a) commercial MCM-48, b) a-synthesized Cu-MCM-48, and c) calcined Cu-MCM-48 (synthesis condition: Si: Cu: CTAB: ethanol: H_2O: H_2SO_4=1: 0 (or 0.0073): 0.2: 4.3: 83: 0.1, aging time 3 h, hydrothermal synthesis temperature 110 °C, synthesis time 36 h)

On the other hand, the absorption bands at approximately 1050 and 1220 cm^{-1} in the commercial MCM-48 sample that are associated to internal and external asymmetric Si–O–Si stretching modes and the bands at 800 cm^{-1} that is assigned to symmetric Si–O–Si stretching. All these bands appeared in the spectrum of the calcined Cu-MCM-48 sample. In addition, a band centred at around 960 cm^{-1} was also observed in the spectrum of uncalcined Cu-MCM-48, which was taken by some authors as a proof for the incorporation of metal atoms in the framework of mesoporous molecular sieve because the band is usually absent in pure silicates [54-56]. However, in the case of calcined Cu-MCM-48, just like that of MCM-48, the assignment of this band was not ambiguous, indicating that the metal incorporation maybe very low which probably affected by the calcination. Furthermore, compared to the MCM-48 sample, a slightly blue shift to higher wavenumber emerged in the bands of the calcined Cu-MCM-48 sample, which could also be ascribed to a slight increase

of Si–O distance caused by the substitution of Si atoms (ionic radius = 40 pm [39]) by Cu atoms (ionic radius = 71 pm [40]) [43,57].

6.3.5 Active metal content - ICP-OES

Table 6.3. Properties of the synthesized Cu-MCM-48 catalysts.

Catalyst	Supported metal loading	Substituted metal loading	Total metal loading
CM-23* (Cu-MCM-48)	1.0%	0.0090%	1.0%
CM-2* (Si/Cu=0.0073)	1.1%	0.077%	1.2%
CM-3* (Si/Cu=0.146)	1.7%	0.36%	2.1%
CM-4* (Si/Cu=0.292)	4.3%	0.22%	4.5%
CM-12* (H_2O/Si=249)	0.97%	0.014%	0.98%
CM-15* (H_2SO_4/Si=0.15)	0.84%	0.054%	0.89%
CM-16* (H_2SO_4/Si=0.3)	0.58%	0.012%	0.59%
CM-25* (time 168 h)	1.6%	0.33%	1.9%

* catalyst numbers see table 6.6.

As suggested by the XRD and IR results of the Cu-MCM-48, a few heteroatoms substitutions occurred in the hydrothermal synthesis process. In support of it, the total metal loading, supported metal loading and substituted metal loading of the Cu-MCM-48 catalyst were all tested by ICP-OES. The supported metal loading was measured by soaking the synthesized Cu catalyst into *aqua regia* (1 mL per 0.1 g of sample) under continuous stirring for 24 h to dissolve all the Cu species on the support. The *aqua regia*-treated Cu-MCM-48 catalyst was collected after washing and drying, then further immersed in the solution of HF acid to destroy the framework of mesoporous phase and release the ‘trapped’ Cu species in the framework. The Cu that was digested from the sample by the HF acid was tested by ICP-OES and regarded as the amount of Cu that substituted into the framework. The sum of the supported metal loading and the substituted metal loading is the total metal loading (table 6.3).

The nominal total metal loading (1.0 wt%) of the Cu-MCM-48 (CM-23) was higher than that of expected (0.78 wt%, calculated from the Si/Cu ratio of 137 in the synthesis gel), as displayed in table 6.3. However, with the hydrothermal synthesis method, most of the metal species were on the surface rather than incorporated into the framework, as the supported metal loading (1.0 wt%) was far higher than the substituted metal loading (0.012 wt%). The ICP-OES data corroborated the results obtained from XRD and FTIR.

6.3.6 Silica Yield

The yield of synthesized material is another important factor characterizing the efficiency of a synthesis method, especially for expensive MCM-48 mesoporous materials. In particular, the yield of a typical synthesis of MCM-48 is usually low (< 50%) as reported in literature [58,59], which caused increased cost and severe waste of resources.

The yield of MCM-48 is usually defined as the ratio of the output and the input of silica in each batch of synthesis, as shown in Equation 6.5,

$$Yield = \frac{\text{output}_{SiO_2}}{\text{input}_{SiO_2}} \times 100\% = \frac{m_{\text{sample},f}}{m_{SiO_2,i}} \times 100\% \qquad \text{(Eq. 6.5)}$$

Where $m_{sample,f}$ (g) is the amount of sample finally obtained after calcination, $m_{SiO2,i}$ (g) is the amount of SiO_2 initially added into the synthesis gel. Whereas in the synthesis process, the $m_{SiO2,i}$, originating from sodium silicate, is 0.6 g.

The product yield in the synthesis batch of Cu-MCM-48, as listed in table 6.4, was less than 50% on the basis of the silica recovery. Except for a slight loss of material during the transfer of synthesis gel, about half of the Si precursor was lost as dissolved silica in the supernatant liquid under the hydrothermal reaction condition. The value is quite close to the yield of a typical synthesis of MCM-48 (40-50%). Meanwhile, the yield of the Cu-MCM-48 was similar with the undoped MCM-48, suggesting that the introduction of metal precursors did not lead to a decrease in the production of the material.

Table 6.4. Yield of synthesized MCM-48 and Cu-MCM-48 sample (synthesis condition: Si: Cu: CTAB: ethanol: H_2O: H_2SO_4=1: 0.0073: 0.2: 4.3: 83: 0.1, aging time 3 h, hydrothermal synthesis temperature 110 ^oC, synthesis time 36 h)

Sample name	Amount of Si source (water glass)	Amount of SiO_2 in the synthesis gel	Amount of as-synthesized material per batch	Yield
MCM-48	1.64 mL	0.6 g	0.4667 g	42%
Cu-MCM-48	1.64 mL	0.6 g	0.5509 g	44%

Overall, the Cu-MCM-48 catalyst with fine cubic structure and high ordering, high surface area and uniform pore size was synthesized, while the metal incorporation and yield need to be further optimized.

6.4 Improvements of metal incorporation of Cu-MCM-48

Since the development of the first mesoporous materials in the early 1990s, one of the main objectives has been a further rationalization of the synthesis procedure, thus maximizing reproducibility and yield without reducing the structural order of the samples, as reported [9,16,23,48,60,61]. However, very little attention has been paid to the optimization of Cu-MCM-48 due to its challenging synthesis and the difficulties in heteroatom substitution, whereas the heteroatom substitution is crucial for the performance of a metal-substituted catalyst in the CWPO of phenol. However, the low yield and in particular, the low metal incorporation of the synthesized material, as discussed in section 6.3, are still challenges of the synthesis process based on the above analysis in the chapter. Hence different synthesis parameters were investigated in order to obtain materials of defined meso-structure (highly ordered cubic phase), superior yield and desirable morphology (high percentage of metal substitution) in the following study. The synthesis conditions of different Cu-MCM-48 were presented in table 6.5. The parameters, including: concentration of template, metal loading, water content, pH of synthesis solution, aging time, synthesis time and temperature were investigated.

Table 6.5. Synthesis conditions of different Cu-MCM-48 catalysts. The catalyst synthesized under different conditions were denoted as CM-X, respectively. The sample CM-1 is the blank MCM-48 without Cu species introduced into the synthesis gel. The sample CM-23 is the Cu-MCM-48 discussed in section 6.2 and 6.3, which is used for comparison in this section to evaluate if the yield and the incorporation percentage increased or not. The variable of each sample is marked blue.

Catalyst number	Molar ratio of the composition of synthesis gel						Aging time	Synthesis time	hydrothermal synthesis temperature	Calcination temperature
	Sodium silicate	Cu nitrate	CTAB	ethanol	H_2O	H_2SO_4				
CM-1 (blank)	1	0	0.2	4.3	83	0.1	3 h	36 h	110 ºC	550 ºC
CM-2	1	0.0073	0.2	4.3	83	0.1	3 h	72 h	110 ºC	550 ºC
CM-3	1	0.0146	0.2	4.3	83	0.1	3 h	72 h	110 ºC	550 ºC
CM-4	1	0.0292	0.2	4.3	83	0.1	3 h	72 h	110 ºC	550 ºC
CM-5	1	0.0073	0.15	4.3	83	0.1	3 h	36 h	110 ºC	550 ºC
CM-6	1	0.0073	0.1	4.3	83	0.1	3 h	36 h	110 ºC	550 ºC
CM-7	1	0.0073	0.05	4.3	83	0.1	3 h	36 h	110 ºC	550 ºC
CM-8	1	0.0073	0.2	0	83	0.1	3 h	36 h	110 ºC	550 ºC
CM-9	1	0.0073	0.2	4.3 (methanol)	83	0.1	3 h	36 h	110 ºC	550 ºC
CM-10	1	0.0073	0.2	4.3 (isopropanol)	83	0.1	3 h	36 h	110 ºC	550 ºC
CM-11	1	0.0073	0.2	4.3	166	0.1	3 h	36 h	110 ºC	550 ºC
CM-12	1	0.0073	0.2	4.3	249	0.1	3 h	36 h	110 ºC	550 ºC
CM-13	1	0.0073	0.2	4.3	332	0.1	3 h	36 h	110 ºC	550 ºC
CM-14	1	0.0073	0.2	4.3	83	0.05	3 h	36 h	110 ºC	550 ºC
CM-15	1	0.0073	0.2	4.3	83	0.15	3 h	36 h	110 ºC	550 ºC

Catalyst	Molar ratio of the composition of synthesis gel						Aging	Synthesis	hydrotherm	Calcination
CM-16	1	0.0073	0.2	4.3	83	0.3	3 h	36 h	110 °C	550 °C
CM-17	1	0.0073	0.2	4.3	83	0.1	10 min	36 h	110 °C	550 °C
CM-18	1	0.0073	0.2	4.3	83	0.1	1 h	36 h	110 °C	550 °C
CM-19	1	0.0073	0.2	4.3	83	0.1	2 h	36 h	110 °C	550 °C
CM-20	1	0.0073	0.2	4.3	83	0.1	6 h	36 h	110 °C	550 °C
CM-21	1	0.0073	0.2	4.3	83	0.1	3 h	9 h	110 °C	550 °C
CM-22	1	0.0073	0.2	4.3	83	0.1	3 h	18 h	110 °C	550 °C
CM-23 (for comparison)	1	0.0073	0.2	4.3	83	0.1	3 h	36 h	110 °C	550 °C
CM-24	1	0.0073	0.2	4.3	83	0.1	3 h	72 h	110 °C	550 °C
CM-25	1	0.0073	0.2	4.3	83	0.1	3 h	168 h	110 °C	550 °C
CM-26	1	0.0073	0.2	4.3	83	0.1	3 h	36 h	Room temp	550 °C
CM-27	1	0.0073	0.2	4.3	83	0.1	3 h	36 h	60 °C	550 °C
CM-28	1	0.0073	0.2	4.3	83	0.1	3 h	36 h	90 °C	550 °C
CM-29	1	0.0073	0.2	4.3	83	0.1	3 h	36 h	145 °C	550 °C
CM-30	1	0.0073	0.2	4.3	83	0.1	3 h	72 h	110 °C	350 °C
CM-31	1	0.0073	0.2	4.3	83	0.1	3 h	72 h	110 °C	450 °C
CM-32	1	0.0073	0.2	4.3	83	0.1	3 h	72 h	110 °C	650 °C

6.4.1 Effects of protocol on the synthesis of Cu-MCM-48

A typical synthesis protocol for Cu substituted MCM-48 requires a minimum of four reagents: an organic template, a silica precursor, a metal precursor, and a solvent (most often water and/or ethanol). Depending on the protocol, some acid/base reagents maybe also needed as the synthesis occurs in solution of certain pH range. To investigate the most favourable conditions, the optimal dose of these reagents in the synthesis of mesoporous material was explored. In addition, parameters varied in this protocol whereas the silica precursor was fixed as sodium silicate (Na_2SiO_3, 1.64 mL, corresponding to 0.6 g of silica) as it is much cheaper than the most commonly used Si precursor, tetraethyl orthosilicate (TEOS, $Si(OC_2H_5)_4$), in the lab.

6.4.1.1 Concentration of template: CTAB/Si

The synthesis of MCM-48 was first reported by Mobil Company in 1992 [5] and was carried out by using quaternary ammonium surfactant compounds ($C_nH_{2n+1}(CH_3)_3NX$, X = Cl or Br) as the templates (also called structure directing agents). However, the use of a large number of surfactants (molar ratio of surfactant/silica > 1) significantly increased the cost of MCM-48 synthesis and was not environmentally friendly. Though some optimized ratios (for example, 0.177 [62], 0.2 [48], 0.275 [9], 0.45 [53]) were reported in the last decades, a high molar ratio of surfactant/Si and a high concentration of surfactant are still the prerequisite conditions for making MCM-48 catalyst.

The cationic surfactant, CTAB ($C_{19}H_{42}BrN$), was used as the organic template in this study due to the strong ionic interactions between CTA^+ ions and silicate anions. The dependence of the structural order and output of the material on CTAB concentration was investigated in this section. The Cu-MCM-48 samples were obtained at CTAB/Si molar ratio varying from 0.05 to 0.2 in the initial gel, with the XRD patterns plotted in figure 6.7a.

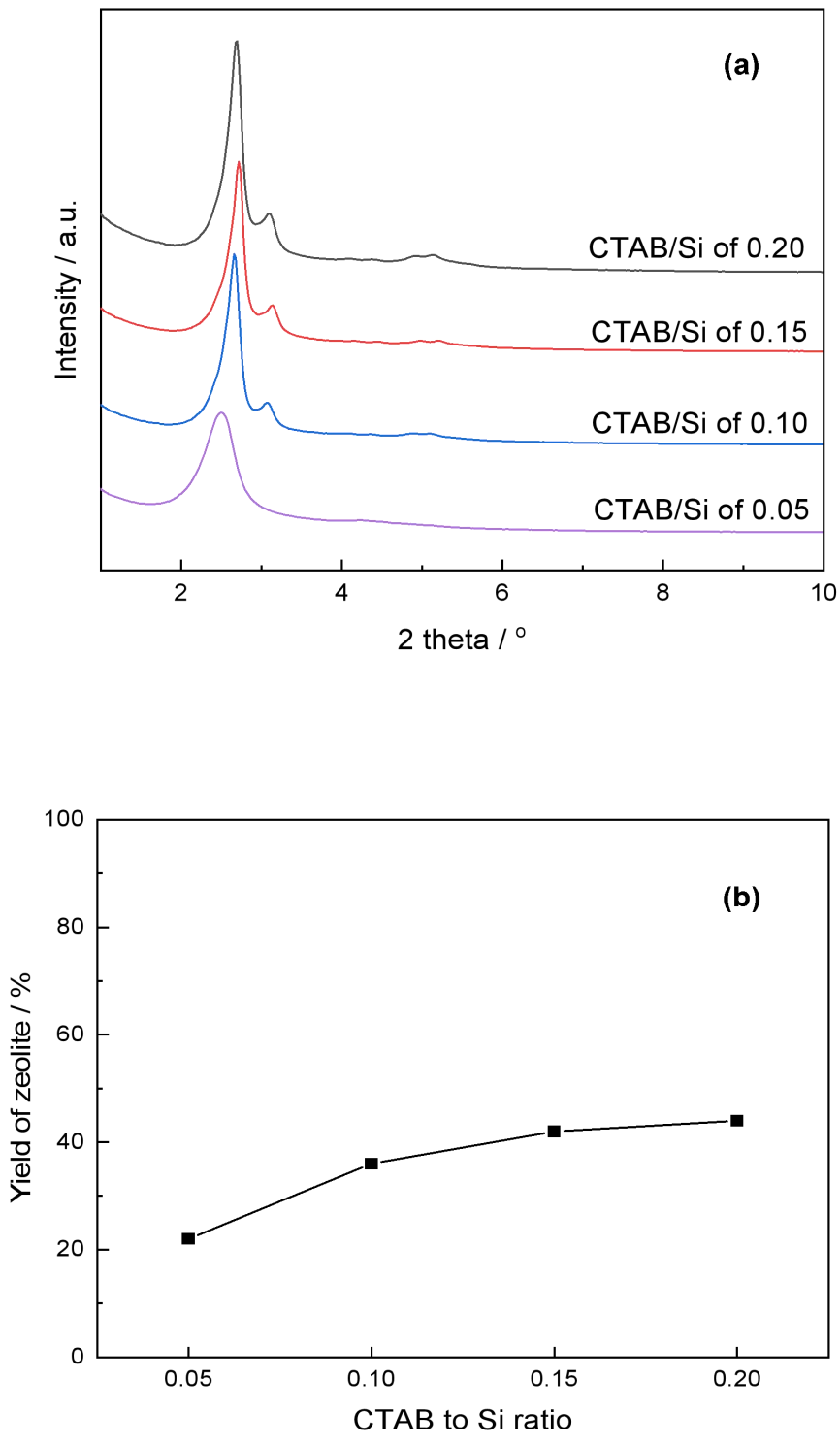

Figure 6.7. a) XRD patterns and b) yields of Cu-MCM-48 catalysts with different CTAB/Si ratios (synthesis condition: Si: Cu: CTAB: ethanol: H_2O: H_2SO_4=1: 0.0073: 0.05~0.2: 4.3: 83: 0.1, aging time 3 h, hydrothermal synthesis temperature 110 °C, synthesis time36 h)

As shown in figure 6.7a, the sample with a CTAB/Si ratio of 0.2 presented a typical MCM-48 pattern with high regularity since the five planes (211), (220), (321), (400), (420) and (332) all clearly appeared. Cubic MCM-48 silica was also obtained with only a slight loss of intensity when the CTAB/Si molar ratio was reduced to 0.15 and 0.1. It means that an appropriate decrease in the CTAB concentration would not result in an obvious loss of the ordering of the silica material. Meanwhile, the obvious contraction and expansion of the unit cell parameter was not observed neither (in table 6.6), indicating the minor influence of the amount of CTAB on the structure once MCM-48 was formed. On the other hand, the yield of the sample (36%, table 6.6 and figure 6.8b) insignificantly reduced under the optimal CTAB/Si molar ratio (0.1, the amount of template halved). However, further lowering down the CTAB/Si molar ratio to 0.05 led to the formation of the MCM-41 analogue phase. As a result, it is concluded that the lowest molar ratio of surfactants/Si for the successful synthesis of cubic mesostructure in this study is just 0.1, which is much lower than the reported value in the literature. From environmental concerns, the surfactant amount should be minimized thus the CTAB/Si ratio of 0.1 is optimal in this synthesis route.

Table 6.6. The characteristics of the MCM-48 catalysts synthesized at different conditions. The sample CM-1 is the blank MCM-48 (bold) whereas the sample CM-23 (bold) is the Cu-MCM-48 used for comparison to evaluate if the yield and the incorporation percentage increased or not.

catalyst number	phase	2θ[a]	d_{211}[b] (nm)	a_0[c] (nm)	yield
CM-1 (blank)	**cubic**	**2.68º**	**3.29**	**8.06**	**42%**
CM-2 (Cu/Si 0.0073)	cubic	2.66º	3.32	8.13	45%
CM-3 (Cu/Si 0.0146)	cubic	2.70º			46%
CM-4 (Cu/Si 0.0292)	cubic	2.66º	3.32	8.13	51%
CM-5 (CTAB/Si 0.15)	cubic	2.72º	3.24	7.95	42%
CM-6 (CTAB/Si 0.10)	cubic	2.66º	3.32	8.13	36%
CM-7 (CTAB/Si 0.05)	poorly ordered	--	--	--	22%
CM-8 (without alcihol)	poorly ordered	--	--	--	44%
CM-9 (with methanol)	poorly ordered	--	--	--	48%
CM-10 (with isopropanol)	poorly ordered	--	--	--	28%
CM-11 (H_2O/Si 166)	cubic	2.70º	3.27	8.01	54%
CM-12 (H_2O/Si 249)	cubic	2.72º	3.24	7.95	59%
CM-13 (H_2O/Si 332)	cubic	2.76º	3.2	7.83	66%
CM-14 (H_2SO_4/Si 0.05)	poorly ordered	--	--	--	30%
CM-15 (H_2SO_4/Si 0.15)	cubic	2.52º	3.5	8.58	57%
CM-16 (H_2SO_4/Si 0.30)	hexagonal	--	--	--	91%
CM-17 (age 10 min)	cubic	2.72º	3.24	7.95	45%
CM-18 (age 1 h)	cubic	2.72º	3.24	7.95	45%
CM-19 (age 2 h)	cubic	2.72º	3.24	7.95	45%
CM-20 (age 6 h)	cubic	2.70º	3.27	8.01	44%
CM-21 (synthesis 9 h)	cubic	2.76º	3.2	7.83	47%
CM-22 (synthesis 18 h)	cubic	2.78º	3.17	7.78	48%
CM-23 (for comparison)	**cubic**	**2.70º**	**3.27**	**8.01**	**44%**
CM-24 (synthesis 72 h)	cubic	2.66º	3.32	8.13	44%
CM-25 (synthesis 168 h)	pore collapsed	--	--	--	48%
CM-26 (20 ºC synthesis)	poorly ordered	--	--	--	54%
CM-27 (60 ºC synthesis)	poorly ordered	--	--	--	47%
CM-28 (90 ºC synthesis)	cubic	2.70º	3.27	8.01	43%
CM-29 (145 ºC synthesis)	pore collapsed	--	--	--	44%
CM-30 (350 ºC calcination)	cubic	2.62º	3.37	8.25	44%
CM-31 (450 ºC calcination)	cubic	2.62º	3.37	8.25	44%
CM-32 (650 ºC calcination)	cubic	2.78º	3.17	7.78	44%

a, position of 211 plane - data from XRD; b, d_{211} spacing - calculated by Eq. 6.1; c, unit cell parameter (a_0) - calculated by Eq. 6.3.

6.4.1.2 Concentration of water: H_2O/Si

Water is an important constituent of any hydrothermal system as it plays multiple roles in the synthesis of porous material. On the one hand, it acts as a solvent, thus assists the dissolution of solid components of a mixture and facilitates their transport and mixing, meanwhile, it modifies phase equilibrium temperatures. On the other hand, it acts as space fillers to stabilize the porous lattice. Through its presence, especially at high temperatures, water may be incorporated into siliceous materials to hydrolyse and reform Si-O-Si bonds so that chemical reactivity is enhanced [63].

The influence of water content on the formation of Cu-MCM-48 materials was investigated by varying the molar composition of the synthesis gel: SiO_2: CuO: CTAB: ethanol: H_2SO_4: H_2O: =1: 0.0073: 0.2: 4.3: 0.1: x, where $83 \leq x \leq 332$. The samples with the similar MCM-48 structure were obtained from the gels with molar H_2O/Si ratios of 83 to 332 (figure 6.8a), whereas the intensity and width of the characteristic peaks varied. Well-ordered MCM-48 was obtained from gels with molar H_2O/Si ratios of 83 to 249 as confirmed by the presence of well-defined peaks corresponding to (211) and (220). Furthermore, the intensity and the width of the peaks maintained almost constant. The intensity of the peaks decreased and the width broadened when further increasing the H_2O/Si ratio to 332, which reflects the formation of a lower-quality cubic mesostructure. The different behaviour of prepared samples with the highest water content may be explained by the strong electrostatic interaction between the cationic surfactant and anionic silicate species. A longer aging time is required for the formation of well-ordered materials in the gel at higher water content [49]. On the other hand, the d-spacing and unit parameter a_0 (table 6.6) at H_2O/Si ratio from 83 to 249 kept almost constant, suggesting a constant metal incorporation, which can also be supported by their substituted metal loading (around 0.01%, see table 6.3).

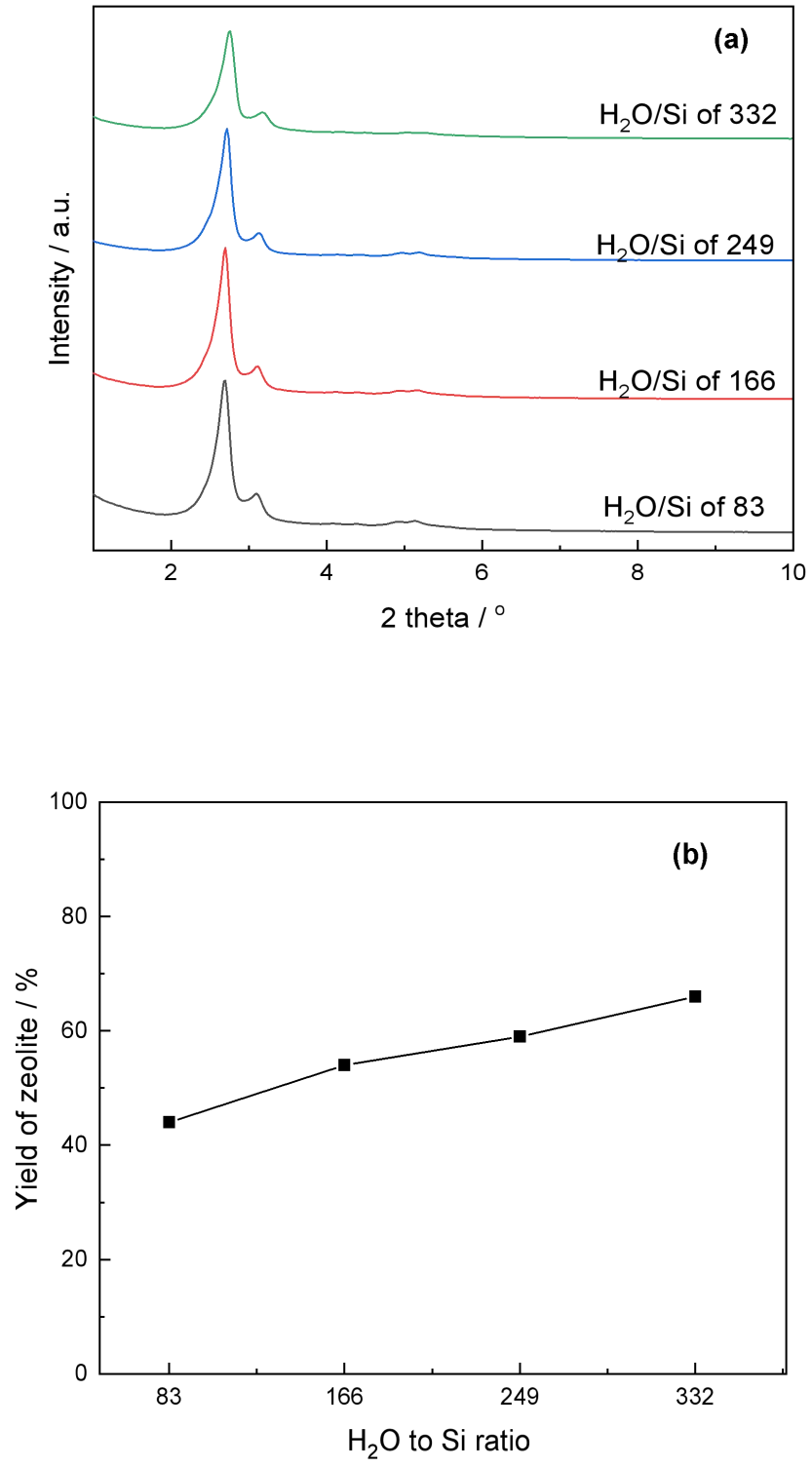

Figure 6.8. a) XRD patterns and b) yield of Cu-MCM-48 catalysts with different H_2O/Si ratios (synthesis condition: Si: Cu: CTAB: ethanol: H_2O: H_2SO_4=1: 0.0073: 0.2: 4.3: 83~332: 0.1, aging time 3 h, hydrothermal synthesis temperature 110 °C, synthesis time 36 h)

The big challenge of MCM-48 synthesis, namely, the low yield of the final products in a single batch (around 45% in this research, see table 6.6), was efficiently tackled with an increase of the H_2O/Si ratio. As shown in figure 6.8b, the yield of MCM-48 increased by 50% (from 44% to 66%) when the amount of water quadrupled, indicating the higher utilization of both silica and organic template. This behaviour may be explained by an enhanced reactivity due to a lower viscosity or decreased synthesis pH at diluted solutions [64].

Though no obvious differences were observed from the perspective of mesoporous structures after increasing water content, the pore structures of the samples also deserved a test to confirm the advantages of samples with higher water contents. In the N_2 adsorption-desorption isotherms of materials synthesized at different H_2O/Si (83 and 249) were selected as representative, as shown in figure 6.9a. Typical type IV isotherms were clearly observed, indicating the high quality of the mesoporous samples. The higher adsorption capability of the sample with H_2O/Si of 249 suggested that MCM-48 synthesized at higher water content presented even slightly higher surface area (1338 $m^2 \cdot g^{-1}$) than the sample with H_2O/Si ratio of 83 (1219 $m^2 \cdot g^{-1}$), as listed in table 6.2. Besides, the pore size distribution also indicated that changing the water content had no negative effects on the uniformity of pore width of samples whereas the desorption pore size of Cu-MCM-48 with H_2O/Si of 83 and 249 were 2.66 and 2.55 nm, respectively.

Overall, it is concluded that an increase of water content improves the yield of MCM-48 dramatically without loss of quality of the final material.

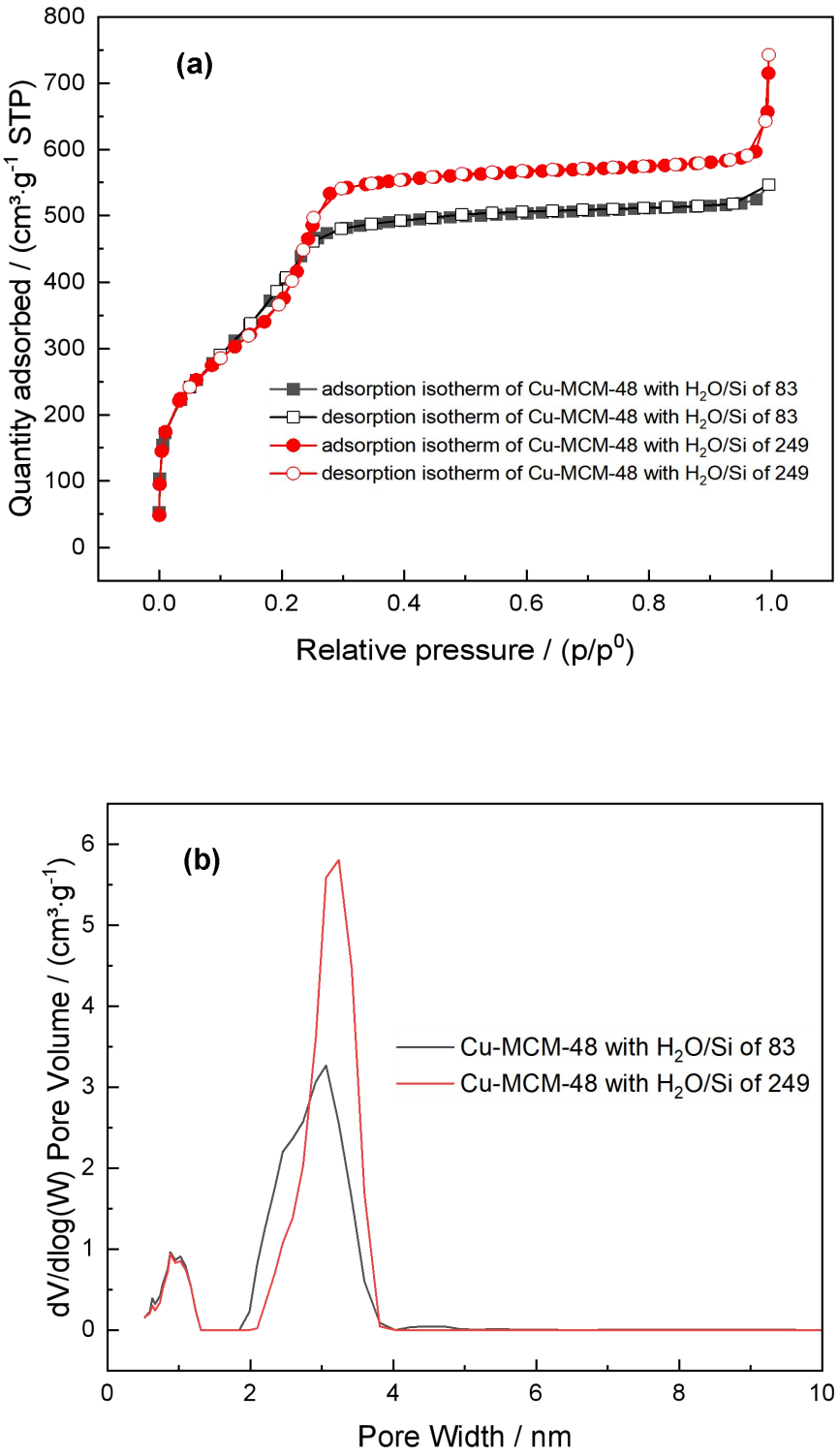

Figure 6.9. a) N_2 adsorption–desorption isotherms and b) pore distribution of the Cu-MCM-48 with different H_2O/Si (synthesis condition: Si: Cu: CTAB: ethanol: H_2O: H_2SO_4=1: 0.0073: 0.2: 4.3: 83 or 249: 0.1, aging time 3 h, hydrothermal synthesis temperature 110 °C, synthesis time 36 h)

6.4.1.3 Alcohol additive

With almost no exception, all of the studies in the literature for the preparation of MCM-48 silica made use of ethanol when using cetyltrimethylammonium (CTA^+) surfactant molecule as a template [23]. Ethanol is either added directly into the synthesis gel as an additive or obtained from the hydrolysis of other Si sources (such as TEOS). In this project, the Si source was sodium silicate (Na_2SiO_3) rather than the costly TEOS ($Si(OC_2H_5)_4$), thus ethanol was added into the synthesis gel from the beginning of preparation. Although ethanol was previously found useful for the synthesis of cubic MCM-48 nanoparticles under highly basic conditions, its role is not addressed in detail [61]. On the one hand, it acts as a co-solvent to dissolve CTAB because CTAB is difficult to be dissolved at room temperature. On the other hand, the role of the added ethanol in the formation of MCM-48 is in the ability to cause a systematic rearrangement in the structure of the micelle by penetrating the micelle surface [58]. It acts as a co-surfactant entering into the organic phase and swell micelles and drives a mesophase transformation from.

The formation of MCM-48 depends strongly on the nature of alcohol, as shown in figure 6.10. The sample without alcohol additive yielded a material with only a single broad peak in the diffraction pattern, which showed that ethanol is required for the phase transformation to occur. In comparison, the MCM-48 structure was formed, if ethanol was added. This is because the use of ethanol as a co-surfactant increases the surfactant packing parameter and directs mesostructure assembly to a cubic MCM-48. Another attempt was performed with other alcohol (methanol and iso-propanol) as additives replacing ethanol but the formation of cubic structural MCM-48 failed. The use of methanol to form cubic mesostructure was reported in other researches [58] but it did not give MCM-48 in this study which might be attributed to the high polarity and hydrophilicity of methanol or the inappropriate alcohol/Si ratio.

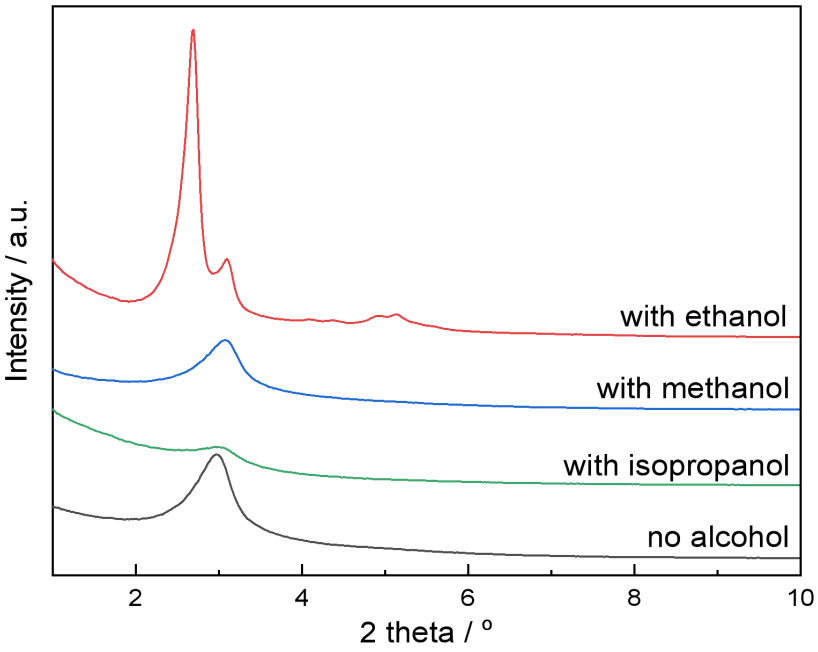

Figure 6.10. XRD patterns of Cu-MCM-48 catalysts: black line, without alcohol; green line, with ethanol; blue line,with methanol; red line, with isopropanol (synthesis condition: Si: Cu: CTAB: alcohol: H_2O: H_2SO_4=1: 0.0073: 0.2: 4.3: 83: 0.1, aging time 3 h, hydrothermal synthesis temperature 110 °C, synthesis time 36 h)

6.4.1.4 Cu/Si ratio

Figure 6.11a showed the XRD patterns of Cu substituted mesoporous materials prepared by adding the required amount of $Cu(NO_3)_2$ corresponding to theoretical loading of 1, 2, and 4 wt% Cu in the synthesis gel and actual loading of 1.2%, 2.1% and 4.5% Cu in the sample (table 6.3). As can be seen, the two intense diffraction peaks at 2θ of 2.7° and 3.1° indexed as (211) and (220) reflections were clearly observed, indicating the maintaining of the ordered cubic mesoporous structures. However, the peak intensity of the (211) reflection was gradually attenuated when increasing the copper content of the samples, implying a relatively disordered mesostructure arising from the excessive incorporation. This behaviour is possibly attributed to the partial collapse and/or disorder of the cubic ordered phase [65-67] aroused by the introduction of the copper salt into the synthesis gel. On the other hand, no significant

changes were observed in the shift of peaks (figure 6.11a) and the unit cell parameter a_0 (table 6.6) when the ratio of Cu/Si ratio increased from 0.0073 to 0.0292, implying that the excess amount of copper nitrate would not lead to further enlargement in the unit cell. Furthermore, the growth of the sample yields with the change of Cu loading is negligible (in figure 6.11b).

Therefore, though it is more viable to prepare cubic Cu-MCM-48 materials with low loading (1 wt% Cu) under the experimental conditions in this study, the successful synthesis of Cu-MCM-48 with high loading (such as 4%) is also achieved. Furthermore, this suggests that the synthesis of Cu-MCM-48 with even higher metal loading would be possible as metal loadings of 10% [25] to 20% [24] have been reported in the literature.

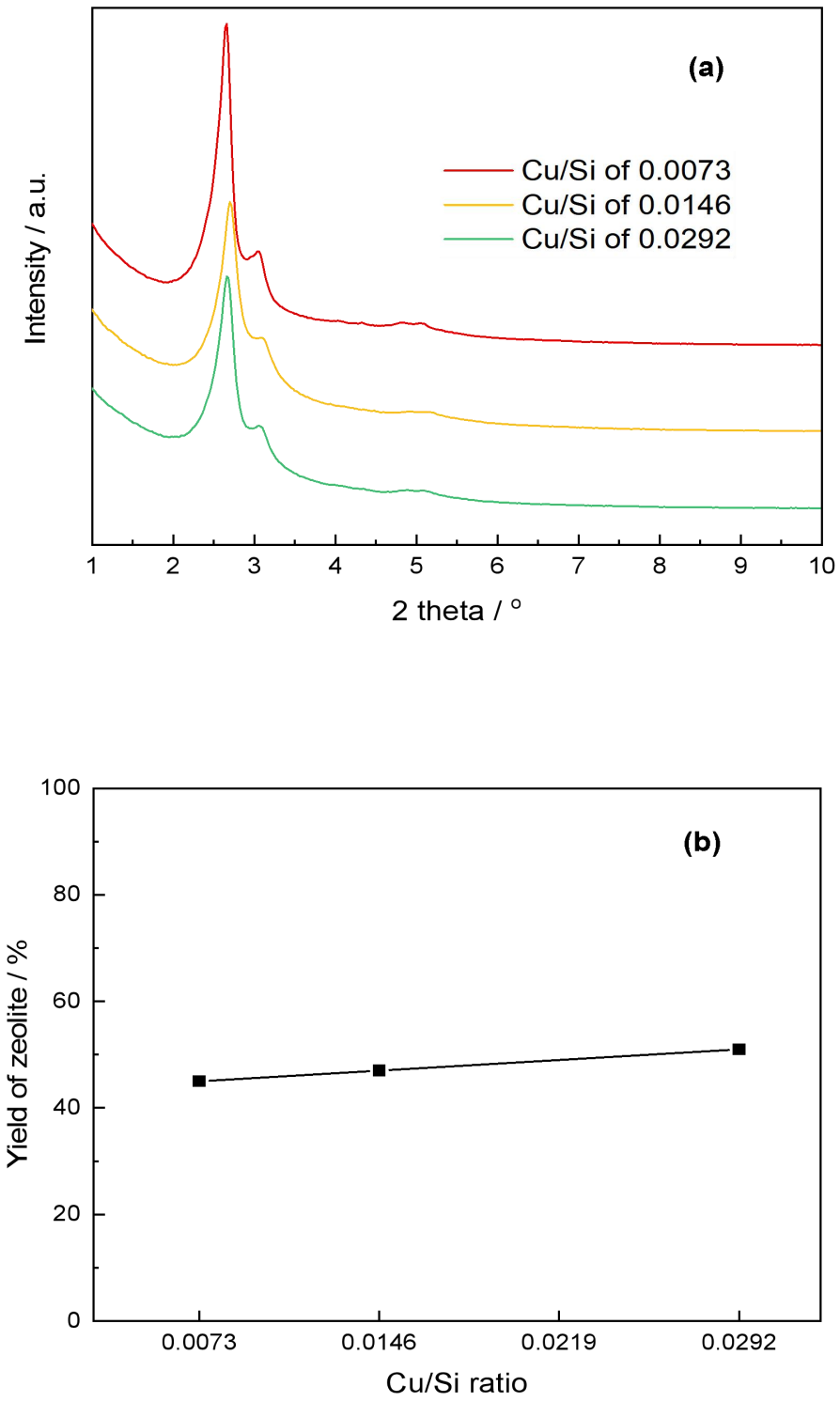

Figure 6.11. a) XRD patterns and b) yield of Cu-MCM-48 catalysts with different Cu/Si ratios (synthesis condition: Si: Cu: CTAB: ethanol: H_2O: H_2SO_4=1: 0.0073~0.0292: 0.2: 4.3: 83: 0.1, aging time 3 h, hydrothermal synthesis temperature 110 °C, synthesis time 72 h)

6.4.1.5 Alkalinity

The synthesis of MCM-48 is usually carried out in a basic media while the formation of MCM-41 is preferential at a lower pH [49]. However, the strong basic media may lead to the precipitation of copper hydroxide [68] which is detrimental for the substitution of Cu into the silica framework. Thus, an appropriate pH for this synthesis is necessary to balance the formation of a cubic structure and an improvement in metal incorporation. In this section, the effects of the alkalinity of the gel to the formation of mesoporous materials were studied. The protocol we used for synthesis of the MCM-48 involved the use of sodium silicate (Na_2SiO_3, 13.4-14.4% NaOH basis) as Si source, which is a basic solution with pH around 12.5, whereas the diluted H_2SO_4 (2 M) was used to adjust the pH in the synthesis process. The samples in this section were synthesized using the procedure described in section 2.1 in chapter 2 at the pH of the synthesis gel (10.2–12.2) adjusted to the desired value.

The powder XRD patterns of our samples were collected (figure 6.12). As shown, when the synthesis was carried out at pH 12.2 (H_2SO_4/Si ratio of 0.05), the obtained material had neither hexagonal array nor cubic structure as no relative diffraction peaks were present in the pattern, suggesting that a decreased synthesis pH is necessary for the synthesis of mesoporous materials. When decreasing the synthesis pH to 11.9 (H_2SO_4/Si to 0.1), a typical XRD pattern of MCM-48 structure was observed, indicating that the pH of around 12 is in the appropriate range for the synthesis of MCM-48 which is also consistent with the literature [9,15]. The intensity of the Cu-MCM-48 characteristic peaks decreased greatly, when more H_2SO_4 was added to the synthesis gel and the pH reached 11.6 (H_2SO_4/Si of 0.15), which suggested the impairment of the ordered structure. This can be attributed to the production of large depolymerization of the silica species at higher pH as compared to that at low pH [49]. Further decreasing the pH of the synthesis gel to 10.2 (H_2SO_4/Si of 0.3) led to the formation of MCM-41, similar findings were reported elsewhere [13,49]. As it can be seen, an XRD pattern with four peaks at 2.3°, 3.9°, 4.5° and 6.0° corresponding to the (1 0 0), (1 1 0), (2 0 0) and (2 1 0) planes on hexagonal unit cell [28] was present in the sample at pH 10.2, indicating

the formation of a highly ordered MCM-41. It is evidenced that the formation of MCM-41 is preferential at lower pH value (around 10) and the optimal pH for the synthesis of MCM-48 is around 12.

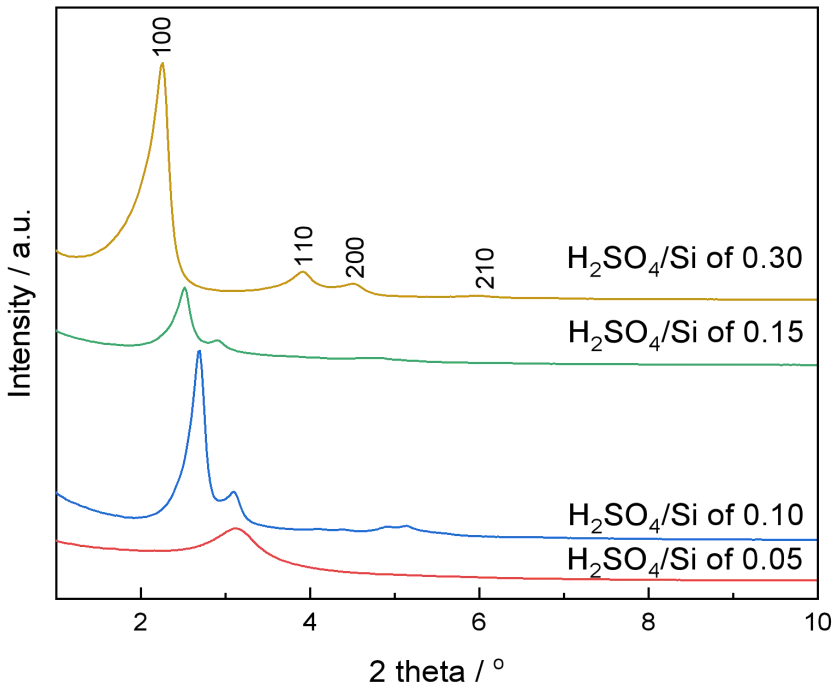

Figure 6.12. XRD patterns of Cu-MCM-48 catalysts with H_2SO_4/Si ratio of a) 0.05, b) 0.1, c) 0.15 and d) 0.30 (synthesis condition: Si: Cu: CTAB: ethanol: H_2O: H_2SO_4=1: 0.0073: 0.2: 4.3: 83: 0.05~0.3, aging time 3 h, hydrothermal synthesis temperature 110 °C, synthesis time 36 h)

Besides the changes in peak intensities, the XRD patterns of MCM-48 at lower pH shifted to a smaller angle, which was also reflected in the unit cell parameter and substituted Cu loading. The values, a_0 (table 6.6), increased sharply from 8.01 to 8.58 nm and the incorporated Cu loading increased from 0.0091% to 0.054% (table 6.3) with the pH decreased slightly from 11.9 to 11.6, suggesting that the expansion of the lattice is highly sensitive to pH of the synthesis gel. Similar results were also reported in the synthesis of B-Ge-MFI [69]. The lattice expansion may be attributed to the metal substitution since more dissociate Cu^{2+} exists at lower pH condition. Furthermore, the yield of sample increased sharply with the decline of

synthesis pH (figure 6.13). In particular, the yield of MCM-41 was noticed, as it reached over 90%, far higher than that of MCM-48 samples, indicating the high utilization of the raw materials.

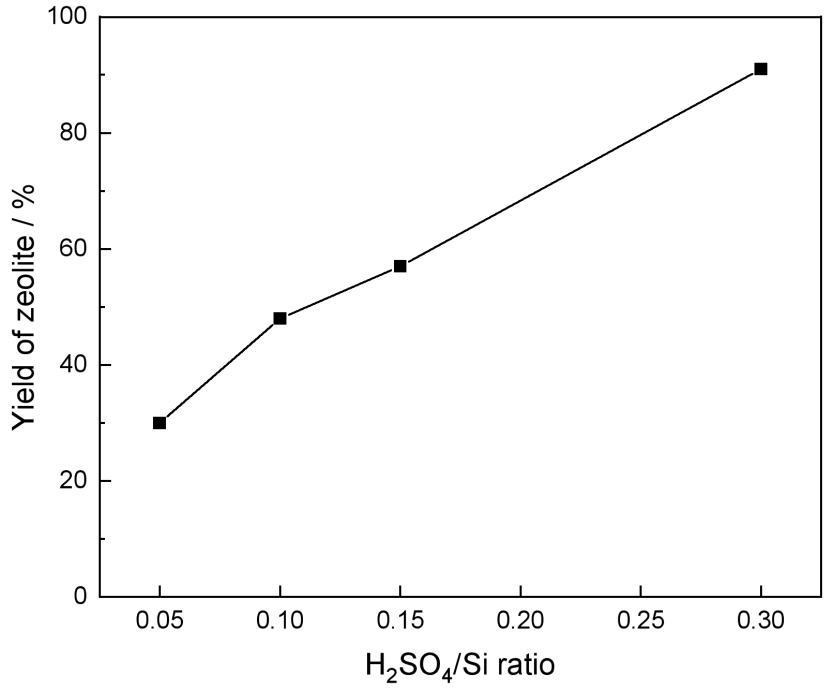

Figure 6.13. Yield of synthesized catalysts with H_2SO_4/Si of a) 0.05, b) 0.10, c) 0.15 and d) 0.30 (synthesis condition: Si: Cu: CTAB: ethanol: H_2O: H_2SO_4=1: 0.0073: 0.2: 4.3: 83: 0.05~0.3, aging time 3 h, hydrothermal synthesis temperature 110 ^oC, synthesis time 36 h)

Additionally, the pore size and framework structure of the Cu-MCM-41 sample synthesized at pH of 10.2 was further characterized by BET and TEM, respectively. As shown, the N_2 adsorption-desorption isotherms and pore size distribution of Cu-MCM-41 sample are consistent with a typical type IV isotherm (figure 6.14a). Adsorption on MCM-41 materials at low relative pressures ($p/p_0 < 0.3$) is assigned by monolayer adsorption of nitrogen on the walls of the mesopores while the sharp increase in the adsorption amount of nitrogen at the relative pressure of around 0.3 is characteristic of capillary condensation within uniform mesopores whereas the sharpness of the step reflects the uniformity of the pores [70,71].

The high N_2 adsorption suggested a high surface area of 1219 $m^{2}\cdot g^{-1}$ (table 6.3). Besides, the sample had narrow pore size distribution mainly at around 3-5 nm as shown in figure 6.14b, with an average pore size obtained at 3.73 nm.

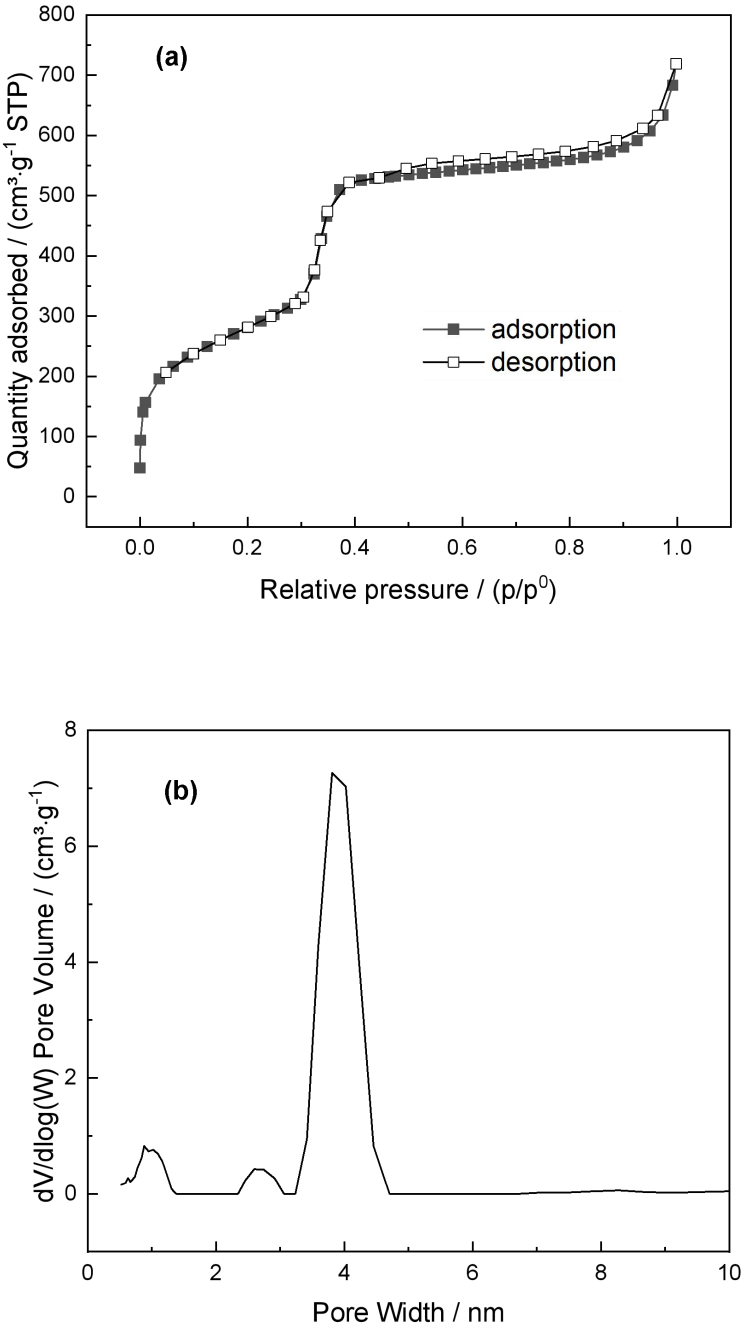

Figure 6.14. a) N_2 adsorption–desorption isotherms and b) pore distribution of Cu-MCM-41 catalyst (synthesis condition: Si: Cu: CTAB: ethanol: H_2O: H_2SO_4=1: 0.0073: 0.2: 4.3: 83: 0.3, aging time 3 h, hydrothermal synthesis temperature 110 ^{o}C, synthesis time 36 h)

Hexagonal arrays of Cu-MCM-41 were imaged (figure 6.15), and these electron microscopy patterns were in good agreement with results reported in literature [72,73].

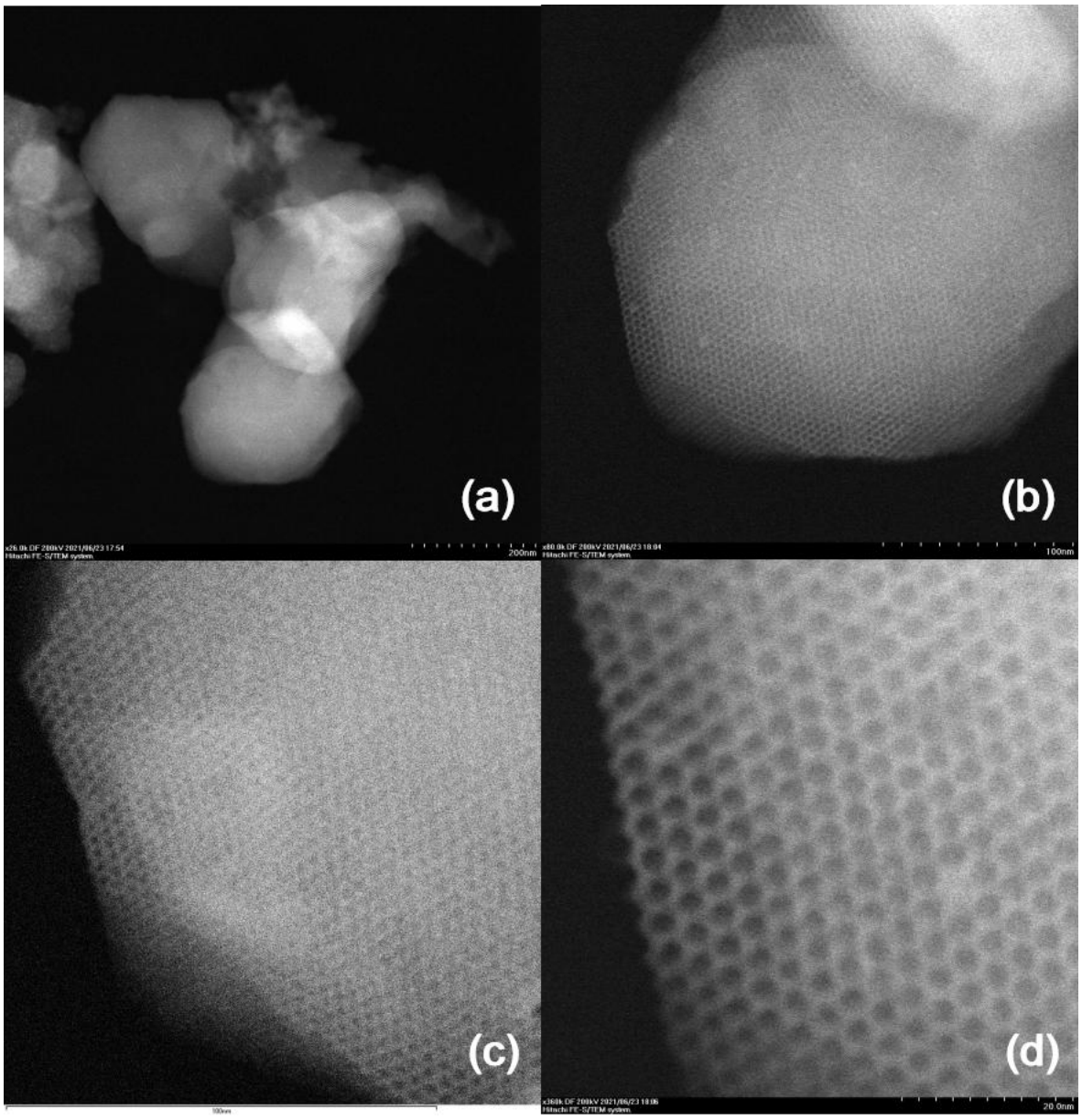

Figure 6.15. TEM images of the synthesized Cu-MCM-41 (magnification from (a) to (d): ×26k, ×80k, ×180k, ×360k) (synthesis condition: Si: Cu: CTAB: ethanol: H_2O: H_2SO_4=1: 0.0073: 0.2: 4.3: 83: 0.3, aging time 3 h, hydrothermal synthesis temperature 110 ^oC, synthesis time 36 h)

The hexagonal symmetry could be clearly identified in a TEM image (Figure 6.15a-d) which indicated the uniform phase of the MCM-41 material. The magnification of the images further showed that the material is structured with a highly ordered hexagonal array of pores. In

addition, several particles were observed in figure 6.15b, which might be due to the formation of CuO particles on the surface of the sample. However, the hexagonally ordered mesostructure of the host material MCM-41 was not affected by the presence of Cu inside the pores. Thus it was indicated that the metal substitution does not cause significant deterioration of the MCM-41 framework, which is consistant with the XRD and porosimetry results.

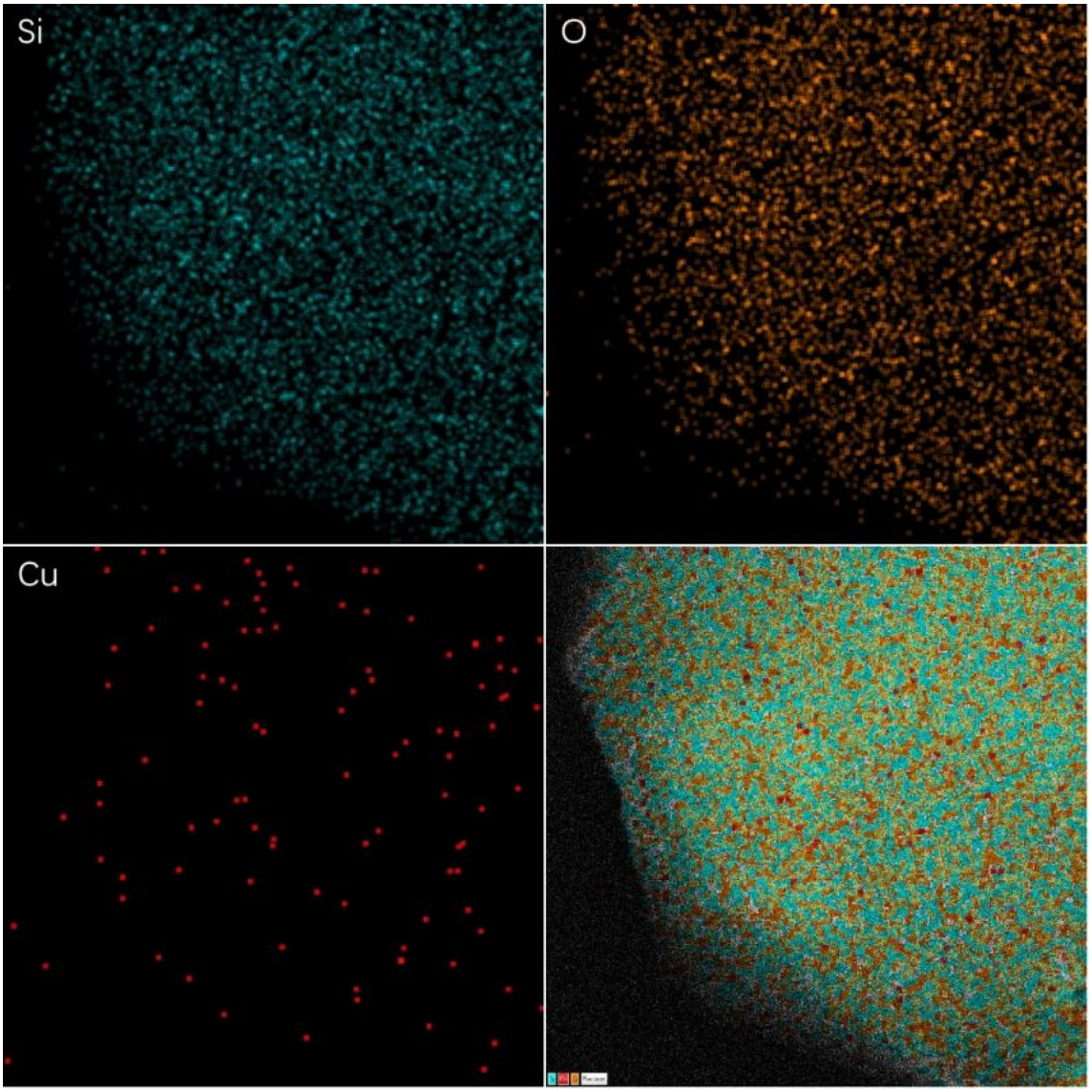

Figure 6.16. EDX elemental mapping of Cu-MCM-41 (synthesis condition: Si: Cu: CTAB: ethanol: H_2O: H_2SO_4=1: 0.0073: 0.2: 4.3: 83: 0.3, aging time 3 h, hydrothermal synthesis temperature 110 ^oC, synthesis time 36 h), Si in blue, O in orange, Cu in red.

An EDX analysis performed on the mesoporous region (where no CuO particles were externally visible, figure. 6.15c) was plotted in figure 6.16, where Si, O and Cu signals were detected. The Si and O atoms were originated from silica material (MCM-41), while the Cu-atoms were derived from the substituted active species. The appearance of uniformly distributed Cu atoms indicated the confinement of metal oxide nanoparticles inside the pores of MCM-41.

6.4.2 Effects of aging process on the synthesis of Cu-MCM-48

The aging process is defined as a stirring or pre-heating process at low temperature (typically, below 100 ^{o}C) prior to high temperature-hydrothermal treatments [74]. Aging is a nucleation aiding step in the synthesis of porous material, which could influence the hydrothermal synthesis process and the final properties of the product [75]. For instance, previous studies revealed advantages of controlling the aging process such as suppression of impurity-phase formation, reduction of synthesis time and control of particle sizes and their distribution [75-78].

The aging process in this study was accomplished by stirring (at 500 rpm) the synthesis gel for a certain time (0 to 6 h) at room temperature. Samples with different aging time were assessed by XRD (figure 6.17a); as it can be seen, the XRD patterns of the MCM-48 samples kept almost constant as the aging time increased for a fixed synthesis condition, which indicated that the aging process had no effects on the formation of cubic mesoporous structure when hydrothermal synthesis temperature and time were 110 ^{o}C and 36 h, respectively. On the other hand, the yield (figure 6.17b) and lattice spacing (table 6.6) of ordered mesoporous material remained constant, whereas the impurity phases such as MCM-41 and MCM-50 were not found, indicating the robustness of the synthesis method. The insignificant effect of the aging process on the structure of the final products might be attributed to the high solubility of sodium silicate in water since one of the important steps

occurring during the aging period is the (partially) dissolution or depolymerization of the silica sol [63].

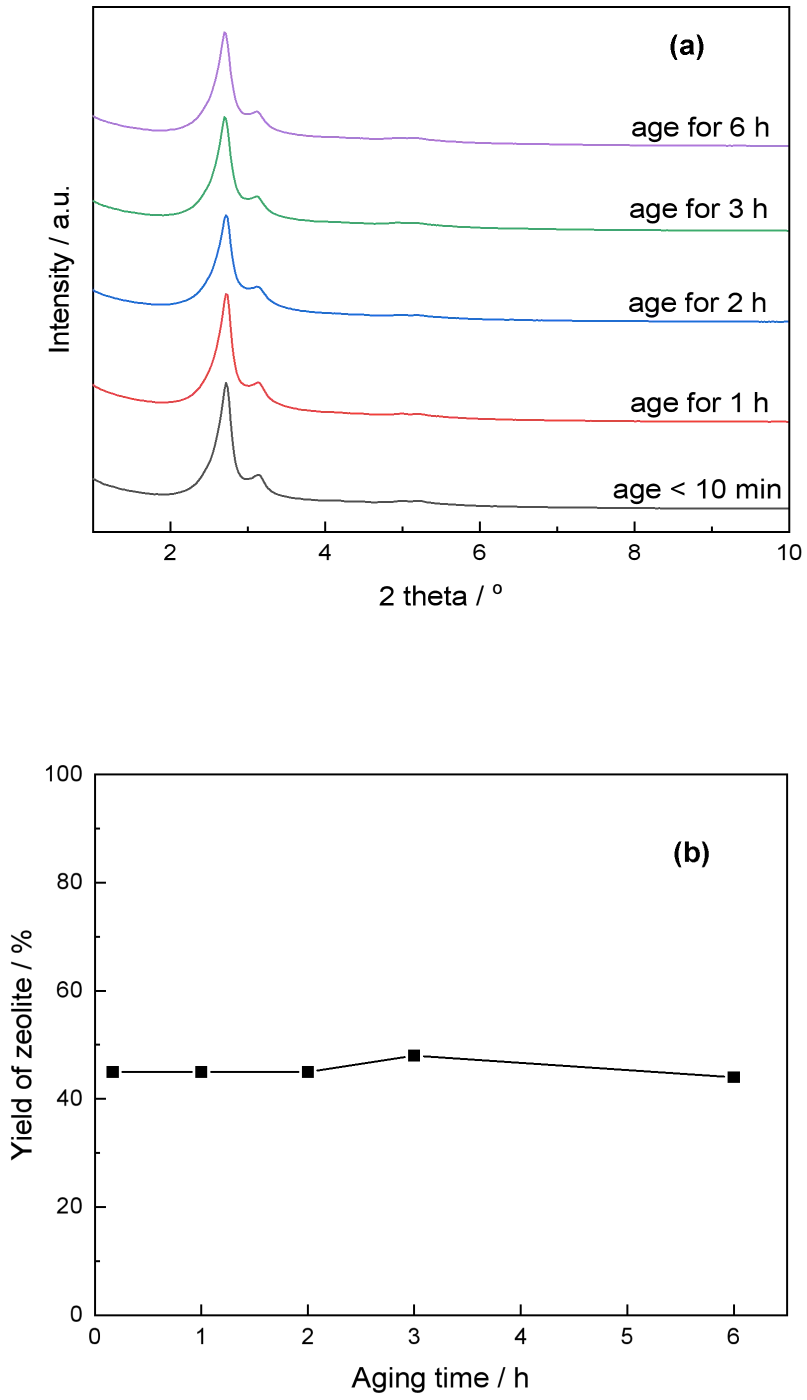

Figure 6.17. a) XRD patterns and b) yield of Cu-MCM-48 catalysts with different aging time (synthesis condition: Si: Cu: CTAB: ethanol: H_2O: H_2SO_4=1: 0.0073: 0.2: 4.3: 83: 0.1, aging time 10 min~6 h, hydrothermal synthesis temperature 110 °C, synthesis time 36 h)

6.4.3 Effects of hydrothermal conditions on the synthesis of Cu-MCM-48

For most of the microporous materials (pore diameter < 2 nm), the hydrothermal synthesis temperature and the synthesis time have positive influences on their formation process, while for mesoporous silica (pore diameter between 2 to 50 nm), the effects of the temperature and the hydrothermal time are uncertain due to the intermediate nature of MCM-48. On the one hand, a rise in temperature will increase both the synthesis efficiency and the linear growth rate, hence, the ordering of samples normally increases with time [63]. Nevertheless a rise of temperature may also destroy the structure of the mesoporous material. Besides, a certain synthesis time is necessary for the transformation of hexagonal phase to cubic while prolonged time may lead to the further transformation from cubic to lamellar phase [15,18,19]. As a consequence, the investigation of the hydrothermal conditions for MCM-48 synthesis is crucial because the intended mesoporous phase can only be synthesized under a defined range.

6.4.3.1 Hydrothermal synthesis temperature

Temperature is one of the key factors to tune the rate of mesoporous silica formation in the hydrothermal synthesis process. With an increase of the synthesis temperature, the rate for phase transformation from cubic MCM-48 to lamellar MCM-50 is accelerated. On the other hand though, the rate of micelles formation is slowed down as a result of the decreased synthesis temperature. Therefore, the effects of temperature on MCM-48 are the net results of the two integrated factors. The effects of synthesis temperature on the formation of MCM-48 were studied with the molar ratio of 1 Si: 0.0073 Cu: 0.2 CTAB: 4.3 ethanol: 83 H_2O: 0.1 H_2SO_4 in this project.

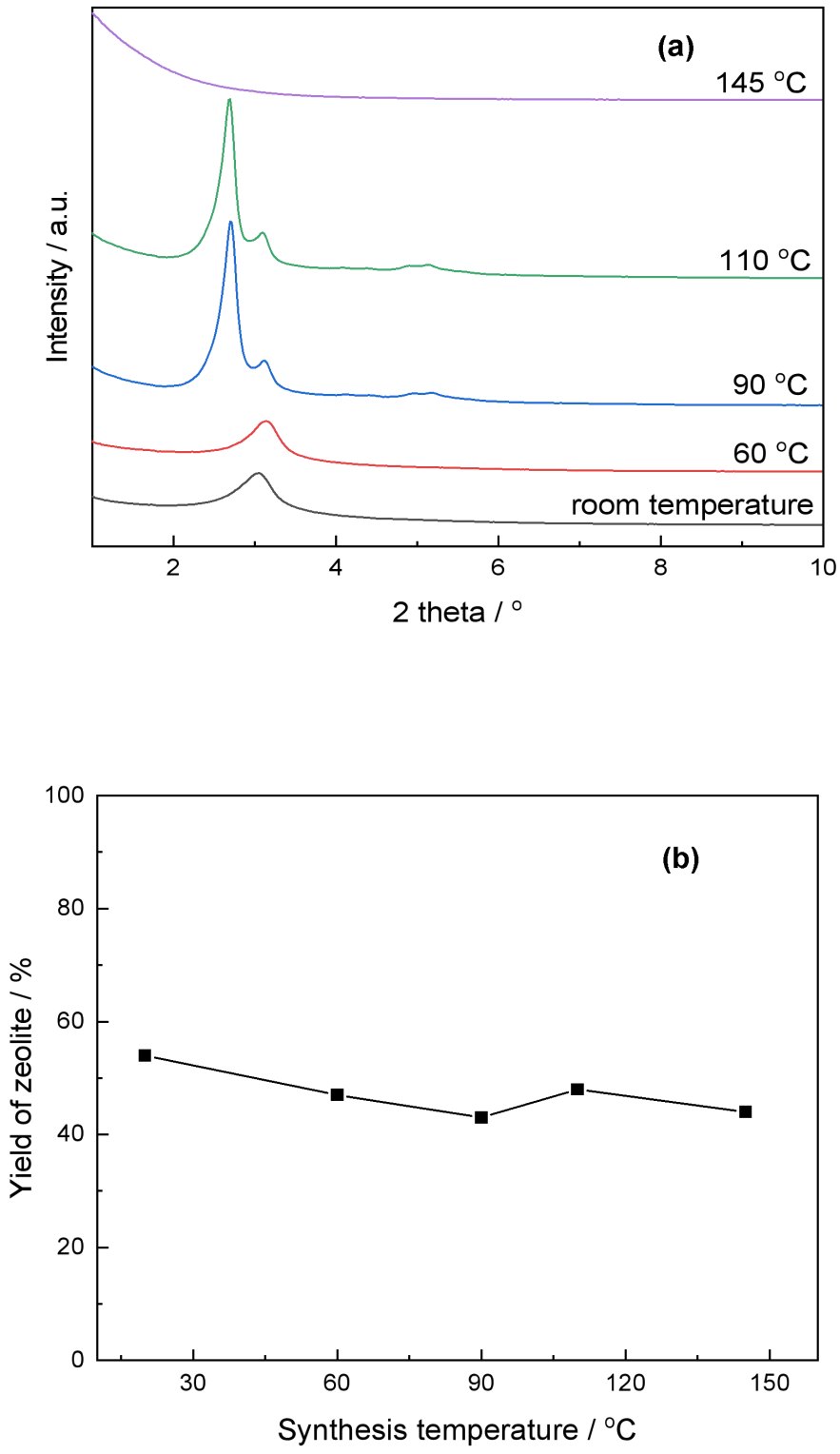

Figure 6.18. a) XRD patterns and b) yields of Cu-MCM-48 with different hydrothermal synthesis temperature (synthesis condition: Si: Cu: CTAB: ethanol: H_2O: H_2SO_4=1: 0.0073: 0.2: 4.3: 83: 0.1, aging time 3 h, hydrothermal synthesis temperature of 20~145 °C, synthesis time 36 h)

Figure 6.18a presented the XRD patterns of the Cu-MCM-48 samples synthesized at different temperatures (room temperature, 60, 90, 110 and 145 ^{o}C) during 36 hours followed by a post-thermal treatment at 550 ^{o}C to remove the template. The results showed poor-resolved diffraction peaks which are assigned to MCM-41 analogue were obtained after 36 h due to the low synthesis temperature (room temperature and 60 ^{o}C). When the synthesis temperature increased to 90 and 110 ^{o}C, the typical MCM-48 materials were formed as the diffraction characteristic peaks of the cubic phase were all present. Moreover, the intensity of peaks, unit cell parameters (in table 6.6) were almost constant, indicating that the cubic phase of MCM-48 was steadily formed within the temperature of 90-110 ^{o}C. Whereas at higher temperature (145 ^{o}C), MCM-48 mesostructure was not formed, since all the peaks disappeared. This is probably due to the pore structure collapses at high temperatures caused by the poor hydrothermal stability of the mesoporous silica. In addition, the yields of the samples, as shown in figure 6.18b, maintained at around 45% and were insignificantly affected by the hydrothermal synthesis temperature. From the above analysis, it is indicated that the formation of MCM-48 is sensitive to the hydrothermal synthesis temperature and hence the hydrothermal synthesis temperature used in this project is 110 ^{o}C.

6.4.3.2 Hydrothermal synthesis time

As the formation of MCM-48 goes through a transformation of hexagonal phase, the MCM-48 with cubic phase is only a mesophase (a hybrid phase between main phases, which is also called interphase [79]) during the hydrothermal synthesis process. Thus, the hydrothermal synthesis time is an important parameter for the synthesis of MCM-48. In principle, a certain synthesis time should be assured for the transformation of the hexagonal phase to the cubic phase while prolonged time may lead to the destruction of the cubic phase. As a result, the time needed for the hydrothermal process must be adjusted to minimize the production of impurity while also ensure the formation of sufficient desired phase.

The XRD patterns were collected for Cu-MCM-48 samples with synthesis time of 3 h to 168 h (Figure 6.19a). The cubic structure was not well defined when the synthesis time was short (in case of 3 h). The samples produced typical MCM-48 diffractions after a synthesis time of 9 h, and the difference in the regularity of the samples was significant. As shown, the intensity of characteristic peaks of the MCM-48 phase was found to increase with the synthesis time rising from 9 h to 36 h. However, the diffraction peaks of (420) and (332) were not seen in the samples synthesized less than 36 h. The MCM-48 synthesized for 36 h showed the strongest diffraction of (211), and the diffractions of (420) and (332) were all well developed. The cubic mesostructure was stable for 72 h, though the ordering of the samples weakened. This demonstrated that the samples were well synthesized between 36 to 72 h. Prolonged hydrothermal treatment for over 168 h resulted in pore collapse completely.

Moreover, the synthesis time also influenced the unit cell parameter of samples. The (211) peak of the well defined cubic samples was found to shift towards lower 2θ with the rising of synthesis time (in figure 6.19). The calculated unit cell parameters (in table 6.6) of the samples with a synthesis time of 9, 18, 36 and 72 h were 7.83, 7.78, 8.01 and 8.13 nm, respectively, which is in agreement with the literature [80,81] and indicating a positive effects of synthesis time within a certain range on the metal incorporation. The increase of unit cell parameters demonstrated that the substitution of heteroatoms occurs with time, it was also evidenced in table 6.3 since the substituted Cu loading went up from 0.0091% (36 h) to 0.077% (72 h) and 0.33% (168 h), respectively. Furthermore, the yield of samples maintained stable when varying the synthesis time, suggesting the dependence of silica output on the composition of the synthesis gel rather than on the hydrothermal conditions.

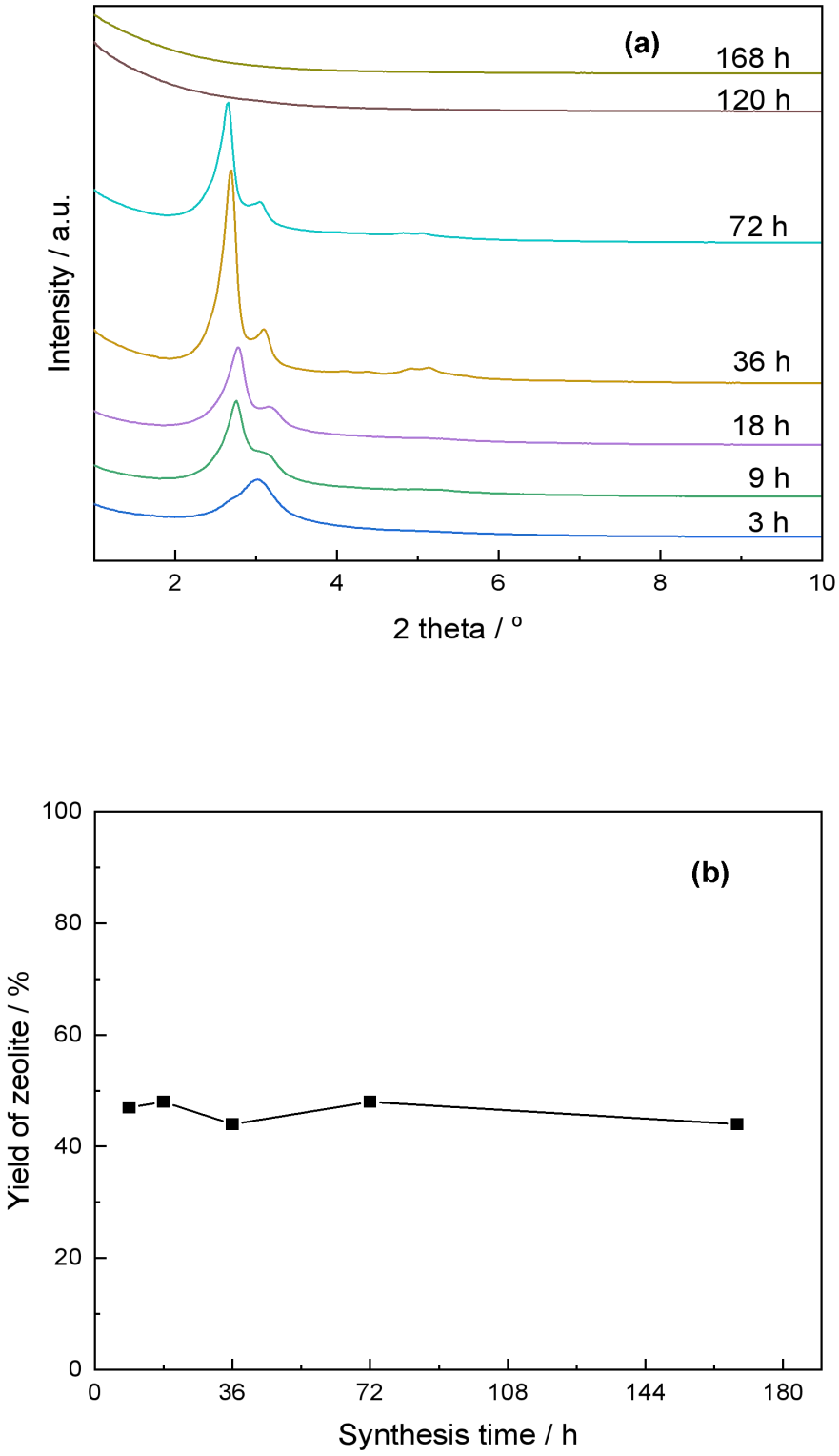

Figure 6.19. a) XRD patterns of and b) yields of Cu-MCM-48 catalysts with different synthesis time (synthesis condition: Si: Cu: CTAB: ethanol: H_2O: H_2SO_4=1: 0.0073: 0.2: 4.3: 83: 0.1, aging time 3 h, hydrothermal synthesis temperature 110 °C, synthesis time 3~168 h)

To sum up, the temperature adversely interacts with the hydrothermal time of the synthesis gel due to the intermediate nature of the MCM-48 material. This means that when moving from higher levels of both temperature and time simultaneously (for example, 145 °C for 36 h), there is no MCM-48 structure formation. Therefore, for high-temperature synthesis, the reaction time should be reduced to form the material structure. While in the synthesis performed at lower temperatures, a longer hydrothermal synthesis time should be assured. On the other hand, a higher temperature and longer synthesis time both improved the metal substitution positively. Therefore, the hydrothermal synthesis temperature of 110 °C and synthesis time of 72 h are optimal in this study in consideration of the balance between the higher regularity and the higher metal substitution.

6.4.4 Effects of calcination temperature on the removal of organic template

Calcination in air at high temperature (typically > 500 ^{o}C) is the most common method used for template removal [82]. The calcination process especially the calcination temperature has a huge impact on the porous structure. In principle, the calcination temperature should be higher than the decomposition temperature of the organic template (> 235 ^{o}C for CTAB [83]), whereas calcination temperature higher than 750 ^{o}C may lead to the collapse of the cubic structure [84]. Hence the appropriate temperature for CTAB removal has to be studied to completely remove the organic molecules and to protect the frameworks from being destroyed.

The mesoporous Cu-MCM-48 silica prepared under 110 ^{o}C for 72 h was calcined at different temperatures (350-650 ^{o}C) and assessed by FTIR-ATR (figure 6.20). The CTAB template was completely removed at temperature over 350 ^{o}C, as the bands of CTAB all disappeared in the spectra. Besides, the weight losses of the as-synthesized Cu-MCM-48 samples were stable at around 50% after calcination, which confirmed the above conclusions.

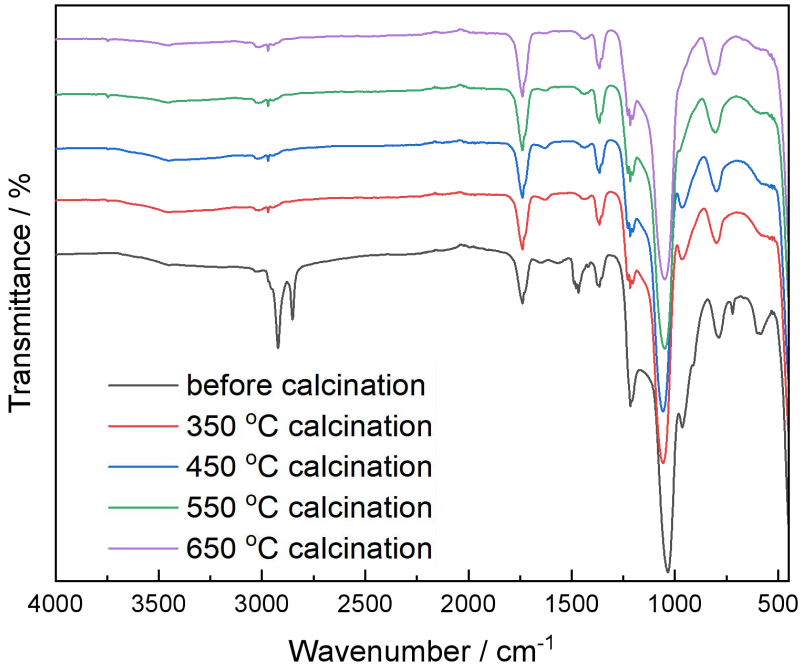

Figure 6.20. FTIR spectra of Cu-MCM-48 catalysts with different calcination temperatures (synthesis condition: Si: Cu: CTAB: ethanol: H_2O: H_2SO_4=1: 0.0073: 0.2: 4.3: 83: 0.1, aging time of 3 h, hydrothermal synthesis temperature 110 °C, synthesis time 72 h)

In addition, the structural ordering of the calcined samples was assessed by powder XRD, as shown in figure 6.21. All the Cu-MCM-48 silica kept their cubic structure after calcination, as all the samples showed two intense diffraction peaks, which correspond to the planes (211) and (220) that can be indexed to cubic structure of MCM-48. It is consistent with the literature [84] that the cubic mesoporous material is thermally stable at no more than 750 °C. It should be noted that, even though the structure well maintained, the intensities of the d211 peak and the d-spacing values (see table 6.6) of different samples varied, suggesting the effects of calcination temperature on the ordering and the structure of the material. The sample calcined at 550 °C exhibited the highest peak intensity which is because a higher calcination temperature promotes the silica condensation and prevents greater shrinkage of the mesostructure. The a_0 of the samples decreased with the rising of calcination temperature,

which is due to the shrinkage of material structure during template removal [46,85,86]. The intensity of the diffraction peaks dramatically reduced when further raising the temperature to 650 °C, indicating the optimal calcination temperature of the synthesized MCM-48 is 550 °C.

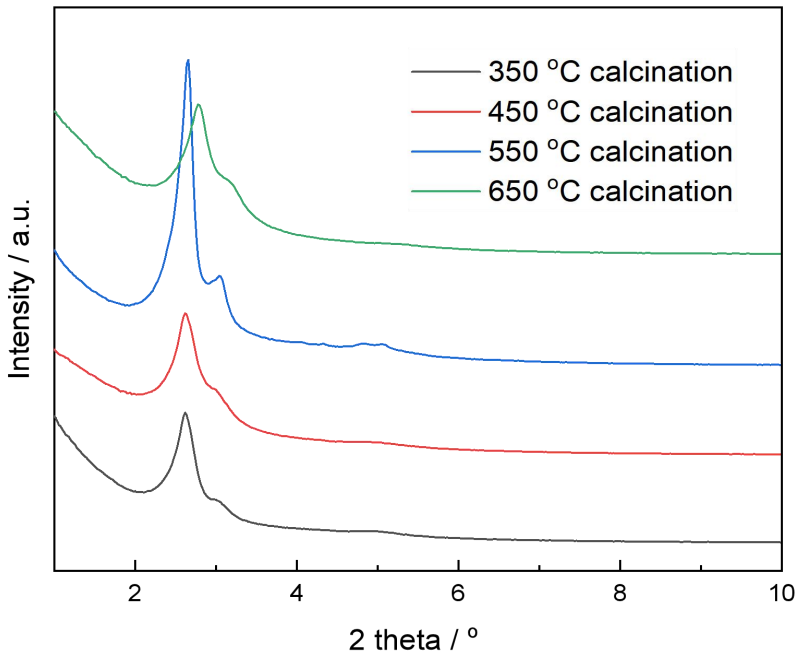

Figure 6.21. XRD patterns of Cu-MCM-48 catalysts with different calcination temperatures (synthesis condition: Si: Cu: CTAB: ethanol: H_2O: H_2SO_4=1: 0.0073: 0.2: 4.3: 83: 0.1, aging time 3 h, hydrothermal synthesis temperature 110 °C, synthesis time 72 h)

6.5 Conclusions

A hydrothermal synthesis method for Cu-MCM-48 preparation has been developed using sodium silicate (Na_2SiO_3) as silica source, copper nitrate ($Cu(NO_3)_2$) as metal precursor, CTAB ($C_{19}H_{42}BrN$) as template. The synthesized sample presented regular ordering, high phase purity, high surface area and uniform pore size, however, it also suffered from low yield (< 50%), low metal incorporation into the framework thus the synthesis parameters were optimized. To this scope, the use of a sufficient amount of surfactant is crucial for the MCM-48 formation and the least CTAB/Si ratio is 0.1. Increasing water content resulted in the obvious rise in yield without loss of quality. In addition, the cubic phase was more likely to be

formed when ethanol was used in the preparation procedure, whereas an MCM-41 alike phase was obtained when using methanol and isopropanol instead. The alkalinity of the synthesis gel had the most significant influence on the synthesis. On the one hand, it controlled the type of phases of the synthesized materials as MCM-41 and MCM-48 were obtained at pH of 10.2 and 11.6-11.9, respectively. On the other hand, the increase of both the yield (57%) and the metal incorporation (0.0091% substituted Cu loading) of Cu-MCM-48 were achieved when lowering the synthesis pH from 11.9 (44% yield, 0.054% Cu sustitution loading) to 11.6, respectively. Moreover, the synthesis of mesoporous materials was found to be very sensitive to hydrothermal conditions, whereas highly ordered MCM-48 could be acquired at 90-110 ^{o}C for 18-72 h. Throughout the optimization process, the highest yield of MCM-48 reached around 70% while the highest metal loading of heteroatom achieved 0.36%.

6.6 References

[1]. K. Schumacher, C. D. F. V. Hohenesche, K. K. Unger, R. Ulrich, A. D. Chesne, U. Wiesner and H. W. Spiess, *Adv Mater*, 1999, **11**, 1194-1198.

[2]. Y. Shao, L. Wang, J. Zhang and M. Anpo, *J Phys Chem B*, 2005, **109**, 20835-20841.

[3]. Y. KONG, X. XU, Y. WU, R. ZHANG and J. WANG, *Chinese J Catal*, 2008, **29**, 385-390.

[4]. C. T. Kresge, M. E. Leonowicz, W. J. Roth, J. C. Vartuli and J. S. Beck, *Nature*, 1992, **359**, 710-712.

[5]. J. S. Beck, J. C. Vartuli, W. J. Roth, M. E. Leonowicz, C. T. Kresge, K. D. Schmitt, C. Chu, D. H. Olson, E. W. Sheppard and S. B. McCullen, *J Am Chem Soc*, 1992, **114**, 10834-10843.

[6]. H. S. Kibombo, V. Balasanthiran, C. Wu, R. Peng and R. T. Koodali, *Micropor Mesopor Mat*, 2014, **198**, 1-8.

[7]. K. Schumacher, P. I. Ravikovitch, A. Du Chesne, A. V. Neimark and K. K. Unger, *Langmuir*, 2000, **16**, 4648-4654.

[8]. H. I. Meléndez-Ortiz, Y. A. Perera-Mercado, L. A. García-Cerda, J. A. Mercado-Silva and G. Castruita, *Ceram Int*, 2014, **40**, 4155-4161.

[9]. U. S. Taralkar, M. W. Kasture and P. N. Joshi, *J Phys Chem Solids*, 2008, **69**, 2075-2081.

[10]. M. Anpo, H. Yamashita, K. Ikeue, Y. Fujii, S. G. Zhang, Y. Ichihashi, D. R. Park, Y. Suzuki, K. Koyano and T. Tatsumi, *Catal Today*, 1998, **44**, 327-332.

[11]. A. Sakthivel, S. E. Dapurkar and P. Selvam, *Catal Lett*, 2001, **77**, 155-158.

[12]. T. Kim, P. Chung and V. S. Lin, *Chem Mater*, 2010, **22**, 5093-5104.

[13]. T. Kim, F. Kleitz, B. Paul and R. Ryoo, *J Am Chem Soc*, 2005, **127**, 7601-7610.

[14]. S. Yismaw, R. Kohns, D. Schneider, D. Poppitz, S. G. Ebbinghaus, R. Gläser, U. Tallarek and D. Enke, *J Nanopart Res*, 2019, **21**, 1-13.

[15]. J. Xu, Z. Luan, H. He, W. Zhou and L. Kevan, *Chem Mater*, 1998, **10**, 3690-3698.

[16]. O. Collart, P. Van Der Voort, E. F. Vansant, D. Desplantier, A. Galarneau, F. Di Renzo and F. Fajula, *J Phys Chem B*, 2001, **105**, 12771-12777.

[17]. M. Shaban, M. R. Abukhadra, A. Hamd, R. R. Amin and A. A. Khalek, *J Environ Manage*, 2017, **204**, 189-199.

[18]. K. W. Gallis and C. C. Landry, *Chem Mater*, 1997, **9**, 2035-2038.

[19]. A. A. Romero, M. D. Alba, W. Zhou and J. Klinowski, *J Phys Chem B*, 1997, **101**, 5294-5300.

[20]. R. Ryoo, S. H. Joo and J. M. Kim, *J Phys Chem B*, 1999, **103**, 7435-7440.

[21]. I. Díaz, J. Pérez-Pariente and O. Terasaki, *J Mater Chem*, 2004, **14**, 48-53.

[22]. K. Zhang, E. H. Yuan, L. L. Xu, Q. S. Xue, C. Luo, B. Albela and L. Bonneviot, *Eur J Inorg Chem*, 2012, **2012**, 4183-4189.

[23]. A. Sayari, *J Am Chem Soc*, 2000, **122**, 6504-6505.

[24]. J. Shan, L. Chen, L. Sun and X. Liu, *Energ Fuel*, 2011, **25**, 3093-3099.

[25]. L. CHEN and X. LIU, *Chinese J Chem Eng*, 2008, **16**, 570-574.

[26]. Y. Ding, A. Kong, H. Zhang, H. Shen, Z. Sun, S. D. Huang and Y. Shan, *Appl Catal A-Gen*, 2013, **455**, 58-64.

[27]. K. Byrappa and M. Yoshimura, *Handbook of Hydrothermal Technology, Uniersity of Mysore Manasagangotri, Mysore, India, Apparatus*, 2001, 82-160.

[28]. K. S. Hui and C. Y. H. Chao, *J Hazard Mater*, 2006, **137**, 1135-1148.

[29]. D. Kumar, K. Schumacher, C. du Fresne Von Hohenesche, M. Grün and K. K. Unger, *Colloids and Surfaces A: Physicochem Engi Aspects*, 2001, **187-188**, 109-116.

[30]. Y. Kim, K. Kim and R. Ryoo, *Chem Mater*, 2017, **29**, 1752-1757.

[31]. B. L. Newalkar and S. Komarneni, *Chem Mater*, 2001, **13**, 4573-4579.

[32]. V. Gutierrez, M. Dennehy, A. Diez and M. A. Volpe, *Appl Catal A-Gen*, 2012, **437**, 72-78.

[33]. V. S. Gutiérrez, A. S. Diez, M. Dennehy and M. A. Volpe, *Micropor Mesopor Mat*, 2011, **141**, 207-213.

[34]. F. Chen, F. Song and Q. Li, *Micropor Mesopor Mat*, 1999, **29**, 305-310.

[35]. A. M. Doyle, E. Ahmed and B. K. Hodnett, *Catal Today*, 2006, **116**, 50-55.

[36]. F. Tavakoli, M. Mamaghani and M. Sheykhan, *Appl Organomet Chem*, 2019, **33**, e5083.

[37]. W. Zhao, Q. Li, L. Wang, J. Chu, J. Qu, S. Li and T. Qi, *Langmuir*, 2010, **26**, 6982-6988.

[38]. V. Zeleňák, D. Halamová, M. Almáši, L. Žid, A. Zeleňáková and O. Kapusta, *Appl Surf Sci*, 2018, **443**, 525-534.

[39]. M. Zhang, W. Luo, Z. Li, T. Yu and Z. Zou, *Appl Phys Lett*, 2010, **97**, 42105.

[40]. A. A. El-Bayaa, N. A. Badawy and E. A. AlKhalik, *J Hazard Mater*, 2009, **170**, 1204-1209.

[41]. W. Qian, H. Wang, J. Chen and Y. Kong, *Materials*, 2015, **8**, 1752-1765.

[42]. D. Zhao, S. Budhi, A. Rodriguez and R. T. Koodali, *Int J Hydrogen Energ*, 2010, **35**, 5276-5283.

[43]. T. Jiang, D. Wu, J. Song, X. Zhou, Q. Zhao, M. Ji and H. Yin, *Powder Technol*, 2011, **207**, 422-427.

[44]. R. Longloilert, T. Chaisuwan, A. Luengnaruemitchai and S. Wongkasemjit, *J Sol-Gel Sci Techn*, 2012, **61**, 133-143.

[45]. W. Zhang and T. J. Pinnavaia, *Catal Lett*, 1996, **38**, 261-265.

[46]. H. Kosslick, G. Lischke, H. Landmesser, B. Parlitz, W. Storek and R. Fricke, *J Catal*, 1998, **176**, 102-114.

[47]. M. Mureseanu, M. Filip, S. Somacescu, A. Baran, G. Carja and V. Parvulescu, *Appl Surf Sci*, 2018, **444**, 235-242.

[48]. H. I. Meléndez-Ortiz, Y. A. Perera-Mercado, L. A. García-Cerda, J. A. Mercado-Silva and G. Castruita, *Ceram Int*, 2014, **40**, 4155-4161.

[49]. U. S. Taralkar, M. W. Kasture and P. N. Joshi, *J Phys Chem Solids*, 2008, **69**, 2075-2081.

[50]. K. Wang, Y. Lin, M. A. Morris and J. D. Holmes, *J Mater Chem*, 2006, **16**, 4051-4057.

[51]. J. Sun and M. Coppens, *J Mater Chem*, 2002, **12**, 3016-3020.

[52]. H. Li, S. Wang, F. Ling and J. Li, *J Mol Catal A-Chem*, 2006, **244**, 33-40.

[53]. G. A. Eimer, L. B. Pierella, G. A. Monti and O. A. Anunziata, *Catal Lett*, 2002, **78**, 65-75.

[54]. M. S. A. Salam, M. A. Betiha, S. A. Shaban, A. M. Elsabagh and R. M. Abd El-Aal, *Egypt J Pet*, 2015, **24**, 49-57.

[55]. G. A. Eimer, L. B. Pierella, G. A. Monti and O. A. Anunziata, *Catal Lett*, 2002, **78**, 65-75.

[56]. A. Derylo-Marczewska, W. Gac, N. Popivnyak, G. Zukocinski and S. Pasieczna, *Catal Today*, 2006, **114**, 293-306.

[57]. Q. Zhao, X. Zhou, M. Ji, H. Ding, T. Jiang, C. Li and H. Yin, *Appl Surf Sci*, 2011, **257**, 2436-2442.

[58]. J. M. Kim and R. Ryoo, *Chem Commun*, 1998, 259-260.

[59]. M. Hartmann, S. Racouchot and C. Bischof, *Micropor Mesopor Mat*, 1999, **27**, 309-320.

[60]. F. Wei, Z. Liu, J. Lu and Z. Liu, *Micropor Mesopor Mat*, 2010, **131**, 224-229.

[61]. L. Luo, Y. Liang, E. S. Erichsen and R. Anwander, *J Colloid Interf Sci*, 2017, **495**, 84-93.

[62]. J. Wang, J. Lu, J. Yang, W. Xiao and J. Wang, *Mater Lett*, 2012, **78**, 199-201.

[63]. K. Byrappa and M. Yoshimura, *Handbook of hydrothermal technology*, William Andrew, 2012.

[64]. S. Wang, D. Wu, Y. Sun and B. Zhong, *Mater Res Bull*, 2001, **36**, 1717-1720.

[65]. W. Zhan, Y. Guo, Y. Wang, X. Liu, Y. Guo, Y. Wang, Z. Zhang and G. Lu, *J Phys Chem B*, 2007, **111**, 12103-12110.

[66]. X. Yang, W. Dai, R. Gao, H. Chen, H. Li, Y. Cao and K. Fan, *J Mol Catal A-Chem*, 2005, **241**, 205-214.

[67]. H. Wang, W. Qian, J. Chen, Y. Wu, X. Xu, J. Wang and Y. Kong, *Rsc Adv*, 2014, **4**, 50832-50839.

[68]. T. W. J. Albrecht, J. Addai-Mensah and D. Fornasiero, *Chemeca 2011: Engineering a Better World: Sydney Hilton Hotel, NSW, Australia, 18-21 September 2011*, 2011, 2100.

[69]. N. Garcia Vargas, S. Stevenson and D. F. Shantz, *Micropor Mesopor Mat*, 2013, **170**, 131-140.

[70]. S. Hitz and R. Prins, *J Catal*, 1997, **168**, 194-206.

[71]. Y. Cesteros and G. L. Haller, *Micropor Mesopor Mat*, 2001, **43**, 171-179.

[72]. H. Parala, H. Winkler, M. Kolbe, A. Wohlfart, R. A. Fischer, R. Schmechel and H. von Seggern, *Adv Mater*, 2000, **12**, 1050-1055.

[73]. M. R. Mello, D. Phanon, G. Q. Silveira, P. L. Llewellyn and C. M. Ronconi, *Micropor Mesopor Mat*, 2011, **143**, 174-179.

[74]. N. Hikichi, K. Iyoki, Y. Naraki, Y. Yanaba, K. Ohara, T. Okubo and T. Wakihara, *Micropor Mesopor Mat*, 2019, **284**, 82-89.

[75]. Y. Wu, X. Ren and J. Wang, *Micropor Mesopor Mat*, 2008, **116**, 386-393.

[76]. B. Wang, J. Wu, Z. Yuan, N. Li and S. Xiang, *Ultrason Sonochem*, 2008, **15**, 334-338.

[77]. A. Á. B. Maia, R. N. Dias, R. S. Angélica and R. F. Neves, *J Mater Res Technol*, 2019, **8**, 2924-2929.

[78]. G. Zhu, Y. Li, H. Chen, J. Liu and W. Yang, *J Mater Sci*, 2008, **43**, 3279-3288.

[79]. P. S. Theocaris, *J Appl Polym Sci*, 1985, **30**, 621-645.

[80]. M. Mathieu, P. Van Der Voort, B. M. Weckhuysen, R. R. Rao, G. Catana, R. A. Schoonheydt and E. F. Vansant, *J Phys Chem B*, 2001, **105**, 3393-3399.

[81]. U. S. Taralkar, P. Kalita, R. Kumar and P. N. Joshi, *Appl Catal A-Gen*, 2009, **358**, 88-94.

[82]. S. Heng, P. P. S. Lau, K. L. Yeung, M. Djafer and J. Schrotter, *J Membrane Sci*, 2004, **243**, 69-78.

[83]. Safety Data Sheet of CTAB, https://www.gbiosciences.com/image/pdfs/msds/DG095_msds.pdf.

[84]. K. Schumacher, M. Grün and K. K. Unger, *Micropor Mesopor Mat*, 1999, **27**, 201-206.

[85]. Y. Zhang, M. Wang, S. Liu, H. Qiu, M. Wang, N. Xu, L. Gao and Y. Zhang, *Sep Purif Technol*, 2019, **228**, 115758.

[86]. W. Zhao, Y. Luo, P. Deng and Q. Li, *Catal Lett*, 2001, **73**, 199-202.

Chapter 7. Catalytic activity of Cu-substituted MCM-48 catalysts prepared by hydrothermal synthesis in the CWPO of phenol

7.1 Overview

Various porous materials are widely reported in the literature as catalysts support (such as MFI [1,2], LTA [3,4], FAU [5,6], BEA [7,8] and MOR [9,10] and so on) for the decomposition of water contaminants due to their large surface area, pore volume and adjustable pore size. Among them, mesoporous materials have attracted increasing interest for the design of heterogeneous catalysts, being an ideal support candidate for the preparation of catalysts as their larger pore size (2-4 nm) allows large molecular reactions (such as phenol with molecular diameter of 0.62 nm [11,12]) to occur within the pores. In particular, the MCM-48 with attractive and unique cubic arrangement of continuous three-dimensional and interwoven structure which can effectively reduce the chances of pore blockage by guest molecules makes it one of most the promising catalytic materials [13,14]. Though the MCM-48 silica has potential for catalysis applications due to its pore size range and shape, it also has a lower activity due to the lack of obvious acid sites that in zeolites are otherwise provided by the presence of Al centres. This factor makes the development of catalytically active mesoporous materials necessary. Bearing this in mind, acidic functions can be introduced by incorporating metals either as extra-framework nanoscale oxide clusters or in their appropriate valence state as tetrahedral framework species [15]. In recent years, studies involving the modification of MCM-48 with active species such as Mn [16,17], Fe [18,19], V [20,21], Co [22,23], Cr [24,25] and the catalytic tests of these materials are increasingly reported.

The catalytic performance of heterogeneous catalysts in the CWPO of phenol reaction is highly sensitive to the interaction mode of metal species and catalyst support, thus the preparation and control of the metal atoms with a more stable chemical environment are decisive to obtain materials with high catalytic stability. Against this background, a series of MCM-48 materials with heteroatom substituted into the silica matrix via the hydrothermal

synthesis method have been reported (as shown in chapter 6). In the synthesis process, the condensation of silicon and metal species around the organic micelles occur simultaneously, thus it is likely that some of the metal species are incorporated in the silica matrix. This method offers advantages like the expansion of unit cell parameter [26-28] and wall thickness [29-31] of the material, which may contribute to a higher metal dispersion and a more stable location of metal species into the framework of silica matrix. Despite the very attractive structure of the MCM-48 with unique channel network, few studies of their modifications using heteroatoms have been employed in the application of phenol oxidation and none, to our knowledge, concerns copper.

Therefore, the aims of this chapter are to: 1) confirm the high activity of the prepared materials, 2) assess the stability of the Cu substituted catalysts, 3) investigate the effects of the synthesis conditions on the performance of the Cu-MCM-48 catalysts and 4) explore the activity, stability and reusability of the Cu species that incorporated into the framework of MCM-48.

7.2 Activity and stability of Cu-substituted MCM-48 catalysts

7.2.1 Control tests - activity of MCM-48 catalysts in the CWPO of phenol

The activity of Cu substituted MCM-48 was evaluated with undoped (commercial and synthesized) MCM-48 as control tests, as shown in figure 7.1. It is clear that the blank mesoporous silica exhibited low activity in both the phenol conversion (< 20%) and the H_2O_2 consumption (< 15%), which was just slightly higher than that without catalyst (phenol conversion 4%, H_2O_2 consumption 7%, see figure 4.4). In addition, the difference between the commercial and synthesized MCM-48 was negligible, confirming the inactivate nature of the pure silica materials to form hydroxyl radicals due to the absence of active sites.

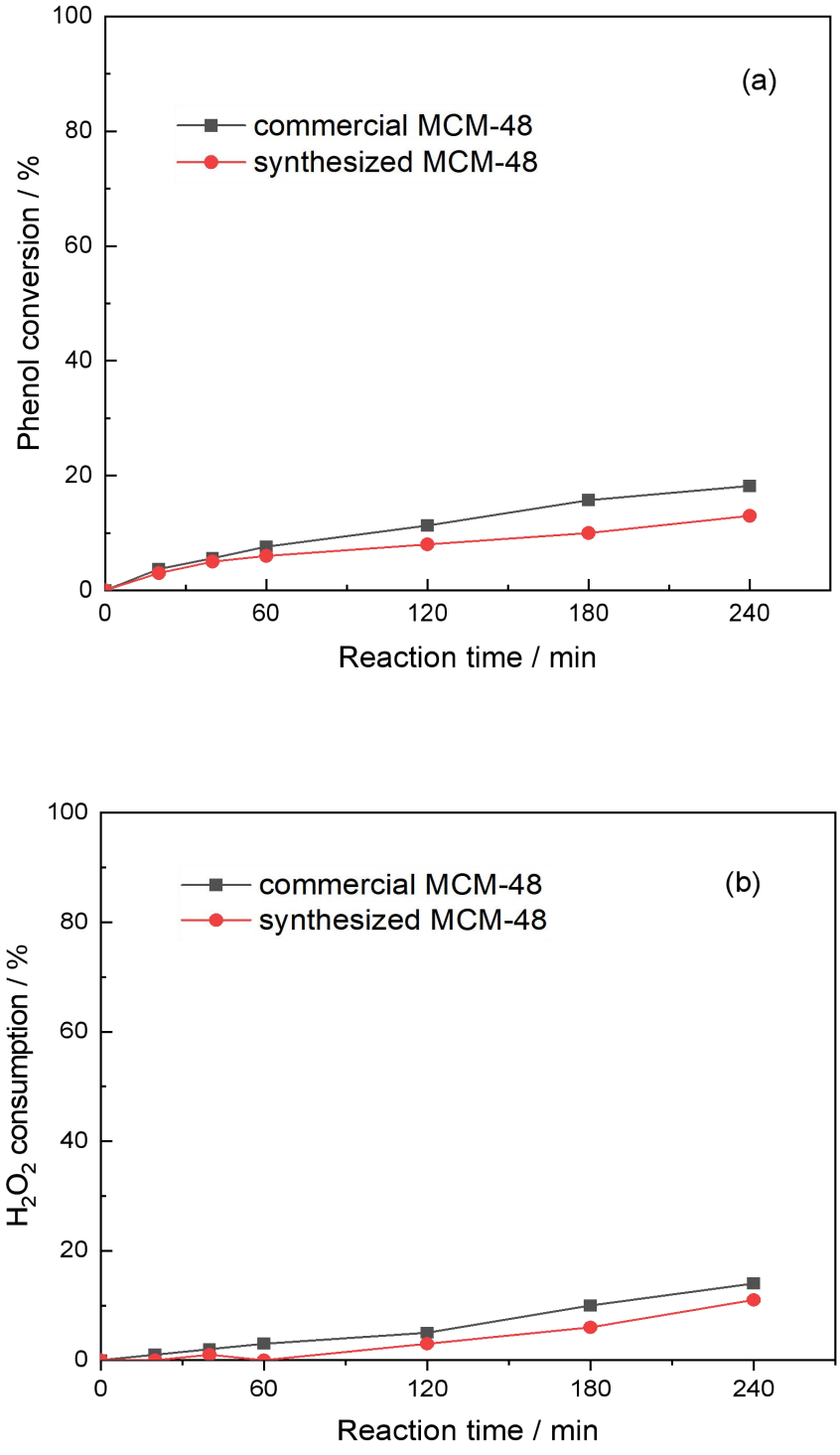

Figure 7.1. a) Phenol conversion and b) H_2O_2 consumption over commercial MCM-48 and synthesized MCM-48 in the CWPO of phenol (Si: CTAB: ethanol: H_2O: H_2SO_4=1: 0.2: 4.3: 83: 0.1, aging time 3 h, hydrothermal synthesis temperature 110 ºC, synthesis time 36 h, calcination at 550 ºC, 6 h)

7.2.2 Activity of Cu-MCM-48 catalyst in the CWPO of phenol

The assessment of the activity of the Cu-MCM-48 catalyst prepared by hydrothermal synthesis in the CWPO of phenol is necessary although the mesostructure was confirmed in chapter 6. In this section, the reference Cu-MCM-48 catalyst with the best structure of ordering, CM-23 (table 6.5 and table 6.6), had high activity in phenol oxidation, as shown in figure 7.2 since a complete phenol degradation was achieved in 20 min, together with high H_2O_2 consumption (82%) and high CO_2 formation (88%), suggesting a strong capability of the catalysts in the generation of hydroxyl radicals. By the way, the CO_2 slightly decreased with time due to the error of the HPLC analysis. Moreover, the aromatic intermediates were completely oxidized to acids with the increase of reaction time to 4 h and most of the organic acids were degraded to CO_2 and H_2O with the further decomposition of H_2O_2, leading to complete H_2O_2 consumption, as well as 90% of CO_2 formation, after 4 h at 80 ^{o}C. As a result, the compounds that remained in the reaction mixture after 4 h were mainly acetic acid (around 2.7×10^{-3} mol·L^{-1}) and malonic acid (7.7×10^{-4} mol·L^{-1}) whereas the concentrations of other intermediates were negligible. The high activity of the catalyst indicated that the Cu-MCM-48 is a promising candidate in the CWPO process with the ability to remove all the toxic organic compounds including phenol and quinones and to achieve high CO_2 selectivity.

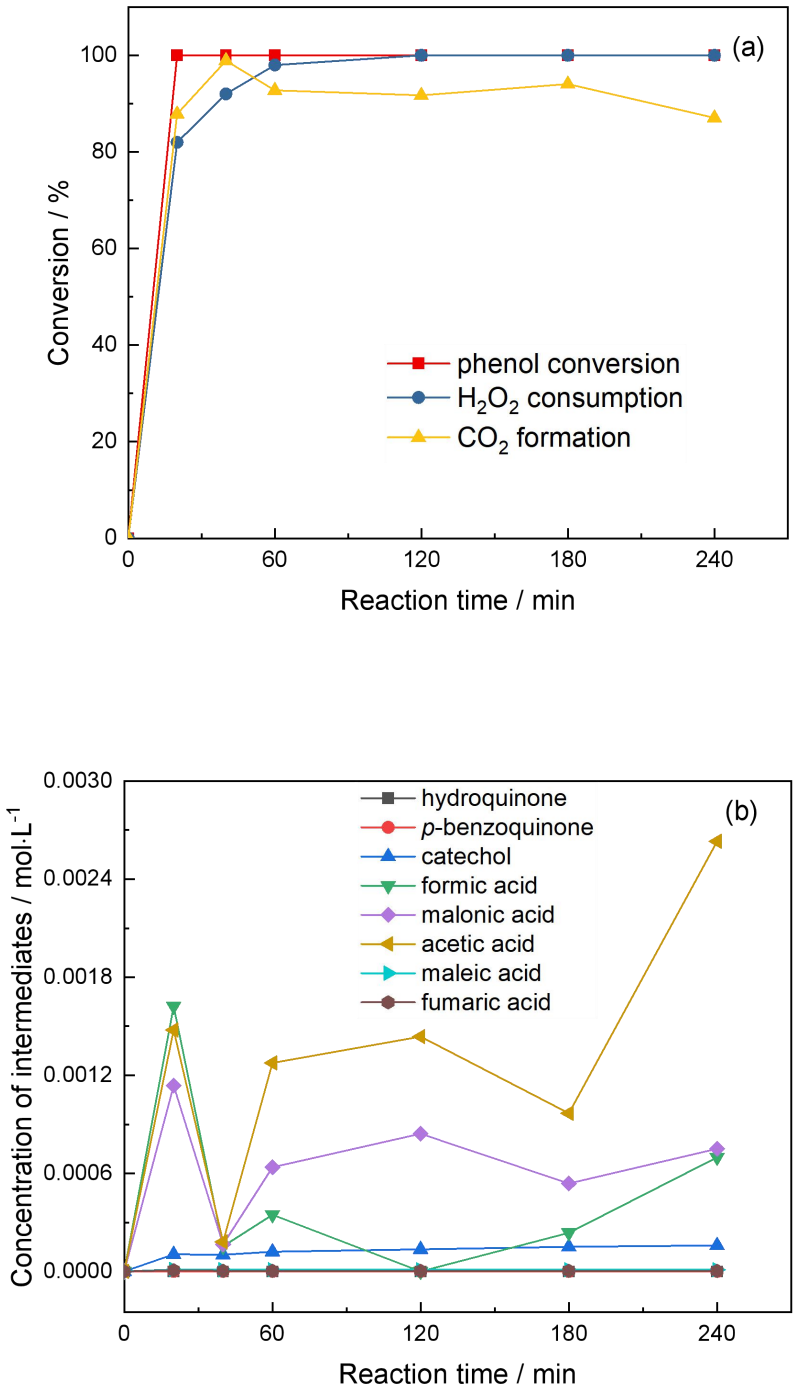

Figure 7.2. Catalytic activity of Cu-MCM-48 in the CWPO of phenol: a) phenol conversion, H_2O_2 consumption and CO_2 formation and b) intermediates concentration (Si: Cu: CTAB: ethanol: H_2O: H_2SO_4=1: 0.0073: 0.2: 4.3: 83: 0.1, aging time 3 h, hydrothermal synthesis temperature 110 ºC, synthesis time 36 h, calcination at 550 ºC, 6 h). CO_2 formation maintained stable within an acceptable error as it is calculated from CMB.

7.2.3 Stability of Cu-MCM-48 in the CWPO of phenol

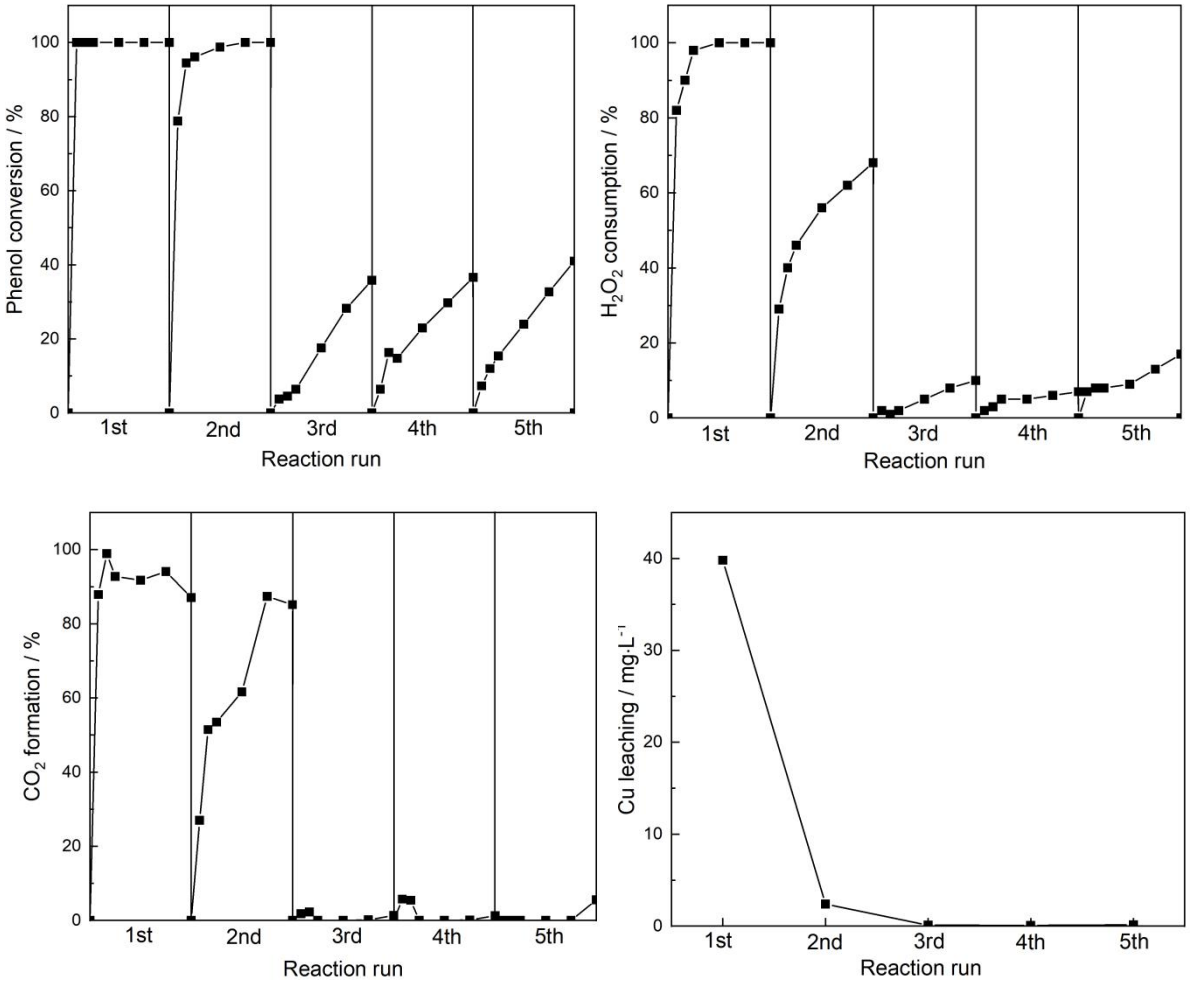

Figure 7.3. Reusability of Cu-MCM-48 in successive runs of reactions in the CWPO of phenol, a) phenol conversion, b) H_2O_2 consumption, c) CO_2 formation and d) Cu leaching (Si: Cu: CTAB: ethanol: H_2O: H_2SO_4=1: 0.0073: 0.2: 4.3: 83: 0.1, aging time 3 h, hydrothermal synthesis temperature 110 ^oC, synthesis time 36 h, calcination at 550 ^oC, 6 h)

Though the high activity of the synthesized Cu-MCM-48 sample was confirmed, it may be caused by the Cu species supported on the surface of the support as the ratio of the heteroatom within the silica matrix was low according to the unit cell parameter (a_0, in table 6.6), FTIR spectra (figure 6.6) and the substituted Cu loading (0.0091%) of the sample. In that case, the activity of the catalyst may decrease after the Cu on the surface leaches out gradually thus the catalyst may deactivate like the Cu catalysts reported in chapter 4 (section 4.5). Due to these analogies, the Cu-MCM-48 catalysts were tested in the CWPO of phenol

reaction in 5 runs of reactions to investigate its stability in terms of reusability and Cu leaching.

As it can be seen in figure 7.3a, the catalyst lost most of its actvity, as the phenol conversion decreased from 100% in the first 2 runs of reaction to 40% in the last 3 runs of reaction, which is due to the leaching of metal on the mesoporous material. In the first run, the complete phenol conversion, high H_2O_2 consumption and CO_2 formation were mainly due to the homogeneous contribution of the leached metal, evidenced by the high Cu concentration (40 $mg \cdot L^{-1}$) in the reaction mixture (figure 7.3d). While in the second run, the activity may be enhanced by the leached Cu (2.4 $mg \cdot L^{-1}$), and after that the Cu-MCM-48 catalyst lost all Cu species on the surface. Thus in the last three runs, the low activity was detected since the low H_2O_2 consumption (12%), low CO_2 formation (close to 0%), were observed. The activity of the heterogeneous catalyst was unsatisfactory which might be attributed to the low metal incorporation into the silica framework, as evidenced in the section 6.3 in chapter 6. Hence, improving the activity of Cu-MCM-48 catalysts by increasing the metal into the framework is necessary in order to increase both the activity and the stability of these materials.

7.3 Improvements of the activity of Cu-MCM-48 catalysts

Following the data reported in chapter 6, the Cu-MCM-48 samples with higher unit cell parameter (a_0, see table 6.6) were selected and tested because they are more likely to have higher percentage of metal substitution (ranging from 0.0091% to 0.36%).

7.3.1 Varying calcination temperature

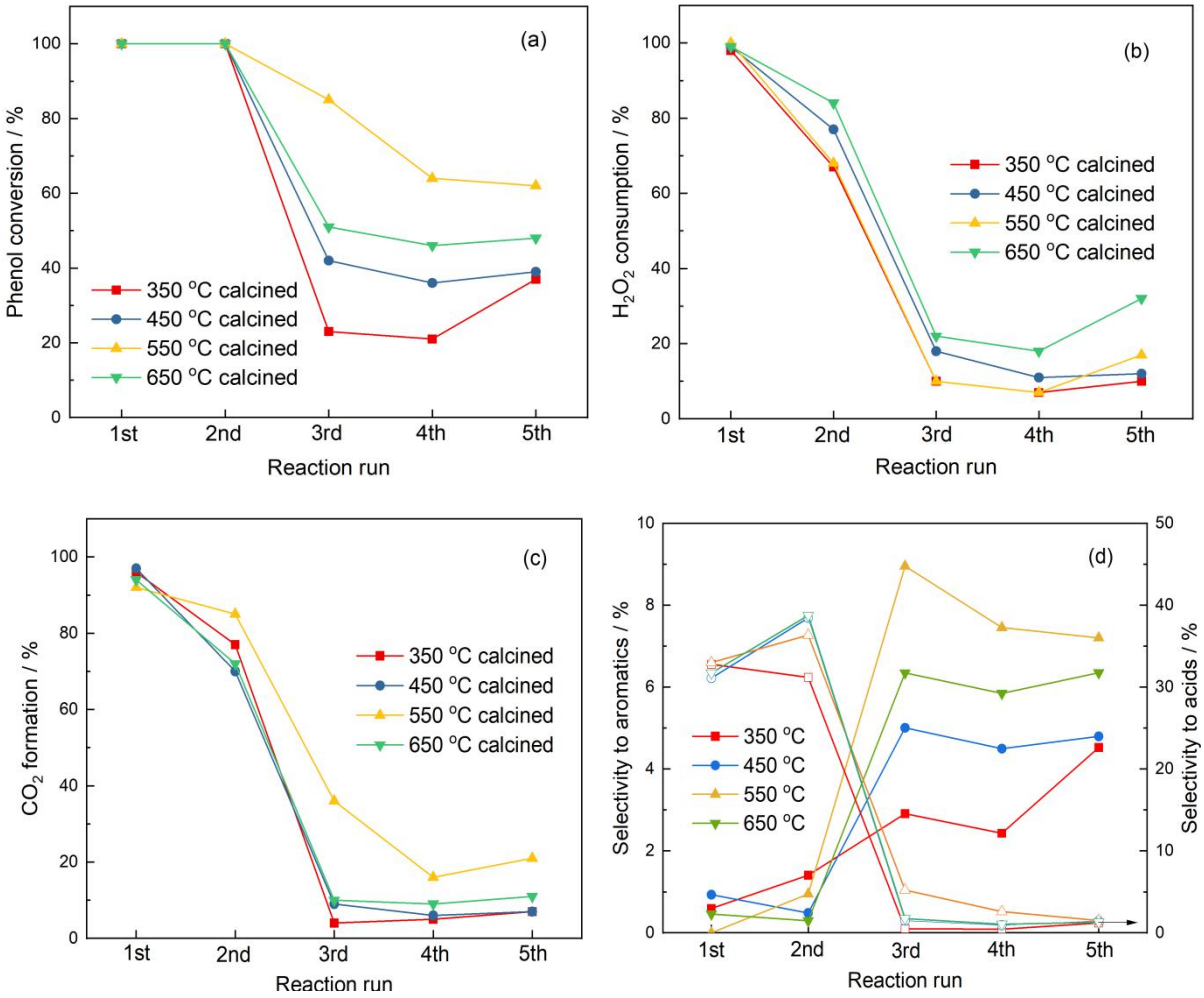

Figure 7.4. Reusability of Cu-MCM-48 with different calcination temperature in successive runs of reactions in the CWPO of phenol, a) phenol conversion, b) H_2O_2 consumption, c) CO_2 formation and d) intermediates selectivity (Si: Cu: CTAB: ethanol: H_2O: H_2SO_4=1: 0.0073: 0.2: 4.3: 83: 0.1, aging time 3 h, hydrothermal synthesis temperature 110 °C, synthesis time 72 h, calcination at 350~650 °C 6 h)

The unit cell parameters (a_0, the centre-to-centre pore distance) of the Cu-MCM-48 samples decreased from 8.25 nm to 7.78 nm when rising the calcination temperatures from 350 to 650 °C (calcined after hydrothermal synthesis), as displayed in table 6.6, implying that the samples may present different activities due to their different metal substitution ratios. However, the activity of the Cu-MCM-48 catalysts which is inconsistent with the change of a_0 since the phenol conversion of the catalyst followed the order: Cu-MCM-48 (550 °C) >

Cu-MCM-48 (650 °C) > Cu-MCM-48 (450 °C) > Cu-MCM-48 (350 °C). The results are contrary to expectation which is because that the change of unit cell parameter a_0 of the MCM-48 is influenced mainly by two reasons: i) metal incorporation into the silica framework [26-28] or ii) the shrinkage of material structure during the removal of organic template [26,32]. In this case, the change of unit cell parameter a_0 (from 8.25 nm to 7.78) with calcination temperature (from 350 to 650 °C) is caused by the second reason. This indicates that the unit cell parameter a_0 can be used as evidence of metal incorporation only when the Cu-MCM-48 samples were calcined at the same temperature and this is also one of the reasons for maintaining the calcination process (550 °C, 6 h) the same in both the catalyst activation process and regeneration process. Moreover, the activity of the catalyst calcined at 550 °C gave the highest activity, which is probably because it achieved the balance between the removal of the organic template (CTAB) and the maintaining of pore structure of the sample.

7.3.2 Varying hydrothermal synthesis temperature

The Cu-MCM-48 catalysts synthesized at different hydrothermal synthesis temperatures, showed very different unit cell parameter a_0 (table 6.6), suggesting that the metal incorporation into the framework is affected by the hydrothermal conditions. The Cu-MCM-48 synthesized at 145 °C, as shown in figure 7.5, presented higher activity in from the 3rd run of reactions since the phenol conversion (69%) and H_2O_2 consumption (50%) both improved by approximately 30% than that synthesized at 110 °C (36% and 10% respectively), indicating that the higher synthesis temperature improves the stability of the catalyst. This behaviour is possibly due to an increased metal incorporation with temperature, as deduced from the increased unit cell parameter a_0 (in table 6.6) of samples with higher hydrothermal synthesis temperatures. Furthermore, the pore of the material synthesized at 145 °C collapsed, as proved in figure 6.18a, thus it may indicate that not only the ordered structure but the heteroatom loading of the Cu-MCM-48 catalysts makes difference in the CWPO of phenol.

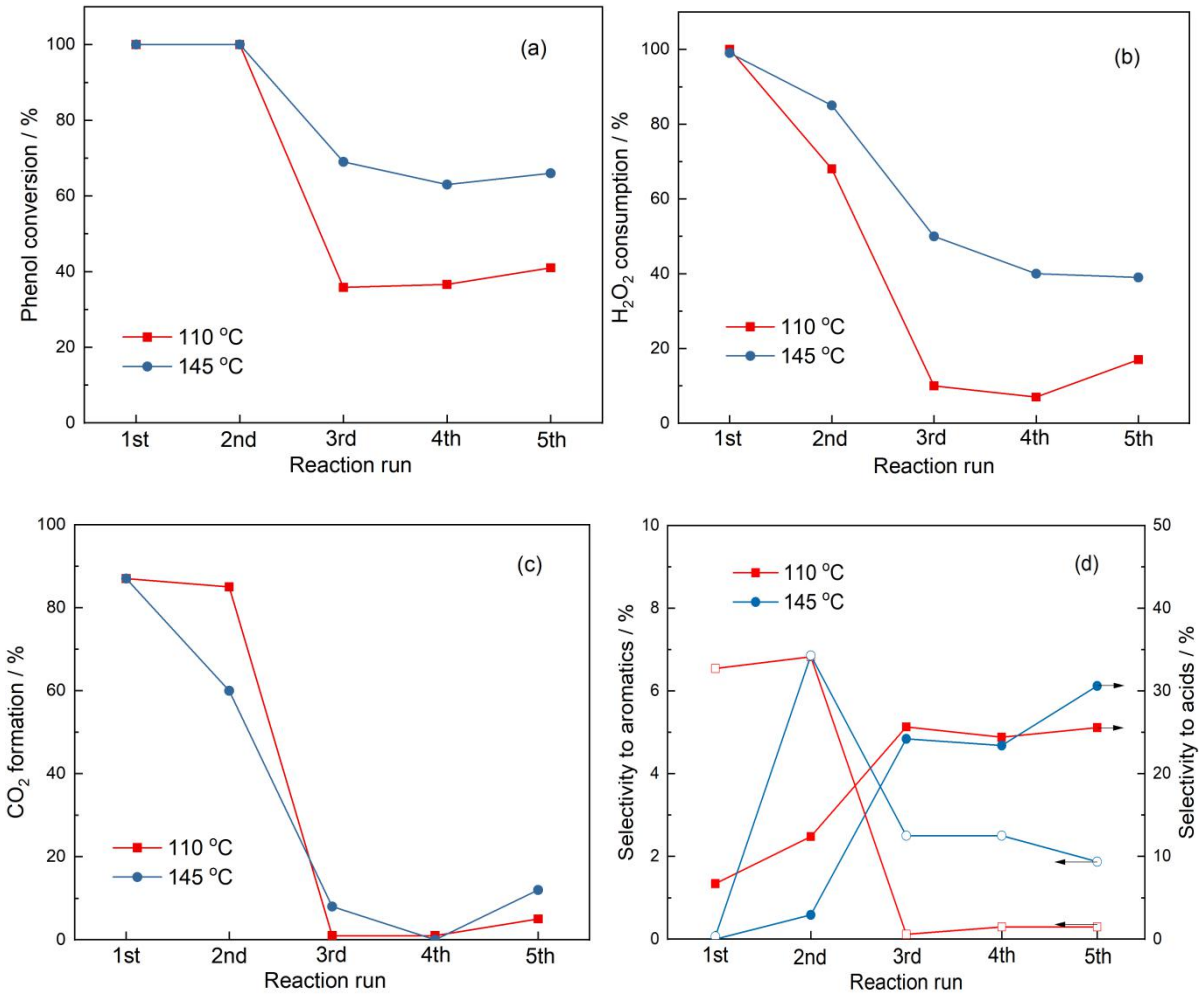

Figure 7.5. Reusability of Cu-MCM-48 with different hydrothermal synthesis temperatures in successive runs of reactions in the CWPO of phenol, a) phenol conversion, b) H_2O_2 consumption, c) CO_2 formation and d) intermediates selectivity (Si: Cu: CTAB: ethanol: H_2O: H_2SO_4=1: 0.0073: 0.2: 4.3: 83: 0.1, aging time 3 h, hydrothermal synthesis temperature 110 and 145 °C, synthesis time 36 h, calcination at 550 °C, 6 h)

7.3.3 Varying synthesis time

Except for the hydrothermal synthesis temperature, the synthesis time also dramatically affected the unit cell parameter a_0 and the heteroatom loading, as indicated in table 6.6 and table 6.3. The catalyst with longer synthesis time presented larger d_{211} and bigger a_0, indicating that a higher metal incorporation can be achieved from longer synthesis time. In particular, the samples with synthesis time of 36 and 72 h had unit cell parameters of 8.01 nm and 8.13 nm and substituted metal loading of 0.0091% and 0.077%, respectively, and these

were considered for catalytic testing as they were supposed to have higher loading of heteroatom. It should also be noted that a high heteroatom loading of 0.33% (table 6.3) was achieved when extending synthesis time to 168 h in this study, hence the sample at 168 h, though suffered pore collapse, was also explored.

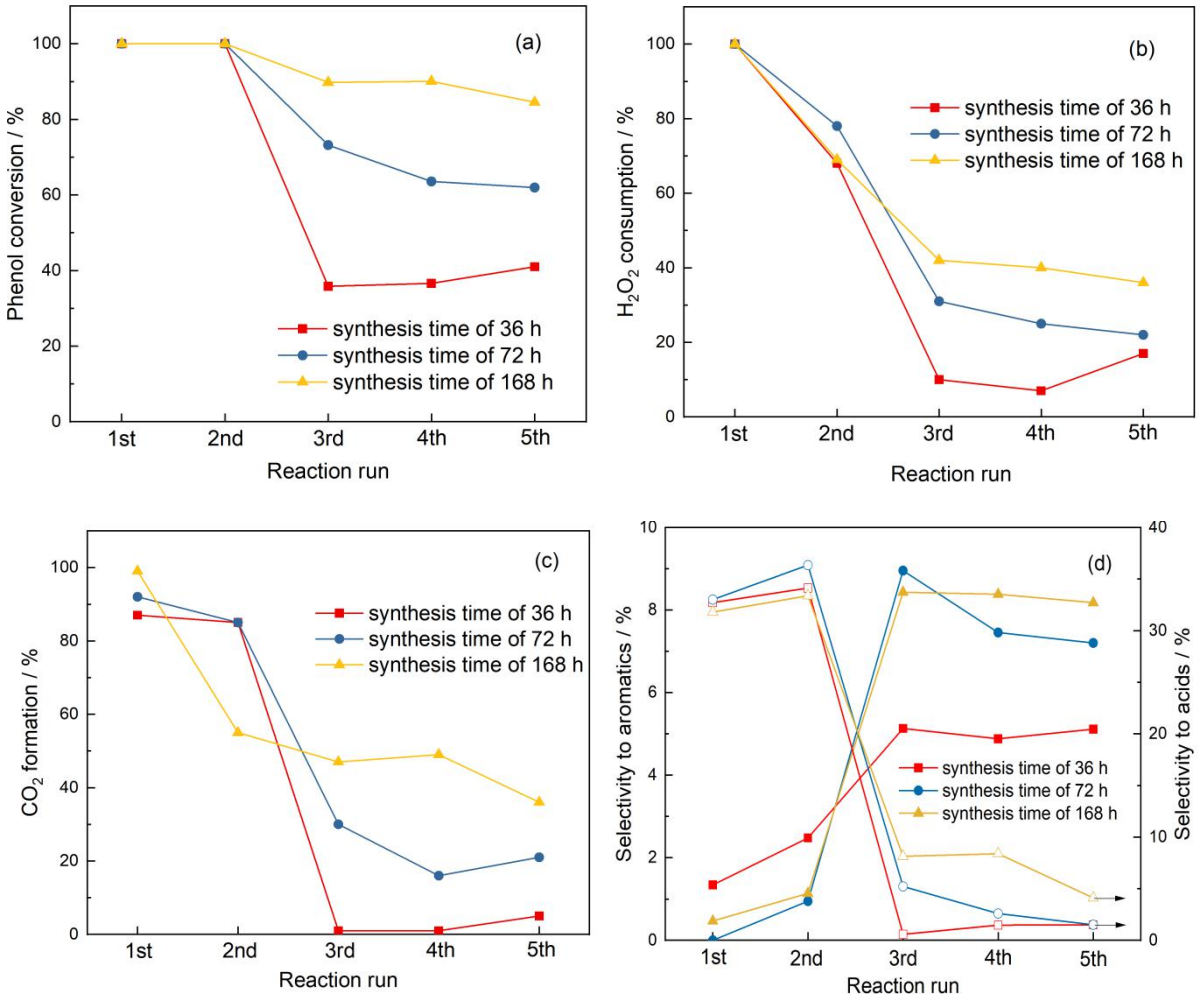

Figure 7.6 Reusability of Cu-MCM-48 with different synthesis time in successive runs of reactions in the CWPO of phenol, a) phenol conversion, b) H_2O_2 consumption, c) CO_2 formation and d) intermediates selectivity (Si: Cu: CTAB: ethanol: H_2O: H_2SO_4=1: 0.0073: 0.2: 4.3: 83: 0.1, aging time 3 h, hydrothermal synthesis temperature 110 ^oC, synthesis time 36~168 h, calcination at 550 ^oC, 6 h)

By analysing the catalytic results from the catalysts synthesized at 36 h, 72 h and 168 h (figure 7.6), it is possible to observe that the synthesis time affected the activity and stability of the prepared Cu-MCM-48 catalysts greatly. First of all, extending the synthesis time had

positive effects on the stability of the Cu catalyst as the catalyst of 168 h presented over 90% phenol conversion throughout the 5 runs of reaction while the catalyst of 72 h and 36 h had much lower phenol conversions in the fifth run (~70% and 40%, respectively). Meanwhile, although the Cu-MCM-48 catalyst with synthesis time of 168 h, suffered pore structure damage (just like that with temperature of 145 ^{o}C), it nevertheless showed the highest performances among all the Cu-MCM-48 materials tested so far, which confirmed again that except for porous structure, the metal incorporation appears to be the other relevant structural feature dictating the catalytic activity of these materials in phenol decomposition. In addition, the H_2O_2 consumption and the CO_2 formation in the 3rd to the 5th run of reactions increased with synthesis time, which is consistent with the trend of phenol conversions. It should be noted that, the activity of the samples after 2nd run did obey the trend of unit cell parameter a_0, evidencing the feasibility of using the unit cell parameter as an index to assess metal substitution.

7.3.4 Varying synthesis pH

As discussed in chapter 6, the pH of the synthesis gel is a crucial factor for the synthesis of mesopore materials, since it does not only affect the ordering of the uniform structure and the size of the unit cell of the MCM-48 but it also influences the type of the mesotructures (hexagonal or cubic, see table 6.6 and figure 6.12). For this reason, the activity of the Cu samples synthesized at different H_2SO_4/Si ratios was investigated. The Cu-MCM-48 catalyst with the highest synthesis pH (pH of 11.9, figure 7.7), had low activity in the last run of reaction with phenol conversion and H_2O_2 consumption of 41% and 17%, respectively, that is probably because the MCM-48 sample had small unit cell parameter (a_0 of 8.01 nm) and low metal-substitution loading (0.0091%, table 6.3). Whereas the sample with the synthesis pH of 11.6 gave much higher phenol conversion (70%) and H_2O_2 consumption (28%) in the 5th run owing to the higher heteroatom substitution (Cu-substitution loading of 0.054%, see table 6.3), as expected from the higher a_0 value (8.68 nm). However, further increasing the synthesis pH to 10.2 led to the lowest stability of the catalyst with phenol conversion maintained at around

30% after the first run of reaction, which might be explained by the formation of hexagonal MCM-41 rather than MCM-48 whereas the MCM-41 had low Cu loading in the framework (0.012%, see table 6.3).

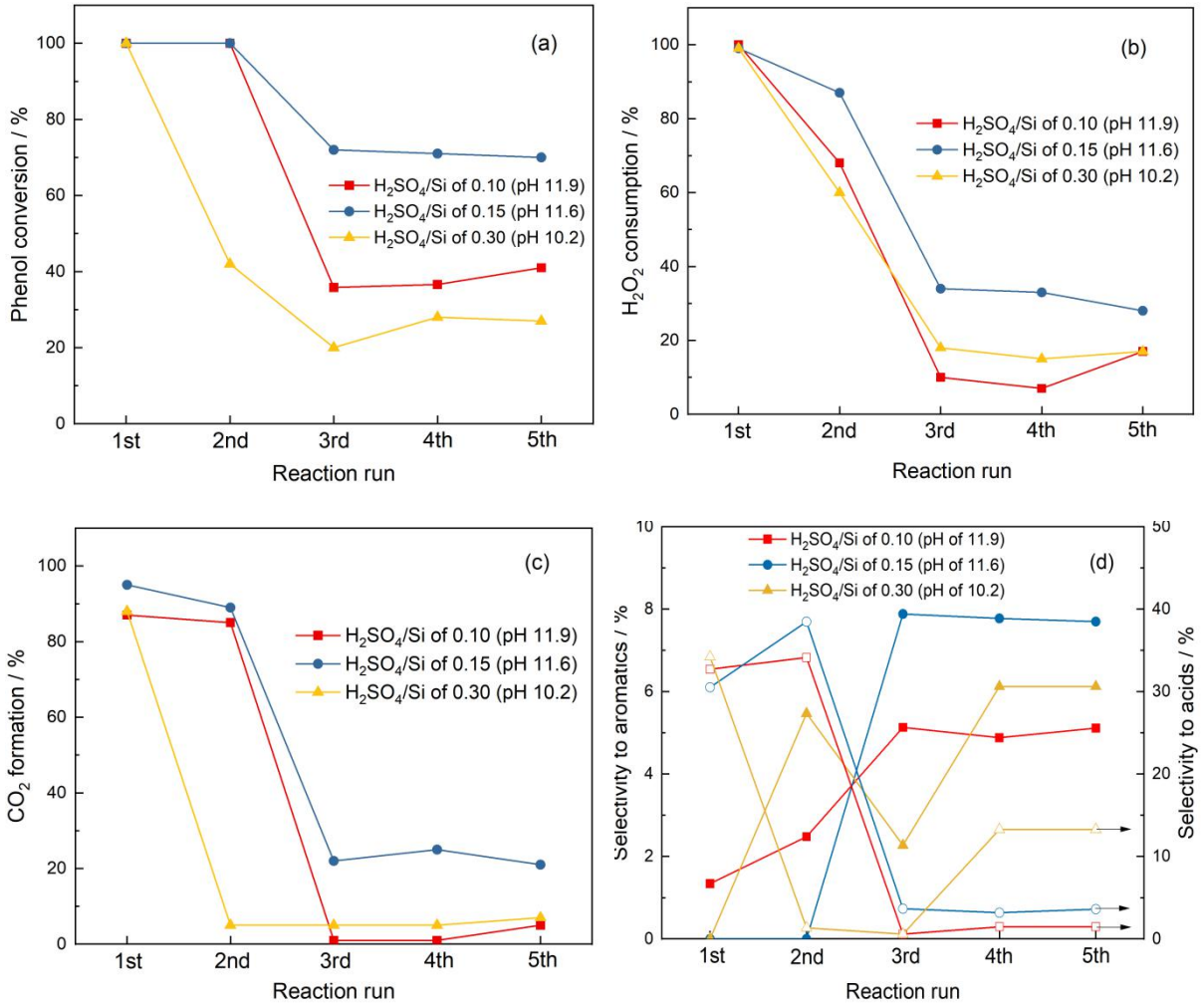

Figure 7.7. Reusability of Cu-MCM-48 with different synthesis pH in successive runs of reactions in the CWPO of phenol , a) phenol conversion, b) H_2O_2 consumption, c) CO_2 formation and d) intermediates selectivity (Si: Cu: CTAB: ethanol: H_2O: H_2SO_4=1: 0.0073: 0.2: 4.3: 83: 0.1~0.3, aging time 3 h, hydrothermal synthesis temperature 110 ^oC, synthesis time 36 h, calcination at 550 ^oC, 6 h)

7.3.5 Varying water content

Increasing the water content from 83 to 249 improved the yield of sample by 50% (figure 6.8b) while it had no obvious effects on the regularity of the ordering (figure 6.8a), unit cell

parameter a_0 (table 6.6,), metal loading (table 6.3) and pore structures of the cubic materials (figure 6.9). This implies that a higher yield of MCM-48 could be achieved for an increased water content without loss of textural properties and performance. As shown in figure 7.8, the Cu-MCM-48 with H_2O/Si ratio of 83 and 249 presented almost completely the same phenol conversion, H_2O_2 consumption and CO_2 formation throughout the 5 runs of the reaction, which means that the water content did not affect the distribution of metal in the framework. Nevertheless, a higher H_2O/Si is recommended in the synthesis of Cu-MCM-48 in this research as it contributes to a higher yield without negative influences being found so far.

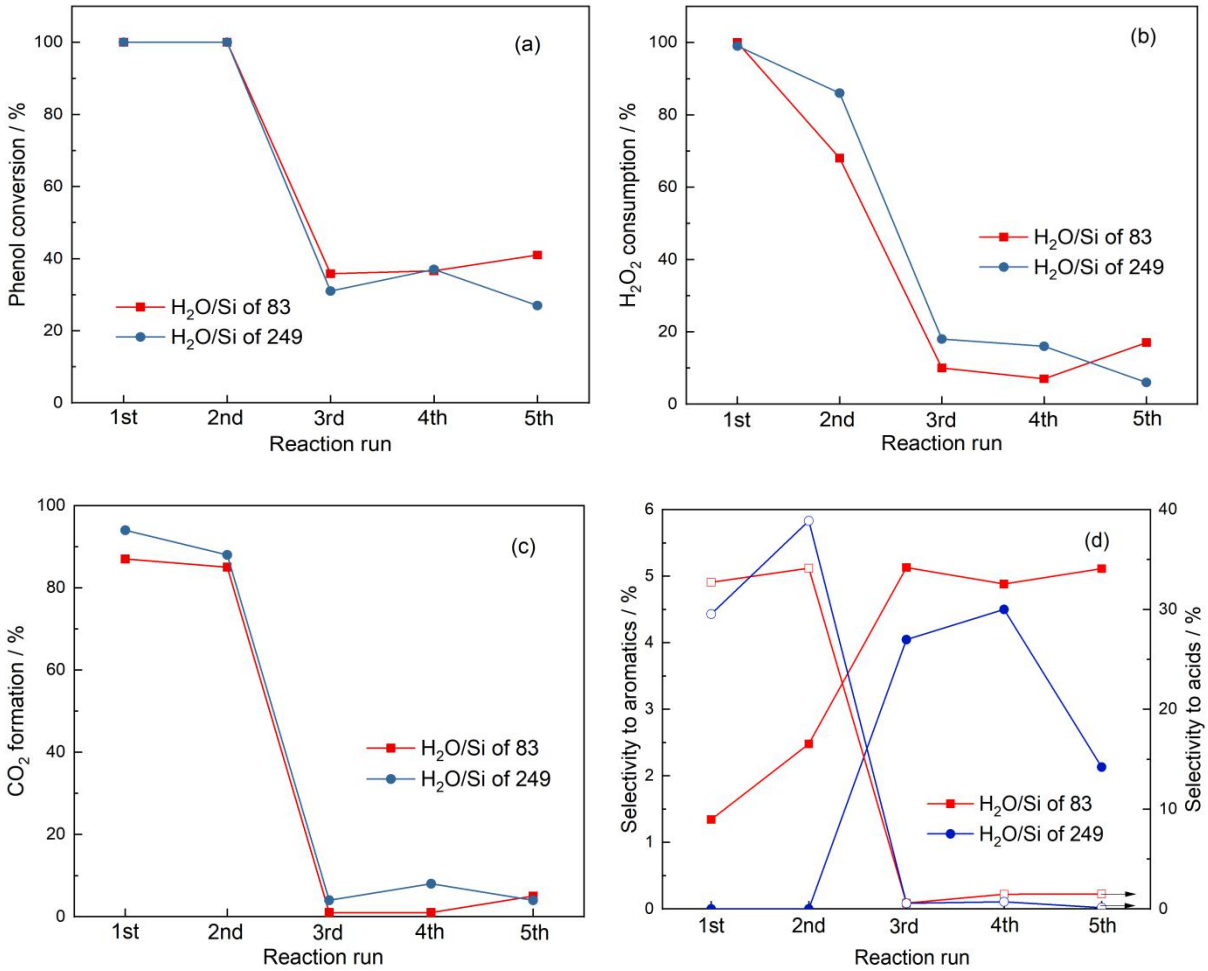

Figure 7.8. Reusability of Cu-MCM-48 with different water content in successive runs of reactions in the CWPO of phenol, a) phenol conversion, b) H_2O_2 consumption, c) CO_2 formation and d) intermediates selectivity (Si: Cu: CTAB: ethanol: H_2O: H_2SO_4=1: 0.0073: 0.2: 4.3: 83 or 249: 0.1, aging time 3 h, hydrothermal synthesis temperature 110 ºC, synthesis time 36 h, calcination at 550 ºC, 6 h)

7.3.6 Varying Si/Cu ratio

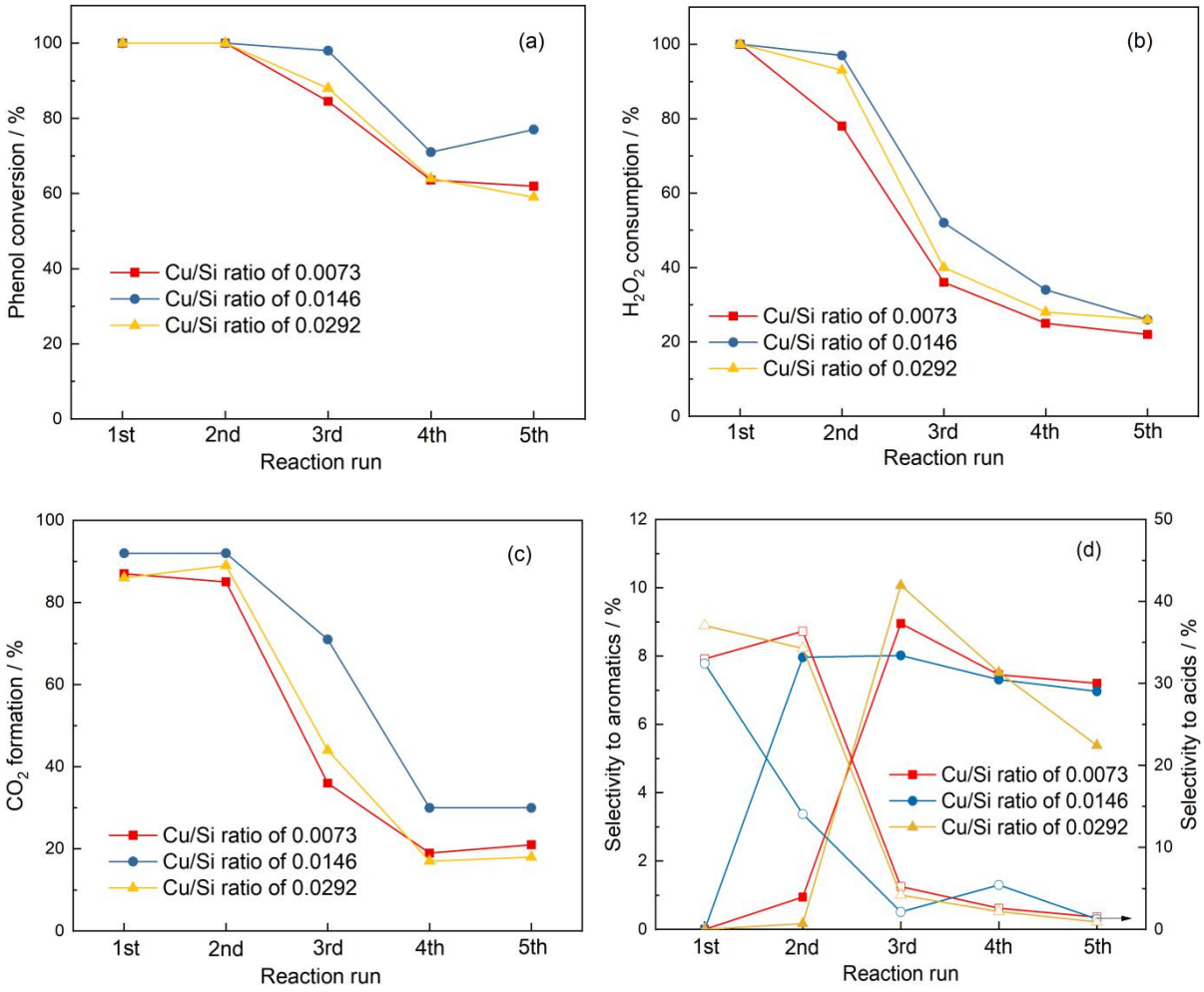

Figure 7.9. Reusability of Cu-MCM-48 with different Si/Cu ratios in successive runs of reactions in the CWPO of phenol, a) phenol conversion, b) H_2O_2 consumption, c) CO_2 formation and d) intermediates selectivity (Si: Cu: CTAB: ethanol: H_2O: H_2SO_4=1: 0.0073~0.0292: 0.2: 4.3: 83: 0.1, aging time 3 h, hydrothermal synthesis temperature 110 ^oC, synthesis time 36 h, calcination at 550 ^oC, 6 h)

The synthesized Cu-MCM-48 materials suffered from the low Cu incorporation ratio in the synthesis, though the stability of the heteroatom was proved, hence other possible methods for improving metal substitution were investigated. In this context, the Cu-MCM-48 catalysts with different Cu/Si ratios of 0.0073, 0.0146 and 0.0292 (corresponding to total Cu loading of 1.2, 2.1 and 4.5%, table 6.3) were evaluated. Increasing the metal loading of the Cu-MCM-48 had influence on the stability of catalysts, since the phenol conversion, H_2O_2 consumption,

CO_2 formation and intermediates selectivity over the three catalyst follows the trend: Cu loading 2.1%>4.5≈1.2% (Figure 7.9), which roughly matched up with their incorporated metal loading (0.36%, 0.22%, 0.077%, table 6.3). It is clear that only a small amount of Cu species was substituted into the framework under the same synthesis condition whether the concentration of Cu precursor (within the range) in the synthesis gel, which is in agreement with the data in table 6.6.

To sum up, the activity and stability of the Cu-MCM-48 catalysts could be improved by increasing substituted metal loading through the optimization of synthesis parameters (such as the hydrothermal temperature, hydrothermal time and synthesis pH), which is reflected by the activity of the catalysts after 5 runs of reactions. Although the activity and the stability needs further improvements, the Cu-MCM-48 materials showed potential in phenol oxidation reaction. The most promising catalyst among these synthesized materials is Cu-MCM-48 synthesized for 168 h, which presented over 90% phenol conversion in successive 5 runs of reactions.

7.4 Regeneration of catalysts

It is clear from the above results that the activity of the Cu-MCM-48 declined significantly throughout the five runs of reactions since the highest phenol conversion in the fifth run of reaction was only approximately 90% using all these Cu substituted cubic MCM-48 catalysts tested in this chapter. It is true that the metal leaching accounts for the loss of activity, however, the activity of the synthesized Cu-MCM-48 in the last reaction run does not match up with the substituted metal loading (in table 6.3), indicating that Cu leaching is not necessarely the only reason for the loss of activity in the reaction. Another quite common reason for catalyst deactivation in a liquid phase reaction is the formation of carbonaceous deposits over the catalyst surface, which also triggers loss of activity of catalyst with the accumulation of intermediates. The loss of activity caused by metal leaching is usually irreversible whereas the catalyst deactivated by carbon deposit has elements of reversibility

as often a catalyst affected by carbonacoues deposition can be regenerated at high temperature calcination. In this section, the possibility of deactivation caused by carbonaceous deposit is investigated in detail by using the generated Cu-MCM-48 catalysts after calcination at 550 °C for 6 h. In principle, the deposited carbon could be removed completely after calcination thus an improved activity could be observed.

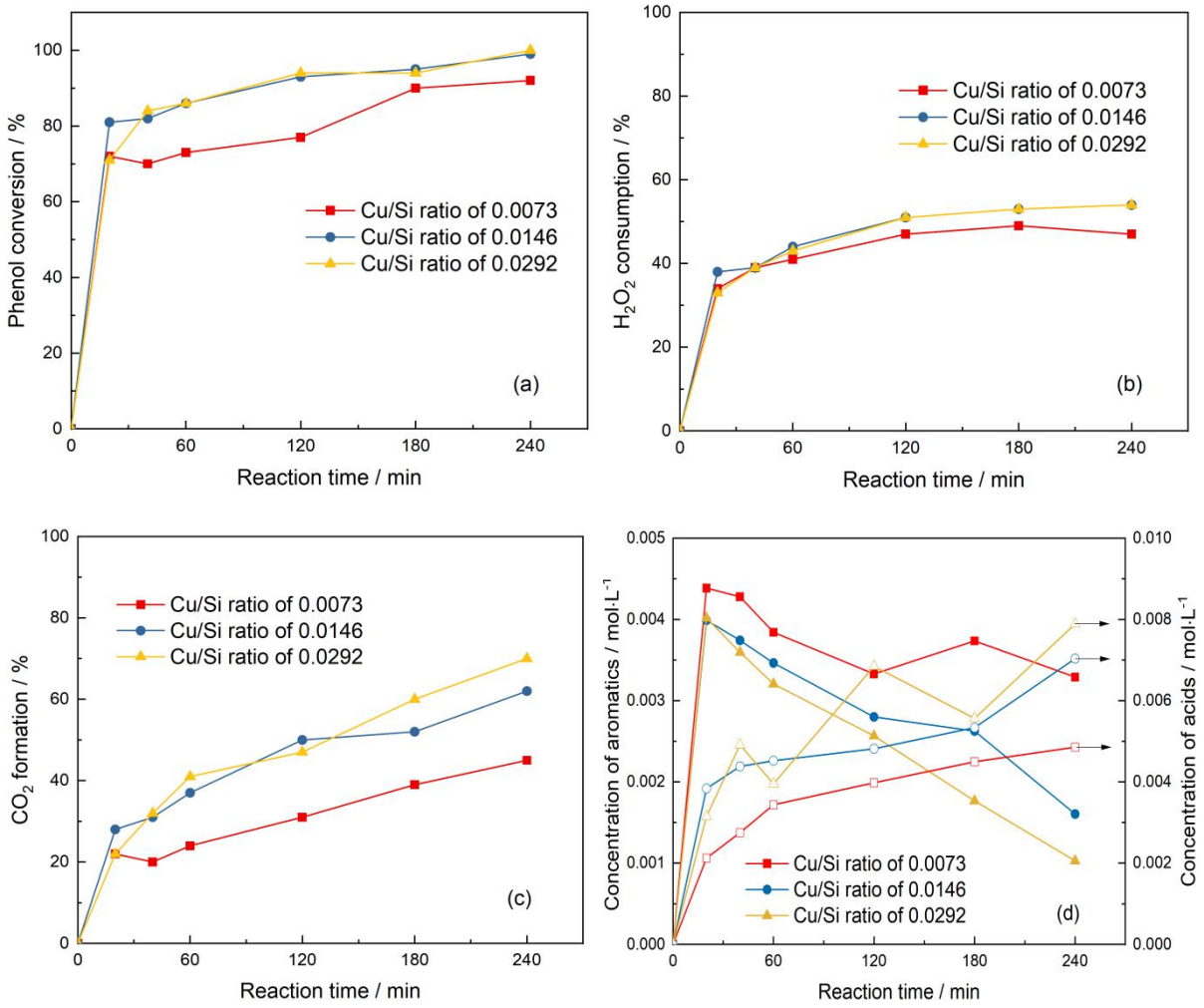

Figure 7.10. Activity of regenerated Cu-MCM-48 catalyst with different Si/Cu ratio in successive runs of reactions in the CWPO of phenol, a) phenol conversion, b) H_2O_2 consumption, c) CO_2 formation and d) intermediates selectivity (Si: Cu: CTAB: ethanol: H_2O: H_2SO_4=1: 0.0073~0.0292: 0.2: 4.3: 83: 0.1, aging time 3 h, hydrothermal synthesis temperature 110 °C, synthesis time 36 h, calcination 550 °C, 6 h, regeneration by calcination at 550 °C, 6 h)

Three regenerated catalysts with different Cu loadings (1.2, 2.1, and 4.5%) were tested in the CWPO of phenol (figure 7.10). As it can be seen, the regenerated catalysts presented good performance in phenol decomposition since over 70% of phenol was degraded in merely 20 min. Among the three regenerated catalysts, the catalyst with Cu/Si ratio of 0.0073 had slightly lower activity since the phenol conversion 92%, the H_2O_2 consumption of 47% as well as the CO_2 formation of 45% were achieved in 4 h while the catalysts with Cu/Si ratio of 0.0146 and 0.0292 showed higher phenol conversion (99% and 100%), higher H_2O_2 consumption (54% and 54%) as well as higher CO_2 formation (62% and 70%), respectively. In particular, the concentration of aromatic intermediates kept low (1.0×10^{-3} mol·L^{-1}) in the final reaction mixture when using the regenerated Cu-MCM-48 with the highest Cu/Si ratio, while the acids concentration was high (7.9×10^{-3} mol·L^{-1}), suggesting the high activity and selectivity of the regenerated catalyst. Overall, the regenerated Cu-MCM-48 catalysts, in comparison with the spent counterparts, exhibited higher activity in phenol decomposition, which suggested that carbonaceous deposit is also one of the reasons for catalyst deactivation in the CWPO of phenol, while it can be simply solved by regeneration at high temperature calcination.

7.5 Activity and stability of the optimized Cu-MCM-48 catalyst

As discussed in sections 7.3 and 7.4, the stability of Cu-MCM-48 could be improved by adjusting synthesis parameters while the synthesis pH, synthesis time are of great help. Meanwhile, the prepared catalysts could be regenerated by simply calcination in the air at high temperatures. In order to defend the conclusion, a Cu-MCM-48 material synthesized under the optimal conditions (hydrothermal synthesis temperature of 110 °C, synthesis time of 72 h, synthesis pH of 11.6), denoted as Cu-MCM-48-optimized, was characterized and tested. Moreover, the catalyst, denoted as Cu-MCM-48-*aqua regia*, was Cu-MCM-48-optimized treated by *aqua regia* (a mixture of hydrochloric acid and nitric acid, with HCl: HNO_3 volume ratio of 3: 1) at room temperature for 24 h in order to remove the Cu supported on the surface since aqua regia treatment is an efficient solution to extract metal

from solid material, thus the Cu-MCM-48 catalyst was obtained with only intra-framework metal, in principle.

7.5.1 Characterization of Cu-MCM-48 catalysts

7.5.1.1 XRD

The ordered structure of the material was achieved since the typical peaks assigned to (211), (220), (321), (400), (420) and (332) diffraction planes were all detected, as displayed in the XRD pattern of the Cu-MCM-48-optimized sample in figure 7.11. The intensity of the peaks of the Cu-MCM-48 was slightly weakened in comparison to a pure MCM-48 sample, suggesting that adjusting the synthesis parameters based on the above results had no obvious influence on the regularity of the mesoporous materials. However, an apparent shift of the peaks to the smaller angle was observed in the XRD pattern of the Cu-MCM-48-optimized sample, presenting a great increase of the unit cell parameter a_0 from 8.06 nm to 8.79 nm thus indicating a higher metal incorporation (table 7.1). The XRD pattern of the Cu-MCM-48-*aqua regia* in figure 7.11 showed the intensity of the characteristic peaks reduced, indicating that the cubic structure of the sample remained though the regularity of the structure was impaired after treatment using *aqua regia*. In addition, the acid treatment process had effects on the unit cell parameter a_0 since it decreased from 8.79 nm to 8.45 nm after *aqua regia* treatment at room temperature for 24 h, but still higher than the a_0 of the pure MCM-48 (8.06 nm). The decrease of the peak intensity and the unit cell parameter is likely due to the effects of acid treatment on the elution of Cu from the framework since similar examples about elution of Al from zeolite by acid were widely reported [33-37].

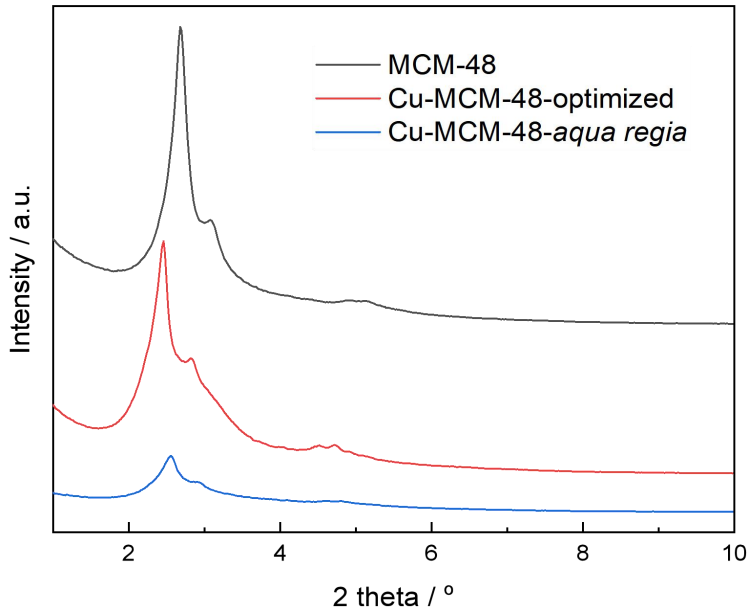

Figure 7.11. XRD patterns of MCM-48 and Cu-MCM-48 samples (synthesis condition of Cu-MCM-48: Si: Cu: CTAB: ethanol: H_2O: H_2SO_4=1: 0.0073: 0.2: 4.3: 83: 0.15, aging time 3 h, hydrothermal synthesis temperature 110 ºC, synthesis time 72 h, calcination at 550 ºC, 6 h)

7.5.1.2 Surface area and porosimetry

Isotherms of the pure MCM-48, the Cu-MCM-48-optimized with and without acid treatment were collected (figure 7.12a). The adsorption analysis confirmed mesopores highy uniform, and this characteristic was further reflected by the sharp condensation step at p/p^0 of 0.2-0.3 in the adsorption branch for the MCM-48 material, while the uniformity was weakened for the metal substituted samples since the condensation step flattened. On the other hand, the isotherms of the Cu-MCM-48-optimized sample presented a much lower N_2 adsorption in comparison with the pure silica, especially the sample after *aqua regia* treatment. Thus corroborating our conclusion that the uniformity of pore channels of the mesoporous silica was impaired by the substitution of Cu atoms into the silica and/or by the acid wash, which is in agreement with the XRD results.

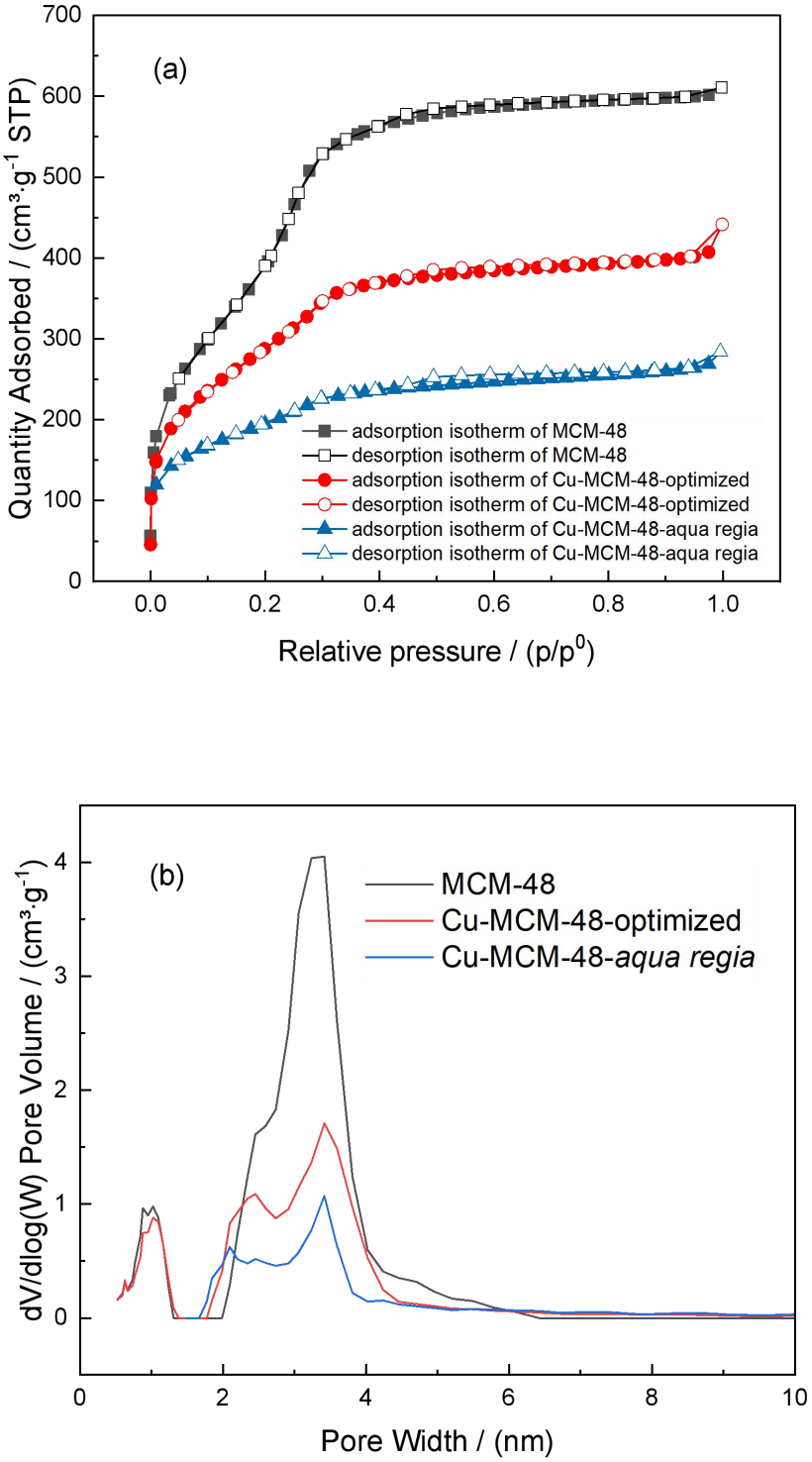

Figure 7.12. a) N_2 adsorption–desorption isotherm sand b) pore distribution of the synthesized mesoporous Cu-MCM-48 catalysts (synthesis condition: Si: Cu: CTAB: ethanol: H_2O: H_2SO_4=1: 0.0073: 0.2: 4.3: 83: 0.15, aging time 3 h, hydrothermal synthesis temperature 110 °C, synthesis time 72 h, calcination at 550 °C, 6 h)

Pore parameters were summarized in table 7.1. It should be noticed that the introduction of the metal species led to a decrease in pore diameter, surface area and pore volume. For example, the BET specific surface area and pore size of a pure (undoped) MCM-48 were 1435 $m^2 \cdot g^{-1}$ and 2.59 nm, respectively. Whereas after incorporation of Cu the BET surface area of the Cu-MCM-48-optimized decresed to 1053 $m^2 \cdot g^{-1}$, this may be caused by a partial blockage of the MCM-48 pores by copper oxide clusters existing in the channels and/or a partial collapse of the mesoporous structure [22,31]. In comparison, the wall thickness, w_t, of the Cu samples slightly increased to 1.65 nm with MCM-48 as reference (1.31 nm) which is in agreement with that reported in the literature [29-31] and might be due to the expansion of pore structure caused by metal incorporation. The pore structure was negatively affected after treatment by *aqua regia* with the surface area further decreasing to 696 $m^2 \cdot g^{-1}$.

Overall, the nitrogen adsorption/desorption isotherms clearly indicated a retain of porosity of the samples upon metal substitution and acid treatment. Meanwhile, the analysis of the Barret-Joyner-Halenda (BJH) pore size distributions showed the negative effects of the Cu introduction and the treatment of *aqua regia* since the surface area and pore diameters decreased after each of these steps.

Table 7.1. Porosimetry data of synthesized Cu-MCM-48 (synthesis condition: Si: Cu: CTAB: ethanol: H_2O: H_2SO_4=1: 0.0073: 0.2: 4.3: 83: 0.15, aging time 3 h, hydrothermal synthesis temperature 110 °C, synthesis time 72 h, calcination at 550 °C, 6 h)

Sample name	2θ of (211) plane [a]	d(211) [b]	a_0 (nm) [c]	S_{BET}[d] ($m^2 \cdot g^{-1}$)	V_p[e] ($cm^3 \cdot g^{-1}$)	D_p[d] (nm)	W_t[f] (nm)
MCM-48	2.68°	3.29	8.06	1435	1.06	2.59	1.31
Cu-MCM-48-optimized	2.46°	3.59	8.79	1053	0.60	2.39	1.65
Cu-MCM-48-*aqua regia*	2.56°	3.45	8.45	696	0.26	2.38	1.54

a - data from XRD.

b - calculated by Eq. 2.3.

c - calculated by Eq. 2.5.

d - determined by BET method.

e - determined by BJH method.

f - calculated by Eq. 2.6.

7.5.1.3 TEM

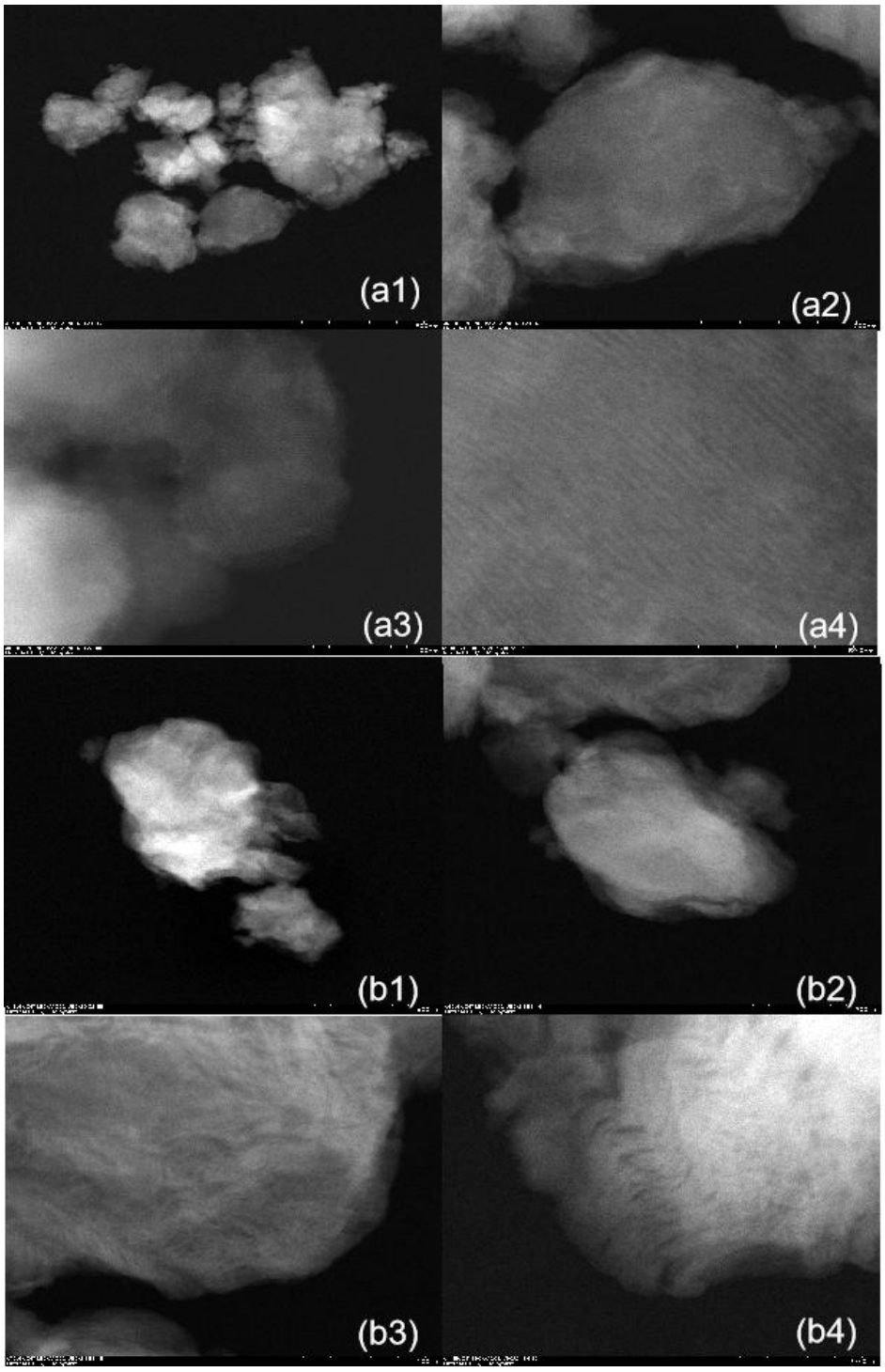

Figure 7.13. TEM micrographs of a) Cu-MCM-48-optimized (magnification from (a1) to (a4) ×14K, ×50K, ×80K, ×200K) and b) Cu-MCM-48-*aqua regia* (magnification from (b1) to (b4) ×16K, ×40K, ×70K, ×140K) (synthesis condition: Si: Cu: CTAB: ethanol: H_2O: H_2SO_4 =1: 0.0073: 0.2: 4.3: 83: 0.15, aging time 3 h, hydrothermal synthesis temperature 110 ºC, synthesis time 72 h, calcination at 550 ºC, 6 h)

Transmission electron images of Cu-MCM-48-optimized before (figure 7.13a) and after acid wash (figure 7.13b) indicated the effects of the treatment process on the morphology and pore structure of the cubic mesoporous materials. The typical structure of MCM-48 was maintained after introducing Cu atoms, as the Cu-MCM-48 sample without acid treatment exhibited ordered pore structure and uniform channel system, though the support structure was partially collapsed when compared to those with very low metal incorporation (figure 6.5), as slight irregularity of the framework was seen. The results well matched up with the XRD and BET data, whereas the slight irregularity can be explained by a distortion of the structure caused by a higher percentage of metal substitution into cubic framework, as proved by the ICP-OES data in table 7.2. In comparison, the mesostructured ordering was not observed in the TEM image of samples after soaking in *aqua regia* for 24 h. As can be seen, the acid treated sample showed a floc-like channel structure, indicating the ordered cubic mesoporous inorganic framework has been destroyed after stirring in *aqua regia* for one day. It suggested that some of the pores, especially those located at the edge of the particles have collapsed due to the effects of acid treatment. The reason is that the acid treatment causes loss of ordering and the formation of amorphous material, which is in agreement with some conclusions from the literature [38].

7.5.1.4 Active metal content - ICP-OES

The unit cell parameter a_0 (table 7.1) implied that there were heteroatoms substituted into the silica matrix of the Cu-MCM-48 sample, thus both the Cu supported metal loading (metal leached by *aqua regia*) and Cu substituted metal loading (framework metal leached by HF acid) were tested by ICP-OES, with the results listed in table 7.2. It is stated that the supported and substituted Cu coexisted in the sample whereas the Cu on the surface (1.0%) accounted for 83% and the Cu substituted in the framework (0.20%) took up 17% of the total Cu loading (1.2%). Among the Cu-MCM-48 samples

that maintained Cu/Si ratio of 0.0073 and cubic structure (table 7.2 and table 6.3), the Cu-MCM-48-optimized synthesized at H_2SO_4/Si ratio of 0.15, H_2O/Si of 83, and synthesis time of 72 h exhibited the highest substituted metal loading, suggesting that adjusting synthesis parameters is effecient method to improve the metal incorporation ratio, and at last would improve the activity and stability of the Cu-MCM-48 catalysts in the CWPO of phenol reaction.

Table 7.2. Properties of the synthesized Cu-MCM-48 catalyst (synthesis condition: Si: Cu: CTAB: ethanol: H_2O: H_2SO_4=1: 0.0073: 0.2: 4.3: 83: 0.15, aging time 3 h, hydrothermal synthesis temperature 110 ^oC, synthesis time 72 h, calcination at 550 ^oC, 6 h)

Catalyst	Supported metal loading	Substituted metal loading	Total metal loading
Cu-MCM-48	1.0 wt%	0.20%	1.2%

7.5.2 Activity of Cu-MCM-48 catalyst

The Cu-MCM-48-*aqua regia* sample presented high activity in phenol decomposition with complete phenol conversion achieved in only 20 min. After the decomposition of phenol, the aromatic intermediates such as *p*-benzoquinone and catechol formed, which were further degraded to acids (mainly formic acid, malonic acid and acetic acid) in reaction time of 2 h with the continuous consumption of H_2O_2. Acid intermediates were gradually oxidized to CO_2 in the last 2 h with the concentration of formic acid and malonic acid fell down, leading to the growth of the CO_2 formation. At last, the phenol conversion of 100%, H_2O_2 consumption of 87%, CO_2 formation of 87% (oxalic acid was not included) were achieved in 4 h, meanwhile, all the aromatic compounds were removed from water and the main intermediates remained in the reaction mixture were harmless acids such as acetic acid and formic acid.

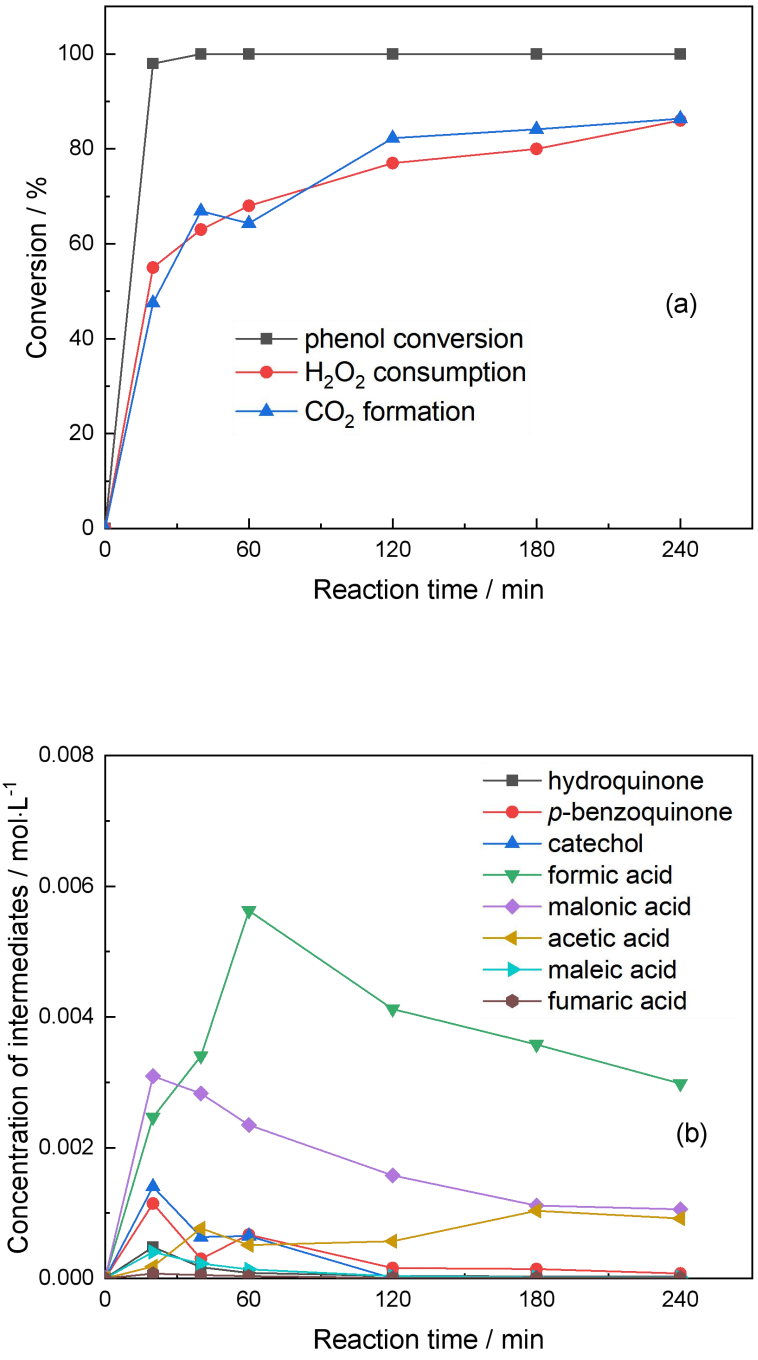

Figure 7.14. Catalytic activity of Cu-MCM-48-*aqua regia* in the CWPO of phenol, a) phenol conversion, H_2O_2 consumption and CO_2 formation and b) intermediates concentration (Si: Cu: CTAB: ethanol: H_2O: H_2SO_4=1: 0.0073: 0.2: 4.3: 83: 0.15, aging time 3 h, hydrothermal synthesis temperature 110 ºC, synthesis time 72 h, calcination at 550 ºC, 6 h)

7.5.3 Stability and re-usability of Cu-MCM-48-*aqua regia*

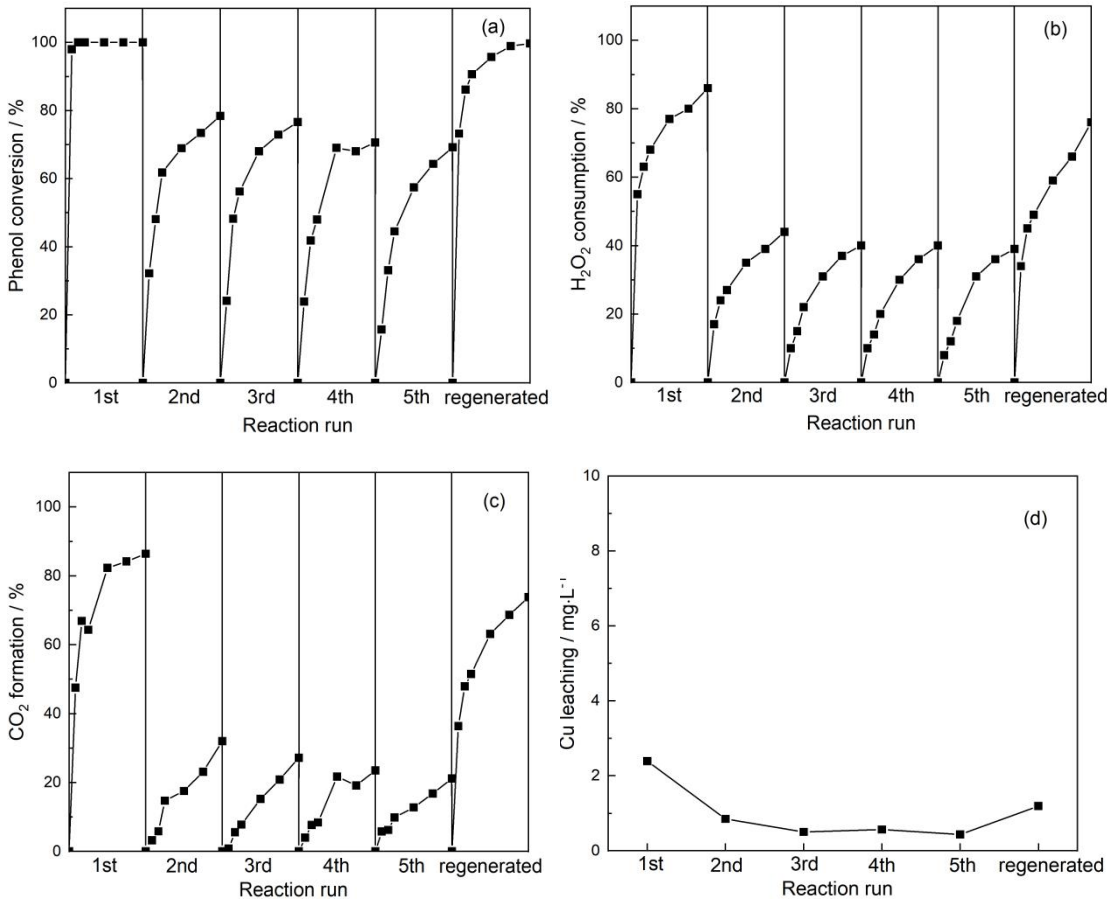

Figure 7.15. Reusability of Cu-MCM-48-*aqua regia* in successive runs of reactions in the CWPO of phenol, a) phenol conversion, b) H_2O_2 consumption, c) CO_2 formation and d) Cu leaching (Si: Cu: CTAB: ethanol: H_2O: H_2SO_4=1: 0.0073: 0.2: 4.3: 83: 0.15, aging time 3 h, hydrothermal synthesis temperature 110 ^oC, synthesis time 72 h, calcination at 550 ^oC, 6 h)

The Cu-MCM-48-*aqua regia* was recycled through a filtration/washing/drying process after 4 h reaction and reused in the next run of CWPO of phenol. The catalyst, as displayed in figure 7.15, showed high activity in phenol decomposition since phenol was completely removed in 20 min in the first run, while after 4 h the phenol conversion of 100%, the H_2O_2 consumption of 86% and the CO_2 formation of 86% were achieved together with a low Cu leaching (2.4 mg·L^{-1}). The used catalyst, after the first run, presented decreased activity with the phenol conversion, H_2O_2

consumption, as well as CO_2 formation, maintained almost constant at around 75%, 40% and 30%, respectively, which may be due to the lower adsorption capacity of the used catalyst [39]. Meanwhile, the metal concentration detected in the reaction mixture using the used catalyst kept lower than 0.5 $mg \cdot L^{-1}$, suggesting the negligible effect of leached Cu and the good performance of the metal incorporated into the silica matrix. On the other hand, the steady performance of the used catalyst in the 2nd to the 5th run of reaction also implied the potential of the Cu-MCM-48 catalyst although catalyst deactivation occurred. Moreover, the Cu-MCM-48-*aqua regia* catalyst, after regenerated simply at 550 ^oC for 6 h, exhibited performance as good as in the first run, with phenol conversion of 100%, H_2O_2 consumption of 76%, CO_2 formation of 74%, whereas metal leaching of merely 1.2 $mg \cdot L^{-1}$. The activity of the regenerated catalyst stated that the causes of deactivation of the Cu-MCM-48-*aqua regia* catalyst might be carbonaceous deposit thus can be regenerated by calcination in air.

7.6 Conclusions

The Cu-MCM-48 catalyst (CM-23) synthesized by hydrothermal synthesis with the best ordering of structure presented high activity in the CWPO of phenol since it resulted in high phenol conversion (100%), high H_2O_2 consumption (82%), high CO_2 formation (88%) as well as harmless reaction mixture (aromatic compounds removed and only organic acids remained). Despite the high activity, the Cu-MCM-48 sample suffered high Cu leaching (40 $mg \cdot L^{-1}$) in the first run of the reaction, leading to low stability and low reusability of the catalyst as the activity of the sample drastically reduced from the second run of reaction. In comparison, the Cu-MCM-48 samples with higher unit cell parameters (a_0), though slightly inferior in the regularity of the mesostructure, showed improved stability as an obvious increase in the phenol conversion, H_2O_2 consumption and CO_2 formation was shown after the first run of the reaction. In particular, the Cu-MCM-48 samples with longer synthesis time, higher

hydrothermal synthesis temperature, as well as lower synthesis pH were favour of improvement of stability. It suggests that the unit cell parameter indicates the performance of Cu-MCM-48 samples to some extent and is evidence of metal incorporation. The Cu-MCM-48 sample synthesized at the optimal conditions (110 ^{o}C, 72 h, pH 11.6) presented the typical cubic structure and uniform mesopores, had a high percentage of metal incorporation as proved by the unit cell parameter (8.79 nm) and substituted metal loading (0.2%) thus the activity and the stability were improved as expected. Therefore, the Cu-MCM-48 catalyst with Cu substitution into the framework is one of the efficient catalysts that presented both high activity and high stability in the CWPO of phenol, though the further increase of the percentage of metal incorporation should be pursued. Moreover, the used Cu-MCM-48 catalysts could be regenerated simply by calcination at 550 ^{o}C at ambient air to recover the activity loss caused by carbonaceous deposit, which further indicates the potential of the catalysts in the catalytic reaction.

7.7 References

[1]. K. M. Valkaj, A. Katovic and S. Zrnčević, *J Hazard Mater*, 2007, **144**, 663-667.

[2]. N. H. Phu, T. T. K. Hoa, N. V. Tan, H. V. Thang and P. L. Ha, *Appl Catal B-Environ*, 2001, **34**, 267-275.

[3]. L. Huang, L. Zhang, D. Li, Q. Xin, R. Jiao, X. Hou, Y. Zhang and H. Li, *J Environ Chem Eng*, 2020, **8**, 103933.

[4]. Y. Ghaffari, N. K. Gupta, J. Bae and K. S. Kim, *Catalysts*, 2019, **9**, 859.

[5]. K. M. Valkaj, A. Katovic and S. Zrncevic, *Ind Eng Chem Res*, 2011, **50**, 4390-4397.

[6]. M. Alvaro, E. Carbonell, M. Esplá and H. Garcia, *Appl Catal B-Environ*, 2005, **57**, 37-42.

[7]. W. Najjar, S. Azabou, S. Sayadi and A. Ghorbel, *Appl Catal B-Environ*, 2009, **88**, 299-304.

[8]. S. Yuvaraj, M. Palanichamy and V. Krishnasamy, *Chem Commun*, 1996, 2707-2708.

[9]. H. Xu, Y. Zhang, H. Wu, Y. Liu, X. Li, J. Jiang, M. He and P. Wu, *J Catal*, 2011, **281**, 263-272.

[10]. M. V. P. Sharma, V. Durgakumari and M. Subrahmanyam, *J Hazard Mater*, 2008, **160**, 568-575.

[11]. U. Beker, B. Ganbold, H. Dertli and D. D. Gülbayir, *Energ Convers Manage*, 2010, **51**, 235-240.

[12]. J. Przepiórski, *J Hazard Mater*, 2006, **135**, 453-456.

[13]. H. I. Meléndez-Ortiz, Y. A. Perera-Mercado, L. A. García-Cerda, J. A. Mercado-Silva and G. Castruita, *Ceram Int*, 2014, **40**, 4155-4161.

[14]. U. S. Taralkar, M. W. Kasture and P. N. Joshi, *J Phys Chem Solids*, 2008, **69**, 2075-2081.

[15]. B. Echchahed, A. Moen, D. Nicholson and L. Bonneviot, *Chem Mater*, 1997, **9**, 1716-1719.

[16]. J. Park, J. Jurng, G. Bae, S. H. Park, J. Jeon, S. C. Kim, J. M. Kim and Y. Park, *J Nanosci Nanotechno*, 2012, **12**, 5942-5946.

[17]. J. Xu, Z. Luan, M. Hartmann and L. Kevan, *Chem Mater*, 1999, **11**, 2928-2936.

[18]. B. Echchahed, A. Moen, D. Nicholson and L. Bonneviot, *Chem Mater*, 1997, **9**, 1716-1719.

[19]. X. Li, W. Chen, Y. Tang and L. Li, *Chemosphere*, 2018, **206**, 615-621.

[20]. W. Qian, H. Wang, J. Chen and Y. Kong, *Materials*, 2015, **8**, 1752-1765.

[21]. M. Mathieu, P. Van Der Voort, B. M. Weckhuysen, R. R. Rao, G. Catana, R. A. Schoonheydt and E. F. Vansant, *J Phys Chem B*, 2001, **105**, 3393-3399.

[22]. H. Li, S. Wang, F. Ling and J. Li, *J Mol Catal A-Chem*, 2006, **244**, 33-40.

[23]. X. ZHOU, Q. ZHAO, D. WU, M. JI and T. JIANG, *J Chinese Ceram Soc*, 2011, **39**, 995-999.

[24]. S. E. Dapurkar, A. Sakthivel and P. Selvam, *New J Chem*, 2003, **27**, 1184-1190.

[25]. Y. Shao, L. Wang, J. Zhang and M. Anpo, *Micropor Mesopor Mat*, 2008, **109**, 271-277.

[26]. W. Zhao, Y. Luo, P. Deng and Q. Li, *Catal Lett*, 2001, **73**, 199-202.

[27]. H. Kosslick, G. Lischke, H. Landmesser, B. Parlitz, W. Storek and R. Fricke, *J Catal*, 1998, **176**, 102-114.

[28]. M. Mureseanu, M. Filip, S. Somacescu, A. Baran, G. Carja and V. Parvulescu, *Appl Surf Sci*, 2018, **444**, 235-242.

[29]. W. Zhang and T. J. Pinnavaia, *Catal Lett*, 1996, **38**, 261-265.

[30]. U. S. Taralkar, P. Kalita, R. Kumar and P. N. Joshi, *Appl Catal A-Gen*, 2009, **358**, 88-94.

[31]. W. Zhan, Y. Guo, Y. Wang, X. Liu, Y. Guo, Y. Wang, Z. Zhang and G. Lu, *J Phys Chem B*, 2007, **111**, 12103-12110.

[32]. Y. Zhang, M. Wang, S. Liu, H. Qiu, M. Wang, N. Xu, L. Gao and Y. Zhang, *Sep Purif Technol*, 2019, **228**, 115758.

[33]. C. Wang, S. Leng, H. Guo, L. Cao and J. Huang, *Appl Surf Sci*, 2019, **478**, 319-326.

[34]. R. Baran, Y. Millot, T. Onfroy, J. Krafft and S. Dzwigaj, *Micropor Mesopor Mat*, 2012, **163**, 122-130.

[35]. M. R. Apelian, A. S. Fung, G. J. Kennedy and T. F. Degnan, *J Phys Chem*, 1996, **100**, 16577-16583.

[36]. C. Coutanceau, J. M. Da Silva, M. F. Alvarez, F. R. Ribeiro and M. Guisnet, *J Chim Phys*, 1997, **94**, 765-781.

[37]. C. Wang, L. Cao and J. Huang, *Surf Interface Anal*, 2017, **49**, 1249-1255.

[38]. A. Ates and C. Hardacre, *J Colloid Interf Sci*, 2012, **372**, 130-140.

[39]. S. A. Messele, O. S. G. P. Soares, J. J. M. Órfão, F. Stüber, C. Bengoa, A. Fortuny, A. Fabregat and J. Font, *Appl Catal B-Environ*, 2014, **154-155**, 329-338.

Chapter 8. Conclusions and future work

Conclusions

The research project has developed on the following three areas: i) identification and determination of phenol and intermediates formed during the abatement reaction ii) seeking for highly efficient catalysts for complete removal of phenol and aromatic intermediates and high selectivity to CO_2/organic acids, iii) investigation of catalyst deactivation mechanism and develop catalyst with high stability accordingly.

On this basis, the main achievements of the project are summarized as follows:

1) An efficient analysis method for the qualitative and quantitative determination of phenol and intermediates was developed by HPLC which only took 30 min for the analysis of each sample.

2) Almost all the expected intermediates (including hydroquinone, *p*-benzoquinone, catechol, oxalic acid, formic acid, malonic acid, acetic acid, maleic acid and fumaric acid) were identified by the HPLC analysis method which enables the calculation of carbon mass balance and CO_2 formation. And this is always neglected in current literature.

3) The complete decomposition of phenol could be achieved under mild reaction conditions (80 ^oC, endogenous pressure, 4 h) over Cu and Fe catalysts, especially the Cu-ZSM-5-WI catalyst that exhibited 100% phenol conversion, 94% H_2O_2 consumption, 90% CO_2 formation and complete removal of aromatic intermediates under the experimental conditions. However, the low stability of the catalyst during the reaction process due to high metal leaching (> 80%) limits the potential of the industrial application of the catalyst.

4) The causes of the Cu leaching of the Cu-supported ZSM-5 catalyst were studied, and the decreased pH of the reaction mixture with the formation of organic acids during the reaction process led to increased Cu leacing. The Cu leaching (25% at pH 3) was severe at pH below 4, whereas adjustment of the reaction parameters (such

pH, temperature, M: S ratio and so on) had no obvious influences on the stability of the Cu catalyst. The formation of intermediates especially the formation of oxalic acid was the main reason for metal leaching. The oxalate ions formed in the reaction process complexed with Cu with 2:1 ratio, indicating that the formation of Cu oxalate ($Cu(oxa)_2$) was one of the direct reasons for Cu leaching. It is very likely this occurs for many other similar catalysts reported in literature.

5) High leaching (> 50%) was observed over all the Cu-supported ZSM-5 zeolite catalysts in this project regardless of the oxidation state of Cu and the catalyst preparation methods (WI, IE, DP), indicating the poor stability of the metal oxides that suported on zeolite. A factor to be considered for future catalyst development is designing zeolite catalyst with metal incorporated into the silica matrix.

6) The Fe-ZSM-5-HTS catalyst prepared by hydrothermal synthesis showed high activity (100% phenol conversion, 100% H_2O_2 consumption, 60% CO_2 formation) and high stability (leaching < 0.4 $mg \cdot L^{-1}$) in the CWPO of phenol in successive 8 runs of reaction without loss of activity, which evidenced the potential of the metal incorporated zeolite catalyst. The Fe-ZSM-5/SiC presented somehow similar performances though slightly lower activity was seen due to the higher diffusion resistance. Whereas the Cu-ZSM-5/SiC presented low activity and low stability in phenol oxidation due to the failure of Cu incorporation which drove us to seek for other guest for Cu substitution.

7) The Cu-MCM-48 catalysts with uniform ordering and mesopore structure were prepared by hydrothermal synthesis and the pH adjustment and the hydrothermal conditions were key parameters influencing the synthesis of MCM-48 and the metal incorporation. The MCM-48 structure was formed with pH at 11.6-11.9, hydrothermal treatment at 90-110 ^oC for 18-72 h, whereas the lower pH, higher temperature, longer time within these ranges positively influenced the metal incorporation (characterized by the unit cell parameter, a_0). At last, the highest yield of 70% and the highest

heteroatom loading of 0.36% were achieved via adjusting the synthesis parameters.

8) The Cu-MCM-48 catalysts with higher metal incorporation were assessed in the CWPO of phenol. They all presented high activity (100% phenol conversion) in the first run of reaction due to the metal on support surface, whereas the activity was then decreased and stablized form the 2^{nd} and 5^{th} run owing to the heterogeneous contribution of the substituted Cu species. Among those tested Cu-MCM-48 catalysts, the samples with higher a_0 and higher metal incorporation showed improved stability and the most stable catalyst was that synthesized for 168 h which had > 90% phenol conversion in successive 5 reaction runs. The Cu-MCM-48 catalyst synthesized at the optimal conditions (pH 11.6, 110 ^oC, 72 h) showed steady activity (> 70% phenol conversion in 5 runs), suggesting the possibility of improving activity via increasing metal incorporation through adjusting synthesis parameters. These are excellent results, especially if considered with the added bonus that Cu-MCM-48 could be regenerated by simple calcination in air at 550 ^oC.

Future work

The future work of this project will focus on:

1) Screen catalyst rapidly with high selectivity to acids/CO_2 and high efficiency of H_2O_2 to hydroxyl radicals based on the calculation of CMB, OMB and H_2O_2 efficiency;

2) Seek other potential catalysts in the CWPO process in the form of metal-free catalysts and/or intra-framework Cu catalyst with high substituted metal loading (> 0.5%), with aims to achieve both high activity and high stability;

3) Design a catalyst with high activity in the decomposition of both phenol and oxalic acid, such as bimetallic catalys with one metal for phenol decomposition and the other one for decomposition of any oxalic acid when it was formed in the reaction mixture to improve catalyst stability;

4) Apply the ideal catalysts (Fe-ZSM-5-HTS(80) and Cu-MCM-48 for instance) and

the technique (CWPO) into the abatement of other possible water pollutants. To confirm the efficiency of the CWPO technique and the universal applicability of the prepared catalysts, other common organic compounds in wastewater other than phenol, either in terms of single or combinations, will be studied. For example: bisphenol A, quinone and 2-chlorophenol, and so on;

5) Study the possible mechanisms and the routes of phenol oxidation. The reaction pathway of phenol oxidation under different condition or based on different catalysts, and the oxidation mechanism of H_2O_2 will be proposed. On the basis of this research, an integrated process for phenolic wastewater, or even for organic wastewater treatment may be designed.

Appendix

A.1 Design of reaction setup

The reaction setup for phenol oxidation reaction includes a stirrer hot plate, an aluminium block (custom made) and four glass reactor vessels (custom made). The hot plate is used to provide magnetic stirring and heat the reaction mixture to the desired temperature by inserting the temperature probe into the aluminium block. The aluminium block (in figure A1), which is placed on the top of the hot plate, has four holes (with diameters of 40.4 mm) to place four reactor vessles. The diameter of the block (160 mm) matches up with the diameter of the hot plate, while the height (120 mm) of the block is designed to fit the reactor, to minimize as much as possible the difference of the temperature between the reaction setups. The reactor vessel (figure A2) is equipped with a Young tap valve on the top, which is used to seal the glassware during the reactions. The reactor with diameter of 40 mm and volume of 100 mL are made of transparent glass and used for conducting liquid phase reactions.

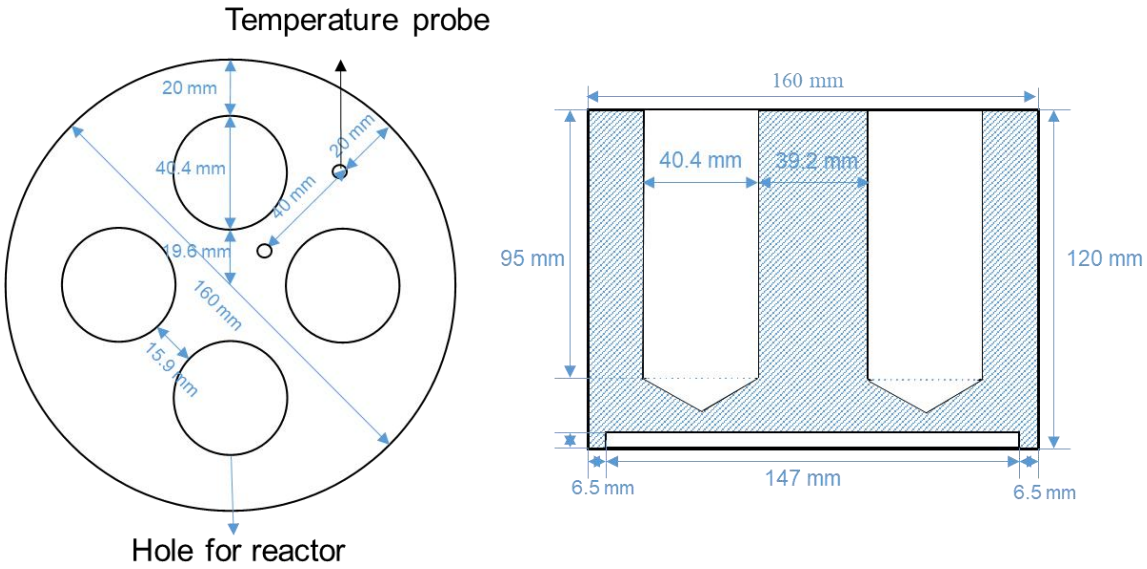

Figure A1. Sketch of the four-hole aluminium block (custom made), vertical view (left) and sectional view (right)

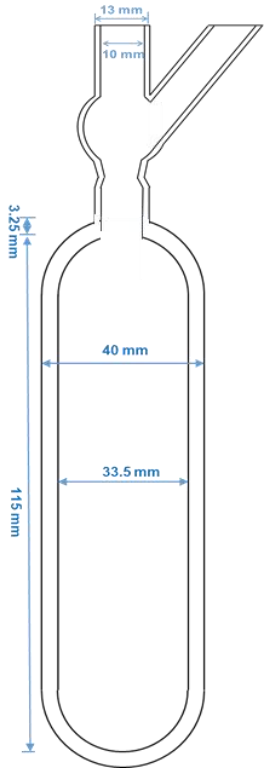

Figure A2. Sketch of the custom made glassware

A.2 Temperature calibration of the reaction setup

The difference between the actual temperature of reaction mixture, and the set temperature deserves attention as there is heat loss between different zones of the reactor setup, and this require a temperature calibration. Temperature calibration was carried out by measuring the actual temperature of the deionized water (50 mL) in the glassware. The actual temperature was tested with a temperature detector under continuous stirring (500 rpm) with set temperatures ranging from 30 ^{o}C to 100 ^{o}C (with increments of 10 ^{o}C). The actual temperatures of the water in the four different reactor vessels were recorded 10 min after the reading of the temperature reaches the set temperature. The actual temperature with function of set temperature was then plotted (figure A3a). From the calibration curve ($T_{measured}$ = 0.932 T_{set}+2.5). For example, the actual temperature reaches 80 ^{o}C when the temperature was set as 83 ^{o}C. Besides, the actual temperature of water with set temperature of 83 ^{o}C was also recorded every half hour to investigate its fluctuation range (figure A3b).

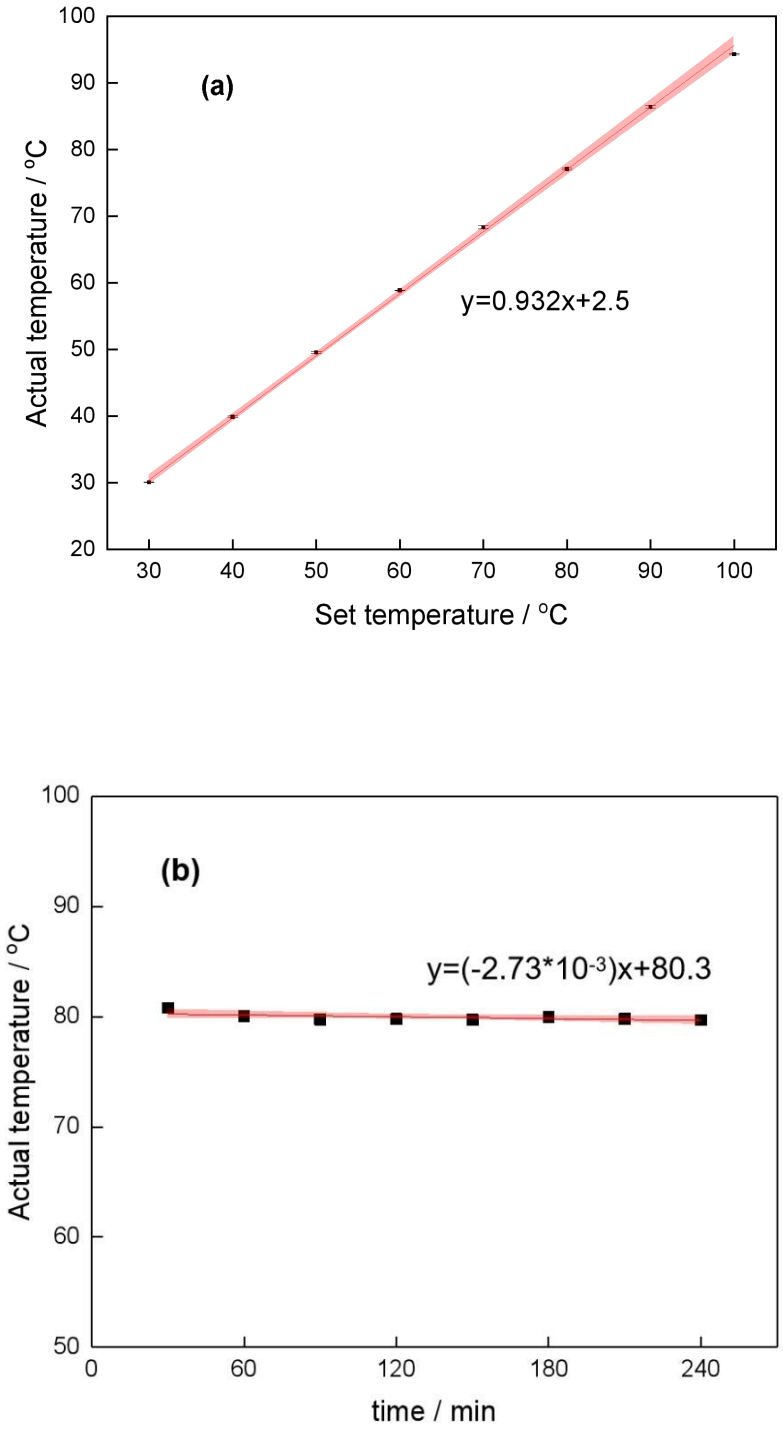

Figure A3. a) The actual temperatures of water per different set temperatures ranging from 30-100 °C, and b) the actual temperature of water with time from 0.5-4 h when setting temperature at 83 °C (50 mL of deionized water, stirring rate of 500 rpm)

A.3 Principle of catalyst preparation

A.3.1 Wet impregnation (WI)

Wet impregnation usually refers to contacting a solid with a liquid containing a metal precursor and then eliminating the excess liquid (which practically acts as a solvent for the precursor), by evaporation. This concentrates the metal precursor and deposits metal species on the surface of the solid or within pores, if a material has a suitable (size and polarity) pore structure [1]. The deposition of active species on the surface of a solid by wet impregnation usually results from weak interactions such as Coulomb force, van der Waals forces, or H-bonds [2]. A typical wet impregnation process is shown in figure A4.

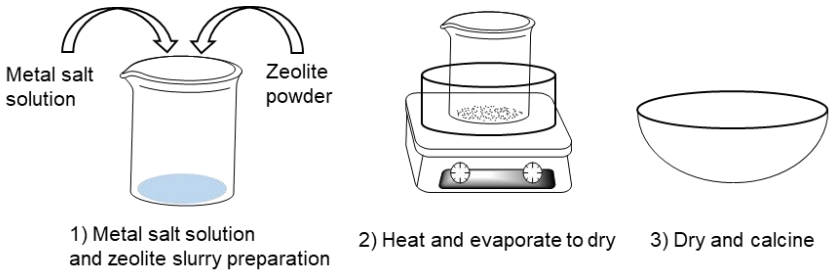

Figure A4. Schematic diagram of metal-supported catalyst preparation by wet impregnation in three steps. The concentration of metal salts decides the metal loading of the WI catalyst.

Despite being a quite straight forward preparation method, it is reported, however, that this protocol leads to an uncontrolled distribution of the metal sites both inside the pores and on the external surface due to the absence of specific metal–zeolite interactions [3]. Besides, it also leads to large metal particles formed via agglomeration [4]. However, it is still the most widely used due to its simplicity and

economic advantages. This sequence of operations may then be followed by a post reduction step (most often by H_2 gas or $NaBH_4$ in solution) to alter the oxidation state of the deposited metal [5].

A.3.2 Deposition-precipitation (DP)

Deposition-precipitation method involves the conversion of a highly soluble metal salt precursor into a less-soluble substance which precipitates only on the support and not in solution [6]. Typically, this process is achieved by a change in solution pH, most often basic, by addition of a precipitation agent (such as NaOH [7,8], Na_2CO_3 [9,10], urea [11,12], ammonia [13,14] and so on), addition of a reducing agent [15,16], or change in the concentration of a complexation agent [17]. A typical deposition-precipitation process is shown in figure A5.

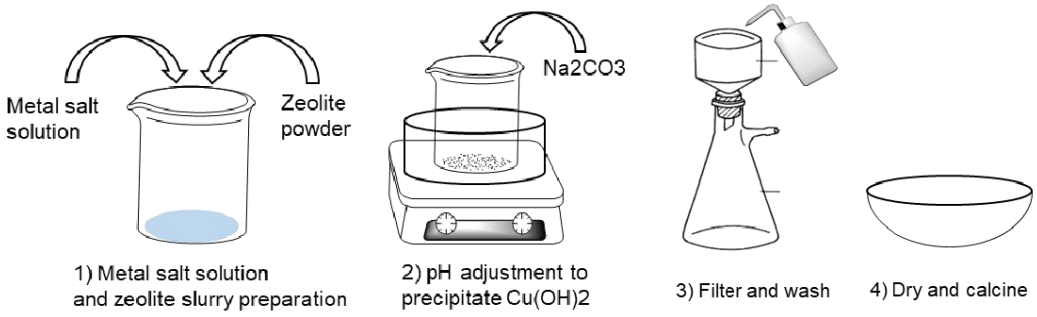

Figure A5. Schematic diagram of metal-supported catalyst preparation by deposition-precipitation in four steps. pH adjustment is the key step in the preparation of DP catalyst.

Catalysts prepared by DP method exhibit some advantages compared to more conventional wet impregnation: smaller metal particles are obtained with a narrower

size distribution. Besides, it is possible to obtain catalysts with higher metal loadings (20 wt % for instance) in comparison with those prepared by ion exchange method as they usually have metal loading below 5% [18,19]. In addition, the metal particles of catalysts prepared by deposition precipitation are usually highly dispersed and do not easily sinter because of the strong interaction with the support [6,18]. However, it also presents some disadvantages that not all the metal ions present in solution are deposited on the support. Indeed, the maximum metal loading is usually much lower than the nominal amount of metal present in solution.

A.3.3 Ion exchange (IE)

The ion exchange method consists in a process when ionic species from an aqueous solution are attracted electrostatically by charged sites on the support surface [20]. This protocol involves the replacing of an ion in an electrostatic interaction with the surface of a support by another ion species. For example, for a support like HZSM-5, which containing H^+ ions, is mixed with an excess volume of a metal precursor solution, metal ions gradually penetrate into the pore space of the support, while ions H^+ pass into the solution, until equilibrium is established corresponding to a given distribution of the two ions between the solid and the solution [21]. Heating is sometimes required to increase the ion exchange rate. A typical ion exchange process is schematized in figure A6.

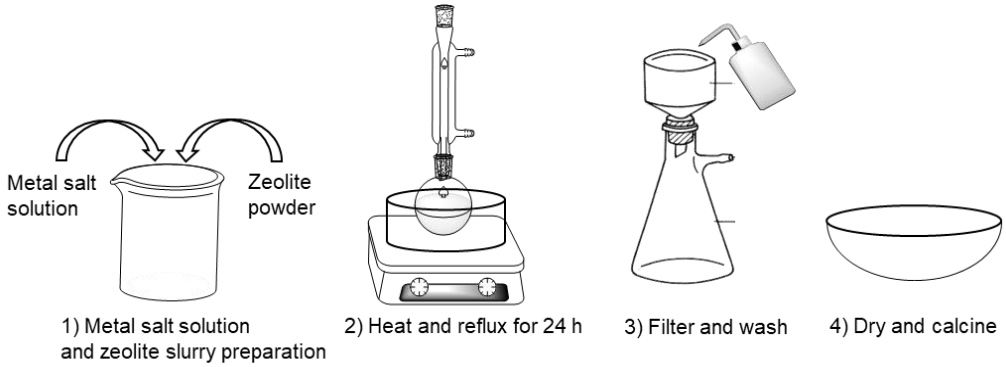

Figure A6. Schematic diagram of metal-supported catalyst preparation by ion exchange in four steps. The parameters including the concentration of metal salts, temperature, and time in the first and second steps influence the metal loading of the catalyst significantly.

Ion-exchange is historically one of the first methods of introducing the transition-metal sites inside the pores of zeolites. Furthermore, it improves the metal dispersion and produces isolated metal species, which may positively affect the activity of the zeolite catalysts. In addition, the ion-exchange technique normally brings about a stronger metal-support interaction than impregnation , which may lead to a higher stability of the zeolite catalysts. Whereas the main drawback is that catalyst prepared by this method commonly displays a low metal loading (usually below 5% [18]) as a result of the limited ion exchange capacity of the zeolite (depending on the molar SiO_2/Al_2O_3 ratio) [4,22].

A.3.4 Hydrothermal synthesis (HTS)

A typical hydrothermal zeolite synthesis (in figure A7) can be described as follows [4]: amorphous reactants containing silica and alumina (or metal oxide) are mixed together with a cation source, usually in a basic medium (high pH over 9), the pH of

the aqueous reaction mixture is then adjusted to optimal pH. After that the synthesis gel is aged, which is a process defined as a stirring or pre-heating process at low temperature (typically, below 100 °C) prior to high temperature-hydrothermal treatments [23], to decrease the duration of crystallization (ranging from hours to days) at a given temperature and the size of crystals in the final products [24]. After aging, the solution is heated (for reaction temperatures above 100 °C if using water as solvent), often in a sealed autoclave. For some time (for example several hours for ZSM-5) after raising to synthesis temperature, the reactants remain amorphous. Afterwards, crystalline zeolite products can be detected. Finally, some of the amorphous materials are replaced by an approximately equal mass of zeolite crystals (which are recovered by filtration, washing and drying).

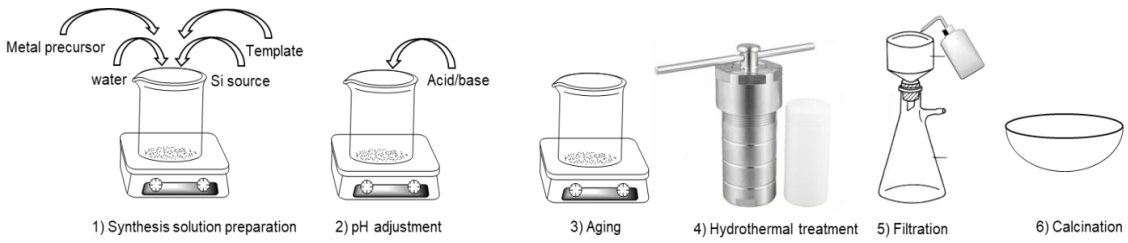

Figure A7. Schematic diagram of metal-substituted zeolite catalyst preparation by hydrothermal synthesis in six steps. The pH adjustment and hydrothermal synthesis steps are crucial for the growth of the desired crystalline materials.

Unlike other metal-zeolite configurations that exclusively lead to extra-framework species, the hydrothermal synthesis approach sometimes permits creating truly single framework metal sites [24]. The most common heteroatom applied for the

isomorphous substitution is obviously trivalent Al. Other trivalent elements such as B, Fe, Ga, and La can be also introduced into the framework, resulting in an array of lattice acidity and stability. Further, isomorphously substituted zeolites contain catalytically active Brønsted (proton donors) and/or Lewis acid (electron acceptor) sites that are also suitable for the coordination of highly dispersed transition metal centres.

A.4 Principle of characterization techniques

A.4.1 XRD

X-ray powder diffraction (XRD) is a non-destructive technique used for the determination of composition or crystalline structure of material. X-ray diffraction is based on constructive interference of monochromatic X-rays when crossing or being reflected by a crystalline sample. The interaction of the incident rays with the sample produces a diffracted ray (figure A8) and a pattern from constructive interference when conditions satisfy Bragg's Law. According to the Bragg's law, the lattice spacing in a crystalline sample is correlated to the wavelength of the electromagnetic radiation used to carry out the experiment and the diffraction angle at which a diffraction peak is detected. It follows that by scanning a sample in a range of 2θ angles, while converting the diffraction peaks to *d*-spacing allows identification of crystalline materials owing to their unique *d* -spacing and structure.

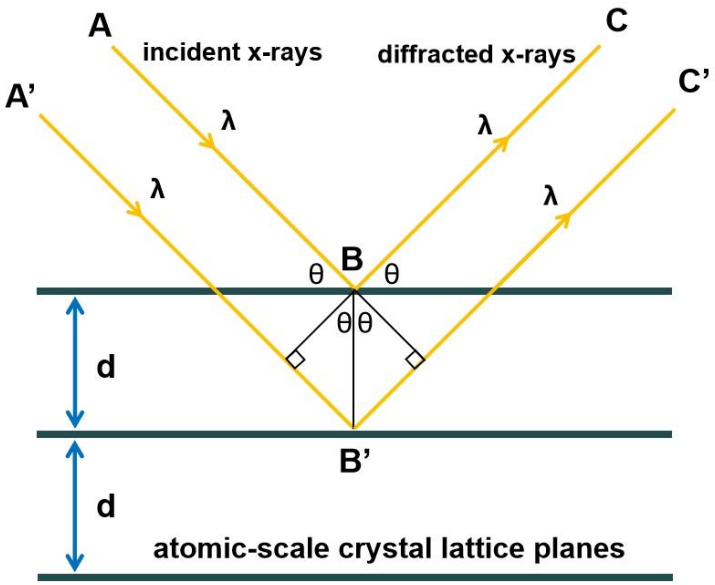

Figure A8. Bragg's Law of diffraction from reflection. The diffracted X-rays exhibit constructive interference when the distance between paths ABC and A'B'C' differs by an integer number of wavelengths (λ).

A.4.2 Porosimetry and BET surface area

Surface area and pore size determination with the Brunauer–Emmett–Teller (BET) method is a widely used characterization technique for micro- and meso-porous materials. The BET theory is correlated to the adsorption of a gas on the surface of the adsorbent material whereas the amount of the adsorbed gas on the surface of the material is associated with the surface area. BET theory is an extension of the Langmuir theory. The Langmuir theory is based on the assumption that gas molecules form a monolayer adsorption which is an ideal situation. Whereas the BET theory is based on the assumption of a multilayer adsorption and all layers are in equilibrium (and do not interact with each other), thus the Langmuir equation is applicable for each layer. The BET equation is expressed as Eq. A1 [25-27]:

$$\frac{P/P_0}{\mathrm{n}(1-P/P_0)} = \frac{1}{n_m C} + \frac{C-1}{n_m C}(P/P_0) \qquad \text{(Eq. A1)}$$

In the above equation, P and P_0 are the equilibrium and saturation pressure of the adsorbates at the adsorption temperature, n is the specific amount of the adsorbates at the relative pressure P/P_0, n_m is the monolayer capacity (the amount of adsorbate required to occupy all adsorption sites on the solid surface) of the adsorbed gas, and C is the BET constant. The shape of an isotherm in the BET range is acquired from the parameter C.

A.4.3 Transmission electron microscopy (TEM)

Transmission electron microscopy (TEM) is one of the most common imaging techniques used for studying porous materials at atomic scale and has been widely applied for characterization of zeolite structures such as pore structures of hierachical micro- and meso-porous zeolites and analysis of metal sites in zeolites. The basic principles behind the TEM operation is the same as the light microscope except that the TEM uses electrons as excitation source instead of light. In principle, the maximum resolution, d, that can be achieved with a light microscope is limited by the wavelength of the photons (λ) that used to probe the sample and the numerical aperture NA of the system (Eq. A2).

$$\mathrm{d} = \frac{\lambda}{2n\sin\alpha} \approx \frac{\lambda}{2NA} \qquad \text{(Eq. A2)}$$

Where n is the index of refraction of the medium in which the lens is working and α is the maximum half-angle of the cone of light that can enter the lens.

Whereas this limitation can be overcome by using electrons and a higher resolution (0.1 nm) can be obtained due to the smaller de Broglie wavelength of electrons. It able to capture fine detail - even as small as a single column of atoms, which is thousands of times smaller than a resolvable object seen in a light microscope [28]. When a beam of electrons is transmitted through a very thin specimen (50 nm), part of the beam absorbed are scattered due to an interaction between specimen atoms and electrons of the illuminating beam. The electrons beam is then transmitted through objective aperture and projected by projector lens after corrected by intermediate lenses on the fluorescence screen. The spatial variation in the image is then magnified by a series of magnetic lenses and recorded to produce two-dimensional, black and white images [29].

A.4.4 X-ray photoelectron spectroscopy (XPS)

X-ray photoelectron spectroscopy (XPS) is one of the most widely used surface analysis techniques which provides both elemental and chemical state information. When a beam of X-rays illuminate the surface of a sample, the electrons in the surface can absorb the photon energy and be excited. In some cases, these electrons (known as photoelectrons) can escape the host material, as shown in figure A9.

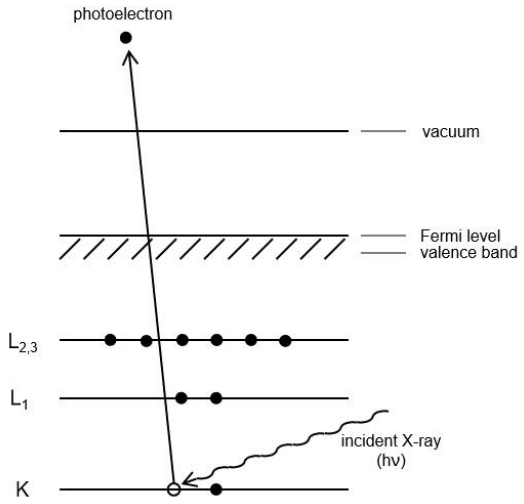

Figure A9. Schematic of the photoelectron emission process involved in XPS surface analysis [30]. An electron can be ejected when an atom or molecule absorbs an X-ray photon. The surface elements and chemical states can be identified by detecting the kinetic energy (E_k) of the emitted electrons.

The kinetic energy (E_K) of the ejected photoelectrons is related to the electron binding energy (E_b), as shown in the Einstein's photoelectric equation (Eq. A3 [31,32]), whereas E_b reflects the type and valence of the elements in the tested sample.

$$E_k = hv - E_b - \varphi \qquad \text{(Eq. A3)}$$

Where E_k is the kinetic energy of emitted electron; E_b is the binding energy of the emitted electron; h is Planck's constant; υ is the frequency of incident X-ray and φ is the work function of the spectrometer.

In this context, the technique can be used to [32]:

1) detect all elements except hydrogen and helium.

2) detect chemical bonding states.

3) give depth information in the nanometer region. The photoelectrons are easily scattered and absorbed by the atoms of the sample, whereas only the photoelectrons that originate from the top of the surface can escape from the material without either being scattered or absorbed by the sample. Thus the typical analysis depth of XPS is less than 10 nm.

A.4.5 Attenuated total reflectance - Fourier transform infrared (ATR-FTIR)

Attenuated total reflectance–Fourier transform infrared (ATR–FTIR) spectroscopy is a versatile tool for measuring infrared spectra of solids and liquids. ATR–FTIR requires a sample to be placed onto an internal reflection element (IRE), as shown in figure A10. The IR beam from the spectrometer is directed onto the element at an angle, θ, greater than the critical angle, θ_c, so that the infrared light undergoes internal reflection. At each point of internal reflection an evanescent wave is produced, from which, the radiation can be absorbed by a sample that is placed in direct contact with the IRE [33,34]. As such, based on the infrared absorbance of a sample it is possible to determine both chemical and structural information of a sample.

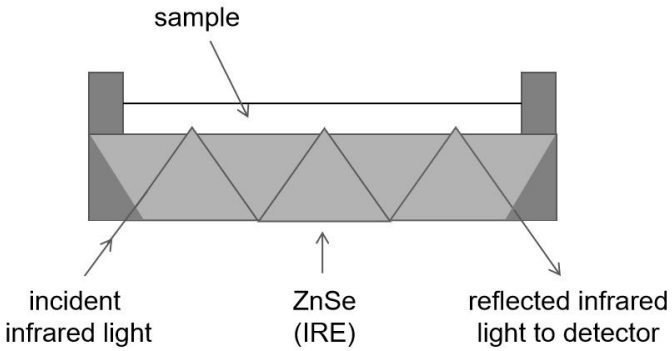

Figure A10. A pictorial representation of internal reflections through a high refractive index medium, for example, ZnSe, used as the internal reflection element (IRE) [33]

A.4.6 Inductively coupled plasma optical emission spectroscopy (ICP-OES)

ICP/OES is one of the most powerful and popular analytical tools for the determination of multiple elements in a variety of (liquid and solid) sample matrices, whereas the solid sample requires a digestion process (by HF acid to digest zeolite for example) to dissolve the analytes into a liquid solution.

Plasma, which is usually produced by an argon stream, is a highly energized and electrically neutral gas composed of ions, electrons, and neutral particles [35]. The ICP-OES technique uses a high-frequency inductively coupled plasma as the light source, while the principle of it involves the spontaneous emission of photons from atoms and ions that have been excited in a radiofrequency (RF) discharge. In principle, the sample solution is atomized and injected into a RF-induced argon plasma, the atomized sample reaching the plasma is then quickly dried, vaporized, and energized through collisional excitation at high temperature (over 6000 K [36]). The analyte atoms are promoted from the ground states to excited states under the collisional excitation within the plasma, whereas the atomic and ionic excited state species may then relax to the ground state via the emission of a photon. These photons have characteristic energies that are determined by the quantized energy level structure for the atoms or ions. Thus the wavelength of the emitted photons can be used for the qualitative analysis of the elements from which they originated, while the number of photons which is directly proportional to the concentration of the element in the sample is the basis of quantitative analysis [37].

A.5 Determination of H_2O_2 concentration

Two traditional methods, potassium permanganate titration [38] and iodometry titration [39], were used to determine the H_2O_2 concentration in the reaction mixture.

A.5.1 H_2O_2 determination by potassium permanganate titration

The determination of the concentration of H_2O_2 in the effluents by potassium permanganate titration involves the standardization of $KMnO_4$ and titration of H_2O_2:

1) Standardization of $KMnO_4$ concentration:

$$5\ C_2O_4^{2-} + 2\ MnO_4^{-} + 16\ H^{+} = 2\ Mn^{2+} + 8\ H_2O + 10\ CO_2 \quad \text{(Eq.A4)}$$

The process is used to detect the accurate concentration of the titrant ($KMnO_4$). the procedure is described as follows:

a) Prepare $KMnO_4$ (0.02 M), $Na_2C_2O_4$ (0.01 M) and H_2SO_4 (3 M) solution, respectively. Store $KMnO_4$ solution in brown bottle or in dark place to avoid its decomposition under the effects of Mn^{2+} and/or MnO_2 under sunlight.

b) Pipette 20 mL $Na_2C_2O_4$ (0.01 M) solution into a 250 mL flask, and add 5 mL H_2SO_4 (3 M) solution into the flask as well. Keep the temperature of the mixture at 75-85 ^oC for 10 min.

c) Titrate the sample mixture with prepared $KMnO_4$ solution (0.02 M) with a slow speed at the beginning to make sure the formation of Mn^{2+}, which act both as product in the reaction and as catalyst to further accelerate the reaction.

d) Continue to titrate with $KMnO_4$ solution (0.02 M) till a pale red colour is observed and the color doesn't fade within 30 seconds, which indicates the end of the titration.

e) Recorded the volume of $KMnO_4$ solution, then calculate the concentration of $KMnO_4$ (C_{KMnO4}) by the following formula:

$$C_{KMnO_4} = \frac{2}{5} \times \frac{C_{Na_2C_2O_4} \cdot V_{Na_2C_2O_4}}{V_1} = \frac{0.08}{V_1} \qquad \text{(Eq.A5)}$$

Where $C_{Na2C2O4}$ (mol·L^{-1}) and $V_{Na2C2O4}$ (mL) represent the concentration and the volume of $Na_2C_2O_4$ solution, while V_1 is the volume of $KMnO_4$ solution (mL).

2) Titration of H_2O_2 concentration:

$$5\ H_2O_2 + 2\ MnO_4^- + 6\ H^+ = 2\ Mn^{2+} + 8\ H_2O + 5\ O_2 \quad \text{(Eq.A6)}$$

The concentration of H_2O_2 was determined with $KMnO_4$ (accurate concentration C_{KMnO4} confirmed by standardization) as titrant. The process is as follows:

a) Dilute 5 mL of the reaction mixture into 100 mL with deionized water (dilution ratio of 20).

b) Pipette 20 mL of diluted sample solution into a 250 mL flask and add 5 mL H_2SO_4 (3 M).

c) Titrate the sample mixture with $KMnO_4$ solution (with concentration of C_{KMnO4}) under room temperature till a pale red solution is observed and the color doesn't fade in 30 seconds, which indicates the end of the titration.

d) Record the volume of $KMnO_4$ solution, then calculate the concentration of H_2O_2 following the formula:

$$C_{H_2O_2} = \frac{5}{2} \times \frac{C_{KMnO_4} \times V_2}{V_{H_2O_2}} \times D_1 = \frac{C_{KMnO_4} \times V_2}{8} \quad \text{(Eq.A7)}$$

Where C_{KMnO4} (mol·L^{-1}) and V_2 (mL) represent the concentration and the volume of $KMnO_4$ solution, while V_{H2O2} (mL) and D_1 (=20) are volume and the dilution ratio of H_2O_2 solution (or reaction mixture), respectively.

A.5.2 H_2O_2 determination by iodometry titration

The determination of the concentration of H_2O_2 in the effluents by iodometry titration involves the standardization of $Na_2S_2O_3$ and titration of H_2O_2:

1) Standardization of $Na_2S_2O_3$ concentration:

$$Cr_2O_7^{2-} + 6\ I^- + 14\ H^+ = 2\ Cr^{3+} + 3\ I_2 + 7\ H_2O \qquad \text{(Eq.A8)}$$

$$2\ S_2O_3^{2-} + I_2 = S_4O_6^{2-} + 2\ I^- \qquad \text{(Eq.A9)}$$

The process is used to detect the accurate concentration of the titrant ($Na_2S_2O_3$). The procedure is as follows:

a) Prepare $Na_2S_2O_3$ (0.002 mol·L^{-1}), $K_2Cr_2O_7$ (0.001 mol·L^{-1}), KI (100 g·L^{-1}), H_2SO_4 (10%, m/m) and starch (10 g·L^{-1}) solution, respectively.

b) Pipette 2 mL of $K_2Cr_2O_7$ (0.001 mol·L^{-1}) solution into the iodine flask, then add 3 mL KI (100 g·L^{-1}) and 1 mL H_2SO_4 (10%, m/m), respectively. Keep the flask in the dark for 10 min [40] to obtain a yellow solution due to the formation of I_2.

c) Titrate the solution with $Na_2S_2O_3$ (0.002 mol·L^{-1}) to reduce the I_2 till the solution becomes pale yellow.

d) Add 1 mL starch (10 g·L^{-1}) solution as indicator and a blue solution is observed. Added more $Na_2S_2O_3$ solution until the colour changed into colourless.

e) Keep titration until the solution becomes colourless, and the colorless solution maintains for half minutes to indicate the end of the titration.

f) Record the volume (V_3) of $Na_2S_2O_3$ solution that consumed in the titration, then calculate the concentration of $Na_2S_2O_3$ following the formula:

$$C_{Na_2S_2O_3} = \frac{6 \times C_{K_2Cr_2O_7} \times V_{K_2Cr_2O_7}}{V_3} = \frac{0.012}{V_3} \qquad \text{(Eq.A10)}$$

Where $C_{K2Cr2O7}$ (mol·L^{-1}) and $V_{K2Cr2O7}$ (mL) represent the concentration and the volume of $K_2Cr_2O_7$ solution, while V_3 is the volume of $Na_2S_2O_3$ solution (mL).

2) Determination of H_2O_2 concentration:

$$H_2O_2 + 2\ I^- + 2\ H^+ = I_2 + 2\ H_2O \qquad \text{(Eq.A11)}$$

$$I_2 + 2\ S_2O_3^{2-} = S_4O_6^{2-} + 2\ I^- \qquad \text{(Eq.A12)}$$

The concentration of H_2O_2 was determined with $Na_2S_2O_3$ (concentration calibrated by $K_2Cr_2O_7$) as titrant. The process is as follows:

a) Dilute 0.25 mL of the reaction mixture into 25 mL with deionized water (dilution

ratio of 100).

b) Pipette 5 mL of diluted reaction mixture into the iodine flask, then add 3 mL KI (100 $g \cdot L^{-1}$) and 1 mL H_2SO_4 (10%, m/m). Keep the flask in a dark place for 10 min to allow the oxidation of I^- to I_2.

c) Titrate with $Na_2S_2O_3$ (0.002 $mol \cdot L^{-1}$) to reduce the I_2 back to I^- till the solution becomes pale yellow.

d) Add 1 mL starch (10 $g \cdot L^{-1}$) into the solution and the color of the solution changes from pale yellow to blue.

e) Keep titration till the blue colour disappear.

f) Record the volume (V_4) of $Na_2S_2O_3$ solution that consumed in the titration, then calculate the concentration of H_2O_2 following the formula:

$$C_{H_2O_2} = \frac{1}{2} \times \frac{C_{Na_2S_2O_3} \times V_4}{V_{H_2O_2}} \times D_2 = 10 \times C_{Na_2S_2O_3} \times V_4 \quad \text{(Eq.A13)}$$

Where $C_{Na2S2O3}$ ($mol \cdot L^{-1}$) and V_4 (mL) represent the concentration and the volume of $Na_2S_2O_3$ solution, while V_{H2O2} (mL) and D_2 (=100) are volume and the dilution ratio of H_2O_2 solution (or reaction mixture), respectively.

A.6 Determination of phenol and intermediates

The qualitative and quantitative analysis of the reaction mixture is a challenging task due to the similar properties amongst the tens of potential products during oxidation and the low concentration of some components (see section 3.2 in chapter 3). Hence several methods including UV-vis (in A.4.1), NMR (in A.4.2) and HPLC (in chapter 3) were tried to determine the phenol and intermediates in the reaction mixture.

A.6.1 Ultra-Violet and Visible spectrophotometry (UV-Vis)

All the measurements were carried out on a PerkinElmer Lambda 35 UV-Vis Spectrometer equipped with a 1 cm quartz cuvette. UV spectra were collected from

700 nm to 200 nm at a scan speed of 480 $nm \cdot min^{-1}$. Absorbance measurements for phenol, hydroquinone, *p*-benzoquinone, catechol and organic acids were carried out at a fixed wavelength of 270 nm, 288 nm, 280 nm, 275 nm, and 200 nm, respectively.

The concentration of the phenol (or intermediates) was calculated by the Beer-Lambert law, the principle behind absorbance spectroscopy. This law correlates absorbance and concentration of substances in a linear manner, which can be described using the following equation (Eq. A14):

$$A = \varepsilon bc \qquad \text{(Eq. A14)}$$

Where A is absorbance, ε is molar absorption coefficient, b is path length of the cuvette (1 cm), and c is the concentration of determined substance.

The UV spectra of phenol solutions with concentration of 10-50 $mg \cdot L^{-1}$ was shown in figure A11. Two main absorption bands of phenol solution were observed at the range of 200-700 nm, one is at 210 nm while the other is at 270 nm. The former results from π - π* transition owing to the conjugated double bonds of benzene ring while the latter one is caused by n - π* transition of hydroxyl OH and conjugated double bond of benzene ring.

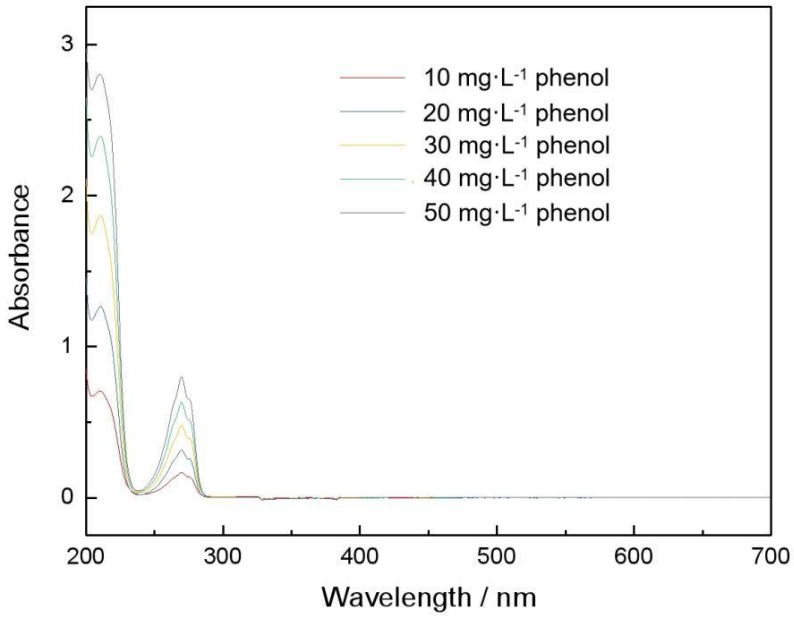

Figure A11. UV spectra of phenol solution in water with different concentrations (10-50 mg·L^{-1})

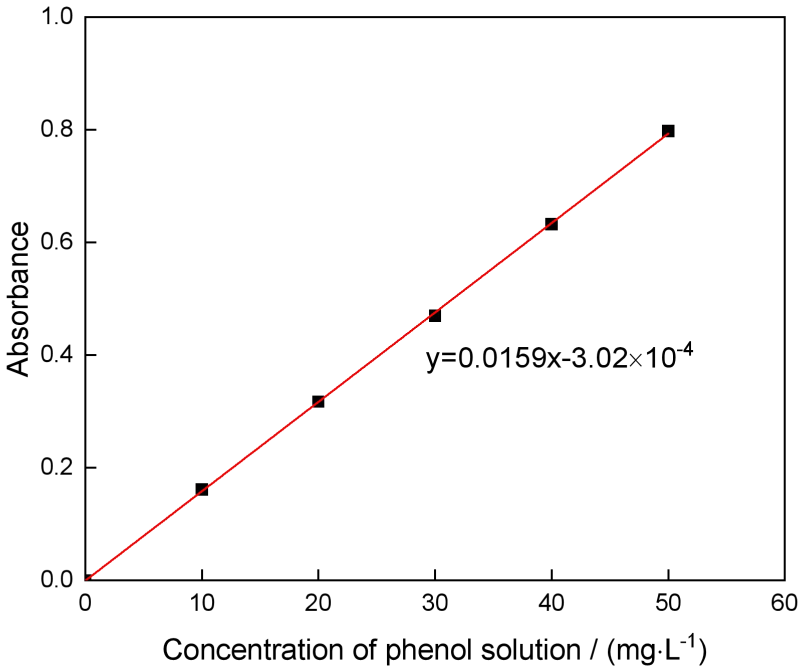

Figure A12. Calibration curve of phenol solution with concentration of 10-50 mg·L^{-1} determined by UV-vis (absorbance collected at 270 nm)

In general, the peak at maximum absorption wavelength of λ_{max} = 270 nm is regarded as the characteristic absorption peak of phenol. As displayed in figure A12, the absorbance at λ = 270 nm increased proportionally with the increase of phenol concentration, laying a foundation for quantitative analysis of phenol.

Other main aromatic intermediates, such as hydroquinone and *p*-benzoquinone, can also be determined by UV-Vis spectrophotometry. As observed in Figure A13, the spectra of hydroquinone and *p*-benzoquinone standard solution were determined with maximum absorption wavelength of 347 nm and 288 nm, respectively. However, the absorbance peaks of these substances overlapped and interfered with each other, making it hard to analyse the concentration of a certain substance in a mixture.

Though the concentration of phenol in the mixture can be calculated after Gaussian deconvolution analysis, this is nevertheless a reasonably complex fitting procedure, as many peaks are involved simultaneously and of different intensity, and the obtained concentration differed from its set value. As stated in Figure A14, the calculated phenol concentration was 26.8 $mg \cdot L^{-1}$ after Gaussian deconvolution while the actual concentration was 20 $mg \cdot L^{-1}$. In addition, organic acids such as acetic acid was not identified with this method. It is concluded that the use of a sole UV-Vis determination is a good method for rapid determination of pure phenol and aromatic intermediates solution but inappropriate for phenol and intermediates analysis in phenol CWPO process.

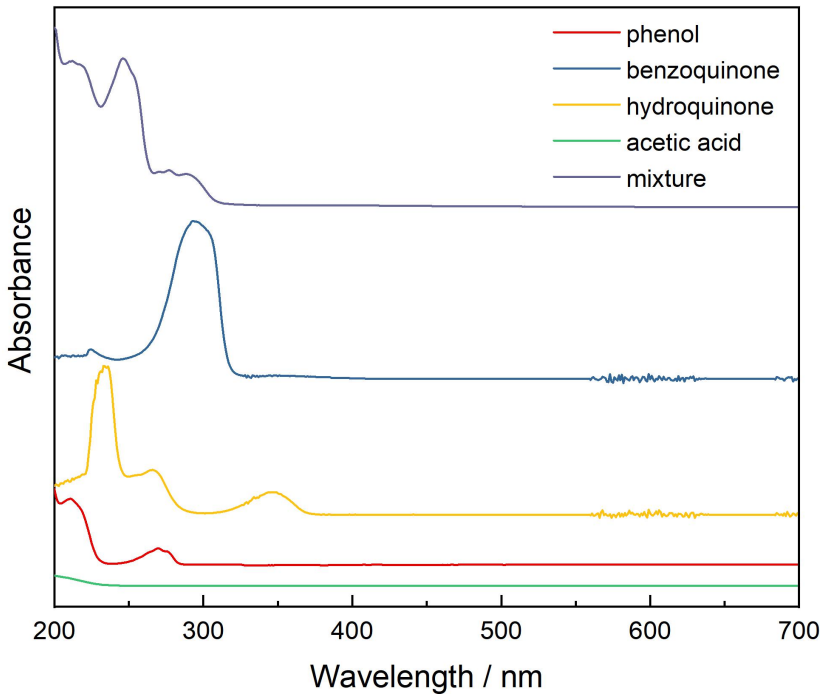

Figure A13. UV spectra of solution of phenol (20 mg·L^{-1}), *p*-benzoquinone (20 mg·L^{-1}), hydroquinone (20 mg·L^{-1}), acetic acid (100 mg·L^{-1}) and the mixture of the above solution

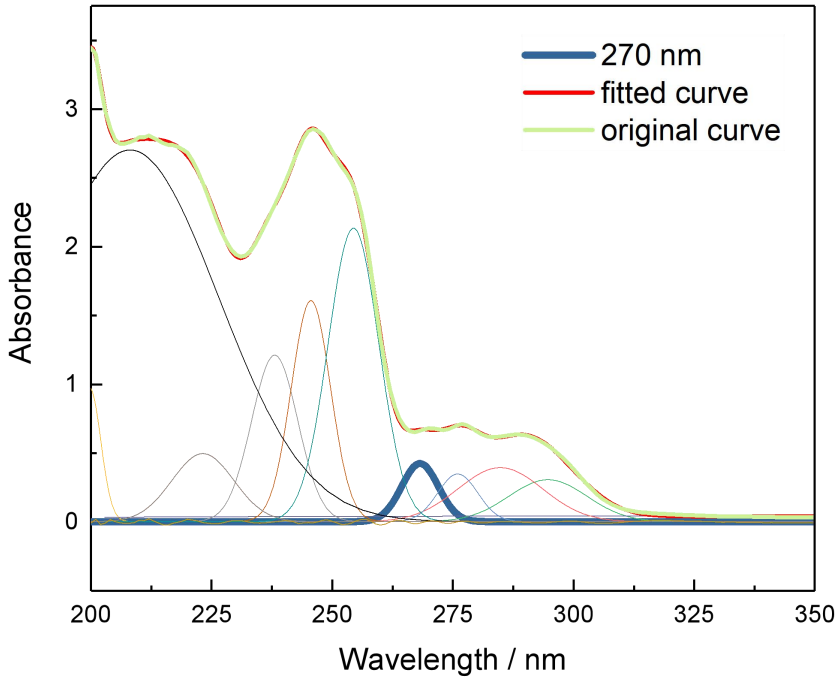

Figure A14. Gaussian deconvolution of UV spectrum of the mixture solution: phenol (20 m mg·L^{-1}), *p*-benzoquinone (20 mg·L^{-1}), hydroquinone (20 mg·L^{-1}) and acetic acid (100 mg·L^{-1})

A.6.2 Nuclear Magnetic Resonance (NMR)

^{1}H NMR spectra were collected using a Bruker Advance III 400 spectrometer fitted with a 5mm PABBO BB/19F-1H/D-GRD probe and a frequency of 400MHz. DMSO-d_6 and $CDCl_3$ was used as solvent in standard NMR tubes. All spectra were referenced to DMSO-d_6 present in DMSO-d_6 solvent (2.54 ppm), or referenced to $CDCl_3$ present in $CDCl_3$ solvent (7.26 ppm), as shown in Table A1.

Table A1. List of possible by-products and their peak shift in different solvent.

Products	Technique	Peak shift in DMSO (δ, ppm)	Peak shift in $CDCl_3$ (δ, ppm)
Phenol	^{1}H NMR	9.30, 7.16, 6.76, 6.75	7.24, 6.93, 6.84, 5.35
Hydroquinone	^{1}H NMR	8.59, 6.58	---
Resorcinol	^{1}H NMR	9.15, 6.30, 6.20, 6.21	---
Maleic acid	^{1}H NMR	11.0, 6.29	---
Fumaric acid	^{1}H NMR	13.0, 6.65	---
Malonic acid	^{1}H NMR	11.5, 3.26	---
Succinic acid	^{1}H NMR	12.2, 2.43	---
p-benzoquinone	^{1}H NMR	---	6.80
Formic acid	^{1}H NMR	---	11.0, 8.06
Acetic acid	^{1}H NMR	---	11.4, 2.10
Oxalic acid	^{13}C NMR	D_2O as solvent: peak shift 162	

Phenol and almost all the potential intermediates e.g. hydroquinone, *p*-benzoquinone, resorcinol, maleic acid, fumaric acid, oxalic acid, acetic acid, formic acid, malonic acid can be clearly identified and determined by this technique based on their peak shift. The qualitative and quantitative determination of phenol by NMR technique is used as example.

In order to quantify the concentration of phenol, an eligible internal standard substance, dichloromethane (Figure A15), was selected and added into phenol solution before analysis. This compound exhibited good capability as an internal standard substance.

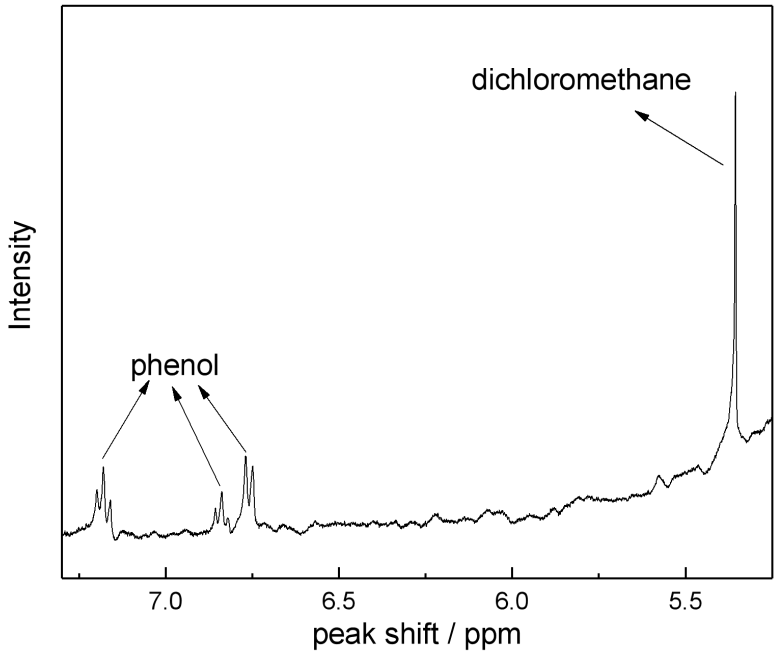

Figure A15. NMR spectrum of 1g·L^{-1} phenol solution with dichloromethane as internal standard

In addition, peak shift of phenol in DMSO at 7.16, 6.76, 6.75 ppm, are clearly observed, as exhibited in figure A16, which is the fundamental of qualitative analysis of phenol via NMR. However, ^{1}H NMR has a limit of detection (LOD), which in this experiment could only be used for the determination of phenol with concentration over 200 mg·L^{-1}, since the peaks of phenol in 150 mg·L^{-1} and 100 mg·L^{-1} solution were not detectable or not identifiable. It means that the ^{1}H NMR is only applicable for reaction mixtures with phenol conversion lower than 80% (the residual phenol concentration is 200 mg·L^{-1} then) when the initial phenol concentration in this project is 1 g·L^{-1} in the

CWPO procedure. Otherwise, an additional concentration step or extraction step is necessary to analyze the low phenol concentration. Furthermore, *p*-benzoquinone, acetic acid, and formic acid are detected in $CDCl_3$, which means the extraction of intermediates with an organic solvent is required because $CDCl_3$ is insoluble in water. The additional concentration/extraction step is time-consuming and causes waste and further contamination.

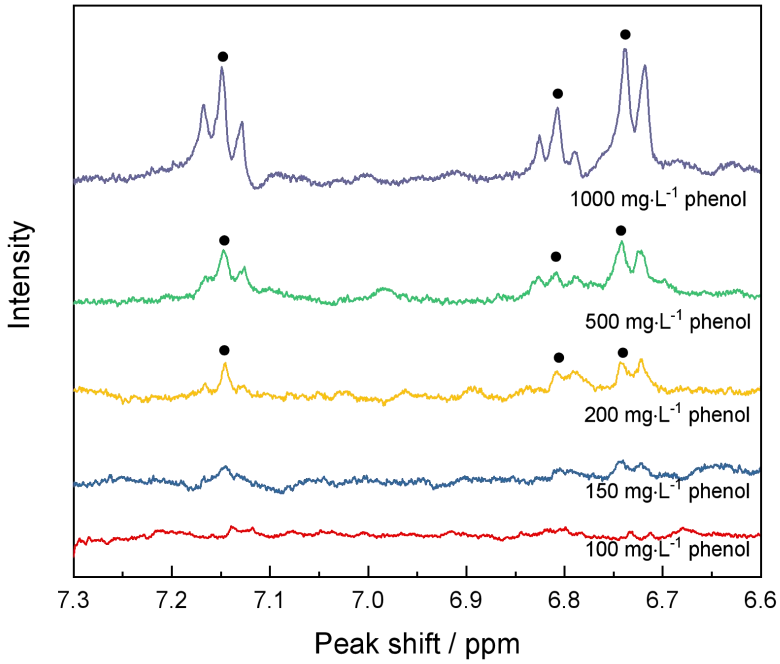

Figure A16. ^{1}H NMR spectra of phenol solutions with different concentrations in DMSO (peaks of phenol were marked by black dots)

Overall, ^{1}H NMR is an optional technique for phenol and intermediates analysis, however, the technique is limited by the relatively high detection limit and the complicated pre-analysis condition, which makes it impractical for large number of samples, like in the case of this research project.

A.6.3 High-performance liquid chromatography (HPLC)

The HPLC chromatograms of intermediates are shown in figure A17-A25 and their retention times are presented in table A2.

Table A2. Retention times of expected intermediates in standard solutions

Component	Retention time / min
Oxalic acid	2.6 ± 0.1
H_2O_2	--
Formic acid	3.1 ± 0.1
Malonic acid	3.8 ± 0.1
Acetic acid	4.4 ± 0.1
Maleic acid	5.1 ± 0.1
Fumaric acid	6.1 ± 0.1
hydroquinone	8.9 ± 0.2
p-benzoquinone	12.2 ± 0.1
Catechol	13.2 ± 0.1
phenol	16.0 ± 0.1

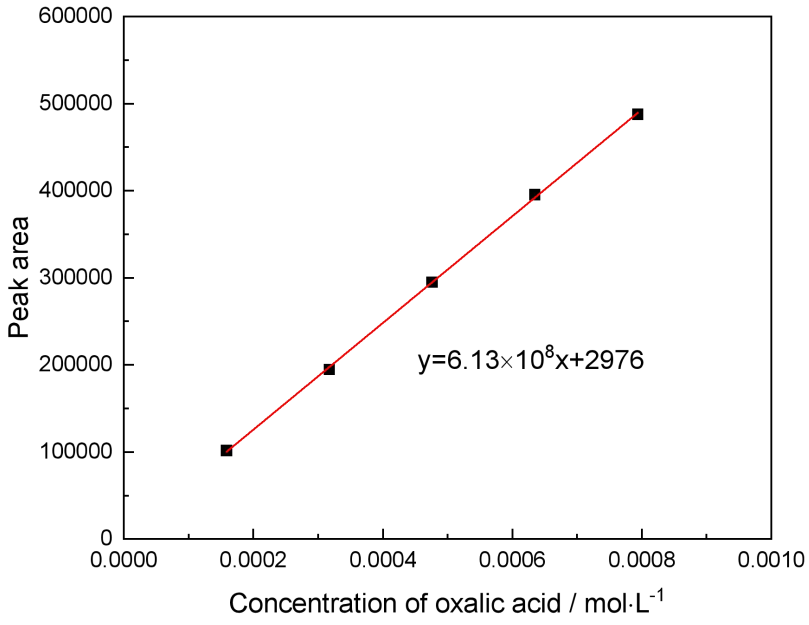

Figure A17. Calibration curve of oxalic acid solution with concentration ranging at 2.22×10^{-4} - 1.11×10^{-3} mol·L^{-1} (20 - 100 mg·L^{-1})

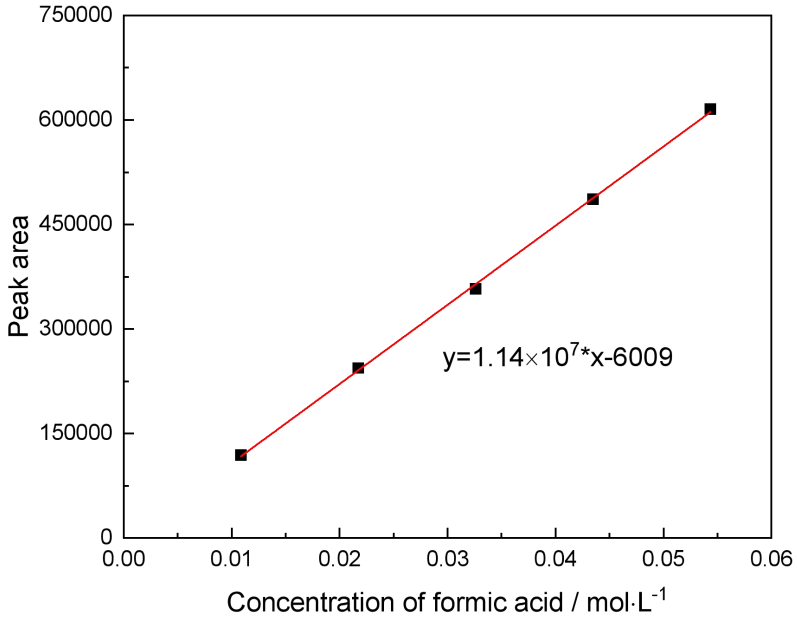

Figure A18. Calibration curve of formic acid solution with concentration ranging at 1.09×10^{-2} - 5.43×10^{-2} mol·L^{-1} (500 - 2500 mg·L^{-1})

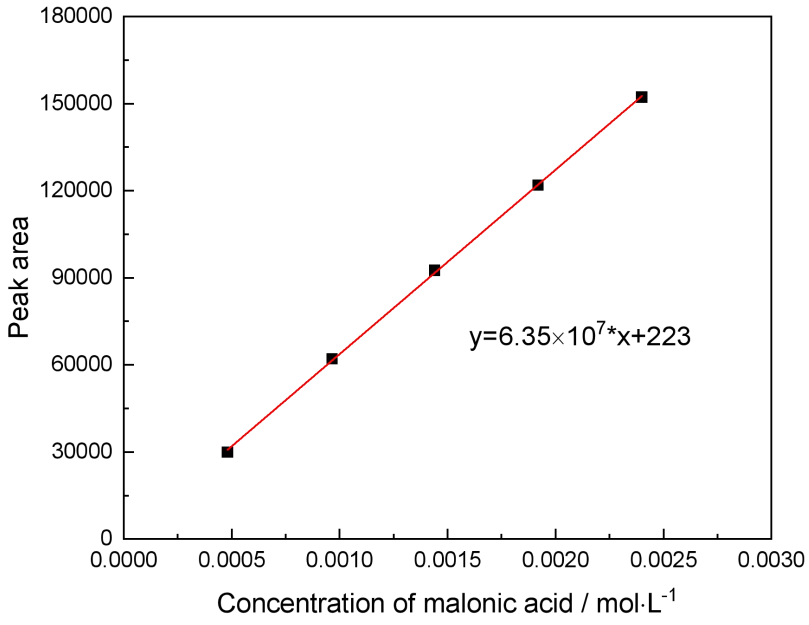

Figure A19. Calibration curve of malonic acid solution with concentration ranging at 4.81×10^{-4} - 2.40×10^{-3} mol·L^{-1} (50 - 250 mg·L^{-1})

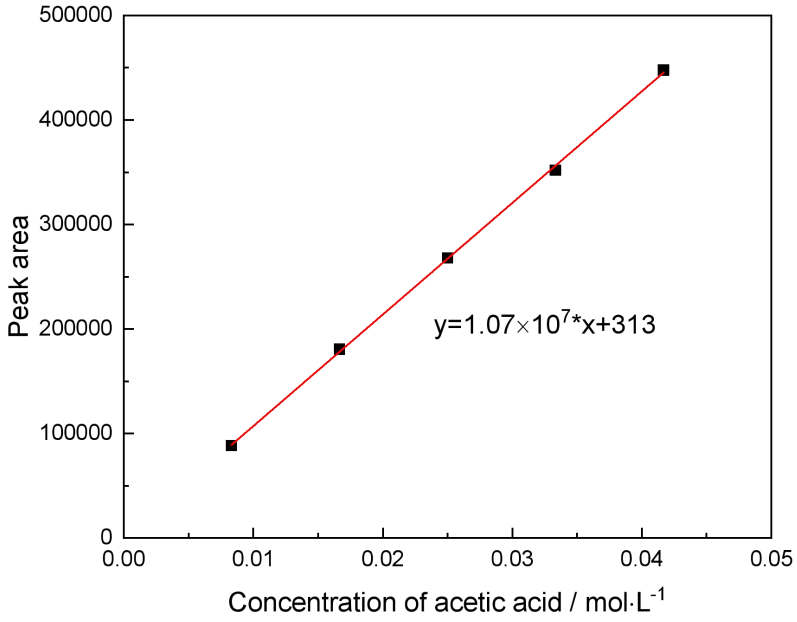

Figure A20. Calibration curve of acetic acid solution with concentration ranging at 8.33×10^{-3} - 4.17×10^{-2} mol·L^{-1} (500 - 2500 mg·L^{-1})

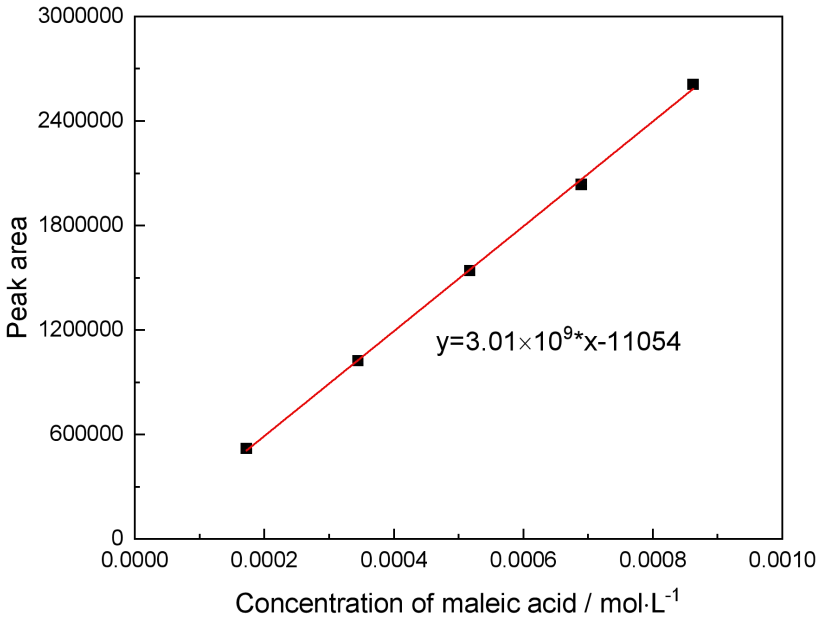

Figure A21. Calibration curve of maleic acid solution with concentration ranging at 1.72×10^{-4} - 8.62×10^{-4} mol·L^{-1} (20 - 100 mg·L^{-1})

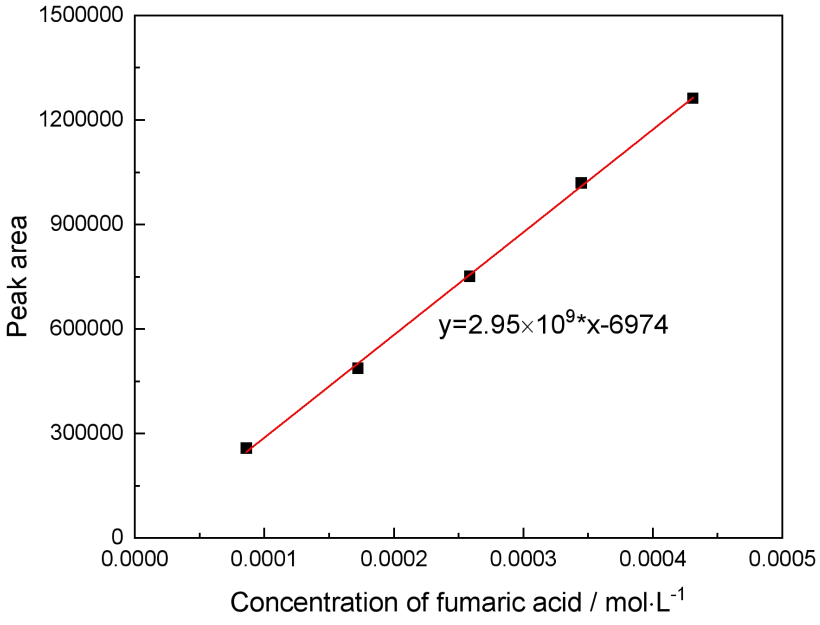

Figure A22. Calibration curve of fumaric acid solution with concentration ranging at 8.62×10^{-5} - 4.31×10^{-4} mol·L^{-1} (10 - 50 mg·L^{-1})

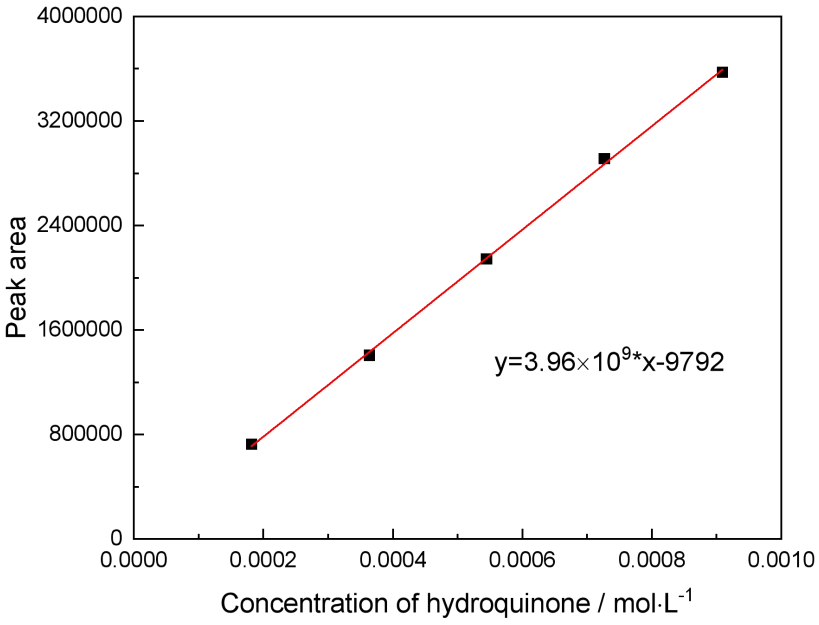

Figure A23. Calibration curve of hydroquinone solution with concentration ranging at 1.82×10^{-4} - 9.09×10^{-4} mol·L^{-1} (20 - 100 mg·L^{-1})

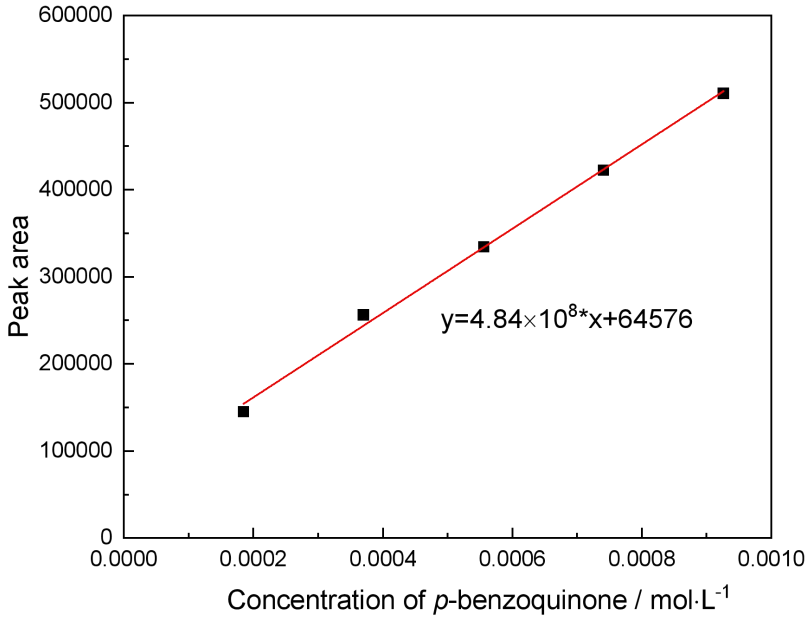

Figure A24. Calibration curve of *p*-benzoquinone solution with concentration ranging at 1.85×10^{-4} - 9.26×10^{-4} mol·L^{-1} (20 - 100 mg·L^{-1})

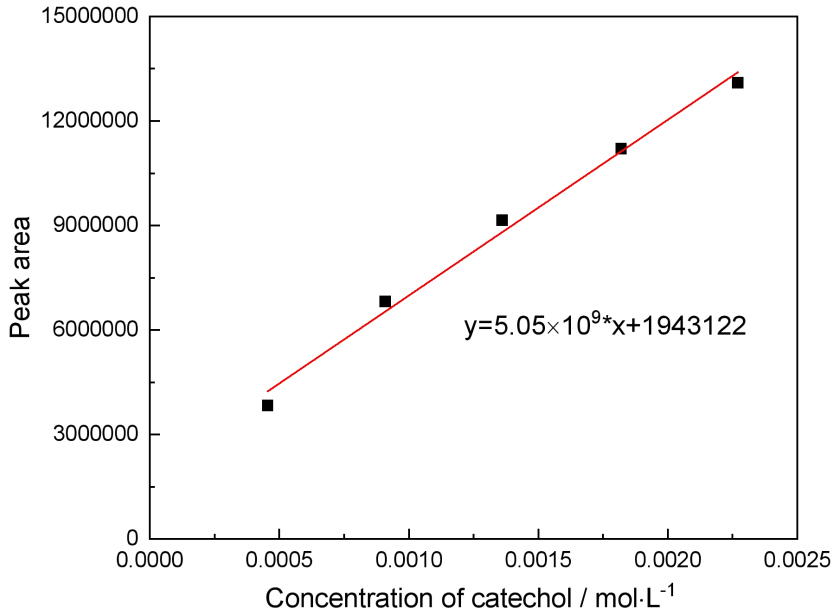

Figure A25. Calibration curve of catechol solution with concentration ranging at 4.55×10^{-4} - 2.27×10^{-3} mol·L^{-1} (50 - 250 mg·L^{-1})

A.7 HPLC chromatograms of reaction mixtures over different metal supported ZSM-5 catalysts

The HPLC chromatogram of the reaction mixtures using different metal supported ZSM-5 catalysts were shown in figure A26. As it can be seen, phenol was completely removed when using Cu- and Fe- supported ZSM-5 catalysts in the reaction, while it was observed when using other metal supported catalyst. Besides, most of acid intermediates (such as oxalic acid and malonic acid) were detected in the reaction mixtiures over Cu and Fe catalysts, which indicated the high activity of the two metal species in the decomposition of phenol and the high selectivity to acids. In comparison, aromatic compounds (such as hudroquinone and catechol) were detected in reaction mixtures using catalysts (Co-, Mn-, Ag-, Au- and Pd- supported ZSM-5) with lower activity, which suggested that phenol was decomposed to aromatic intermediates in these tests.

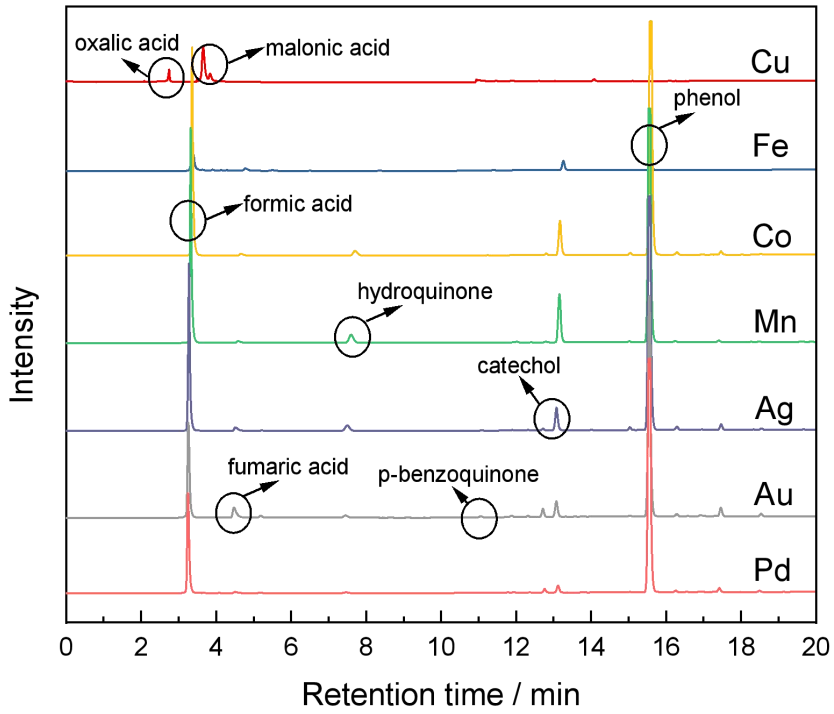

Figure A26. HPLC chromatogram sof reaction mixtures over Cu, Fe, Co, Mn, Ag, Au, Pd supported ZSM-5 catalysts after CWPO of phenol (50 mL of 1 g·L^{-1} phenol, M: S = 1:100, phenol: H_2O_2 = 1:14, P = endogenous, 80 °C, 4 h, 500 rpm)

A.8 References

[1]. D. Song and J. Li, *J Mol Catal A: -Chem*, 2006, **247**, 206-212.

[2]. J. Haber, J. H. Block and B. Delmon, *Pure Appl Chem*, 1995, **67**, 1257-1306.

[3]. N. Kosinov, C. Liu, E. J. M. Hensen and E. A. Pidko, *Chem Mater*, 2018, **30**, 3177-3198.

[4]. P. Yan, J. Mensah, A. Adesina, E. Kennedy and M. Stockenhuber, *Appl Catal B-Environ*, 2020, **267**, 118690.

[5]. A. R. Naghash, T. H. Etsell and S. Xu, *Chem Mater*, 2006, **18**, 2480-2488.

[6]. C. Louis, *CATALYST PREPARATION*, 2007, 319.

[7]. W. Li, M. Comotti and F. Schüth, *J Catal*, 2006, **237**, 190-196.

[8]. Z. Huang, F. Cui, J. Xue, J. Zuo, J. Chen and C. Xia, *Catal Today*, 2012, **183**, 42-51.

[9]. W. J. Shen, Y. Ichihashi, M. Okumura and Y. Matsumura, *Catal Lett*, 2000, **64**, 23-25.

[10]. A. Gurbani, J. L. Ayastuy, M. P. González-Marcos, J. E. Herrero, J. M. Guil and M. A. Gutiérrez-Ortiz, *Int J Hydrogen Energ*, 2009, **34**, 547-553.

[11]. V. K. Kaushik, C. Sivaraj and P. K. Rao, *Appl Surf Sci*, 1991, **51**, 27-33.

[12]. Z. Wang, D. Brouri, S. Casale, L. Delannoy and C. Louis, *J Catal*, 2016, **340**, 95-106.

[13]. S. S. R. Putluru, L. Schill, A. D. Jensen, B. Siret, F. Tabaries and R. Fehrmann, *Appl Catal B-Environ*, 2015, **165**, 628-635.

[14]. Q. Xin, A. Papavasiliou, N. Boukos, A. Glisenti, J. P. H. Li, Y. Yang, C. J. Philippopoulos, E. Poulakis, F. K. Katsaros, V. Meynen and P. Cool, *Appl Catal B-Environ* 2018, **223**, 103-115.

[15]. K. P. de Jong, *Synthesis of solid catalysts*, 2009, 111-134.

[16]. H. Huang, X. Ye, H. Huang, L. Zhang and D. Y. C. Leung, *Chem Eng J*, 2013, **230**, 73-79.

[17]. B. A. T. Mehrabadi, S. Eskandari, U. Khan, R. D. White and J. R. Regalbuto, in *Advances in Catalysis*, ed. C. Song, Academic Press, 2017, pp. 1-35.

[18]. P. Burattin, M. Che and C. Louis, *J Phys Chem B*, 1997, **101**, 7060-7074.

[19]. S. Chytil, W. R. Glomm, I. Kvande, T. Zhao, J. C. Walmsley and E. A. Blekkan, *Top Catal*, 2007, **45**, 93-99.

[20]. J. A. Schwarz, C. Contescu and A. Contescu, *Chem Rev*, 1995, **95**, 477-510.

[21]. M. Campanati, G. Fornasari and A. Vaccari, *Catal Today*, 2003, **77**, 299-314.

[22]. P. Cañizares, A. de Lucas, F. Dorado, A. Durán and I. Asencio, *Appl Catal A- Gen*, 1998, **169**, 137-150.

[23]. N. Hikichi, K. Iyoki, Y. Naraki, Y. Yanaba, K. Ohara, T. Okubo and T. Wakihara, *Micropor Mesopor Mat*, 2019, **284**, 82-89.

[24]. H. Chen, C. Song and W. Yang, *Micropor Mesopor Mat*, 2007, **102**, 249-257.

[25]. F. Ambroz, T. J. Macdonald, V. Martis and I. P. Parkin, *Small Methods*, 2018, **2**, 1800173.

[26]. K. E. Hart, L. J. Abbott and C. M. Colina, *Mol Simulat*, 2013, **39**, 397-404.

[27]. D. D. Do, H. D. Do and D. Nicholson, *Chem Eng Sci*, 2010, **65**, 3331-3340.

[28]. W. Wan, J. Su, X. D. Zou and T. Willhammar, *Inorg Chem Front*, 2018, **5**, 2836-2855.

[29]. M. Kannan, *A Textbook on Fundamentals and Applications of Nanotechnology*, 2018, 93-102.

[30]. J. F. Watts, *Surface science techniques*, 1994, **45**, 5.

[31]. J. Chastain and R. C. King Jr, *Perkin-Elmer Corporation*, 1992, **40**, 221.

[32]. J. D. Andrade, in *Surface and interfacial aspects of biomedical polymers*, Springer, 1985, 105-195.

[33]. J. D. Schuttlefield and V. H. Grassian, *J Chem Educ*, 2008, **85**, 279.

[34]. H. Kaur, B. Rana, D. Tomar, S. Kaur and K. C. Jena, *Modern Techniques of Spectroscopy: Basics, Instrumentation, and Applications*, 2021, **13**, 3.

[35]. C. G. Novaes, M. A. Bezerra, E. G. P. Da Silva, A. M. P. Dos Santos, I. L. Da Silva Romao and J. H. S. Neto, *Microchem J*, 2016, **128**, 331-346.

[36]. J. A. Broekaert, *Analytical atomic spectrometry with flames and plasmas*, John Wiley & Sons, 2006.

[37]. X. Hou and B. T. Jones, *Encyclopedia of analytical chemistry*, 2000, **11**, 9468-9485.

[38]. N. V. Klassen, D. Marchington and H. C. McGowan, *Anal Chem*, 1994, **66**, 2921-2925.

[39]. R. J. Kieber and G. R. Helz, *Anal Chem*, 1986, **58**, 2312-2315.

[40]. Y. Pan, H. Xie, X. Tan, L. Liu and C. F. Zheng, *Physical Testing and Chemical Analysis Part B Chemical Analysis*, 2003, **39**, 404-405.